Aluminum Content Tunability of Structural and Optical Properties in Wide-Gap Semiconducting $(Al_xGa_{1-x})_2O_3$

Benjamin W. Krueger

A dissertation
submitted in partial fulfillment of the
requirements for the degree of

Doctor of Philosophy

University of Washington

2015

Reading Committee:

Marjorie A. Olmstead, Chair

Fumio S. Ohuchi

Scott T. Dunham

Program Authorized to Offer Degree:
Physics

University of Washington

Abstract

Aluminum Content Tunability of Structural and Optical Properties in Wide-Gap Semiconducting $(Al_xGa_{1-x})_2O_3$

Benjamin W. Krueger

Chair of the Supervisory Committee:
Professor Marjorie A. Olmstead
Physics

$(Al_xGa_{1-x})_2O_3$ alloys have attracted renewed interest due to their potential for use in deep-ultraviolet optical devices and high-powered transistors, but realization of these technologies depends on the ability to tune the band gap (E_g) and crystal phase of alloy films for specific applications. In this work, fundamental relationships between structural and optical properties of $(Al_xGa_{1-x})_2O_3$ were explored in a series of experiments on single-phase sintered powders produced by solution combustion synthesis, and continuous-composition-spread (CCS) thin films deposited at room temperature on silicon and sapphire by pulsed-laser deposition and post-annealed to successively higher temperatures in air, to see how crystallinity develops with alloy composition and measure the corresponding change in band gap. As the annealing temperature is raised (to a maximum of 1000 °C), amorphous $(Al_xGa_{1-x})_2O_3$ films transition first to the metastable γ phase, and then to the β phase, for alloy compositions in the range $0.1 < x < 1$ with the specific (am.) $\rightarrow \gamma$ and $\gamma \rightarrow \beta$ transition temperatures increasing steadily with Al content. A different phase was identified in the Ga-rich region ($0 < x < 0.1$) after annealing to 400–800 °C, tentatively assigned to a κ/γ mix; at higher temperatures these films also relax to the β phase. A maximum solubility limit of $x = 0.8$ was found for Al in the monoclinic $\beta - (Al_xGa_{1-x})_2O_3$ structure after sintering at 1600 °C for 12 hours, followed by a transition to corundum $\alpha - Al_2O_3$ above $x > 0.8$. Within each phase the band gap increases steadily with Al concentration, with greater bowing in the amorphous films than crystalline films, and linear variation with no bowing in 1600 °C sintered powders. No discontinuity

in the band gap was observed through the $\beta \rightarrow \gamma$ transition, but a 0.1–0.2 eV jump to lower E_g occurs when films become amorphous.

$(Al_xGa_{1-x})_2O_3$ films were also grown on silicon and sapphire at elevated temperature, with and without a Ga_2O_3 buffer layer, to determine limits on epitaxy with these two substrates and to see if films grown at high temperature exhibit similar properties as post-annealed films grown at room temperature. Epitaxial $(Al_xGa_{1-x})_2O_3$ CCS films on sapphire are initially $(\bar{2}01)$-oriented on the Ga-rich side, with an in-plane epitaxial relationship $[201]_{Ga_2O_3} \parallel [\bar{2}10]_{sapphire}$ and six-fold rotational symmetry. Films with thickness greater than 100 nm start to lose their orientation by twinning on the (101) plane, parallel to one of the faces of the distorted oxygen fcc sublattice, with the twinned regions growing faster than $[\bar{2}01]$-oriented regions as the thickness increases further. As the Al concentration is increased, films on sapphire immediately begin to lose crystallinity, due to a relatively low growth temperature of 500–600 °C, but a Ga_2O_3 buffer layer extends the solubility limit to $x \approx 0.15$. $(Al_xGa_{1-x})_2O_3$ films on silicon are initially unoriented on the Ga-rich side due to the oxidization of the Si surface (SiOx), but develop a spontaneous [400]/[002] orientation as the Al content is raised above $x > 0.1$, which grows stronger with film thickness. Above $x = 0.35$ a transition to the γ phase occurs, which is extended to $x = 0.4$ by the presence of a Ga_2O_3 buffer layer. The higher solubility of Al in CCS films on SiOx than sapphire is attributed to a higher substrate temperature of 800 °C during growth, and is consistent with the solubility limit of post-annealed room-temperature-deposited films at the same temperature.

TABLE OF CONTENTS

Page

LIST OF FIGURES

ACKNOWLEDGMENTS

This author would like to thank the National Science Foundation for financial support (grant nos: DMR 1104628, OISE 1209856). Part of this work was conducted at the UW Molecular Analysis Facility, which is supported in part by funds from the Molecular Engineering & Sciences Institute, the Clean Energy Institute, the National Science Foundation and the National Institutes of Health.

I would also like to express my sincerest gratitude to my advisor Marjorie Olmstead for her unwavering support and her enthusiasm for teaching. She has taught me how to ask the right questions, design experiments (and sometimes new equipment) to find the answers, extract new and interesting physics from imperfect data, and generally think like a physicist. In my opinion she is one of the most brilliant scientists at UW, and it was a special privilege to be her only current student.

I also owe a huge thanks to my "second advisor" and faculty mentor Fumio Ohuchi, for his never-ending creativity and ability to generate new ideas, his ability to challenge me on the most important aspects of my research, and his different perspective as an engineer, focusing not just on the fundamental science but also on why it's useful—helping me see the whole forest, not just the trees.

Thanks also goes to Prof. Scott Dunham for agreeing to read the first draft of my thesis, for teaching me about modeling physical systems and density functional theory (DFT), and for collaborating (with his student Evan Nelson) to perform DFT simulations on $\beta - (Al_xGa_{1-x})_2O_3$ to compare with my data on single-phase powders.

Thanks also to the other (current and former) graduate students in our lab, including Sam Zheng, Hien Pham, Chris Dandeneau, Bo Zhao, YiHsun Yang, and Jessica Tjalsma. It was a great pleasure to work with each of you, and I am fortunate to count you all as friends in addition to colleagues. Chris—I am really going to miss our long conversations at Schultzy's and Flowers. We will have to do it again whenever we are both in town.

To Ryan Abe, thank you so much for your unconditional love and support even through the most stressful of times. You have been beyond patient, waiting for me as I spent years in school studying an esoteric topic. Now the wait is over, and the next phase of our life together can begin, and I am so excited to see what the future holds. I could not have done it without your help.

Finally, thank you to my parents, who taught me to be ambitious, always do my best, believe in myself, and never give up. There were times when those words were much easier said than done, and none of us knew at the start how long it would take to finish, or difficult it would be. However, I always knew I could count on your encouragement and support whenever I needed someone to talk to, and I always felt re-energized to tackle challenging problems when returning to Seattle after spending time at home.

Chapter 1

INTRODUCTION

1.1 Why Aluminum Gallium Oxide?

Gallium oxide is a member of a commercially important class of materials known as transparent conducting oxides (TCOs), a group that also includes zinc oxide, tin oxide, indium oxide, cadmium oxide, and others [1]. In these materials, a distinct band structure featuring wide energy gaps (greater than 3 eV) between the valence band and first and second conduction bands prevents the absorption of visible light by direct interband transitions even when electrons occupy the lowest-lying conduction band, allowing for strong n-type conductivity while remaining 80 % transparent or better in the visible range (approximately 390–700 nm). In contrast to other types of semiconductors, which mainly belong to the zinc-blende and wurtzite systems, TCOs come in a wide variety of crystal structures and with a large number of possible elemental constituents, leading to a great deal of flexibility in their chemical, optical, electronic and magnetic properties [2]. A further advantage is their chemical stability in air at elevated temperatures, where other materials tend to oxidize and suffer degraded performance [3]. Amorphous oxides tend to have superior transport properties compared to other amorphous semiconductors as well, because their conduction "bands" are generally made up of extended s-orbitals of metal cations whose spatial overlap is less affected by disorder than directional sp^3 or p-type orbitals in other semiconductors [2, 4, 5]. However, valence bands of TCOs are primarily composed of oxygen $2p$ orbitals with small overlaps, leading to large effective masses and low mobilities for holes; overcoming this problem to realize p-type conductivity in oxides is notoriously difficult and remains an active area of research. So far, the best examples of p-type oxides belong to the delafossite family $CuMO_2$ (M = Al, Ga, In, Y, Sc, La, etc.), taking advantage of hybridization between O $2p$ and Cu $3d$ orbitals at the top of the valence band [4–6]. However the mobility is still low, and active technologies based on homogeneous oxide p-n junctions such as bipolar transistors, LEDs and lasers are uncompetitive when compared with equivalent GaN and SiC devices [7]. Therefore transparent oxide electronics remain limited to passive technologies

for now, such as transparent top contacts, electromagnetic shielding, functional glass coatings, and photodetectors [8].

The most widely-used TCO in modern technology is indium tin oxide or ITO, typically containing Sn in quantities of 1–10 cat. %. Of all the TCOs available, crystalline ITO has the lowest resisitivity (1–3 $\times 10^{-4}\,\Omega\,\mathrm{cm}$), although amorphous ITO performs nearly as well and offers practical manufacturing advantages [9]. Sputtered ITO films are often used as transparent top electrodes in flat panels and touchscreen displays, and in solar cells, for example [8]. Due to the relative scarcity of indium, zinc oxide doped with Al or Ga (AZO or GZO, respectively), having a slightly smaller band gap and higher resistivity than ITO, is increasingly being used instead for the same purposes [10]. However, both of these materials become opaque in the ultraviolet: ZnO at wavelengths shorter than 360 nm, and ITO at wavelengths shorter than 310 nm. In contrast, Ga_2O_3 has the largest band gap of the TCOs at 4.8 eV, and therefore remains transparent to wavelengths down to 260 nm [11, 12]. Its conductivity can be controlled through orders of magnitude by doping with Si [13] or Sn [14, 15]. Furthermore, alloying with aluminum offers the ability to extend the transparent range to 200 nm and below, making $(Al_xGa_{1-x})_2O_3$ an attractive material for deep-UV optical applications.

A great deal of research demonstrating the usefulness of Ga_2O_3 single crystals and thin films has already taken place. N-type conductive Ga_2O_3 thin films fabricated with Sn [16, 17] or Si [18, 19] impurities can be used as UV-transparent electrodes, e.g. to increase the useful wavelength range of solar cells [20]. Solar-blind UV photodetectors and/or flame detectors based on Ga_2O_3 single crystals [21, 22], thin films [23–25], and nanowires [26, 27] have been demonstrated. Good lattice matching means Ga_2O_3 single crystals can serve as transparent conducting substrates for devices based on GaAs [28], ZnO, [28] or GaN [29]; in the latter case the remaining mismatch can be eliminated by surface nitridation prior to GaN deposition [30, 31]. A low interface state density with GaAs means Ga_2O_3 can be used to effectively passivate GaAs surfaces [32], and a refractive index close to $\sqrt{n_{\mathrm{GaAs}}}$ opens the possibility of single-layer Ga_2O_3 anti-reflective coatings for GaAs [33]. Ga_2O_3 may be used as a host for a variety of transition metal or rare-earth phosphors [34]. The combination of a large band gap and ability to control the conductivity by doping also finds application to the development in high-power metal-semiconductor field-effect transistors (MESFETs) [35, 36] and metal-oxide-semiconductor field-effect transistors (MOSFETs) [37, 38], with a breakdown field more than three times larger than competing GaN or SiC devices and stable operation up to 250 °C

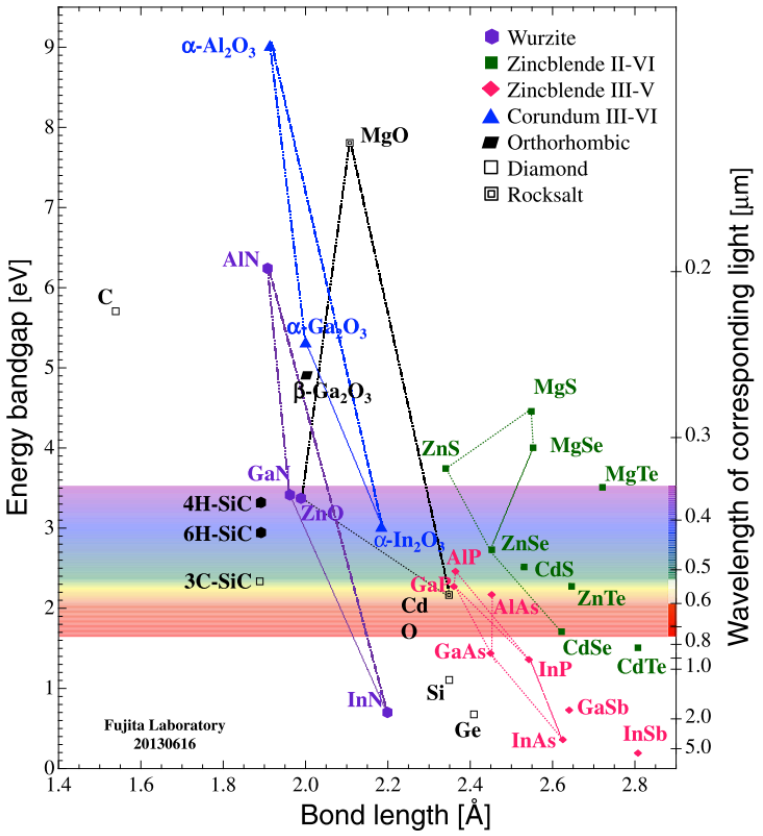

Figure 1.1: Overview of band gaps and bond lengths for several alloy systems including $(Al_xGa_{1-x})_2O_3$. Markers indicate the crystal structure, and lines connect endpoints belonging to a particular system. SiC, C (diamond), Si, and Ge are also shown for comparison. From Fujita [7].

[37]. A dramatic conductivity change upon heating of amorphous Ga_2O_3 [39], and bipolar resistive switching behavior in Pt/GaOx/ITO stacks [40] show potential for its use as a non-volatile memory element. In addition to its various electrical and optical properties, the chemistry of Ga_2O_3 may be exploited to fabricate oxygen [41] and reducing [42] gas sensors, as a photocatalyst to break down volatile aromatic pollutants in air [43], or as a photoelectrode for water splitting [44].

Much in the same way that varying Al content allows for continuous band gap tunability of $Al_xGa_{1-x}As$ alloys within the visible range ($1.4\,\text{eV} < E_g < 2.2\,\text{eV}$), and of $Al_xGa_{1-x}N$ alloys in the ultraviolet range ($3.4\,\text{eV} < E_g < 6.2\,\text{eV}$), band gap tunability is also possible with $(Al_xGa_{1-x})_2O_3$.

As shown in fig. 1.1, the upper limit of $\alpha - (Al_xGa_{1-x})_2O_3$ is near 9 eV, far beyond the maximum of any other system, enabling the design of devices such as UV-photodetectors which operate in that part of the spectrum [45]. As a conductive material able to transmit light emitted by ArF (193 nm), KrF (248 nm), and fourth-harmonic Nd^{3+} : YAG (266 nm) lasers, $(Al_xGa_{1-x})_2O_3$ could find application in the field of laser lithography [14]. The ability to push the band gap past 4.8 eV will further increase the breakdown field of MOSFETs based on $(Al_xGa_{1-x})_2O_3$ relative to those fabricated from Ga_2O_3 [37]. In addition, evidence of carrier accumulation at an $(Al_xGa_{1-x})_2O_3$:Ga_2O_3 interface has been reported [46], which could enable the design of high-electron mobility transistors (HEMTs) with superior power handling ability than equivalent devices based on $Al_xGa_{1-x}As$ and $Al_xGa_{1-x}N$. Double-layered $(Al_xGa_{1-x})_2O_3$–Ga_2O_3–$(Al_xGa_{1-x})_2O_3$ films may also be fabricated to form quantum well hetero-structures, with tunable energy levels determined by geometry and alloy composition. Variation of the lattice parameters can be used to provide superior lattice matching when used as a substrate for epitaxial $Al_xGa_{1-x}N$ and other films.

In the case of $Al_xGa_{1-x}As$, the useful range for optical devices is limited by the band gap becoming indirect above $x = 0.41$ [47]. However, the endpoints of the $(Al_xGa_{1-x})_2O_3$ system have different stable crystal structures, with the monoclinic β phase favorable for Ga_2O_3 and the trigonal α (corundum) phase favorable for Al_2O_3; a phase change is therefore expected to occur at an intermediate value of x leading to a discontinuous jump in the band gap, though it is also possible to fabricate metastable alloys with uniform structure throughout the entire composition range. It is the goal of this research to determine the limits of stability in the α, β, and meta-stable phases of $(Al_xGa_{1-x})_2O_3$ thin films and powders, and to learn how the band gap and optical constants change as the aluminum content is varied within each phase. The ability to reliably achieve a desired band gap through control of the crystal phase and aluminum content is an important step in the development of $(Al_xGa_{1-x})_2O_3$-based technology, and will provide an alternative to $Al_xGa_{1-x}N$ for deep ultraviolet applications.

1.2 Thesis Overview

In the next chapter, I provide a brief introduction to the physics relevant to optical semiconductors synthesized from a small number of books which I found useful. In chapter 3, I review the Ga_2O_3 literature beginning with a description of Ga_2O_3 and Al_2O_3 crystal structures, and moving on to describe previous results on Ga_2O_3 single crystals, Ga_2O_3 thin films, and alloys. Due to the vastness of the field, emphasis is placed on key papers relating to the electrical and optical properties of the material, which are most relevant to this work. In chapter 4, I provide details on the manufacture of $(Al_xGa_{1-x})_2O_3$ thin films and powders as well as their characterization. Experimental results are described in chapters 5–7, beginning with single-phase powders in chapter 5, followed by post-annealed composition-spread films in chapter 6, and composition-spread films deposited at high temperature in chapter 7. Finally in chapter 8, I summarize the key findings and give suggestions for further work.

Chapter 2

OPTICAL PROPERTIES OF SEMICONDUCTORS

[1] Light traveling through a dielectric medium is governed by Maxwell's equations, which take the form (assuming $E \propto e^{-i\,\omega t}$ and no free charges or currents)

$$\nabla \cdot \mathbf{D} = 0 \tag{2.1a}$$

$$\nabla \cdot \mathbf{B} = 0 \tag{2.1b}$$

$$\nabla \times \mathbf{E} = i\,\omega \mathbf{B} \tag{2.1c}$$

$$\nabla \times \mathbf{H} = -i\,\omega \mathbf{D} \tag{2.1d}$$

Bound charges responding to an applied field $\mathbf{E}$ produce a dipole moment $\mathbf{p}$ in the direction of $\mathbf{E}$; summing over all atoms gives the total polarization $\mathbf{P}$. If the fields are weak enough, the response of $\mathbf{P}$ may be taken to be proportional to $\mathbf{E}$

$$P_j = \varepsilon_0 \chi_{i,j} E_j \tag{2.2}$$

where the constant of proportionality is the electric susceptibility, and is in general a tensor. By analogy to $\mathbf{P}$, an applied magnetic induction $\mathbf{B}$ produces a total magnetization $\mathbf{M}$ whose linear response may be described by a magnetic susceptibility χ_m

$$M_i = \frac{1}{\mu_0}(\chi_m)_{i,j} H_j \tag{2.3}$$

The electric displacement $\mathbf{D}$ and magnetic field $\mathbf{H}$ are defined in terms of the electric field $\mathbf{E}$ and the magnetic induction $\mathbf{B}$ by constitutive relations

$$\begin{aligned} \mathbf{D} &= \varepsilon_0 \mathbf{E} + \mathbf{P} = \varepsilon_0\, \varepsilon \mathbf{E} \\ \mathbf{H} &= \frac{1}{\mu_0}\mathbf{B} - \mathbf{M} = \frac{1}{\mu_0}\frac{1}{\mu}\mathbf{B} \end{aligned} \tag{2.4}$$

---

[1] This chapter is summarized primarily from Jackson [48] Ch. 7, Yu and Cardona [49] Ch. 6, and Dresselhaus [50] Pt. 2–Optical Properties

Here ε is the relative permittivity or dielectric constant, and μ is the relative permeability; in free space both are equal to 1. They are related to the electric and magnetic susceptibilities by $\varepsilon = 1 + \chi$ and $\mu = 1 + \chi_m$, respectively. In principle the entire linear optical response of a material is determined by the behavior of $\varepsilon_{i,j}(\mathbf{k}, \omega)$ and $\mu_{i,j}(\mathbf{k}, \omega)$ as a function of ω; the study of its optical properties is tantamount to the determination of these two quantities. Furthermore, for most non-ferromagnetic materials μ differs from one by 10^{-5} or less. For example, the magnetic permeability of sapphire differs by just 2.4×10^{-7}. Therefore for comparison with experiment it is usually sufficient to assume $\mu \approx 1$ and only consider ε.

Combining eqs. (2.1c) and (2.1d) using the constitutive relations (2.4) produces the Helmholtz wave equation

$$(\nabla^2 + \frac{\mu\varepsilon\omega^2}{c^2}) \left\{ \begin{array}{c} \mathbf{E} \\ \\ \mathbf{B} \end{array} \right\} = 0, \tag{2.5}$$

and substituting the plane wave solution $e^{ikx-i\omega t}$ yields the dispersion relation

$$k = \frac{\sqrt{\mu\varepsilon}}{c}\,\omega = \frac{\tilde{n}}{c}\,\omega \tag{2.6}$$

which shows that a complex-valued $\tilde{\varepsilon}$ (or $\tilde{\mu}$) results in an exponential decrease in plane wave amplitude with distance

$$\mathbf{E} = \mathbf{E_0} e^{-\kappa\omega z/c} e^{i\omega(n/c)z - i\omega t} \tag{2.7}$$

As a result, the imaginary part of $\tilde{n}$, or κ, is known as the extinction coefficient. (The real part of $\tilde{n}$ is just the index of refraction n.) One may also take the exponential decay of light intensity with distance as an axiom and define the absorption coefficient α as

$$I(z) = I_0 e^{-\alpha z} \tag{2.8}$$

The relationship between extinction coefficient and absorption coefficient is therefore

$$\alpha = 2\kappa\omega/c \tag{2.9}$$

A simple model of absorption may be derived by considering a cloud of electrons bound to an atom as a damped, driven harmonic oscillator, with mass m, damping coefficient γ, resonant requency ω_0, and the incident electric field ($\mathbf{E} \propto e^{-i\omega t}$) providing the driving force

$$m[\ddot{\mathbf{x}} + \gamma\dot{\mathbf{x}} + \omega_0^2 x] = -e\mathbf{E}(\mathbf{x}, t) \tag{2.10}$$

whose solution is

$$\mathbf{p} = -e\mathbf{x} = \frac{e^2}{m}\frac{1}{\omega_0^2 - \omega^2 - i\omega\gamma}\mathbf{E} \tag{2.11}$$

Real compounds have more than one type of atom, and/or electrons bound to atoms in different sites, with different bonding strengths and degrees of ionicity. Therefore a more realistic model will include multiple oscillators with varying strengths f_j, resonant frequencies ω_j and damping coefficients γ_j

$$\varepsilon = 1 + \chi = 1 + \frac{Ne^2}{\varepsilon_0 m}\sum_j \frac{f_j}{\omega_j^2 - \omega^2 - i\omega\gamma_j} \tag{2.12}$$

where N is the total number of atoms per unit volume, and oscillator strengths must satisfy the sum rule $\sum_j f_j = Z$, where Z is the number of electrons per atom. Equation (2.12) may be written in terms of its real and imaginary parts as

$$\begin{aligned}
\varepsilon_1 \equiv \text{Re } \varepsilon &= 1 + \frac{Ne^2}{\varepsilon_0 m}\sum_j \frac{f_j(\omega_j^2 - \omega^2)}{(\omega_j^2 - \omega^2)^2 + \omega^2\gamma^2} \\
\varepsilon_2 \equiv \text{Im } \varepsilon &= \frac{Ne^2}{\varepsilon_0 m}\sum_j \frac{f_j\omega\gamma_j}{(\omega_j^2 - \omega^2)^2 + \omega^2\gamma^2}
\end{aligned} \tag{2.13}$$

This basic result provides the theoretical foundation for modeling a dielectric function as a superposition of oscillators of varying strengths, widths and center frequencies. In practice, oscillators are added to ε_2 until a satisfactory match to experiment is found, and ε_1 is computed from ε_2 using the Kramers-Kronig relations

$$\varepsilon_1(\omega) = 1 + \frac{2}{\pi}\, P\int_0^\infty \frac{\omega'\ \varepsilon_2(\omega')}{\omega'^2 - \omega^2}\ d\omega' \tag{2.14a}$$

$$\varepsilon_2(\omega) = -\frac{2\omega}{\pi}\, P\int_0^\infty \frac{\varepsilon_1(\omega') - 1}{\omega'^2 - \omega^2}\ d\omega' \tag{2.14b}$$

This semi-empirical approach to parameterizing the dielectric function has been extended to many types of oscillator functions, described in section 4.6.3.

Many features of the dielectric function may be understood by identifying its structures with specific transitions between valence and conduction bands. Fermi's Golden Rule gives the transition probability per unit time between two states $|i\rangle$ and $|f\rangle$ connected by a Hamiltonian $\mathcal{H}_{if}$

$$R_{i\to f} = \frac{2\pi}{\hbar}|\langle f|\mathcal{H}_{if}|i\rangle|^2\rho_f \tag{2.15}$$

where ρ_f is the final state density for a transition from a discrete level (e.g. a defect state) to a continuum of final states; in the case of an optical transition between continua of initial and final states it is replaced by a joint density of states. For electric dipole transitions $\mathcal{H} = \frac{e}{mc}\mathbf{A}\cdot\mathbf{p}$, and $|i\rangle$ and $|f\rangle$ are states in the valence $|v\rangle$ and conduction bands $|c\rangle$ at the same crystal momentum $\mathbf{k}$, i.e. $\mathbf{k_c} = \mathbf{k_v}$, which differ by an energy $\hbar\omega$. The matrix element for $\mathcal{H}$ becomes

$$|\langle c|\mathcal{H}_{cv}|v\rangle|^2 = \left(\frac{e}{mc}\right)^2 |A|^2 |P_{cv}|^2 \tag{2.16}$$

where $|P_{cv}|$ is the momentum matrix element, which is assumed not to vary with respect to $\mathbf{k}$. Summing over all states in the Brillouin zone (per unit volume) gives the total probability to absorb a photon per unit time per unit volume

$$R = \frac{2\pi}{\hbar}\left(\frac{e}{m\omega}\right)^2 \left|\frac{E(\omega)}{2}\right|^2 \sum_{\mathbf{k}} |P_{cv}|^2 \; \delta(E_c(\mathbf{k}) - E_v(\mathbf{k}) - \hbar\omega) \tag{2.17}$$

which multiplied by $\hbar\omega$ gives the power lost in the field due to absorption per unit volume. To relate this to the dielectric function, one may use eqs. (2.8) and (2.9) to calculate the intensity $I \equiv \frac{P}{A}$ of the incident beam per unit time per unit distance z

$$-\frac{dI}{dt} = -\left(\frac{dI}{dz}\right)\left(\frac{dz}{dt}\right) = (\alpha I_0)\left(\frac{c}{n}\right) = \frac{\varepsilon_2\omega}{n^2} I_0 = \frac{\varepsilon_2\omega}{2}\mathbf{E}(\omega)^2 \tag{2.18}$$

where in the last equality we used the fact that the intensity of an electric field in a linear dielectric may be written as $I = \frac{1}{2}\mathbf{D}\cdot\mathbf{E} = \frac{1}{2}n^2\mathbf{E}^2$. Thus the imaginary part of the dielectric function may be related to the probability of electric dipole transitions between states

$$\varepsilon_2 = \pi\left(\frac{e}{m\omega}\right)^2 \sum_{\mathbf{k}} |P_{cv}|^2 \; \delta(E_c(\mathbf{k}) - E_v(\mathbf{k}) - \hbar\omega) \tag{2.19}$$

The real part of the dielectric function is obtained by substituting eq. (2.19) into the Kramers Kronig relation (2.14a)

$$\varepsilon_1 = 1 + \sum_{\mathbf{k}} \frac{2e^2}{m^2\hbar\omega_{cv}} \frac{|P_{cv}|^2}{\omega_{cv}^2 - \omega^2} \tag{2.20}$$

Comparing this expression with the expression for ε calculated in the harmonic oscillator approximation (2.12), one identifies the quantum mechanical oscillator strength f_j as

$$\frac{N f_j}{\varepsilon_0} = \frac{2|P_{cv}|^2}{m\hbar\omega} \tag{2.21}$$

To further elucidate the connection between band structure and optical absorption we replace the sum over $\mathbf{k}$ in eq. (2.19) with an integral, giving the joint density of states per unit energy and volume

$$D_j = \frac{2}{(2\pi)^3} \int d^3k \; \delta(E_c(\mathbf{k}) - E_v(\mathbf{k}) - \hbar\omega) \tag{2.22}$$

Next we introduce a constant-energy surface S in $\mathbf{k}$ space such that $d^3k = dS \; dk_n$ with dk_n normal to the surface S, and since $|\nabla_k(E_c - E_v)|dk_n = d(E_c - E_v)$ we have

$$d^3k = dS \; \frac{d(E_c - E_v)}{|\nabla_k(E_c - E_v)|} \tag{2.23}$$

Equation (2.22) is then transformed to a surface integral over the constant energy surface defined by $E_{cv} = E_c - E_v = \hbar\omega$

$$D_j(E_{cv}) = \frac{2}{(2\pi)^3} \int \frac{dS}{|\nabla_k(E_{cv})|_{E_{cv}=\hbar\omega}} \tag{2.24}$$

The imaginary part of the dielectric function is now written as an integral over E_{cv}

$$\varepsilon_2 = \pi \left(\frac{e}{m\omega}\right)^2 \frac{2}{(2\pi)^3} \int dE_{cv} \; D_j(E_{cv}) \tag{2.25}$$

Points in $\mathbf{k}$-space where the gradient in the denominator of eq. (2.24) vanishes are referred to as critical points, and corresponding singularities in the joint density of states are known as Van Hove singularities. They are identified by looking for places in the band structure where the slopes of the valence and conduction bands are parallel, and are usually found around high-symmetry points in the Brillouin zone (fig. 2.1a). Around critical points, light induces transitions over a relatively large region in $\mathbf{k}$-space, giving rise to strong absorption features in the dielectric function (fig. 2.1b). As a result, spectroscopic optical measurements have become an important tool for the determination of band structures in semiconductors.

Van Hove singularities are classified by the number of negative coefficients in the first three terms of the expansion of $E(\mathbf{k})$ about a critical point (see fig. 2.2)

$$E_c(\mathbf{k}) - E_v(\mathbf{k}) = E_g(\mathbf{k_0}) + \sum_{i=1}^{3} a_i(k_i - k_0 i)^2 \tag{2.26}$$

Assuming approximately parabolic bands, near a M0 critical point E_c and E_v take the form

$$E_c(\mathbf{k}) = \frac{E_g}{2} + \frac{\hbar^2 k^2}{2m_c} \tag{2.27a}$$

$$E_v(\mathbf{k}) = -\frac{E_g}{2} - \frac{\hbar^2 k^2}{2m_v} \tag{2.27b}$$

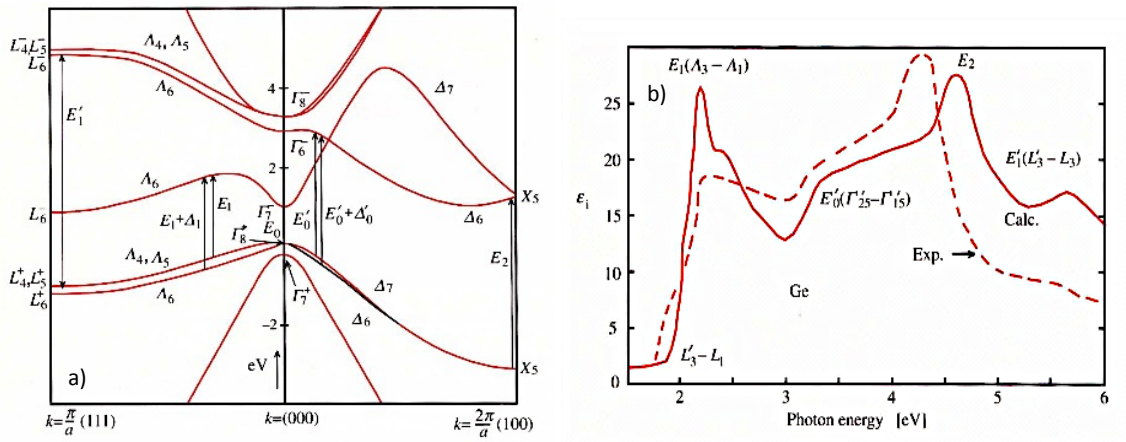

Figure 2.1: a) Band structure of Ge showing allowed optical transitions, and b) its corresponding absorption coefficient (calculated and experimental) with associated structures labeled. From *Yu and Cardona*, ch. 6. [49]

which leads to the approximate form of $\varepsilon_2(\omega)$ around an M0 critical point

$$\varepsilon_2(\omega) \propto (\hbar\omega - E_g)^{1/2} \tag{2.28}$$

The forms of $\varepsilon(\omega)$ near other types of critical points are shown on the right hand side of fig. 2.2. Recalling that the absorption coefficient is proportional to ε_2/ω in eq. (2.9), eq. (2.28) implies that a plot of $(\alpha\hbar\omega)^2$ vs. $\hbar\omega$ produces a straight line for a direct transition around a critical point, whose extrapolation to zero gives the optical band gap E_g. Such a plot is known as a Tauc plot, and is widely used to estimate the band gap of direct-gap semiconductors.

Equation (2.24) follows from the condition that the difference in energy between the initial and final states is equal to the incident photon energy $\hbar\omega$, which defines a direct transition. In the case of an indirect transition, a momentum change $\mathbf{q}$ occurs due to a collision with a phonon, which results in an additional energy E_p. This leads to a qualitatively different dependence of ε_2 on $\hbar\omega$ near the band edge. One can model an indirect transition across a gap defined by energy E_g as a process involving two steps:

1. A direct virtual transition with energy $\hbar\omega$

2. A momentum transfer $\mathbf{q}$ accompanied by an additional change in energy E_p

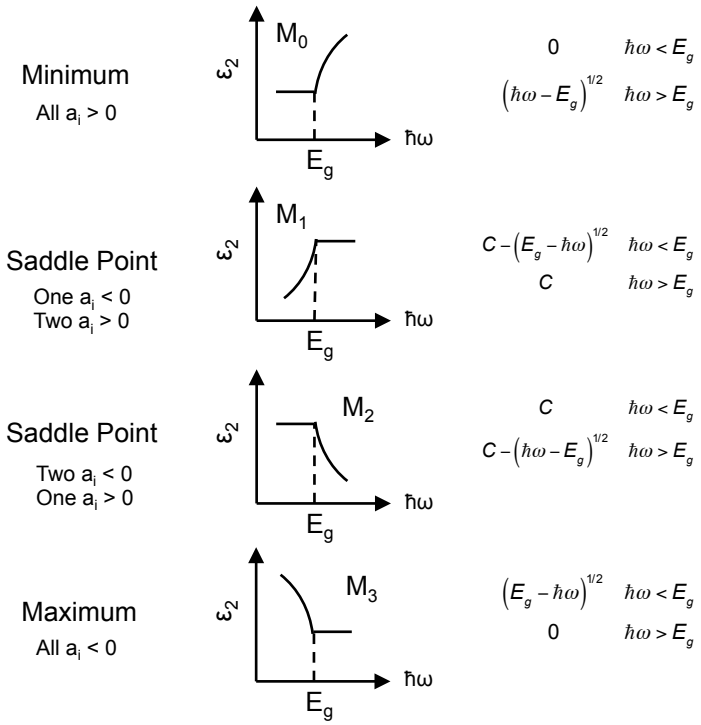

Figure 2.2: Types of 3D Van Hove Singularities

Therefore the new conservation of energy condition is written $E_c - E_v = \hbar\omega \pm E_p$, and the integral in eq. (2.25) becomes

$$\iint dE_c\, dE_v\, D_v(E_v) D_c(E_c) \delta(E_c - E_v - \hbar\omega \pm E_p) \tag{2.29}$$

Again, assuming parabolic valence and conduction bands

$$D_v(E_v) \propto \begin{cases} (-E_v)^{1/2} & \text{for } E_v < 0 \\ 0 & \text{for } E_v > 0 \end{cases} \tag{2.30a}$$

$$D_c(E_c) \propto \begin{cases} 0 & \text{for } E_c < E_g \\ (E_c - E_g)^{1/2} & \text{for } E_c > E_g \end{cases} \tag{2.30b}$$

Substituting eqs. (2.30a) and (2.30b) into eq. (2.29) gives

$$\iint dE_c\, dE_v\, (-E_v)^{1/2} (E_c - E_g)^{1/2} \delta(E_c - E_v - \hbar\omega \pm E_p) \tag{2.31}$$

and performing the integral over E_v

$$\int_0^{\hbar\omega\mp E_p-E_g} dE_c\ (E_c - E_g)^{1/2}(\hbar\omega \mp E_p - E_c)^{1/2} \tag{2.32}$$

where the lower limit of integration comes from eq. (2.30b) and the upper limit of integration comes from eq. (2.30a). Substituting

$$x = \frac{E_c - E_g}{\hbar\omega \mp E_p - E_g}$$

into eq. (2.32) gives

$$(\hbar\omega \mp E_p - E_g)^2 \int_0^1 x^{1/2}(1-x)^{1/2}dx \tag{2.33}$$

The integral on the right hand side evaluates to $\pi/8$. Therefore in the case of an indirect transition, ε_2 depends on $\hbar\omega$ as

$$\varepsilon_2(\omega) \propto \begin{cases} (\hbar\omega \mp E_p - E_g)^2 & \text{for } \hbar\omega \geq E_g \pm E_p \\ 0 & \text{otherwise} \end{cases} \tag{2.34}$$

This result implies that when momentum is not conserved, as in an indirect transition involving a phonon, a Tauc plot of $(\alpha\hbar\omega)^{1/2}$ vs. $\hbar\omega$ should produce a straight line, whose intersection with the abscissa yields the indirect band gap energy $\pm$ the photon energy E_p. The lower energy edge at $E_g - E_p$ is associated with phonon absorption and is appreciable only at high temperatures. The higher edge at $E_g + E_p$ is associated with phonon emission, and occurs at high and low temperatures at a rate proportional to the number of phonons present.

Gallium oxide is technically an indirect-gap semiconductor; however the difference between the indirect gap and the direct gap at Γ is only $\sim$0.04 eV [51]. Since the absorption coefficient for the direct transition is orders of magnitude greater, the indirect gap is nearly impossible to distinguish. Therefore most authors measure the band gap of Ga_2O_3 by plotting $(\alpha\hbar\omega)^2$ vs. $\hbar\omega$ and extrapolating a linear fit to zero. However, I found that $\alpha(\omega)$ is already almost-linear in most of my data, and $(\alpha\hbar\omega)^2$ defines a parabolic curve resulting in a very ambiguous fit. Therefore I opted to simply estimate the band gap from $\alpha(\omega)$ directly. This is justified by considering that the entire purpose of forming a Tauc plot is to linearize the data. Regardless of the physical assumptions that lead to the derivation of $(\alpha\hbar\omega)^2$, in general there will be only one function proportional to a power of α resulting in a straight line and an unambiguous linear fit.

Chapter 3

LITERATURE REVIEW

3.1 Ga_2O_3 and Al_2O_3 Polymorphs

3.1.1 Monoclinic $\beta - Ga_2O_3$ and $\theta - Al_2O_3$

The thermodynamically stable phase of Ga_2O_3 is shown in fig. 3.1. The unit cell dimensions, shape and similarity to $\theta - Al_2O_3$ were first reported in 1957 by Kohn et al. [52] based on powder X-ray diffraction and polarizing microscopy data, although $\beta - Ga_2O_3$ has been known to be the most stable polymorph since at least 1952 [53]. A detailed description of the atomic arrangement and bond lengths was published three years later by Geller [54] based on the three-dimensional X-ray diffraction of $\beta - Ga_2O_3$ single crystals. $\beta - Ga_2O_3$ has monoclinic symmetry belonging to space group $C2/m$. The conventional unit cell contains 20 atoms (8 Ga and 12 O) and has edge dimensions $a = 12.23 \pm 0.02$ Å, $b = 3.04 \pm 0.01$ Å, $c = 5.80 \pm 0.01$ Å, and the angle between **a** and **c** is $\beta = 103.7 \pm 0.3°$ (fig. 3.1). The primitive unit cell contains 10 atoms (4 Ga and 6 O). Its axes are obtained vectorially from the conventional unit cell axes by $\mathbf{a}_{prim} = (\mathbf{a}_{conv} + \mathbf{b}_{conv})/2$, $\mathbf{b}_{prim} = (-\mathbf{a}_{conv} + \mathbf{b}_{conv})/2$, and $\mathbf{c}_{prim} = \mathbf{c}_{conv}$. Either description is sufficient to understand the atomic structure, however the primitive cell should be used for band structure calculations to include the full Brillouin zone [51]. There are two gallium sites, one tetrahedrally coordinated (Ga_I) and the other octahedrally coordinated (Ga_{II}), and three oxygen sites, which are distinguished from each other by the number and types of polyhedra connected to them: O_I is threefold-coordinated, connecting one Ga_I and two Ga_{II}; O_{II} is threefold-coordinated, connecting two Ga_I and one Ga_{II}; and O_I is fourfold-coordinated, connecting one Ga_I and three Ga_{II}. The oxygen atoms form a distorted face-centered cubic (fcc) sublattice, with cation vacancies on distorted octahedral sites forming hollow channels in the **b**-direction. The structure may be equally well described as parallel chains of tetrahedral and octahedral Ga polyhedra running along the **b**-direction, connected by O atoms at the vertices. The existence of parallel chains gives rise to electrical and optical anisotropy in $\beta - Ga_2O_3$ single crystals.

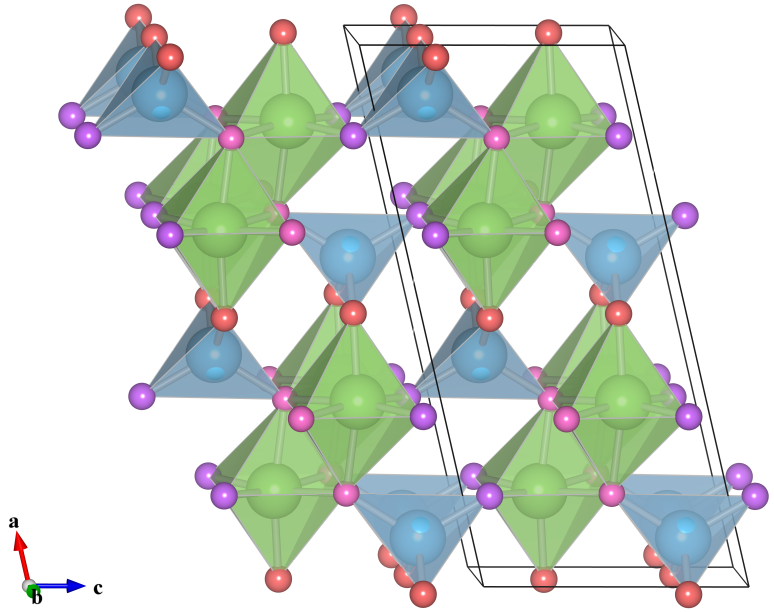

Figure 3.1: The structure of $\beta - Ga_2O_3$ viewed along the [010] direction. Black lines show the conventional unit cell. Tetrahedral Ga_I and octahedral Ga_{II} sites are indicated by green and blue polyhedra, respectively, and the three nonequivalent oxygen sites O_I, O_{II}, and O_{III} are indicated in purple, red, and pink, respectively.

$\theta - Al_2O_3$ is isostructural to $\beta - Ga_2O_3$, with approximately 3 % smaller unit cell dimensions [52]. It has unit cell dimensions $a = 11.795$ Å, $b = 2.910$ Å, and $c = 5.621$ Å, with angle $\beta = 103.79°$ [55]. Unlike $\beta - Ga_2O_3$, $\theta - Al_2O_3$ is not the stable phase of Al_2O_3, and will convert to $\alpha - Al_2O_3$ upon heating above 1000 °C [56].

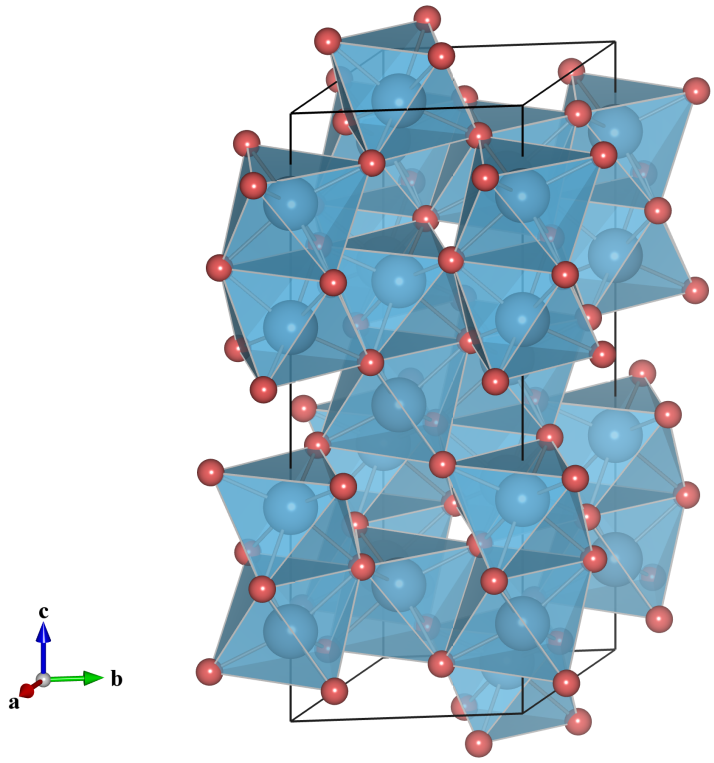

Figure 3.2: The conventional unit cell of $\alpha - Al_2O_3$.

3.1.2 Rhombohedral $\alpha - Ga_2O_3$ *and* $\alpha - Al_2O_3$

The α phase is the thermodynamically stable phase of Al_2O_3, and a metastable phase of Ga_2O_3, which converts to the β phase at temperatures above 600 °C (bulk) [57] or 500 °C (thin films) [58, 59]. It has the corundum structure with $R\bar{3}c$ symmetry. The conventional unit cell is pictured in fig. 3.2, which contains 30 atoms (12 Al and 18 O). The $\alpha - Al_2O_3$ lattice parameters are $a = b = 4.759$ Å and $c = 12.992$ Å [60], and the $\alpha - Ga_2O_3$ lattice parameters are $a = b = 4.983$ Å and $c = 13.433$ Å [61]. The $\gamma - Ga_2O_3$ unit cell is therefore 4.7 % wider and 3.4 % taller than $\alpha - Al_2O_3$. As opposed to the cubic arrangement in $\beta - Ga_2O_3$ and $\gamma - Ga_2O_3$, the oxygen anions in $\alpha - Ga_2O_3$ form a hexagonal close-packed sublattice, and all gallium atoms are octahedrally coordinated.

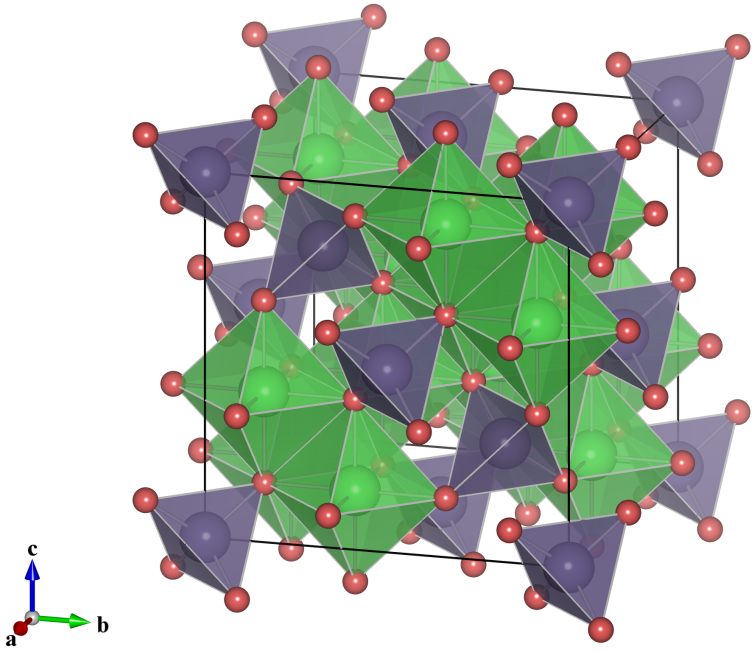

Figure 3.3: The unit cell of spinel $MgAl_2O_4$. Tetrahedral cation sites are shown in purple, and octahdral sites in green. $\gamma - Ga_2O_3$ and $\gamma - Al_2O_3$ also have spinel structure, but with cation vacancies randomly distributed over $\frac{1}{6}$ of the octahedral sites.

3.1.3 Cubic $\gamma - Ga_2O_3$ *and* $\gamma - Al_2O_3$

The γ phase is a low-temperature metastable phase which has been described as a defective spinel, in which $\frac{1}{9}$ of the cation sites are vacant. The conventional unit cell contains 32 anion sites in a face-centered cubic arrangement, 16 octahedral cation sites, and 8 tetrahedral cation sites. The undefected spinel structure can be described as a repeating layered structure in the {111} planes, in which two cation layers are sandwiched within an fcc oxygen sublattice: one containing only octahedra, and the other containing both octahedra and tetrahedra in alternating orientations (fig. 3.3) [56]. It is a cubic unit cell with side length 7.94 Å for $\gamma - Al_2O_3$, [62] and 8.238 Å for $\gamma - Ga_2O_3$ [63], and its space group is $Fd\bar{3}m$. $\gamma - Al_2O_3$ converts to $\delta - Al_2O_3$ upon annealing past 750 °C, and $\theta - Al_2O_3$ upon heating above 900–1000 °C [64]. The transformation takes place by a

migration of Al atoms through neighboring interstitial sites, with minimal displacement of the O atoms, in marked contrast to the $\theta \rightarrow \alpha$ transformation [56, 65].

In the case of $\gamma-Al_2O_3$, there have been numerous conflicting experimental and theoretical studies regarding the nature of the disorder and the distribution of cation vacancies. Experimental data based on neutron, electron, X-ray diffraction, as well as high-resolution electron microscopy indicate that vacancies are primarily located on octahedral sites [62, 66–69], however other experiments using many of the same techniques in addition to nuclear magnetic resonance (NMR) argue instead that vacancies are either located on tetrahedral sites [70, 71], or distributed over both tetrahedral and octahedral sites [72–75]. Early molecular dynamics (MD) simulations favor vacant tetrahedral sites [76, 77]; however, later first-principles calculations as well as calculations based on empirical pair potentials conclude that octahedral vacancies are favorable [74, 78–81]. Along the way there have been observations that the cubic unit cell is tetrahedrally distorted [82], and that cations occupy non-spinel sites [83, 84]. In 2001, Krokidis et al. [85] suggested an orthorhombically distorted fcc oxygen sublattice allowing cations to occupy non-spinel sites, a model also supported by Digne et al. [86]. In 2003, Paglia et al. [87] suggested that $\gamma - Al_2O_3$ should actually be described by a tetragonal structure belonging to $I4_1/amd$, a maximal subgroup of $Fd\bar{3}m$ with $a_{cubic} \approx \sqrt{2}a_{tetragonal}$. Two years later, the same authors followed their experimental work with an exhaustive computational study considering 1.47 billion possible structural possibilities satisfying either $Fd\bar{3}m$ and $I4_1/amd$ symmetry, with the results supporting their earlier hypothesis and also showing that 40% of Al ions occupy non-spinel sites regardless of the type of symmetry [88]. However, they allow that an amorphous-starting material (such as the thin films considered in the present work) as opposed to boehmite ($\gamma - AlO(OH)$) would still be expected to have cubic $Fd\bar{3}m$ symmetry upon annealing. Since then a number of theoretical and experimental studies have been published explicitly comparing spinel and non-spinel models to experimental data [89–94]. Except for Sun et al. [90] (which has been heavily criticized [95, 96]) there seems to be general agreement that a distorted cubic $Fd\bar{3}m$ structure allowing for Al ions in non-spinel sites provides the best match to experimental data. This is also in agreement with the result of Smrčok et al. [97], who managed to grow single-crystal $\gamma-Al_2O_3$ whiskers by the thermal decomposition of boehmite and study them using X-ray diffraction. Electronic structure calculations for both spinel and non-spinel models show similar features, with the particular result that the smaller band gap of $\gamma - Al_2O_3$ results from electrostatic effects caused

by disorder due to cation vacancies and tetrahedrally-bonded Al ions. [89, 92, 98]

There is dramatically less literature on the structure of $\gamma - Ga_2O_3$ compared to $\gamma - Al_2O_3$. Assignment to the cubic spinel phase with space group $Fd\bar{3}m$ was done by Arean et al. [99] based on X-ray diffraction analysis. A theoretical study by Yoshioka et al. [100] compared 14 inequivalent cation vacancy distributions over spinel sites and concluded a slight (0.05 eV) preference for both vacancies to be on the octahedral site, separated by an average distance of 8.06 Å, with the second-lowest energy configuration distributing vacancies over both octahedral and tetrahedral sites with an average separation of 3.57 Å. Detailed refinement of the micro-structure of three different $\gamma - Ga_2O_3$ gels of varying crystal quality was carried out by Playford et al. [101], using reverse Monte Carlo refinement and Bragg analysis of total neutron scattering data, who found that the occupation ratio of tetrahedrally- to octahedrally-coordinated sites increases in the bulk with decreasing crystallite size, with a balancing increase in octahedrally-coordinated cation sites at the surface, as well as a significant increase in the population of non-spinel sites.

3.2 Review of the literature on Ga_2O_3 *and* $(Al_xGa_{1-x})_2O_3$

Although the phenomenological study of gallium oxide dates back to the 1950s, a detailed understanding of the physics had to wait for improvements in technology for the growth and characterization of high quality samples and the development of accurate computer modeling. In the remainder of this chapter I will review the most important developments in our understanding of the electronic and optical behavior of $\beta - Ga_2O_3$ single crystals, followed by Ga_2O_3 thin films and alloys, in roughly chronological order.

3.2.1 Early Experiments

The early work of Roy et al. [53] identified one stable (β) and four metastable (α, γ, δ, ϵ)[1] phases of Ga_2O_3 powders and their transformation sequences when derived from different precursors, including an aqueous gallium nitrate ($Ga(NO_3)_3$) solution, gels prepared from $Ga(NO_3)_3$ by adding ammonia, dried gels that crystallized in the diaspore GaO(OH) structure, and solid solutions of $(Al_xGa_{1-x})_2O_3$ powder. A different paper that year by the same group (Hill et al. [102]) mapped the phase diagram of $(Al_xGa_{1-x})_2O_3$ solid solutions precipitated from a melt, as the composition varied from $0 < x < 1$ and the temperature varied from $200\,^{\circ}\mathrm{C} < T < 2200\,^{\circ}\mathrm{C}$, finding that the β phase is stable from $0 < x < 0.67$, a mixture of $\alpha + \beta$ phases appears from $0.67 < x < 0.75$, and the α (corundum) phase is stable from $0.75 < x < 1$. Following the transition sequences in their other paper they fabricated metastable $(Al_xGa_{1-x})_2O_3$ powders in the α, β, ϵ, and diaspore phases over the entire composition range $0 < x < 1$ and determined the change in lattice parameters with Al composition in each phase. A different study by Mizuno et al. [103], using $(Al_xGa_{1-x})_2O_3$ powder mixed from pure Al_2O_3 and Ga_2O_3 by grinding and sintering in appropriate ratios, found the stable region of the β phase to extend from $0 < x < 0.75$, with a mixed phase from $0.75 < x < 0.85$ and a stable α phase from $0.85 < x < 1$. These results agree more closely with a much later study by Jaromin and Edwards [104], who found the stable region of the β phase to extend from $0 < x < 0.78$, with a mixed phase from $0.78 < x < 0.88$ and the stable α phase from $0.88 < x < 1$, again using $(Al_xGa_{1-x})_2O_3$ powder mixed by grinding and sintering. To my knowledge no study other than the present work has investigated $(Al_xGa_{1-x})_2O_3$ powders derived by mixing precursors in solution (chapter 5).

[1] The phase they denoted ϵ was renamed κ in 2013 by Playford et al. [63]

The first description of the $\beta - Ga_2O_3$ (and isostructural $\theta - Al_2O_3$) unit cell appeared in 1956 by Kohn et al. [52], who fashioned small single crystals by a vapor-phase growth method and studied them using X-ray diffraction. The crystals showed apparent orthorhombic symmetry due to twinning on the (001) plane; however the true symmetry is monoclinic with lattice parameters $a = 5.80 \pm 0.01$ Å, $b = 3.04 \pm 0.01$ Å, $c = 12.23 \pm 0.02$ Å, $\beta = 103°42'$, belonging to space group $A2/m$. The $\theta - Al_2O_3$ pattern was shown to be isomorphic to $\beta - Ga_2O_3$, with approximately 3 % smaller lattice parameters. However, a detailed description of the structure had to wait until 1960 for a paper by Geller [54], who examined single crystals (prepared by a flux growth method by [105]) using three-dimensional XRD with both Cu Kα and Mo Kα radiation. Geller found complete agreement with the results of Kohn et al. [52], but renamed the axes $a = 12.23 \pm 0.02$ Å and $c = 5.80 \pm 0.01$ Å, and assigned the symmetry $C2/m$. With this new assignment the twinning plane is identified as (100). Two sites were identified for Ga, one tetrahedral (Ga_I) and one octahedral (Ga_{II}), and three sites for oxygen, two three-coordinated and one tetrahedral, with a total of 20 atoms per unit cell. Atomic positions and nearest-neighbor distances were given. Until a reinvestigation in 1996 by Ahman et al. [106], the paper by Geller remained the key reference for the Ga_2O_3 structure; Ahman found complete agreement, but with significantly improved precision. (In 1976 a paper was published by Wolten and Chase [107] which disputed the assignment of $C2/m$ in favor of $P1$ based on the results of an electron microscope study; however a response by Geller [108] referencing a variety of diffraction and spectroscopic experiments in support of $C2/m$ appeared to settle the argument.)

At this time the largest single crystals were either grown by the Verneuil technique (Chase [109]), or by a flux growth method (Katz and Roy [110]), which yielded smaller fragments but with fewer inhomogeneities and imperfections. The first study on the optical properties of Ga_2O_3 single crystals was performed in 1965 by Tippins [11], who measured the absorption edge of Ga_2O_3 at room temperature and at 77 K, finding a 100 Å blue shift at the lower temperature. The band gap was reported to be 4.7 eV, but with a shoulder that could not be explained at the time. A charge transfer model was developed to explain the lower band gap of Ga_2O_3 relative to Al_2O_3 by the lower coordination of Ga_I ions in the $\beta - Ga_2O_3$ structure. Two years later, a study by Lorenz et al. [111] measured the electrical properties of Ga_2O_3 single-crystals grown (1) by the Verneuil method, (2) by a solution method using Ga_2O_3-saturated Ga solutions, and also (3) by a vapor-transport method using iodine as the transport agent. In all cases it was observed that crystals grown in oxidizing

conditions were clear, with resistivities greater than $10^6\,\Omega\,\mathrm{cm}$, and crystals grown in reducing atmospheres were light blue and conducting, with resistivities of $1\,\Omega\,\mathrm{cm}$ and electron concentrations on the order of $10^{18}\,\mathrm{cm}^{-3}$. Annealing the conducting crystals in an oxygen atmosphere restored their insulating behavior, so the conductivity was attributed to oxygen vacancies introduced by the reducing environment during growth. Based on Hall and resistivity measurements they deduced that conduction proceeds in a shallow impurity band at 4.2 K, with mobility $\mu = 2\,\mathrm{cm}^2/\mathrm{Vs}$; in both the impurity band and the conduction band at 110 K, with $\mu = 40\,\mathrm{cm}^2/\mathrm{Vs}$ and $140\,\mathrm{cm}^2/\mathrm{Vs}$, respectively; and in the conduction band above 160 K, with $\mu = 110\,\mathrm{cm}^2/\mathrm{Vs}$ at 160 K and $\mu = 80\,\mathrm{cm}^2/\mathrm{Vs}$ at 200 K. They also calculated the activation energy of the donor states to be 0.02–0.03 eV, and measured the band gap to be 4.8 eV, in agreement with Tippins [11].

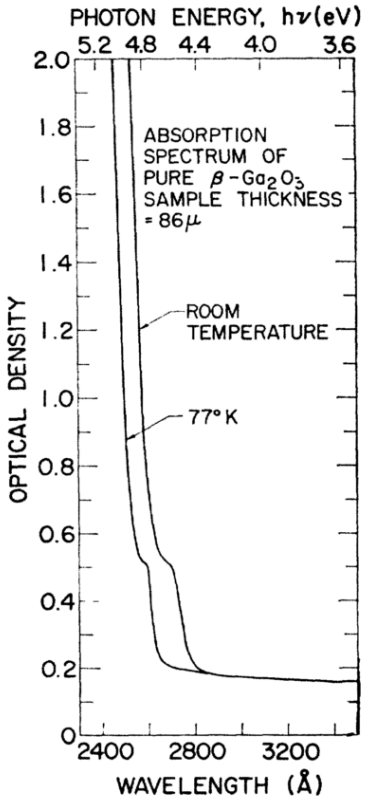

Figure 3.4: Absorption edge normal to the (100) plane of $\beta - Ga_2O_3$ at room temperature and 77 K. From Tippins [11]

In 1971, Hoeneisen et al. [112] measured the dielectric constant of Ga_2O_3 perpendicular to the (100) plane, finding a frequency and temperature independent result of 10.2 ± 0.3. The next optical measurements came in 1974 by Matsumoto et al. [113], who measured the refractive index from 280 nm to 680 nm in both polarizations normal to the (100) plane. Later in the following year, the same group measured the absorption of vapor-grown $\beta - Ga_2O_3$ platelet crystals in six orientations using polarized light. They found the absorption edge to be dichroic, with absorption at 4.55 eV for light polarized parallel to the c axis and for light polarized perpendicular to both b and c, and at 4.90 eV for light polarized parallel to the b axis, at room temperature. At 77 K the absorption edge parallel to b only moves by 0.04 eV to higher energy, and the other absorption moves by 0.22 eV to higher energy. These results are in agreement with the measurement by Tippins (fig. 3.4), and gives evidence that the shoulder is caused by optical anisotropy in the (100) plane.

Early attempts to explain the conductivity in $\beta - Ga_2O_3$ single crystals are inextricably linked to luminescence studies, the first of which was carried out in 1970 by Blasse and Bril [114] who identified efficient blue (420 nm) and green (500 nm) emission bands which depend on the doping, and a composition-independent near-UV emission band (365 nm) at low temperature. However, they made no attempt to explain the origins of the observed luminescence. In 1976, Harwig et al. [115], [116] reported that $\beta - Ga_2O_3$ crystals grown by the Verneuil method can be made insulating by doping with Mg, or conducting by doping with Zr. The same group also re-examined the ultraviolet luminescence [117] and the blue and green luminescence [118] of $\beta - Ga_2O_3$ single crystals and powders containing a variety of aliovalent dopants. By correlating with photoconductivity measurements they attributed the UV emission to an intrinsic interband transition between an electron and a self-trapped hole, a hypothesis that also explains its independence of the impurity concentration. As the temperature was raised above 120 K the UV luminescence was quenched, and visible luminescence began. Blue emission is observed in blue-colored Zr- or Si-doped single crystals and correlates with conductivity and infrared absorption. It can't be due to the presence of Si or Zr alone because it disappears when crystals are heat treated in air above 1200 °C, and it can't be due to intrinsic charged defects because it is not observed in Mg-doped single crystals. Therefore the authors proposed that the blue emission is due to recombination of electrons at neutral O vacancies or Ga interstitials with holes trapped on Ga vacancies, which act as charge compensators after substitutional doping with Si or Zr. The green luminescence remained unexplained, but the

observation that it appears only upon doping with specific elements lead the authors to speculate that it may be due to donor-acceptor pair recombination. A later report by Vasiltsiv [119] suggested that the green emission originates from pairs of charged vacancies (V_O, V_{Ga})' instead.

Both UV and blue emissions are broad and exhibit strong Stokes shifts characteristic of electron-phonon coupling, suggesting that recombining electrons and holes are localized. These results are in apparent contradiction with an EPR study by Aubay and Gourier [120], which suggested that electrons are in fact delocalized, because shallow donors in Ga_2O_3 are sufficiently concentrated to satisfy the Mott criterion and form an impurity band [121]. A reconciliation of these two properties was finally proposed in 1998 by Binet and Gourier [122] who suggested that donor impurities form clusters, leading to delocalized electron states within the clusters, while blue emission results from a two-step process in which (1) an electron in a donor cluster tunnels to a neutral acceptor, forming a trapped exciton, and then (2) the electron and trapped hole recombine at the acceptor site, giving a localized character to the luminescence. Indirect evidence for the spatial organization of defects was provided two years later by Binet and Gourier [123], who observed an intrinsic quantum well structure below the band edge in $\beta - Ga_2O_3$ at low temperature (fig. 3.5 a, b) which can be explained by transitions between discrete levels in low-dimensional acceptor clusters and the conduction band. More direct evidence of defect clustering in $\beta - Ga_2O_3$ was later provided by Villora et al. [124] who observed forbidden reflections in the electron diffraction pattern consistent with a structural modulation with domain size $< 5\,\text{nm}$, and an inhomogeneous appearance in dark-field TEM images (fig. 3.5 c, d). In these reports the natural assumption was that the donors in question were oxygen vacancies, as the sample conductivity and cluster density generally increases when growing crystals in a reducing atmosphere, and decreases upon annealing in oxygen; however, nothing about the cluster model rules out other kinds of defects, and it is now known that oxygen vacancies form deep donors and cannot contribute to conductivity [125]. It has also been shown that hydrogen interstitials, which could be introduced during flame growth using a 2:3 H_2:O_2 flow in the Verneuil torch, form shallow donors in Ga_2O_3 which may explain the conductivity instead.

An early band structure calculation was carried out by Binet et al. [126] in 1994 based on the semi-empirical extended Hückel method, in an attempt to explain the observed magnetic bistability of conduction electrons in Ga_2O_3 [127]. The calculated dispersion in the conduction bands is shown in fig. 3.6. The greatest dispersion is in the b direction, signifying greater delocalization and a lower

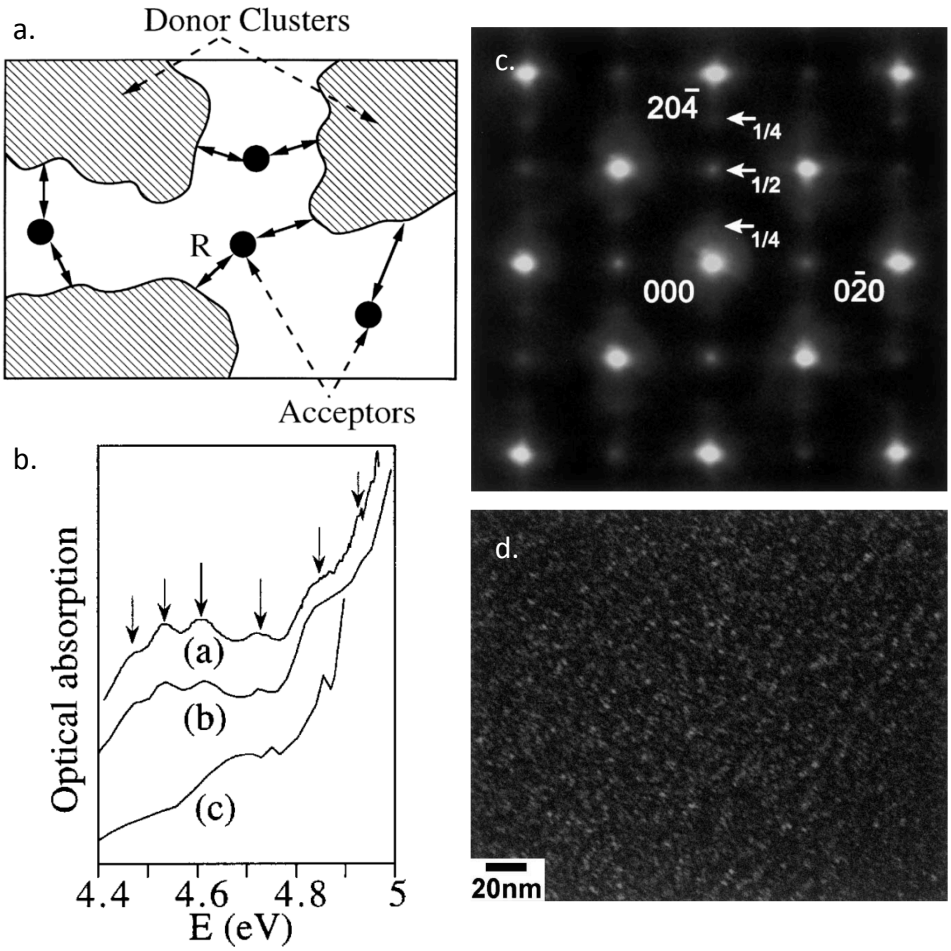

Figure 3.5: a) Cluster model for donors in gallium oxide proposed by Binet and Gourier [122]. b) Absorption spectra of thin $\beta - Ga_2O_3$ single crystals at 17 K (a), 12 K (b), and 300 K (c), showing discrete levels characterstic of intrinsic quantum wells formed by low-dimensional clusters. (From Binet and Gourier [123].) c) Electron diffraction from the (100) surface of $\beta - Ga_2O_3$, showing forbidden 1/2 and 1/4 reflections arising from inhomogeneous structural modulation. d) Dark-field TEM image showing inhomogeneous appearance with typical domain size less than 5 nm. (From Villora et al. [124]).

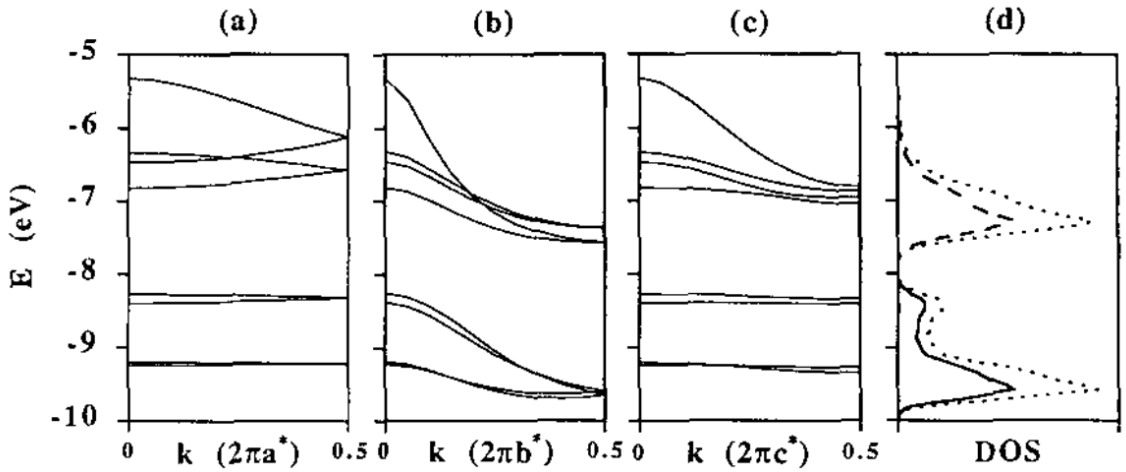

Figure 3.6: Dispersion curves in the conduction band of $\beta - Ga_2O_3$. Density of states: Total (dotted line), projected on $4s$ Ga_I (dashed line), projected on $4s$ Ga_{II} (solid line). From Binet et al. [126]

effective mass in this direction than in either a or c, which is attributed to the existence of parallel tetrahedral and octahedral chains along b in the $\beta - Ga_2O_3$ structure. The calculated band gap is indirect, with the conduction band minimum along b. Furthermore, the conduction and valence bands are neatly split by atomic orbitals with gaps in between. The valence band is comprised of O $2p$, the upper conduction band is comprised of Ga $4s$ from tetrahedrally-coordinated Ga_I, and the lower lying band is Ga $4s$ from octahedrally-coordinated Ga_{II}. These results contradict the simple electrostatic model described by Tippins, which predicted that the band gap is set by the lower-coordinated gallium ions, and which did not take into account shorter Ga–O bond lengths at Ga_I sites compared to Ga_{II}, which lead to a higher degree of covalency and destabilize the Ga $4s$ levels more strongly into anti-bonding states.

Heteroepitaxy of Ga_2O_3 thin films on sapphire was first investigated by Chaplygin and Semiletov [128] in 1976, who measured resistivities varying from 10^5 to $10^7\,\Omega\,\mathrm{cm}$ and found the following epitaxial relationships:

$$\left.\begin{array}{l}(20\bar{1})\ \beta\text{-}Ga_2O_3 \parallel (0001)\ Al_2O_3 \\ (310)\ \beta\text{-}Ga_2O_3 \parallel (11\bar{2}3)\ Al_2O_3 \\ (\bar{1}12)\ \beta\text{-}Ga_2O_3 \parallel (11\bar{2}3)\ Al_2O_3 \\ (111)\ \beta\text{-}Ga_2O_3 \parallel (11\bar{2}0)\ Al_2O_3\end{array}\right\} \langle 132\rangle\ \beta\text{-}Ga_2O_3 \parallel \langle 1\bar{1}00\rangle\ Al_2O_3$$

$$(11\bar{2}0)\ \alpha\text{-}Ga_2O_3 \parallel (11\bar{2}0)\ Al_2O_3 \qquad \langle 0001\rangle\ \alpha\text{-}Ga_2O_3 \parallel \langle 0001\rangle\ Al_2O_3$$

The optical properties of $\beta - Ga_2O_3$ and $\alpha - Ga_2O_3$:Co thin films grown by spray pyrolysis on glass substrates were investivated in 1987 by Kim and Kim [129], who found energy gaps of 4.23 eV for $\beta - Ga_2O_3$ and 2.41 eV for $\alpha - Ga_2O_3$:Co, with the latter also exhibing absorption in the near-infrared region due to impurities. Ga_2O_3 films prepared by spray pyrolysis were again investigated in 1990 by Wu et al. [130], on silicon and silica substrates. These films were initially amorphous after deposition at 450 °C, but transformed to the β phase after annealing at 800 °C. The band gap was measured to be 4.79 eV. In 1989, scanning tunnelling microscopy was used to measure the morphology of insulating Ga_2O_3 films prepared by RF sputtering by Hanrieder et al. [131]. A reversible change in the conductivity with the surrounding atmosphere at high temperatures was reported by Fleischer et al. [132], and the material was soon proposed for use as an oxygen sensor [41]. Over the next several years the same authors published a number of additional papers on Ga_2O_3 thin films, focused on developing their utility as sensors for oxygen and reducing gases. Among them was an interesting study on the electron mobility in single-crystal and polycrystalline Ga_2O_3 by Fleischer and Meixner [133]. Impedance spectroscopy revealed that the current remains in-phase with voltage, meaning that the observed conductivity is primarily electronic rather than ionic, and in the case of sintered ceramics is not affected by grain boundaries or contacts. The thermal activation energy of carriers in Ga_2O_3 ceramics (2.1 eV) was comparable to similar measurements by the same authors on sputtered thin films and to earlier reports by different authors. A surprising result was that the carrier mobility is identical for both monocrystalline and polycrystalline samples within the experimental error, meaning it is not limited by grain boundaries but by the Ga_2O_3 structure itself. This observation explained the reproducibility of the electric properties of Ga_2O_3 thin films: a consistent crystal lattice is easier to reproduce between different samples than a consistent grain boundary structure. In a different application, dielectric Ga_2O_3 films were deposited on GaAs substrates by electron-beam evaporation by Passlack et al. [134] and shown to have extremely low interface state densities ($< 10^{11}\,cm^{-2}\,eV^{-1}$), high resistivity and breakdown fields ($> 6 \times 10^{13}\,\Omega$

and 2.1 MV/cm, respectively), and static dielectric constants between 9.93 and 10.2. XPS analysis revealed that e-beam evaporation in vacuum leads to thin films with elemental gallium intermixed with Ga_2O_3, but that an oxygen partial pressure of 0.2 mT leads to a fully oxidized film [134, 135].

3.2.2 Density Functional Theory and Single Crystals Studies

Toward the end of the 1990s, better quality Ga_2O_3 single crystals were becoming available, fabricated using either float-zone [14, 136, 137] and Czochralski [28, 138] methods. In addition, first-principles calculations using density functional theory were becoming feasible with rapid advances in computing speeds, providing explanations for a number of observed phenomena that had so far eluded researchers.

In 1997 Ueda et al. [14] synthesized pure and Sn-doped Ga_2O_3 by the float zone method. They showed that the conductivity could be changed from $10^{-9}\,\Omega^{-1}\,cm^{-1}$ when grown in a pure O_2 environment, to $38\,\Omega^{-1}\,cm^{-1}$ when grown in a 40 % N_2 : 60 % O_2 environment. A conductivity of $0.96\,\Omega^{-1}\,cm^{-1}$ was achieved with 0.05 mol % Sn doping, even when grown in pure O_2. Annealing in oxygen at 900 °C reduced the free carrier density from $5 \times 10^{18}\,cm^{-3}$ to zero after 136 hours, evidenced by a complete disappearance of infrared absorption, and a slight red-shift in the absorption edge due to the Burstein-Moss effect. Anisotropy of the electrical and optical properties of nominally undoped $\beta - Ga_2O_3$ single crystals was also measured by Ueda et al. [12] in the same year. From Hall measurements, the conductivity and mobility were found to be $38\,\Omega^{-1}\,cm^{-1}$ and $46\,cm^2/Vs$ in b, and $2.2\,\Omega^{-1}\,cm^{-1}$ and $2.6\,cm^2/Vs$ in c, respectively, and roughly constant in temperature, as expected for a degenerate semiconductor. This result is in agreement with the semi-empirical calculation performed in 1994 by Binet et al. [126]. Next, the dichroism was measured with polarized light (fig. 3.7). Absorption was found to start at 253 nm and 270 nm for light polarized parallel to b and c, respectively. Based on an unpublished tight binding calculation by the same authors, it was discovered that direct transitions from valence bands with Γ_1^- symmetry only occur for light polarized parallel to c, while direct transitions from valence bands with Γ_2^- symmetry occur for light polarized parallel to a and b. Since the conduction band has Γ_1^+ symmetry, transitions from valence bands with Γ_1^+ and Γ_2^+ symmetry are forbidden. Therefore the observed dichroism results from the energy difference between valence bands with Γ_1^- and Γ_2^- symmetry. Furthermore, based on the

different Burstein-Moss shifts with carrier concentration for light polarized parallel to b and c it was deduced that the effective mass of electrons in the conduction band is smaller along the b direction than along c, consistent with the observed difference in conductivity.

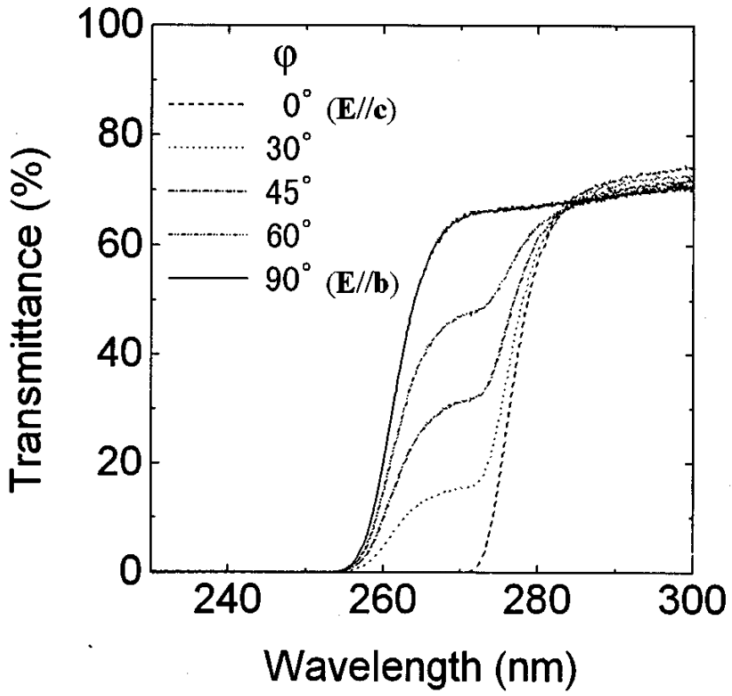

Figure 3.7: Absorption edge of polarized light incident on the (100) face of Ga_2O_3, where the direction of polarization was rotated from the c axis to the b axis. From Ueda et al. [12]

Villora et al. [137] performed a cathodoluminescence study on Ga_2O_3 single crystals grown at different oxygen partial pressures in 2001. The familiar UV, blue and green bands were observed, but blue was resolved into three distinct bands for the first time, and green was dominant in intensity over the blue. The intensities of all luminescence peaks increased with oxygen partial pressure, but green much more quickly than blue. Earlier papers by Harwig et al. showed that the blue luminescence is correlated with infrared absorbance and carrier concentration, and in this study samples grown at different O_2 pressures did not vary much in electrical conductivity, so presumably the increase was attributable to a reduced defect density as the O_2 pressure was increased leading to less non-radiative recombination. The splitting of blue into three distinct bands is attributed to the

existence of two inequivalent cation sites and three inequivalent anion sites in $\beta - Ga_2O_3$, which is consistent with the model of an electron recombining with a trapped hole at an acceptor site. The authors explain that cathodoluminescence is more surface sensitive than photoluminescence due to the smaller penetration depth of the electron beam, and hypothesize that the large green emission is caused by a high surface state density relative to the bulk. An explanation of why the conductivity did not change with O_2 pressure was not given, but in a different paper on the infrared reflectance and conductivity of $\beta - Ga_2O_3$ the same authors found that an increase in carrier concentration was offset by a decrease in mobility as the O_2 pressure is reduced [139].

A photoluminescence study performed in 2002 by Villora et al. [140] examined the luminescence spectra from three single crystals, one grown in 1 atm O_2 pressure, one grown in 2 atm O_2 pressure, and one which was annealed at 900 K in O_2. Although the 2 atm pressure suppressed the evaporation of volatile species from the floating zone and reduced the blue coloration of the crystal, both crystals that were not post-annealed exhibited similar carrier concentrations ($10^{18}\,cm^{-3}$), mobilities ($100\,cm^2/Vs$) and resistivities ($0.1\,\Omega\,cm$). However, the sample which was post-annealed in O_2 had resistivity greater than ($10^6\,\Omega\,cm$) and correspondingly reduced infrared absorption. Absorption spectra show the characteristic shoulder below the band edge observed by Tippins and Ueda. Luminescence emission and excitation spectra were collected for all samples at several wavelengths, to identify which features increase and decrease together. Unlike previous reports, the UV emission band was not sample independent, but decreased with higher oxygen pressure and disappeared completely after post-annealing. The authors therefore attributed the existence of the UV band to recombination between between a trapped hole and an electron, as with the blue emission, with the difference in energy being related to the size of defect clusters. Furthermore, the shoulder below the band edge disappeared in luminescence excitation spectra after post-annealing, an observation which led the authors to conclude that the absorption shoulder cannot be intrinsic to $\beta - Ga_2O_3$. It also cannot be due to oxygen vacancies, as the shoulder remains in the absorption spectra after post annealing. Therefore it is attributed to transitions from a valence band perturbed by Ga^{3+} vacancies, whose concentration is not expected to change upon annealing. It is not clear how this model accounts for the dichroism described in Ueda et al. [12], however. In addition to the disappearance of the 273 nm shoulder, the green emission band increased in intensity after post-annealing. The simultaneous decrease of the UV-emission and increase of the green emission after annealing suggests

that with fewer oxygen vacancies, tunnel recombination between electrons and trapped holes are suppressed and recombination of self-trapped excitons become more likely.

Around this time semi-empirical calculations were being performed to elucidate the origin of conductivity in $\beta - Ga_2O_3$. Hajnal et al. [141] calculated the formation energies of neutral and doubly-charged, but not singly-charged, oxygen vacancies at each of the three oxygen sites in $\beta - Ga_2O_3$. The two defects with the lowest formation energies were the doubly-charged O vacancy on a tetrahedral O_{III} site (connecting two Ga_I and two Ga_{II}), and the neutral vacancy on the three-fold coordinated O_{II} site (connecting two Ga_I and one Ga_{II}). The energy levels were calculated to be 4.2 eV, 4.3 eV, and 2.8 eV above the valence band edge for oxygen sites O_I, O_{II}, and O_{III} respectively. Vacancies on O_I, although theoretically able to contribute to the conductivity at elevated temperatures, were disregarded due to their high formation energy. Therefore it was concluded that conductivity arises from a thermal equilibrium distribution between neutral vacancies on O_{III} and doubly-charged vacancies on O_{II}, with the latter providing free carriers to the crystal. However, on the basis of EPR results Yamaga et al. [142] argued that singly-charged vacancies on O_{III} sites are more likely the origin of free carriers, and furthermore that donor electrons on O_{III} transfer along chains parallel to b through hopping and tunnelling. Hajnal et al. [141] also performed a PM3 semiempirical band structure calculation on a 120 atom supercell, finding again that the conduction band edge is predominantly made up of Ga $4s$ states. However, no considerable difference was predicted between tetrahedral Ga_I and octahedral Ga_{II}, unlike the conclusions of the earlier study by Binet et al. [126]. They also determined that the conduction band edge is made up of extended $ss\sigma$ states of chains of Ga atoms in the b direction, thus explaining the observed optical anisotropy by the structure of the conduction band rather than the valence band, which showed almost negligible dispersion. Based on this result, and the photoluminescence results of Villora et al. [140], Yamaga concluded that (1) the blue photoluminescence excitation bands are due to transitions between the valence band and donor levels, which lie just below the conduction band minimum and probably show similar anisotropy to the conduction band minimum due to preferential vacancy formation; and (2) that donor and acceptor bands overlap in the range 260–280 nm, explaining why the shoulder in absorption spectra persists after post-annealing when the impurity band created by oxygen vacancies is expected to disappear. This second observation is also consistent with the interpretation by Binet and Gourier [123] that the intrinsic quantum wells they observed are formed

by acceptor clusters.

In 2004, a first-principles study using density functional theory (DFT) was carried out by Yamaguchi [143] using the full-potential linearized augmented plane-wave method (FLAPW) within the local density approximation (LDA), to determine the electronic structure of $\beta - Ga_2O_3$ and resolve discrepancies between previous calculations. The calculated band structure is shown in fig. 3.8. Unlike the results of Binet and Ueda, here the conduction band is found to be nearly isotropic, with a minimum at Γ and a small effective mass ($m^* < 0.25m_0$) in all directions. On the other hand, the valence band is found to be relatively flat with a heavy effective mass for holes, with a maximum along the E line which is parallel to b. These results are in qualitative agreement with the band structure calculated by Hajnal et al. [141] and indicate that the anisotropy in the electrical conductivity is not due to the intrinsic structure of $\beta - Ga_2O_3$, but instead caused by vacancy ordering as suggested by Yamaga et al. [142]. However, the optical anisotropy is intrinsic to $\beta - Ga_2O_3$, and results from the symmetry of the valence bands as suggested by Ueda et al. [12]. The difference in energy between valence bands with and without a y-component in their basis functions is approximately 0.7 eV, giving rise to dichroism in the b direction as illustrated on the right-hand side of fig. 3.8. These results are in overall agreement with later DFT calculations using the plane-wave pseudopotential approach within the generalized gradient approximation (GGA) [144], and using the periodic linear combination of atomic orbitals approximation (LCAO) with B3LYP hybrid functionals [145]. However, in the later calculations the maximum in the valence band is located on the Brillouin zone boundary at M, rather than along a line parallel to b connecting to M, and only higher than the valence band at Γ by about 0.03 eV. In addition, the bottom of the conduction band was shown to be made up of $4s$ states from octahedrally-coordinated Ga_{II}, as initially predicted by Binet, with the $4s$ states from Ga_I atoms at 3.28 eV higher energy. The latter reference [145] also contained the first band structure calculations of Ga_2O_3 in the alpha phase, showing similar band structure and dielectric function to $\beta - Ga_2O_3$ but without anisotropy in the onset of absorption, and a calculated band gap of 5.03 eV.

The energetics and migration paths of native point defects and dopants in $\beta - Ga_2O_3$ were investigated theoretically in 2005 by Blanco et al. [146]. Favored locations for interstitials were identified based on minimization of the electron density, lying in one of three distinct channels running parallel to b. Minimization of the structure shows that oxygen interstitials can be accomodated

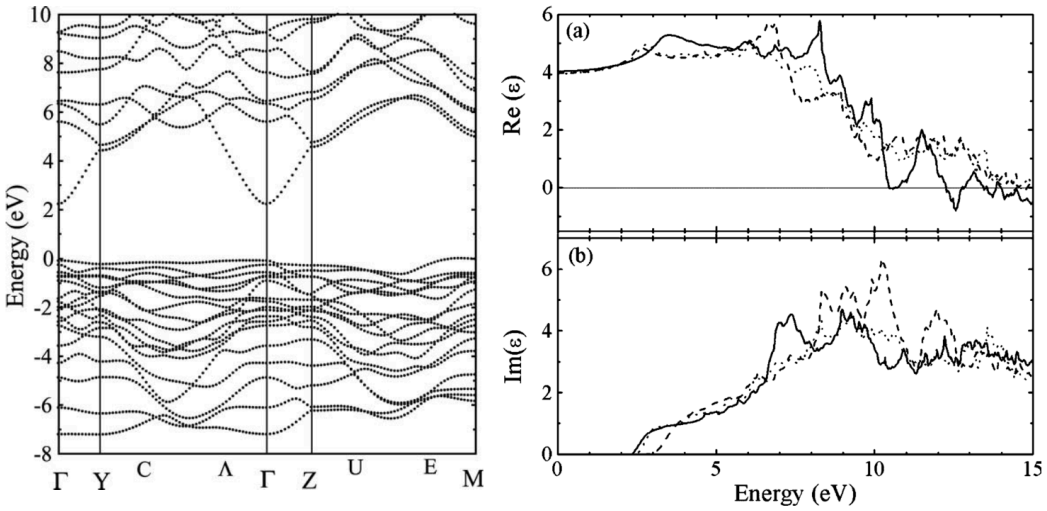

Figure 3.8: Left: Band structure of Ga_2O_3 calculated from first principles using the local density approximation. Right: Calculated real (a) and imaginary (b) parts of the dielectric function. The dotted, broken, and solid lines represent the optical functions via polarized dipoles along the x, y, and z-directions, respectively. From Yamaguchi [143]

in these channels, with the largest channel having the lowest formation energy; however, gallium interstitials cause significant lattice distortion and associated defect complexes. In addition, site preferences for divalent (Be, Mg), trivalent (In, Cr) and tetravalent (Si, Ge, Sn, Zr) substitutional dopants were investigated, for both substitutional and interstitial doping. In all cases except Be, the octahedral site was preferred. The preference for each type of dopant is determined by the size effect, the strength of short range repulsion of surrounding ions, and the coordination index of the original lattice site. As with the case of gallium interstitials, interstitial doping leads to defect complexes including displacements of nearby Ga_I and Ga_{II} from their ideal positions. In general, substitutional doping is found to be energetically favorable.

Progress was being made in the growth of single crystals as substrates for epitaxial deposition. In 2004, Villora et al. [3] demonstrated the float-zone growth of $\beta - Ga_2O_3$ single crystals along all three principal directions, as well as the growth of large-size boules up to 1 in in diameter in the $\langle 100 \rangle$ direction, which could be cut and polished in the (100), (010), and (001) planes to create wafers for subsequent film growth. This allowed, for the first time, the determination of conductivity by the bar method in each of the three directions, which were all found to be similar despite the

crystallographic anisotropy. This was also observed in a more extended study on the electrical properties of Czochralski-grown $\beta-Ga_2O_3$ crystals by Irmscher et al. [147], and is consistent with the isotropic band structure calculated by Yamaguchi (fig. 3.8) and others. However, it contradicts the observation of a 20x higher conductivity measured along the b axis by [12]. In a separate 2004 paper, Villora et al. [148] found that nitridation of single-crystal $\beta-Ga_2O_3$ surfaces under high temperature and NH_3 gas results in the substitution of O by N atoms at the surface and a reconstruction to create six-fold symmetry. In this way, single crystal $\beta - Ga_2O_3$ can be used as a substrate for epitaxial GaN growth with no lattice mismatch. However, in their first paper demonstrating GaN epitaxial growth on Ga_2O_3, nitridation was not performed, but instead a low-temperature (600 °C) GaN buffer layer was deposited before a 1000 nm GaN "epi-layer" at 1070 °C (Shimamura et al. [29]). It was found that the GaN epi-layer was oriented in the $\langle 0001 \rangle$ direction, with a narrow emission spectrum peaking at 326 nm corresponding to the band edge of wurtzite GaN. Nitridation for an extended time to create an epitaxial GaN film was carried out the following year by Ohira et al. [31], and the resulting 50 nm surface layer was characterized using XRD and TEM. It was found that the nitride layer consists of an aggregation of single-crystalline GaN particles ranging from 5 to 50 nm in size, with preferred $(10\bar{1}0)$ and (0001) orientation normal to the $\beta - Ga_2O_3$ (100) surface. Quasi-homoepitaxial GaN deposition on nitridized Ga_2O_3 surfaces without a buffer layer was performed by Villora et al. [30] in 2006 using molecular beam epitaxy (MBE). It was discovered that the substrate preparation depended sensitively on the NH_3 pressure, and needed to be greater than 10^3 Pa for effective nitridation. GaN layers grown on Ga_2O_3 substrates that were insufficiently nitridized took the zinc blende structure, with $\langle 111 \rangle$ oriented normal to the Ga_2O_3 (100) surface; layers grown on sufficiently nitridized substrates were $\langle 0001 \rangle$-oriented wurtzite.

Further work to develop Ga_2O_3 as a substrate for epitaxial growth was carried out by Ohira et al. [149], who published a recipe for achieving an atomically-smooth $\beta - Ga_2O_3$ (100) surfaces using chemical-mechanical polishing followed by a high temperature anneal in an oxygen atmosphere. AFM images reveal a terrace structure, with step heights corresponding to half of the projection of the a axis normal to the (100) plane: $\left(\frac{1}{2}\right) 12.23 \sin(103.83°)$ (fig. 3.9). This result is in accord with a 2006 computational study performed by Bermudez [150] who examined the relaxation of surfaces of $\beta - Ga_2O_3$ single crystals terminated on the (100), (010), (001), and $(10\bar{1})$ planes. The two lowest energy surfaces were both in the (100) plane, explaining the tendency of $\beta - Ga_2O_3$

single crystals to cleave in this direction. The lowest energy surface, denoted "B", is terminated in nearest-neighbor rows of Ga_{II} and O_{III} atoms. The second-lowest energy surface, denoted "A", is terminated in rows of O_{II} lying in the [010] direction (shown in red in fig. 3.1). Two A surfaces and two B surfaces exist per unit cell, which explains the terrace structure observed by Ohira et al. In both A and B terminations, one O and one Ga_{II} site is left with an unsaturated bond; Ga_I and O_I are never unsaturated. These theoretical predictions were tested experimentally in our group by Lovejoy et al. [151] in 2009 by atomically-resolved LEED and STM measurements. After cleaving on the (100) plane, $\beta - Ga_2O_3$ single crystals were inserted into ultrahigh vacuum and annealed at high temperature (800–1000 °C) by direct current to improve the surface order. In these samples, as in Ohira et al. [149], step heights of 5.9 Å corresponding to half of $a \sin \beta$ were found, though at some edges smaller steps of 1.5 Å and 4.4 Å were also observed. Based on the relative step heights and the relative distances of the A and B planes it was determined that the predominant surface termination is B-type, and that A-terminated surfaces only appear at step edges. This confirms the theoretical prediction by Bermudez [150]. An unrelated but interesting observation by the same authors was that undoped $\beta - Ga_2O_3$ single crystals became insulating after prolonged annealing in ultrahigh vacuum, in apparent contradiction to the oxygen-vacancy model of electronic conduction in $\beta - Ga_2O_3$.

Experiments in doping $\beta - Ga_2O_3$ single crystals with extrinsic impurities were beginning in 2006, in an effort to improve their conductivity. Zhang et al. grew nominally undoped [152] and 5 mol % and 10 mol % Sn-doped [153] single crystals using the float zone method and characterized their electronic and optical properties. In 2007, 2–10 mol % Sn-doped $\beta - Ga_2O_3$ crystals were grown by Suzuki et al. [15]. Both groups observed significant evaporation of SnO_2 during growth leading to drastically reduced Sn content in the resulting crystals, on the order of 0.1 mol % (Zhang) to 0.01 mol % (Suzuki). Deteriorating crystal quality, as indicated by X-ray rocking curve measurements, was measured with increasing Sn content; however, no secondary phases were observed in XRD by either group. Hall measurements by Suzuki et al. indicated that for an Sn concentration of 45 ppm, the conductivity increased by a full order of magnitude (the mobility decreased by a factor of two, and the carrier density increased by a factor of 20) relative to the nominally undoped crystal. IR absorption increases with Sn content indicating the presence of free carriers, and no change was observed in the position of the absorption edge. An experiment the following year by the

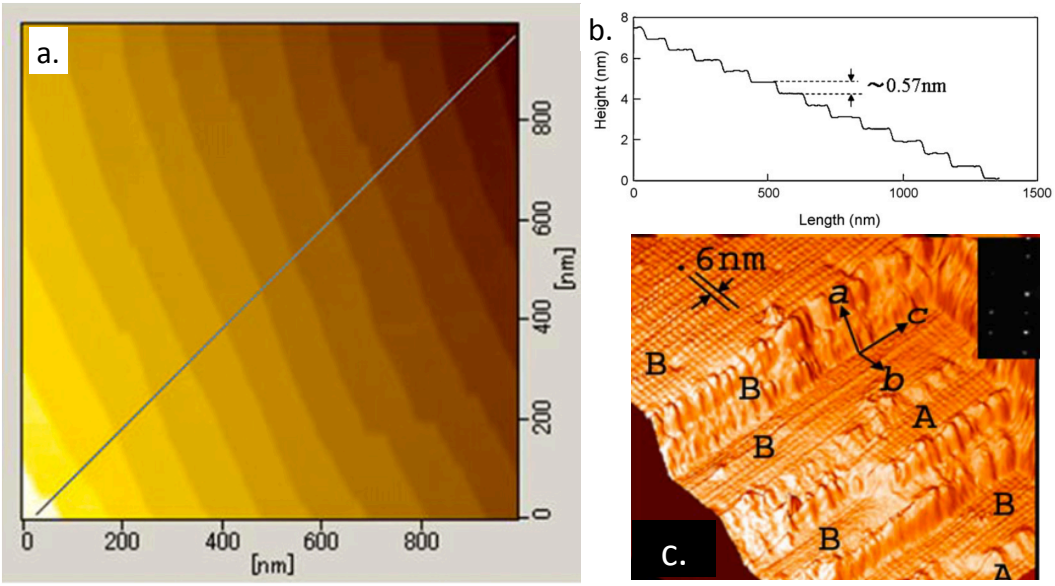

Figure 3.9: a) AFM image of an atomically smooth $\beta - Ga_2O_3$ surface after chemical-mechanical polishing and annealing in oxygen at 1100 °C for 6 h. The terrace structure results from a small misorientation when cutting the wafer along the (100) plane. b) Step height along the blue line shown in a. From Ohira et al. [149] c) Atomically-resolved STM image showing terrace structure of cleaved $\beta - Ga_2O_3$ (100) surface after vacuum annealing. Two surface terminations denoted by "A" and "B" are indicated. From Lovejoy et al. [151]

same group (Ohira et al. [154]) was carried out to investigate the stability of Sn-doped $\beta - Ga_2O_3$ single crystals upon annealing at 1100 °C in O_2. It was found that surface morphology, roughness, electrical, and optical characteristics of as-grown crystals did not change as a result of annealing. However, segregation of Sn-atoms to the surface was evidenced by SIMS depth profiling, leading to intensification and shifting of the cathodoluminescence emission band to longer wavelength.

Si-doping of $\beta - Ga_2O_3$ single crystals was carried out by Vllora et al. [13] in 2008. It was found that Si incorporates up to a maximum concentration of about 0.2 mol % before phase segregation occurs, and that within that range the conductivity varies over three orders of magnitude, from $0.03\,\Omega^{-1}\,cm^{-1}$ for 99.9999 %-pure undoped crystals up to $50\,\Omega^{-1}\,cm^{-1}$ with the maximum Si doping. Furthermore, Hall measurements showed almost no change in the mobility of free carriers after Si incorporation. Comparing the free carrier concentration to the concentration of Si impurities revealed that only 25 % to 50 % of Si impurities contributed donors to the conduction band; this

observation is explained by assuming a distribution of Si over Ga_I and Ga_{II} sites, with only one site giving donors to the bulk. The observation that conductivity depends sensitively on the Si doping level, in combination with the fact that Si constitutes the main impurity in commercial Ga_2O_3 powder at levels comparable to the intentional doping in this study, suggests that the main source of conductivity in nominally-undoped $\beta - Ga_2O_3$ in the literature is probably due to unintentional Si impurities rather than oxygen vacancies which had been previously assumed. In a separate paper, the same group (Shimamura et al. [155]) also reported the absorption and luminescence properties of undoped and Si-doped (0.1 mol %) single crystals. A blue shift in the absorption edge is observed with Si doping which is probably due to the Burstein-Moss effect. An overall decrease in luminescence intensity is observed due to the increase in non-radiative recombination centers, and a further decrease in the blue emission band is attributed to a proportional decrease in oxygen vacancies with Si doping, which is necessary to maintain charge neutrality. This model suggests that the blue emission is due to the recombination of trapped electrons on donor sites with trapped holes on acceptor sites, which is consistent with earlier luminescence measurements showing a correlation between oxygen vacancies and blue luminescence intensity. A shift to longer wavelength and broadening of the blue emission band, coupled with an observation of absorption sub-bands in the excitation spectrum of the Si-doped sample suggest that the lower concentration of oxygen vacancies leads to an increase in the number of unpaired acceptor clusters with states just above the valence band maximum. The UV emission band is independent of Si concentration and is attributed to the recombination of self-trapped excitons, in agreement with conclusions by earlier authors.

An updated electronic structure calculation was performed in 2009 for $\beta - Ga_2O_3$ and $\alpha - Ga_2O_3$ by Litimein et al. [156] using the FLAPW method within the local density approximation. In general, quite good agreement was obtained with Yamaguchi [143] and He et al. [145], and origins of prominent features in the imaginary part of the dielectric function were given. Several basic DFT studies were carried out by various authors examining the effects of charged impurities on the electronic structure of Ga_2O_3 following the increasing experimental interest in doped single crystals and thin films, including Sn [157], Zn [158] and Cu [159]. In addition, experimental data on the band structure of Ga_2O_3 based on angle-resolved photoemission spectroscopy (ARPES) was becoming available to compare with theory. Figure 3.10 shows a comparison between experimental

band structures measured at synchrotron facilities by Lovejoy et al. [151] and Mohamed et al. [160]. The data by Lovejoy is overlaid on top of calculated structure from Yamaguchi [143], which was calculated using the FLAPW method in the local density approximation, whereas the newer data was overlaid with a calculation by the same group using projector-augmented wave (PAW) potentials and a HSE hybrid functional. The calculated band structures appear quite similar in all directions. A significant difference in the relative intensities of different bands exists between the two experiments, due to the higher photon energy employed by Lovejoy than Mohamed. Close agreement between measured and calculated band structures at Γ and along the c^* direction was obtained in both studies, but along b^* Lovejoy found more dispersion in the experimental band structure than predicted by theory. However, a similar discrepancy does not appear in the data by Mohamed.

After the discovery that conductivity is controlled by unintentional Si doping rather than by oxygen vacancies [13], Varley et al. [125] published a DFT study calculating formation energies and energy levels of gap states arising from several types of impurities, based on the PAW method with the HSE06 hybrid functional. It was found that oxygen vacancies form a defect level more than 1 eV below the conduction band minimum and therefore act as deep donors, incapable of contributing to the n-type conductivity. However, hydrogen impurities incorporated either substitutionally or interstitially form shallow donors; in addition, interstitial hydrogen has a low formation energy in both O-rich and O-poor conditions (substitutional hydrogen is only favorable in O-poor conditions). If hydrogen is unintentionally incorporated in Ga_2O_3 during growth, an increase in the resistivity would still be observed upon annealing in an oxygen atmosphere, and would also be observed upon annealing in vacuum in accordance with the observations of Lovejoy et al. [151]. Their calculations also show that Si, Ge, Sn, F, and Cl all act as shallow donors and are readily incorporated in $\beta - Ga_2O_3$. A second paper by the same group showed that cation vacancies have low formation energies and exist in appreciable concentrations in $\beta - Ga_2O_3$, acting as compensating acceptors and increasing the resistivity [162]. They proposed that the resistivity increases after annealing in oxygen due to the formation of Ga vacancies, rather than by the reduction in O vacancies. Hydrogenated vacancies (Ga vacancies bound to interstitial hydrogen) act as deep acceptors and have an even lower formation energy than isolated vacancies alone, remaining stable up to 730–1000 °C.

DFT studies by other authors investigating the role of point defects soon followed. Zhang et al.

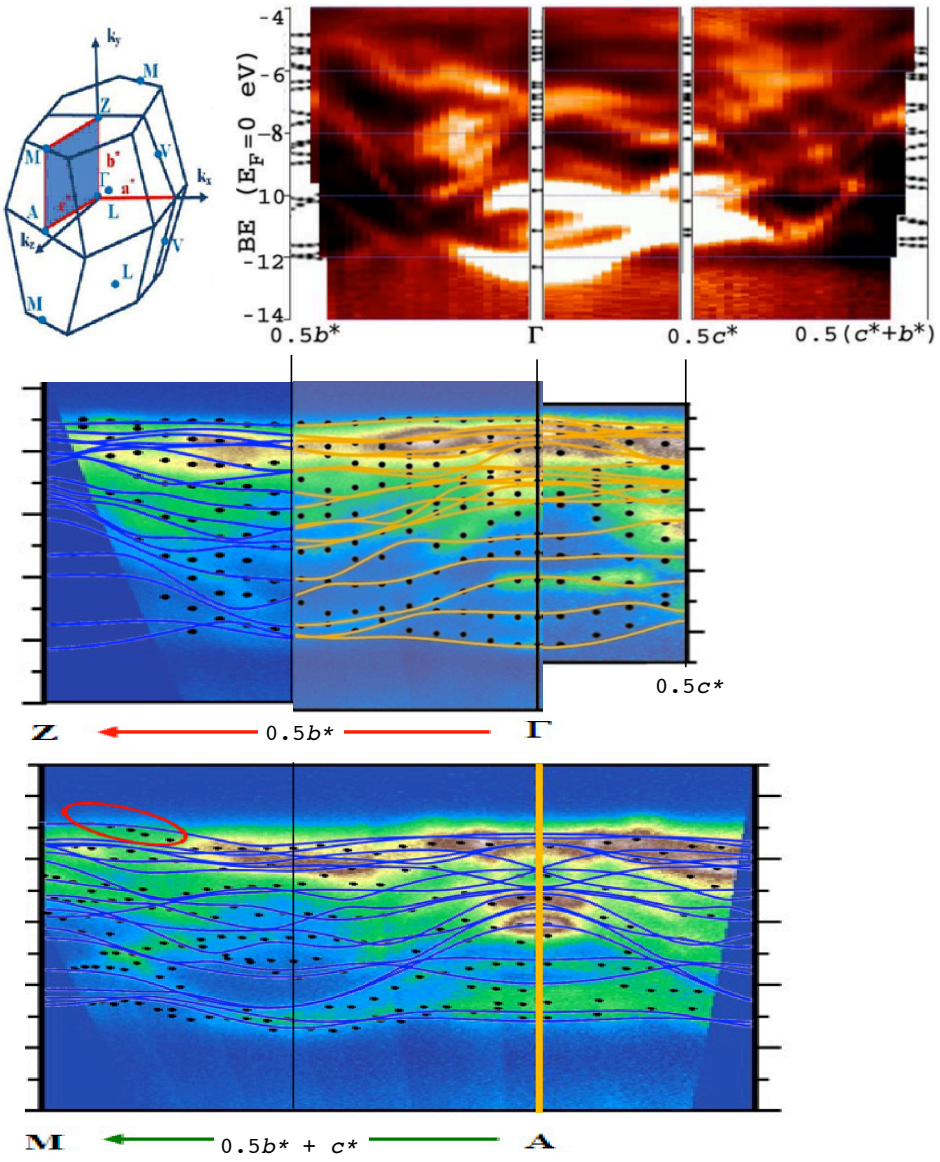

Figure 3.10: Top (red): Experimental valence band structure from Lovejoy et al. [151], overlaid on top of the calculated band structure from Yamaguchi [143]. Bottom (blue): Experimental valence band structures from Mohamed et al. [160] and Janowitz et al. [161], overlaid with a theoretical band structure calculated by the same authors using hybrid functionals (solid lines). Black dots show experimental band locations derived from a fit procedure. The Brillouin zone of $\beta - Ga_2O_3$ is shown in the upper left. Original figures have been stretched to a uniform scale for comparison.

investgated the role of N doping on anion sites [163], and N-Zn co-doping on anion and cation sites [164] to form p-type Ga_2O_3. Calculations were performed using ultra-soft pseudopotentials, a plane-wave basis set and the generalized gradient approximation (GGA) to describe exchange-correlation interactions. For N doping alone, deep acceptor levels are formed at 0.7 eV above the VBM for 1 at.% N, and at 0.6 eV above the VBM for 2 at.% N; however, for 1 at.% N + 1 at.% Zn doped Ga_2O_3 two impurity levels were found, one at 0.483 eV and the other at 0.149 eV above the VBM, a significant improvement, although in both calculations the band gap is severely underestimated and the true acceptor levels may lie deeper. Finite-size-corrected formation energies and entropies of intrinsic point defects in $\beta - Ga_2O_3$ were investigated by Zacherle et al. [165] using both PBE functionals within the GGA (as in Zhang et al.) and also using HSE06 hybrid functionals (as in Varley et al.) which are known to give a more accurate band gap result. Their result for formation energies of O vacancies as the Fermi level varies within the gap is in good agreement with Varley et al. [125] in both O-rich and O-poor conditions, and the variation in formation energies of other intrinsic defects is also shown. Equilibrium defect concentrations were computed based on the Gibbs free energy, taking into account both formation energies and entropies at finite temperature, and found to be very low (10^{13}–$10^{14}\,cm^{-3}$), yielding a carrier concentration dependence $\sigma \sim pO_2^{-1/6}$ in contradiction with experimental studies. Such a low equilibrium intrinsic defect concentration in Ga_2O_3 explains why the measured conductivity is so sensitive to unintentional extrinsic dopants; repeating the calculation but including a typical donor concentration of $10^{18}\,cm^{-3}$ reproduces the correct experimental dependence $\sigma \sim pO_2^{-1/4}$. At O_2 partial pressures greater than 10^{-9} bar, V_{Ga} are the dominant compensating acceptors for extrinsic impurities. Carbon impurities have also been investigated in Ga_2O_3 and found to be shallow donors, and in addition C_{Ga} is found to have a lower formation energy than Sn, Si, Ge, and interstitial hydrogen in O-rich conditions Lyons et al. [166]. A DFT study on non-metallic doping at oxygen-sites in $\beta - Ga_2O_3$ was carried out recently by Guo et al. [167], investigating C, N, F, Si, P, S, Cl, Se, Br, and I using both PBE functionals within the GGA, and HSE06 functionals. Formation energies are computed at each oxygen site, and their effect on the band gap is summarized in fig. 3.11. It was also shown that doping with C, Si, and P leads to deep levels within the gap.

Experimental evidence for interstitial hydrogen acting as a shallow donor was provided by King et al. [168], who actually showed by muon-spin rotation and relaxation spectroscopy that

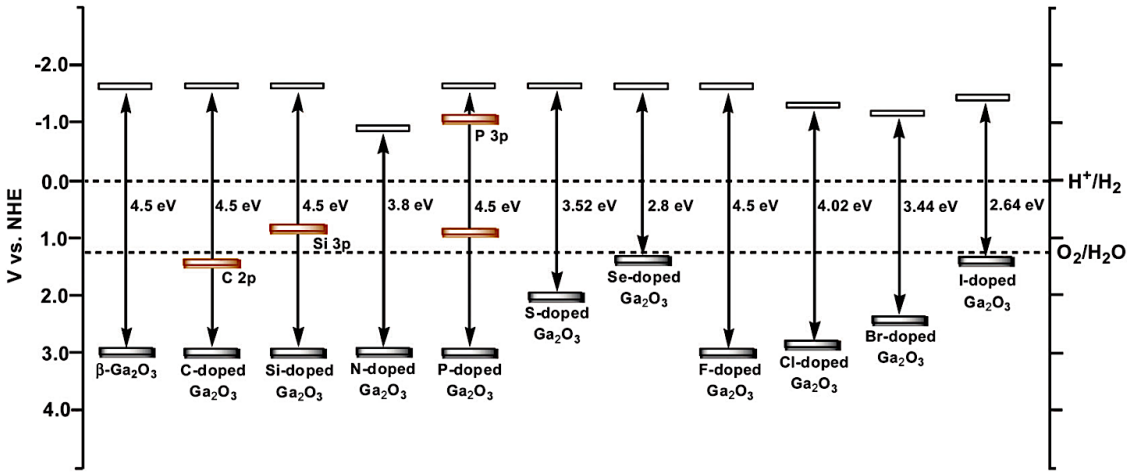

Figure 3.11: Band gap of $\beta - Ga_2O_3$ doped with several non-metallic impurities on anion sites, relative to the undoped crystal at left. From Guo et al. [167]

.

muonium acts as a shallow donor approximately 15–30 meV below the conduction band minimum. As explained by King, defect levels for muonium are expected to be the same as those for hydrogen except for small corrections due to the zero point energy. This result agrees with the electrical characterization by Irmscher et al. [147], who measured carrier concentrations for several undoped samples over a wide range of temperatures and deduced that the donor state ionization energy varies from 36 meV for a donor concentration of zero, to an energy of 16 meV for a donor concentration of $10^{18}\,\mathrm{cm}^{-3}$. Using deep-level transient spectroscopy, trap states at 0.55 ± 0.03 eV, 0.74 ± 0.03 eV, and 1.04 ± 0.03 eV below the conduction band minimum were also detected, but this type of measurement did not allow for an identification of their origin.

Direct observation of silicon donors at the $\beta - Ga_2O_3$ surface by STM was reported by Iwaya et al. [169] on a single crystal grown by the edge-fed film growth method [170] and doped to an Si concentration of $10^{19}\,\mathrm{cm}^{-3}$. Silicon atoms up to four layers below the surface were detected in a 30×30 nm window, and their density was in excellent agreement with the nominal value. Furthermore, conductance maps were recorded at a fixed substrate voltage set to coincide with Si features in the dI/dV spectrum, and line profiles were measured through the center of donor impurities and fit to hydrogenic wave functions. It was found that the fitted decay length was slightly

higher for impurities in the top-most layer, but remained relatively constant in layers 2–4; in addition, the Mott criterion $n_c^{1/3} a_B^* = 0.26$ [121] with $n_c = 1 \times 10^{-19}\,\mathrm{cm}^{-3}$ predicts a Bohr radius of 1.2 nm, in perfect agreement with the decay length measured for Si impurities located below the first layer. Momentum-space localization of Si-donor states was also reported by Richard et al. [171]. A weak, two-peak structure was observed at $18 \pm 3\,\mathrm{meV}$ and $120 \pm 9\,\mathrm{meV}$ below the Fermi level (1000x less intense than valence band features) by photoemission spectroscopy on Si-doped $\beta - Ga_2O_3$ samples from the same batch as Iwaya et al. [169]. Dispersion in x and y was characterized by angle-resolved measurements, and dispersion in z by varying the incident photon energy. Peak intensities fell off quickly as the angle was varied away from normal indicating strong localization of defect states at the Brillouin zone center, although the deeper state persisted slightly longer. In addition no shift in the energy was observed as the angle was varied, indicating a lack of dispersion. At low temperature ($T = 10\,\mathrm{K}$), a smaller third peak $220 \pm 20\,\mathrm{meV}$ below E_F could also be resolved. Based on the roughly equal spacing in energy, and the simultaneous localization in real- and momentum-space of the donor states, a quantum-well donor structure was proposed. From angle-resolved measurements it was determined that the momentum space localization is approximately $0.05\,\mathrm{Å}^{-1}$; therefore the uncertainty principle predicts a real-space localization on the order of $\Delta r = 1/\Delta k = 20\,\mathrm{Å}$, in close agreement with the spatial extent of Si donors reported by Iwaya et al.

Cathodoluminescence experiments on nominally undoped (001), Si-doped (conducting) (100), and Mg-doped (insulating) (010) $\beta - Ga_2O_3$ single crystals was carried out over a wide range of temperatures in 2013 by Onuma et al. [172]. The UV-luminescence was found to be independent of dopant and attributed to the recombination of electrons and self-trapped holes, as reported by previous authors [117], and not band-edge recombination by excitons. This interpretation found convincing theoretical support in a DFT study the following year by Varley et al. [173], who predicted luminescence at almost exactly the same wavelenth by that mechanism, finding also that it is especially energetically favorable in Ga_2O_3 relative to other TCOs. In the study by Onuma, the blue emission band became brighter as resistivity increased, in the order Si-doped $\rightarrow$ undoped $\rightarrow$ Mg-doped, and was attributed to recombination at deep donors and acceptors, respectively. Correlation between O vacancy concentration and blue luminescence has been observed before, but at the time O vacancies were thought to contribute to free carriers. The DFT calculation by Varley et al. [125] showing that O vacancies are deep donors provides a different explanation: as

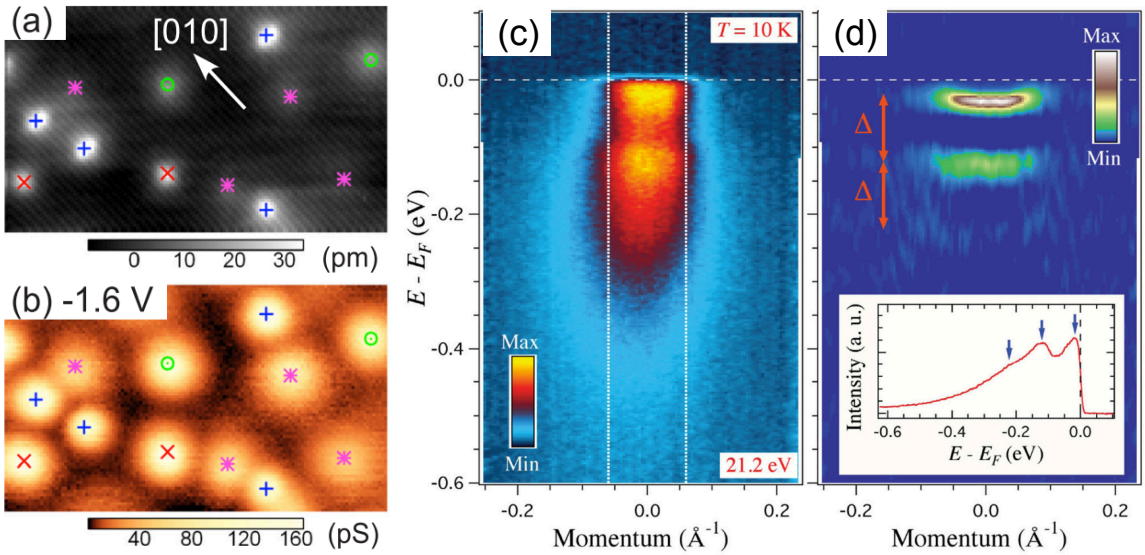

Figure 3.12: Left: Localization of Si-impurities in real-space, from Iwaya et al. [169]. a) STM image of a $30 \times 17\,\text{nm}$ area at $V_s = -1.6\,\text{V}$. b) Corresponding conductance map. Right: Localization of Si-impurity donor states in momentum-space, from Richard et al. [171]. c) Photoemission intensity from ARPES. d) Corresponding curvature plot. (Inset: integrated density of states between the white dotted lines in c.)

the resistivity increases, and the Fermi level moves deeper into the gap toward the valence band, the formation energy of O vacancies is lowered, and recombination between electrons trapped at O vacancies and deep acceptors such as V_{Ga}, V_O–V_{Ga} complexes, or Mg_{Ga} is enhanced.

Amid mounting experimental and theoretical evidence that O vacancies form deep donors in $\beta - Ga_2O_3$, the question arises of how Ga_2O_3 has been so successful in oxygen-sensing applications. The answer may be related to upward surface band bending, as observed by Lovejoy et al. [174] and Navarro-Quezada et al. [175] who performed XPS on nominally undoped $\beta - Ga_2O_3$ single crystals. Lovejoy et al. [174] obseved nearly-flat bands in highly-doped single crystals, but upward band bending by at least 0.5 eV in undoped crystals which increased by a further 0.15 eV after vacuum annealing. A model was proposed in which negatively-charged surface defects give rise to an extended depletion layer in undoped crystals, and in fact such defects were observed in STM empty state images. DFT calculations show that a steep band bending could lead to the freeing of electrons from energetically favorable neutral O vacancies near the surface, thus increasing surface

conductivity.

A theoretical explanation of why the monoclinic structure is stable in Ga_2O_3, but not in Al_2O_3 or In_2O_3 was recently provided by Sabino et al. [176]. In general, smaller cations favor the corundum structure, whereas larger cations favor the bixbyite structure; however, the monoclinic $\beta - Ga_2O_3$ structure becomes more stable with increasing hybridization between Ga $3d$ and O $2s$ states, which is maximized in the presence of tetrahedral sites. Of the three structures considered, only the monoclinic $\beta - Ga_2O_3$ structure contains four-fold symmetric cation sites, which explains its stability in Ga_2O_3. Hybridization between Ga $3d$ and O $2s$ has in fact been observed in XPS in this work and by Navarro-Quezada et al. [175], Petitmangin et al. [177], due to the small energy separation between those two orbitals.

A new band structure calculation was carried out this year by Peelaers and Van de Walle [51], who noticed that previous calculations of the band structure were based on the conventional unit cell of $\beta - Ga_2O_3$, which is larger than the primitive unit cell of $\beta - Ga_2O_3$, and therefore did not span the full range of the Brillouin zone. The HSE06 hybrid functional was used with a plane wave basis set to achieve an accurate band gap, and the result is shown in fig. 3.13. The calculated band gap is indirect with a value of 4.84 eV with a minimum in the conduction band at Γ and a maximum in the valence band along the $I - L$ line on the surface of the Brillouin zone. However, the direct gap at the zone center is only 0.04 eV larger at 4.84 eV. The effective mass of electrons is almost isotropic with values between 0.27–0.28 eV depending on the direction, in agreement with previous band structure calculations. Peelaers et al. [178] also used DFT to investigate $(In_xGa_{1-x})_2O_3$ alloys, to determine the limits of structural stability of the monoclinic and bixbyite phases, and to predict the change in band gap with alloy parameter x. Linear decrease in the optical band gap was predicted with alloy composition in the monoclinic structure, in agreement with experimental data, with a maximum indium solubility of 50 at.%. A different theoretical study by Maccioni et al. [179] found a maximum solubility limit of just 10 %, based on a 1.1 eV higher formation energy of In_{GaI} compared to In_{GaII} and a thermal equilibrium occupation of just 3/16 over the remaining octahedral sites. Bulk powder growth has achieved single-phase incorporation up to $x = 0.43$, while alloy thin films have had lower limits ($0.1 < x < 0.2$, as shown in the next section), so the true limit appears to lie in between the two theoretical studies. Finally, in a third paper this year, Varley and Schleife [180] computed absorption spectra for both Ga_2O_3 and In_2O_3 within the Bethe-Salpeter framework.

The imaginary part of the dielectric function is shown in fig. 3.14. Strong biaxial anisotropy was observed, with the lowest gap for light polarized parallel to the c-axis, a slightly larger gap for light polarized parallel to the a-axis, and a much larger value gap for light polarized parallel to the b-axis, in agreement with the calculations by Yamaguchi [143]. When excitonic effects are included the gap is reduced by 0.5 eV in all directions, but with different structure in b than the other two.

Finally, in addition to fundamental investigations there have been a number of studies focused on developing single-crystal $\beta - Ga_2O_3$-based devices. Solar-blind Schottky photodetectors fabricated by evaporating Au contacts on $\beta - Ga_2O_3$ crystals have been demonstrated by [21] and [181]. Schottky-barrier diodes (SBDs) were fabricated by evaporating metal contacts on $\beta - Ga_2O_3$ crystals (Sasaki et al. [182]), and on Sn-doped homoepitaxial $\beta - Ga_2O_3$ thin films Sasaki et al. [183]. Metal-semiconductor field-effect transistors (MESFETs) have been demonstrated using Sn-doped homoepitaxial films Higashiwaki et al. [35], Sasaki et al. [36, 183]. Sasaki et al. also demonstrated the formation of an Ohmic contact to $\beta - Ga_2O_3$ by Si-ion implantation [184], taking advantage of the lower band bending in heavily doped samples observed by Lovejoy et al. [174]. Using ion-implantation, depletion mode metal-oxide-semiconductor field-effect-transistors (MOSFETs) were fabricated on Sn-doped homoepitaxial Ga_2O_3 films on insulating Fe-doped $\beta - Ga_2O_3$ substrates (Higashiwaki et al. [37]). These devices all had extremely low drain leakage, leading to a high drain-current on/off ratios (10^4 for MESFETs, and 10^10 for MOSFETs) and breakdown voltages (125–150 V for SBDs, 250 V for MESFETs, and 370 V for MOSFETs). In addition, stable operatation for MOSFETs was shown up to 250 °C, demonstrating the potential usefulness of Ga_2O_3 for power electronics.

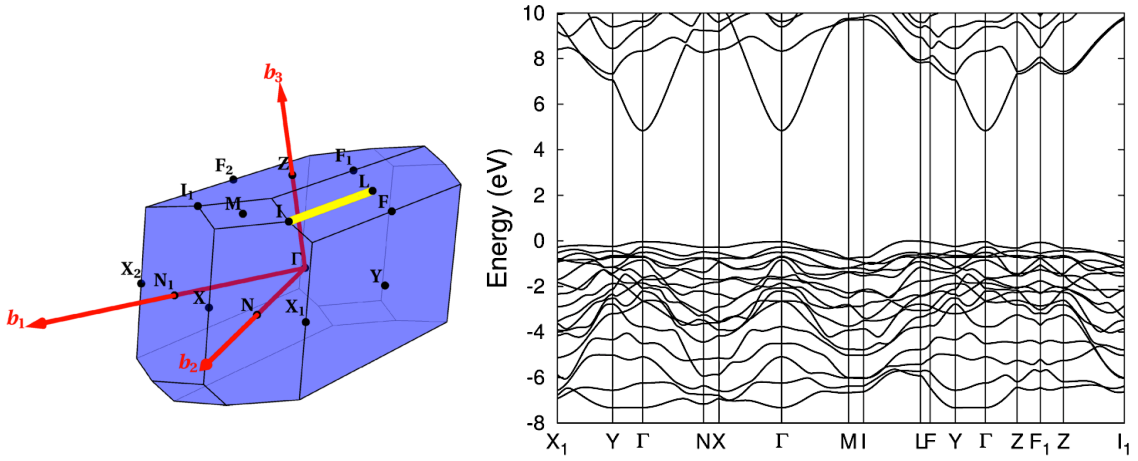

Figure 3.13: Left: Full Brilluoin zone calculated from the primitive cell of $\beta - Ga_2O_3$. Right: Corresponding band structure. From Peelaers and Van de Walle [51].

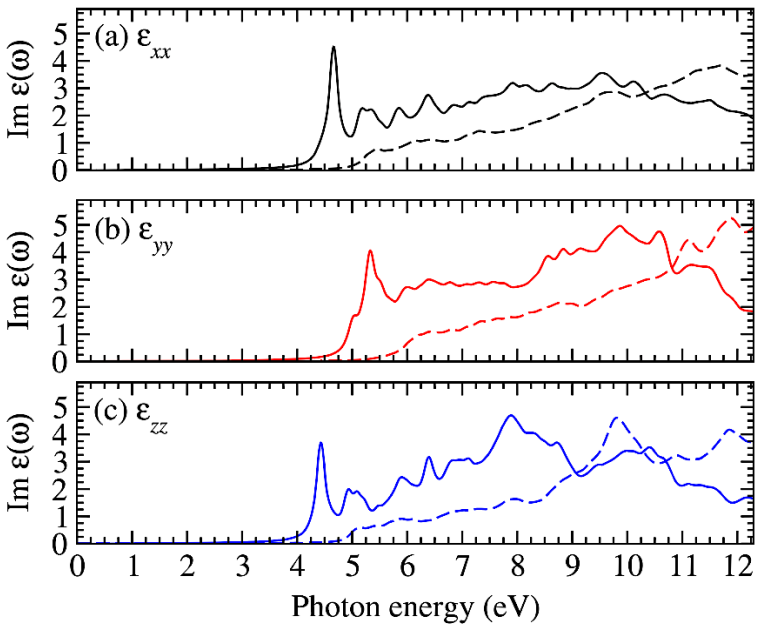

Figure 3.14: Calculated imaginary part of the dielectric function of $\beta - Ga_2O_3$ within the Bethe-Salpeter framework for light polarized along each of the three crystallographic axes. From Varley and Schleife [180].

3.2.3 Thin Films and Alloys

Unlike single crystals, thin films often contain numerous randomly-oriented grains, high defect concentrations, non-uniform surface morphology, poor crystallinity, substrate-related effects, and other non-idealities depending on the preparation method. Therefore the study of high-quality single crystals in combination with theoretical calculations is critical to achieve a working understanding of many of the fundamental material properties of Ga_2O_3. However, the study of thin films offers a number of different advantages. Only a few reliable growth techniques are available for the preparation of single crystals, whereas a great multitude exist for the deposition of thin films. This offers a great deal of flexibility to fabricate films in metastable phases, or in the amorphous phase, in addition to the stable phase, and to study their properties and phase transformation mechanisms. Furthermore, it is often quite easy to blend materials together in a thin film, e.g. to increase or change the type of conductivity through doping, to study the luminescence characteristics of transition metals or rare-earth phosphors, or to investigate new alloy systems for efficient combinatorial materials exploration. These investigations are more difficult to carry out with bulk samples, which must be prepared individually for every doping level and alloy concentration to be studied, and in the case of single crystals may contain dramatically different impurity concentrations than the melt due to differences in evaporation rates (e.g. in the case of Sn-doped Ga_2O_3 [15] or Si-doped Ga_2O_3 [13]).

Thin films of intrinsic and doped Ga_2O_3 have been prepared by a great variety of physical and chemical deposition methods (table 3.1). Many reports of this nature follow a common pattern: "Thin film *a* was prepared on substrate *b* using technique *c* and subsequently characterized by *d*, and here are the data." Therefore to avoid becoming repetitive this part of the review is organized by topic (i.e. homoepitaxy, heteroepitaxy, impurity-doping, Ga_2O_3-based alloys, etc.), summarizing common findings from multiple studies under each heading rather than covering every report in detail.

Table 3.1: Thin film deposition techniques used to prepare Ga_2O_3 films, organized by research group.

Method	References
Electron-beam evaporation	Hong et al. [32], Passlack et al. [134, 135]
	Al-Kuhaili et al. [185]
	Nakagomi and Kokubun [186, 187], Nakagomi et al. [188]
	Dakhel [189, 190]
	Cheng et al. [191, 192, 193]
	Rao and Kumar [194]
Radio-frequency sputtering	Fleischer et al. [132]
	Ogita [195]
	Miyata et al. [34, 196], Minami et al. [197]
	Kim and Holloway [198]
	Takakura et al. [199, 200]
	Takeuchi et al. [201]
	Zhang et al. [202, 203]
	Kumar et al. [204], Rubio and Ramana [205], Ramana et al. [206]
	Sun et al. [207]
	Kang [208]
Molecular beam epitaxy	Villora et al. [30], Vllora et al. [209]
	Sasaki et al. [183], Oshima et al. [210, 211]
	Tsai et al. [212], Kaun et al. [213]
	Sasaki et al. [36], Okumura et al. [214]
Pulsed laser deposition	Orita et al. [16, 17, 215], Ohta et al. [216]
	Matsuzaki et al. [217, 218]
	Li et al. [219]
	Lam et al. [220]
	Gollakota et al. [221]
	Huang et al. [222], Hayashi et al. [223]
	Petitmangin et al. [224]
	Ou et al. [225]
	Wang et al. [226]
	Oshima et al. [19]
Atomic layer deposition	Nieminen et al. [227]
	Shan et al. [228]
	Altuntas et al. [229]
Metal-organic chemical vapor deposition (CVD)	Battiston et al. [230]
	Mîinea et al. [231]
	Kim et al. [232], Kim and Kim [233]
	Binions et al. [234]
	Gottschalch et al. [235]
	Kong et al. [236], Mi et al. [237, 238, 239, 240]
	Du et al. [241, 242], Feng et al. [243]
	Guo et al. [25], Chen et al. [244]
	Gogova et al. [245], Wagner et al. [246], Korhonen et al. [247]
Ultrasonic mist CVD	Shinohara and Fujita [248]
	Oshima et al. [249]
	Cusco et al. [250]
Halide vapor phase epitaxy	Oshima et al. [251]
	Murakami et al. [252]
Spray pyrolysis	Kim and Kim [129]
	Wu et al. [130]
	Ortiz et al. [253]
	Hao and Cocivera [254]
	Ji et al. [23]
	Thomas et al. [255]
Sol gel, solution deposition	Minami et al. [256]
	Sinha et al. [58, 257]
	Kokubun et al. [24]
	Ohya et al. [258]

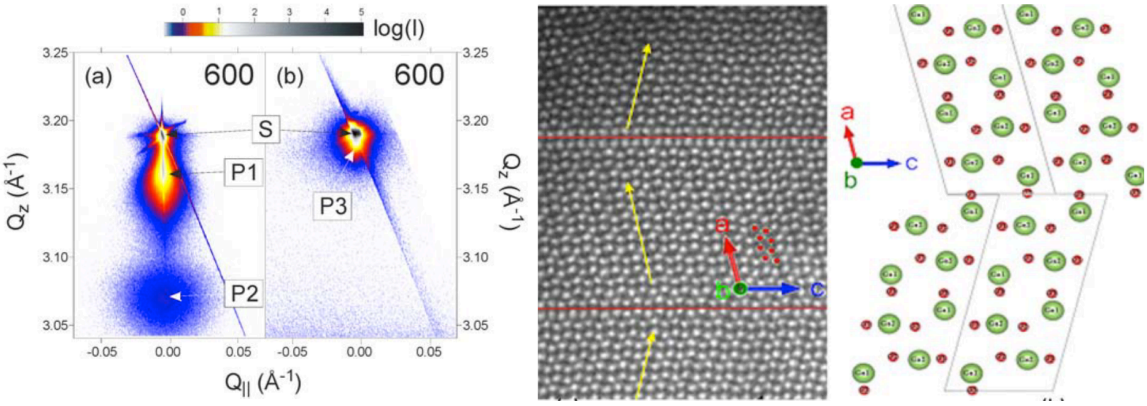

Figure 3.15: Left: Reciprocal space XRD of as-grown (a) and post-annealed (b) homoepitaxial Ga_2O_3 films. In addition to the substrate S, the as-grown films show additional reflections P1 and P2, arising from defects. Right: Cross-sectional TEM image showing twinning on the (100) plane of homoepitaxial films. From Wagner et al. [246]

.

Homoepitaxy of $\beta - Ga_2O_3$ and $\beta - (Al_xGa_{1-x})_2O_3$ Films

For a long time only a few groups had access to single-crystal $\beta - Ga_2O_3$ to deposit films on, but the situation changed recently as Czochralski-grown $\beta - Ga_2O_3$ wafers can now be purchased commercially in (100), (010), or (001) orientations. Intrinsic Ga_2O_3 homoepitaxial films have been grown by molecular beam epitaxy (MBE) [209, 211, 212, 214], megal-organic chemical vapor deposition (MOCVD or MOVPE) [241, 245–247] and halide vapor-phase epitaxy (HVPE) [252]; Sn-doped films have been grown by MBE [183, 214, 259] and MOCVD [242]; and Si-doped films have been grown by MOCVD [245]. Band gaps for intrinsic homoepitaxial films were 4.70 ± 0.03 eV [241], while Sn-doping decreased the band gap from 4.66 eV (1 %) to 4.16 eV (10 %) [242]. Evidence of vertical stacking faults and twinning were observed in 700–800 °C MOVPE-grown epitaxial films, which healed upon annealing at 950 °C for 1 hr in oxygen (fig. 3.15); similar defects were not observed in HVPE growth at 1000 °C [252]. In general faster growth is achieved in the [010] direction than either the [100] or [001] directions [183], and the growth mode depends on the degree of miscut of the $\beta - Ga_2O_3$ substrate [212, 214]. As the growth temperature increases, surface roughness becomes more severe due to step bunching (fig. 3.16).

$(Al_xGa_{1-x})_2O_3$ layers were grown at 800 °C on (100)-oriented $\beta - Ga_2O_3$ substrates by Oshima

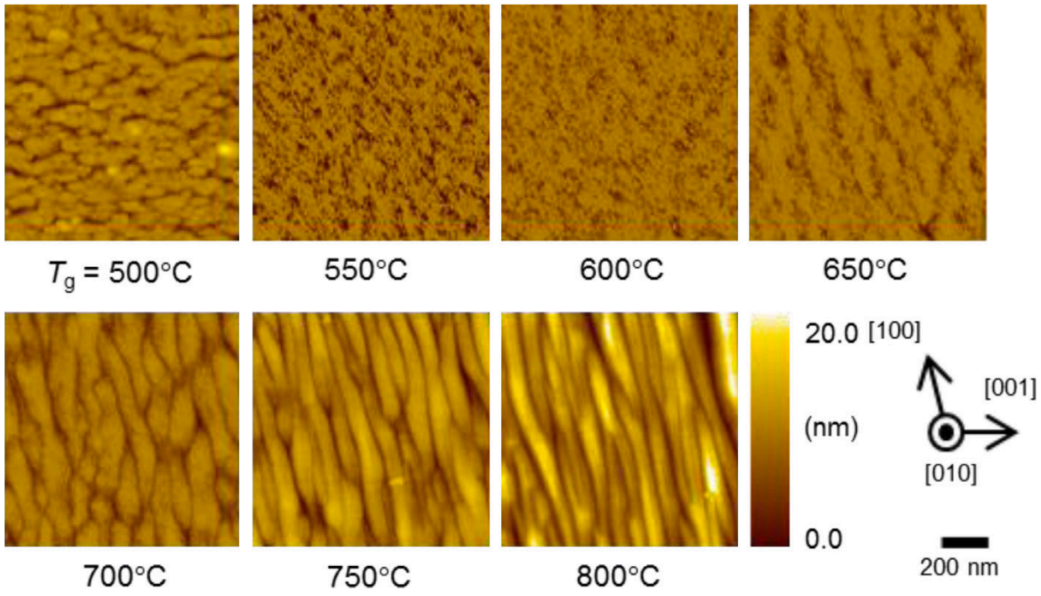

Fig. 2. Surface AFM images of Ga_2O_3 epitaxial films grown at various T_g.

Figure 3.16: AFM images of homoepitaxial Ga_2O_3 films on (010) $\beta - Ga_2O_3$ substrates grown by MBE. As the growth temperature is raised, step bunching leads to increased roughness. From Sasaki et al. [259]

.

et al. [46], and at 600 °C on (010)-oriented $\beta - Ga_2O_3$ substrates by Kaun et al. [213]. At 800 °C a β-phase solubility limit of $x = 0.61$ was observed, but at 600 °C the β phase disappeared above $x = 0.18$. This is in accordance with the results of this work (chapter 6). Faster in-plane growth proceeded along the [010] direction than [001], due to the existence of cleavage planes along {001}. At low Al concentrations, film growth proceeded by a step-flow mechanism, which transitioned to a three-dimensional growth mechanism above $x = 0.39$ (fig. 3.17). Surface roughness of (010)-oriented $(Al_xGa_{1-x})_2O_3$ films increased as the growth temperature was raised, caused by bunching of gallium suboxide Ga_2O at the step edges of miscut substrates during growth, which was suppressed with the addition of Al [213]. Capacitance-voltage measurements indicated that electrons can accumulate at the interface between $(Al_xGa_{1-x})_2O_3$ and Ga_2O_3 (100) with $x = 0.29$, suggesting the possibility of fabricating a HEMT device [46].

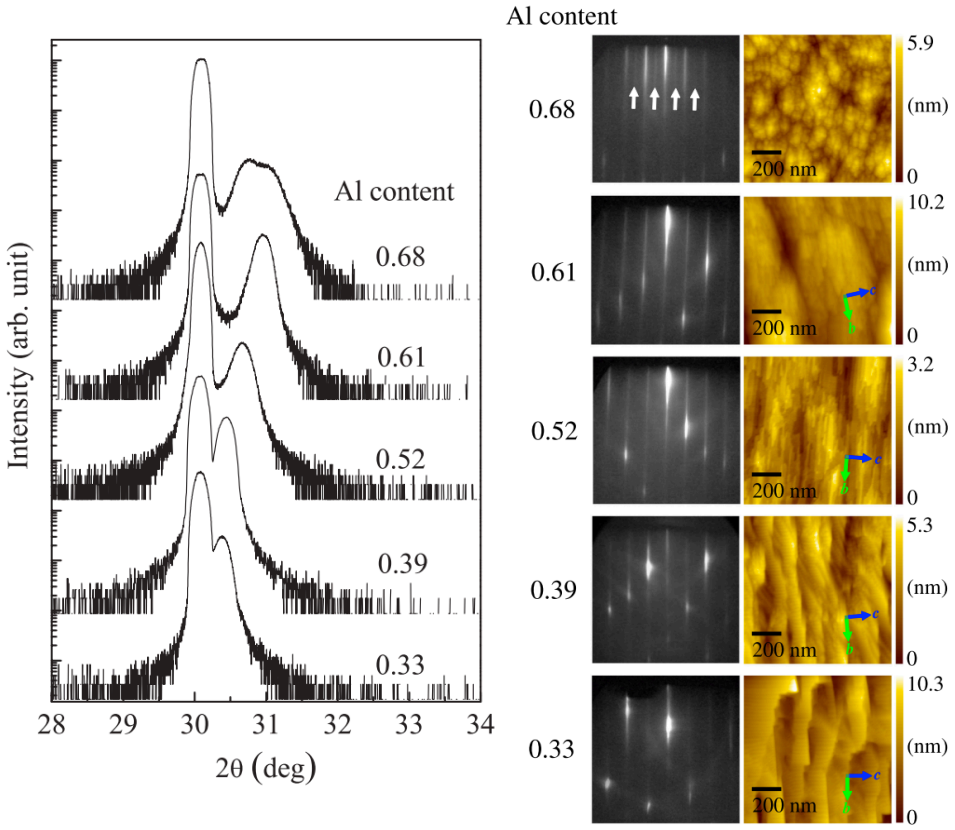

Figure 3.17: Left: XRD of homoepitaxial $(Al_xGa_{1-x})_2O_3$ on (100) $\beta - Ga_2O_3$ substrates grown by MBE at 800 °C. Right: RHEED and AFM images of epitaxial films as a function of Al concentration. Step flow growth is observed for films with $x < 0.39$, while three-dimensional growth starts above $x > 0.52$, with large grains up to $x = 0.61$. From Oshima et al. [46]

Heteroepitaxy of Ga_2O_3 Films

Growth of intrinsic epitaxial $\beta - Ga_2O_3$ films on sapphire has been investigated by PLD [215, 216, 222, 225, 260–262], MBE [209, 210, 212], RF sputtering [208], e-beam evaporation [186–188], and MOCVD [235, 244, 245]; Sn-doped films have been grown by PLD [17, 217, 218]; Si-doped films have been grown by PLD [18] and MOCVD [245]; and Zn-doped films have been grown by PLD [226].

In almost all cases, films on *c*-plane sapphire are $(\bar{2}01)$-oriented with six-fold rotational symmetry in plane, two for each of the three equivalent directions on $\alpha - Al_2O_3$ (001) [186]. Epitaxial relationships are $(\bar{2}01)_{\beta-Ga_2O_3} || (0001)_{\alpha-Al_2O_3}$ and $[010]_{\beta-Ga_2O_3} || [10\bar{1}0]_{\alpha-Al_2O_3}$ [235], or equivalently $[102]_{\beta-Ga_2O_3} || [2\bar{1}\bar{1}0]_{\alpha-Al_2O_3}$ [222]. Seiler et al. [262] recently reported a second (101) texture in $50 - 500$ nm PLD-grown films, based on pole figures very similar to figures presented in this work (section 7.1), but their $\theta - 2\theta$ XRD scan contains only $(\bar{2}01)$ and higher-order peaks, while (202) and others are missing. Other authors published pole figures from $200 - 400$ nm e-beam evaporated films and did not show any textures other than $(\bar{2}01)$ [186] (fig. 3.18). In this work, PLD-grown epitaxial films were found to develop additional peaks as the thickness surpassed 100 nm, but not thinner films; therefore I believe the extra peaks in the paper by Seiler et al. are probably explained by twinning and the loss of the initial epitaxial relationship, as in section 7.1, rather than a second texture.

Epitaxial relationships of e-beam evaporated $\beta - Ga_2O_3$ films on (110) *a*-plane, (100) *m*- and (102) *r*-plane sapphire substrates have all been found [186, 188]. On *a*-plane sapphire $\beta - Ga_2O_3$ films are strongly $(\bar{2}01)$-oriented and six-fold symmetric, rotated around the $[\bar{1}10]$ direction. On *m*-plane sapphire the $\beta - Ga_2O_3$ $(\bar{2}01)$ plane is inclined along two sapphire (110) *a*-planes, resulting in twelve distinct types after six-fold rotation. On *r*-plane sapphire $\beta - Ga_2O_3$ $(\bar{2}01)$ is inclined along the (113) *n*-plane, and is again six-fold symmetric. Lattice matching between oxygen atoms at the interface between $\beta - Ga_2O_3$ and sapphire is shown.

Gottschalch et al. [235] found mixed α and β phase films on *a*-plane sapphire, and pure α phase on *m*- and *r*-plane sapphire, for MOVPE films grown at 700 °C, with lattice-matched epitaxial relationships between $\alpha - Ga_2O_3$ and $\alpha - Al_2O_3$. This is a rather high temperature for α phase growth, comparable to the temperature used by Nakagomi et al. [188] to obtain β phase

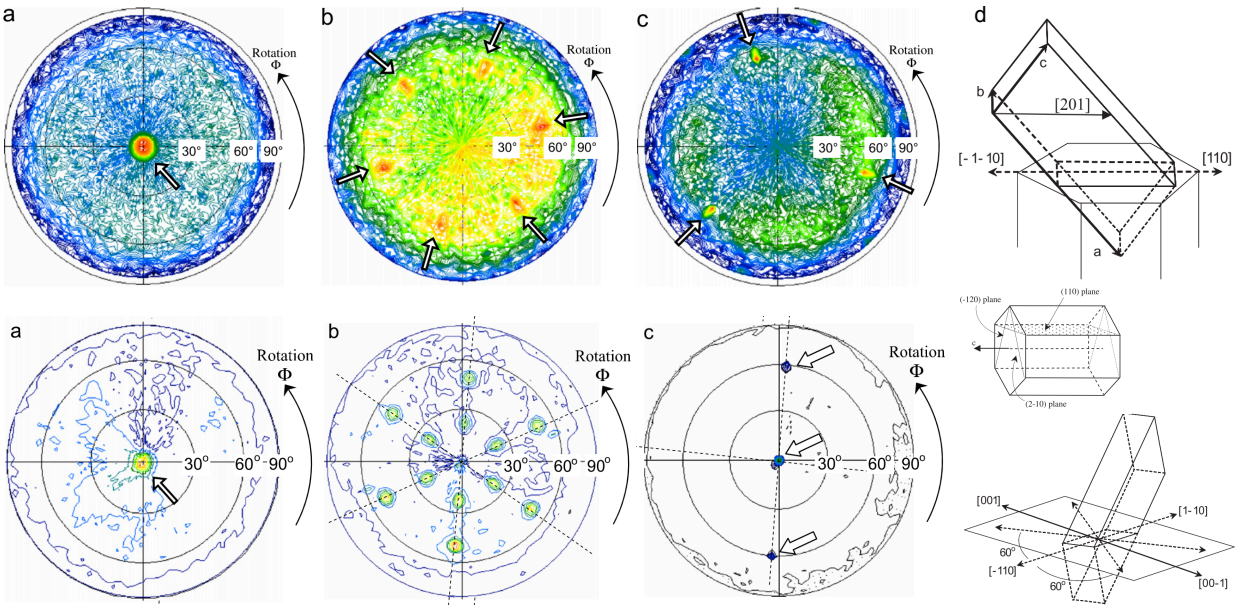

Figure 3.18: Top row: Pole figures of epitaxial $(\bar{2}01)$-oriented $\beta - Ga_2O_3$ film on c-plane sapphire. a) $\beta - Ga_2O_3$ $(\bar{2}01)$ b) $\beta - Ga_2O_3$ (001) c) $\alpha - Al_2O_3$ (102). Second row: Pole figures of epitaxial $(\bar{2}01)$-oriented $\beta - Ga_2O_3$ film on a-plane (110) sapphire. a) $\beta - Ga_2O_3$ $(\bar{2}01)$ b) $\beta - Ga_2O_3$ (001) c) $\alpha - Al_2O_3$ (110) From Nakagomi and Kokubun [186]

films on the same substrates. In other MOVPE studies the β phase was exclusively obtained at growth temperatures from 550–800 °C [244, 245], but no sapphire orientation other than c-plane was investigated. Gottschalch et al. also measured the epitaxial relationship on GaAs, finding $(\bar{2}01)_{\beta-Ga_2O_3}||\ (\bar{1}11)_{GaAs}$ and $[010]_{\beta-Ga_2O_3}||\ [110]_{GaAs}$.

Heteroepitaxial $\beta - Ga_2O_3$ films have been grown on MgO substrates by MBE [209], RF sputtering [201] and MOCVD (MOVPE) [237, 238, 243, 263]. On (100)-oriented MgO substrates, $\beta - Ga_2O_3$ films are (100)-oriented, with $[001]_{\beta-Ga_2O_3}||\ [011]_{MgO}$ and $[010]_{\beta-Ga_2O_3}||\ [01\bar{1}]_{MgO}$ with four-fold rotational symmetry [209, 263]. On (110)-oriented MgO substrates, $\beta - Ga_2O_3$ films are $(\bar{1}02)$-oriented with $[010]_{\beta-Ga_2O_3}||\ [001]_{MgO}$ and $[201]_{\beta-Ga_2O_3}||\ [\bar{1}10]_{MgO}$ with two-fold rotational symmetry [238]. On (111)-oriented MgO substrates, $\beta - Ga_2O_3$ films are $(\bar{2}01)$-oriented with $[010]_{\beta-Ga_2O_3}||\ [112]_{MgO}$ and six-fold rotational symmetry [237].

Sn-doped films grown on c-plane sapphire by PLD were found to take the orthorhombic $\kappa - Ga_2O_3$ phase (identified as ϵ in the cited references) at temperatures above 410 °C, with epitaxial relationships

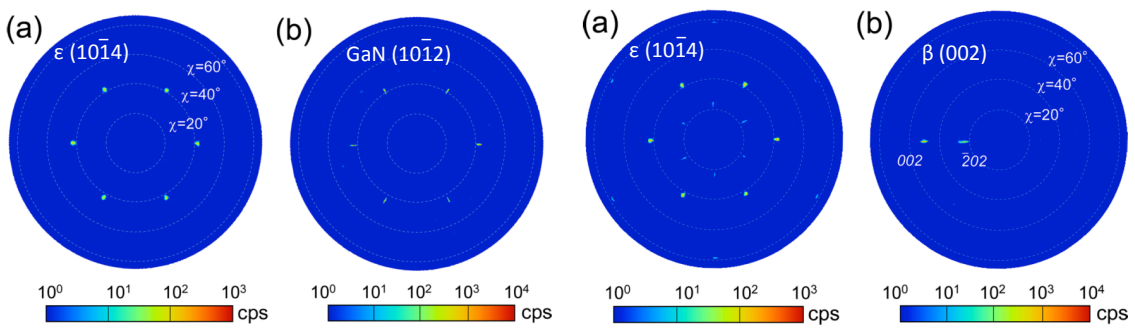

Figure 3.19: Pole figures showing orientation of epitaxial $\epsilon-Ga_2O_3$ films on GaN (left), and on $\beta - Ga_2O_3$ (right). From Oshima et al. [251]

$(001)_{\kappa-Ga_2O_3}||\ (0001)_{\alpha-Al_2O_3}$ and $[010]_{\kappa-Ga_2O_3}||\ [10\bar{1}0]_{\alpha-Al_2O_3}$ [17, 218]. However, both undoped and Sn-doped oriented $\beta - Ga_2O_3$ films grown on $MgAl_2O_4$ spinel substrates are amorphous below 600 °C, and between 600–700 °C by MOCVD take the β phase, with epitaxial relationships $(100)_{\beta-Ga_2O_3}||\ (100)_{MgAl_2O_4}$ and $[001]_{\beta-Ga_2O_3}||\ [011]_{MgAl_2O_4}$ and four-fold rotational symmetry [239, 240]. Both undoped and Mn-doped Ga_2O_3 films grown on spinel substrates by PLD were found to take the γ phase, and cross-sectional TEM showed "cube-on-cube" lattice matching between the $\gamma - Ga_2O_3$ defected spinel structure and the $MgAl_2O_4$ substrate. Mn-doping lead to greatly improved crystallinity of the γ phase. A selected area electron diffraction (SAED) pattern revealed uniform tetragonal distortion in the [100] direction, normal to the interface [223]. Mn-doping also lead to γ-phase films grown by PLD on c-plane sapphire, with epitaxial relationships $(111)_{\gamma-Ga_2O_3}||\ (0001)_{\alpha-Al_2O_3}$ and $[2\bar{1}\bar{1}]_{\gamma-Ga_2O_3}||\ [2\bar{1}\bar{1}0]_{\alpha-Al_2O_3}$ [222]. Twinning on {111} was observed for Mn-doped $\gamma - Ga_2O_3$ on sapphire, but not on spinel substrates.

Lattice-matched $\alpha - Ga_2O_3$ films were grown on sapphire substrates using mist-CVD by carefully controlling the growth temperature between 390–400 °C [249] or 430–470 °C [248]; at higher temperatures the β phase inevitably began to appear. When growing on $MgAl_2O_4$ rather than sapphire, γ-phase films with "cube-on-cube" epitaxial relationships were obtained under identical deposition conditions [249]. Recently, hexagonal (0001)-oriented $\epsilon-Ga_2O_3$ films[2] were grown by HVPE on c-plane AlN/SiC, c-plane GaN, and $\beta - Ga_2O_3$ ($\bar{2}01$) substrates, at temperatures up

[2]Here ϵ refers to the hexagonal phase ($P6_3mc$), similar to wurtzite GaN; not κ, which is orthorhombic ($Pna2_1$)

to 700 °C by Oshima et al. [251]. Epitaxial relationships were $(0001)_{\epsilon-Ga_2O_3}||\ (0001)_{GaN,\ AlN}$ and $[10\bar{1}0]_{\epsilon-Ga_2O_3}||\ [10\bar{1}0]_{GaN,\ AlN}$ and $(0001)_{\epsilon-Ga_2O_3}||\ (\bar{2}01)_{\beta-Ga_2O_3}$ and $[10\bar{1}0]_{\epsilon-Ga_2O_3}||\ [102]_{\beta-Ga_2O_3}$. Interestingly, X-ray rocking curve measurements show the smallest width for $\epsilon - Ga_2O_3$ films frown on $(\bar{2}01)$-oriented $\beta - Ga_2O_3$. CVD/VPE therefore appears to be a very flexible technique for producing Ga_2O_3 films in metastable phases.

Temperature Dependence of the Crystal Phase and Band Gap of Heteroepitaxial Ga_2O_3 Films

There is a large variation in the temperature reported for the onset of the β phase, depending on the growth method. Ou et al. [225] and Zhang et al. [260] found that PLD-grown films on sapphire remain amorphous to 400 °C, and then become β phase at temperatures above 500 °C (fig. 3.20), with correspondingly increasing band gaps. Kumar et al. [204] and Ramana et al. [206] found the same temperature dependence for films deposited by RF-sputtering on silicon, but an opposite variation in the band gap (fig. 3.21). In this case, the larger band gap in the amorphous phase may be due to excess oxygen; Al-Kuhaili et al. [185] deposited amorphous Ga_2O_3 films in vacuum and in 0.38 mT O_2 by e-beam evaporation, and found that the films in vacuum had lower band gap (4.84 eV) than films deposited in O_2 (5.04 eV). A different study on RF-sputtered films on MgO substrates by Takeuchi et al. [201] found that films remain amorphous to 390 °C and suddenly change to the β phase at 400 °C. E-beam evaporated films deposited on glass by Rao and Kumar [194] crystallized to the β phase at 500 °C, with a peculiar dendritic morphology depending on whether a Mo or Ta boat was used.

MOCVD-grown films grown on alumina plates remained amorphous to 600 °C [230], and MOCVD films grown on Si (100) remained amorphous up to 800 °C [232], but turned crystalline at 1050 °C [264, 265]. The temperature at which an amorphous Ga_2O_3 film transitions to the β phase has been shown to depend on the orientation of the substrate [236–239]. Metal-organic-deposited (MOD) amorphous Ga_2O_3 films were fabricated on sapphire and post-annealed from 850 °C to 1250 °C, and it was found that crystallization did not set in until above 950 °C [25] (fig. 3.22).

Sol-gel films on quartz crystallize in the $\alpha-GaO(OH)$ phase at 300 °C, the $\alpha - Ga_2O_3$ phase at 500 °C, and the $\beta - Ga_2O_3$ phase at 700 °C, with a monotonically decreasing bandgap moving

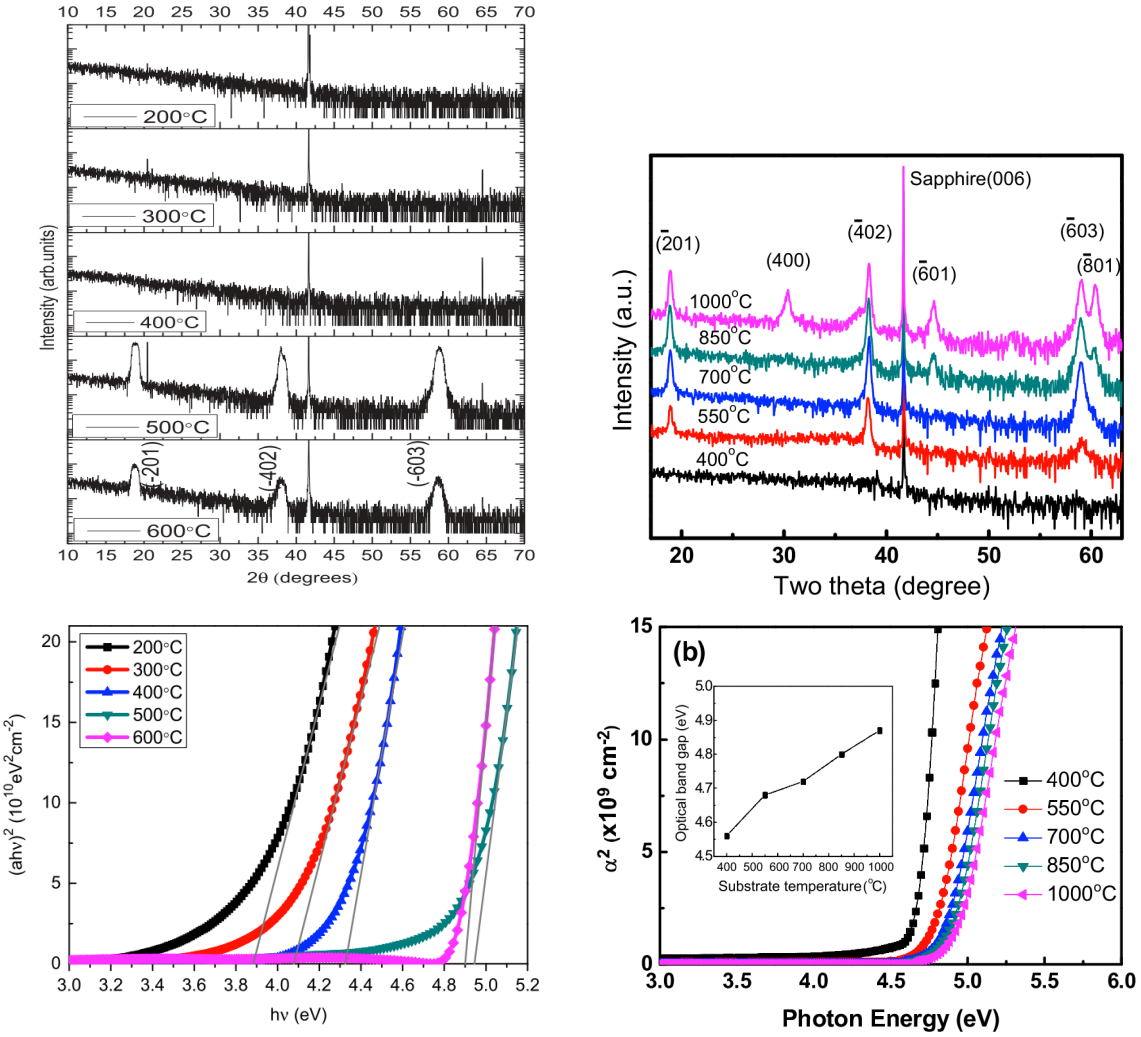

Figure 3.20: XRD $\theta - 2\theta$ scans and direct-gap Tauc plots of PLD Ga_2O_3 films deposited on sapphire at different temperatures. Left: data from Ou et al. [225] Right: data from Zhang et al. [260] (Deposition conditions were not the same in both references.)

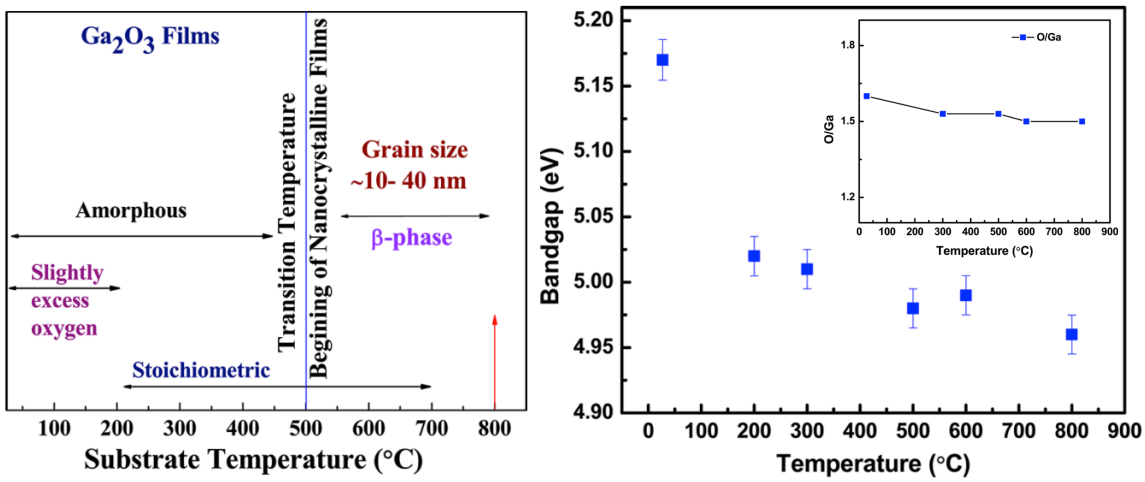

Figure 3.21: Left: Summary of film conditions for RF-sputtered Ga_2O_3 films on Si substrates deposited at temperatures up to 800 °C. Right: Band gap of sputtered films determined from direct-gap Tauc plots. Inset: O/Ga atomic ratio determined by RBS. From Kumar et al. [204]

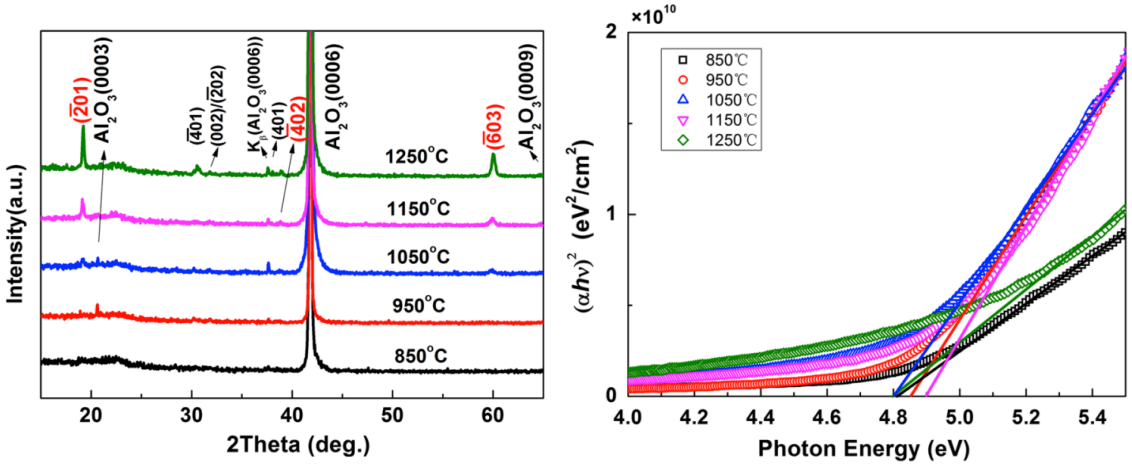

Figure 3.22: XRD $\theta - 2\theta$ scans and direct-gap Tauc plots of MOD-derived Ga_2O_3 films deposited on sapphire at different temperatures. From Guo et al. [25]

from 5.3 eV → 4.8 eV → 4.7 eV as the annealing temperature is raised (fig. 3.23) [58, 257]. In this case, the decrease may be due to a slightly larger bandgap of the α phase compared to the β phase [145, 248]. A different study on sol-gel films on sapphire found a transition directly from amorphous to β at 600 °C, followed by a monotonic increase in the band gap from 4.95 eV to 5.15 eV as the temperature was raised from 600 °C to 900 °C (fig. 3.24) [24].

Early Ga_2O_3 films produced by spray pyrolysis on borosilicate glass at 350 °C took the β phase, but with a very low band gap of 4.23 eV [129]. A different group depositing by spray pyrolysis on silicon found that films were amorphous at 400 °C, and converted to the β phase after annealing to 800 °C, with a band gap of 4.87 eV [130]. A more modern study found that films on Si crystallize at 850 °C [253]. A higher index of refraction was measured for crystalline films ($n = 1.92$ at 632 nm) than as-deposited amorphous films ($n = 1.85$). Annealing to 425 °C lead to an increase in the refractive index to $n = 1.87$, and a blue shift in the absorption edge from 4.94 eV to 4.99 eV. The following year, Hao and Cocivera [254] prepared Ga_2O_3 films by spray pyrolysis on a variety of substrates and post-annealed to 400 °C, 600 °C, and 900 °C, finding that $\beta - Ga_2O_3$ peaks first appear in XRD at 600 °C. The band gaps corresponding to each temperature were 4.44 eV (400 °C), 4.48 eV (600 °C), and 4.75 eV (900 °C). Spray pyrolysis at an elevated substrate temperature is possible by using pulses rather than a continuous spray; in this way Ji et al. [23] was able to deposit at 700–800 °C, producing crystalline as-deposited films with larger band gap of 5.16 eV.

Atomic-layer-deposited Ga_2O_3 thin films on silicon and sapphire were reported by Shan et al. [228], and post-annealed from 500 °C to 900 °C. Films prepared in this way remained amorphous to 700 °C, transitioning to the β phase at higher temperatures, with a corresponding increase in the band gap from 5.0 eV to 5.15–5.25 eV (fig. 3.25).

Several authors noticed Al diffusion from sapphire into Ga_2O_3 thin films when post-annealing at 1000 °C or higher [24, 132, 230, 266], and a few didn't but should have based on a dramatic increase in the band gap [191–193]. Goyal et al. [266] performed post-annealing at 600 °C, 800 °C, and 1000 °C for 24 h each, and measured the diffusion between film and substrate using secondary ion mass spectroscopy (SIMS) depth profiling. They found evidence of Al diffusion from sapphire into the film already at 800 °C, and diffusion in both directions at 1000 °C (fig. 3.26). No data is presented on diffusion when annealing at 800 °C for more reasonable annealing times (~ 1 hr), but it is likely not as significant or it would have been noticed sooner.

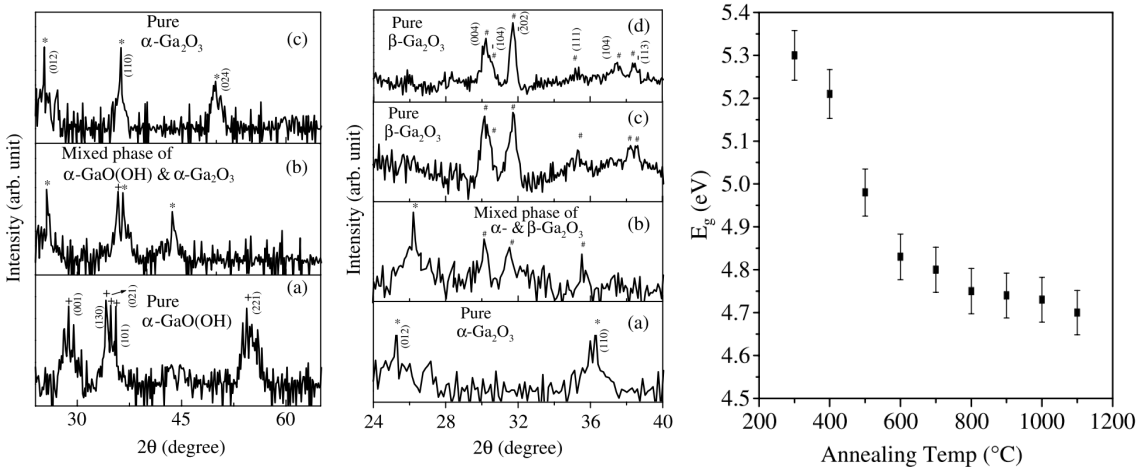

Figure 3.23: Left: XRD $\theta - 2\theta$ scans for sol-gel derived Ga_2O_3 film annealed at 300 °C, 400 °C, and 500 °C, going from bottom to top. Middle: XRD $\theta - 2\theta$ scans for sol-gel derived Ga_2O_3 film annealed at 500 °C, 600 °C, 700 °C, and 1100 °C, going from bottom to top. Right: Band gap estimated from direct Tauc plots at each annealing step. From Sinha et al. [257]

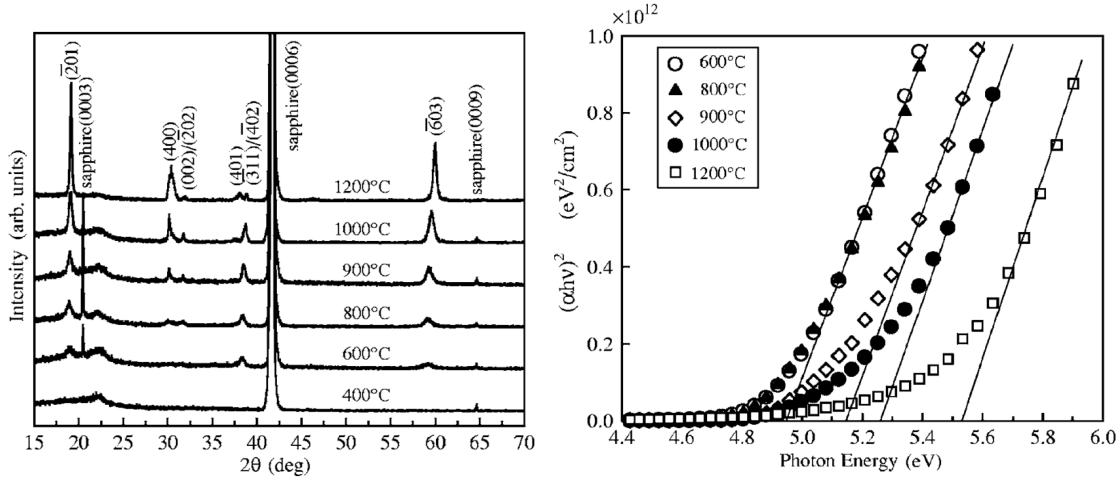

Figure 3.24: Left: XRD $\theta - 2\theta$ scans for sol-gel derived Ga_2O_3 film after post-annealing at the indicated temperatures. Right: Tauc plots showing the increasing band gap with annealing temperature. From Kokubun et al. [24]

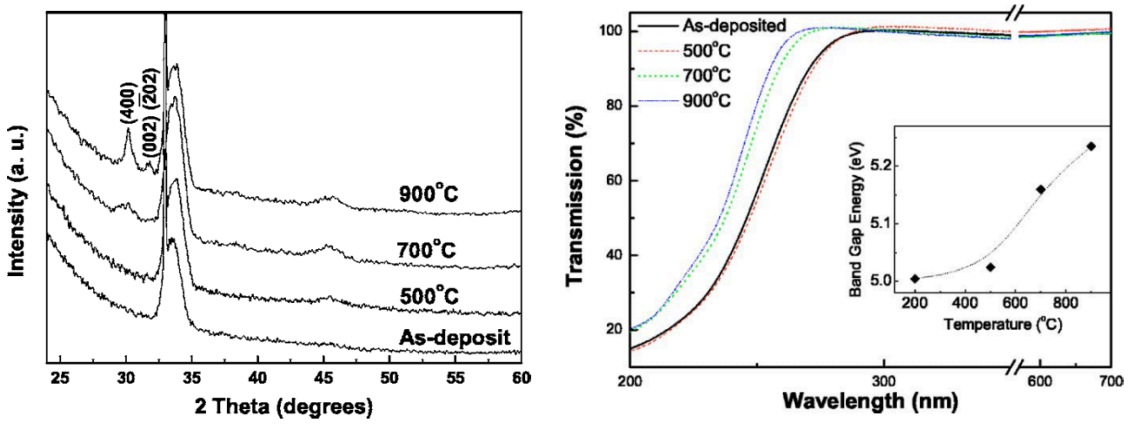

Figure 3.25: Left: XRD $\theta - 2\theta$ scans for ALD Ga_2O_3 film before post-annealing and after annealing to 500 °C, 700 °C, and 900 °C. Right: Transmission intensities and band gaps after each annealing step. From Shan et al. [228]

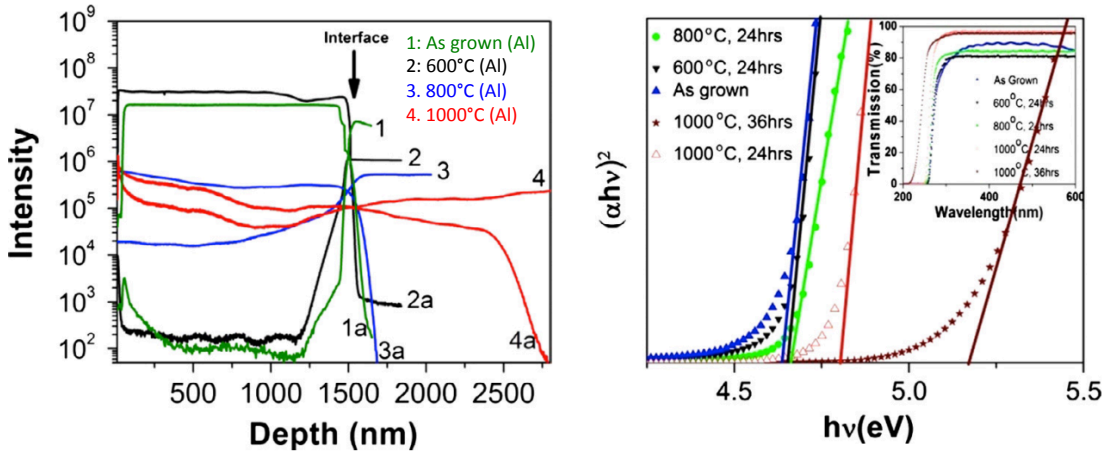

Figure 3.26: Left: SIMS depth profile showing Al and Ga species for 24-hour post-annealed films at each temperature. Diffusion of Al into the Ga_2O_3 film begins at 800 °C; diffusion of Ga into the substrate begins at 1000 °C. Right: Band gap increase after post-annealing due to Al diffusion. From Goyal et al. [266]

Metallic Clusters in Substoichiometric Ga_2O_3

Substoichiometric Ga_2O_x films were obtained when deposited by PLD under vacuum, and a combination of TEM, SAED, XPS, and resistance measurements provided evidence that phase segregation into Ga_2O_3 and β-Ga phases occurs when $x \leq 2.3$. fig. 3.27 [177, 224]. These were the first XPS studies showing a distinct shoulder on the low-binding-energy side of Ga $3d$, separate from the metallic Ga peak, which is now understood to come from hybridization between Ga $3d$ and O $2s$ [175].

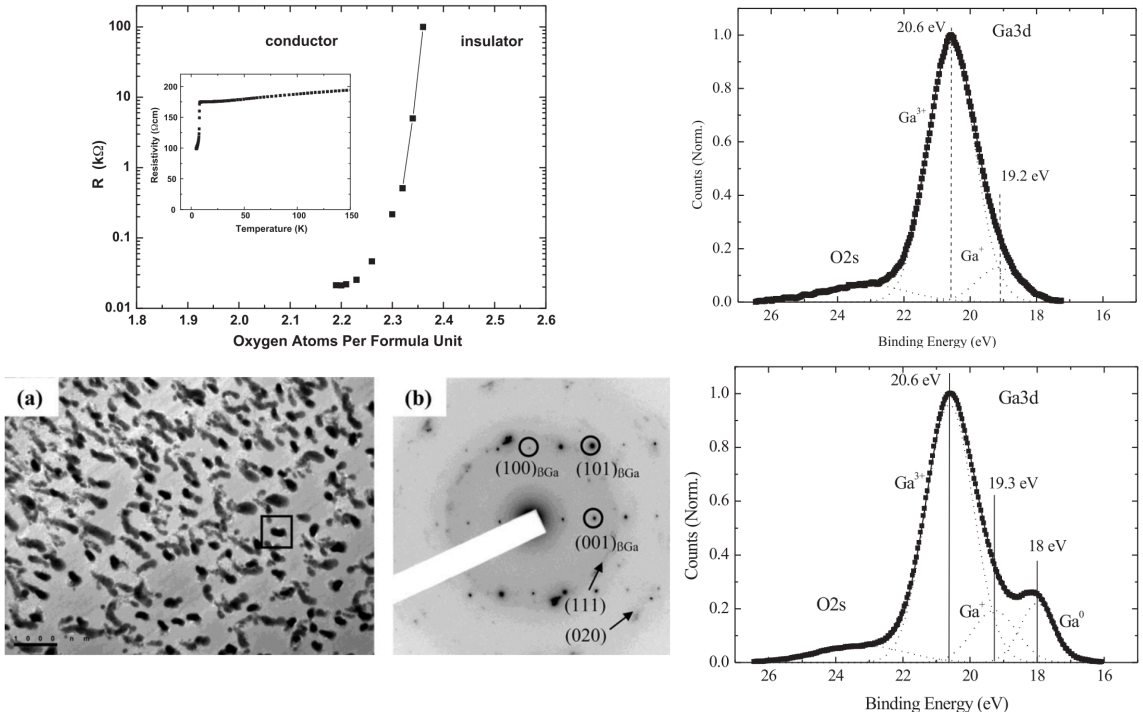

Figure 3.27: Evidence of metallic clusters in substoichiometric Ga_2O_x films, with $x \leq 2.3$. Upper left: Resistivity as a function of x. Lower left: a) Bright-field TEM image of substoichiometric Ga_2O_3 film showing clusters, b) SAED image of squared area revealing β-Ga diffraction peaks. Upper right: Ga $3d$ XPS spectrum from a $Ga_2O_{2.7}$ film. Lower right: Ga $3d$ XPS spectrum from a $Ga_2O_{2.3}$ film. From Petitmangin et al. [177]

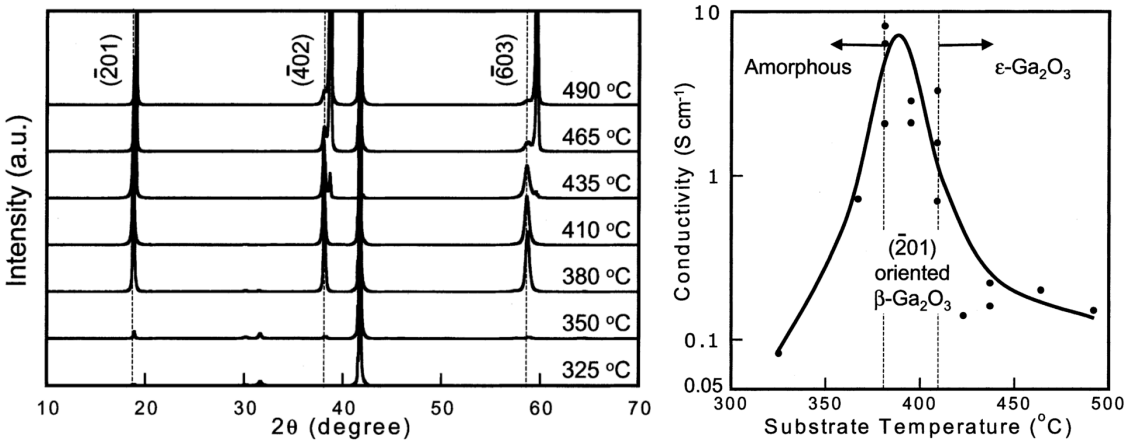

Figure 3.28: Left: XRD $\theta - 2\theta$ scans at the indicated deposition temperatures. Right: Conductivity vs. deposition temperature. As the temperature was raised from 350 °C to 500 °C the concentration increased from 2.5 % to 4.0 % due to improved incorporation from the 5 % SnO_2 PLD target. From Orita et al. [17]

N-type Ga_2O_3 Films Doped with Sn and Si

Some of the earliest Ga_2O_3 PLD papers actually investigated Sn-doped films before undoped films. Using a 1 % SnO_2 target, and depositing on quartz at 880 °C in a low oxygen pressure of 5×10^7 T, a carrier concentration of $1.4 \times 10^{19}\,\mathrm{cm^2/Vs}$, a mobility of $0.44\,\mathrm{cm^2\,V^{-1}\,s}$, and a conductivity of 1.0 S/cm was achieved [16]. However, when the oxygen pressure was raised to 0.1 mT the conductivity fell to 3.6×10^{-3} S/cm. Increasing the doping level to 2.5 % and depositing highly-oriented films on sapphire resulted in a new maximum conductivity of 8.2 S/cm when depositing in a narrow temperature range 380–410 °C (fig. 3.28) [17]. As the temperature increased further, a new orthorhombic phase appeared and the conductivity fell by an order of magnitude, indicating that Sn no longer acts as a shallow donor in the new phase. Matsuzaki et al. [217] later identified the new phase as $\kappa{-}Ga_2O_3$ belonging to space group $Pna2_1$, with epitaxial relationships $(001)_{\kappa-Ga_2O_3} || (0001)_{\alpha-Al_2O_3}$, $[100]_{\kappa-Ga_2O_3} || [11\bar{2}0]_{\alpha-Al_2O_3}$ and $[010]_{\kappa-Ga_2O_3} || [10\bar{1}0]_{\alpha-Al_2O_3}$. Growth conditions were surveyed to optimize electrical properties for application as an transparent n-channel in a FET, and a prototype was demonstrated [217, 218].

MBE-growth of Sn-doped films on $\beta - Ga_2O_3$ substrates was taken up by in 2012 by Sasaki et al.

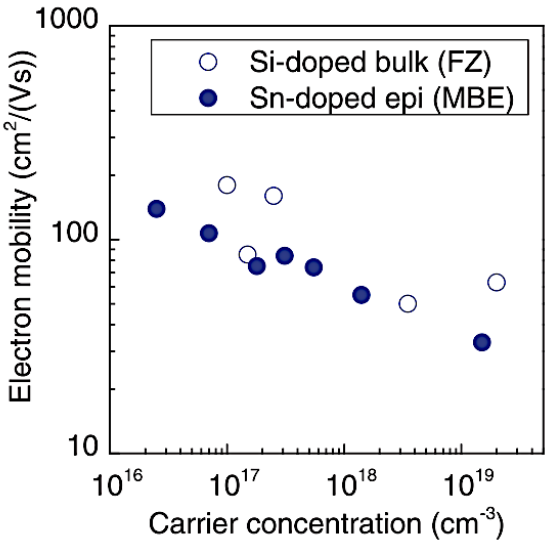

Figure 3.29: Conductivity vs. mobility for Sn-doped homoepitaxial film grown by MBE. From Sasaki et al. [36]

[183], who found that the carrier concentration could be controlled from 10^{16} to $10^{19}\,\mathrm{cm}^{-3}$ with a corresponding drop in mobility from $150\,\mathrm{cm}^2/\mathrm{Vs}$ to $20\,\mathrm{cm}^2/\mathrm{Vs}$ (fig. 3.29).

Ga_2O_3 films alloyed with 0–12 % Sn on spinel $MgAl_2O_4$ [240] and $\beta - Ga_2O_3$ (100) [242] were characterized recently, and key findings are displayed in fig. 3.30. $\beta - Ga_2O_3$ films on $MgAl_2O_4$ were only stable up to 3 %, and a structural change occured at 5 %, followed by amorphous Ga_2O_3:Sn above 8 %. Interestingly, the intermediate structure at 5 % appears to be different from the orthorhombic phase observed in 4 % Sn-doped films by Orita et al. [17]. Homoepitaxial $\beta - Ga_2O_3$ films remained stable all the way to 10 %. On $MgAl_2O_4$, the conductivity was observed to jump by two orders of magnitude upon doping with 1 % Sn, and not improve further from 1–5 %. From 5–10 %, amorphous films on $MgAl_2O_4$ exhibited a sharp increase in conductivity by nine orders of magnitude, peaking at 32 S/cm for the 10 % sample, followed by an equally sharp drop from 10–12 %. The conductivity of the homoepitaxial film followed a similar pattern, but with less pronounced changes; from 0–1 % the conductivity improved by one order of magnitude, with no further change from 1–5 %, and a sharp increase from 5–10 % to a maximum of 8.3 S/cm at 10 %, followed by a sharp drop again at 12 %. The band gap was found to decrease from 4.66 eV to 4.16 eV as the Sn content increased from

1 % to 10 %, showing that Sn incorporation lowers the band gap much like In. SnO_2, like Ga_2O_3, has a conduction band minimum primarily made up of Sn 5s states, with a band gap of 3.6 eV [267]; therefore the conduction band minimum should be lowered by alloying with Sn.

Ga_2O_3 films alloyed with 0–50 % Si were sputtered on silicon and quartz substrates and post-annealed at 600 °C [199, 200]. The authors reported that films remain stable in the β phase throughout the studied composition range; however, it appears that they mis-identified the lone peak in their XRD $\theta - 2\theta$ scans attributed to $\beta - Ga_2O_3$, so in fact the films are either amorphous or in some other phase. Opposite to the case of Sn, alloying with Si was found to substantially increase the band gap to 6.1 eV for a 50 %-doped film. The absorption coefficient and Tauc plots after post-annealing are shown in fig. 3.31. Comparing 15 min to 60 min annealing shows that the longer time leads to slightly higher values of the bandgap from 0–40 %, and little change at 50 %. It's unclear whether the leveling off is merely an artifact of fitting to the band edge running off the right side of the window, or whether it's caused by a fundamental solubility limit, although taking into account the lack of $\beta - Ga_2O_3$ XRD peaks and the fact that only the tail of the absorption coefficient is still visible at 50 % I suspect the former. The shape and trend of the absorption coefficient with increasing Si concentration after post-annealing to 600 °C for 1 hr bears a similarity to my fitted ellipsometry results for post-annealed $(Al_xGa_{1-x})_2O_3$ films. Despite the huge variation in Si content, no improvement to the conductivity was found [268].

Doping with Si at more moderate levels (10^{17}–10^{20} cm^{-3}) to improve the conductivity was attempted in MOVPE films grown at 800 °C on both sapphire and $\beta - Ga_2O_3$ (100) [245]. No change in the band gap was observed. $\beta - Ga_2O_3$ XRD peaks disappeared at doping levels above 5×10^{19} cm^{-3}, and extended defects are visible in high-resolution TEM images. As in the study by Takakura et al. [268], Si-doped films remained resistive throughout the doping range studied, and it is suggested that compensating acceptors could be the reason. It was not described how contacts were made, however. A positron-annihilation study on Si-doped films by the same group this year identified Ga vacancies in sufficient numbers to explain the compensation [247].

An Si ion-implantation study found that the resistivity could be lowered to 1.4 mΩ cm, measured using Ti/Au contacts annealed at 450 °C which are known to be Ohmic [184]. In addition, the conductivity of PLD-grown Si-doped $\beta - Ga_2O_3$ films can be varied over four orders of magnitude by changing the O_2 pressure during growth [18]. These observations are possibly explained by surface

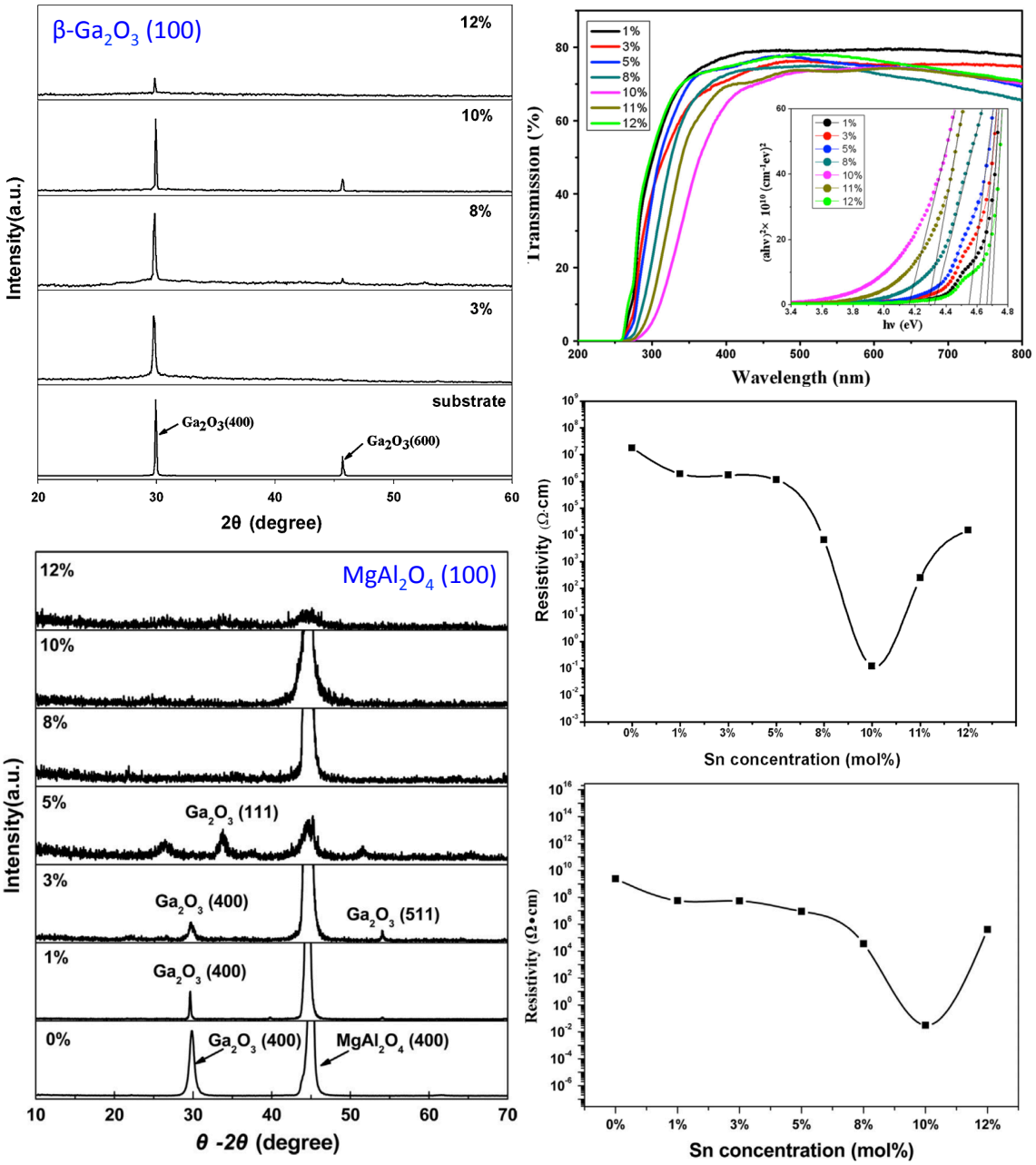

Figure 3.30: $(Sn_xGa_{1-x})_2O_3$ alloy films with $0 < x < 0.12$ on $\beta - Ga_2O_3$ (100) and $MgAl_2O_4$ (100) substrates. Upper left: XRD $\theta - 2\theta$ scans of homoepitaxial Ga_2O_3 films on $\beta - Ga_2O_3$ (100) substrates. Lower left: XRD $\theta - 2\theta$ scans of heteroepitaxial films on $MgAl_2O_4$ (100) substrates. Upper right: Band gap decreases with Sn incorporation on homoepitaxial films. Lower right: Resistivity vs. Sn concentration for homoepitaxial (upper) and heteroepitaxial (lower) films. From Mi et al. [240] and Du et al. [242].

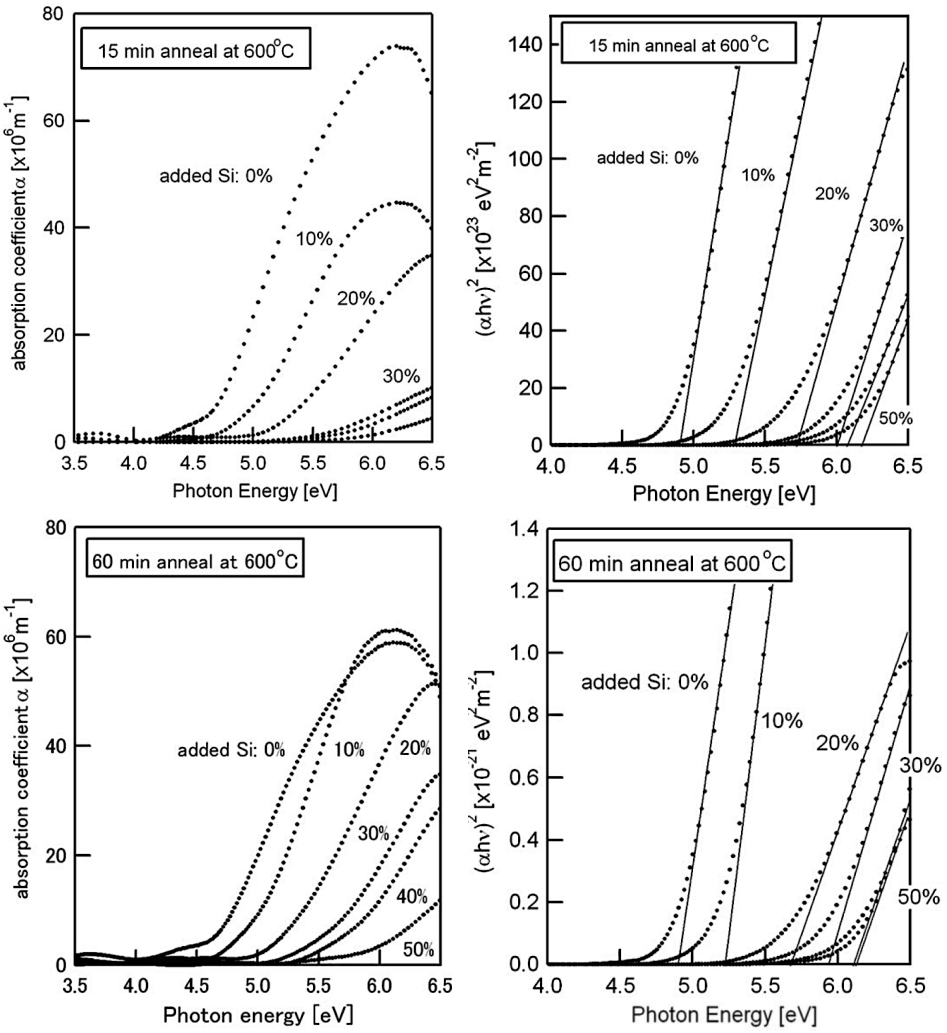

Figure 3.31: Absorption coefficient and band gap of RF-sputtered $(Si_xGa_{1-x})_2O_3$ alloy films with $0 < x < 0.5$ on quartz substrates, post-annealed to 600 °C for 15 min (top) and 60 min (bottom). From Takakura et al. [200]

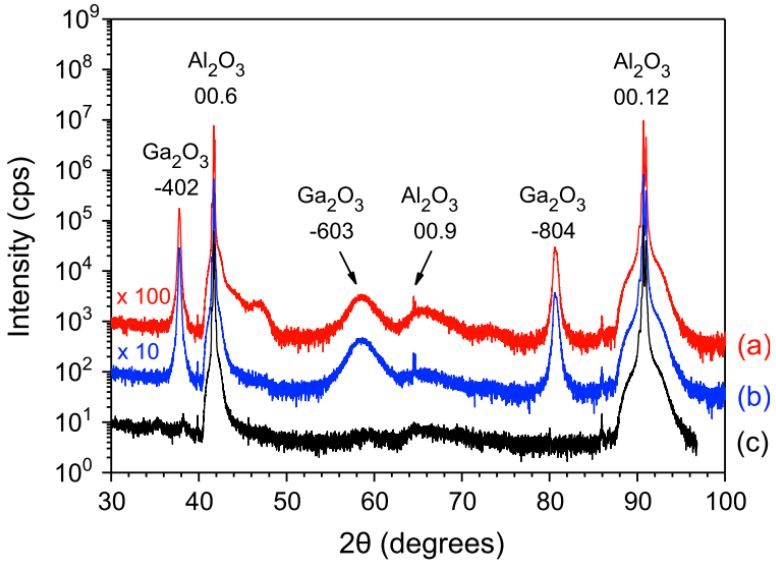

Figure 3.32: XRD $\theta - 2\theta$ scans for Si-doped Ga_2O_3 films with a) $4 \times 10^{17}\,cm^{-3}$, b) $3 \times 10^{18}\,cm^{-3}$, and c) $5 \times 10^{19}\,cm^{-3}$ Si concentrations. From Gogova et al. [245]

band bending as described by Lovejoy et al. [174], which is large enough to activate deep V_O donors at the surface for films grown in reducing conditions. Conversely, Si ion implantation would reduce the band bending in stoichiometric films and increase the conductivity, explaining the observations by Sasaki et al.

Successful Si doping of $\gamma - Ga_2O_3$ films on $MgAl_2O_4$ was reported this year as well, achieving a carrier concentration of $1.8 \times 10^{19}\,cm^{-3}$, a mobility of $1.6\,cm^2/Vs$, and a resistivity of $0.21\,\Omega\,cm$ [19]. This development opens the possibility of fabricating quasi-homoepitaxial $\gamma - (Al_xGa_{1-x})_2O_3/\gamma - Ga_2O_3$ heterojunctions.

Al_2O_3 Thin Films

Numerous groups have fabricated Al_2O_3 thin films by many of the same methods used to prepare Ga_2O_3 films (table 3.1) giving rise to an equally extensive literature. Of the two compounds Al_2O_3 growth is more challenging, requiring a higher temperature for crystallization into the stable α phase than is needed for $\beta - Ga_2O_3$. In this section I will focus mostly on the growth of Al_2O_3 films by pulsed laser deposition, which is most relevant to this work. $\alpha - Al_2O_3$ films [269–279], $\gamma - Al_2O_3$ films [271–274, 276, 277, 280–285], and amorphous Al_2O_3 films [276, 277, 281, 283, 285–288] have been studied. The resulting phase is a sensitive function of the the growth temperature, overall pressure, laser fluence, and the choice of substrate.

$(11\bar{2}0)$-oriented $\alpha - Al_2O_3$ films on Si (111) were achieved at temperatures higher than 850 °C in a high vacuum environment (10^{-8} T); at lower temperatures metallic Al embedded in the Al_2O_3 film were detected by XPS and XRD [269]. (A similar result was obtained for vacuum-deposited Ga_2O_3 films by Petitmangin et al. [224].) An overlap between Al (111) and Al_2O_3 $(11\bar{2}0)$ XRD reflections prevented the precise identification of the lower limit of crystallization. PLD $\alpha - Al_2O_3$ films on fused silica were achieved at 1140 °C and 10^{-4} T [272]. Amorphous PLD films all the way to 1000 °C followed by a transition to α above 1100 °C have been reported [275]. Recently highly-oriented $\alpha - Al_2O_3$ PLD films grown at 700 °C on *c*-plane sapphire, *r*-plane sapphire, $SrTiO_3$, and MgO, were also reported, but the only evidence was a tiny shoulder present on each of the respective substrate peaks in XRD $\theta - 2\theta$ scans, and oddly the (012) reflections were missing from the (024)-oriented film data [279]; I'm not sure that the possibility of satellite peaks from the X-ray source can be definitively ruled out without additional data, e.g. from electron diffraction. The same authors [283, 285] as well as several others [272, 281, 282, 284] previously reported γ-phase films grown under similar conditions. PLD growth on Si (100) and SiO_2 (quartz) substrates from room temperature up to 700 °C yielded amorphous films below 400 °C and γ-phase films above 500 °C [285]. A temperature-dependent growth study on MOCVD films from 900 °C to 1100 °C showed amorphous phase films up to 950 °C, pure γ-phase from 950 °C $< T_s <$ 1050 °C, and mixed α/γ phase at 1100 °C [277].

It has been previously shown that the growth temperature to achieve α phase films can be lowered by a judicious choice of substrate, or by optimizing other deposition parameters. Growth at

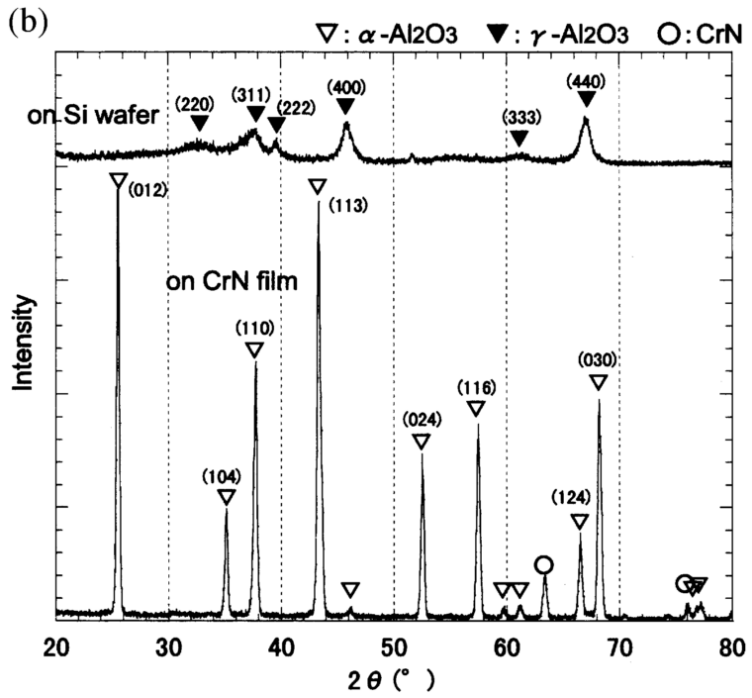

Figure 3.33: XRD $\theta - 2\theta$ scans from reactive magnetron sputtered Al_2O_3 films on silicon (top) and CrN (bottom) substrates, under identical deposition conditions. From Kohara et al. [271].

750 °C by reactive magnetron sputtering leads to γ phase films on silicon, but α phase films on CrN and oxygen-treated steel, due to the development of lattice matched Cr_2O_3 and Fe_2O_3 templates, respectively (fig. 3.33) [271]. α-phase growth on Cr_2O_3 by RF sputtering was demonstrated by lowering the overall gas pressure below 3 mT, thereby increasing energetic bombardment [273]. At a slightly higher pressure of 5 mT, films took the γ-phase. The lowest reported temperature for PLD growth of $\alpha - Al_2O_3$ is 400 °C, on a lattice matched epitaxial NiO (111) layer using a high laser fluence of 4 J/cm^2 [276]. The same study also showed that a laser fluence of 3 J/cm^2 resulted in a mixed-phase γ/α film, and a laser fluence of 2 J/cm^2 resulted in amorphous Al_2O_3. Balakrishnan et al. [283] showed that increasing the oxygen partial pressure past 250 mT for PLD films deposited at 700 °C on Si (100) substrates results in the amorphous phase, but keeping the oxygen partial pressure below 25 mT results in the γ phase. These studies demonstrate that controlling the energy of deposited particles, either through a higher fluence or smaller background gas pressure, in combination with a lattice matched substrate, allows an additional degree of control over the

resulting phase of the film.

The substrate is found to have an effect on the quality of γ-phase films as well. Improved crystallinity and epitaxy was found on thermally-oxidized SiO_2 compared to cleaned Si (111), for ion-beam deposited $\gamma - Al_2O_3$ films grown at 850 °C [280]. RHEED showed that films grown at temperatures under 600 °C were amorphous; from 700–800 °C began to develop streaking indicative of the γ-phase, and at 850 °C were single-crystalline. XPS depth profiling and TEM studies indicated that Al_2O_3 consumes oxygen atoms from SiO_2, forming an abrupt interface between Si and Al_2O_3 when SiO_2 is used as a substrate. When depositing on cleaned Si, no oxide is formed between the film and substrate even in an oxidizing atmosphere, and Si diffuses readily into the Al_2O_3, leading to a thick interface layer and poor crystallinity. On SiO_2 the $\gamma - Al_2O_3$ film took the Hausmanite structure, a tetragonal distortion of spinel, with $a = 0.795$ nm and $c = 0.779$ nm and 2.4 % lattice mismatch, and epitaxial relationships $(111)_{\gamma-Al_2O_3} || (111)_{Si}$, $[\bar{1}10]_{\gamma-Al_2O_3} || [\bar{1}10]_{Si}$ and $[11\bar{2}]_{\gamma-Al_2O_3} || [11\bar{2}]_{Si}$. MBE-grown Al_2O_3 films at 850 °C on Si (100) initially grew pseudomorphically in the γ phase, but transitioned to the α phase after the first 2 nm; however, on Si (111) films remained in the γ phase to 7 nm, with epitaxial relationships $(111)_{\gamma-Al_2O_3} || (111)_{Si}$ and $[1\bar{1}0]_{\gamma-Al_2O_3} || [1\bar{1}0]_{Si}$, and a -23.5 % lattice mismatch. PLD growth of $\gamma - Al_2O_3$ films was also demonstrated at 800 °C on Si and SiO_2 substrates [281], at 700 °C on $SrTiO_3$ and MgO substrates [282], and at 500 °C on $SrTiO_3$ [284].

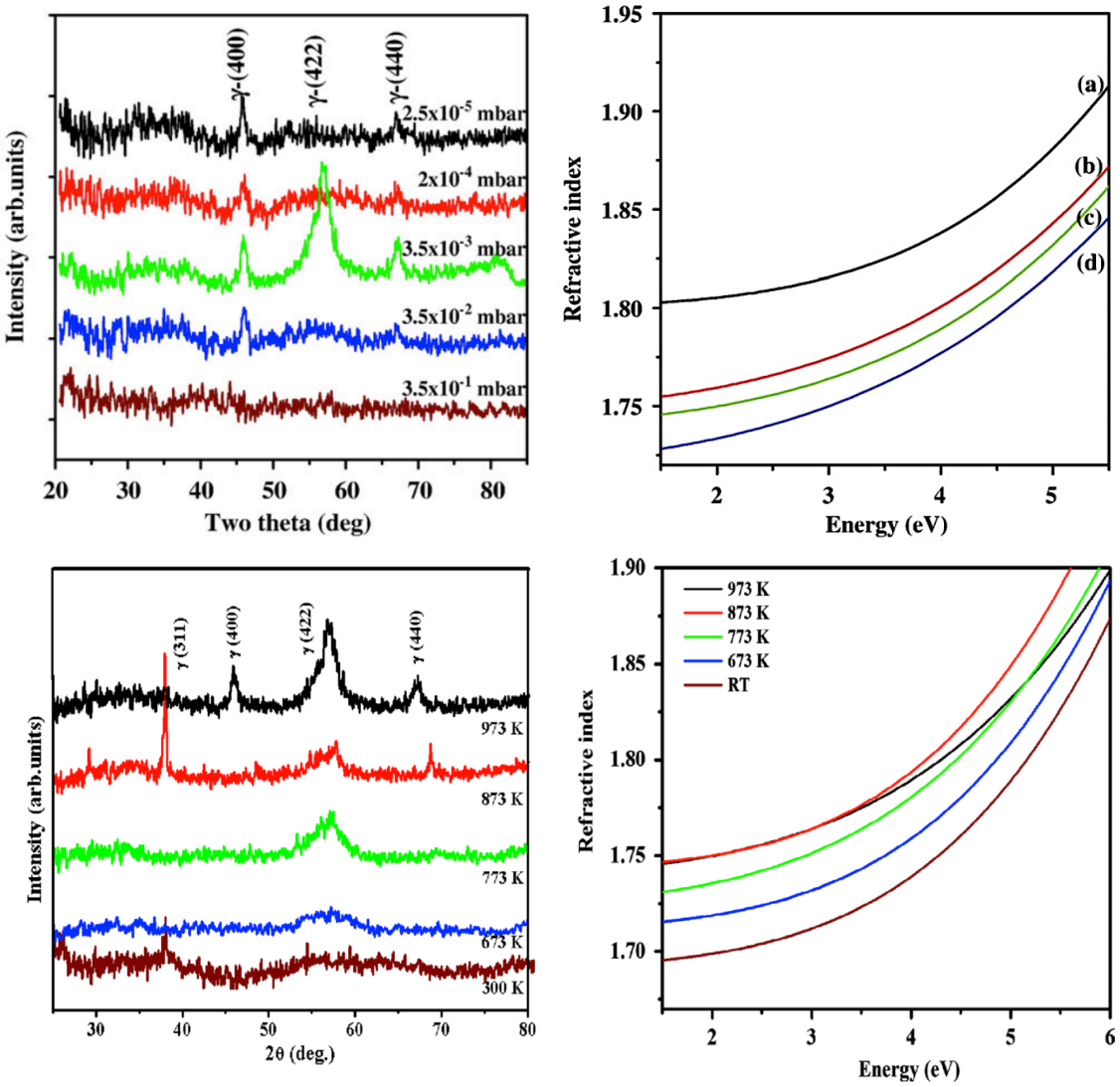

Figure 3.34: Relationship between index of refraction and crystallinity and density of PLD-grown Al_2O_3 films. Top: films deposited at 700 °C under varying oxygen pressure, from Balakrishnan et al. [283]. Bottom: films deposited at 2.25 mT at varying growth temperatures, from Balakrishnan et al. [285]. Colors are consistent from left to right in both sets of data.

Band Offsets to SiC, SiO_2, and Al_2O_3

Band offsets between sputtered Ga_2O_3 thin films and SiC substrates were measured using photoemission, finding $\Delta V = 2.8\,\text{eV}$ and $\Delta C = 0.89\,\text{eV}$ [289]. Band offsets between ALD Al_2O_3 thin films ($E_g = 6.8\,\text{eV}$) and single-crystal $\beta - Ga_2O_3$ were measured both by photoemission and capacitance-voltage (CV) measurements [290, 291]. Kamimura et al. [290] measured $\Delta V = 1.6 \pm 0.2\,\text{eV}$ and $\Delta C = 1.5 \pm 0.2\,\text{eV}$ by photoemission, and $\Delta C = 1.6 \pm 0.2\,\text{eV}$ by CV measurements. Hung et al. [291] also found $\Delta C = 1.7\,\text{eV}$ by CV. Band offsets between atomic-layer deposited SiO_2 ($E_g = 8.6\,\text{eV}$) were also measured using both photoemission and CV, finding $\Delta V = 0.43\,\text{eV}$ and $\Delta C = 3.63\,\text{eV}$ with photoemission, and $\Delta C = 3.76\,\text{eV}$ from CV measurements [292]. Band alignments at each interface are shown in fig. 3.35.

$(In_xGa_{1-x})_2O_3$ Alloy Films

Band gap variation and crystal stability has been explored in $(In_xGa_{1-x})_2O_3$ single crystals [293, 294] and thin films [236, 295–303]. $(In_xGa_{1-x})_2O_3$ single crystals with $0 < x < 0.2$ were grown by the float zone technique, and the change in the absorption edge for light polarized parallel to the b and c crystallographic directions was measured (fig. 3.36) [293]. In addition to a red shift in the band-to-band absorption edge, a second absorption onset at 3.6 eV in both polarizations developed, which was attributed to transitions between O $2p$ and In $5s$ from indium atoms in distorted octahedral sites based on a tight binding calculation similar to Tippins [11]. X-ray diffraction showed approximately a 1.5 % increase in lattice cell dimensions. $(In_xGa_{1-x})_2O_3$ single crystals using the float zone technque over a larger composition range $0 < x < 0.5$ were also grown [294]. Optical characterization was not performed, but it was shown that the solubility limit of indium in $\beta - Ga_2O_3$ is around $x = 0.35$, with a different phase appearing at $x = 0.5$, and that increasing the In content changes the conductivity from n-type to p-type.

$(In_xGa_{1-x})_2O_3$ thin films have been prepared by MBE [295], PLD [301–303], MOCVD [236, 296, 297, 299, 300], and sol-gel synthesis Kokubun et al. [298]. Films with nominal In concentrations $x = 0.1$, $x = 0.3$, $x = 0.5$, $x = 0.7$, and $x = 0.9$ were deposited on c-plane sapphire and ZrO_2 (100) [296, 297]. $\beta - Ga_2O_3$ peaks were not observed in XRD at any concentration, and the band gap decreased from 4.9 eV to 3.7 eV. However, these papers were somewhat confusing because RBS

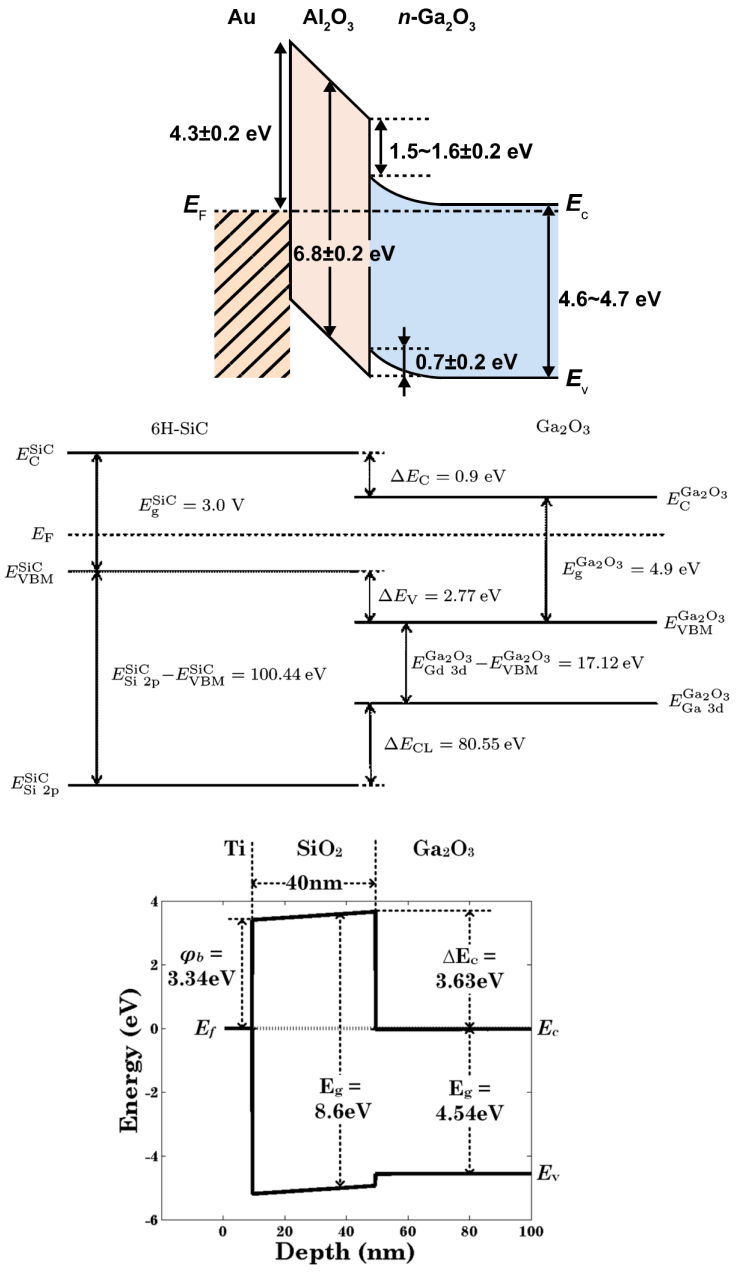

Figure 3.35: Top: Band alignment between atomic layer deposited Al_2O_3 and $\beta - Ga_2O_3$ from Kamimura et al. [290]. Middle: Band alignment between sputtered Ga_2O_3 on 6H-SiC from Chang et al. [289]. Bottom: Band alignment between atomic layer deposited SiO_2 and $\beta - Ga_2O_3$ from Jia et al. [292]

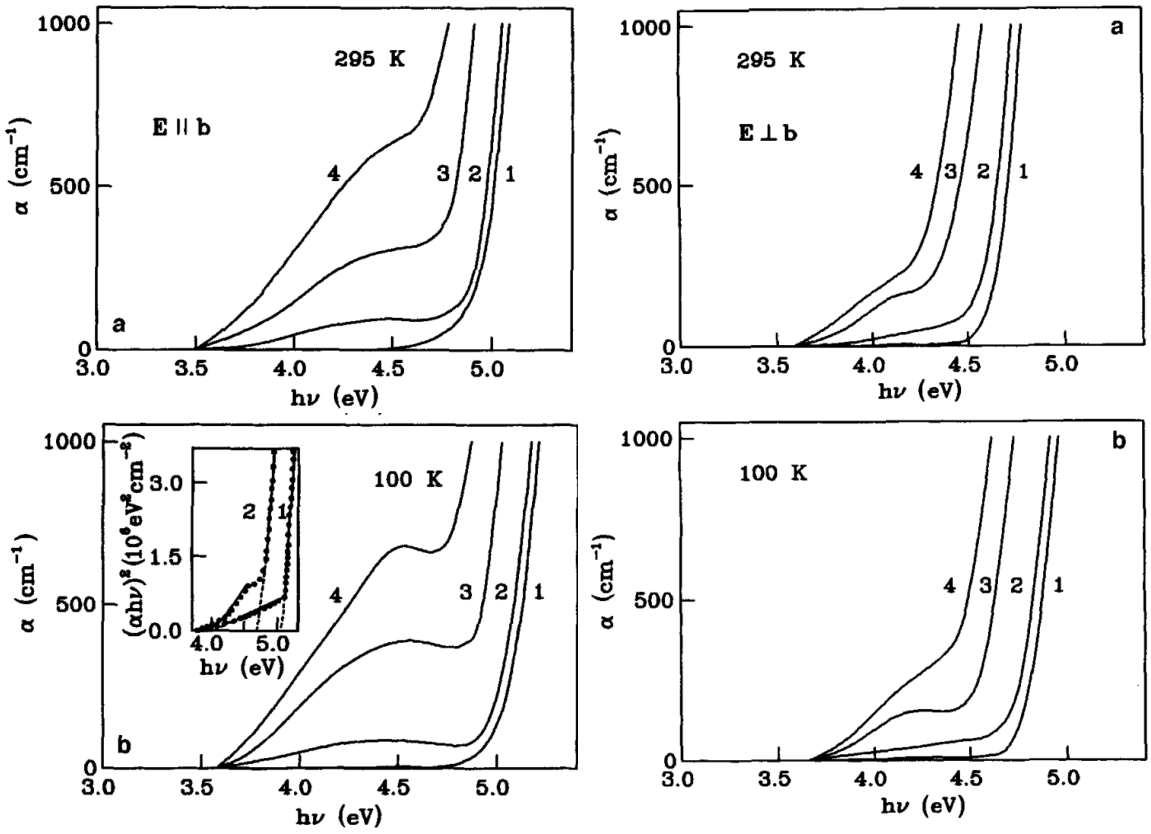

Figure 3.36: Absorption coefficient of $(In_xGa_{1-x})_2O_3$ single crystals with $x = 0$ (1), $x = 0.05$ (2), $x = 0.12$ (3), and $x = 0.2$ (4). From Vasyltsiv et al. [293]

measurements showed significant deviations of the actual In concentration from the nominal values appearing in plots of band gap vs. concentration. This issue was corrected in a subsequent study examining $(In_xGa_{1-x})_2O_3$ films on MgO (100) [236]. Here, RBS showed actual In concentrations of $x = 0.00$, $x = 0.09$, $x = 0.18$, $x = 0.37$ corresponding to nominal values $x = 0.0$, $x = 0.1$, $x = 0.3$, $x = 0.5$, and this time data were plotted as a function of the RBS values. XRD revealed that indium remains stable in the β phase up to $x = 0.09$, and secondary phases appear at $x = 0.18$. The band gap decreases monotonically in the sequence $4.87\,\text{eV} \rightarrow 4.83\,\text{eV} \rightarrow 4.79\,\text{eV} \rightarrow 4.74\,\text{eV}$, accompanied by a change in the shape of the absorption coefficient above $x = 0.18$ as crystallinity is lost. More recently, a series of $(In_xGa_{1-x})_2O_3$ films were fabricated on c-plane sapphire with x varying from 0.02 to 0.14, and in this study the upper solubility limit was also found to be about 10 %, with increasing lattice parameters and decreasing band gap from about 4.98 eV to 4.89 eV as x varied from 0.02 to 0.09 [299]. This is a larger shift ($\Delta E_{g\,\text{Baldini}} \sim 0.09\,\text{eV}$) than was observed by Kong et al. [236] ($\Delta E_{g\,\text{Kong}} \sim 0.04\,\text{eV}$) over the same interval.

Sol-gel $(In_xGa_{1-x})_2O_3$ films were prepared on c-plane sapphire from $x = 0$ to $x = 1$ and post-annealed to 900 °C for 1 hr, and the lattice expansion and band gap variation measured [298]. For these films the upper solubility limit was substantially higher at $x = 0.3$, which is closer to results obtained for sintered powders and for MBE-grown epitaxial films on sapphire by Oshima and Fujita [295]. Within the β phase ($0 < x < 0.3$) the lattice parameters are shown to increase linearly with In content by 3.5–4 %, and the band gap decreases linearly from 5.0 eV to 4.2 eV, which is a 3x faster variation than Baldini et al. [299] and a 6x faster variation than Kong et al. [236].

Epitaxial PLD $(In_xGa_{1-x})_2O_3$ films with a continuous composition spread (CCS) over a wide composition range on MgO (100) and c-plane sapphire were prepared [301–303]. CCS films are readily fabricated by PLD taking advantage of the natural anisotropy of the plume, enabling characterization over a range of alloy compositions within the same sample. Some of the data are shown in fig. 3.38. $\beta-(In_xGa_{1-x})_2O_3$ films were (100)-oriented on MgO, and $(\bar{2}01)$-oriented on sapphire. At $x = 0.2$, $(In_xGa_{1-x})_2O_3$ on sapphire transitioned to rhombohedral In_2O_3, although traces were already visible at $x = 0.1$, and finally transitioned to bixbyite at $x = 0.9$. On MgO, the β phase persisted until $x = 0.3$. Lattice parameters were observed to increase linearly until the second phase appeared, with a slight change in slope at that point. The band gap decreased from 4.97 eV at $x = 0$ to 4.54 eV at $x = 0.15$, in reasonable agreement with the result by Kokubun et al.

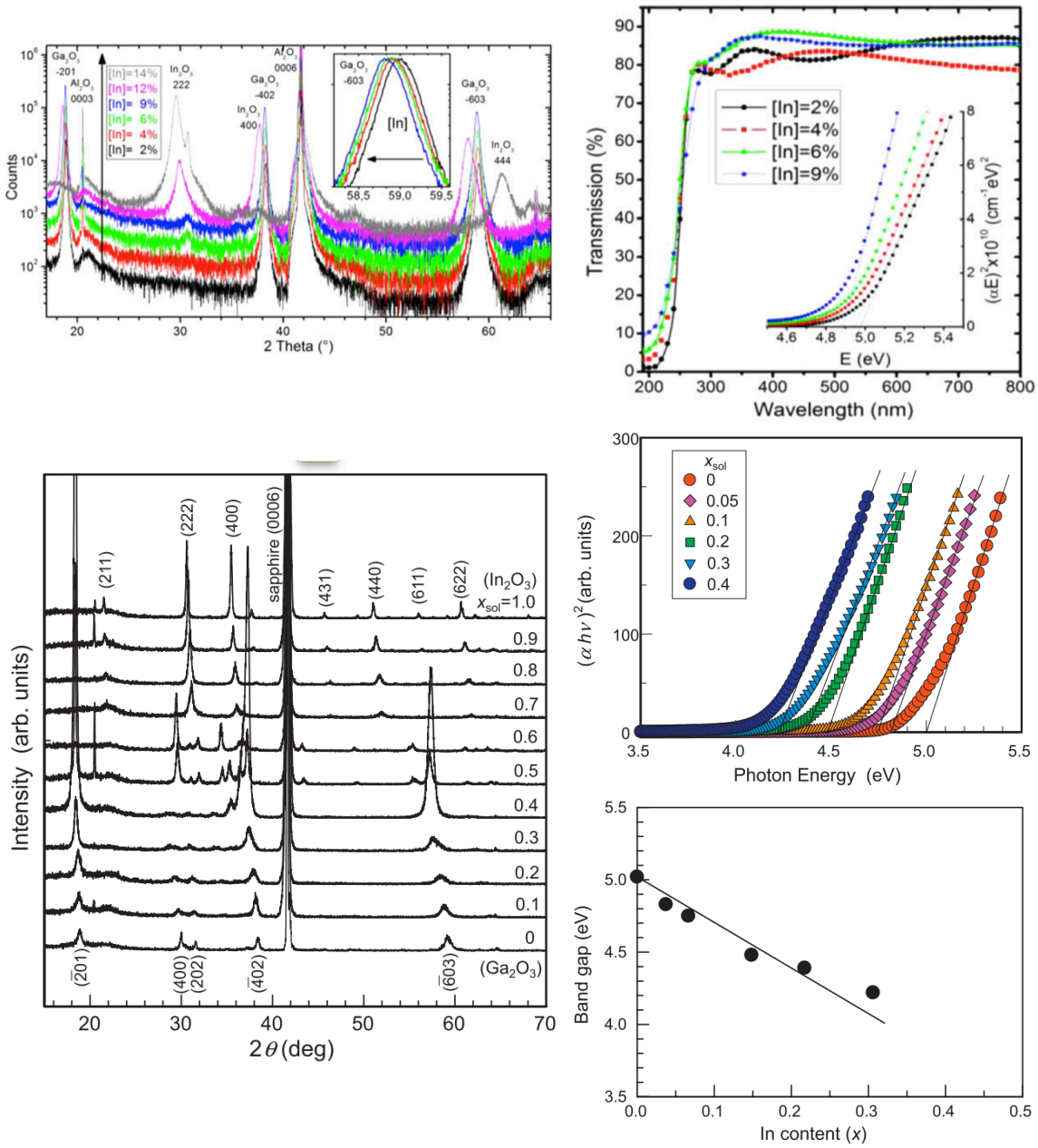

Figure 3.37: Top: XRD $\theta - 2\theta$ scans and band gap variation of a series of $(In_xGa_{1-x})_2O_3$ films grown by MOVPE on sapphire, from Baldini et al. [299]. Bottom: Similar results from a series of sol-gel films on sapphire, from Kokubun et al. [298].

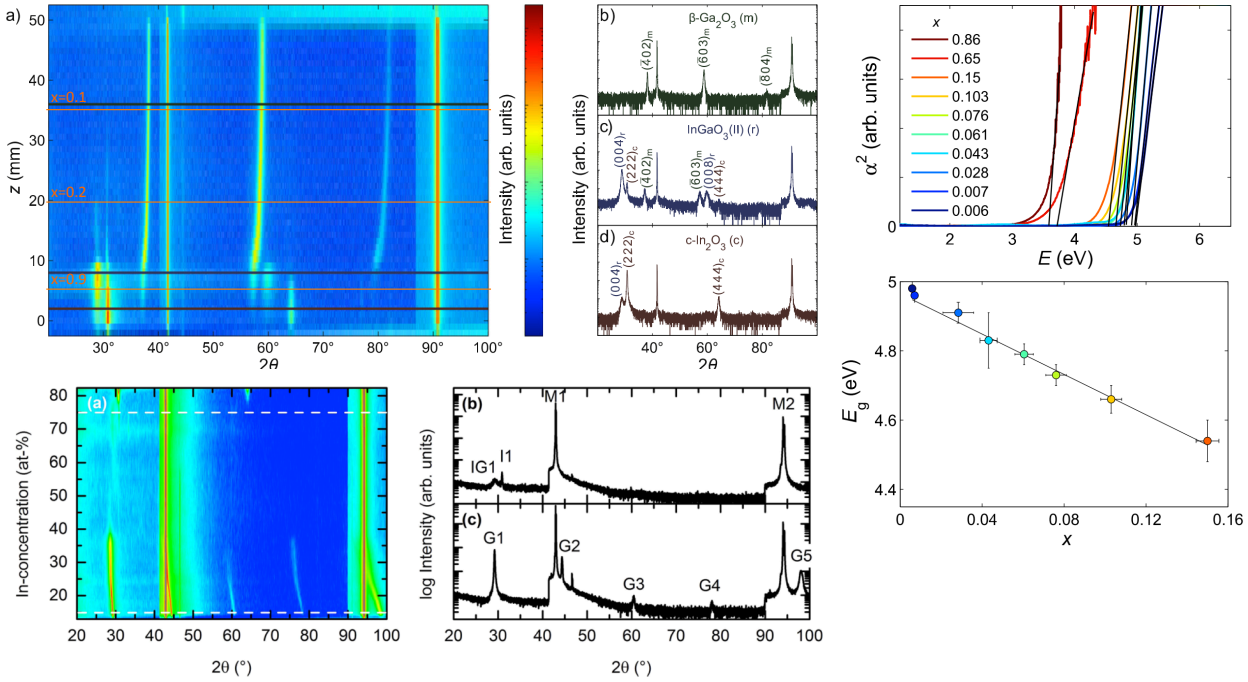

Figure 3.38: Top: XRD false color image assembled from a series of 55 $\theta - 2\theta$ scans from an $(In_xGa_{1-x})_2O_3$ CCS film on sapphire showing distinct crystallographic regions: $\beta - Ga_2O_3$ from $55 > z > 20$ $(0 < x < 0.2)$, rhombohedral In_2O_3 from $15 > z > 5$ $(0.2 < x < 0.9)$, and bixbyite In_2O_3 at $5 > z > 0$ $0.9 < x < 1$. Right: Band gap variation with In content of CCS films on sapphire. From Wenckstern et al. [303]. Bottom: Similar XRD false color image from an $(In_xGa_{1-x})_2O_3$ CCS film on MgO (100), plotted against composition on the y-axis. From Kranert et al. [301].

[298].

$(Al_xGa_{1-x})_2O_3$ Alloy Films

$\beta-(Al_xGa_{1-x})_2O_3$ alloy films have been fabricated by MBE [46], PLD [213, 304–306], by the thermal oxidation of AlGaN [45], and by intentionally diffusing Al from sapphire into a Ga_2O_3 film [266]. The earliest study found a solubility limit of Al in $\beta-(Al_xGa_{1-x})_2O_3$ of $x = 0.61$ for MBE films on $\beta-Ga_2O_3$ (100) substrates, and a b-axis lattice mismatch between film and substrate of just 0.1 % at $x = 0.61$ [46]. The natural lattice parameter is around 2 % smaller at that composition, therefore the low mismatch indicates that the film is under tensile strain to maintain epitaxy. In addition, CV measurements showed evidence of carrier accumulation at the interface between $\beta-(Al_{0.29}Ga_{0.71})_2O_3$ and $\beta-Ga_2O_3$, demonstrating that a high-electron-mobility transistor may be possible. VUV solar-blind photodetectors were fabricated by thermally oxidizing an AlGaN layer, showing a band gap increase to 5.6 eV for an Al content of $x = 0.24$ [45].

A series of $(Al_xGa_{1-x})_2O_3$ films were deposited by PLD on sapphire with $x = 0.22$, $x = 0.53$, $x = 0.72$, $x = 0.86$, $x = 0.96$ and $x = 1.0$ [304]. The substrate temperature was rather low (400 °C), and XRD showed that the crystallinity deteriorates with increasing Al content. Optical measurements showed the band gap to be 5.34 eV and 5.74 eV for $x = 0.22$ and $x = 0.53$, respectively, but above $x = 0.53$ the absorption edge moved past the edge of the window. Therefore XPS was also used to measure the band gap, by finding the onset of inelastic loss structure from electron-electron collisions behind the bright O 1s photoemission peak. The resulting trend exhibited a nearly linear increase from 5.25 eV ($x = 0.2$) to 6.25 eV ($x = 0.9$), with a sharp increase above $x = 0.9$.

Recently, $(Al_xGa_{1-x})_2O_3$ continuous-composition spread films on MgO (100) were fabricated by PLD, and characterization using XRD and spectroscopic ellipsometry was performed, following a strategy very similar to the present work [305, 306]. In these films the β phase was found to be stable to $x = 0.5$, followed by a transition to γ. Within the β phase the band gap increases from 5.0 eV to 5.8 eV at $x = 0.5$, in reasonable agreement with Zhang et al. [304] (fig. 3.39). The higher stability of the β phase in this work is probably due to a higher growth temperature of 650 °C; however, Kaun et al. [213] found that at 650 °C the β phase in MBE-grown $(Al_xGa_{1-x})_2O_3$ films on $\beta-Ga_2O_3$ (010) is only stable to $x = 0.18$, and our data suggests the limit is approximately $x = 0.3$ on sapphire.

In addition, $\alpha-(Al_xGa_{1-x})_2O_3$ alloy films have been fabricated epitaxially on c-plane sapphire

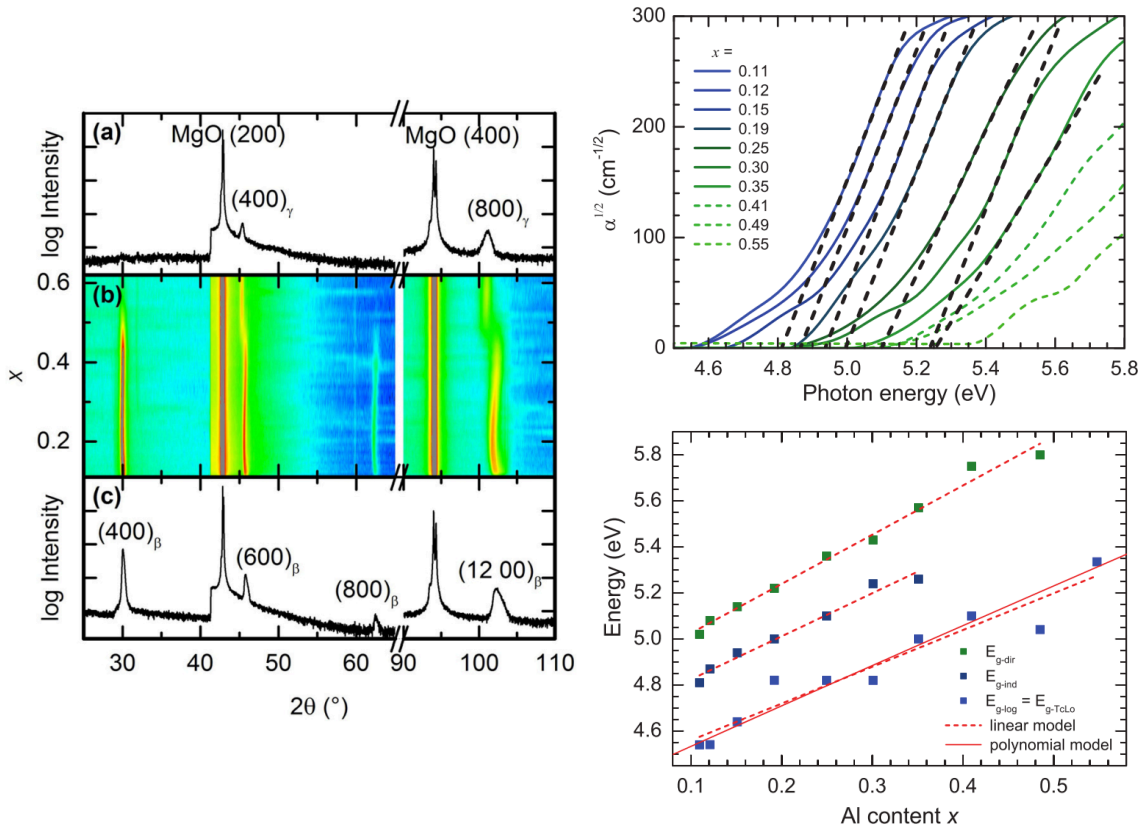

Figure 3.39: XRD false color image assembled from a series of $\theta - 2\theta$ scans from an $(Al_xGa_{1-x})_2O_3$ CCS film on MgO (100) showing distinct crystallographic regions: $\beta - Ga_2O_3$ (100) for $x < 0.5$ and $\gamma - Al_2O_3$ (100) for $x > 0.5$. Right: Band gap variation with Al content from ellipsometry fitting. From Kranert et al. [305] and Schmidt-Grund et al. [306].

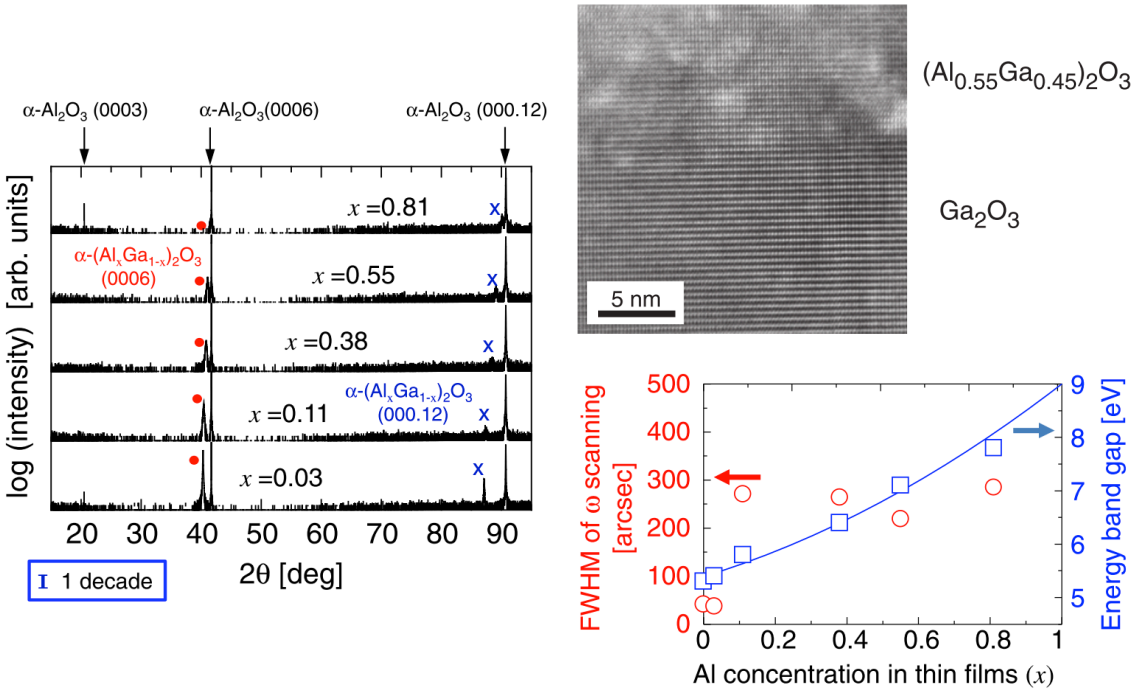

Figure 3.40: Left: XRD $\theta - 2\theta$ scans for epitaxial $\alpha - (Al_xGa_{1-x})_2O_3$ films on sapphire. Upper right: Cross sectional TEM image at the interface between a $(Al_{0.55}Ga_{0.45})_2O_3$ and a Ga_2O_3 film on a sapphire substrate. Lower right: Band gap and XRD rocking curve widths for the α (0006) reflection of $\alpha - (Al_xGa_{1-x})_2O_3$ films. From Ito et al. [307]

by mist-CVD [248, 307–309]. Since the stable phase at the $x = 1$ endpoint is also corundum, the composition can be varied all the way from $0 < x < 1$ without a phase change. The band gap of $\alpha - Ga_2O_3$ is 5.3 eV [248], higher than $\beta - Ga_2O_3$ band gap by approximately 0.5 eV, and the band gap of $\alpha - Al_2O_3$ is 8.8 eV [310], much larger than $\theta - Al_2O_3$ which is predicted to be around 6.5 eV (chapter 5). As in $\beta - (Al_xGa_{1-x})_2O_3$ films, variation within the α phase proceeds almost linearly with Al concentration between the $x = 0$ and $x = 1$ endpoints. Growth of α phase films also opens up the possibility of alloying with other corundum-structured metal-oxides, including $\alpha - Cr_2O_3$, $\alpha - Fe_2O_3$, $\alpha - V_2O_3$, and $\alpha - Ti_2O_3$ [308, 311], although the window of growth temperatures yielding α phase films is rather low, which may inhibit incorporation. However, it was recently shown that alloying with Al can substantially enhance the thermal stability $\alpha - (Al_xGa_{1-x})_2O_3$ films, up to at 900 °C (fig. 3.41) [309].

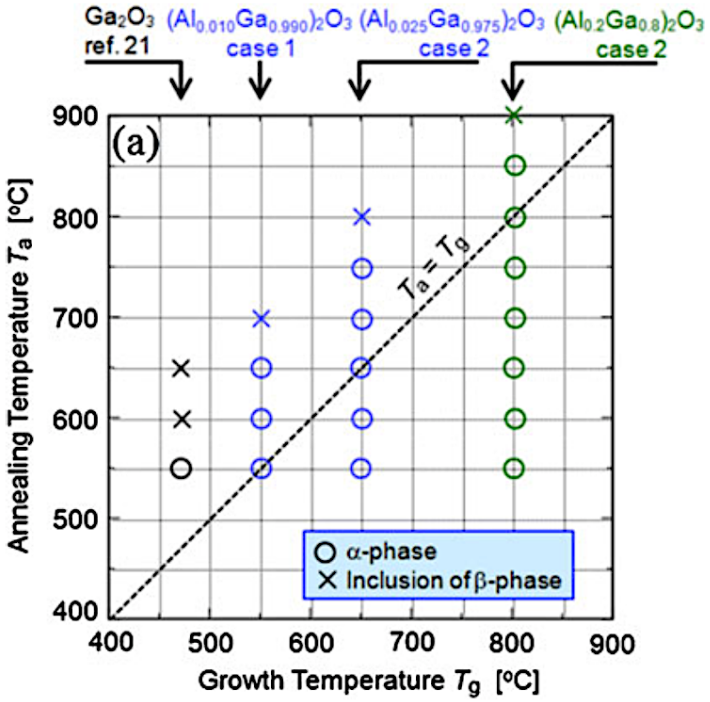

Figure 3.41: Thermal stability of the α phase in mist-CVD-grown $(Al_xGa_{1-x})_2O_3$ films. From Lee et al. [309]

Ga_2O_3 Thin Films Alloyed with Other Elements

Several other Ga_2O_3-based alloys have been reported. In attempts to achieve p-type conductivity, Ga_2O_3:Zn films with 0–7 at.% Zn were fabricated by Wang et al. [226], and Ga_2O_3:Cu films with 5 at.% Cu were fabricated by Zhang et al. [202]. Both authors claimed success; however, the data are unconvincing. Ga_2O_3:Zn films remain in the β phase to at least 7 at.%, but XRD peaks for Ga_2O_3:Cu start to diminish already at 5 at.%. Additionally, no change is observed in the absorption edge of Ga_2O_3:Zn films, but Ga_2O_3:Cu films show a pronounced red shift, as well as higher absorption in the gap and smaller grain sizes compared to undoped Ga_2O_3 films.

Doping with N on the anion site was attempted in RF-sputtered films by Zhang et al. [203] and Sun et al. [207]. Both reports showed red shifting of the absorption edge with N-incorporation due to the stronger ionicity of the Ga–O bond relative to Ga–N; however, neither study measured the composition of their films, instead reporting data as functions of ammonia or N_2 partial pressure in the growth atmosphere, so it's not clear how the band gap, conductivity, or crystal phase change with N concentration.

Ga_2O_3:W films have been fabricated by Rubio and Ramana [205] and Dakhel [189], and both authors showed a decreasing band gap with W incorporation. Dakhel reported that the β phase is stable all the way to 30 % W, due to the similar ionic radii of W and Ga, and that the band gap decreases from 4.9 eV to 4.4 eV from $0 < x < 0.3$. In addition, a wild variation in the dielectric permittivity was measured, decreasing from 10 ($x = 0$) to 1.5 ($x = 0.18$) and then climbing back to 6 ($x = 0.3$).

$\gamma - Ga_2O_3$:Mn films were fabricated by PLD at 500 °C by Huang et al. [222] and Hayashi et al. [223], and $\beta - Ga_2O_3$:Mn films were fabricated at 900 °C by Guo et al. [312]. Films grown at 900 °C remained single phase up to 53 % Mn, showing a linear increase with lattice parameters and a decrease in the band gap from 4.92 eV to 4.72 eV at $x = 0.31$. In addition, room temperature ferromagnetism was observed for Mn concentrations above $x = 0.11$.

Ga_2O_3:X films were also fabricated to investigate their phosphorescent properties, where X $\in$ {Mn, Cr, Co, Eu, Nd, Sm, Dy, Ce, Er, Ho, Pr, Tb, or Tm} [34, 196, 197, 221, 254, 256], and cathodoluminescence spectra with peak intensities spanning the entire visible range were demonstrated [34].

Ga_2O_3:Ti films with 0–15.7 at.% Ti were evaporated by Dakhel [190]. XRD showed that 600 °C post-annealed films crystallize in the $\kappa-Ga_2O_3$ phase ($Pna2_1$) and that peak intensities grow with Ti-incorporation, suggesting that Ti stabilizes the orthorhombic phase. The band gap is shown to decrease with Ti concentration, with significant sub-gap absorption beginning at 15.7 at.%, and a change in the dielectric permittivity similar to the case of W-incorporation.

Amorphous Ga_2O_3:Cd films were fabricated by Yanagi et al. [313]. The band gap of CdO is 2.3 eV, even lower than In_2O_3, therefore a wider range of tunability was achieved in Ga_2O_3:Cd films than Ga_2O_3:In, from 4.3 eV ($x = 0.3$) down to 2.5 eV ($x = 0.8$). Carrier concentration and conductivity fell by an order of magnitude as the Cd concentration increased past 50 %.

Ga_2O_3:Mg films were fabricated from 1–10 at.% Mg by Feng et al. [243], and the effect of post-annealing was investigated. After post-annealing to 900 °C, $\beta - Ga_2O_3$ peaks were visible in XRD until $x = 0.07$, but with decreased intensity at each step implying poorer crystallinity. Before annealing, the band gap showed a linear increase with Mg concentration from 4.93 eV to 5.32 eV; after annealing the endpoints were slightly lowered to 4.87 eV and 5.22 eV, respectively. Doping with Mg is known to reduce the unintentional conductivity of Ga_2O_3 single crystals [314], though no significant change in the conductivity was observed in the Ga_2O_3:Mg alloy films.

$\alpha - Ga_2O_3$:Fe films from 0–100 at.% Fe were fabricated by mist-CVD by Kaneko et al. [311], demonstrating the ability to fabricate corundum-phase alloy films over a wide composition range using this technique. The band gap of $\alpha - Fe_2O_3$ is 2.2 eV, close to CdO, and the band gap varied smoothly between the $\alpha - Ga_2O_3$ and $\alpha - Fe_2O_3$ end points. In addition, ferromagnetism at 110 K was demonstrated in an $x = 0.24$ film.

Optical Characterization of Ga_2O_3 Films

The refractive index of amorphous Ga_2O_3 deposited by e-beam evaporation, RF sputtering, atomic layer deposition, and spray pyrolysis has been reported by several authors. Passlack et al. [135] measured an increase from $n = 1.841$ to $n = 1.885$ at 980 nm for e-beam evaporated films post-annealed at 125 °C to 350 °C, respectively. An absorption spectrum revealed that the band gap of the 125 °C post-annealed film was 4.4 eV. Ortiz et al. [253] found an increase in the refractive index from $n = 1.846$ to $n = 1.864$ (at 632 nm) of Ga_2O_3 films deposited by spray pyrolysis as the substrate temperature was raised from 300 °C to 425 °C, followed by a lower n at higher temperatures due to developing porosity. Shan et al. [228] also found an increase from $n = 1.84$ to $n = 1.89$ at 632.8 nm as the substrate temperature was raised from 500 °C to 700 °C, and amorphous atomic-layer-deposited films transitioned to crystalline. Al-Kuhaili et al. [185] evaporated Ga_2O_3 films in vacuum and O_2, and found that the n dispersion curve of the O_2-deposited films was offset vertically by approximately -0.2 from the corresponding curve for vacuum-deposited films. In all of these experiments, the authors attributed the increase of the refractive index to a change in the film density caused by either post-annealing or deposition conditions, and all remain lower than $n = 1.92$–1.95 for bulk $\beta - Ga_2O_3$ [253].

The refractive index of meta-stable Al_2O_3 thin films is also proportional to density. Cibert et al. [281] found variation from $n = 1.69$ to $n = 1.72$–1.73 at 632.8 nm for PLD films grown at room temperature and at 800 °C, respectively. Balakrishnan et al. [283, 285] found variation from $n = 1.69$ to $n = 1.75$ at 632 nm through an amorphous to γ transition by varying the substrate temperature, and from $n = 1.73$ to $n = 1.81$ when varying the O_2 partial pressure (fig. 3.34). Gottmann and Kreutz [286] found that even for films deposited at room-temperature the index of refraction at 633 nm could vary from $n = 1.72 \pm 0.02$ for 94 % dense films, to $n = 1.3$–1.4 for 40–50 % dense films.

Rebien et al. [33] studied e-beam evaporated and RF-sputtered Ga_2O_3 films by spectroscopic ellipsometry. It was determined by XRD and TEM analysis that both films consisted of nanocrystallites embedded in an amorphous matrix. Despite the different deposition methods, both films had nearly the same band gap (4.74 eV and 4.72 eV, respectively) and consistent dispersion in n, with Cauchy model parameters $A = 1.89$, $B = 0.011$, and $C = 0.0004$. These values are consistent with the parameters of my PLD Ga_2O_3 films as well. These results show that sample-to-sample

variation in n and other properties of amorphous films may probably be attributed to microstructural differences, and that consistency can be achieved by comparing films with similar microstructure even if deposited by quite different methods.

Dispersion curves of $(Al_xGa_{1-x})_2O_3$ and $(In_xGa_{1-x})_2O_3$ PLD films as a function of In and Al concentration, based on spectroscopic ellipsometry data fitted to a Cauchy model, have been reported by Schmidt-Grund et al. [302, 306] and are shown in fig. 3.42. These figures are directly comparable to my own data reported in section 7.4 and chapter 6.

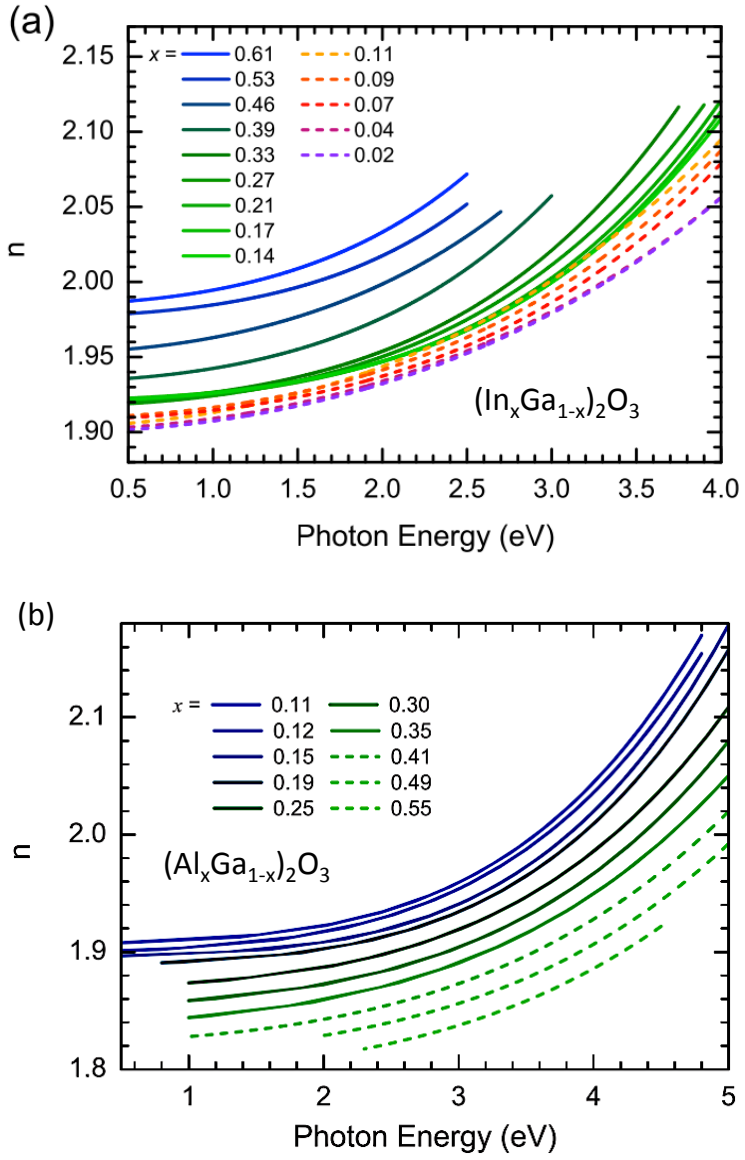

Figure 3.42: Top: Refractive index of $(In_xGa_{1-x})_2O_3$ films, from Schmidt-Grund et al. [302]. Bottom: Refractive index of $(Al_xGa_{1-x})_2O_3$ films, from Schmidt-Grund et al. [306].

Chapter 4

EXPERIMENTAL METHODS

4.1 Preparing $(Al_xGa_{1-x})_2O_3$ Powders: Solution Combustion Synthesis

Solution combustion synthesis is a simple, low-cost method to produce high-purity, stoichiometric oxide powder without the need for multiple grinding and calcination steps. Advantages of combining precursors in solution are uniform, atomic level mixing and precise control of their relative quantities [315–317]. Gallium nitrate [$Ga(NO_3)_3$] and aluminum nitrate [$Al(NO_3)_3$] precursors (99.9999% purity, from Alfa Aesar) were dissolved in DI water in the desired Al:Ga atomic ratio x. Urea [$CO(NH_2)_2$] was added as a fuel in the molar ratio 2.5:1. This fuel concentration establishes a stoichiometric redox mixture, ensuring that maximum energy is released in the combustion reaction [318–320]. This property can be exploited to give control over the phase of the reaction products. For example, Srihari et al. [321] found that either $\gamma - Ga_2O_3$ or $\beta - Ga_2O_3$ is produced by adding a sub-stoichiometric or super-stoichiometric molar ratio of urea, respectively. A similar result was obtained for Al_2O_3 by Zhuravlev et al. [322]. Upon heating the solution above 500 °C, the solution boils away and the remaining gel auto-ignites, causing the following exothermic reaction to take place

$$2x\ Al(NO_3)_3 + 2(1-x)\ Ga(NO_3)_3 + 5\ CO(NH_2)_2 \longrightarrow 8\ N_2 + 5\ CO_2 + 10\ H_2O + (Al_xGa_{1-x})_2O_3$$

Temperatures reached during the combustion of Al_2O_3 and other oxides are generally in the range 1200–1300 °C [319, 320, 322]. The reaction was carried out in a furnace in a loosely-covered alumina crucible to avoid introducing the dopant Si, or other impurities contained within a standard glass beaker. The result after combustion is a loosely-connected network which collapses into powder as soon as it is touched.

After combustion, powder was rolled by hand in wax paper to break up large agglomerates. Rolling by hand is clearly inferior to grinding in a mortar and pestle if a uniform, fine grain size is desired, but optimization of the grain size was deemed less important than avoiding Si contamination

from the porcelain. Next the powder was placed in a 13 mm diameter die press and pressed into a pellet with approximate pressure 8 kN/cm^2, placed on an alumina plate, and sintered in air at 1600 °C for 12 h, ramping at a rate of 5 °C/min. This sintering temperature is approximately 200 °C below the melting point of Ga_2O_3, and 500 °C below the melting point of Al_2O_3 [103].

4.2 Preparing $(Al_xGa_{1-x})_2O_3$ Thin Films: Pulsed Laser Deposition

4.2.1 Overview and Background

Pulsed laser deposition (PLD) is a versatile technique for the deposition of thin films and is especially well suited for complex oxides, which are difficult to grow by evaporative techniques. On a basic level the idea appears somewhat brute-force: a target made of the desired material is placed in a deposition chamber with a controlled atmosphere and exposed to high-intensity laser pulses, which ablate the target surface, creating an energetic plume that propagates away from the target and condenses onto a substrate. Heating rates as high as 10^{11} K/s and instantaneous gas pressures of 10–500 atm have been observed at the target surface [323] creating a dense plasma of atoms, ions, molecules and clusters [324–326]. The highly nonequilibrium and anisotropic nature of the ablation process and the sensitivity of the final product to a large number of experimental parameters means achieving high quality samples can be challenging. Usually a significant amount of trial and error is required before one finds a suitable recipe, which may differ from those published by others. As a result, a large theoretical and experimental literature has developed to elucidate the mechanics of the PLD process.

Although a small community of thin films researchers employing pulsed laser methods existed as early as 1965 [327], the explosion in popularity of modern PLD began in 1987 after a paper by Dijkkamp et al. [328], demonstrating the stoichiometric transfer of Y-Ba-Cu-O from target to film and preserving its superconducting property. Soon afterward a theoretical study by Singh and Narayan [329] was published which successfully explained a number of experimental observations such as the changing plume shape as a function of spot size, the linear relationship between pulse energy and evaporated flux, the dependence of film thickness and thickness variation on the target-substrate distance, and the spatial variation of the composition in a deposited film, by modeling the plume as an ideal gas expanding adiabatically into a vacuum. Modeling the plume using gas

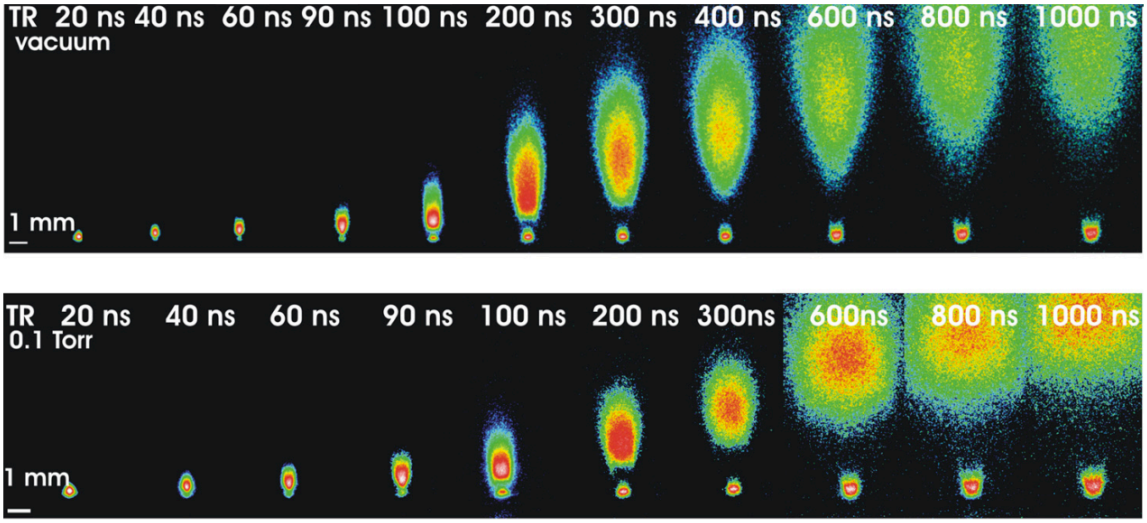

Figure 4.1: Expansion of a laser ablated brass plume into vacuum (10^{-5} Torr) and 0.1 Torr Ar gas. From Diwakar et al. [337]

dynamics was undertaken again three years later by Anisimov et al. [330], who derived a thickness profile [const. $\times (1 + k^2 \tan^2\theta)^{-3/2}$] used by almost every author since. Since then the study of plume dynamics has become an entire field unto itself. Strikovski and Miller [331] used an adiabatic thermalization model to predict an optimum deposition rate of 1 Å/pulse for oxides independent of the pulse energy which agrees with experimental results [331, 332]. Interesting review papers on the subject are written by Marla et al. [333] and Balling and Schou [334]. Recently it has even become possible to image and characterize the expansion of a plume into an atmosphere through a wide range of gas pressures directly using ultrafast cameras [335–337].

The main experimentally controlled parameters may be divided into broad categories including: laser settings, background gas atmosphere, geometry of the substrate over the target, substrate type and temperature, and target composition (table 4.1). Most of these have been explored in the literature for their various effects on the final product. The influence of laser energy density over a 1–6 J/cm^2 range was undertaken by Gonzalo et al. [338] in BiSrCaCuO films, who found that the velocity of ejected particles increases with absorbed energy but that composition and angular distribution are unaffected. Laser energy density has been reported to affect the crystal phase of Al_2O_3 films, transforming them from amorphous into the α phase as energy density varies

Table 4.1: Experimentally controlled PLD deposition parameters.

Laser Settings	Wavelength
	Pulse Energy
	Pulse Repetition Rate
	Spot Size
Environment	Background Gas
	Pressure
Geometry	Target-Substrate Distance
	Target Rotation
	Deposition Angle
	Rastering
	Shutter
Substrate	Deposition Temperature
	Substrate
Target	Composition
	Density

over 2–4 J/cm^2 range despite a low substrate temperature of just 400 °C [276] (however, we were unsuccessful in producing α-phase Al_2O_3 films using a similar laser fluence even at much higher temperatures). Changing the shape of the laser spot from one elliptical orientation to the other has been observed to affect the width of the plume—the so-called "flip-over effect" [339]. The angular distribution of the plume has been studied for a number of different metals [339–342] and oxides [343–345]. The effect of atomic mass and pressure of the background gas on the overall shape and distribution of the plume has been studied [346–348], as well as the effect of intrinsic preferential resputtering [340, 349]. In addition to influencing the sticking coefficient and crystallinity of deposited films, raising the substrate temperature has been found to affect the propagation of the plume by counteracting the background gas pressure [350]. Geometrical parameters affect the number and velocity of particles incident on the substrate, which can have a dramatic effect on film properties. Target-substrate distance has been observed to strongly affect conductivity at the $LaGaO_3/SrTiO_3$ interface [351], and a lateral offset has led to an unexpected tilting of the optical axis in ZnO [352]. This is not a complete tour of the PLD literature, and is only intended to highlight the wide array of processing conditions achievable through PLD, and the (often unexpected) interplay between various deposition parameters. A review of the physics of PLD with emphasis on achieving stoichiometric transfer from target to film has been written by Schou [353], and another review focusing on the PLD of oxides was written by Christen and Eres [323].

Background oxygen is critical to the production of oxide films; without it, films are severely sub-stoichiometric [354]. Authors have reported phase segregation leading to metallic clusters embedded in a stoichiometric oxide in ITO [355, 356], TiO_2 [357], and Ga_2O_3 [177, 224, 357, 358]. A detailed study of the oxygen uptake as a function of pressure was undertaken by Morales-Paliza et al. [359], making use of Rutherford backscattering and ^{18}O gas to determine the relative amounts of oxygen coming from gas and target. They found that the relative amount of oxygen coming from the gas begins to increase above 5 mT partially displacing oxygen coming from the target, but with an increase in the total oxygen content up to a maximum pressure around 50 mT above which plume scattering becomes too great.

One of the strengths of PLD is the limitless flexibility to create new alloys. One way is to mix together powders of different materials in desired ratios, and press the entire mixture into a single sintered pellet to act as a PLD target, taking advantage of stoichiometric transfer from target to

film. Another way is to rotate multiple targets into the laser spot, building an alloy film layer by layer and controlling the film composition by the relative number of pulses incident on each target. A variation on the second method to center the axis of each plume at different positions over the substrate surface allows for the creation of thin films with a continuous composition spread (CCS), due to the anisotropic nature of the PLD plume. The first report on the advantages and disadvantages of this method is by Christen et al. [360], who explored the binary $Ba_xSr_{1-x}TiO_3$ and ternary $In_2O_3 - SnO_2 - ZnO$ systems. This method is sometimes referred to as the natural composition spread technique, as no mask is used and the composition gradient is set by the natural shape of the plume and the background gas pressure. Investigating new alloys in this way allows for the mapping of a large number physical properties with alloy composition within a single sample, eliminating the possibility of unintentional sample-to-sample variation. Four years later, the same authors showed that inserting a programmable moving shutter gives added flexibility to the design of the final film, including better control of dimensions and a more uniform thickness profile [361]. However, our system does not possess a programmable shutter, so CCS films in this work were fabricated using the natural composition spread technique.

4.2.2 Sample Preparation Details

All film growth was carried out on a PLD-MBE 2300 deposition system by PVD Products, Inc. (Wilmington, MA). An illustration of our process is shown in fig. 4.2. Optimization of deposition conditions was first carried out for Ga_2O_3 by systematically varying the substrate temperature, oxygen pressure, and laser fluence over ranges reported in the literature. Optimized parameters were then used to fabricate CCS $(Al_xGa_{1-x})_2O_3$ films. Ideal conditions for stoichiometric Al_2O_3 probably vary somewhat from Ga_2O_3, in particular the background O_2 pressure and substrate temperature. As a result oxygen stoichiometry is not always consistent throughout the film—especially for films grown at room temperature—and a transition to a low-temperature metastable or amorphous phase is always observed at some point along the composition gradient. In the future, moving to a higher temperature might alleviate the latter problem, as long as substrate-film interdiffusion remains minimal. In this work films were grown at 20 mT in 99.9999% O_2, either at room temperature or at a setpoint of 800 °C. The incident KrF laser energy was 200 mJ (est. 3 J/cm^2), the pulse repetition

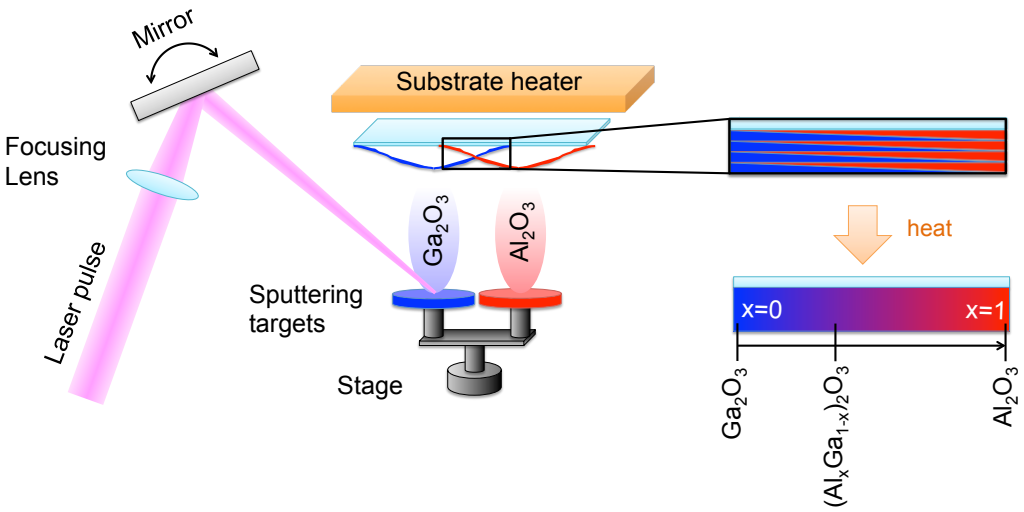

Figure 4.2: Fabrication of a $(Al_xGa_{1-x})_2O_3$ continuous-composition-spread thin film by pulsed laser deposition. Alternating layers may be deposited either by rastering the laser spot from one target to the other, or by leaving the mirror fixed and rotating the sample and targets together by 180° in between layers.

rate was set to a low 2 Hz, and the target-substrate distance was 5.5 cm.

Important additional parameters for CCS films include the thickness of each layer, and the separation between opposite plume axes along the substrate surface. The requirement of uniform incorporation means that the layer thickness should be smaller than 1–2 monolayers at the thickest point, to avoid creating a superlattice structure. The separation between plume axes depends on the size of the substrate and the range of composition spread desired. A combination of large substrate and large separation leads to a wide composition range (up to $0.005 < x < 0.995$ in room-temperature sample pa-S1), and a correspondingly extreme film thickness variation (300–3000 nm). When the plume axes are brought closer together a smaller composition range is achieved, but the thickness variation is smaller (e.g. sample pa-A1 varies in composition from $0.05 < x < 0.90$ and in height from 400–800 nm).

It is helpful to be able to predict the thickness variation and composition range of a CCS thin film before deposition. The problem of the thickness of a PLD film as a function of lateral distance

has already been solved [323, 330]

$$t(\theta) \approx \text{Amp.} \times k^2 \left(1 + k^2 \tan^2\left(\frac{s}{d}\right)\right)^{-3/2} \tag{4.1}$$

where d is the target-substrate distance, s is the distance away from the plume axis, and k is a parameter that describes the shape of an elliptical plume centered on the laser spot, equal to the z-extent divided by the x-extent. A spherical plume has $k = 1$, and larger values of k denote greater ellipticity.

A series of oxide films were produced under identical conditions and the natural thickness variation measured as a function of position. The deposition parameters used were close to those used for my $(Al_xGa_{1-x})_2O_3$ films: 36 000 pulses at a rate of 5 Hz and a pulse energy of 160 mJ, a substrate temperature of 800 °C, an O_2 pressure of 20 mT, and a target-substrate distance of 5.5 cm. The result is shown in fig. 4.3. Acceptable fits using eq. (4.1) were achieved for each type of oxide and a trend was found between k and cation atomic mass, as expected for collisions with the background gas. In addition, an inverse trend between film thickness and band gap was observed (fig. 4.4). In PLD it is preferable for laser light to be absorbed in the fundamental absorption region of the material, with high optical absorption coefficient $\alpha \sim 10^5\,\text{cm}^{-1}$ [362]. Our KrF laser produces 248 nm radiation, which is ideal for SnO_2 and Ga_2O_3 but a low energy for ZrO_2 and Al_2O_3, so in those materials heating and ablation occurs through the absorption of incident light at grain boundaries or other defects, rather than in the bulk.

The composition at any point along the composition gradient can be predicted if we know how the thickness t varies with position for each plume (based on eq. 4.1) and the spatial separation s of the plume axes, by the formula [360]

$$\%\ \text{Material 1} = L \times \frac{n_1 t_1(x)}{n_1 t_1(x) + n_2 t_2(s - x)} \tag{4.2}$$

Where n_1 and n_2 are the number of pulses in each layer and L is the total number of layers. Based on the above film thickness measurements, a 7:1 pulse ratio of Al_2O_3 to Ga_2O_3 would be expected to produce an approximately 50 % alloy $(Al_xGa_{1-x})_2O_3$ film if the substrate were equidistant between the two plumes. In fact, we found the ratio to be closer to 2:1 by trial and error. However, to emphasize points near the Ga_2O_3 end of the composition range, pulse ratios ranging from 1:1 to 1.5:1 were actually used. As a result, thicknesses are much greater on the Ga_2O_3 side than on the

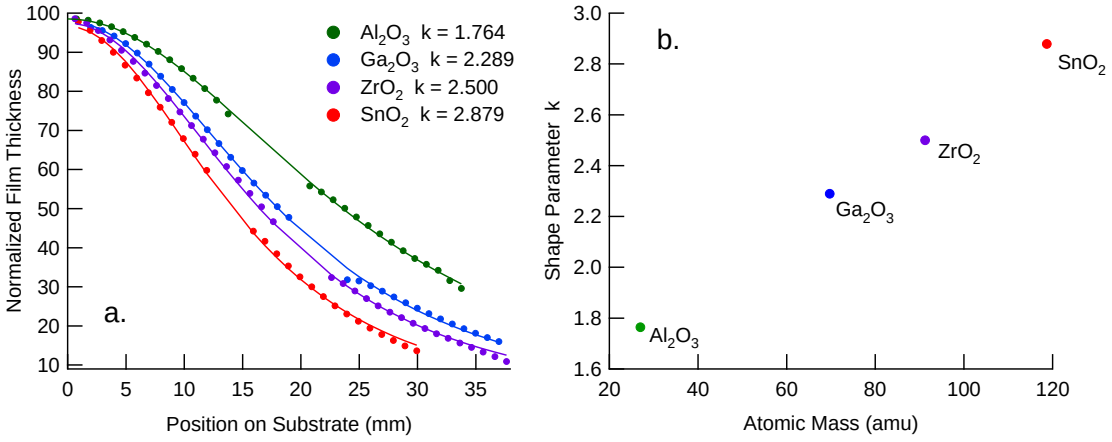

Figure 4.3: a) Comparison of eq. (4.1) model fit to normalized film thicknesses for a series of oxides as a function of distance from the center of the plume, and b) Relationship between the plume shape parameter k and cation atomic mass.

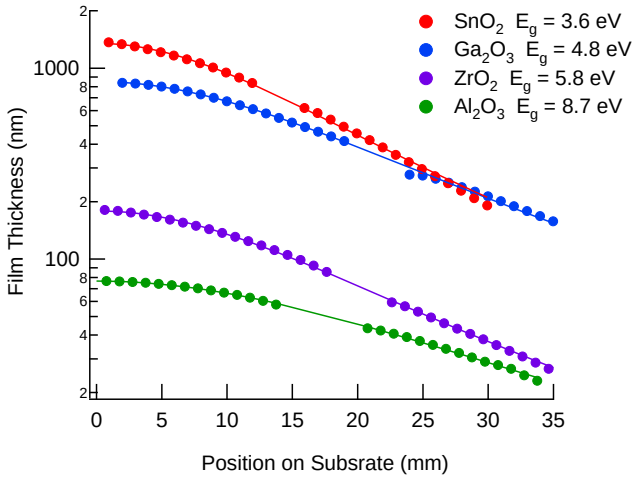

Figure 4.4: Thickness as a function of distance from the center of the plume for a various oxide films deposited using a fixed number of pulses (36 000) and a laser fluence of 3 J/cm^2. Band gaps are taken from refs. [363] (SnO_2), [310] (ZrO_2), [364] (Al_2O_3), and [12] (Ga_2O_3).

Table 4.2: Summary of CCS film deposition parameters. (BL = Buffer Layers)

Group	Sample	Substrate	Layers/BL	Pulses per Layer	Ga:Al Plume Separation	T-S Dist.	Composition Range	Thickness Variation
800 °C	S0	SiOx	1950	8:8	42 mm	55 mm	4–80 %	–
	S1	SiOx	1500	8:8	42 mm	55 mm	5–65 %	215–100 nm
	A1	Sapphire	1500	8:8	42 mm	55 mm	5–70 %	130–50 nm
	S2	SiOx	3600/60	10:15	38 mm	55 mm	11–78 %	480–230 nm
	A2	Sapphire	4000/60	10:12	52 mm	55 mm	5–81 %	795–270 nm
Room Temp.	pa-A1	Sapphire	2200	4:6	50 mm	50 mm	4–90 %	890–200 nm
	pa-A2	Sapphire	2000	4:6	50 mm	50 mm	4–88 %	870–190 nm
	pa-S1	Silicon	3000	4:6	68 mm	40 mm	0.5–99.5 %	3200–400 nm

Al_2O_3 side for all CCS films studied (fig. 4.5). Table 4.2 summarizes the various deposition settings used to produce CCS films in this work. The largest composition range is found in sample pa-S1, due to a combination of a low target-substrate distance and large separation between the Ga_2O_3 and Al_2O_3 plumes, which also resulted in an extreme thickness variation from 3200 nm over the Ga_2O_3 plume, to 400 nm at a point equidistant between the two plumes, and 1300 nm over the Al_2O_3 plume. The flux ratio over the Ga_2O_3 and Al_2O_3 plumes in this sample is also close to 2:1.

Before deposition, substrates in group 1 (800 °C) were rinsed with organic solvents and placed into the deposition chamber. After reaching a base pressure of 5×10^{-8} T, the substrate temperature was slowly raised to 800 °C and held for one hour to burn off any remaining surface contamination, before proceeding to film deposition following table 4.2. Due to confusing XRD data in samples A1 and S1 as the Al content increased beyond 10 %, a 60-layer Ga_2O_3 buffer layer was inserted in samples A2 and S2 between the substrate and overlying CCS film, to determine whether the unexpected results were substrate related. Substrates in group 2 (room temp.) were rinsed in organic solvents and then acid-etched before deposition. Sapphire surfaces were cleaned in a hot 3:1 H_2SO_4:H_3PO_4 solution (300 °C) for two minutes and rinsed in DI water before introducing into the deposition chamber. Silicon surfaces were cleaned following the standard RCA procedure: (1) 1 NH_3OH:1 H_2O_2:5 H_2O solution at 80 °C, 10 min, (2) 1 % HF dip, 10 s, (3) 1:1:5 HCl:H_2O_2:H_2O solution at 80 °C, 10 min, (4) 1 % HF dip, 10 s. Samples in group 2 were not heated in vacuum prior to deposition.

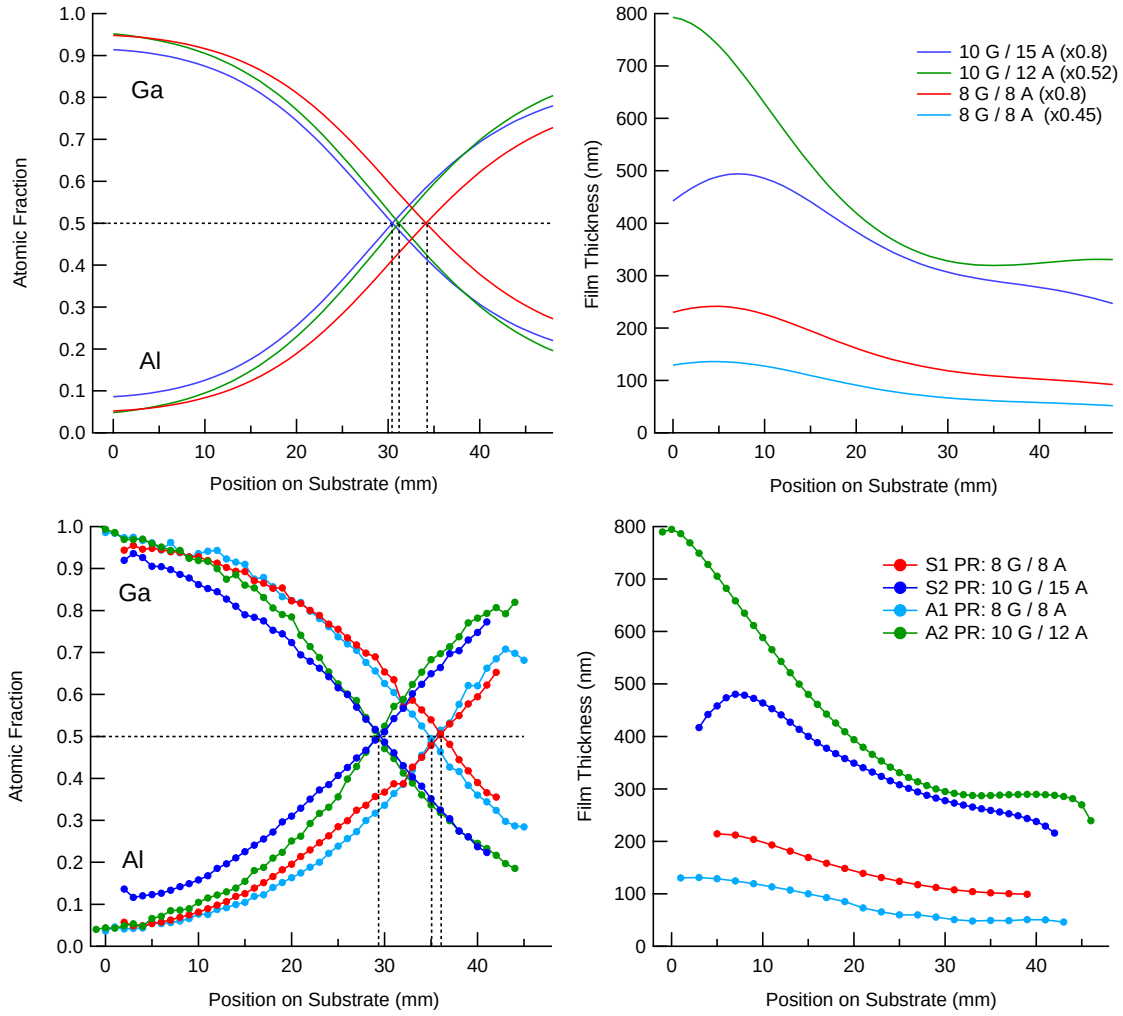

Figure 4.5: Simulated (top) and measured (bottom) alloy compositions and film thicknesses for samples S1, A1, S2, and A2 using eqs. (4.1) and (4.2), assuming a flux per pulse ratio of 2:1 from Ga_2O_3 and Al_2O_3 targets, respectively.

4.3 X-ray Diffraction

4.3.1 Background and Theory

X-ray diffraction was used to obtain information about crystal structure, orientation and phase. The principle is analogous to a diffraction grating with period corresponding to the spacing between atomic planes. Figure 4.6 shows diffraction from two volume elements separated by a vector $\mathbf{r}$. If the waves interfere constructively the sum of the path length differences Δl and $\Delta l'$ must be equal to half multiples of the wavelength, so that together they add to a multiple of the full wavelength

$$\begin{aligned} \frac{n\lambda}{2} &= |\mathbf{r}| \sin \xi \\ \frac{n\lambda'}{2} &= |\mathbf{r}| \sin \xi' \end{aligned} \tag{4.3}$$

Since $|\mathbf{k}| = \frac{2\pi}{\lambda}$ and using the fact that $\mathbf{k} \cdot \mathbf{r} = |\mathbf{k}||\mathbf{r}| \sin \xi$, these equations may be combined into one

$$\left(\mathbf{k} - \mathbf{k}'\right) \cdot \mathbf{r} = 2\pi n \tag{4.4}$$

Replacing $\mathbf{r}$ with $\mathbf{R}$, the direct lattice vector, and rewriting in an equivalent exponential form

$$e^{i(\mathbf{k}-\mathbf{k}')\cdot\mathbf{R}} = 1 \tag{4.5}$$

which is precisely the definition of the reciprocal lattice $\mathbf{K}$. Therefore for constructive interference to occur, the difference between the incoming and outgoing wave vectors is equal to a reciprocal lattice vector

$$\mathbf{k} - \mathbf{k}' = \mathbf{K} \tag{4.6}$$

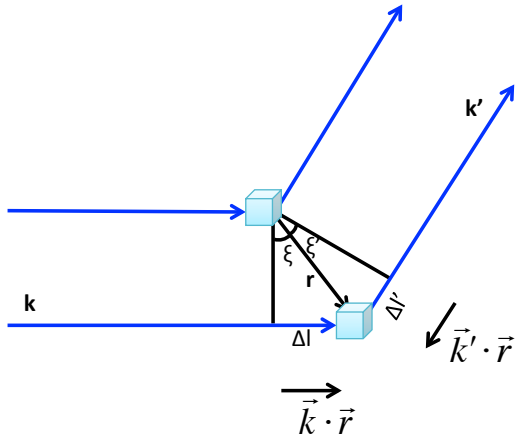

Figure 4.6: Diagram showing the path length difference $\Delta l + \Delta l'$ of incident light of wave vector $\mathbf{k}$ diffracting into $\mathbf{k}'$ from two volume elements separated by a vector $\mathbf{r}$. ξ is the angle between $\mathbf{r}$ and $\mathbf{k} \cdot \mathbf{r}$, and ξ' is the angle between $\mathbf{r}$ and $-\mathbf{k}' \cdot \mathbf{r}$.

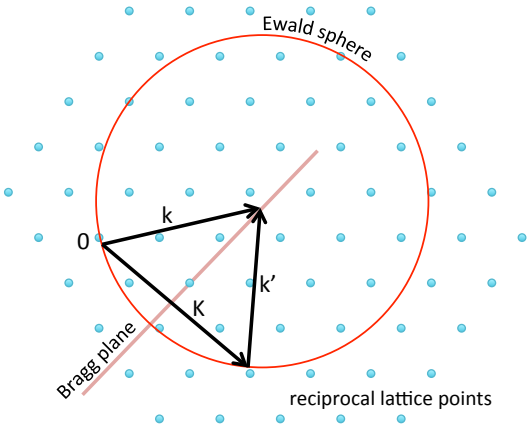

Figure 4.7: Definition of the Ewald sphere.

For elastic scattering, $|\mathbf{k}| = |\mathbf{k}'|$ and $\xi = \xi'$. Then both equations (4.3) are expressions of the familiar Bragg's Law, and the corresponding Bragg plane is the plane perpendicular to the reciprocal lattice vector $\mathbf{K}$. Varying the angle between the incoming and outgoing wave vectors defines a sphere in $\mathbf{k}$-space, and the intersection of the sphere with a point belonging to $\mathbf{K}$ satisfies the condition

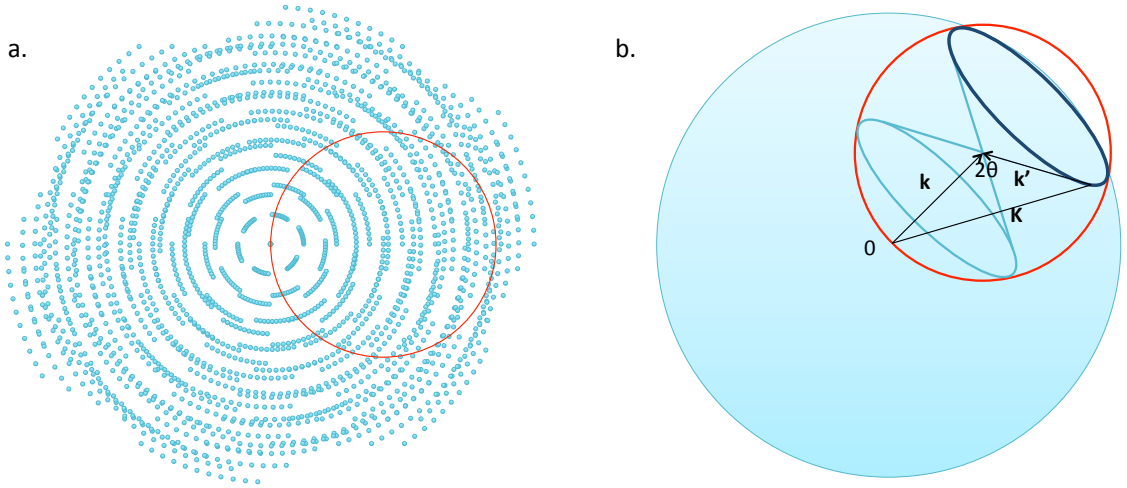

Figure 4.8: a) Rotating sample orientation to sample more **K**-points. b) Ring-shaped intersection of the Ewald sphere with the sphere of a rotated **K**-point in a powder sample.

for constructive interference (fig. 4.7). Diffraction from many more **K**-points may be observed by rotating the sample, bringing additional **K**-points into intersection with the sphere (fig. 4.8a).

X-ray diffraction of poly-crystalline samples and powders involves sampling a large number of small, randomly-oriented grains, so the rotated **k**-space of fig. 4.8b is built in, and the sample orientation becomes less important. The intersection of the Ewald sphere with the sphere of a particular **K**-point is a Debye ring. Figure 4.8b shows that the diffraction pattern of a powder may be calculated by finding the numerical solution to the equation

$$|\mathbf{K}|^2 = |u\mathbf{h} + v\mathbf{k} + w\mathbf{l}|^2 = 2k^2\,(1 - \cos(2\theta)) \tag{4.7}$$

where k is the wave number of the incident radiation, **h**, **k** and **l** are the reciprocal lattice vectors, and (u, v, w) are the Miller indices of the lattice point **K**.

When there is more than one basis atom per Bravais lattice point, or when there is more than one type of atom in the crystal, the intensities of diffraction peaks are modified. In the first case, a phase difference $e^{i\mathbf{K}\cdot\mathbf{r}}$ is associated with each basis atom. The sum of phase differences over all atoms in the unit cell is the geometrical structure factor, representing a relative amplitude

$$S_{\mathbf{K}} = \sum_{j=1}^{n} e^{i\mathbf{K}\cdot\mathbf{r}_j} \tag{4.8}$$

Table 4.3: $C2/m$ symmetry selection rules based on eq. (4.8) [3]

(hkl):	$h+k=2n$	$(hk0)$:	$h+k=2n$
$(h0l)$:	$h=2n$	$(0k0)$:	$k=2n$
$(0kl)$:	$k=2n$	$(h00)$:	$h=2n$

An additional phase difference comes from the size and shape of the electron clouds surrounding individual diffracting atoms. The resulting amplitude, called the atomic form factor, may be written as a volume integral over the continuous charge density distribution surrounding the atom

$$f_{\mathbf{K}} = \int \rho(\mathbf{r}) e^{i\mathbf{K}\cdot\mathbf{r}} d^3r \tag{4.9}$$

If there is diffraction from more than one type of atom, $f_{\mathbf{K}}$ may be replaced by a weighted sum over each type $Af_{a,\mathbf{K}} + Bf_{b,\mathbf{K}} + \cdots$. The quantity $|f_{\mathbf{K}} S_{\mathbf{K}}|^2$ is therefore the relative intensity of diffraction corresponding to a reciprocal lattice vector $\mathbf{K}$.

For a single crystal, mapping the set of reciprocal lattice vectors $\mathbf{K}$ and taking the inverse Fourier transform allows one to solve for the direct lattice $\mathbf{R}$. In the case of poly-crystalline thin films and powders, in which the reciprocal lattice $\mathbf{K}$ is obscured due to the superposition of randomly-oriented grains, the structure may often be determined iteratively by comparing the observed diffraction pattern to indexed materials and using Rietveld refinement [365]. Conversely, if diffraction is not observed for any combination of $\mathbf{k}$ and $\mathbf{k}'$, it may be concluded that long range order is absent and the sample is amorphous.

4.3.2 Equipment Details and Data Collection Methods

In this work a D8 Discover diffractometer by Bruker AXS (Madison, WI) was used to determine crystallographic structure. A diagram is shown in fig. 4.9. It uses a rotating Cu anode to produce high-intensity monochromatic 1.5418 Å radiation, collimated to a 0.5 mm spot size. The distinguishing feature of this diffractometer is a two-dimensional area detector, which captures a large range of scattering angles simultaneously, allowing for instant identification of various types of samples (fig. 4.10). A standard $\theta - 2\theta$ scan is recovered from the 2D pattern by integrating over the χ axis. The circle in $\mathbf{k}$-space equivalent to fig. 4.7 is a shell (fig. 4.11).

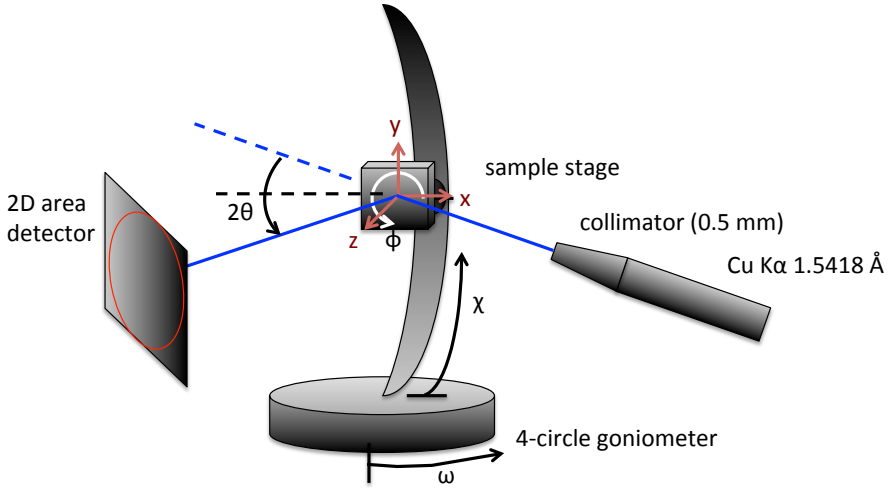

Figure 4.9: Illustration of D8 diffractometer geometry, showing relevant angles.

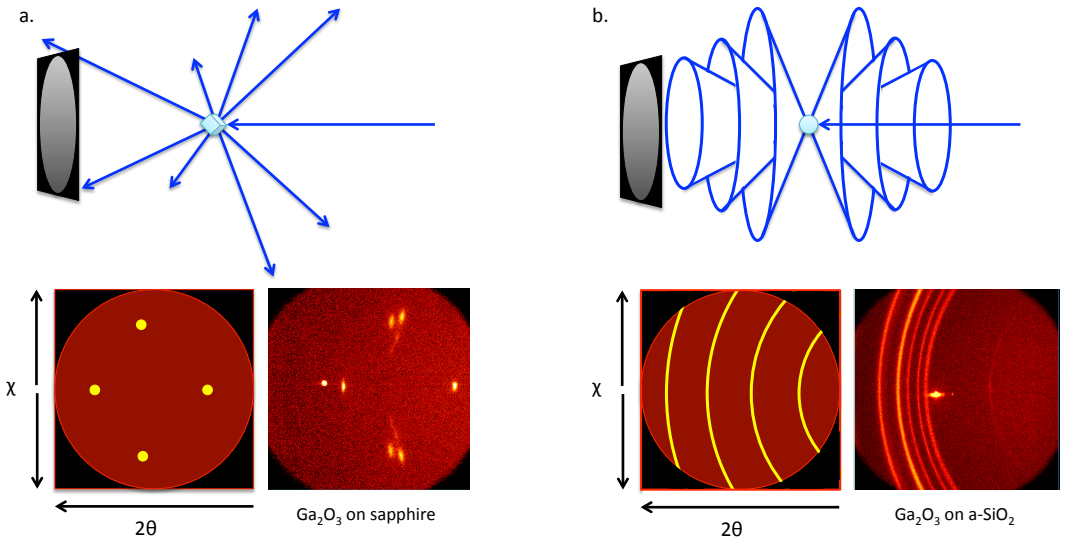

Figure 4.10: Example 2D diffraction patterns. The area detector allows instant identification of whether a thin film is oriented (a), or not (b).

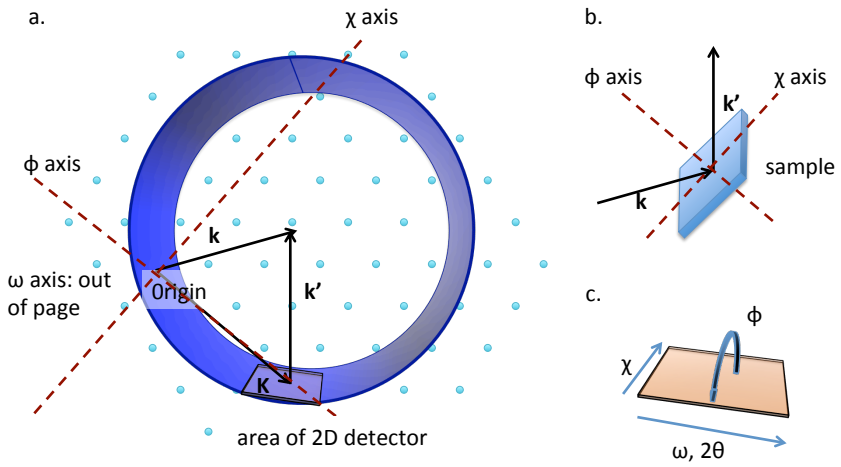

Figure 4.11: a) Two-dimensional shell traced out by an area detector in **k**-space. b) Sample alignment corresponding to the **k** vectors shown in part a. c) Movement of diffraction points in (or out of) the area detector window as individual diffractometer angles are varied.

Depending on the type of sample, different procedures were followed to collect XRD data. For sintered powders, diffraction consists of Debye rings regardless of the sample orientation, so we are free to orient the sample at the optimum angle to maximize the signal intensity. Therefore three 30° frames in 2θ were acquired with the center of each frame at 30°, 55°, and 80°, and the sample ω fixed at half of 2θ (15°, 27.5°, and 40°, respectively). This scheme results in 5° of overlap between adjacent frames. To sample a large number of grains and avoid a granular appearance in the 2D diffraction pattern the sample stage was set to oscillate in x and y with a 1 mm amplitude. After the data were collected, frames were integrated over a 20° window in χ to generate line scans in 2θ, and scans from adjacent frames were merged by normalizing peak intensities in the 5° region of overlap, to generate a single $\theta - 2\theta$ scan covering a 15–95° range in 2θ.

Similar to powders, polycrystalline thin films lacking a preferred orientation exhibit Debye rings in the 2D diffraction pattern. Dramatic improvement in signal intensity is obtained by choosing a low sample ω so that X-ray radiation is at glancing incidence, maximizing the volume of the film penetrated by the beam relative to the substrate. For CCS thin films, ω was set to 10° and ϕ was oriented so that the X-ray beam was perpendicular to the composition gradient. The center of the detection window was fixed at $2\theta = 35°$ so that data were collected over the range $20° \leq 2\theta \leq 50°$.

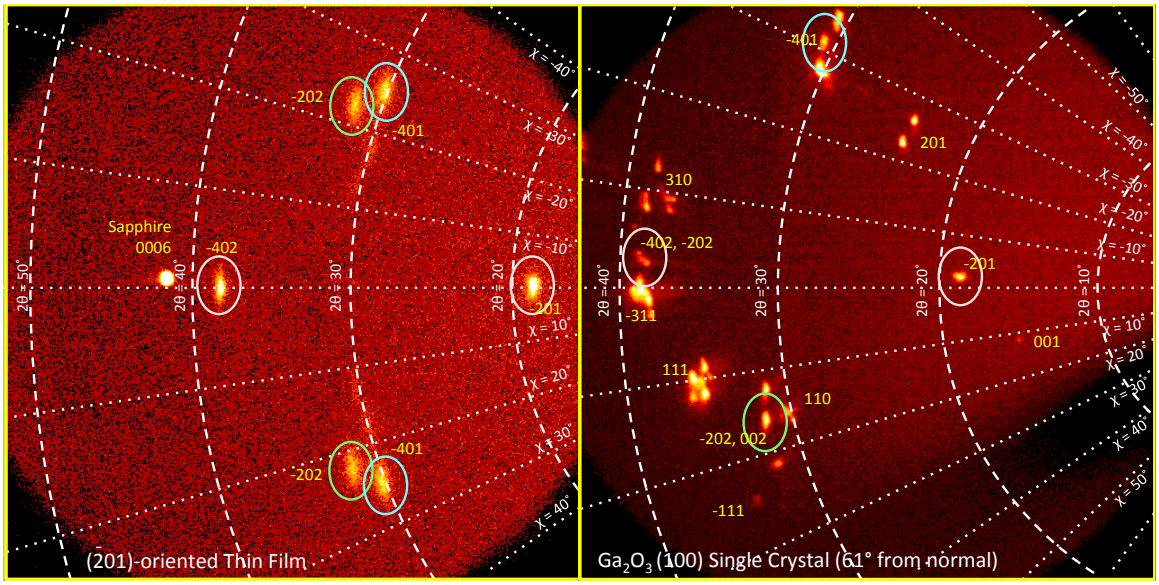

Figure 4.12: Left: $[\bar{2}01]$ orientated $\beta - Ga_2O_3$ thin film on c-plane sapphire. Right: $\beta - Ga_2O_3$ (100) single crystal tilted 61° away from normal. The angle between $[\bar{2}01]$ and [100] is 53.7°, so peaks corresponding to the left frame are tilted slightly up from the central axis. Additional peaks appear on the right because ϕ was rotated around [100] rather than $[\bar{2}01]$, due to the different sample orientation.

Since there is only one frame collected for each 1 mm step, integration was performed over a 60° angle in χ to maxmize the intensity of the peaks. (Choosing such a wide integration window in the previous paragraph would lead to erroneous relative peak intensities when merging adjacent frames, because the maximum range in χ decreases with 2θ.)

For an oriented thin film or single crystal, peaks are observed instead of rings, so the sample must be oriented so that the angle between X-rays and diffracting lattice planes is half of 2θ. To capture all peaks within a given 2θ window, ω is slowly scanned through a range of values so that 2ω moves from one edge of the frame to the other. For example, for a frame at $2\theta = 35°$ spanning a range of 20° to 50°, ω would be scanned from 10° to 25°. Furthermore, as illustrated in fig. 4.11c, diffraction will not be observed unless ϕ is correct, so ϕ was rotating continuously during data acquisition at a relatively fast rate in order to not miss any peaks as ω was slowly scanned. A side-by-side comparison between a $\beta - Ga_2O_3$ thin film and a single crystal is shown in fig. 4.12. Multiple frames can be acquired and assembled together to visualize a much larger area (fig. 4.13).

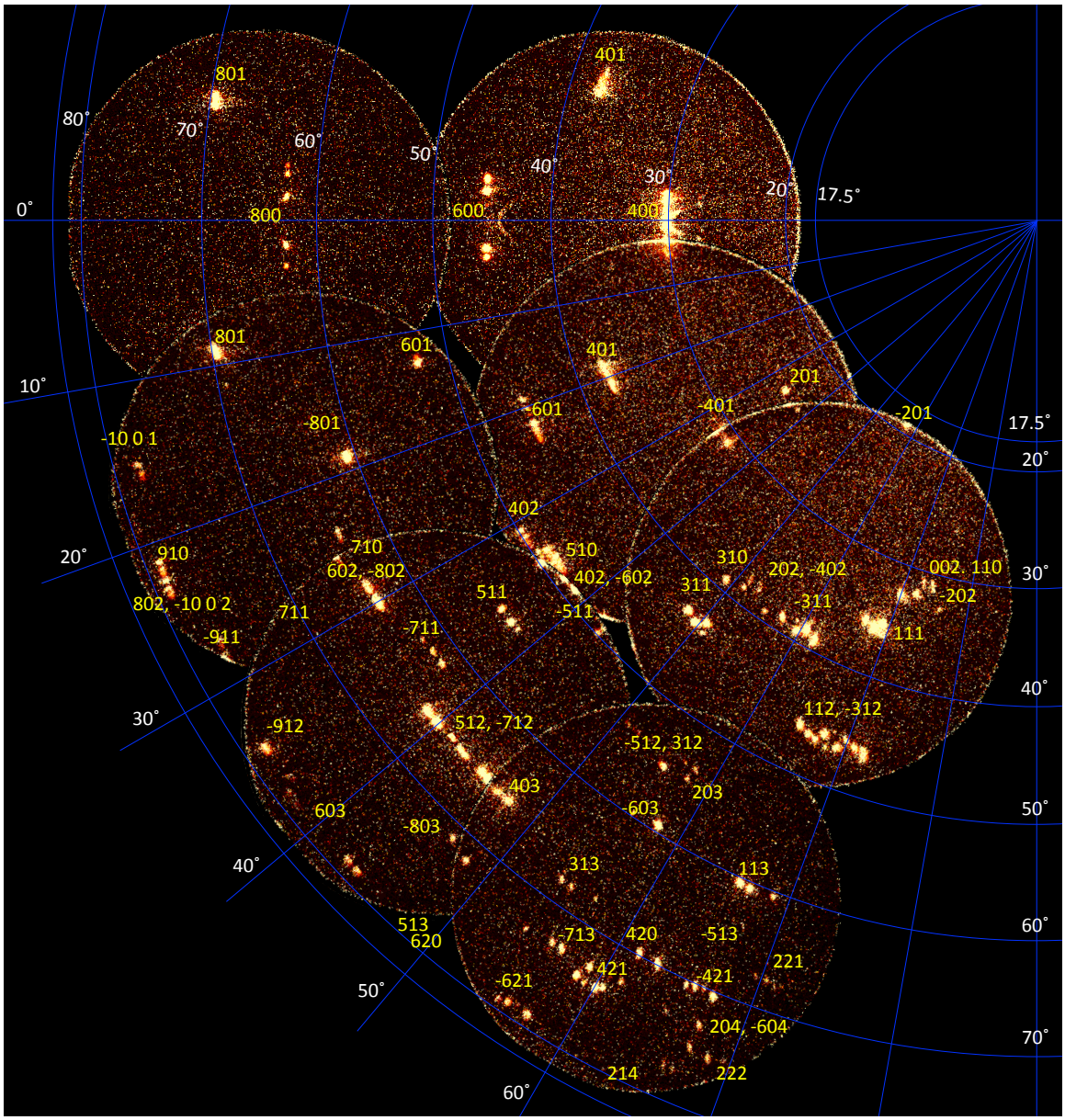

Figure 4.13: Combining 2D-XRD frames to map a large area in 2θ and χ. Shown: Diffraction from a Ga_2O_3 single crystal. Duplicated peaks are caused by imperfections in the crystal and a slight angular offset from the sample normal as ϕ is rotated.

4.4 X-ray Photoemission Spectroscopy

4.4.1 Overview of XPS

X-ray photoemission spectroscopy (XPS) is a technique whereby the kinetic energy spectrum of electrons emitted by a sample under ionizing X-ray radiation is measured. A large amount of information may be learned by XPS because a large number of different processes affect the energy of electrons before they arrive at the analyzer. The basic physical process is illustrated in fig. 4.14. The kinetic energy immediately upon ionization depends on the binding energy of the core level occupied before absorption, plus the constant sample work function Φ. Hence the most basic XPS experiment is elemental identification by identifying core levels in the binding energy spectrum. If more than one element is present, their relative amounts may be deduced by comparing the intensities of peaks assigned to each element. This is the primary method employed in the present work to determine the alloy composition of $(Al_xGa_{1-x})_2O_3$ thin films and powders. In a compound, energy levels shift relative to their positions in an elemental material due to the addition (reduction) or removal (oxidation) of valence electrons during bonding, which alters the screening of the nucleus. The measurement of such chemical shifts may be used to identify the compounds present.

After ionization, electrons travel a distance through the material before reaching the surface. Inelastic collisions with nuclei contribute to broadening of photoemission peaks, while collisions with other electrons form a continuous background. The average distance an electron travels before an inelastic collision is called the mean free path, and increases with kinetic energy as shown in the universal curve (fig. 4.15). Therefore the intensity of unscattered electrons decreases exponentially with escape depth

$$I = I_0 e^{-d/\lambda} \tag{4.10}$$

where λ is the mean free path. Typical values for λ are 1–3 nm for 1486.6 eV Al Kα radiation, meaning that 95 % of electrons come from the top 3–10 nm of the material, depending on the binding energy of the core level. The small escape depth means that depth-sensitive information may be obtained by comparing intensities and chemical shifts of high-binding-energy peaks, which are more surface sensitive, to low-binding-energy peaks. A second method is to collect electrons at an oblique take-off angle, so that a greater fraction of electrons originate from shallower layers, and compare to

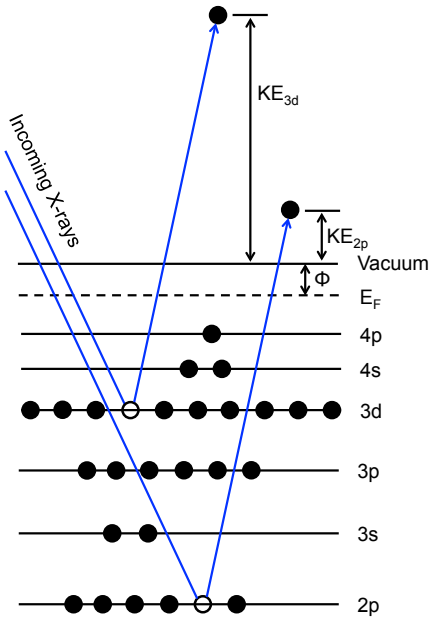

Figure 4.14: The photoionization of electrons from a gallium atom by absorption of incident X-rays. The kinetic energy of the free electron depends on the core level binding energy.

a spectrum obtained at an angle normal to the surface. If the sample is a well-ordered single crystal, varying the take-off and azimuthal angles may also lead to oscillations in the relative intensities of peaks belonging to different elements in the crystal due to the photoelectron diffraction effect, providing information on the surface atomic arrangement.

In addition to primary peaks, an examination of the inelastic loss structure also yields information about a sample. In conducting materials, secondary peaks are observed in multiples behind primary peaks corresponding to surface and bulk plasmon excitations. In materials with a band gap, the size of the gap may be estimated by locating the onset of inelastic losses behind a primary peak. This method is used in chapter 5 to measure the band gap of $(Al_xGa_{1-x})_2O_3$ powders, which scatter light too strongly in solution to permit measurement by optical techniques. Finally, the sample work function may be deduced by finding the minimum kinetic energy of inelastically scattered electrons (the secondary electron cutoff) under an appropriate sample bias.

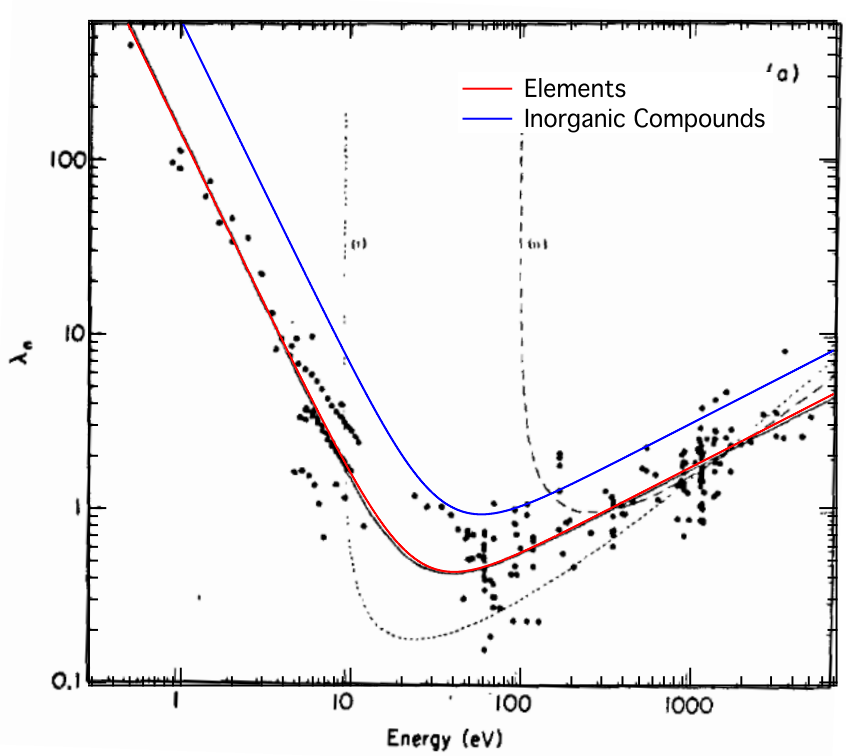

Figure 4.15: The universal curve of inelastic mean free paths (in nanometers) for elements and inorganic compounds. Data points are elemental data taken from Seah and Dench [366]. The superimposed colored curves are best fits for each class of material.

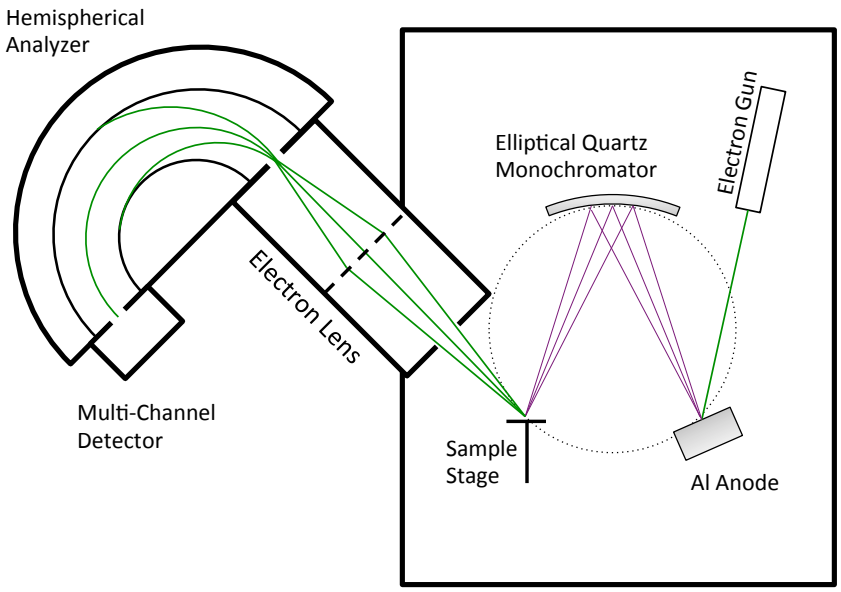

Figure 4.16: A diagram of our X-ray spectrometer.

4.4.2 Equipment Details

XPS was performed on a Versaprobe 5000 spectrometer by Physical Electronics, Inc. (Chanhassan, MN). A diagram showing the important components is shown in fig. 4.16. Intense X-ray radiation is generated in all directions when electrons from a focused electron beam are absorbed by an Al anode, with an energy spectrum characteristic of Al. To filter everything but the desired Al Kα radiation and focus to a 100 µm point, an elliptical quartz monochromator is used. The d-spacing of quartz (100) is 0.4255 nm, and the wavelength of 1486.56 eV radiation is 0.834 nm. Using Bragg's equation, diffraction occurs at an angle of 78.6°. (Actually, 1486.56 eV is a weighted average of Al Kα_1 = 1486.70 eV (100 %) and Al Kα_2 = 1486.27 eV (50 %) which are too close in energy to filter.) The next closest wavelength belongs to Al Kβ radiation, with energy 1557.45 eV and wavelength 0.796 nm. Therefore Bragg's equation predicts diffraction at 69.3°. By aligning anode, sample and monochromator at the proper angles, only Al Kα X-rays will impinge upon the sample. Furthermore, by bending the quartz single crystal into an ellipsoidal shape, with one focal point at the e-beam spot on the anode and the other at X-ray spot on the sample, X-rays emitted from a spread of angles are re-focused to a single point on the sample. In geometric optics, the incident

and reflected angles do not remain constant for reflection from one focal point to the other off of an ellipse, but decrease as the point of reflection moves away from center. However, the diffraction angle is fixed at 78.6° by Bragg's equation, meaning there is still a small deviation from perfect focusing, which limits the size of the X-ray spot.

Upon absorbing Al Kα X-rays, electrons are emitted from the sample at a spectrum of energies and a wide range of take-off angles, and some enter the electron lens through a narrow aperture. The electron lens consists of a series of concentric cylinders held at different voltages, and the voltage differences between adjacent cylinders determine the position of focal points on either side of the boundary. The lens accelerates incoming electrons at a certain energy to the pass energy and refocuses them to a point at the entrance of the hemispherical energy analyzer. As the voltages on the cylinders are scanned, the particular incoming energy that gets focused and accelerated to the pass energy is also scanned. Plotting the measured electron intensity against the voltage on the electron lens (properly calibrated) therefore yields the energy spectrum of electrons emitted from the sample.

The energy analyzer consists of two concentric hemispherical shells of radii a and b held at different electrostatic potentials, producing an electric field pointing out from the center that accelerates electrons at the correct kinetic energy (the pass energy) around the hemisphere to a detector at the opposite side. The pass energy E_0 of an electron traveling along a circular path from the aperture to the detector depends on the voltage difference V on the shells

$$E_0 = \frac{V}{\frac{b}{a} - \frac{a}{b}}$$

There are a range of energies around the pass energy which are passed by the analyzer, due to the finite width w of the aperture and the range of entrance angles α around the central ray. The full-width at half-maximum (FWHM) ΔE is

$$\Delta E = E_0 \left(\frac{w}{a+b} + \frac{\alpha^2}{4} \right)$$

For our spectrometer, this works out to be [367]

$$E_0 = 0.56V$$

$$\Delta E = 0.015E_0$$

Therefore, large pass energies result in poor energy resolution. The trade-off is that when a greater range of electron energies make it to the detector, the signal-to-noise ratio is improved. In the present work, pass energies of 117.4 eV and 187.5 eV were used for survey scans, yielding bright spectra for elemental identification and poor FWHM energy resolutions of 1.761 eV and 2.813 eV, respectively. For high-resolution spectra of individual peaks the pass energy was set to 23.50 eV, meaning the FWHM energy resolution was 0.3525 eV. This setting provides a good balance between sensitivity to details and signal intensity. For our spectrometer, the pass energy can be set as low as 0.5 eV; however, below a certain point the resolution will be limited by the energy width of the X-ray beam, which for our equipment is 0.26 eV [367].

4.4.3 XPS for the Quantitative Determination of Alloy Composition

One of the main purposes of XPS in the present work is to independently determine the alloy composition of thin films and powders to be correlated with structural and optical data. To accomplish this, intensities of Ga and Al photoemission peaks are measured and compared to their corresponding atomic sensitivity factors (ASFs). Tables of ASFs for the elements are available online and in our equipment manual, but their precise values may vary depending on the spectrometer used, sample preparation, takeoff angle, and other experimental conditions. ASFs from reference spectra acquired on our instrument were used instead, taken from intrinsic Ga_2O_3 and Al_2O_3 thin film samples fabricated in our lab, assuming a stoichiometric O to Ga ratio after post-annealing in air. Reference spectra were also collected from single-crystal Ga_2O_3 and sapphire wafers which certainly contain the correct stoichiometry, and compared with our thin films. However, single-crystal ASFs were not used due to the possibility of intensity fluctuations caused by the X-ray photoelectron diffraction effect, and because peak intensities and widths for the thin film references compare better to our composition-spread film data.

Two methods were followed to determine alloy composition from XPS peak intensities. The first method is to find intensity ratios of various Ga and Al photoemission peaks to O 1s in stoichiometric Ga_2O_3 and Al_2O_3, and compare to corresponding $I_{\mathrm{Ga,Al}} : I_{\mathrm{O}}$ ratios in a composition spread film.

The alloy composition is then given by the formula

$$\begin{aligned} \%\,\mathrm{Al} &= \frac{(I_{\mathrm{Al}} : I_{\mathrm{O}})}{(I_{\mathrm{Al}} : I_{\mathrm{O}})_{ref}} \\ \%\,\mathrm{Ga} &= \frac{(I_{\mathrm{Ga}} : I_{\mathrm{O}})}{(I_{\mathrm{Ga}} : I_{\mathrm{O}})_{ref}} \end{aligned} \tag{4.11}$$

Theoretically, adding % Al and % Ga together gives unity for a stoichiometric film, and as a result oxygen deficiency is also measured by this method. For example, for values of % Ga and % Al calculated from eq. (4.11) a sum of % Ga + % Al = 1.05 indicates a 5 % oxygen deficiency. For these calculations, Ga 3s, Ga 3p, and Ga 3d peaks were used to measure the Ga content, and Al 2s and Al 2p peaks were used to measure the Al content. These peaks are all similar in binding energy, falling within a range 0–180 eV below the Fermi level, and therefore probe a similar escape depth; the inelastic mean free path is ~ 2 nm according to the universal curve of fig. 4.15. The brighter Ga $2p_{3/2}$ peak at 1118 eV was not used due to its smaller 1 nm mean free path (fig. 4.15), and correspondingly greater attenuation relative to the other peaks when a thin contamination layer is present on the surface.

The second method is to compare Al and Ga peak intensities directly. Ideally, a reliable $x = 0.5$ $(\mathrm{Al}_x\mathrm{Ga}_{1-x})_2\mathrm{O}_3$ reference sample would be available to find the relative intensities of each peak. However, we do not possess any such sample, so the appropriate $I_{\mathrm{Al}} : I_{\mathrm{Ga}}$ reference ratios must be determined from intrinsic $\mathrm{Ga_2O_3}$ and $\mathrm{Al_2O_3}$ instead by assuming constant cation to oxygen atomic ratios. Then the $I_{\mathrm{Al}} : I_{\mathrm{Ga}}$ ratio corresponding to $x = 0.5$ is found by dividing $(I_{\mathrm{Al}} : I_{\mathrm{O}})_{\mathrm{Al_2O_3}}/(I_{\mathrm{Ga}} : I_{\mathrm{O}})_{\mathrm{Ga_2O_3}}$. With this value in hand the alloy composition at any point can be determined using the formula

$$\%\mathrm{Al} \equiv \frac{[\mathrm{Al}]}{[\mathrm{Al}] + [\mathrm{Ga}]} = \frac{\frac{(I_{\mathrm{Al}}:I_{\mathrm{Ga}})}{(I_{\mathrm{Al}}:I_{\mathrm{Ga}})_{x=0.5}}}{1 + \frac{(I_{\mathrm{Al}}:I_{\mathrm{Ga}})}{(I_{\mathrm{Al}}:I_{\mathrm{Ga}})_{x=0.5}}} \tag{4.12}$$

Method 2 is advantageous because (1) O 1s lies at 531.8 eV and therefore probes a different depth in the film compared to the Al and Ga peaks, and (2) Surface OH overlaps with O 1s, leading to ambiguity in the precise determination of $I_{\mathrm{Ga,Al}} : I_{\mathrm{O}}$ depending on how the fitting is performed. The disadvantage is that the oxygen stoichiometry is not measured, which can sometimes indicate the presence of unwanted species such as $\mathrm{SiO_2}$ if some oxygen is still unaccounted for after adding together $\mathrm{Al_2O_3}$ and $\mathrm{Ga_2O_3}$.

Ga_2O_3 and Al_2O_3 reference films were deposited at room temperature on silicon substrates, and spectra were acquired at a 45° takeoff angle before and after post-annealing in air to 400 °C and 800 °C for one hour each. XPS spectra at each step are shown in fig. 4.17, along with the corresponding spectra for single crystals. Spectra have been shifted together so that C $1s$ lies at 284.8 eV to compensate for varying degrees of sample charging, and scaled so that Ga $3s$ (Ga_2O_3) and Al $2s$ (Al_2O_3) peaks overlap in intensity to compensate for varying levels of atmospheric surface contamination, making the assumption that Ga and Al are not volatile and that their atomic number stays constant during annealing. Indeed, all Ga and Al spectra with the exception of Ga $2p_{3/2}$ appear to line up well using the same scaling factors, except for slight differences due to broadening in the as-deposited spectra. The changing intensity of Ga $2p_{3/2}$ arises due to its lower escape depth and heightened sensitivity to surface contamination, demonstrating why it is unreliable as an intensity reference. Interestingly, relative intensities of Al $2s$ and Al $2p$ peaks for sapphire appear to be different from an Al_2O_3 thin film, which is probably due to an X-ray photoelectron diffraction effect. In both methods 1 and 2, reliable $I_{\mathrm{Ga,Al}} : I_{\mathrm{O}}$ ratios for the reference samples are needed. As seen in fig. 4.17, that ratio changes significantly depending on the post annealing. The closest match to the single crystal is seen in the 400 °C post-annealed data, while the as-deposited data appears to be oxygen-deficient and the 800 °C data appears oxygen-rich. The Ga_2O_3 PLD parameters were optimized at a substrate temperature of 800 °C; it is interesting that a similar deposition performed at room temperature results in poorer oxygen incorporation.

Example fits to the 400 °C post-annealed Al_2O_3 and Ga_2O_3 thin films are shown in fig. 4.18. To determine the intensity, true Voigt lineshapes obtained from the convolution of Gaussian and Lorentzian line shapes were fit to the experimental data

$$f(E) = Af(L(E) * G(E)) = A \int_{-\infty}^{\infty} L(E')G(E - E')\, dE' \tag{4.13}$$

where $L(E)$ and $G(E)$ are given by

$$L(E) = \left[1 + \left(\frac{E - E_0}{W_L/2}\right)^2\right]^{-1} \tag{4.14a}$$

$$G(E) = \exp\left[-\ln 2 \left(\frac{E - E_0}{W_G/2}\right)^2\right] \tag{4.14b}$$

and W_L and W_G are the full width at half maxima (FWHM) corresponding to Lorentzian and

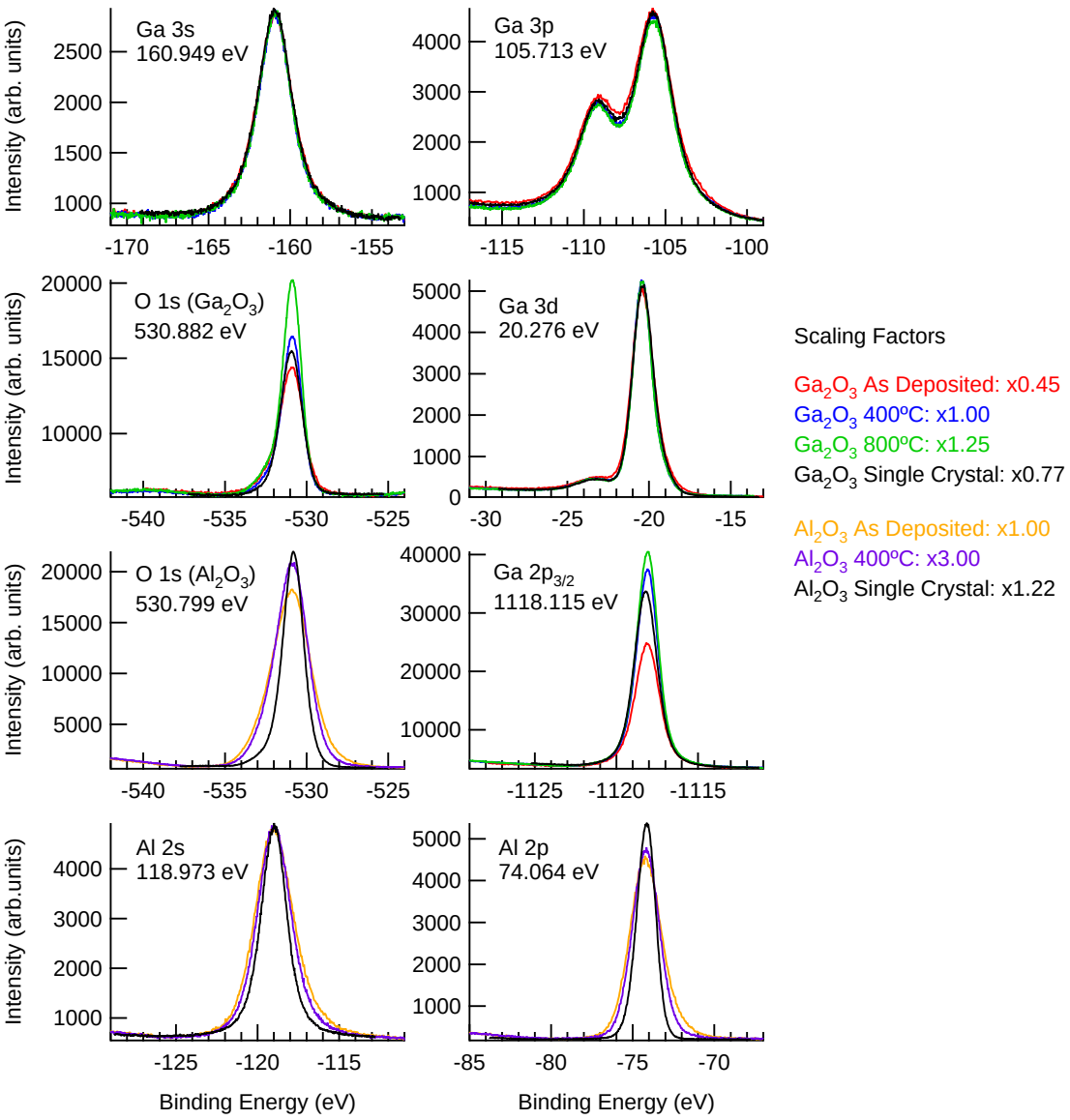

Figure 4.17: XPS reference spectra from Ga_2O_3 and Al_2O_3 single crystals (black), and PLD thin films deposited at room temperature (under the same conditions as other samples) before annealing (red, gold) after post-annealing to 400 °C (blue, violet) and 800 °C (green) in air. Peaks are shifted in binding energy so that C 1*s* lies at 284.8 eV in the as-deposited spectrum, and amplitudes for each set have been scaled together so that Ga 3*s* (Ga peaks) and Al 2*s* (Al peaks) overlap. Binding energies for all spectra are shown on the same scale. Not much difference is seen in the Al and Ga peaks before and after annealing (except for the surface sensitive Ga $2p_{3/2}$; however, O 1*s* grows more intense.

Table 4.4: Lorentzian widths used for the quantitative determination of intensity of photoemission peaks.

	Lorentizian Widths
Al 2p	0.3
Al 2s	1.1
Ga 3s	1.7
Ga 3p	1.6
Ga 3d	0.4
Ga $2p_{3/2}$	0.875
O 1s	0.25

Gaussian line shapes, respectively. In general, W_L depends on the lifetime of the absorption process, and is characteristic for each photoemission peak independent of the sample, whereas W_G represents peak broadening due to disorder caused by a variety of different local electron environments, and therefore is allowed to vary. Lorentizian widths used in the fitting of all spectra in this work are displayed in table 4.4. Fitting to a true Voigt function gives more accurate results than so-called pseudo-Voigt functions formed by simple products or sums of $L(E)$ and $G(E)$ [368], which are nonetheless used all the time by other researchers anyway. Quantitative analysis using XPS is generally taken to be accurate to a few percent [369]. Hesse et al. [368] found that inaccuracy in area determination across a variety of organic and inorganic samples is at worst 7 % when using true Voigt functions, and often better. In our experiment, alloy composition is determined multiple times at each point by comparing different pairs of photoemission peaks. Assuming a 5 % uncertainty in the composition result for each pair, using four pairs of peaks reduces the uncertainty in the average to less than 3 %. $I_{\mathrm{Al,Ga}} : I_{\mathrm{O}}$ ratios calculated using formulas eqs. (4.11) and (4.12) from all reference spectra are displayed in table 4.5. Direct $I_{\mathrm{Al}} : I_{\mathrm{Ga}}$ ratios are computed by dividing the appropriate $(I_{\mathrm{Al}} : I_{\mathrm{O}})/(I_{\mathrm{Ga}} : I_{\mathrm{O}})$ ratios to cancel the O in the denominator. Since the 400 °C set gives the best agreement with the single crystal fitting, that was chosen as the stoichiometric reference.

A satisfactory fit to the Ga 3*d* peak is not possible using a single Voigt component and is therefore fit with two. The low binding energy shoulder has been attributed to Ga^{2+} in sub-stoichiometric Ga_2O_{3-x}, and used as evidence of metallic cluster formation in PLD films grown without O_2 background pressure [177]. This is a reasonable assignment, as unit changes in valence generally result in roughly 1 eV steps in binding energy, and the difference in binding energy from the main

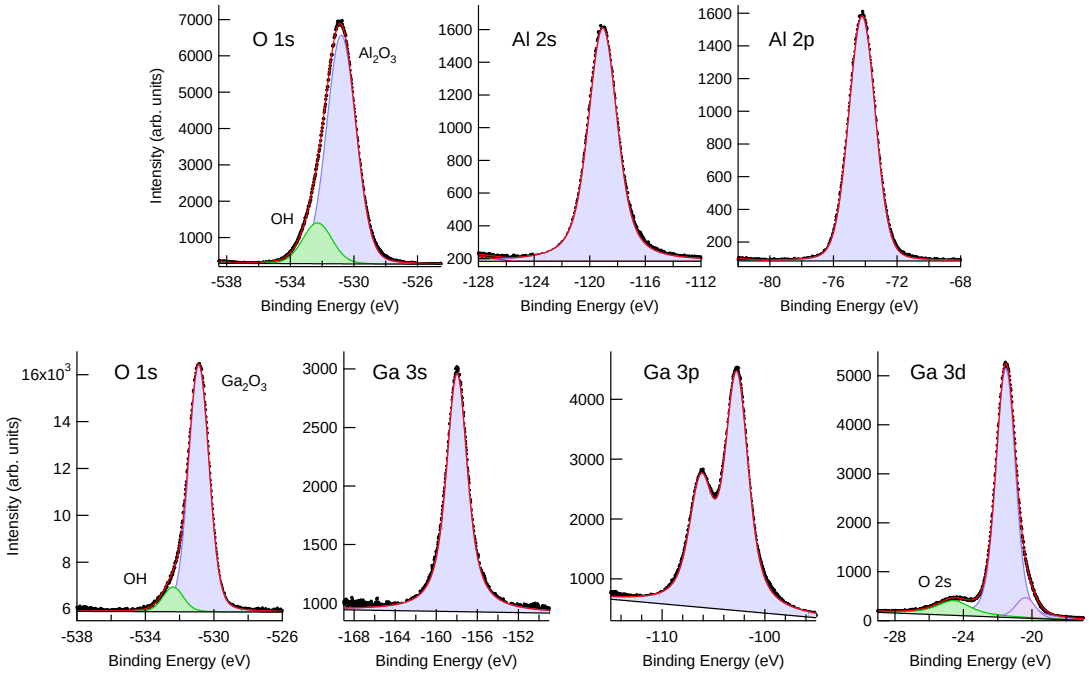

Figure 4.18: Fitting Al_2O_3 and Ga_2O_3 peaks from stoichiometric PLD thin films to determine intensity ratios.

Table 4.5: XPS peak intensity ratios calculated from intrinsic Ga_2O_3 and Al_2O_3 thin films and single crystals.

	As deposited	400 °C	800 °C	Single Crystals
$I_{Ga2p_{3/2}} : I_{O1s}$	3.12	4.01	3.44	3.77
$I_{Ga3s} : I_{O1s}$	0.448	0.393	0.310	0.400
$I_{Ga3p} : I_{O1s}$	1.38	1.19	0.923	1.24
$I_{Ga3d} : I_{O1s}$	0.602	0.516	0.398	0.575
$I_{Al2s} : I_{O1s}$	0.308	0.290		0.277
$I_{Al2p} : I_{O1s}$	0.236	0.218		0.221

Ga 3d peak is 1.15 eV in my reference data. This assignment also agrees with the result of Carli and Bianchi [370] who measured the position of Ga 3d in Ga_2O by reacting metallic Ga with stoichiometric Ga_2O_3. However, these studies only considered Ga 3d and no other Ga or O spectra. If metallic Ga clusters are embedded in our reference samples, similar shoulders would be expected to appear on all other Ga peaks, and they are absent. Furthermore, the shoulder on Ga 3d is persistent upon annealing to high temperatures in oxygen. Curiously, this phenomenon was not noticed or reported on until earlier this year by Navarro-Quezada et al. [175], who attribute the shoulder to a hybridization that takes place between Ga 3d and O 2s peaks and which agrees with DFT band structure calculations performed by the same authors. Similar hybridization has also been observed between In 4d and O 2s in indium oxide [371, 372]. Therefore both components are included in the calculation of % Ga using $I_{\mathrm{Ga3d}} : I_{\mathrm{O1s}}$, and the result agrees with the same calculation using other Ga peaks, as will be shown in subsequent chapters.

4.5 Ultraviolet-Visible Spectroscopy

4.5.1 Background and Theory

Ultraviolet-visible (UV-Vis) spectroscopy is perhaps the most straightforward way to measure the optical band gap of a semiconducting thin film. The film is deposited on a transparent substrate and placed in a beam of monochromatized light. As the wavelength is scanned through a continuous range, the transmitted intensity is measured. A sudden drop in intensity indicates the onset of absorption, meaning that the energy per photon is sufficiently large to excite valence electrons into the conduction band. Usually the incident beam is split into two paths and the second path is left unobstructed, to isolate the absorption due to the sample and exclude intensity fluctuations in the light source. Intensity fluctuations in the transparent region due to constructive and destructive interference in the film are still present.

UV-Vis data are recorded either as transmittance or absorbance vs. wavelength λ. Transmittance is simply the ratio I/I_0, where I is the measured intensity after transmission, and I_0 is the reference beam intensity. Absorbance is defined in terms of the transmittance T, which decreases exponentially with the product of absorption coefficient α and film thickness t

$$A = -\log_{10}(T) = -\log_{10}\left(e^{-\alpha t}\right) \tag{4.15}$$

Therefore the absorption coefficient is given by

$$\alpha = \frac{A}{t}\ln(10) \tag{4.16}$$

The reflection and transmission coefficients for light incident at an interface between medium 1 and medium 2 are denoted $\tilde{r}_{12}$ and $\tilde{t}_{12}$, respectively. At normal incidence they take the form [48]

$$\tilde{r}_{12} = \frac{E_r}{E_i} = \frac{\tilde{n}_2 - \tilde{n}_1}{\tilde{n}_2 + \tilde{n}_1} \tag{4.17a}$$

$$\tilde{t}_{12} = \frac{E_t}{E_i} = \frac{2\tilde{n}_1}{\tilde{n}_2 + \tilde{n}_1} \tag{4.17b}$$

where E_i, E_r, and E_t are the incident, reflected and transmitted electric fields, and $\tilde{n}_1 = n_1 + i\kappa_1$ and $\tilde{n}_2 = n_2 + i\kappa_2$ are the complex indices of refraction for medium 1 and medium 2. Figure 4.19 shows the path of light transmitted through a transparent substrate. At normal incidence, all of the outgoing waves interfere. If one ignores multiple internal reflections, then the incoming wave is

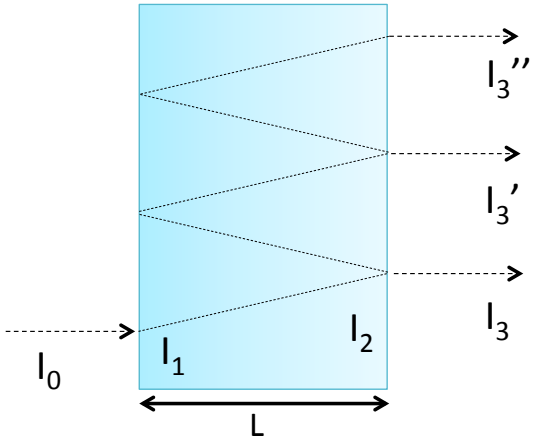

Figure 4.19: Internal reflections and interference of incident light transmitted through a transparent substrate.

diminished by transmission from the air into the substrate, experiences a phase change according to the thickness L, and is diminished a second time by transmission from the substrate back into the air. Hence the outgoing amplitude is written in terms of the incident amplitude as

$$E_3 = \tilde{t}_{23} e^{-i(\omega\tilde{n}(\omega)/c)L} \tilde{t}_{12} E_0 \tag{4.18}$$

If there are two reflections, tracing the light path produces the following expression for the resulting amplitude

$$E_3' = \tilde{t}_{23} e^{-3i(\omega\tilde{n}(\omega)/c)L} \tilde{r}_{12}\tilde{r}_{23}\tilde{t}_{12} E_0 \tag{4.19}$$

If there are n reflections, this expression generalizes to

$$E_3^{(n)} = \tilde{t}_{23} e^{-(2n-1)i(\omega\tilde{n}(\omega)/c)L} \tilde{r}_{12}^{2n-1}\tilde{r}_{23}^{2n-1}\tilde{t}_{12} E_0 \tag{4.20}$$

which is a geometric series and may be summed in closed form to give the total outgoing amplitude

$$E_3 = \frac{\tilde{t}_{12}\tilde{t}_{23} e^{-i(\omega\tilde{n}(\omega)/c)L}}{1 - \tilde{r}_{12}\tilde{r}_{23} e^{-2i(\omega\tilde{n}(\omega)/c)L}} E_0 \tag{4.21}$$

In experiments, we measure outgoing intensity rather than field amplitude, which is found by taking the magnitude squared: $I/I_0 = |E/E_0|^2$.

If the bandwidth of incident light is too great, or the substrate thickness too large, then waves add incoherently and one may neglect interference and replace the previous expression with an expression for intensity, substituting for $\tilde{r}_{ij}$ and $\tilde{t}_{ij}$ the reflectivity $R_{ij} \equiv \tilde{r}_{ij}^* \tilde{r}_{ij}$ and transmittance $T_{ij} \equiv \mathrm{Re}\left(\frac{\tilde{n}_j^*}{\tilde{n}_i^*}\right) \tilde{t}_{ij}^* \tilde{t}_{ij}$, respectively, and keeping only the square of the real part of the exponential factors (the absorption)

$$I_3 = \frac{T_{12} T_{23} e^{-\alpha L}}{1 - R_{12} R_{23} e^{-2\alpha L}} I_0 \tag{4.22}$$

A quantity called the coherence length is used to determine whether a coherent or incoherent treatment is more appropriate. The coherence length is defined as $l_c = \frac{\lambda^2}{2\pi\Delta\lambda}$ where $\Delta\lambda$ is the spectral bandwidth of incident light. If the coherence length is greater than the optical path length nL then interference cannot be neglected [373]. For a typical sapphire wafer, $n \approx 1.7$ and $L \approx 430\,\mu\mathrm{m}$, so the optical path length is 730 µm. In our experiment incident light varies from 190 nm to 600 nm with a spectral bandwidth of 0.5 nm, so the coherence length ranges from 11.491 µm to 114.59 µm. Therefore for the substrate it is not necessary to consider interference. However, for an $(\mathrm{Al}_x\mathrm{Ga}_{1-x})_2\mathrm{O}_3$ thin film n varies from 1.7 to 1.9 and L varies from 0.3 µm to 3 µm, so the optical path length is smaller than the coherence length and a coherent treatment is required.

Light transmitting through a two layer stack is illustrated in fig. 4.20. If the substrate is thick enough to be treated incoherently, then the outgoing amplitude can be found directly by multiplying the intensity after coherent transmission through the film [using eq. (4.21)] and the intensity after incoherent transmission through the substrate [using eq. (4.22)]. This situation of coherent transmission through both layers is more complicated.[1] To assist in the calculation, the outgoing waves in fig. 4.20 have been organized spatially by the number of reflections against the substrate-film interface (i.e., in powers of $\tilde{r}_{23}$), and by color representing the number of transmissions in the backward direction from the film into the substrate (powers of $\tilde{t}_{32}$). The first group is similar to the case of a bare substrate, with an extra transmission coefficient and phase factor

$$\tilde{t}_{12}\tilde{t}_{23}\tilde{t}_{34} e^{i\xi_s L_s} \left(\sum_{q=1}^{\infty} e^{(2q-1)i\xi_f L_f} (\tilde{r}_{34}\tilde{r}_{32})^{q-1} \right)$$

[1] I worked out the expressions to follow and included them here because I found the result to be interesting; if the reader disagrees, this part may be skipped without loss of understanding later.

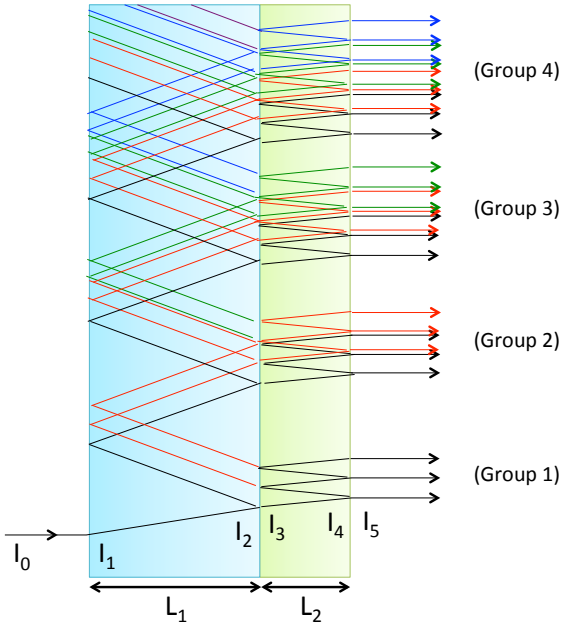

Figure 4.20: Multiple internal reflections and interference of incident light transmitted through a thin film on a transparent substrate. Light that transmits in the backward direction from film to substrate is indicated by a change of color.

where the subscripts s and f refer to substrate and film, respectively, and $\xi \equiv \omega\tilde{n}/c$. The second group contains one subgroup that was reflected once at the film/substrate interface before transmitting into the film (black), and one that was transmitted into the film, reflected at the air/film interface $n \geq 1$ times and then transmitted back from film to substrate, before transmitting into the film again (red)

$$\tilde{t}_{12}\tilde{r}_{23}\tilde{r}_{21}\tilde{t}_{23}\tilde{t}_{34}e^{3i\xi_s L_s}\left(\sum_{q=1}^{\infty} e^{(2q-1)i\xi_f L_f}(\tilde{r}_{34}\tilde{r}_{32})^{q-1}\right) \quad \text{(black)}$$

$$+\tilde{t}_{12}\tilde{r}_{21}\tilde{t}_{23}^2\tilde{t}_{32}\tilde{t}_{34}e^{3i\xi_s L_s}\left(\sum_{q_1=1}^{\infty} e^{2q_1 i\xi_f L_f}(\tilde{r}_{32})^{q_1-1}(\tilde{r}_{34})^{q_1}\right)\left(\sum_{q_2=1}^{\infty} e^{(2q_2-1)i\xi_f L_f}(\tilde{r}_{34}\tilde{r}_{32})^{q_2-1}\right) \quad \text{(red)}$$

The third group contains one subgroup that was reflected twice at the film/substrate interface and then transmitted into the film (black); one that was transmitted into the film, reflected at the air/film interface $n \geq 1$ times, transmitted back into the substrate, reflected off the air/substrate boundary and transmitted into the film again (red), and one that followed the (red) path but was transmitted back from film to substrate a second time, reflected at the air/substrate interface, and

transmitted again from substrate to film (green)

$$\tilde{t}_{12}\tilde{r}_{23}^{2}\tilde{r}_{21}^{2}\tilde{t}_{23}\tilde{t}_{34}e^{5i\xi_s L_s}\left(\sum_{q=1}^{\infty}e^{(2q-1)i\xi_f L_f}(\tilde{r}_{34}\tilde{r}_{32})^{q-1}\right) \quad \text{(black)}$$

$$+\tilde{t}_{12}\tilde{r}_{23}\tilde{r}_{21}^{2}\tilde{t}_{23}^{2}\tilde{t}_{32}\tilde{t}_{34}e^{5i\xi_s L_s}\left(\sum_{q_1=1}^{\infty}e^{2q_1 i\xi_f L_f}(\tilde{r}_{32})^{q_1-1}(\tilde{r}_{34})^{q_1}\right)\left(\sum_{q_2=1}^{\infty}e^{(2q_2-1)i\xi_f L_f}(\tilde{r}_{34}\tilde{r}_{32})^{q_2-1}\right) \quad \text{(red)}$$

$$+\tilde{t}_{12}\tilde{r}_{21}^{2}\tilde{t}_{23}^{3}\tilde{t}_{32}^{2}\tilde{t}_{34}e^{5i\xi_s L_s}\left(\sum_{q_1=1}^{\infty}e^{2q_1 i\xi_f L_f}(\tilde{r}_{32})^{q_1-1}(\tilde{r}_{34})^{q_1}\right)^{2}\left(\sum_{q_2=1}^{\infty}e^{(2q_2-1)i\xi_f L_f}(\tilde{r}_{34}\tilde{r}_{32})^{q_2-1}\right) \quad \text{(green)}$$

Following the same logic, the fourth group may be expressed as

$$\tilde{t}_{12}\tilde{r}_{23}^{3}\tilde{r}_{21}^{3}\tilde{t}_{23}\tilde{t}_{34}e^{7i\xi_s L_s}\left(\sum_{q=1}^{\infty}e^{(2q-1)i\xi_f L_f}(\tilde{r}_{34}\tilde{r}_{32})^{q-1}\right) \quad \text{(black)}$$

$$+\tilde{t}_{12}\tilde{r}_{23}^{2}\tilde{r}_{21}^{3}\tilde{t}_{23}^{2}\tilde{t}_{32}\tilde{t}_{34}e^{7i\xi_s L_s}\left(\sum_{q_1=1}^{\infty}e^{2q_1 i\xi_f L_f}(\tilde{r}_{32})^{q_1-1}(\tilde{r}_{34})^{q_1}\right)\left(\sum_{q_2=1}^{\infty}e^{(2q_2-1)i\xi_f L_f}(\tilde{r}_{34}\tilde{r}_{32})^{q_2-1}\right) \quad \text{(red)}$$

$$+\tilde{t}_{12}\tilde{r}_{23}\tilde{r}_{21}^{3}\tilde{t}_{23}^{3}\tilde{t}_{32}^{2}\tilde{t}_{34}e^{7i\xi_s L_s}\left(\sum_{q_1=1}^{\infty}e^{2q_1 i\xi_f L_f}(\tilde{r}_{32})^{q_1-1}(\tilde{r}_{34})^{q_1}\right)^{2}\left(\sum_{q_2=1}^{\infty}e^{(2q_2-1)i\xi_f L_f}(\tilde{r}_{34}\tilde{r}_{32})^{q_2-1}\right) \quad \text{(green)}$$

$$+\tilde{t}_{12}\tilde{r}_{21}^{3}\tilde{t}_{23}^{4}\tilde{t}_{32}^{3}\tilde{t}_{34}e^{7i\xi_s L_s}\left(\sum_{q_1=1}^{\infty}e^{2q_1 i\xi_f L_f}(\tilde{r}_{32})^{q_1-1}(\tilde{r}_{34})^{q_1}\right)^{3}\left(\sum_{q_2=1}^{\infty}e^{(2q_2-1)i\xi_f L_f}(\tilde{r}_{34}\tilde{r}_{32})^{q_2-1}\right) \quad \text{(blue)}$$

Looking at the first four groups, patterns are emerging. For any group p, labeling colors with the index r, the outgoing amplitude may be expressed

$$\tilde{t}_{12}\tilde{r}_{21}^{p-1}\tilde{t}_{34}e^{(2p-1)i\xi_s L_s}\sum_{r=1}^{p}\tilde{t}_{23}^{r}\tilde{t}_{32}^{r-1}\tilde{r}_{23}^{p-r}\left(\sum_{q_1=1}^{\infty}e^{2q_1 i\xi_f L_f}\tilde{r}_{32}^{q_1-1}\tilde{r}_{34}^{q_1}\right)^{r-1}\left(\sum_{q_2=1}^{\infty}e^{(2q_2-1)i\xi_f L_f}(\tilde{r}_{34}\tilde{r}_{32})^{q_2-1}\right)$$

so the total outgoing amplitude is

$$\frac{E_5}{E_0}=\tilde{t}_{12}\tilde{t}_{34}\sum_{p=1}^{\infty}\tilde{r}_{21}^{p-1}e^{(2p-1)i\xi_s L_s}\left[\sum_{r=1}^{p}\tilde{t}_{23}^{r}\tilde{t}_{32}^{r-1}\tilde{r}_{23}^{p-r}\left(\sum_{q_1=1}^{\infty}e^{2q_1 i\xi_f L_f}\tilde{r}_{32}^{q_1-1}\tilde{r}_{34}^{q_1}\right)^{r-1}\left(\sum_{q_2=1}^{\infty}e^{(2q_2-1)i\xi_f L_f}(\tilde{r}_{34}\tilde{r}_{32})^{q_2-1}\right)\right] \quad (4.23)$$

First evaluating the sums over q_1 and q_2

$$\frac{E_5}{E_0}=\tilde{t}_{12}\tilde{t}_{34}\sum_{p=1}^{\infty}\tilde{r}_{23}^{p}\tilde{r}_{21}^{p-1}e^{(2p-1)i\xi_s L_s}\left[\sum_{r=1}^{p}\left(\frac{\tilde{t}_{23}}{\tilde{r}_{23}}\right)^{r}\tilde{t}_{32}^{r-1}\left(\frac{e^{2i\xi_f L_f}\tilde{r}_{34}}{1-e^{2i\xi_f L_f}\tilde{r}_{32}\tilde{r}_{34}}\right)^{r-1}\left(\frac{e^{i\xi_f L_f}}{1-e^{2i\xi_f L_f}\tilde{r}_{32}\tilde{r}_{34}}\right)\right]$$

Next the sum over r

$$\frac{E_5}{E_0}=\tilde{t}_{12}\tilde{t}_{34}\left(\frac{\tilde{t}_{23}}{\tilde{r}_{23}}\right)\left(\frac{e^{i\xi_f L_f}}{1-e^{2i\xi_f L_f}\tilde{r}_{32}\tilde{r}_{34}}\right)\sum_{p=1}^{\infty}\tilde{r}_{23}^{p}\tilde{r}_{21}^{p-1}e^{(2p-1)i\xi_s L_s}\left[\frac{1-\left(\frac{\tilde{t}_{23}\tilde{t}_{32}}{\tilde{r}_{23}}\right)^{p}\left(\frac{e^{2i\xi_f L_f}\tilde{r}_{34}}{1-e^{2i\xi_f L_f}\tilde{r}_{32}\tilde{r}_{34}}\right)^{p}}{1-\left(\frac{\tilde{t}_{23}\tilde{t}_{32}}{\tilde{r}_{23}}\right)\left(\frac{e^{2i\xi_f L_f}\tilde{r}_{34}}{1-e^{2i\xi_f L_f}\tilde{r}_{32}\tilde{r}_{34}}\right)}\right]$$

And finally the sum over p

$$\frac{E_5}{E_0} = \frac{\tilde{t}_{12}\tilde{t}_{34}\tilde{t}_{23}\left(\frac{e^{i\xi_f L_f}}{1-e^{2i\xi_f L_f}\tilde{r}_{32}\tilde{r}_{34}}\right)}{1-\left(\frac{\tilde{t}_{23}\tilde{t}_{32}}{\tilde{r}_{23}}\right)\left(\frac{e^{2i\xi_f L_f}\tilde{r}_{34}}{1-e^{2i\xi_f L_f}\tilde{r}_{32}\tilde{r}_{34}}\right)} \left(\frac{e^{i\xi_s L_s}}{1-\tilde{r}_{23}\tilde{r}_{21}e^{2i\xi_s L_s}} - \frac{\left(\frac{\tilde{t}_{23}\tilde{t}_{32}}{\tilde{r}_{23}}\right)e^{i\xi_s L_s}\left(\frac{e^{2i\xi_f L_f}\tilde{r}_{34}}{1-e^{2i\xi_f L_f}\tilde{r}_{32}\tilde{r}_{34}}\right)}{1-\tilde{r}_{23}\tilde{r}_{21}\left(\frac{\tilde{t}_{23}\tilde{t}_{32}}{\tilde{r}_{23}}\right)e^{2i\xi_s L_s}\left(\frac{e^{2i\xi_f L_f}\tilde{r}_{34}}{1-e^{2i\xi_f L_f}\tilde{r}_{32}\tilde{r}_{34}}\right)}\right) \quad (4.24)$$

This formula gives the outgoing intensity of light incident normally on a thin film on a thin substrate taking interference from both layers into account. Absorption and scattering are accounted for in the imaginary parts of the exponential factors ξ. If the scattering is zero, the imaginary parts are simply $-\omega\kappa(\omega)/c$ (chapter 2). In reality scattering is usually non-zero, so the imaginary parts may be treated as parameters. A comparison of interference calculated fully-coherently and partially-coherently for a perfectly monochromatic beam of light transmitted through a theoretical double-layer $(Al_{0.15}Ga_{0.85})_2O_3/SiO_2$ stack is shown in fig. 4.21. Clearly, the partially coherent treatment does a better job when the "substrate" is optically thick, which in this case occurs after just a few µm of actual thickness. Real light sources have a finite energy width, and as the SiO_2 layer grows in thickness, the period of oscillations will eventually become smaller than the spread of wavelengths in the beam and interference through that layer will cease.

4.5.2 Experimental Details and Data Collection Methods

In this work, we are interested in the band gap of a CCS thin film as a function of alloy composition. A narrowly collimated beam is therefore critical in order to measure a region which does not vary too much over the beam width. Photos of our experimental apparatus are shown in fig. 4.23. An aluminum block with a slit cut into it is placed in the beam path to restrict the area of the sample illuminated by the beam. The sample is mounted onto a coffee stick using an alligator clip, with the composition gradient is oriented perpendicular to the slit. The other end of the coffee stick is affixed to a micrometer stage (not shown), located well outside of the beam path. Data are collected at regular 1 mm steps by turning the micrometer, moving the sample through the beam from one side of the film to the other. In this way a one-to-one correspondence is established between UV-Vis

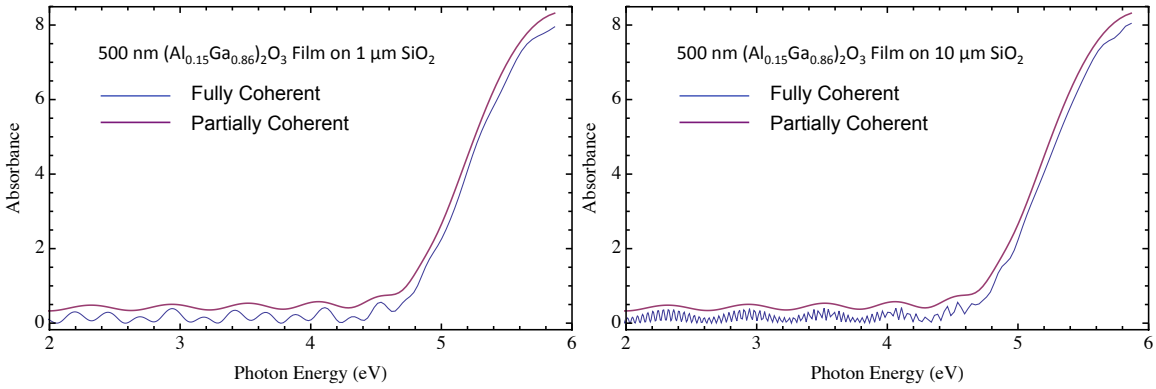

Figure 4.21: Comparison of interference from multiple internal reflections of light transmitted through a 500 nm $(Al_{0.15}Ga_{0.85})_2O_3$ / 1 µm SiO_2 double layer (left), and a 500 nm $(Al_{0.15}Ga_{0.85})_2O_3$/10 µm SiO_2 double layer (right), calculated fully-coherently (using eq. 4.24) and partially coherently (using eq. 4.21 and 4.22).

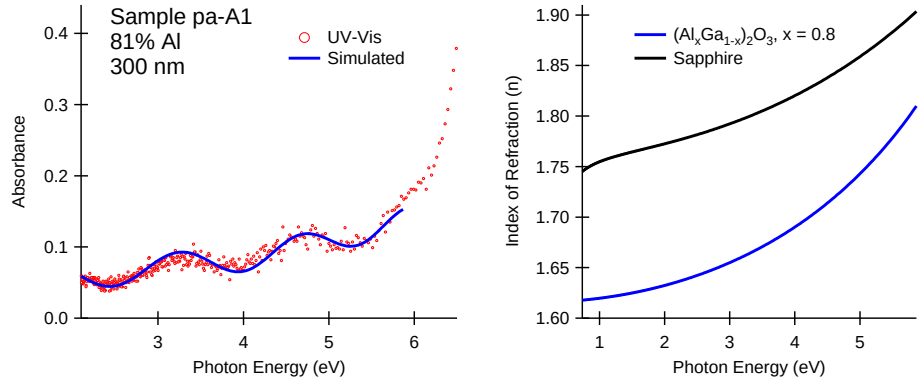

Figure 4.22: Left: Calculated and measured interference fringes in UV-Vis absorbance spectra for a post-annealed $(Al_xGa_{1-x})_2O_3$ thin film on sapphire, using the dispersion in n on the right, obtained from a post-annealed thin film on silicon using spectroscopic ellipsometry.

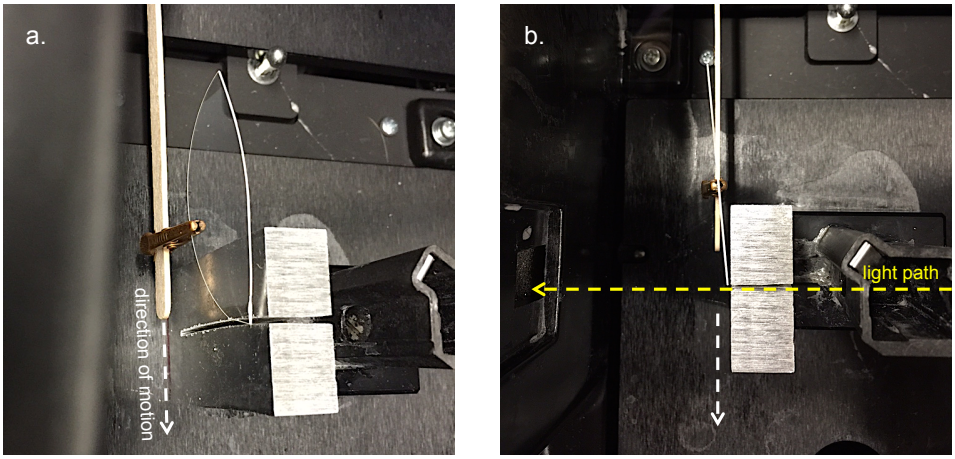

Figure 4.23: Geometry of UV-Vis experiment. a) Angle view b) Top view

data points and alloy compositions obtained in 1 mm steps by XPS.

Even with the Al block in the light path the beam width is not zero, and the effect of a finite width has to be kept in mind. Using the results of eqs. (2.28) and (2.34) to simulate the absorption coefficient for a direct or indirect band gap at 5.0 eV, fig. 4.24 shows how a finite beam width leads to a smearing-out of the absorption edge. We know from the literature that the band gap of $\beta - Ga_2O_3$ is basically direct, but in our data (as will be shown in later chapters) the absorption coefficient exhibits a nearly linear increase from the band gap, so the spreading out of a linear absorption coefficient is also shown. The composition gradient in our CCS films is largest in the middle; the maximum variation is $\frac{\Delta x}{\Delta l} \approx 0.04/\text{mm}$. Assuming that the band gap varies linearly between the endpoints 4.8 eV ($\beta - Ga_2O_3$) and 6.5 eV ($\theta - Al_2O_3$) this corresponds to an estimated width of 0.068 eV for a 1 mm beam width. This may increase, however, due to a small angular offset between the coffee stick and the sapphire substrate, leading to greater separation from the slit as the sample is slowly moved through the beam and giving the outgoing beam more space to diverge.

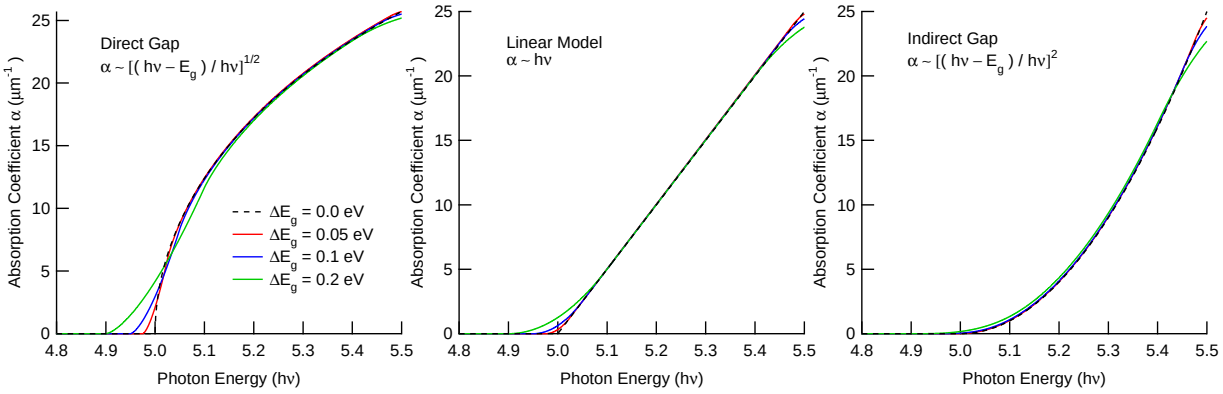

Figure 4.24: Effect of a finite beam width on the measured absorption coefficient of a composition-spread sample with a direct onset (left), linear onset (center), or indirect onset (right) band gap. The beam width is indicated by the variation of the band gap in eV over the portion of the sample illuminated by the beam.

4.6 Spectroscopic Ellipsometry

4.6.1 Ellipsometry Theory

Spectroscopic ellipsometry is a surface-sensitive technique by which the dielectric function of a thin film is determined by measuring the change in polarization of reflected light, and comparing the result to a model prediction. As discussed in chapter 2, the reflectivity (or Fresnel reflection coefficient) $r(\omega)$ is defined as the ratio of the reflected electric field amplitude E_r to the incident electric field amplitude E_i, and is a complex quantity that depends on the initial polarization state

$$\tilde{r}_p = \frac{\tilde{n}^2 \cos\theta - \sqrt{\tilde{n}^2 - \sin^2\theta}}{\tilde{n}^2 \cos\theta + \sqrt{\tilde{n}^2 - \sin^2\theta}} \tag{4.25a}$$

$$\tilde{r}_s = \frac{\cos\theta - \sqrt{\tilde{n}^2 - \sin^2\theta}}{\cos\theta + \sqrt{\tilde{n}^2 - \sin^2\theta}} \tag{4.25b}$$

where θ is the angle of incidence, and p- and s-polarization indicates an **E**-field parallel and perpendicular to the plane of incidence, respectively, as shown in fig. 4.25. The measurement sensitivity is improved by choosing an angle of incidence that maximizes the difference in the reflected p and s components, which falls in the range from 50° to 80° for most materials (fig. 4.26). Usually spectra are taken at multiple angles within that range and fit simultaneously to improve the accuracy of the result.

The two quantities of interest measured in spectroscopic ellipsometry are Ψ and Δ, which contain information on the relative amplitudes and phases of the p- and s-polarized reflected components,

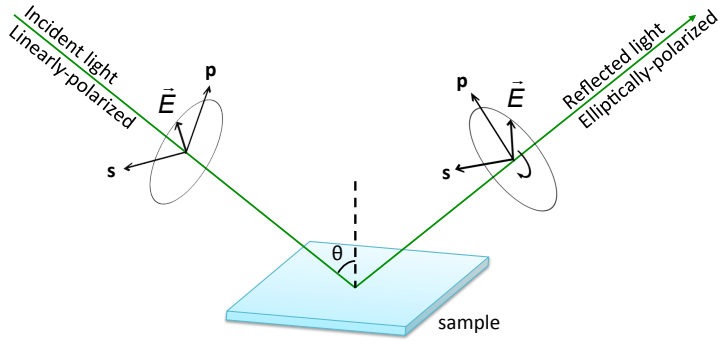

Figure 4.25: Light reflecting off of a sample, changing its polarization state.

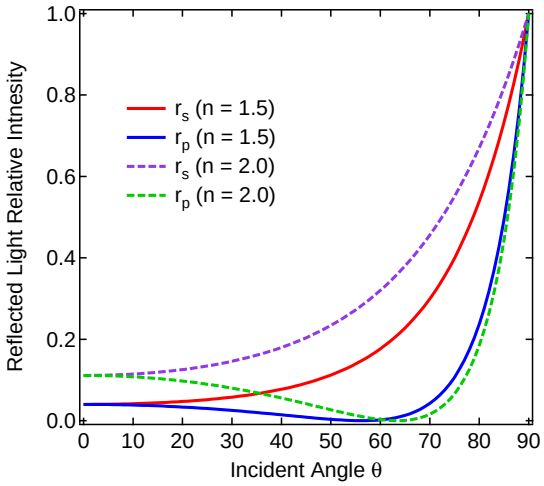

Figure 4.26: Comparison of reflected light intensity as a function of incident angle for p- and s-polarized light at an interface between air and a transparent material with index of refraction either $n = 1.5$, or $n = 2.0$.

respectively

$$\rho = \frac{\tilde{r}_p}{\tilde{r}_s} = \tan(\Psi)e^{i\Delta} \tag{4.26}$$

For an ellipsometric measurement of a semi-infinite bulk sample, this formula may be inverted using eq. (4.25b) to solve for $\tilde{n}$ directly. However, in thin film samples light passes through one or more layers before reflecting off a semi-infinite substrate, and each layer modifies the polarization state in sequence as light passes through it, so it is not possible to determine $\tilde{n}$ by directly inverting eq. (4.26) (the result of performing the calculation anyway is the so-called pseudo-optical function $<\tilde{n}>$). Instead, one builds a layered model to simulate the change in polarization of the light using Jones matrices, and compares the model prediction to the measured data. The agreement between the calculated model and the measured data is quantified by the mean-squared error

$$MSE = \sqrt{\frac{1}{2n-m}\sum_{i=1}^{n}\left[\left(\frac{\Psi_i^{\text{model}} - \Psi_i^{\text{exp}}}{\sigma_{\Psi,i}^{\text{exp}}}\right)^2 + \left(\frac{\Delta_i^{\text{model}} - \Delta_i^{\text{exp}}}{\sigma_{\Delta,i}^{\text{exp}}}\right)^2\right]} \tag{4.27}$$

where n is the number of (Ψ, Δ) pairs, m is the number of fitting parameters and σ is the standard deviation of the experimental data points. An alternative definition for the MSE may be given in

terms of the derived quantities $N = \cos(2\Psi)$, $C = \sin(2\Psi)\cos(\Delta)$, and $S = \sin(2\Psi)\sin(\Delta)$

$$MSE = \sqrt{\frac{1}{3n-m}\sum_{i=1}^{n}\left[\left(N_i^{\text{model}} - N_i^{\text{exp}}\right)^2 + \left(C_i^{\text{model}} - C_i^{\text{exp}}\right)^2 + \left(S_i^{\text{model}} - S_i^{\text{exp}}\right)^2\right]} \times 1000 \quad (4.28)$$

The advantages of using eq. (4.28) are that N, C, and S are all bounded between -1 and 1, and a rotating compensator ellipsometer measures data with approximately the same precision (to about ~ 0.001) in N, C, and S on any sample.

One may represent the polarization state of completely polarized light by a Jones vector

$$\begin{bmatrix} \mathbf{E}_p \\ \mathbf{E}_s \end{bmatrix} = \begin{bmatrix} E_p e^{i\phi_p} \\ E_s e^{i\phi_s} \end{bmatrix}$$

and the change in polarization due to an optical component by a corresponding Jones matrix. For example, the Jones matrix for light reflecting off of an isotropic sample (or an anisotropic sample aligned with its optical axis normal to the surface) is written in terms of the Fresnel reflection coefficients $\tilde{r}_p$ and $\tilde{r}_s$

$$\begin{bmatrix} \tilde{r}_p & 0 \\ 0 & \tilde{r}_s \end{bmatrix} \quad (4.29)$$

Non-diagonal elements arise in the case of an anisotropic sample whose optical axis is not aligned with the sample normal. Representing the optical response of the sample by a Jones matrix with no nonzero components is referred to as generalized ellipsometry. Alternatively, one may define the state and the degree of polarization of partially-polarized incident light by a 4-component Stokes vector

$$\begin{bmatrix} S_0 \\ S_1 \\ S_2 \\ S_3 \end{bmatrix} = \begin{bmatrix} E_p^2 + E_s^2 \\ E_p^2 - E_s^2 \\ 2E_pE_s\cos(\phi_p - \phi_s) \\ 2E_pE_s\sin(\phi_p - \phi_s) \end{bmatrix} \quad (4.30)$$

The first component S_0 measures the reflected intensity of the wave, the second S_1 measures the relative intensities of the two polarization states, and S_2 and S_3 contain information on the relative phases of each component. In general $S_0^2 \geq S_1^2 + S_2^2 + S_3^2$, where equality indicates completely polarized, monochromatic light. The analogue of the Jones matrix for Stokes vectors is the Mueller

matrix, which for an isotropic sample takes the form

$$M_{isotropic} = \begin{bmatrix} 1 & -N & 0 & 0 \\ -N & P & 0 & 0 \\ 0 & 0 & C & S \\ 0 & 0 & -S & C \end{bmatrix} \tag{4.31}$$

where N, C, and S are defined above eq. (4.28) and P measures the degree of depolarization

$$\begin{aligned} P &= \sqrt{N^2 + C^2 + S^2} \\ \%\,\text{Depolarization} &= (1 - P^2) \times 100\% \end{aligned} \tag{4.32}$$

Depolarization is caused by sample non-idealities including non-uniform thickness and roughness, and instrument non-idealities such as bandwidth or angular spread of the incident beam. No light source is perfectly monochromatic, and our ellipsometer uses a broad-band light source, so a certain degree of spectral bandwidth is expected. Furthermore, CCS samples have a thickness variation along the composition gradient, which may be significant within the beam spot unless focus probes are used. Fortunately these effects may be all accounted for in our model by including depolarization data (as defined by eq. 4.32) in our calculation of the MSE.

4.6.2 Rotating Compensator Ellipsometer: Theory of Operation

To measure Ψ and Δ, a number of different types of ellipsometers have been invented, including the null, polarization-modulation, rotating-polarizer, and rotating-analyzer ellipsometers, with various advantages and disadvantages. The type of ellipsometer used in this work is a rotating-compensator ellipsometer (RCE), which represents the current state-of-the-art in terms of measurement accuracy over the entire range of $\Psi = 0 - 90^\circ$ and $\Delta = 10 - 360^\circ$, as well as the ability to accurately measure depolarization.

The RCE configuration consists of a light source, linear polarizer, compensator, sample, analyzer,

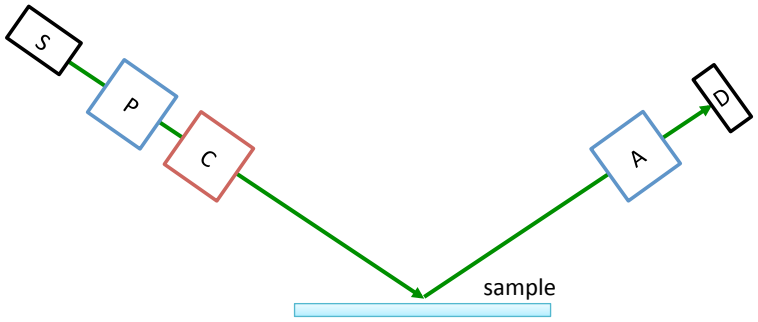

Figure 4.27: Sequence of optical components in a rotating compensator ellipsometer: Source→Polarizer→Compensator→Sample→Analyzer→Detector.

and detector (fig. 4.27). Representing each of these components as Jones matrices

$$\begin{bmatrix} E'_x \\ E'_y \end{bmatrix} = \overbrace{\begin{bmatrix} 1 & 0 \\ 0 & 0 \end{bmatrix}\begin{bmatrix} \cos A & \sin A \\ -\sin A & \cos A \end{bmatrix}}^{\text{Analyzer}}\overbrace{\begin{bmatrix} \tilde{r}_p & 0 \\ 0 & \tilde{r}_s \end{bmatrix}}^{\text{Sample}} \overbrace{\begin{bmatrix} \cos C(t) & -\sin C(t) \\ \sin C(t) & \cos C(t) \end{bmatrix}\begin{bmatrix} e^{i\delta_1} & 0 \\ 0 & e^{i\delta_2} \end{bmatrix}\begin{bmatrix} \cos C(t) & \sin C(t) \\ -\sin C(t) & \cos C(t) \end{bmatrix}}^{\text{RotatingCompensator}} \overbrace{\begin{bmatrix} \cos P & -\sin P \\ \sin P & \cos P \end{bmatrix}\begin{bmatrix} 1 & 0 \\ 0 & 0 \end{bmatrix}\begin{bmatrix} E_x \\ E_y \end{bmatrix}}^{\text{Polarizer}} \tag{4.33}$$

where A, P, and $C(t) = \omega t$ are the azimuthal angles of the analyzer, polarizer, and rotating compensator respectively, relative to the sample normal, and $\delta_1 = d\left(\frac{\omega}{c}\right) n_1$ and $\delta_2 = d\left(\frac{\omega}{c}\right) n_2$ are the phase shifts associated with the two principal axes of the compensator. Equation (4.33) evaluates to

$$\begin{aligned} E'_x = [\ \cos P\ (e^{i\delta_1}\cos C\ (\tilde{r}_p \cos A\ \cos C + \tilde{r}_s \sin A\ \sin C) \\ + e^{i\delta_2}\sin C\ (-\tilde{r}_s \cos C\ \sin A + \tilde{r}_p \cos A\ \sin C)) \\ + \sin P\ (e^{i\delta_1}\sin C\ (\tilde{r}_p \cos A\ \cos C + \tilde{r}_s \sin A\ \sin C) \\ + e^{i\delta_2}\cos C\ (\tilde{r}_s \cos C\ \sin A - \tilde{r}_p \cos A\ \sin C))\ ]\ E_x \end{aligned} \tag{4.34}$$

Using the following identities

$$2\sin C\cos C = \sin(2C)$$
$$\sin^2 C = \frac{1}{2}(1-\cos(2C))$$
$$\cos^2 C = \frac{1}{2}(1+\cos(2C))$$

and collecting terms in $\cos(2C)$ and $\sin(2C)$, the above equation may be written

$$E'_x = \frac{1}{2}\,[\,(e^{i\delta 1}+e^{i\delta_2})(\tilde{r}_p\cos A\cos P+\tilde{r}_s\sin A\sin P) + (e^{i\delta_1}-e^{i\delta_2})(\tilde{r}_p\cos A\cos P-\tilde{r}_s\sin A\sin P)\cos(2C) + (e^{i\delta_1}-e^{i\delta_2})(\tilde{r}_p\cos A\sin P+\tilde{r}_s\sin A\cos P)\sin(2C)\,]\,E_x \quad (4.35)$$

The intensity at the detector is proportional to the magnitude of E'_x squared, and may be expressed in terms that are either constant, or which oscillate at either $2C$ or $4C$

$$|E'_x|^2 = \frac{1}{4}\,[\,I_0+\alpha_2\cos(2C)+\beta_2\sin(2C)+\alpha_4\cos(4C)+\beta_4\sin(4C)\,]|E_x|^2 \quad (4.36)$$

The coefficients I_0, α_2, β_2, α_4, and β_4 are

$$I_0 = 2(1+\cos(\delta))(|\tilde{r}_p|^2\cos^2 A\cos^2 P+|\tilde{r}_s|^2\sin^2 A\sin^2 P+\frac{1}{2}\mathrm{Re}(\tilde{r}_p\tilde{r}_s^*)\sin^2 A\sin^2 P) + (1-\cos(\delta))(|\tilde{r}_p|^2\cos^2 A+|\tilde{r}_s|^2\sin^2 A) \quad (4.37a)$$

$$\alpha_2 = -2\sin(\delta)\sin(2A)\sin(2P)\mathrm{Im}(\tilde{r}_p\tilde{r}_s^*) \quad (4.37b)$$

$$\beta_2 = 2\sin(\delta)\sin(2A)\cos(2P)\mathrm{Im}(\tilde{r}_p\tilde{r}_s^*) \quad (4.37c)$$

$$\alpha_4 = (1-\cos(\delta))[(|\tilde{r}_p|^2\cos^2 A-|\tilde{r}_s|^2\sin^2 A)\cos(2P)-\sin(2A)\sin(2P)\mathrm{Re}(\tilde{r}_p\tilde{r}_s^*)] \quad (4.37d)$$

$$\beta_4 = (1-\cos(\delta))[(|\tilde{r}_p|^2\cos^2 A-|\tilde{r}_s|^2\sin^2 A)\sin(2P)+\sin(2A)\cos(2P)\mathrm{Re}(\tilde{r}_p\tilde{r}_s^*)] \quad (4.37e)$$

where I_0 comes from terms $1\times 1^*$, $2\times 2^*$ and $3\times 3^*$ in eq. (4.35) above, α_2 comes from $1\times 2^*$ and $2\times 1^*$, β_2 comes from $1\times 3^*$ and $3\times 1^*$, α_4 comes from $2\times 2^*$ and $3\times 3^*$, and β_4 comes from $2\times 3^*$ and $3\times 2^*$, and the relations $\tilde{r}_p\tilde{r}_s^*+\tilde{r}_p^*\tilde{r}_s = 2\ \mathrm{Re}(\tilde{r}_p\tilde{r}_s^*)$ and $\pm(\tilde{r}_p\tilde{r}_s^*-\tilde{r}_p^*\tilde{r}_s) = \pm 2i\ \mathrm{Im}(\tilde{r}_p\tilde{r}_s^*) = \mp 2i\ \mathrm{Im}(\tilde{r}_p^*\tilde{r}_s)$ were used to simplify the notation.

Since $C(t)=\omega t$, the continuously rotating compensator modulates the intensity at the detector harmonically in time, so each of the coefficients listed in eqs. (4.37a) to (4.37e) may be found

by Fourier decomposition. As written, it is not possible to solve for $\tilde{r}_p$ and $\tilde{r}_s$ directly. However, by normalizing to the DC reflectance I_0, forming the quantities $\frac{\alpha_2}{I_0}$ $\frac{\beta_2}{I_0}$ $\frac{\alpha_4}{I_0}$ and $\frac{\beta_4}{I_0}$, and dividing numerator and denominator by $|\tilde{r}_s|^2$, the Fourier coefficients may be expressed in terms of Ψ and Δ using eq. (4.26)

$$\frac{I_0}{|\tilde{r}_s|^2} = 2(1+\cos(\delta))(\tan^2(\Psi)\cos^2(A)\sin^2(P) + \sin^2(A)\sin^2(P) + \sin(2A)\sin(2P)\tan(\Psi)\cos(\Delta)) - (1-\cos(\delta))(\tan^2(\Psi)\cos^2(A) + \sin^2(A)) \quad (4.38a)$$

$$\frac{\alpha_2}{|\tilde{r}_s|^2} = -4\sin(\delta)\sin(2A)\sin(2P)\tan(\Psi)\sin(\Delta) \quad (4.38b)$$

$$\frac{\beta_2}{|\tilde{r}_s|^2} = 4\sin(\delta)\sin(2A)\cos(2P)\tan(\Psi)\sin(\Delta) \quad (4.38c)$$

$$\frac{\alpha_4}{|\tilde{r}_s|^2} = (1-\cos(\delta))[(\tan^2(\Psi)\cos^2(A) - \sin^2(A))\cos(2P) - 2\sin(2A)\sin(2P)\tan(\Psi)\cos(\Delta)] \quad (4.38d)$$

$$\frac{\beta_4}{|\tilde{r}_s|^2} = (1-\cos(\delta))[(\tan^2(\Psi)\cos^2(A) - \sin^2(A))\sin(2P) + 2\sin(2A)\cos(2P)\tan(\Psi)\cos(\Delta)] \quad (4.38e)$$

where numerator and denominator of $\frac{\alpha_2}{I_0}$ $\frac{\beta_2}{I_0}$ $\frac{\alpha_4}{I_0}$ and $\frac{\beta_4}{I_0}$ are shown separately for clarity. Hence we have four equations that may be solved for the three quantities $\tan^2(\Psi)$, $\tan(\Psi)\cos(\Delta)$ and $\tan(\Psi)\sin(\Delta)$, which may in turn be solved to find $\tan(\Psi)$, $\cos(\Delta)$ and $\sin(\Delta)$, though the expressions are long and not particularly illuminating and so will not be reproduced here. It is clear, however, that Ψ is uniquely determined within the range 0–90° by its tangent, and Δ determined within its full range 0–360° by the simultaneous measurement of $\cos(\Delta)$ and $\sin(\Delta)$. This offers a distinct advantage over the rotating polarizer and rotating analyzer ellipsometer designs, which map Δ onto the 0–180° range and are thus unable to determine the handedness of the detected elliptical polarization.

4.6.3 Modeling the Dielectric Function

As mentioned earlier, deducing optical functions from ellipsometric data requires building a parameterized model to generate a simulated Ψ and Δ, and varying the model parameters until agreement with experimental data is obtained. At a minimum, the parameters of each layer define a functional form of the real and imaginary parts of the dielectric function ε and the layer thickness. A number of

other characteristics which affect the optical response may also be measured by including additional parameters. The most common is a surface roughness layer, modeled by creating a 50/50 mixture of material and voids in an effective medium approximation (EMA). The most common EMA is the Bruggeman approximation which mixes two materials with dielectric functions ε_a and ε_b in atomic fractions f_a and f_b

$$0 = f_a \frac{\varepsilon_a - \varepsilon}{\varepsilon_a + 2\varepsilon} + f_b \frac{\varepsilon_b - \varepsilon}{\varepsilon_b + 2\varepsilon} \tag{4.39}$$

and can be derived from the Clausius-Mossotti equation by simple considerations [374]. Roughness is modeled by adding a thin EMA layer above the film, with either $\varepsilon_a = \varepsilon_{\text{film}}$ and $\varepsilon_b = 1$. Intermixing between layers may also be modeled by inserting a thin EMA between the two layers. Other model parameters may be included to specify grading, which defines a gradual change in the optical functions with depth; uniaxial or biaxial anisotropy; angular offsets; and experimental non-idealities such as thickness non-uniformity and bandwidth.

If a film is transparent, ε_2 may be modeled by a delta function oscillator in the UV outside the wavelength range being collected with amplitude and center energy specified as parameters, and (optionally) a second delta function oscillator at $\omega = 0$. Then ε_1 is computed from the Kramers Kronig relation eq. (2.14a)

$$\varepsilon_1(\omega) = 1 + \frac{2}{\pi}\, P \int_0^\infty \frac{\omega'\, \varepsilon_2(\omega')}{\omega'^2 - \omega^2}\, d\omega' \rightarrow \varepsilon_\infty + \frac{A_{ir}}{\omega^2} + \frac{A_{uv}}{\omega_{uv}^2 - \omega^2} \tag{4.40}$$

where an additive constant ε_∞ has been added to account for the truncated range of integration. This is the Sellmeier dispersion equation, which is more often expressed as a function of wavelength by substituting $\lambda = 2\pi c/\omega$

$$\varepsilon_1(\lambda) = \varepsilon_\infty + A_{ir}\lambda^2 + \frac{A_{uv}\lambda^2}{\lambda^2 - \lambda_{uv}^2} \tag{4.41}$$

The series expansion of eq. (4.41) about $\lambda = \infty$ (or equivalently, the expansion of eq. (4.40) about $\omega = 0$) is

$$\varepsilon_1(\lambda) \approx A + \frac{B}{\lambda^2} + \frac{C}{\lambda^4} + \cdots \tag{4.42}$$

where multiplicative factors have been absorbed into the constants A, B, and C. This is called the Cauchy dispersion model and is widely used, with A, B and C as the fitted parameters and the $A_{ir}\lambda^2$ term sometimes included as well. Either the Cauchy or Sellmeier models can be used to find the real part of ε_1 and thickness for transparent films and the results are generally indistinguishable,

despite the fact that the Sellmeier equation imposes constraints on A, B, and C that are not enforced by letting those parameters vary freely in the Cauchy model. In reality, zero-width delta function oscillators are unphysical anyway and dispersion calculated from them will be approximate at best, so letting the Cauchy parameters vary freely may in fact allow for a more accurate dispersion.

If the film is absorbing over part of the wavelength range, then a functional form of ε_2 can be specified as a sum of oscillators with each oscillator described by a combination of fitted parameters including the center energy, amplitude, width and possible additional parameters describing the shape, as suggested by eq. (2.12). Then ε_1 is found from the Kramers-Kronig relation eq. (2.14a). The earliest literature modeled ε_2 as large ensembles of Lorentzian (eq. (2.12)) or harmonic oscillators [375, 376] (derived in a self-consistent way by solving the time-dependent Schrödinger equation of an electron in a solid with the electric field of the light treated as a perturbation), but these are inadequate for describing semiconductors near the band edge due to their long tails extending into the transparent region. These models also suffer from the basic weakness that positions and widths of oscillators used are largely decoupled from the intrinsic band structure and are therefore only phenomenological. Other models using oscillators based on the critical point structures (using expressions likeeq. (2.28), for example) have been shown to reproduce derivatives of $\varepsilon_2(\omega)$ well but not ε_2 itself (due to certain approximations used in their derivation), and also require a large number of fitting parameters. Adachi [377, 378] developed a hybrid model combining CP oscillators near the band edge with harmonic oscillators to capture large broad structures but since neither parent model did very well at reproducing ε_2, neither did the model by Adachi.

Substantial improvement arrived when Kim et al. [379] introduced a modified CP model, correcting a few common but erroneous assumptions made in deriving the expressions for the previous CP model and also adding a parameter allowing for interpolation between Lorentzian and (approximate) Gaussian broadening. Fitting with this model involves (1) defining a set of critical points in the band structure (2) Connecting each pair of points with low-order polynomials, and (3) minimizing the total function with respect to ε_2 and its derivatives simultaneously. Thus, using it can be a cumbersome process, eschewing the notion of discrete oscillators altogether. The parametric semiconductor (P-Semi) model of Johs et al. [380] was therefore invented to simplify the fitting procedure while preserving the accuracy of the model of Kim et al. [379].

The P-semi model returns to the oscillator scheme, but retains the Gaussian broadened and

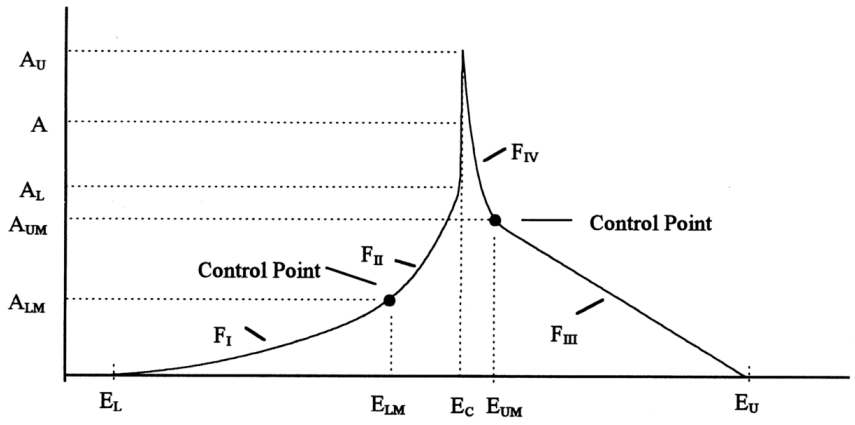

Figure 4.28: Unbroadened P-Semi Tri oscillator composed of four polynomial sections, defined by positions and amplitudes of control points. From Johs et al. [380]

critical point features of [379]. A generic (unbroadened) P-semi oscillator composed of four connected polynomials is shown in fig. 4.28. By appropriately adjusting the various control points defining each polynomial, any of the critical points structures in fig. 2.2 can be accurately modeled. Unlike in the model by [379], in the P-semi model each critical point gets its own oscillator, and variation in fitted parameters such as center energy and amplitude are more easily correlated with changes in the band structure (in the case of alloys such as $Al_xGa_{1-x}As$ [381] and $In_xGa_{1-x}As$ [382], for example). This model is highly flexible however, and one simply may choose to let the control points vary freely to achieve the best fit to ε_2.

In amorphous semiconductors, where long range order is absent, sharp features in absorption spectra arising from band structure become spread out. Absorption is therefore largely determined by short range order—i.e. the degree of overlap and broadening between superposed molecular orbitals. The shape of the absorption edge in amorphous semiconductors was first derived by Tauc et al. [383]

$$\omega^2 \varepsilon_2(\omega) \sim (\hbar\omega - E_g)^2 \tag{4.43}$$

with the assumption that crystal momentum is not conserved in optical transitions in amorphous semiconductors. His result is similar to the case of indirect transitions in crystalline semiconductors eq. (2.34), which also do not conserve momentum. An early oscillator model was developed in 1986

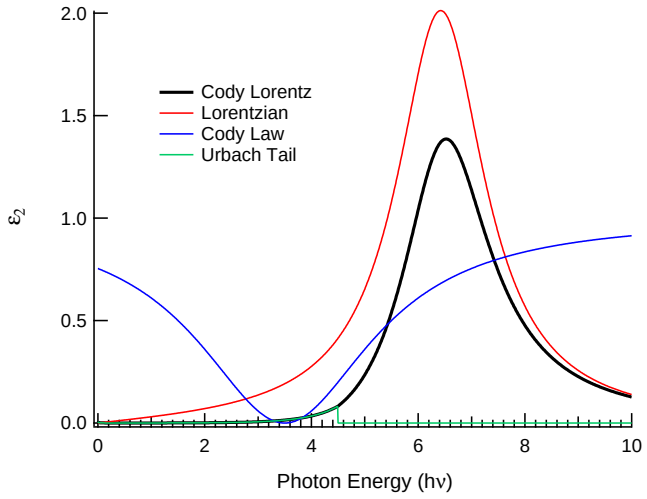

Figure 4.29: Example Cody-Lorentz oscillator with Urbach absorption below the band edge.

by Forouhi and Bloomer [384] to reproduce the Tauc dependence at the absorption edge, but it makes a few unphysical predictions, including finite k as $\omega \to \infty$ and $k > 0$ for $\hbar\omega < E_g$.

In 1996 Jellison and Modine [385] proposed a new model, constructed simply by multiplying eq. (4.43) by the Lorenzian oscillator eq. (2.12), logically named "Tauc-Lorentz," which remedies both problems. Equation (4.43) was derived under the fairly standard assumptions of parabolic bands, and constant momentum matrix element [383]. A different model was proposed by Ferlauto et al. [386] in 2002, making instead an assumption of constant dipole matrix element, which leads to an modified "Cody-Law" absorption edge

$$\varepsilon_2(\omega) \sim (\hbar\omega - E_g)^2 \tag{4.44}$$

This new model, constructed by stitching together the Cody formula eq. (4.44) and a simple Lorentzian at a variable crossover point, is referred to as a "Cody-Lorentz" model. When introducing their formula, Ferlauto et al. [386] also included a second crossover point at lower energy to allow a transition from band-edge Cody Law behavior to an exponentially-decreasing Urbach tail. An example Cody-Lorentz oscillator shape is shown in fig. 4.29 showing how the three pieces combine to create the overall shape.

Both the Tauc-Lorentz and Cody-Lorentz models are still used today to model amorphous and also crystalline materials, often in a completely phenomenological manner, by constructing large

oscillator ensembles to mimic the experimental absorption spectrum (e.g. for a $(Al_xGa_{1-x})_2O_3$ thin film [306]), exactly as was done using Harmonic oscillators in 1984 by Erman et al. [376].

4.6.4 Equipment Details

Spectroscopic ellipsometry was performed on a M-2000XI rotating compensator ellipsometer by Woolam Instruments, Inc. This instrument acquires ellipsometric data between 210 nm and 1690 nm in 697 equal wavelengths simultaneously by dispersing white light from a 75 W xenon light source onto a CCD detector. The beam diameter is 2 mm with a divergence of less than 0.3°, and has a spectral bandwidth of 5 nm; the M-2000 also has the ability to focus the beam spot to 0.125 mm using optional lens optics.

Chapter 5

$(Al_xGa_{1-x})_2O_3$ POWDER

Although technological applications of $(Al_xGa_{1-x})_2O_3$ will undoubtedly require the fabrication of single and multi-layered thin films, the fundamental question remains of the ultimate solubility limit of Al in the monoclinic $\beta - Ga_2O_3$ structure, and whether the band gap variation is linear with Al composition, or exhibits significant bowing, within the thermodynamically stable phase. To answer this question a series of 14 powder pellets were produced by solution combustion synthesis following the recipe outlined in section 4.1, including one Ga_2O_3, one Al_2O_3, and 12 $(Al_xGa_{1-x})_2O_3$ pellets spanning the composition range $0.1 < x < 0.8$. Sintering at 1600 °C (approximately 200 °C less than the melting point of $\beta - Ga_2O_3$, and 500 °C less than the melting point of $\alpha - Al_2O_3$ [103]) for 12 hours (ramping at 5 °C/min) ensures that these powders emerge in the thermodynamically stable phase. X-ray diffraction shows that after sintering the $\beta - Ga_2O_3$ phase is preserved all the way to $x = 0.8$; therefore these powders represent an ideal system to characterize the variation in band gap and lattice parameters of $\beta - (Al_xGa_{1-x})_2O_3$. These same pellets may also be used as PLD targets to prepare uniform $(Al_xGa_{1-x})_2O_3$ films, requiring less deposition time than a layer-by-layer growth method alternating between Ga_2O_3 and Al_2O_3 targets, and allowing for homogenous films with thickness < 5 nm.

5.1 Lattice Parameters

Figure 5.1 shows integrated diffraction patterns for sintered pellets in the composition range $0 \leq x \leq 1$ in steps of 0.1. Also appended are the PDF card reference patterns for $\beta - Ga_2O_3$ (bottom) and $\alpha - Al_2O_3$ (top). As x increases diffraction peaks move to higher 2θ indicating a steady contraction of the lattice parameters. Powders remain in the β phase until $x = 0.8$, when additional smaller peaks appear belonging to the α phase, highlighted in fig. 5.1 by red arrows. Upon closer examination, the 2θ-shift in the $x = 0.7$ to $x = 0.8$ step is comparable in magnitude to shifts at lower steps, suggesting that the upper solubility limit is likely closer to $x = 0.8$ than $x = 0.7$. This result is in agreement

with earlier reports that found an upper solubility limit of 0.78 for alloys fabricated by grinding together and sintering Al_2O_3 and Ga_2O_3 powder in a 4:1 ratio [103, 104], but is higher than the upper limit for alloys fabricated by equilibrium cooling from a melt, in which a mixed phase was observed in the range $0.67 < x < 0.75$ and pure $\alpha - Al_2O_3$ observed above $x \geq 0.75$ [53].

Rietveld refinement was applied to the integrated patterns in fig. 5.1 to determine the change in unit cell and crystallite size with Al content [365]. The expected 3 % smaller size of $\theta - Al_2O_3$ [52] produces too large of a 2θ shift to fit all the patterns directly with $\beta - Ga_2O_3$ as a starting point, so it was necessary to fit the data from the bottom ($x = 0$) to the top ($x = 0.8$) of the figure in sequence. XRD peak widths are related to the average size of crystalline domains through the Scherrer equation

$$\tau = \frac{K\lambda}{\beta \cos\theta} \tag{5.1}$$

where K is a dimensionless shape factor close to unity, λ is the X-ray wavelength, β is the width (FWHM) of XRD peaks, $\theta = \frac{1}{2}(2\theta)$ and τ is the size of crystalline domains. The Scherrer equation therefore provides an estimate of the average size of grains in the powder. Figure 5.2 plots the Scherrer equation result over the alloy composition range $0.1 \leq x \leq 0.8$, showing that the average crystallite size decreases with increasing Al content from approximately 460 nm to 380 nm.

Lattice parameters of the $\beta - (Al_xGa_{1-x})_2O_3$ unit cell after refinement are shown in fig. 5.3 and the fractional change relative to $\beta - Ga_2O_3$ has also been plotted in fig. 5.4. In both figures, the $\theta - Al_2O_3$ ($x = 1$) unit cell dimensions from Husson and Repelin [55] have been appended for reference. Also shown are the results of a density functional theory (DFT) calculation, performed by our collaborators Scott Dunham and Evan Nelson (UW-EE), with the (colored) dotted line connecting the lowest-energy configurations. Total energy was minimized on 20 and 120 atom supercells after substituting Al for Ga in the monoclinic $\beta - Ga_2O_3$ structure at several different lattice sites, using the DFT code VASP [387, 388] with the PW91 GGA functional [389] and ultrasoft Vanderbilt-type pseudopotentials [390, 391]. A 400 eV energy cutoff was used, with $3 \times 11 \times 5$ $k-$space sampling on the 20 atom cells and 2^3 sampling on the 120 atom cells. DFT results are listed in table 5.1.

The lattice parameters of $\beta - (Al_xGa_{1-x})_2O_3$ decrease monotonically as Al content is increased. Close examination of figs. 5.3 and 5.4 reveals a slight change in slope above $x = 0.5$, which might

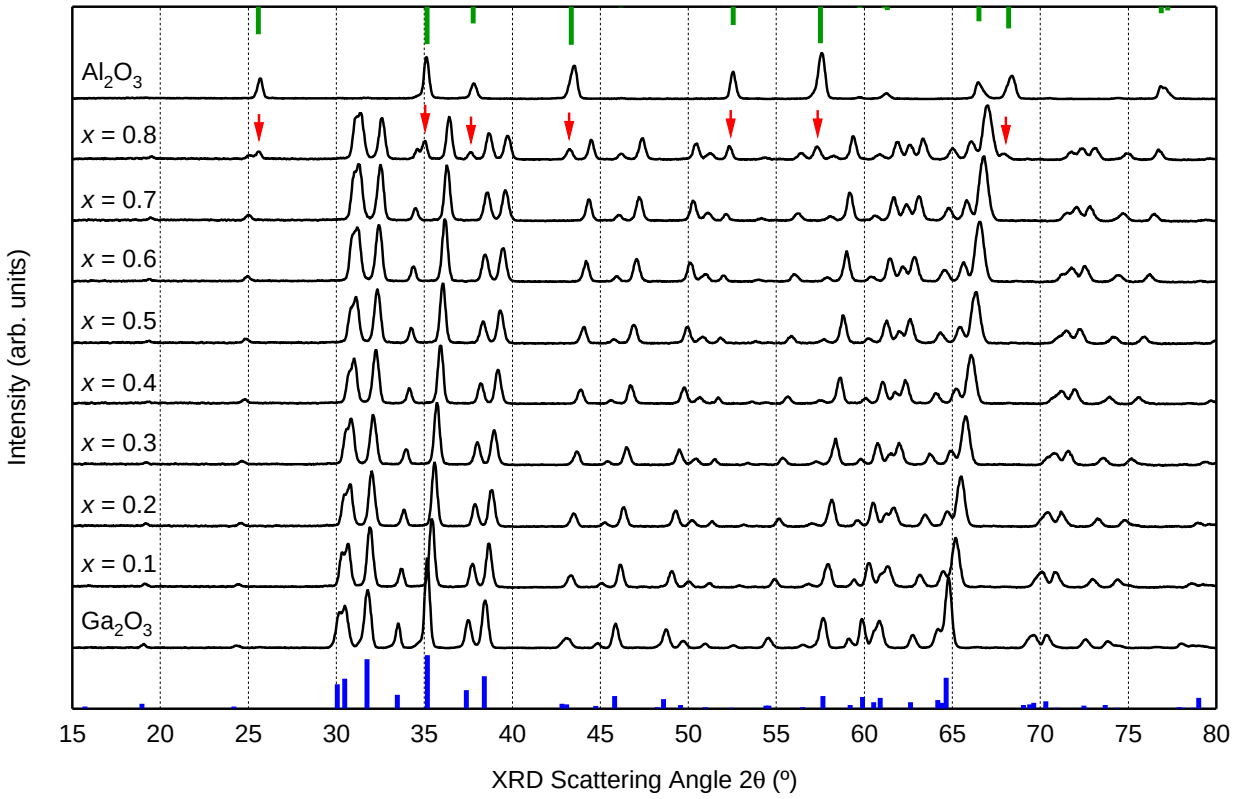

Figure 5.1: X-ray diffraction $\theta - 2\theta$ scans for $(Al_xGa_{1-x})_2O_3$ sintered pellets for $0 \leq x \leq 1$. The JCPDS PDF card references for $\beta - Ga_2O_3$ (00-043-1012) and $\alpha - Al_2O_3$ (00-043-1484) are shown as vertical bars at the bottom and top, respectively. The red arrows indicate the appearance of the α phase at the upper solubility limit, $x = 0.8$

Table 5.1: DFT calculated lattice parameters, energies, and band gaps of $\beta - (Al_xGa_{1-x})_2O_3$. The configuration label (oct) stands for octahedral site, (tet) stands for tetrahedral site, (nn) stands for nearest-neighbor, and (nnn) stands for next-nearest-neighbor. When more than one configuration was tried, the lowest energy is highlighted with an asterisk.

	a (Å)	b (Å)	c (Å)	β (°)	Energy (eV)	Band Gap (eV)
Ga_2O_3	12.33	3.04	5.81	103.65	-124.6351	2.3011
1 Al (oct)	12.11	3.01	5.76	103.85	-127.7422	2.7145
1 Al (tet)*	12.17	3.01	5.76	103.69	-127.6182	2.7030
2 Al (nn)*	12.13	3.00	5.74	103.78	-130.9452	2.8588
2 Al (nnn)	12.10	3.00	5.75	103.82	-130.9192	2.8463
3 Al	12.08	2.99	5.73	103.84	-134.1663	3.0785
4 Al (3 oct)	12.12	2.99	5.75	103.84	-137.2444	3.2296
4 Al (oct)*	12.04	2.97	5.72	103.99	-137.3987	3.3385
4 Al (tet)	12.06	3.00	5.73	103.71	-137.1465	3.3759
5 Al	11.97	2.96	5.70	103.87	-140.4464	3.5888
6 Al	11.95	2.95	5.67	103.85	-143.6178	3.8283
7 Al	11.90	2.94	5.65	103.86	-146.7488	4.2163
Al_2O_3	11.86	2.93	5.64	103.80	-150.0470	5.7354

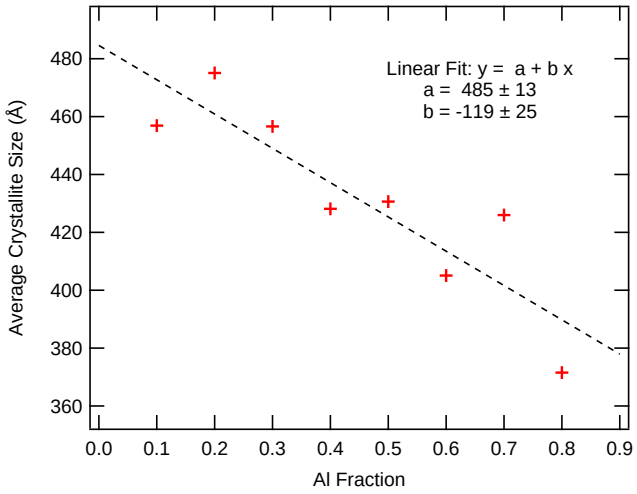

Figure 5.2: Average crystallite size vs. Al fraction x for $0.1 < x < 0.8$ as determined by the Scherrer equation.

be explained by a preferential site occupation of Al atoms in the $\beta - Ga_2O_3$ lattice, as half of the available sites are octahedrally coordinated and the other half are tetrahedrally coordinated. Therefore, a two-line model was used to fit the data with a slope change at $x = 0.5$. The overall slope and change in the slope at $x = 0.5$ is smallest for the c parameter. The a and b parameters change together up to $x = 0.5$, but above $x = 0.5$ the a parameter diverges, contracting faster than both b and c. The angle between **b** and **c** also shows different behavior above and below $x = 0.5$, increasing at low x but then remaining nearly constant. As shown in section 3.1.1, c is the sum of octahedral and tetrahedral edges and b is the edge length of a single octahedron or (equivalently) a tetrahedron. Based on these observations it is surprising that b would change faster than c for either type of site preference, although the octahedra are already distorted and may contract more easily in the b direction than the c direction. On the contrary, it is not clear how a tetrahedral site preference would lead to a preferred contraction direction due to the more symmetrical arrangement of bonds around the tetrahedral site. The much longer a is the sum of two edge-to-edge distances of tetrahedra and two maximal vertex-to-vertex distances of octahedra divided by the sine of β, and therefore would be expected to exhibit the greatest fractional change if all Al atoms occupy octahedral sites.

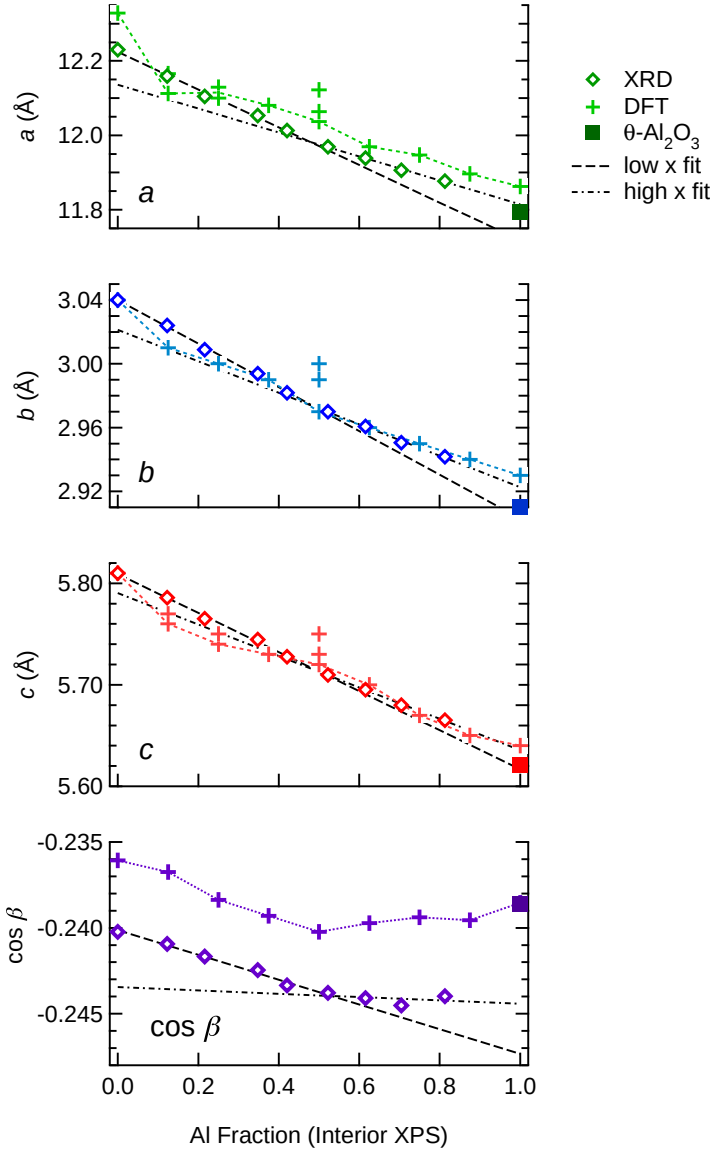

Figure 5.3: Lattice parameters of $\beta - (Al_xGa_{1-x})_2O_3$. Experimental values ($\diamond$) are fits to the X-ray diffraction patterns in fig. 5.1. Theoretical values ($+$) are from DFT calculations; values for the lowest energy Al configuration are connected by a dotted (colored) line. Accepted values for $\theta - Al_2O_3$ are shown as solid squares ($\blacksquare$). Dashed and dash-dotted (black) lines are fits to XRD results for $0 \leq x \leq 0.45$ and $0.5 \leq x \leq 0.8$, respectively, showing a change in slope at $x = 0.5$.

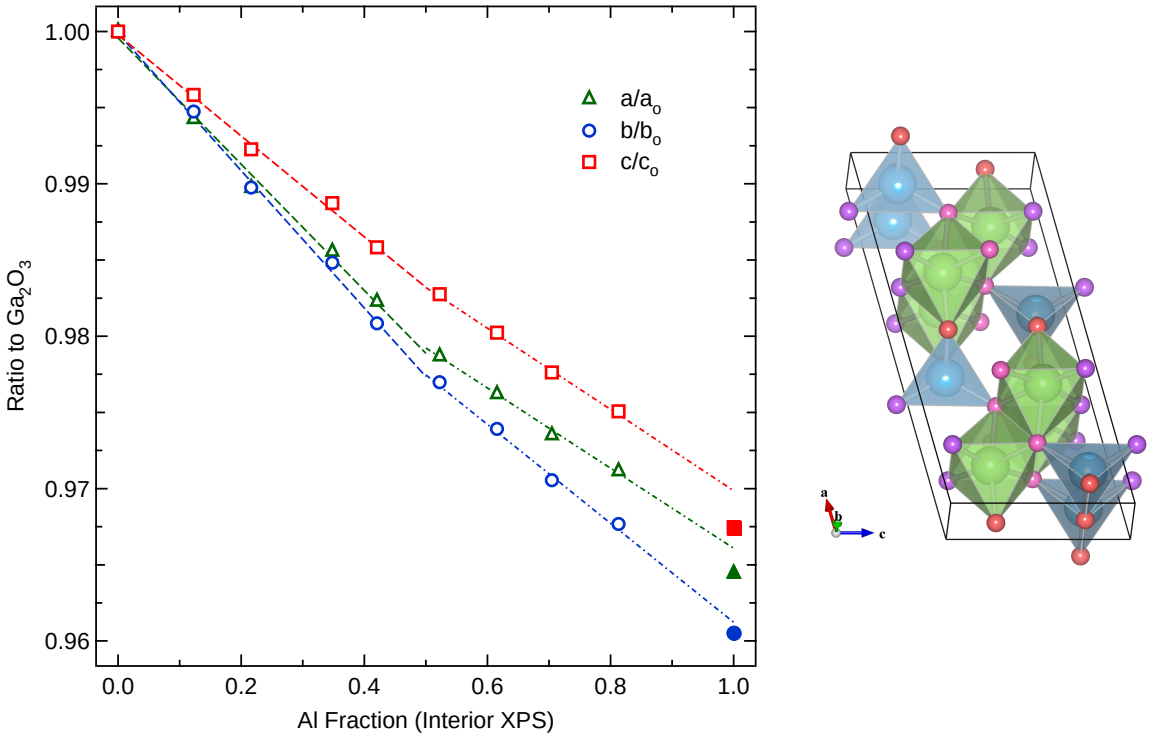

Figure 5.4: Left: Experimental lattice parameters relative to those in Ga_2O_3. Lines are the same linear fits as in fig. 5.3, appropriately scaled and truncated at $x = 0.5$. Right: Unit cell of $\beta - Ga_2O_3$.

The lowest-energy DFT result tracks the experimental lattice parameters in general, except for an artificially low value of β that nonetheless still experiences a change in slope at $x = 0.5$. The other calculated parameters tend to overestimate the contraction below $x = 0.5$ and do not show a clear change in slope. At low x, our calculation predicts a 0.13 eV preference for an isolated Al atom to occupy an octahedral site (table 5.1). When substituting Al in four out of eight cation sites, our calculation predicts a 0.25 eV energy preference for all four Al atoms to occupy octahedral sites rather than tetrahedral sites, and a 0.15 eV energy preference to occupy octahedral sites exclusively relative to a mixed 3:1 octahedral-to-tetrahedral configuration. Furthermore, the contraction in a predicted by the all-octahedral configuration provides the best match to experimental data. It is worth noting that the lowest-energy structure of Al_2O_3 contains only distorted octahedral sites. Unlike Ga, Al does not possess a filled d-orbital, which is responsible for the higher stability of tetrahedral sites in Ga_2O_3 than Al_2O_3 by hybridization with neighboring O $2s$, potentially explaining the preference for Al to occupy octahedral rather than tetrahedral sites in Ga_2O_3 [176].

5.2 XPS Composition

Surface alloy composition and band gap were measured simultaneously using XPS. Details of how XPS can be used to quantitatively determine alloy composition are given in section 4.4.3. However, the highly insulating and loosely-connected nature of our powders resulted in persistent differential charging of XPS spectra even under constant sample neutralization, and fitting to Voigt peaks with well defined Lorentzian widths was not meaningful. However, all regions in a given spectrum distorted in the same way, which permitted analysis using a modified procedure. Regardless of the specific line shape, the intensity of a photoemission peak is proportional to the number of atoms of that species emitting electrons, and therefore may be used as a measure of composition under the X-ray spot. Therefore, numerical integration was performed to find the area under each peak, and the resulting $I_{\mathrm{Al}} : I_{\mathrm{Ga}}$ ratios between Al $2s$, Al $2p$, and Ga $3p$ were used to calculate composition following eq. (4.12). In these samples Ga $3d$ was not used because it was not possible to disentangle Ga $3d$ from the overlapping O $2s$ on the high binding energy side, and O $1s$ was not used because the high surface area of powders relative to thin films resulted in a much larger OH shoulder and was not considered a reliable reference.

Figure 5.5 plots the measured alloy compositions of sintered pellets found by XPS vs. atomic

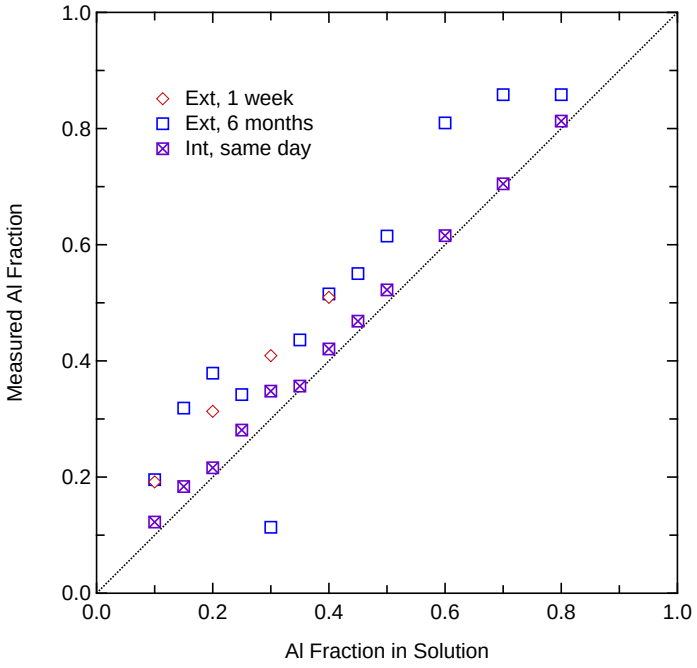

Figure 5.5: Measured surface Al fraction as a function of initial Al concentration in solution. Data are shown for the surface of the sintered pellet (exterior) within a week after fabrication (◇) and several months later (□), and for the interior of the aged pellet immediately after a fresh cleave (⊠).

ratio of precursors in solution, showing composition at the exterior of the pellet shortly after fabrication, composition at the exterior of the pellets approximately six months later after being stored in air, and composition at the interior of the aged pellet measured immediately after a fresh cleave. A significant deviation to higher Al concentration is observed at the exterior of the targets compared to the interior. However, the interior of the targets tracks the solution concentration closely. Fortunately we find that the band gap measured by XPS tracks the local composition under the X-ray spot, rather than overall concentration in solution, so the deviation at the surface allowed for two band gap measurements per pellet rather than one. A possible explanation for the higher Al concentration at the surface may be diffusion into the targets from alumina plates or the alumina tube during sintering, or different reaction rates between Ga, Al, and H_2O vapor in the air at 1600 °C.

5.3 Band Gap

XPS was also used to measure the band gap of the powders. First an attempt to measure the band gap using optical spectroscopy was made by mixing powder in perfluorohexane in a UV-transparent quartz cell, but severe Mie scattering due to the mismatch in refractive index between powder and liquid made it impossible to distinguish any increase in absorption at the band edge. Even if the refractive index of that particular alloy composition had been well matched, however, powder of another alloy composition would be mismatched due to the variation in optical functions with Al content. Since there are not a great many UV-transparent liquids with wide-ranging refractive indices available, optical characterization in general is not well suited for powders.

Inelastic collision of photoexcited electrons with valence electrons on their way out of the material cannot take place without an energy transfer to the other electrons equal to at least the band gap energy, as discussed in section 4.4.1. As a result there is a separation between the primary peak, which is comprised of electrons that did not collide with other electrons, and the onset of a continuous signal at higher binding energy (lower kinetic energy) comprised of electrons originally in the same core level but which collided with other electrons on their way out of the sample. Collisions with heavier nuclei are usually elastic, or suffer a much smaller energy loss, contributing to peak broadening but not enough to overlap with the electron-electron loss structure. Therefore examination of the inelastic loss "tail" arising behind core level peaks in XPS can be used to estimate the band gap of $(Al_xGa_{1-x})_2O_3$ powder samples.

An advantage of this technique is that local composition and band gap are determined simultaneously and at the same location on the sample, and that the sample need not be transparent. Since the sintered pellets had different Al compositions on their exterior surface and interior, this allowed 24 measurements of the band gap on 12 samples within a composition range $0.1 < x < 0.85$. The disadvantage is that the inelastic loss structure is faint, and the onset is difficult to pinpoint precisely unless the spectrum has a high signal-to-noise ratio. The difficulty is compounded when the precise location is obscured by distortion caused by differential charging. To improve the accuracy of our measurement, a deconvolution procedure was developed to remove the effect of differential charging and the brightest Ga and Al peaks were used for the measurement (Ga $2p_{3/2}$ and Al $2p$). O $1s$, while also bright, was not used due to the overlapping Ga LMM Auger structure.

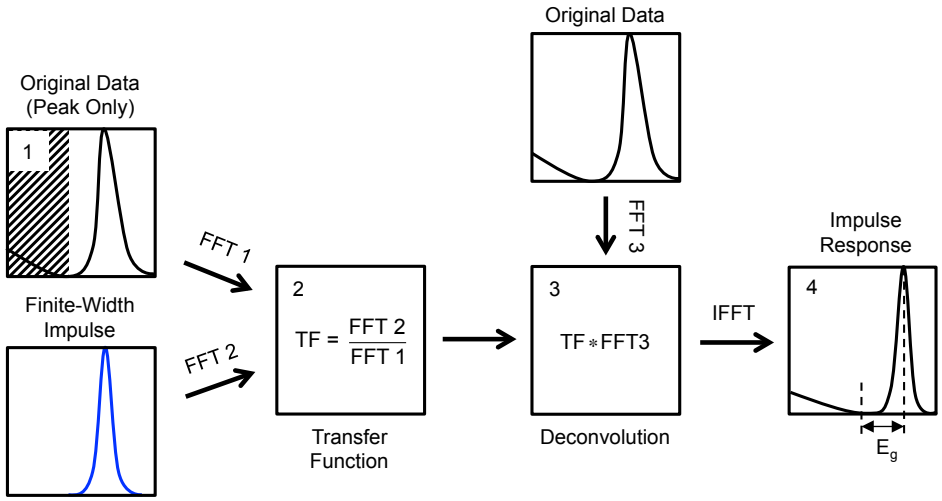

Figure 5.6: Illustration of deconvolution procedure. 1) Distorted spectrum, peak only, 2) Finite-width impulse function, 3) Distorted spectrum including inelastic loss background, 4) Impulse response after taking the inverse Fourier transform. The result is a low-noise inelastic loss spectrum from a symmetric primary peak.

The deconvolution procedure is borrowed from signal processing theory. One may regard the inelastic scattering signal as a time-domain response to an input excitation provided by the primary photoemission peak. We would like to know the impulse response, i.e. the time-domain response to an infinitely sharp excitation, but what we actually observe is a convolution of the impulse response with a broad and distorted peak lineshape. A frequency-domain filter may be used to remove the peak lineshape and restore the impulse response. First, a fast Fourier transform (FFT) is computed of the distorted peak lineshape, after subtracting the background and excluding the inelastic tail. Then another FFT is computed of a symmetric Voigt function fit to the high binding energy (left) side of the photoemission peak only (the differential charging skews spectra to the right, so this fit provides an approximate peak shape if differential charging were absent). This symmetric Voigt peak represents a finite width impulse function (a true impulse would create sharp discontinuities in the time domain, giving rise to high frequency components that are truncated upon taking the inverse FFT, and causing severe oscillations in the filtered spectrum). By forming a quotient in frequency space between the FFTs of the finite impulse and the distorted peak lineshape, a custom filter is created to remove that specific distortion. Taking the FFT of the full distorted spectrum, this time

including the inelastic loss structure, multiplying in frequency space by the filter created from the distorted and symmetric Voigt peaks, and finally taking the inverse FFT of the result, produces a clean spectrum with the differential charging removed (fig. 5.6). Once a clean spectrum is obtained, the band gap energy is found by fitting the primary peak to a Voigt function and the inelastic loss to a linear ramp using least squares minimization, and measuring the separation between the two.

When the input peak is broad, as with Ga $2p_{3/2}$, the width may partially overlap with the onset of inelastic scattering at low x. In these cases part of the fitted Voigt peak was substituted for the original data in step 1 of fig. 5.6 to avoid accidentally removing part of the inelastic loss in the deconvolution. In general care had to be taken throughout the procedure to avoid creating discontinuities, e.g. at the edges during background subtraction, which lead to oscillations in the filtered data.

In some cases (such as Al $2p$ at low x) the peak intensity was not high enough compared to the background noise level to completely avoid spurious oscillations in the filtered data. However, the asymmetric lineshape caused by differential charging can still be approximately removed by fitting the distorted peak to a series of Voigt peaks of identical widths but varying amplitude, and treating each additional Voigt peak as a spin-orbit component to be removed via spin-orbit (SO) deconvolution. In the SO deconvolution procedure, the FFT of the full spectrum is computed $S(\tau)$, and then divided by factors of $A_i \exp[i\tau\Delta_i]$ where A_i and Δ_i are the relative amplitude and spacing of each additional component. Then the inverse FFT is computed to produce the deconvolved spectrum. Several examples of both deconvolution procedures applied to different samples are given at the end of the chapter. The first method, in addition to removing the peak asymmetry, also completely removes the noise in the deconvolved spectrum by virtue of creating a customized filter from the FFT of the noisy peak. The second method does nothing to remove the noise in the spectrum, and therefore fitted band gap results after following the second method contain a greater degree of uncertainty. However, similar fit results were obtained.

The band gaps for all sintered pellets, including results from fitting the filtered Ga $2p_{3/2}$ and Al $2p$ peaks at the exterior surface and the interior of the pellets, are shown as a function of the Al fraction x in fig. 5.7. The band gap result from our theoretical calculation is also appended, after applying a 2.35 eV "scissors" operator to compensate for the artificially low value that is always produced in DFT unless hybrid functionals are used. Both the experimental and theoretical band

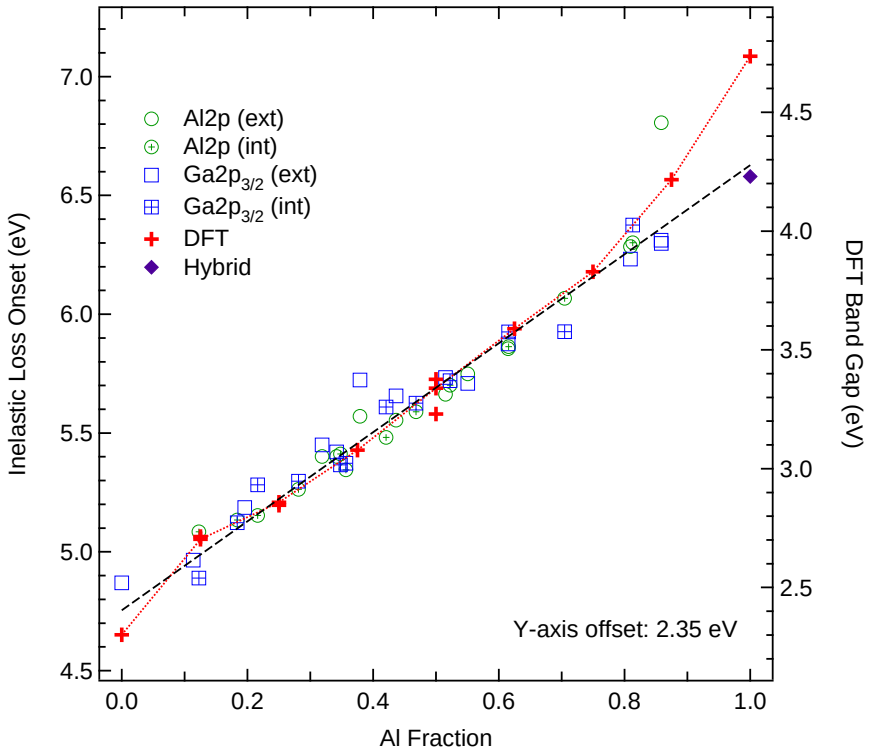

Figure 5.7: $\beta - (Al_xGa_{1-x})_2O_3$ band gap from onset of photoemission inelastic losses (left axis) and DFT calculation (right axis) as a function of Al fraction x. Dotted (red) line denotes DFT gap for lowest energy configuration. Dashed (black) line is a linear fit to the freshly-cleaved Ga $2p_{3/2}$ (interior) data. Hybrid gap for $\theta - Al_2O_3$ is taken from Mo and Ching [392].

gap values show a linear increase with Al content with minimal bowing, within the accuracy of the experiment, up to $x \approx 0.8$. The absence of bowing provides evidence that Al substitutes for Ga without introducing significant structural relaxation and/or charge transfer in the Ga_2O_3 lattice [393], which is to be expected due to the similar bond lengths between Ga–O and Al–O in both the α and β phases [54, 57, 392], and similar electronegativities of 1.61 (Al) and 1.81 (Ga) on the Pauling scale. Above $x = 0.8$ deviations to higher E_g are observed which may be the result of the appearance of secondary phases. A linear trendline was fit to the data which gives the band gap variation of single-phase $\beta - (Al_xGa_{1-x})_2O_3$ as a function of x: $E_g = [\ 4.75 + 1.87\ x\ ]$ eV. Extrapolation of this trendline to $x = 1$ yields a predicted band gap of 6.62 ± 0.05 eV for single-phase $\theta - Al_2O_3$. To our knowledge an experimental value for the $\theta - Al_2O_3$ band gap has not been previously reported;

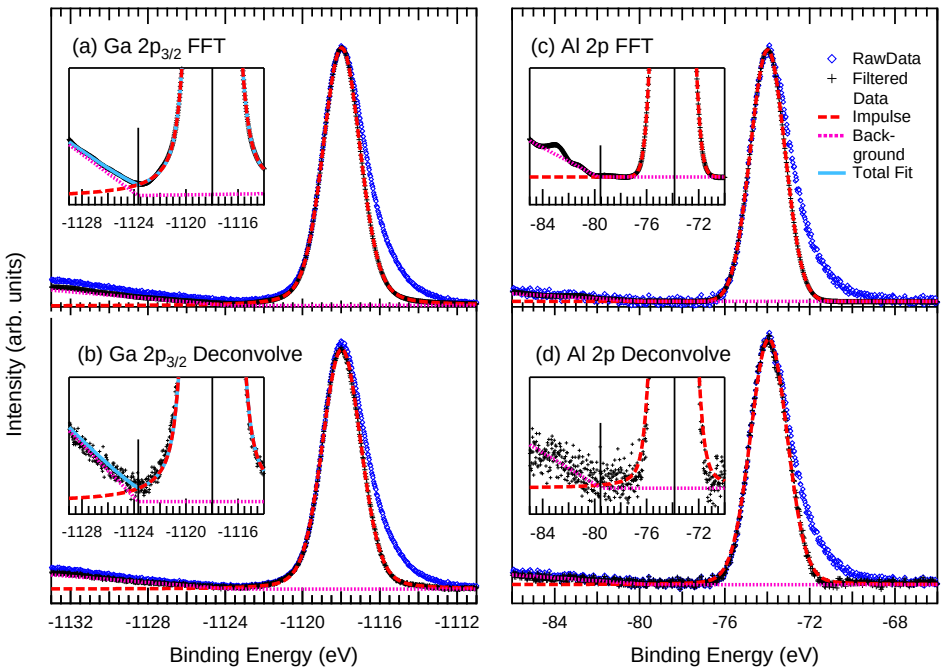

Figure 5.8: Illustration of both deconvolution procedures to determine the band gap of a $(Al_xGa_{1-x})_2O_3$ powder pellet with a measured surface composition of $x = 0.52$.

however, our value agrees well with the DFT result of 6.58 eV, which was calculated using hybrid functionals calibrated to $\alpha - Al_2O_3$ [392, 394]. Our data is also in excellent agreement with a study by Zhang et al. [304] who measured the band gap of $(Al_xGa_{1-x})_2O_3$ thin films by the same method but without any sort of deconvolution, and for a much smaller number of samples, if one ignores the solid line they drew by hand to guide the eye. In their case XRD peak intensities markedly decreased with the Al fraction x, which suggests that the bandgap trendlines connecting the $\beta - Ga_2O_3 \leftrightarrow \theta - Al_2O_3$ and the $\beta - Ga_2O_3 \leftrightarrow$ (am.)Al_2O_3 phases are not too different. The agreement may be spurious however; in chapter 6, it is shown that the band gap of amorphous $(Al_xGa_{1-x})_2O_3$ films measured by optical methods is consistently 0.1–0.2 eV less relative to their crystalline counterparts.

Chapter 6

$(Al_xGa_{1-x})_2O_3$ THIN FILMS DEPOSITED AT ROOM TEMPERATURE

Unlike sintered powders, a variety of techniques exist to grow thin films covering a wide range of deposition conditions, but the resulting films may not be in the most thermodynamically stable phase. In particular, an $(Al_xGa_{1-x})_2O_3$ thin film may relax to the stable β phase for a range of alloy compositions x, but take the metastable γ phase for a different range in x, and the transition point may depend on temperature and other deposition parameters. To obtain a complete picture of the relationships between alloy composition, annealing temperature, crystal structure, and band gap, continuous-composition-spread (CCS) $(Al_xGa_{1-x})_2O_3$ films were deposited at room temperature by PLD and post-annealed to successively higher temperatures in steps of 100 °C in a furnace. X-ray diffraction was performed at each stage to determine the crystal structure, and phase diagrams showing crystal structure vs. annealing temperature and alloy composition were constructed. Double-side polished sapphire substrates were used for UV-Vis measurements, and silicon was used as a substrate for spectroscopic ellipsometry. Both types of optical characterization should yield the same absorption coefficient and band gap for films at a given alloy composition and crystal structure, providing a way to check the accuracy of the ellipsometry fit. Comparing these optical and diffraction data to corresponding data from CCS films grown at high temperature also provides a way to estimate the surface temperature during film deposition (chapter 7).

Deposition parameters used to grow room-temperature CCS films are summarized in table 6.1. Samples pa-A1 and pa-A2 are nearly identical except for a small difference in the overall number of pulses. After deposition and initial measurements at room temperature, sample pa-A1 was post-annealed to 400 °C in air, and already changes in crystallinity and band gap were observed. Therefore pa-A2 was fabricated and post-annealed first to 100 °C, then 200 °C, and so on, to see the initial transformation develop. Both pa-A1 and pa-A2 were then post-annealed in 100 °C steps up to 1000 °C, providing two independent sets of data to test for repeatability. Sample pa-S1 was initially post-annealed to 200 °C, and then in 100 °C steps up to 1000 °C. The wide composition range is due

to a larger substrate (a 3 in Si wafer was used for pa-S1, as opposed to 2 in sapphire wafers for pa-A1 and pa-A2), and the combination of a large plume separation and small target-substrate distance. This geometry also lead to an excessive film thickness variation and unexpected anisotropy in the optical constants at the center of the film, which we attribute to the oblique angle relative to the PLD plume.

Table 6.1: Summary of composition-spread film deposition parameters grown at room temperature.

Sample	Substrate	Buffer Layers	Layers	Ga:Al Pulses per Layer	Plume Separation	T-S Dist.	Composition Range	Thickness Variation
pa-A1	Sapphire	–	2200	4:6	50 mm	50 mm	4%–90%	890–200 nm
pa-A2	Sapphire	–	2000	4:6	50 mm	50 mm	4%–88%	870–190 nm
pa-S1	Silicon	–	3000	4:6	68 mm	40 mm	0.5%–99.5%	3200–400 nm

6.1 XPS Analysis of Composition and Stoichiometry

XPS was used to verify oxygen stoichiometry and measure aluminum content as described in section 4.4.3. Survey scans of sample pa-A1 after the initial deposition, and after the 600 °C and 800 °C annealing steps are shown in fig. 6.1. Other than the expected Ga, Al and O peaks, F 1s and F KLL appear on the Al_2O_3 side of the film likely indicating a small amount of fluorine contamination in the commercial Al_2O_3 target. In addition, a detail scan of Ga 3p (fig. 6.2) shows a small shoulder developing on the low-binding energy side with annealing temperature, which does not appear on other Ga peaks and is likely Si 2p from SiO_2 contamination. The composition spread and stoichiometry of sample pa-A1 as a function of position at each post-annealing step is shown in fig. 6.3. The blue curves show the gallium fraction from $I_{\mathrm{Ga}} : I_{\mathrm{O}}$ intensity ratios, and the green curves show the aluminum fraction from $I_{\mathrm{Al}} : I_{\mathrm{O}}$ ratios. The sum of the gallium and aluminum fractions is shown above the composition spread data, and should be equal to one for a film with correct oxygen stoichiometry. A sum of less than one indicates an oxygen-rich film, and greater than one indicates an oxygen deficiency. Results from fitting with and without the Si 2p shoulder on Ga 3p are included, showing that the expected oxygen-to-cation ratio is only achieved when Si 2p is added, and without it there is unaccounted-for oxygen present even after annealing. Initially after deposition the oxygen content varies along the surface of the film, but post-annealing

to 400 °C in air restores the expected oxygen-to-cation ratio across the entire film. The size of the Si shoulder increases with annealing temperature, as expected from fig. 6.2, which likely indicates Si segregating from the bulk to the surface. In the 800 °C and 900 °C annealing steps there was substantial distortion in all spectra on the Al-rich side, due to sample charging as the film became more insulating, so the deviation above 30 mm is probably artificial.

The average composition at each step was found by comparing the intensities of Al and Ga peaks directly, rather than taking the ratio with O 1s which may also contain a component arising from SiO_2, and the results are plotted in fig. 6.4. Despite the varying oxygen-to-cation ratio, no significant deviation in the Al:Ga composition is observed until the 800 °C step, where charging effects began to distort the individual photoemission peaks. Despite the distortions, the composition result in the 800 °C and 900 °C steps are still within 5 % of the composition in previous steps. The 900 °C data is actually closer to the data from room temperature through 700 °C than the 800 °C data, suggesting that significant changes in the Al-to-Ga ratio after annealing to 800 °C and 900 °C probably did not occur. Composition values taken from room temperature through 700 °C were used in subsequent XRD and UV-Vis analyses due to the high repeatability in the measurement; values from the 800 °C and 900 °C steps were assumed to be less representative of the actual surface stoichiometry and were not used. Since almost no change was observed with annealing temperature in sample pa-A1, XPS was only performed after initial deposition and after annealing to 400 °C for sample pa-A2. The composition results for both measurements were again consistent, and are shown in fig. 6.5.

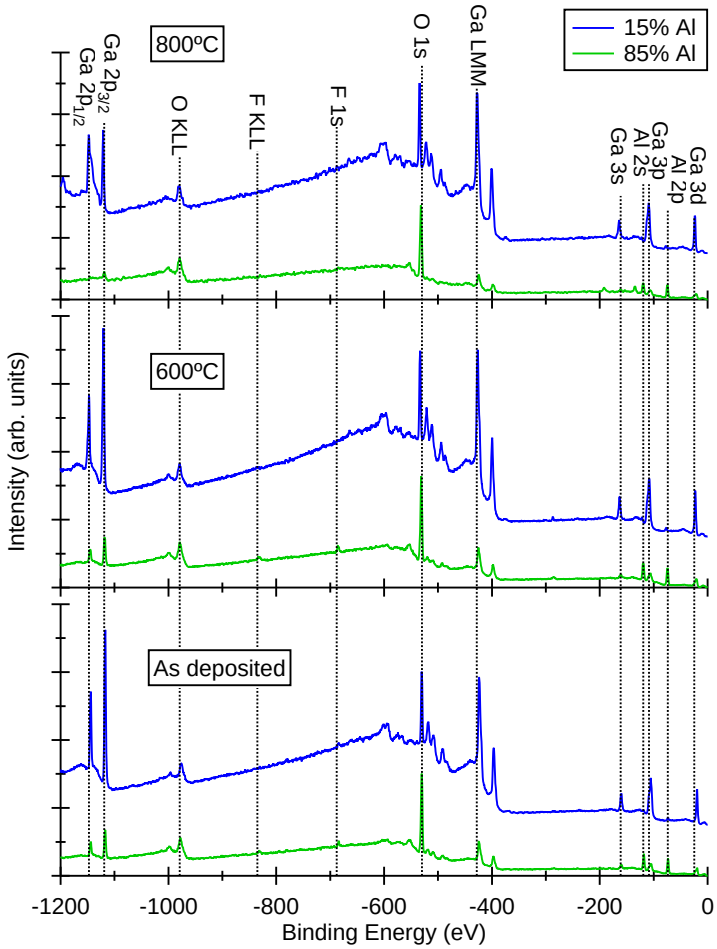

Figure 6.1: XPS survey scans at low and high Al fraction x for sample pa-A1 before post-annealing and after post-annealing to 600 °C and 800 °C for one hour. The only visible impurity is F, which is larger on the Al-rich side of the film and likely comes from the Al_2O_3 target.

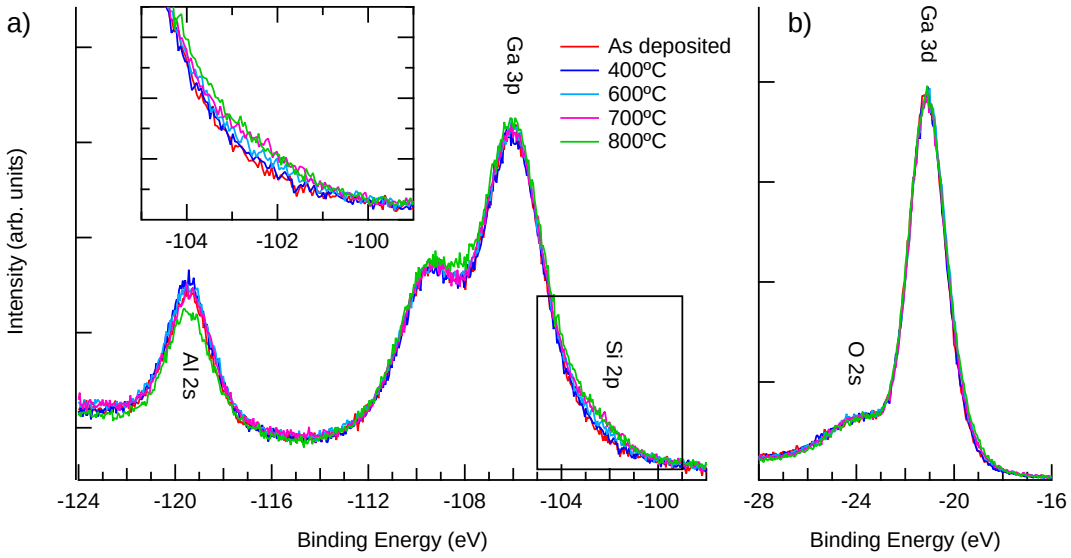

Figure 6.2: a) Ga $3p$ and Al $2s$ and b) Ga $3d$ XPS spectra at position 22 mm along the composition gradient (Al fraction $x = 0.50$) of sample pa-A1. x- and y-axes are set to the same scale for comparison. The shoulder developing on the low-binding energy side of Ga $3p$ at elevated temperatures is absent from Ga $3d$ and is assigned to Si $2p$, indicating segregation of SiO_2 from the bulk to the surface.

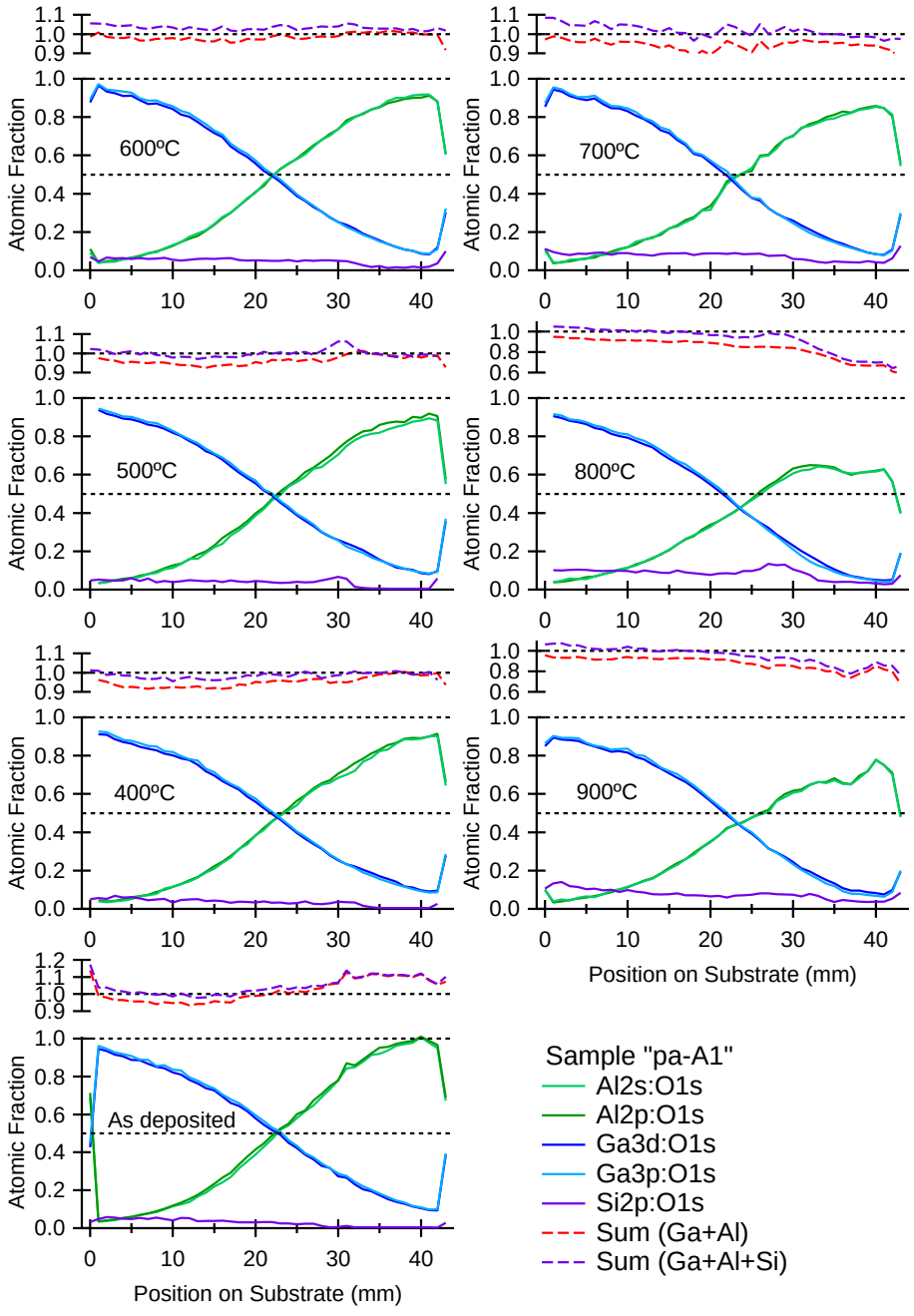

Figure 6.3: Surface alloy composition and oxygen stoichiometry of CCS sample pa-A1 vs. position on the substrate after successive post-annealing steps, as determined by XPS using Al:O and Ga:O peak intensity ratios. Sum > 1 indicates an oxygen deficiency, while Sum < 1 indicates oxygen-rich films.

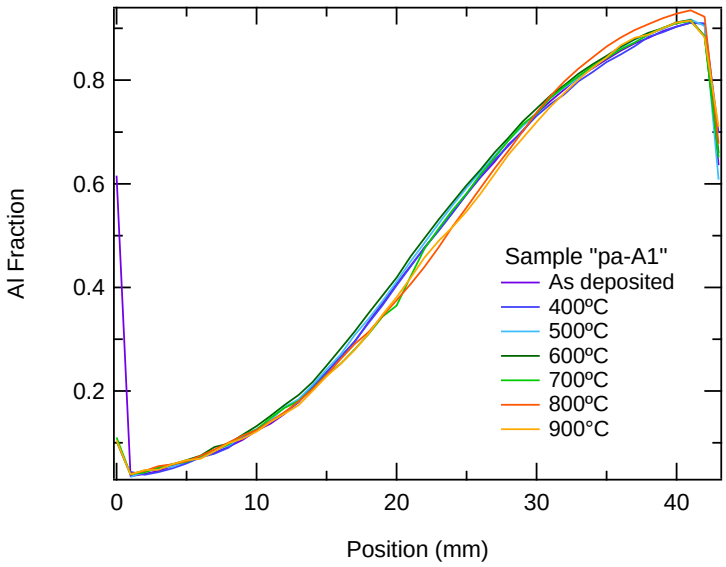

Figure 6.4: Average surface alloy composition vs. position on substrate for a post-annealed CCS film on sapphire (pa-A1), before and after annealing to successively higher temperatures from 400 °C to 900 °C for one hour each as determined by XPS using Al-to-Ga peak intensity ratios.

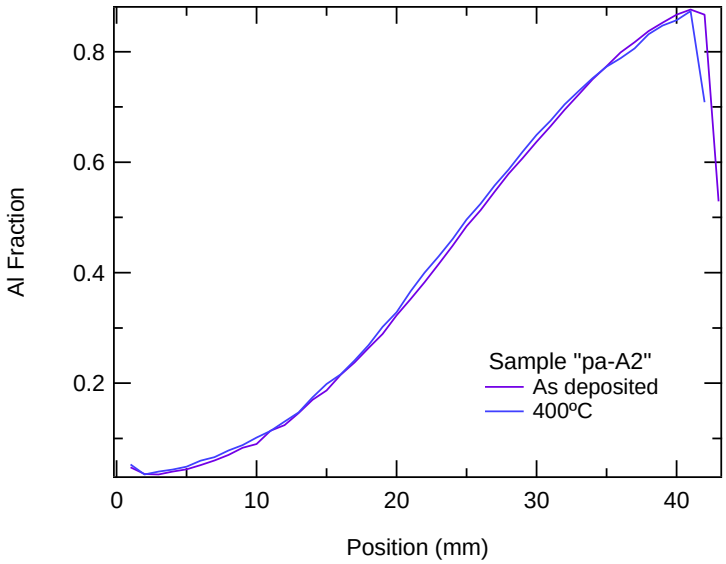

Figure 6.5: Average surface alloy composition vs. position on substrate for a post-annealed CCS film on sapphire (pa-A2), before post annealing and after annealing to 400 °C for one hour, as determined by XPS using Al-to-Ga peak intensity ratios.

6.2 X-ray Diffraction and UV-Visible Spectroscopy of CCS Films on Sapphire

The raw data from a UV-Vis measurement is the dimensionless absorbance A, from which the absorption coefficient is found by the formula (section 4.5)

$$\alpha = \frac{A}{t} \ln 10 \tag{6.1}$$

Film thicknesses were measured on a DekTak XT stylus profiler for samples pa-A1 and pa-A2. A single 45 mm line scan was taken through the center of the film parallel to the composition gradient, starting and ending at points on opposite sides of the substrate where there is no film, and auto-leveling was performed to match the slope of the curved background with the substrate portion on both ends of the line scan. The results for both films are shown in fig. 6.6. Due to the length of the scan and curvature of the substrate, thicknesses derived in this way are only approximate. Ellipsometry would be a more accurate way to measure film thickness at each point along the composition gradient, but was not possible due to severe backside reflections from double-side polished sapphire wafers. Therefore, profilometry data were used with eq. (6.1) to find the absorption coefficient for films on sapphire, in units of μm^{-1}, after first subtracting the small absorbance sapphire so that only the film absorbance would be scaled for thickness.

Although UV-Vis data were taken in 1 mm intervals along the composition gradient, the starting point for each set of data might have varied between data sets since initial alignment was done by eye only. An attempt was made to correct for small (< 1 mm) offset errors by correlating the absorbance at 240 nm (just above the Ga_2O_3 absorption edge) with film thickness (fig. 6.7). XPS data from figs. 6.4 and 6.5 were also interpolated and the same offsets applied to determine the composition at each point.

The absorption coefficient calculated in this way is shown as a function of composition and temperature in figs. 6.8 to 6.10. Due to the large number of measurements, data are highlighted in red at approximately 10 % intervals in Al concentration, and a change in color from blue to green indicates the transition from crystalline to amorphous as determined by XRD. As expected the absorption edge moves to higher energy with Al concentration indicating a widening band gap. A number of observations may be made regarding the change in overall shape. In general, the amorphous region has a softer onset than the crystalline region due to long tails extending into

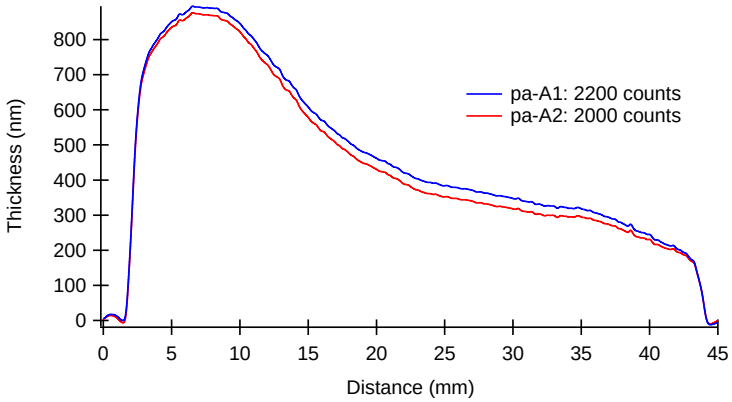

Figure 6.6: Thickness of CCS films pa-A1 and pa-A2, estimated by profilometry.

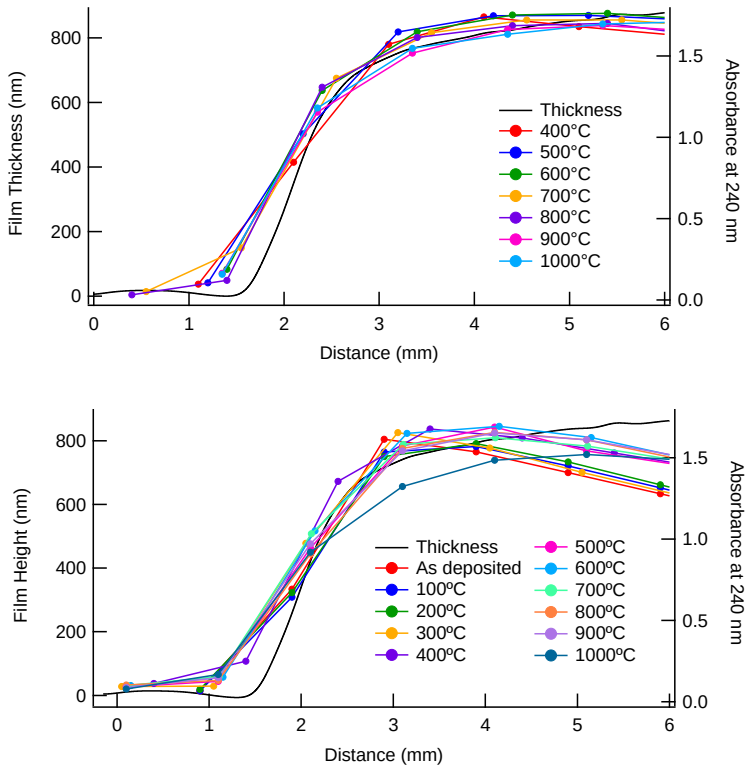

Figure 6.7: Alignment of film thickness and absorbance at 240 nm for samples pa-A1 (top) and pa-A2 (bottom)

the gap. On the Ga_2O_3 side of the film these tails begin to shrink at 300 °C and almost disappear above 400 °C, when diffraction peaks first appear in XRD. A similar change is observed at higher Al concentrations at higher temperatures. The absorption edge is never totally abrupt due to the composition spread in the beam width, which leads to an apparent tail in the data even for an infinitely sharp onset. This apparent tail increases with Al concentration in my data even when the entire film is crystalline, due to the small angle between the sapphire substrate and the aluminum block collimating the beam, which slowly increases the space between the substrate and the slit exit as the micrometer is incremented, allowing the beam to diverge more before impinging on the sample (see fig. 4.23).

After the initial onset, the increase in absorption coefficient with photon energy is nearly linear. On the Ga-rich side of the film the slope decreases from its initial steep value, until the composition is about 20 % Al; above 20 % the slope remains approximately constant throughout the rest of the film. This pattern is observed in both the amorphous and crystalline films and is probably related to a change in the density of states near the conduction band minimum as the Al concentration is increased. A consequence of the change in slope is that the initial part of the absorption onset moves to higher energy relatively slowly compared to the main absorption edge in the 0–20 % region. The blue-shift of the main absorption edge also does not appear to be constant with Al concentration throughout the film, with a greater shift at high x than low x. The exception to this general trend is in the Ga-rich region of amorphous data below 200 °C, where a very rapid shift from 4.5 eV to 4.8 eV is observed as x varies from 0.04 to 0.1.

To quantify the band gap as a function of Al concentration and annealing temperature, Tauc plots for direct $(\alpha\hbar\omega)^2$ vs. $\hbar\omega$ and indirect $(\alpha\hbar\omega)^{1/2}$ vs. $\hbar\omega$ transitions were initially constructed (derived in chapter 2). For the appropriate type of transition, these plots should produce a straight line whose extrapolation to zero yields the band gap. However, the apparent tails caused by the composition spread resulted in significant underestimates of the gap when using an indirect Tauc plot, and the linear increase after the initial onset resulted in a curved shape in the direct Tauc plot that made finding the location of the gap ambiguous. Therefore, the band gap was estimated by linear extrapolation to zero of the absorption coefficient directly. This procedure is justified for the simple reason that absorption by interband transitions starts at the band gap energy. The purpose of Tauc plots is to form a linear function of α that can be extrapolated to zero; however since my

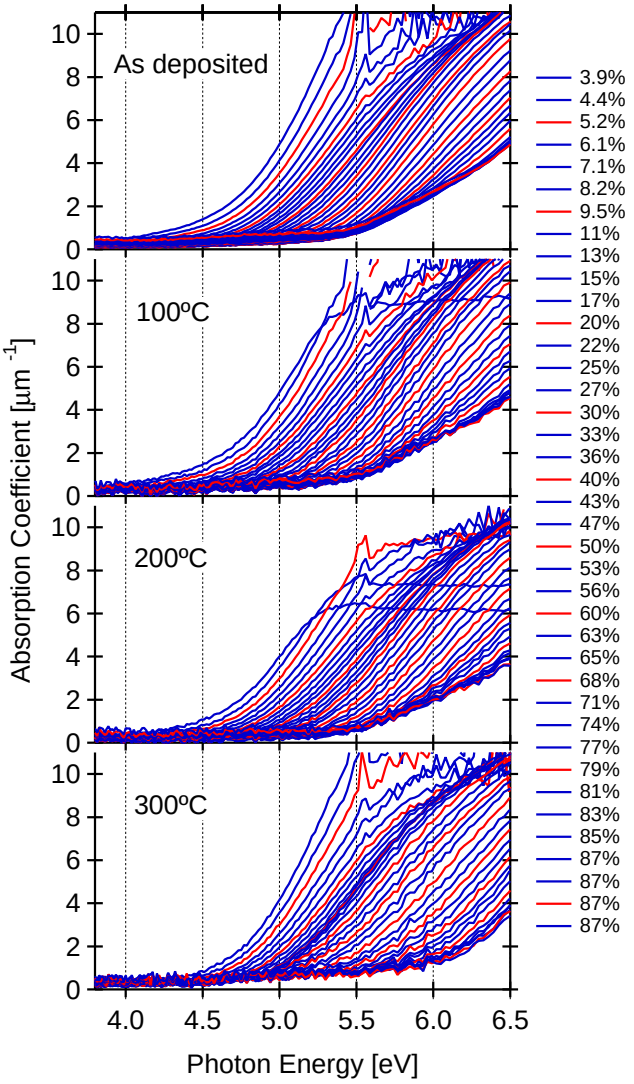

Figure 6.8: Absorption coefficient for post-annealed amorphous CCS $(Al_xGa_{1-x})_2O_3$ film pa-A2 from room temperature to 300 °C. Data are highlighted in red at 5 % and multiples of 10 % for clarity.

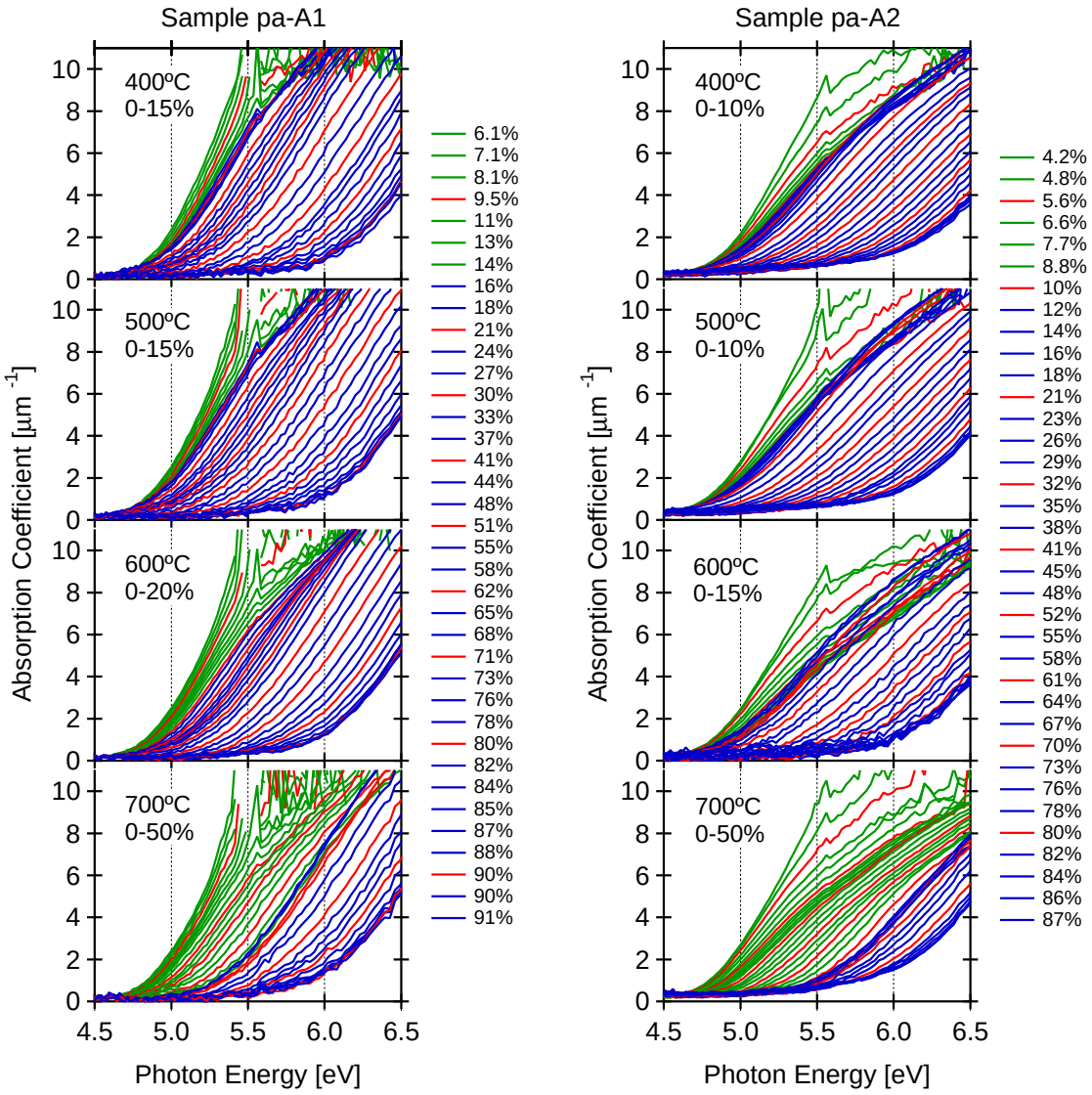

Figure 6.9: Absorption coefficient for post-annealed CCS $(Al_xGa_{1-x})_2O_3$ films from 400 °C to 700 °C. Data are highlighted in red at 5 % and multiples of 10 % for clarity. The portion of the film exhibiting crystal structure in XRD has been changed to green, with the composition range indicated.

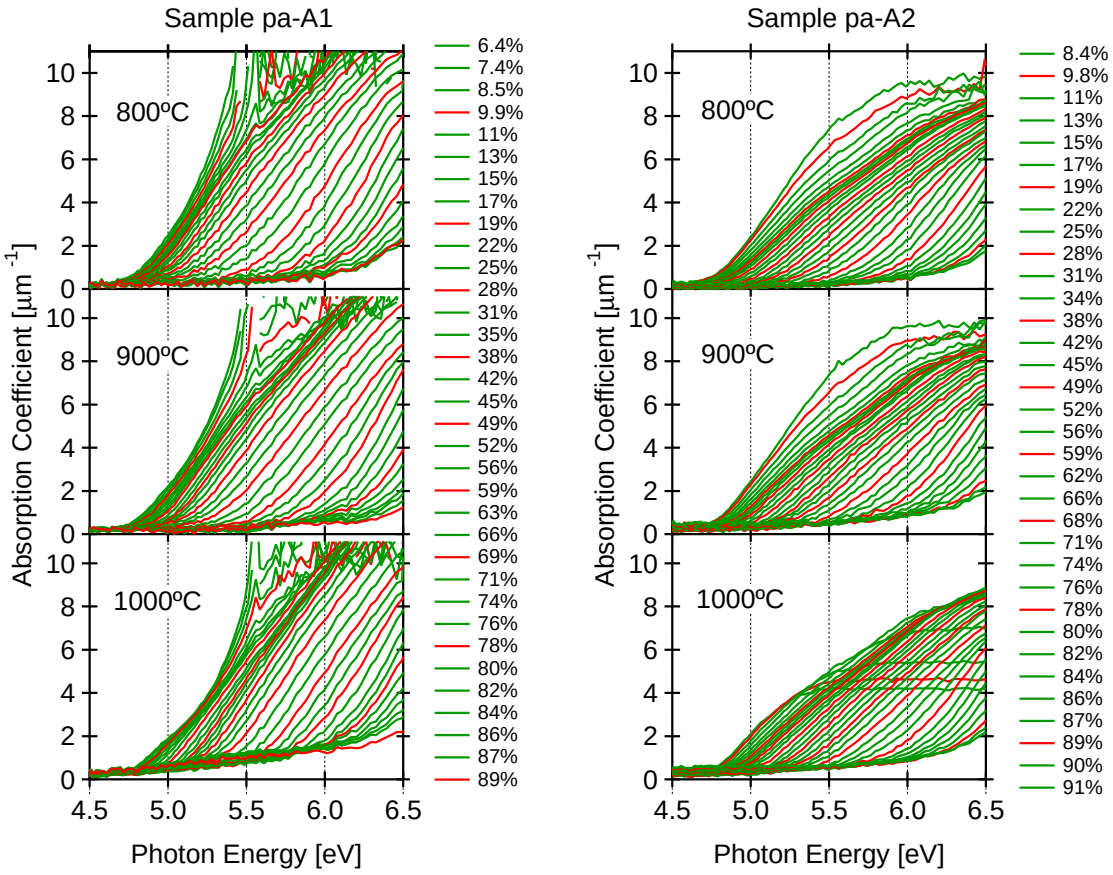

Figure 6.10: Absorption coefficient for post-annealed CCS $(Al_xGa_{1-x})_2O_3$ films from 800 °C to 1000 °C. Data are highlighted in red at multiples of 10 % for clarity.

data is nearly linear already, extrapolation to zero should produce the same result as would have been obtained by a Tauc plot, if Tauc plots had been linear instead.

Several examples of fitting the absorption coefficient to a linear ramp function are shown for sample pa-A1 in fig. 6.11, and for sample pa-A2 in fig. 6.12. In general, the linear fit was quite robust and did not depend strongly on where the endpoints were placed in fitting. The largest source of uncertainty came from fitting the background to a straight line, which worked well for most of the data but was sensitive to the endpoints when large interference oscillations were present, which usually occurred at the Al-rich side of the film after post-annealing to temperatures sufficient to crystallize that region (which is surprising, since those regions would be expected to have index of refraction closest to sapphire). In principle, the interference oscillations could be removed by fitting to eqs. (4.21) and (4.22). However, in practice guessing and checking reasonable functions of $n(\omega)$, $k(\omega)$ and thickness at every point is far too tedious a procedure without the help of fitting software (such as that used to fit ellipsometry data), and furthermore the equations developed in section 4.5 do not take the composition spread in the finite beam width into account. Therefore the linear background was adjusted by hand to keep the slope consistent between adjacent spectra, to locate the absorption onset as precisely as possible. In addition, when the band gap increased to greater than 6 eV there was not much absorption data to fit, so those values are more tentative than the others.

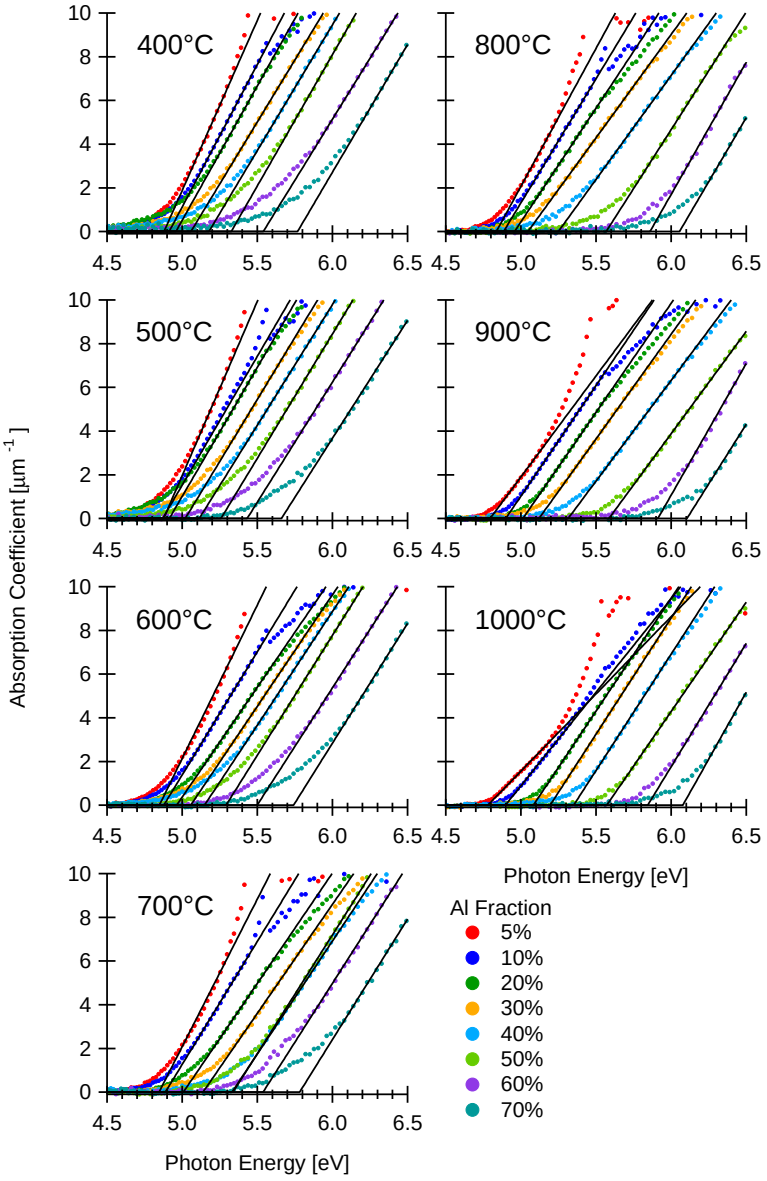

Figure 6.11: Example fits to determine the band gap of sample pa-A1 by linear extrapolation to zero of the absorption coefficient α.

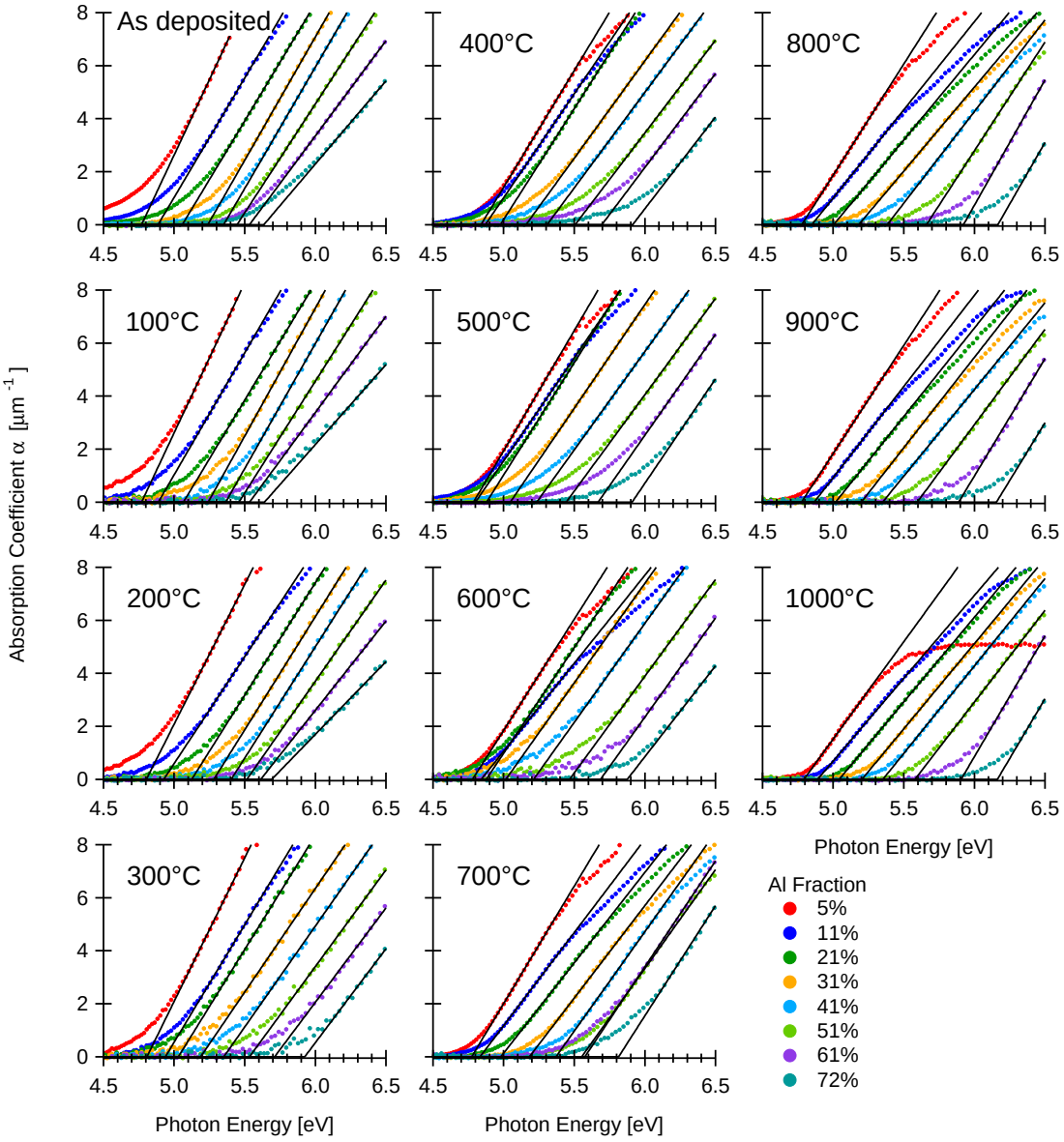

Figure 6.12: Example fits to determine the band gap of sample pa-A2 by linear extrapolation to zero of the absorption coefficient α.

The following pages show several side-by-side images showing the change in absorption coefficient alongside XRD color maps as a function of aluminum concentration, as the annealing temperature is increased. The fitted value for the band gap is also appended, which tracks the shift in absorption closely. A change from upward to downward bowing is observed after annealing to 300 °C, which becomes more pronounced at 400 °C. From 400 °C to 500 °C, samples pa-A1 and pa-A2 show different structure at low Al concentration. Sample pa-A1 has bright diffraction peaks at $2\theta = 29°$, 32°, and 37° which do not match any Ga_2O_3 polymorph in our PDF card database, although the bright spots at 31°, 36°, and 44° roughly match $\gamma - Ga_2O_3$. A clear transition to the distinct β phase occurs at low-x as the temperature increases to 1000 °C. One possibility is it may be a mixture of β, κ, and γ phases. $\kappa{-}Ga_2O_3$ is an metastable phase with orthorhombic symmetry belonging to space group $Pna2_1$, which was discovered when dry-heating solid solutions of $(Al_xGa_{1-x})_2O_3$ before transforming to β at 870 °C [53]. This temperature agrees with the observed transition to the β phase at approximately 900 °C in my data. A $\kappa{-}Ga_2O_3$ pattern from Roy et al. [53] (referred to as the ϵ phase in the paper) is appended below the XRD data for comparison. $\kappa{-}Ga_2O_3$ peaks at 28° and 33° are off from the observed peaks by nearly the same amount in 2θ as $\beta - Ga_2O_3$ peaks at 30° and 31°, but in the opposite direction; a mixture of β and κ phases may explain why intensity maxima appear halfway in between. However, $\kappa{-}Ga_2O_3$ peaks at 35°, 37°, and 40° do line up with observed reflections. This $\kappa{-}Ga_2O_3$ diffraction pattern comes from a very old powder Ga_2O_3 reference and is not of very high quality; small differences in 2θ may arise from a distorted unit cell rather than a totally different phase, if all peaks are accounted for.

At low x, sample pa-A2 does not contain any mysterious peaks when heated to 500 °C, instead showing broad peaks below $x = 0.1$ with maxima at the locations of the $\gamma - Ga_2O_3$ pattern. As x is increased the bright diffraction peaks in sample pa-A1 at 400 °C and 500 °C disappear, and a discontinuous jump to lower band gap is observed. Between $x = 0.15$ and $x = 0.45$ there seems to be more long-range order in sample pa-A1 than pa-A2, indicated by the diffuse background structure. The brightest intensity appears at the location of $\gamma - Ga_2O_3$ [311], but a distinct $\gamma - Ga_2O_3$ [220] peak does not appear until 700 °C in both samples. However, there is not a discontinuous jump in the band gap where the background structure disappears. Therefore, from now on this is referred to as a defected pre-γ phase, which transforms into the γ phase at 600–700 °C depending on the Al concentration. The main differences between the pre-γ and γ phases are that the γ phase has more

defined $[220]_\gamma$ and $[311]_\gamma$ diffraction peaks, and that the band gap of the γ phase at 700 °C is about 0.1–0.2 eV higher than the band gap of the pre-γ phase, which is comparable to the band gap of amorphous $(Al_xGa_{1-x})_2O_3$ films showing no structure in XRD.

At 600 °C, the crystallinity front appears to extend further into the film than in the 400 °C and 500 °C steps, and the first broad $\beta - Ga_2O_3$ diffraction peaks appear at low Al concentration. In sample pa-A2, the γ phase is also visible from about $0.05 < x < 0.15$, and a corresponding jump to higher energy in the absorption edge is observed in the crystalline region, which agrees with the absorption edge of pa-A1 in the same composition range. At 700 °C we see $\beta - Ga_2O_3$ extending to $x = 0.2$ in both samples, followed by a transition to $\gamma - Ga_2O_3$ which extends until roughly $x = 0.5$, and at higher x the films remain amorphous. There is no jump in the band gap through the β to γ transition, but a discontinuous 0.1–0.2 eV jump to lower energy at the γ to amorphous transition in both films.

At 800 °C $\beta - Ga_2O_3$ extends to $x = 0.4$, and $\gamma - Ga_2O_3$ extends all the way to $x = 1$. Interestingly, diffraction peaks belonging to the $\gamma - Ga_2O_3$ and $\gamma - Al_2O_3$ structures have different relative intensities, and a transition from $\gamma - Ga_2O_3$ to $\gamma - Al_2O_3$ can be seen at $x = 0.85$. In sample pa-A1, the transition from β to γ moves to approximately $x = 0.55$ at 900 °C, and $x = 0.65$ at 1000 °C. In pa-A2 the same transitions occur at approximately $x = 0.45$ and $x = 0.55$, respectively. As in the 700 °C step, no abrupt discontinuity is observed in the β to γ transition in the 800–1000 °C data.

Phase diagrams vs. alloy composition and annealing temperature for both CCS films pa-A1 and pa-A2 on sapphire are shown in fig. 6.29. The overall trend is similar in both samples, but phase transformations seem to extend to slightly higher x in pa-A1 than in pa-A2, which may just be a result of experimental inconsistencies, for example if pa-A1 was heated for a longer time than pa-A2 in one of the post-annealing steps.

A summary of fitted band gap results is given in fig. 6.30. The best fit line from our powder data (fig. 5.7) has also been appended for comparison. Similar trends are observed for both samples, although the downward bowing in pa-A1 is greater than in pa-A2. The change from upward bowing to downward bowing may be related to changes in the oxygen stoichiometry after annealing in air at 300 °C; XPS indicates an oxygen-deficiency in as-deposited CCS films on the Al-rich side, which disappears after annealing to 400 °C (fig. 6.3). The band gap variation in the 800–1000 °C

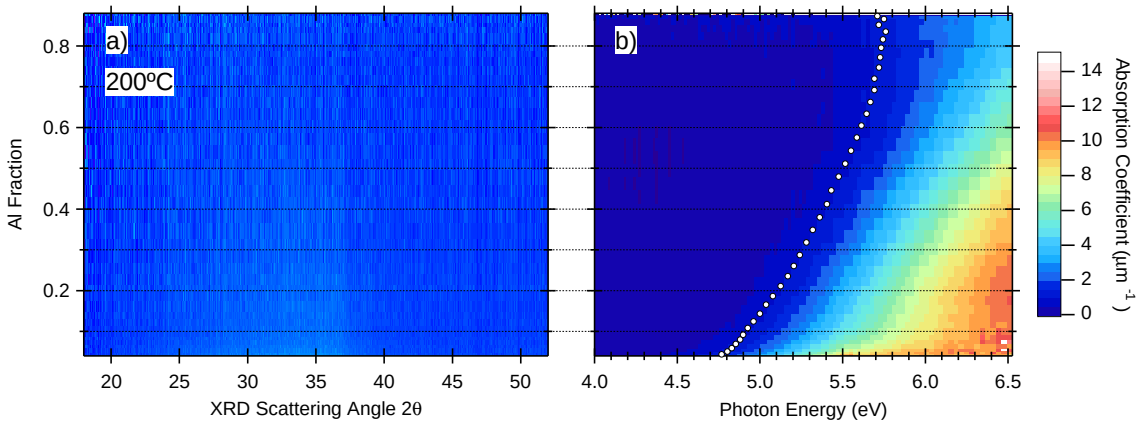

Figure 6.13: a) XRD $\theta - 2\theta$ scans vs. composition for CCS film pa-A2 after post-annealing to 200 °C, and b) absorption coefficient measured by UV-Vis spectroscopy. White markers show the location of the absorption onset.

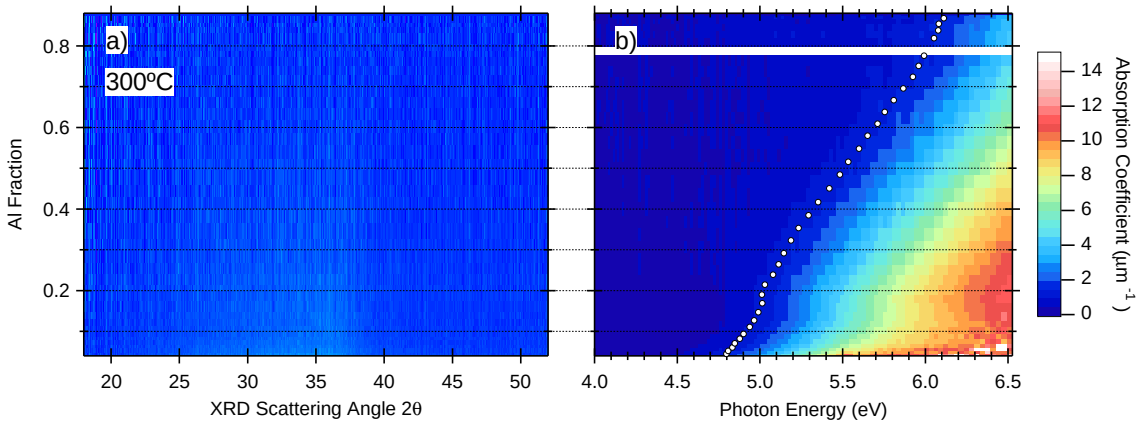

Figure 6.14: a) XRD $\theta - 2\theta$ scans vs. composition for CCS film pa-A2 after post-annealing to 300 °C, and b) absorption coefficient measured by UV-Vis spectroscopy. White markers show the location of the absorption onset.

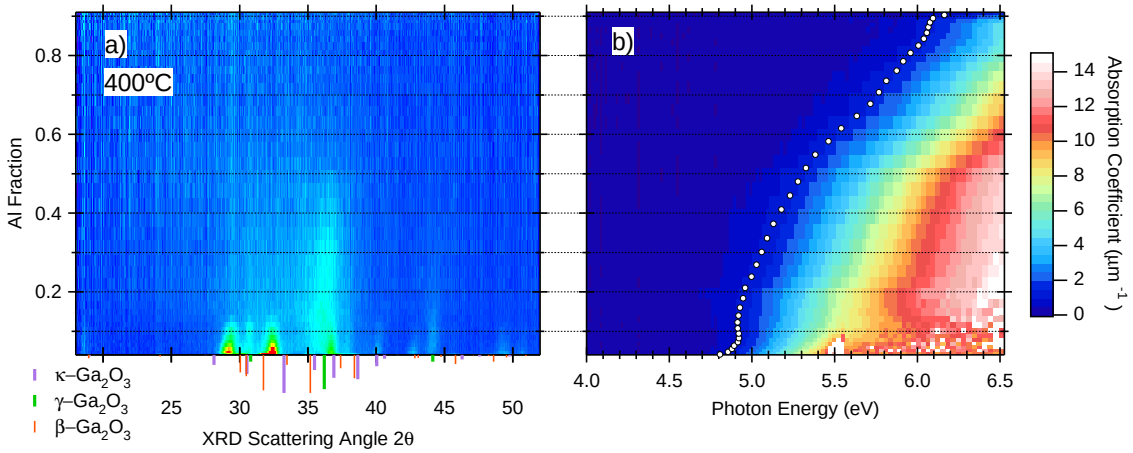

Figure 6.15: a) XRD $\theta - 2\theta$ scans vs. composition for CCS film pa-A1 after post-annealing to 400 °C, and b) absorption coefficient measured by UV-Vis spectroscopy. JCPDS PDF card nos. 00-043-1012 for $\beta - Ga_2O_3$ and 00-020-0426 for $\gamma - Ga_2O_3$, and a pattern for $\kappa - Ga_2O_3$ from refs. [53] and [102] are appended below the XRD data for reference. White markers show the location of the absorption onset.

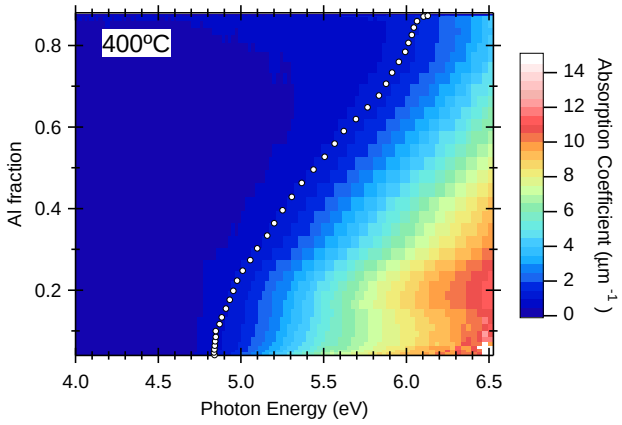

Figure 6.16: Absorption coefficient of CCS film pa-A2 measured by UV-Vis spectroscopy. White markers show the location of the absorption onset. (XRD data for this step are missing.)

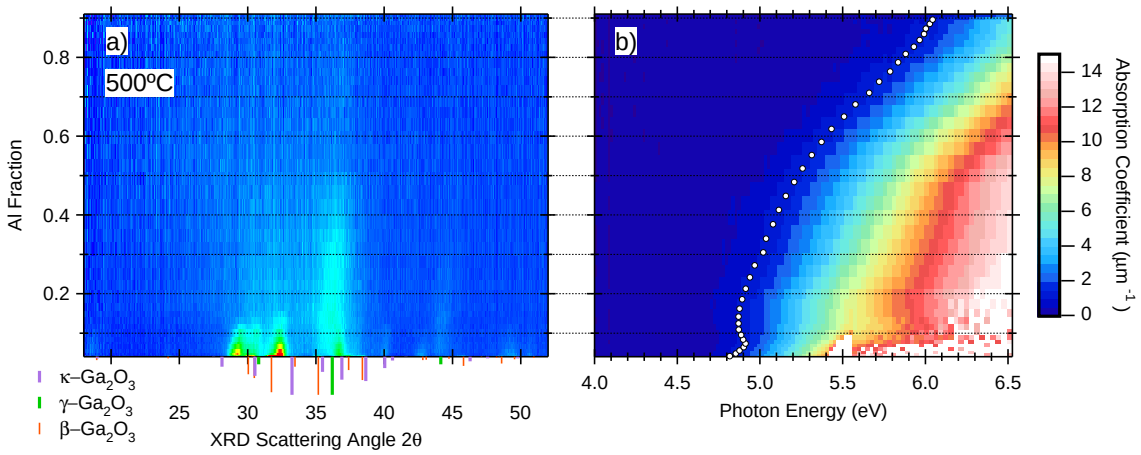

Figure 6.17: a) XRD $\theta - 2\theta$ scans vs. composition for CCS film pa-A1 after post-annealing to 500 °C, and b) corresponding absorption coefficient measured by UV-Vis spectroscopy. JCPDS PDF card nos. 00-043-1012 for $\beta - Ga_2O_3$ and 00-020-0426 for $\gamma - Ga_2O_3$, and a pattern for $\kappa - Ga_2O_3$ from refs. [53] and [102] are appended below the XRD data for reference. White markers show the location of the absorption onset.

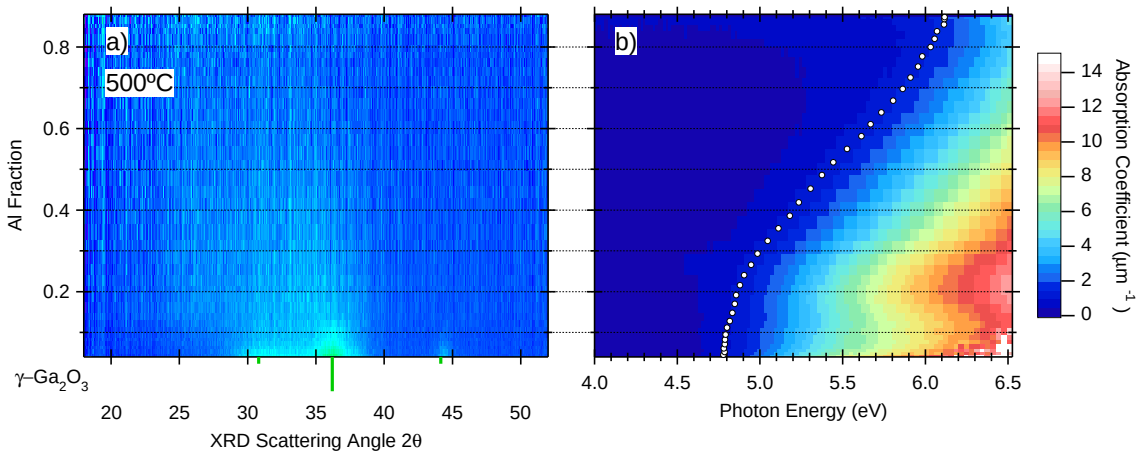

Figure 6.18: a) XRD $\theta - 2\theta$ scans vs. composition for CCS film pa-A2 after post-annealing to 500 °C, and b) corresponding absorption coefficient measured by UV-Vis spectroscopy. JCPDS PDF card no. 00-020-0426 for $\gamma - Ga_2O_3$ is appended below the XRD data for reference. White markers show the location of the absorption onset.

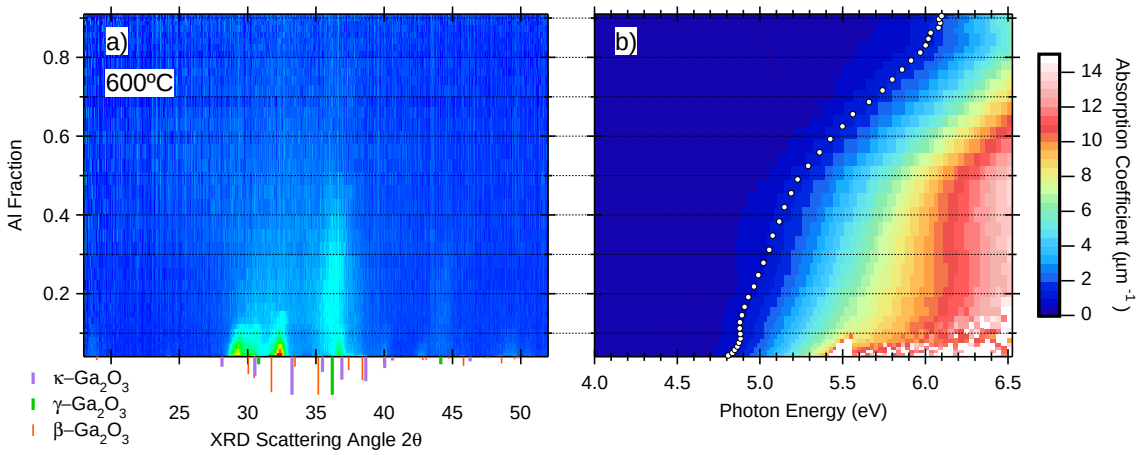

Figure 6.19: a) XRD $\theta - 2\theta$ scans vs. composition for CCS film pa-A1 after post-annealing to 600 °C, and b) corresponding absorption coefficient measured by UV-Vis spectroscopy. JCPDS PDF card nos. 00-043-1012 for $\beta - Ga_2O_3$ and 00-020-0426 for $\gamma - Ga_2O_3$, and a pattern for $\kappa - Ga_2O_3$ from refs. [53] and [102] are appended below the XRD data for reference. White markers show the location of the absorption onset.

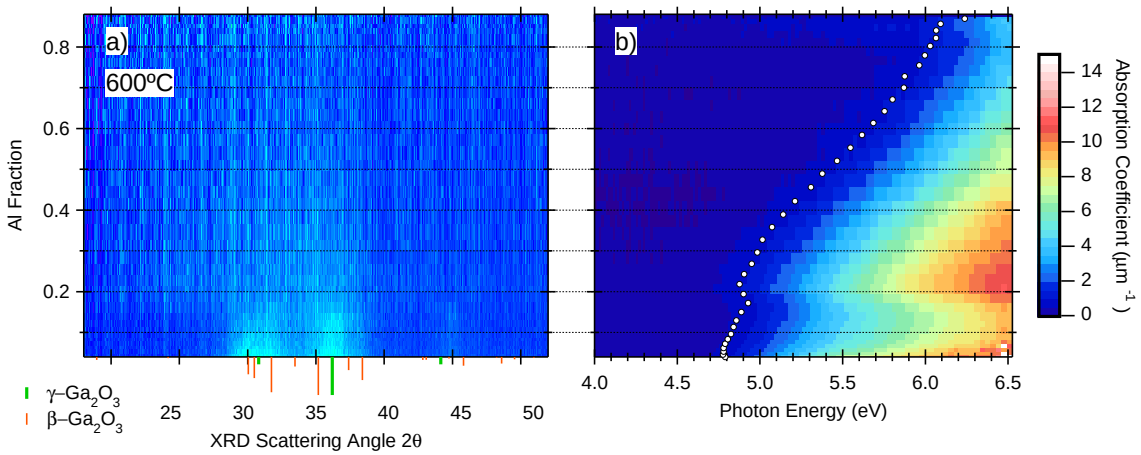

Figure 6.20: a) XRD $\theta - 2\theta$ scans vs. composition for CCS film pa-A2 after post-annealing to 600 °C, and b) corresponding absorption coefficient measured by UV-Vis spectroscopy. JCPDS PDF card nos. 00-043-1012 for $\beta - Ga_2O_3$ and 00-020-0426 for $\gamma - Ga_2O_3$ are appended below the XRD data for reference. White markers show the location of the absorption onset.

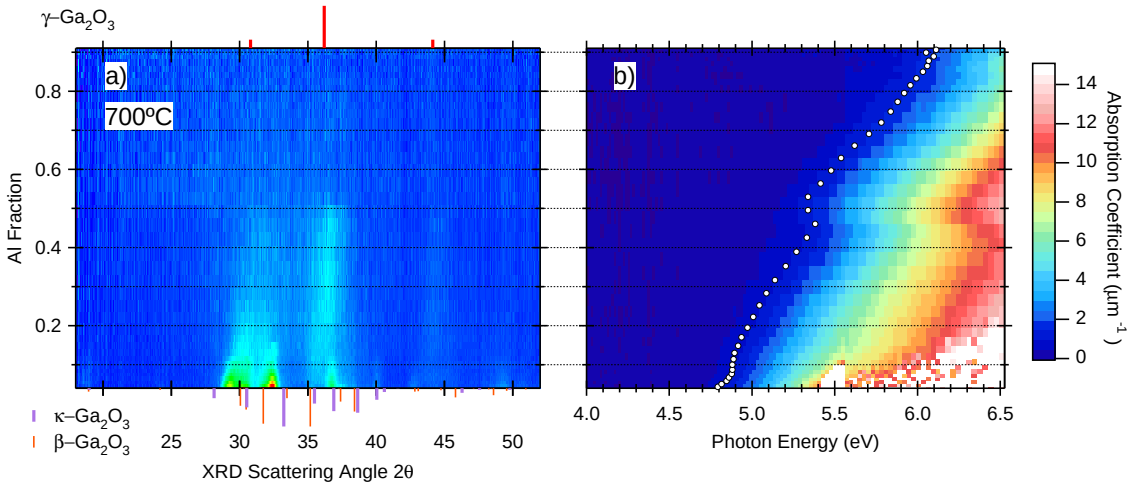

Figure 6.21: a) XRD $\theta - 2\theta$ scans vs. composition for CCS film pa-A1 after post-annealing to 700 °C, and b) corresponding absorption coefficient measured by UV-Vis spectroscopy. JCPDS PDF card no. 00-043-1012 for $\beta - Ga_2O_3$, and a pattern for $\kappa - Ga_2O_3$ from refs. [53] and [102] are appended below the XRD data, and PDF card no. 00-020-0426 for $\gamma - Ga_2O_3$ is appended above the XRD data for reference. White markers show the location of the absorption onset.

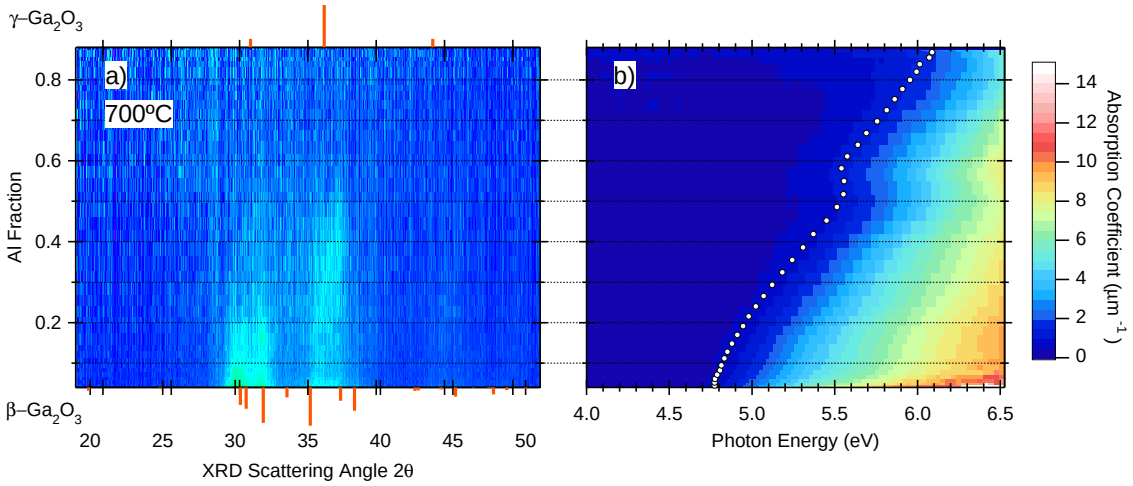

Figure 6.22: a) XRD $\theta - 2\theta$ scans vs. composition for CCS film pa-A2 after post-annealing to 700 °C, and b) absorption coefficient measured by UV-Vis spectroscopy. JCPDS PDF card no. 00-043-1012 for $\beta - Ga_2O_3$ is appended below the XRD data, and PDF card no. 00-020-0426 for $\gamma - Ga_2O_3$ is appended above the XRD data for reference. White markers show the location of the absorption onset.

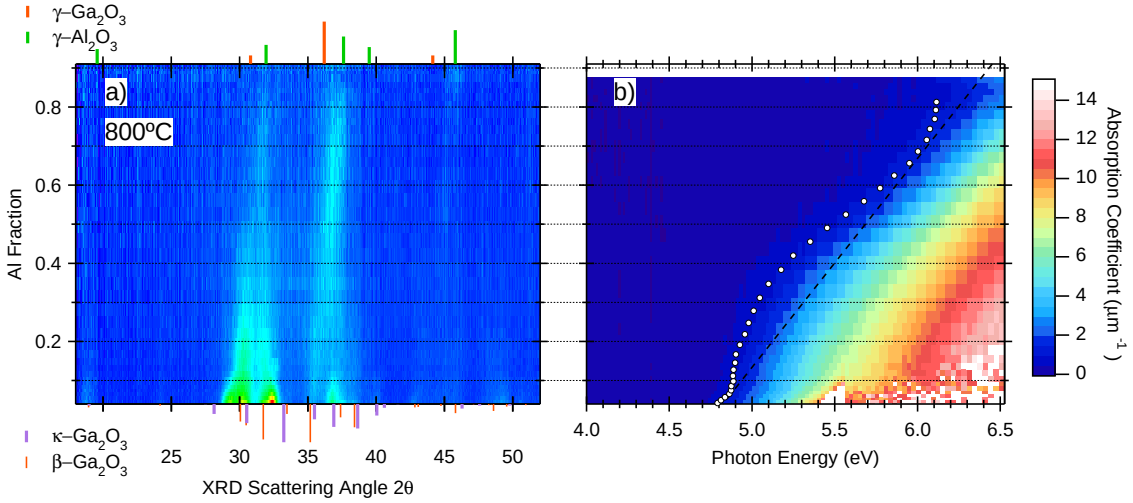

Figure 6.23: a) XRD $\theta - 2\theta$ scans vs. composition for CCS film pa-A1 after post-annealing to 800 °C, and b) absorption coefficient measured by UV-Vis spectroscopy. JCPDS PDF card no. 00-043-1012 for $\beta - Ga_2O_3$, and a pattern for $\kappa - Ga_2O_3$ from refs. [53] and [102] are appended below the XRD data, and PDF card nos. 00-020-0426 and 00-029-0063 for $\gamma - Ga_2O_3$ and $\gamma - Al_2O_3$, respectively, are appended above the XRD data for reference. White markers show the location of the absorption onset.

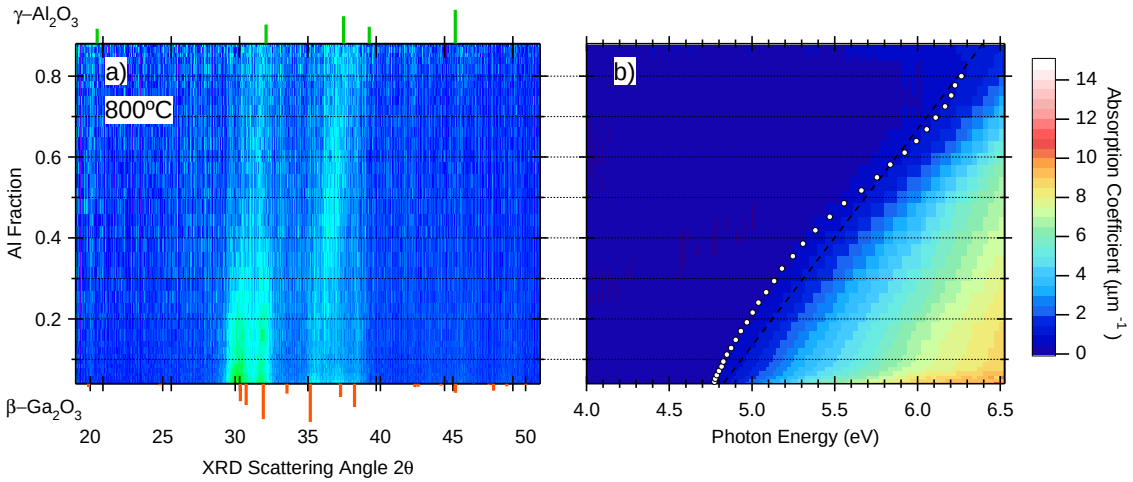

Figure 6.24: a) XRD $\theta - 2\theta$ scans vs. composition for CCS film pa-A2 after post-annealing to 800 °C, and b) absorption coefficient measured by UV-Vis spectroscopy. JCPDS PDF card no. 00-043-1012 for $\beta - Ga_2O_3$ is appended below the XRD data, and PDF card no. 00-029-0063 for $\gamma - Al_2O_3$ is appended above the XRD data for reference. White markers show the location of the absorption onset.

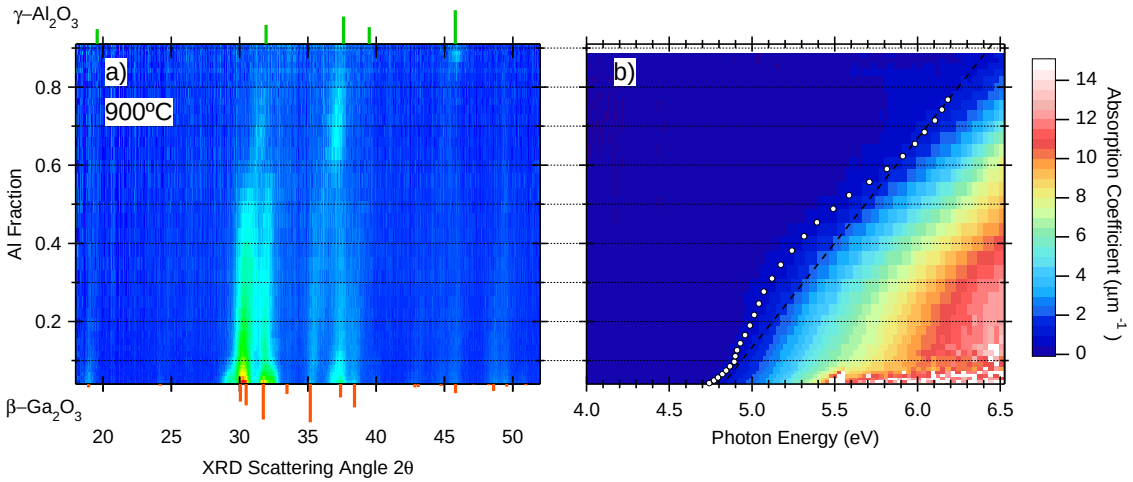

Figure 6.25: a) XRD $\theta - 2\theta$ scans vs. composition for CCS film pa-A1 after post-annealing to 900 °C, and b) absorption coefficient measured by UV-Vis spectroscopy. JCPDS PDF card no. 00-043-1012 for $\beta - Ga_2O_3$ is appended below the XRD data, and PDF card no. 00-029-0063 for $\gamma - Al_2O_3$ is appended above the XRD data for reference. White markers show the location of the absorption onset.

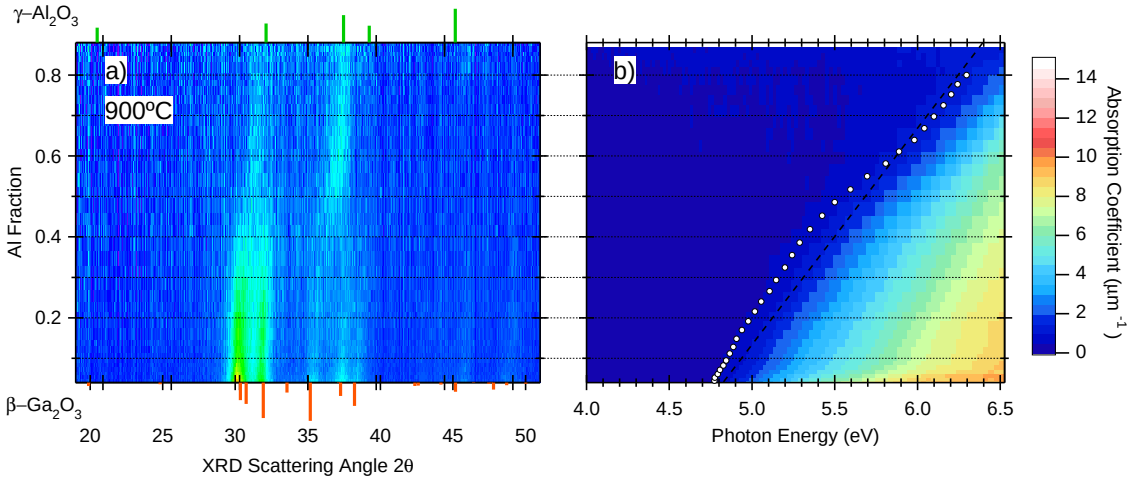

Figure 6.26: a) XRD $\theta - 2\theta$ scans vs. composition for CCS film pa-A2 after post-annealing to 900 °C, and b) absorption coefficient measured by UV-Vis spectroscopy. JCPDS PDF card no. 00-043-1012 for $\beta - Ga_2O_3$ is appended below the XRD data, and PDF card no. 00-029-0063 for $\gamma - Al_2O_3$ is appended above the XRD data for reference. White markers show the location of the absorption onset.

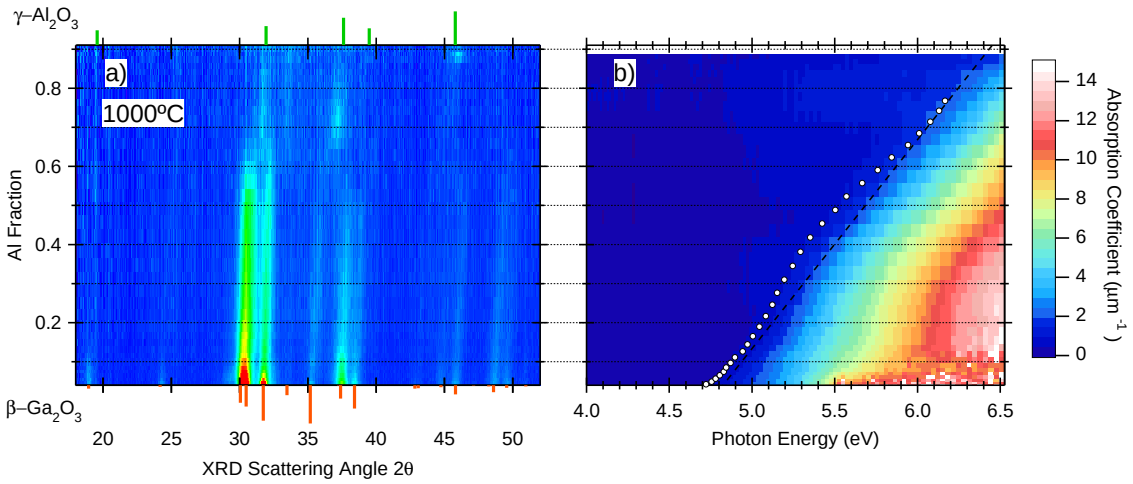

Figure 6.27: a) XRD $\theta - 2\theta$ scans vs. composition for CCS film pa-A1 after post-annealing to 1000 °C, and b) absorption coefficient measured by UV-Vis spectroscopy. JCPDS PDF card no. 00-043-1012 for $\beta - Ga_2O_3$ is appended below the XRD data, and PDF card no. 00-029-0063 for $\gamma - Al_2O_3$ is appended above the XRD data for reference. White markers show the location of the absorption onset.

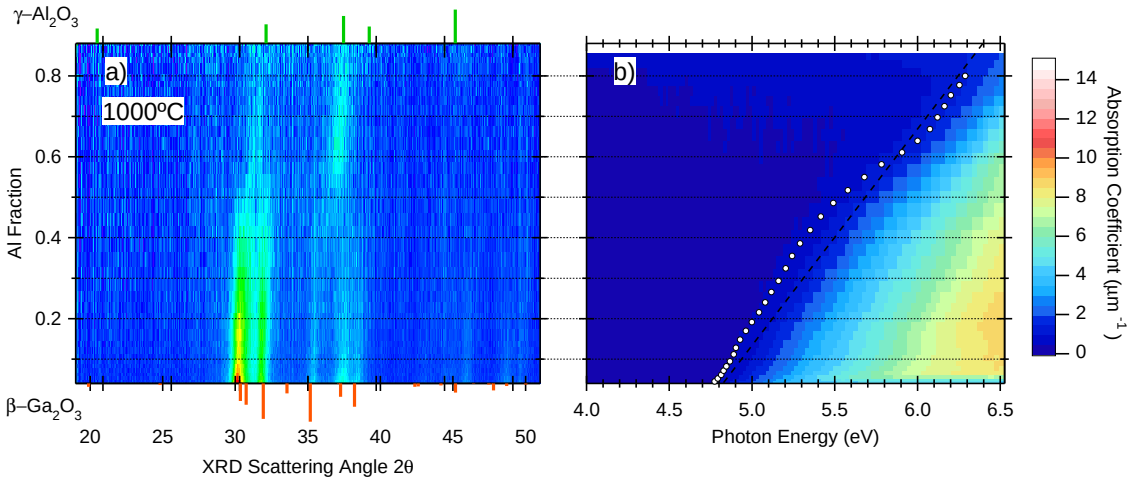

Figure 6.28: a) XRD $\theta - 2\theta$ scans vs. composition for sample pa-A2 after post-annealing to 1000 °C, and b) absorption coefficient measured by UV-Vis spectroscopy. JCPDS PDF card no. 00-043-1012 for $\beta - Ga_2O_3$ is appended below the XRD data, and PDF card no. 00-029-0063 for $\gamma - Al_2O_3$ is appended above the XRD data for reference. White markers show the location of the absorption onset.

temperature steps makes a funny "S" shape, as if there is jump to a higher parallel trendline from $x = 0.5$ to $x = 0.6$. Examination of figs. 6.11 and 6.12 shows that the absorption edge from $0.5 < x < 0.8$ has a longer tail and greater slope than the absorption edge from $0 < x < 0.4$, so the linear extrapolation intercepts zero at higher energy on the Al-rich side of the film. The longer tail may arise from a slowly-growing beam width as the space between the substrate and the Al block slowly increased, or it might indicate diffusion of Al from the sapphire into the film, leading to a nonuniform composition with depth. Goyal et al. [266] found evidence of Al diffusion from sapphire into crystalline $\beta - Ga_2O_3$ PLD films after post-annealing above 800 °C for 24 hr, and a corresponding blue shift in the absorption edge. In addition, evidence of Ga diffusion from a $\beta - Ga_2O_3$ buffer layer all the way through an amorphous $(Al_xGa_{1-x})_2O_3$ film at temperatures less than 700 °C is presented in the next chapter, leading to a 10 % variation in composition with depth, and in that film the absorption edge exhibits an elongated tail as well. It may be that above a certain alloy composition, the crystallization temperature becomes higher than the temperature at which diffusion into the amorphous film starts.

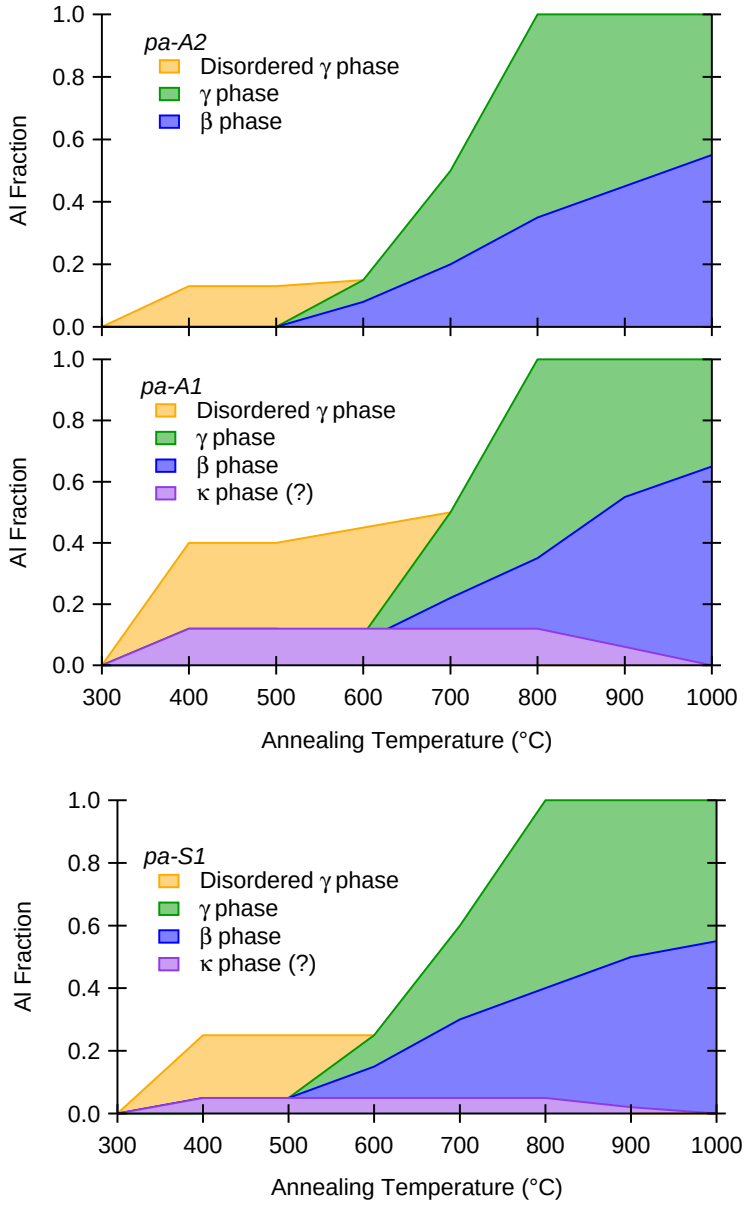

Figure 6.29: Phase diagrams of samples pa-A1 and pa-A2 on sapphire, and pa-S1 on silicon as a function of composition and post-annealing temperature.

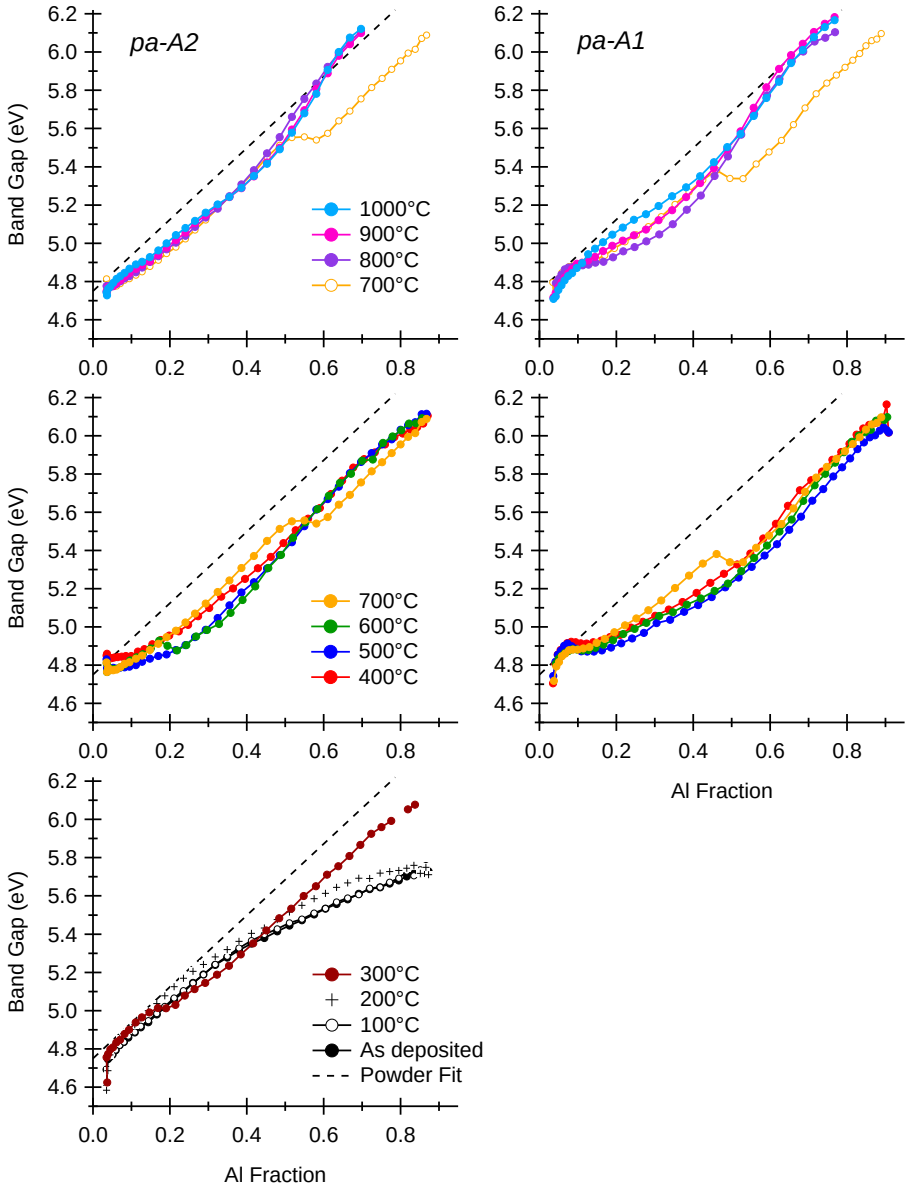

Figure 6.30: Fitted band gaps of CCS $(Al_xGa_{1-x})_2O_3$ films pa-A1 and pa-A2 as a function of composition and post-annealing temperature.

6.3 X-ray Diffraction and Spectroscopic Ellipsometry of a CCS Film on Silicon

A CCS film on silicon was deposited at room temperature to repeat the post-annealing experiment using spectroscopic ellipsometry instead of UV-Vis spectroscopy, and compare the band gap variation obtained by different methods. In ellipsometry, the change in polarization state of reflected light is measured, and optical constants are determined by constructing a model to generate simulated data, and varying model parameters to minimize the difference between simulated and experimental data. If satisfactory agreement is achieved in both reflection and transmission measurements then we may be more confident that the band gap results are trustworthy.

The XPS composition as a function of position is shown in fig. 6.31. Despite the longer length of this sample compared to the others, most of the composition spread still takes place within the central 40 mm region. The long tails at the edges provide information about amorphous $(Al_xGa_{1-x})_2O_3$ in the 0–5$\dot{\%}$ and 95–100 % range, which is missing in my other post-annealed samples. (Unfortunately these regions delaminated after crystallization due to the large film thickness at the ends, leaving only the central region available for characterization after annealing to 400 °C). It is assumed that the choice of substrate does not have a strong influence on films deposited at room temperature, at least before annealing to a temperature high enough to cause reactions between the film and the substrate. XRD color maps showing the crystal phase vs. composition after each annealing step are shown in fig. 6.32. The progression looks very similar to sample pa-A1 on sapphire, and the phase diagram of pa-S1 is displayed alongside phase diagrams for pa-A1 and pa-A2 in the previous section fig. 6.29.

Sample pa-S1 had unexpected non-idealities which complicated the ellipsometric analysis. The first is an extreme variation in film thickness caused by the same geometry that led to a wide composition range. Although CompleteEASE can simulate the effect of a thickness non-uniformity, there are enough correlated variables that it is helpful to have as uniform a thickness as possible. Focus probes were used to reduce the spot size to 0.125 mm to minimize the variation as much as possible. The large thickness also resulted in unfortunate delamination of the film after crystallization. The second non-ideality was apparent anisotropy in the refractive index near the central point between the two plumes. The difference in MSE between isotropic and anisotropic models grows from just 5 in the as-deposited data set to 50 in the 800 °C data set, and a convincing fit could

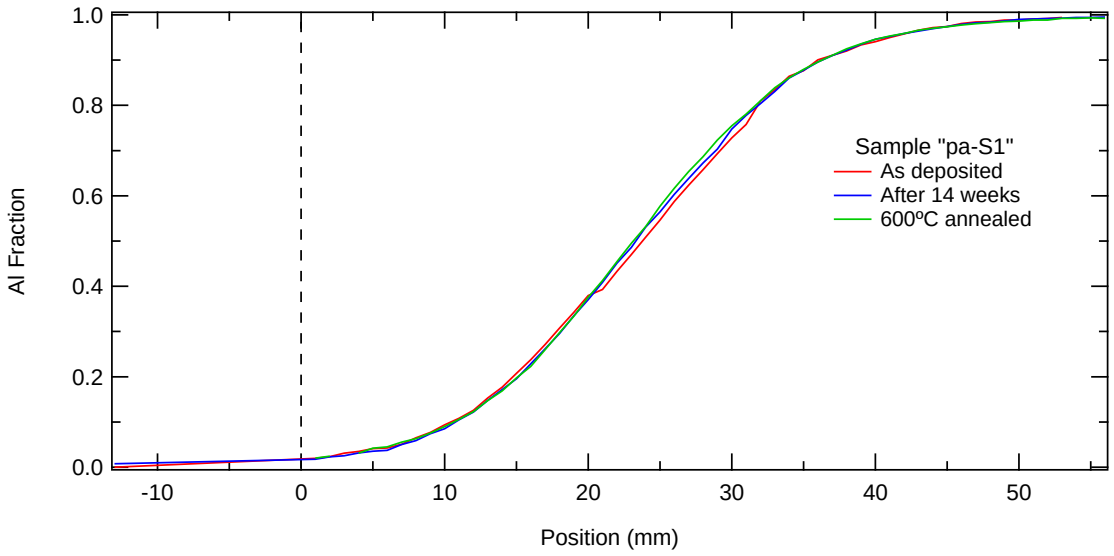

Figure 6.31: Average surface alloy composition vs. position on substrate for a post-annealed composition-spread film on silicon, before post-annealing and after annealing to 600 °C, as determined by XPS using Al-to-Ga peak intensity ratios.

not be achieved without it. Attempts to use more complicated isotropic models, such as effective medium approximations or a continuous variation of optical constants with depth, showed almost no improvement despite the relatively large number of combinations possible. The fact that anisotropy was present even after initial deposition at room temperature suggests that it has to do with deposition conditions and not preferred orientation in the crystal structure (which was not observed in XRD) or interaction with the substrate. The central point in this film had the most oblique angle of incidence of the PLD plume of any sample studied; whereas the angle from the plume axis at the center of samples pa-A1 and pa-A2 was roughly 26°, at the center of pa-S1 the angle was closer to 41°. It's possible the relatively large horizontal velocity component of ablated species led to microstructure in the as-deposited film affecting its optical properties; in general, the refractive index of thin films is proportional to the density (see section 3.2.3). I am not aware of any reports of similar anisotropy in PLD-deposited films in the literature. The closest is Perrière et al. [352], who observed a tilting in the optical axis of ZnO thin films deposited at oblique incidence from the PLD plume.

Figure 6.33 shows a comparison of parameters from three Cauchy fits as a function of position

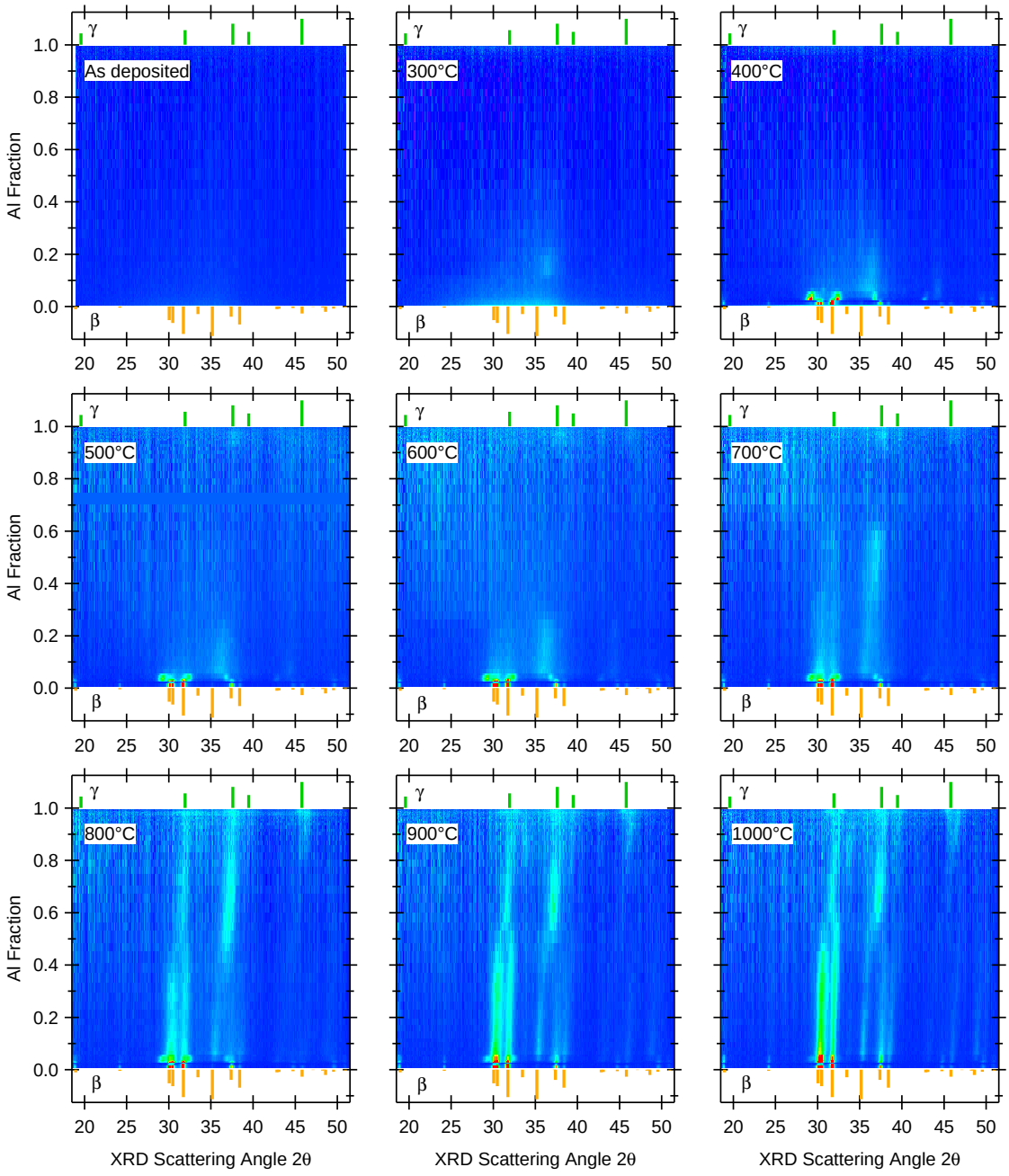

Figure 6.32: XRD color maps of sample pa-S1 before post-annealing and after each annealing step. XRD reference patterns for $\beta - Ga_2O_3$ and $\gamma - Al_2O_3$ from JCPDS PDF card nos. 00-043-1012 and 00-029-0063 are appended below and above the XRD data, respectively.

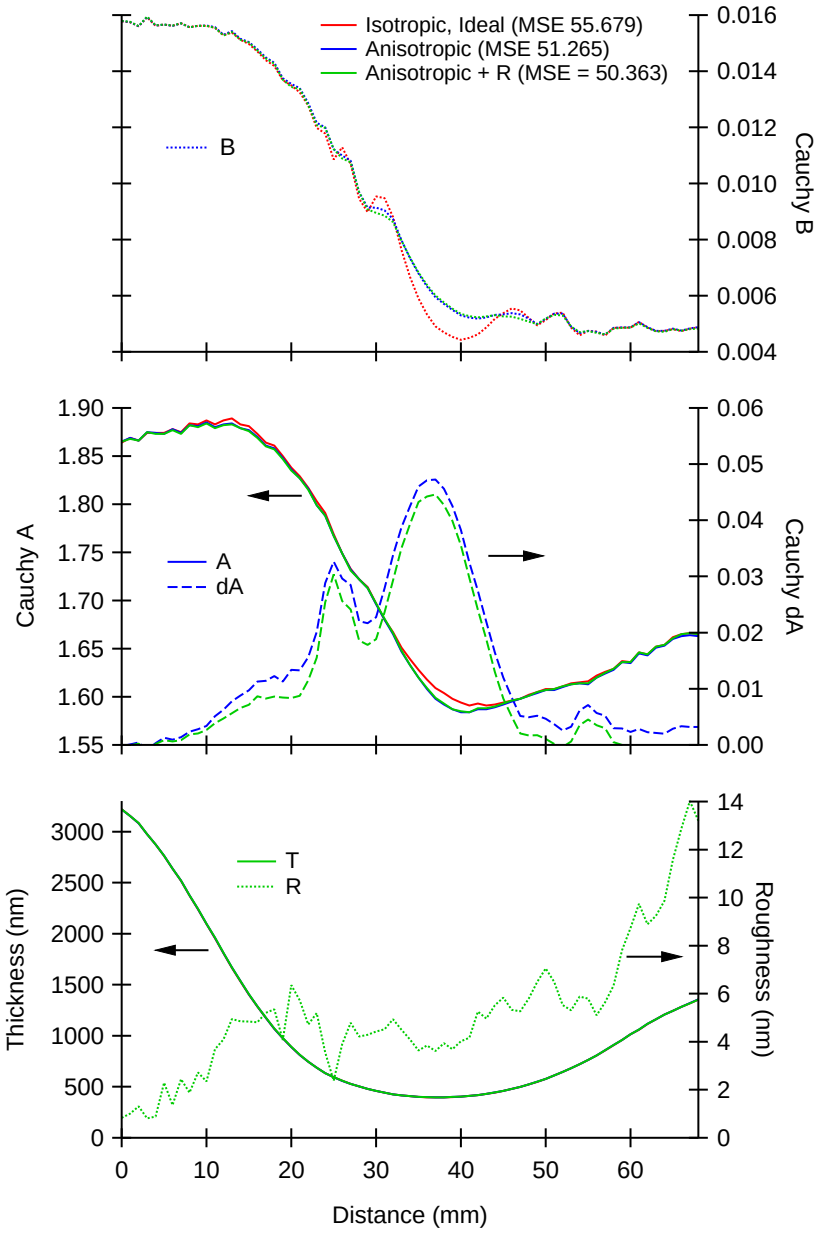

Figure 6.33: Cauchy parameters of sample pa-S1 as a function of position on the substrate, before post-annealing. Red: Ideal fit with no roughness or anisotropy. Blue: Refit with anisotropy included. Green: Refit with both anisotropy and roughness. Uniform fitted C values are 0.00019 for all models. The maximum anisotropy in A is equidistant between the plume axes, showing up to 0.05 higher refractive index in the direction perpendicular to the surface. Anisotropy in B was found to vary around zero with no clear pattern, and was therefore neglected.

on sample pa-S1 in the amorphous state after deposition. As introduced in section 4.6.3, the Cauchy model is an accurate way to determine the optical dispersion and thickness (T) of a thin film in the transparent region, where the index of refraction n is given by the formula

$$n(\lambda) \approx A + \frac{B}{\lambda^2} + \frac{C}{\lambda^4} + \cdots \tag{6.2}$$

In each of these models, fitting was performed over the 1–3 eV range due to the onset of absorption above 3 eV in amorphous Ga_2O_3. The C parameter was found to vary unpredictably around 0.0002, and was therefore fit globally rather than individually. The D parameter (the next term in the series) was found to be on the order of 10^{-7} and was neglected. The first model (red) assumes no non-idealities such as roughness or anisotropy: the only variable parameters are A, B, C, and T. The second model (blue) includes anisotropy, shown as an offset in the A parameter for the perpendicular direction relative to the in-plane direction; the offset in B showed wild, unphysical variations around zero when it was allowed to vary, and was therefore fixed to zero. A and B depend somewhat on the anisotropy, and seem to exhibit a smoother variation with anisotropy turned on. The third model includes both anisotropy and roughness, which are inversely correlated. When roughness is turned on and anisotropy turned off (not shown), values as high as 30 nm are found in the central region, but with a minimal decrease in MSE. Compared to the second model with anisotropy only, including roughness leads to a lower overall anisotropy and smaller MSE, but with minimal change to the other Cauchy parameters. However such a high value on the Al-rich side is not realistic for an amorphous film. Additional non-ideal parameters such as the light source bandwidth and thickness non-uniformity (dT) lead to a drastic reduction in the MSE, from approximately 50 to 30. However, there is almost no effect on the other parameters, and the fitted result for dT was found to peak in the center of the film, not at the maxima of the slope of T as one would expect, and with values too large for the focused size of the spot used. It may be correlated with the anisotropy dA.

A summary of isotropic and anisotropic Cauchy model parameters for sample pa-S1 after each post-annealing step is shown in fig. 6.34. Each set of data were fit to an ideal Cauchy model and a model including anisotropy (models one and two above, respectively). Due to delamination of the thickest parts of the film above 400 °C, only the composition range from $0.05 < x < 0.95$ is shown. The fitted data range was also increased to 1–4 eV because the absorption edge moves quickly to higher energy in the low-x region for amorphous Ga_2O_3, extending the transparent region. Including

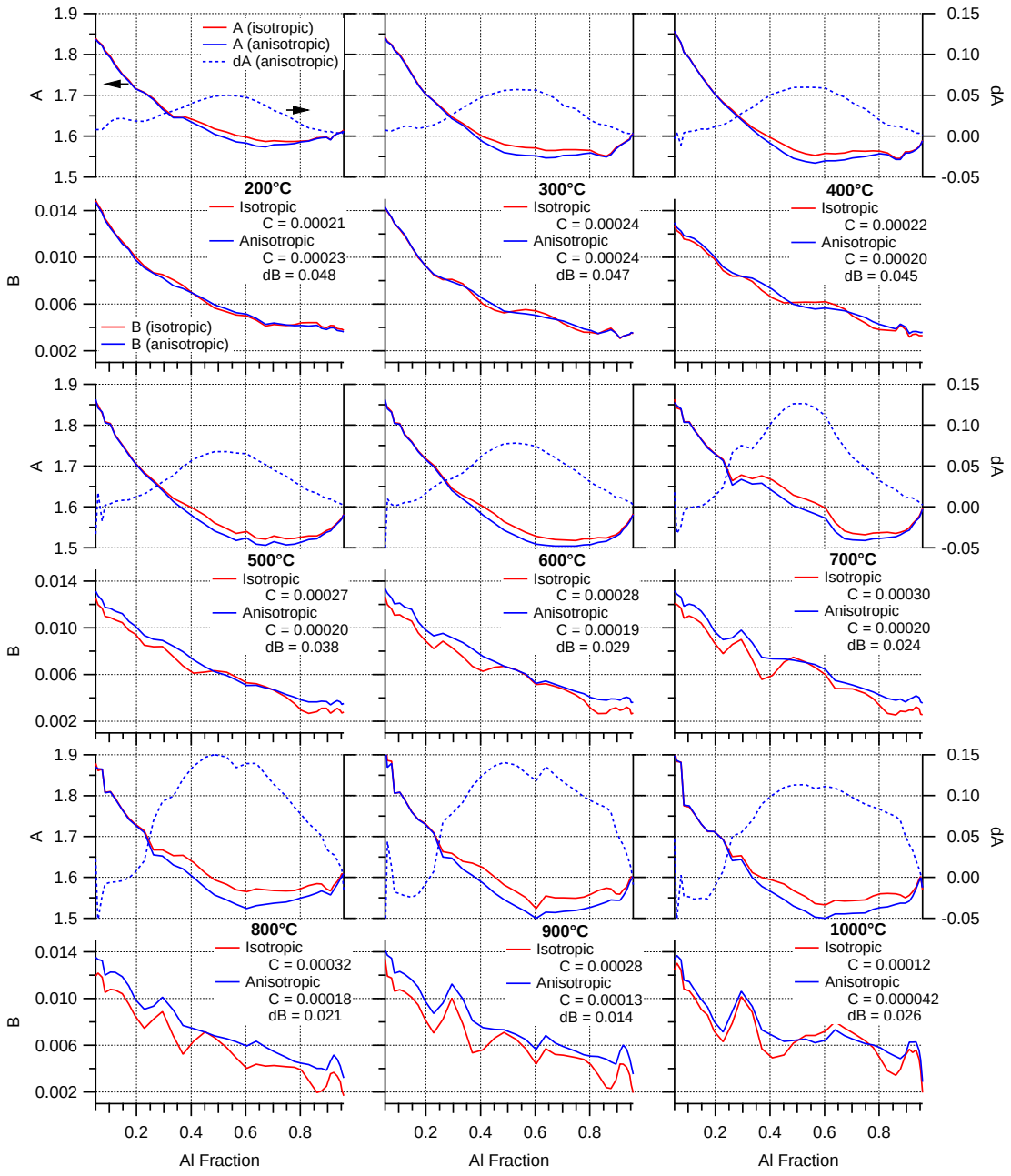

Figure 6.34: Overview of isotropic (red) and anisotropic (blue) Cauchy model parameters for sample pa-S1 in the range $0.05 < x < 0.95$ after each annealing step.

the range $0.95 < x < 1$ of the amorphous film would reveal a steep increase from $A = 1.60$ to 1.65, and including the range $0 < x < 0.05$ would show an increase from $A = 1.86$ to 1.88, which can be seen in fig. 6.33. This non-monotonic variation in A is different from what is observed in CCS films S1, S2, A1 and A2 deposited at high temperature (chapter 7).

In general, the variation in A and B seems to be smoother with the anisotropy turned on, and the increase in the out-of-plane component is balanced by a decrease in the in-plane component. The maximum anisotropy in A appears to be growing with post-annealing temperature, increasing from 0.05 at 200 °C to 0.15 at 800 °C, while the anisotropy in B decreases from approximately 0.048 to 0.020 over the same temperature steps. This may be interpreted as a growing overall offset in the index of refraction n for the in-plane and out-of-plane directions, but a smaller difference in curvature. However, unusual features are present at high post-annealing temperatures. At 700 °C, A jumps to a higher value than in previous data in the range $0.2 < x < 0.6$, roughly matching the region of crystallization, but then returns to its original value at 800 °C and above. The B parameter appears to straighten out as the temperature is increased from initial deposition to 600 °C, but at 700 °C it develops a sharp feature at roughly $x = 0.3$ which grows in magnitude as the annealing temperature is increased further. According to XRD the structure is β-phase below $x = 0.4$ in each of these steps, so it is not clear why B, which describes the curvature in the dispersion, should exhibit non-monotonic variation at all.

Our ellipsometer collects data in equal spacing in wavelength, meaning that the 5–6 eV region containing the band edge of $(Al_xGa_{1-x})_2O_3$ is also the region most sparsely populated with data points, and the mean squared error (MSE) is heavily weighted toward the transparent region. As a consequence, a number of different oscillator functions lead to similar MSE values, which can make it difficult to decide which function is most accurate for the determination of the band gap. Basis spline (B-spline) models have the most flexibility to achieve the lowest MSE without committing to any particular shape in the optical functions, but often exhibit spurious oscillations between fixed control points. Simple oscillator models are preferable because they require few fitting parameters, and because the onset of absorption is continuously tunable in energy rather than defined by a set of fixed control points which may not be located at ideal positions. The gradual variation in optical constants means that the fit result at one point may be used as a starting model for the next point. Furthermore, depending on the type of oscillator used, it is possible to estimate the band gap by

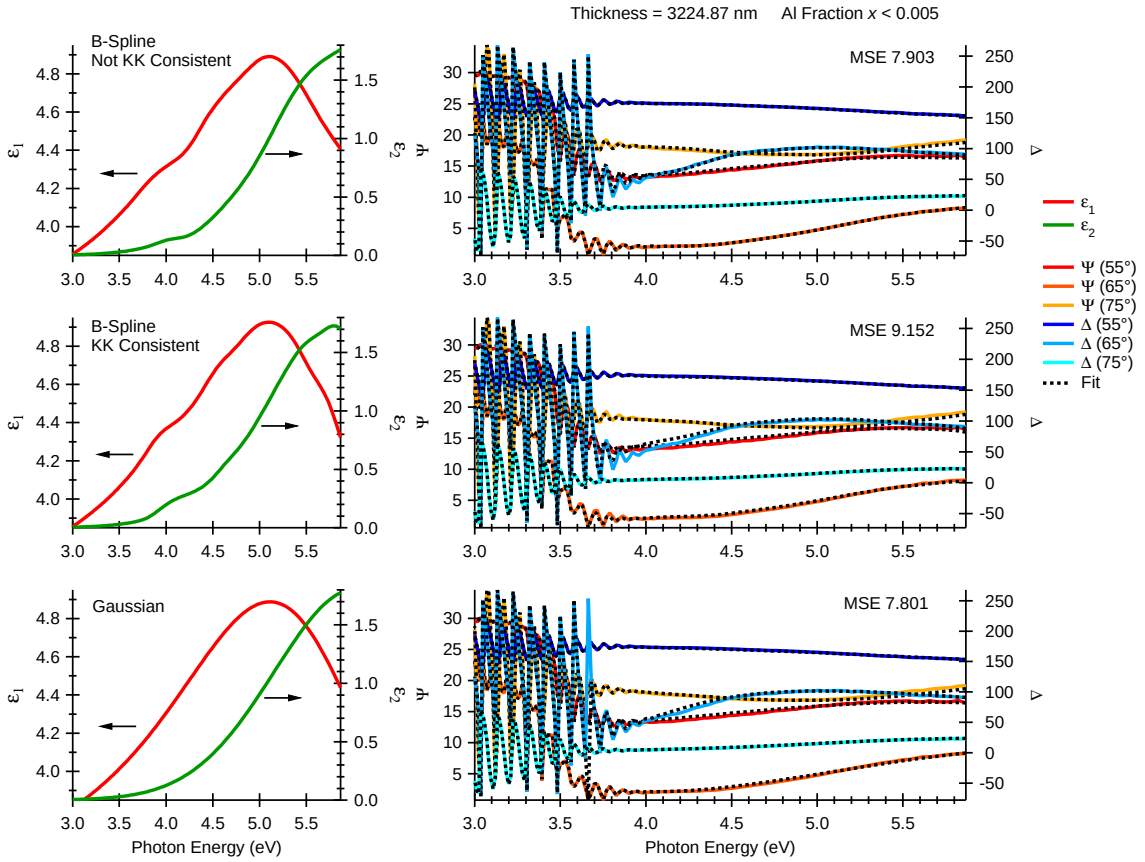

Figure 6.35: Comparison of B-spline and Gaussian fits for an as-deposited thick Ga_2O_3 film. For an amorphous film, a plain Gaussian oscillator provides the best fit.

calculating from model parameters even when there is not sufficient absorption present to draw a linear extrapolation to zero. The main disadvantage of a simple model is a lack of flexibility to accurately follow a change in the shape of the absorption, e.g. through a phase transition, so it should be checked periodically by parametrizing back to a B-spline. Although simple one-oscillator models are used to deduce the band gap energy, this procedure was followed along the way to verify their integrity.

B-spline fits at the first point ($x < 0.005$) of the as-deposited amorphous film are shown in fig. 6.35. There is a remarkable similarity to a basic Gaussian function, and in fact a Gaussian achieves a better MSE than both B-spline models, most likely due to wiggles in the spline fits. In contrast, Tauc-Lorentz (TL) and Cody-Lorentz (TL) oscillators do not achieve MSE better than

11, despite their stronger theoretical foundation. From fig. 6.8 we see that the onset of absorption in an amorphous CCS film on sapphire, measured by UV-Vis spectroscopy, is broader at low Al concentration and sharper above $x = 0.2$. After crystallization (fig. 6.9) there is almost no absorption tail left except for an apparent one due to the composition spread, and the increase from zero follows a nearly-linear trend as noted before. The composition spread under the focused spot of the ellipsometer is expected to be much smaller than in the UV-Vis absorption data, so in the crystalline region of sample pa-S1 a linear ramp with a sharp onset may be more accurate than a Gaussian. More sophisticated models could be constructed based on Cody-Lorentz, Tauc-Lorentz, or Herzinger-Johs parametric semiconductor (P-SEMI) oscillators (section 4.6.3), but unless they provide a substantial improvement to the MSE, there is little to be gained from the added complexity.

Using a Gaussian oscillator to model the absorption edge, the ordinary (in-plane) and extraordinary (out-of-plane) index of refraction for the as-deposited $(Al_xGa_{1-x})_2O_3$ film is shown in fig. 6.36 as the Al concentration is increased. In the 1–4 eV range, these data are nearly identical to the result calculated using the Cauchy parameters displayed in fig. 6.34. The change is non-monotonic, increasing slightly from $0 < x < 0.015$, then decreasing from $0.015 < x < 0.70$, and then increasing again from $0.70 < x < 1$, so each region is plotted separately for clarity.

The absorption coefficient of samples pa-A1 and pa-A2 by UV-Vis spectroscopy, and of pa-S1 by ellipsometry using both Gaussian and linear-ramp oscillator models, are overlaid for several Al concentrations in fig. 6.37 to see which model provides the best agreement with UV-Vis data in the amorphous and crystalline phases. The motivation for trying a linear oscillator comes from the earlier observation that the absorption coefficient increases almost linearly in the UV-Vis spectroscopy data for crystalline films. In these examples, a Herzinger-Johs "P-Semi Tri" oscillator with a small Gaussian broadening is used to model a linear ramp function (described in section 4.6.3), and a second ramp is also included to capture the sub-gap absorption. A B-spline (not shown) usually achieves a better MSE than either model, but often by putting spurious wiggles in the optical functions which obscure the location of the band gap. If desired, additional ramp oscillators may be added to better approximate a non-linear shape, while requiring fewer parameters than a spline and avoiding unphysical oscillations.

Unsurprisingly, examination of fig. 6.37 shows that a linear ramp generally puts a straight line through the equivalent Gaussian (and the equivalent B-spline too) with weight given to the low

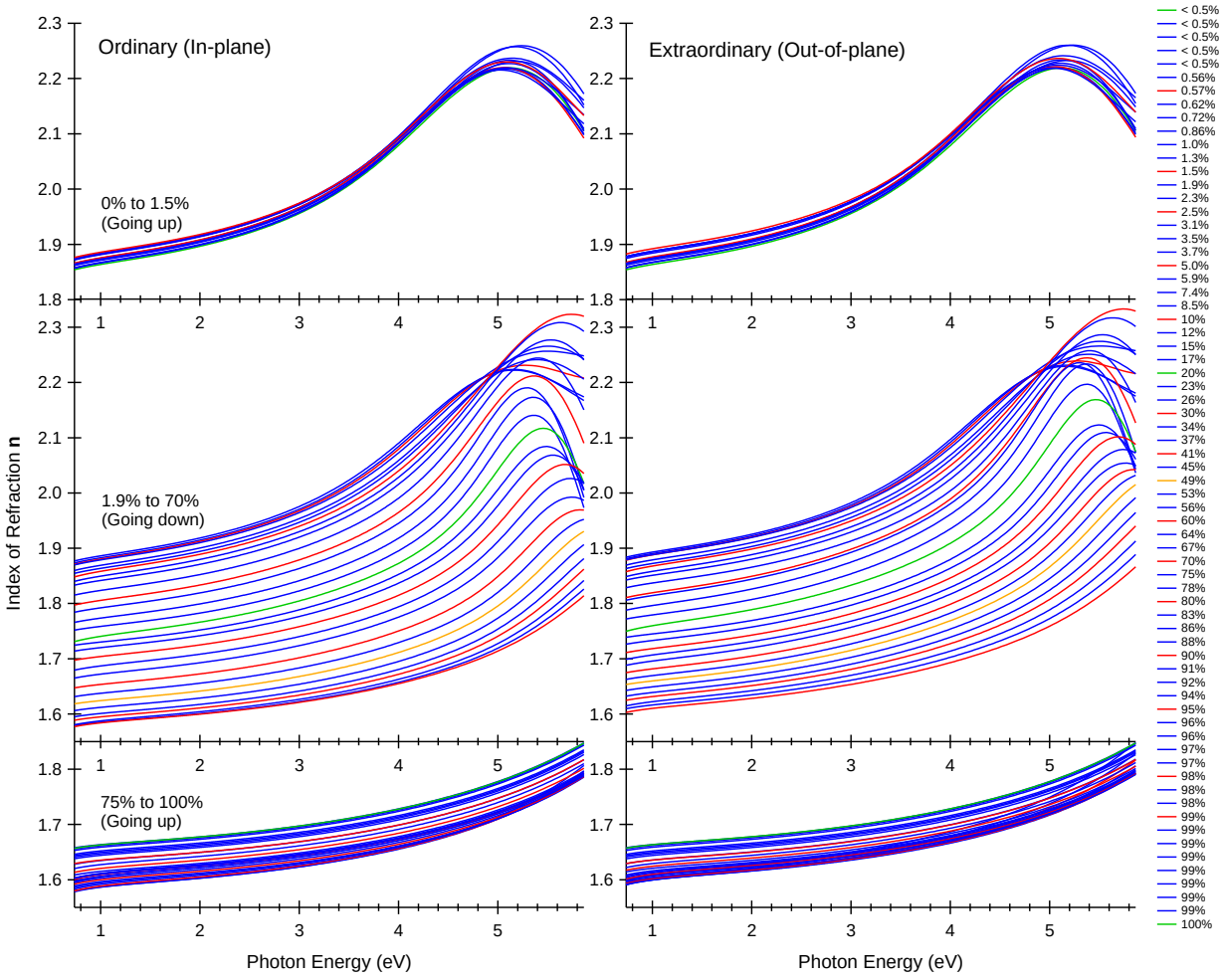

Figure 6.36: Index of refraction of as-deposited amorphous $(Al_xGa_{1-x})_2O_3$ film. Left side: ordinary (in-plane). Right side: extraordinary (out-of-plane). The change as Al concentration is increased is in the order indicated, and data are highlighted in different colors at periodic intervals for readability. The out-of-plane index is larger than the in-plane index from approximately $0.1 < x < 0.9$, possibly indicating lower apparent density out-of-plane due to microstructure in the film induced by the oblique incidence of the PLD plume.

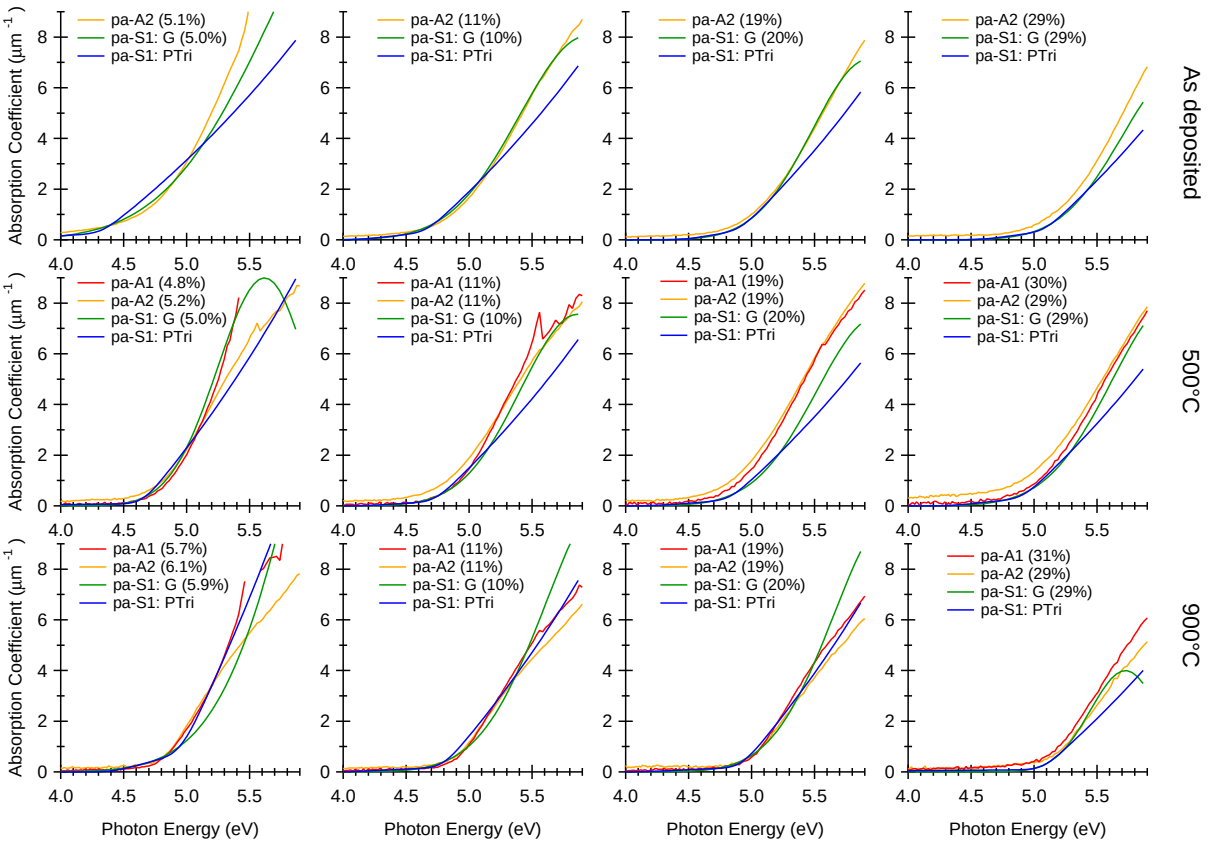

Figure 6.37: Absorption coefficient derived from Gaussian (green) and linear-ramp (blue) oscillator model fits to sample pa-S1 ellipsometry data, and the corresponding absorption coefficient at similar Al concentration from samples pa-A1 (red) and pa-A2 (gold) measured by UV-Vis spectroscopy. Data from pa-A1 have been scaled by 0.8, and data from pa-S1 have been scaled by 0.35 to show the overlap. (The reason for different y-scaling is unclear, but does not matter for determining the band gap.)

energy side, which has a greater density of data points. An advantage of the linear model is that the extrapolation to zero is unambiguous; with a Gaussian, the value of the band gap depends on which part of the curve you fit a line to. In the UV-Vis data, the best estimate of E_g was found by drawing a straight line tangent to the absorption curve at its inflection point. The equation of this line for a Gaussian curve is

$$y = \frac{1}{Bk}\sqrt{\frac{2}{e}}\left(x - \left(E_c - \frac{Bk}{\sqrt{2}}\right)\right) + \frac{1}{\sqrt{e}} \tag{6.3}$$

where B is the full width at half maximum, E_c is the center energy and k is a constant equal to 0.600561294. Solving for zero then gives the band gap energy

$$E_g = E_c - \sqrt{2}Bk \tag{6.4}$$

A linear ramp oscillator gives a band gap estimate that is lower than eq. (6.4) unless the broadening is small, but which tracks the onset of the Gaussian closely.

In the amorphous case, the best agreement with UV-Vis data clearly comes from a single broad Gaussian oscillator. Even at 500 °C it appears that the Gaussian still provides the best match, including at $x = 0.05$ when the film has crystallized to the β-phase. The tails are smaller compared to the as-deposited film, and the difference between the two models is less. However, the band gap result from the linear ramp model appears to agree better with a linear fit to the UV-Vis data at this temperature. At 900 °C the film is crystalline throughout, and the linear model provides the best match. Therefore Gaussian models were used to fit the as-deposited, 200 °C, and 300 °C data sets, which do not show crystal structure in XRD (fig. 6.38); both Gaussian and linear ramp models were used to fit the 400 °C, 500 °C, 600 °C, and 700 °C steps, which contain crystalline and amorphous phases depending on Al concentration (fig. 6.39); and linear models were used to fit the 800 °C and 900 °C steps (fig. 6.40). Fitting the 1000 °C step was attempted, but a satisfactory fit was not achieved without introducing diffusion of SiO_2 from the substrate into the film with a graded effective-medium-approximation layer, which is very computationally heavy to simulate, and it is not known how far the results of such a complicated model could be trusted. Nevertheless, it does show that a reaction takes place between the silicon substrate and $(Al_xGa_{1-x})_2O_3$ film at this temperature that affects the optical properties.

Similar features are observed in the absorption coefficients of each data set regardless of the model used. In the amorphous data sets shown in fig. 6.38, the initial onset appears to be independent of

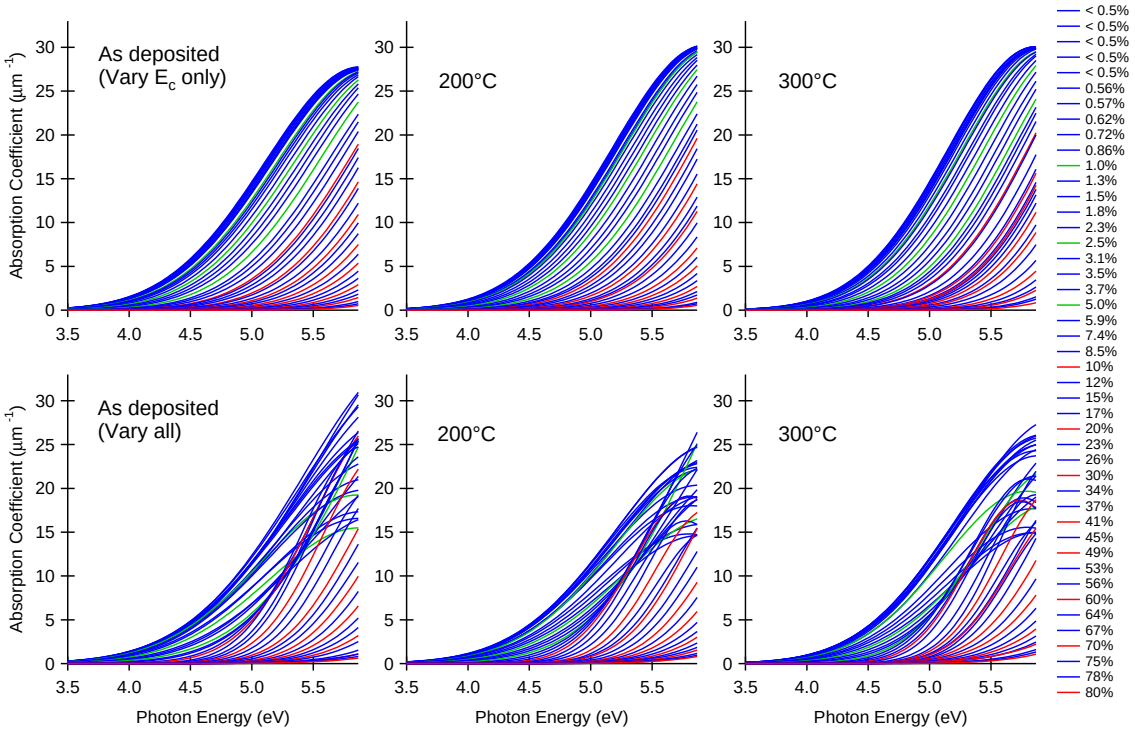

Figure 6.38: Absorption coefficient of sample pa-S1 deduced from ellipsometry using a Gaussian model, before annealing and after annealing to 200 °C and 300 °C. Top: only center energy E_c allowed to vary, with other parameters fixed. Bottom: All Gaussian parameters (E_c, Amp, and Br) allowed to vary to achieve the lowest MSE. Data are highlighted in red at 10 % intervals, and in green at 1.0 %, 2.5 %, and 5.0 %, to show the rapid initial increase in band gap at low Al concentration.

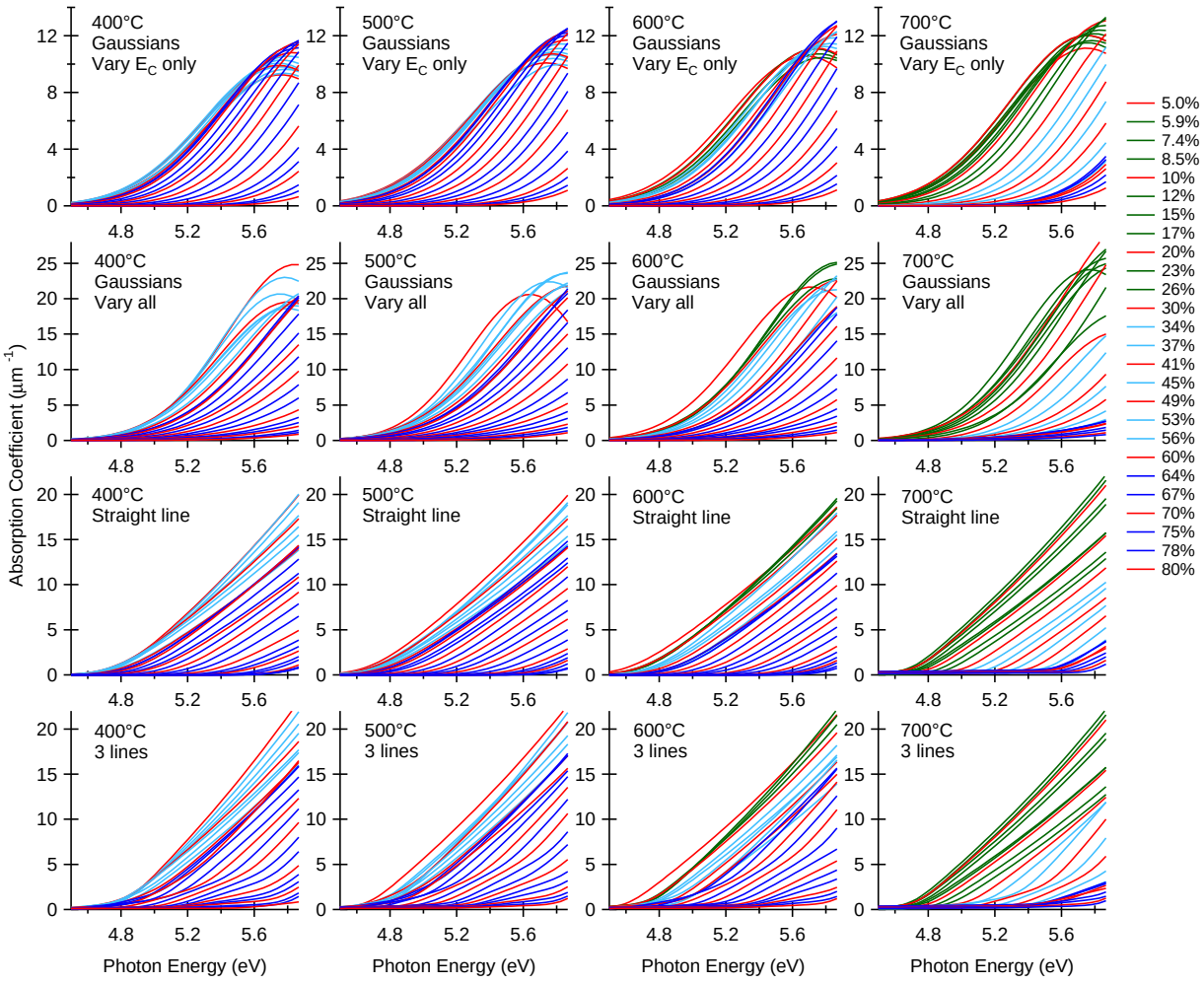

Figure 6.39: Absorption coefficient of sample pa-S1 after annealing to 400 °C, 500 °C, 600 °C, and 700 °C. Four models are shown for comparison. Top row: Gaussian fit, but with all parameters fixed except the center energy E_c. Second row: Gaussian fit with all parameters allowed to vary. Third row: Straight line fit. Fourth row: 3 lines fit. Data are highlighted in red at 10 % intervals, and the other color indicates the crystal phase from XRD: Light blue = $\gamma-$phase, Green = $\beta-$phase, and dark blue = amorphous.

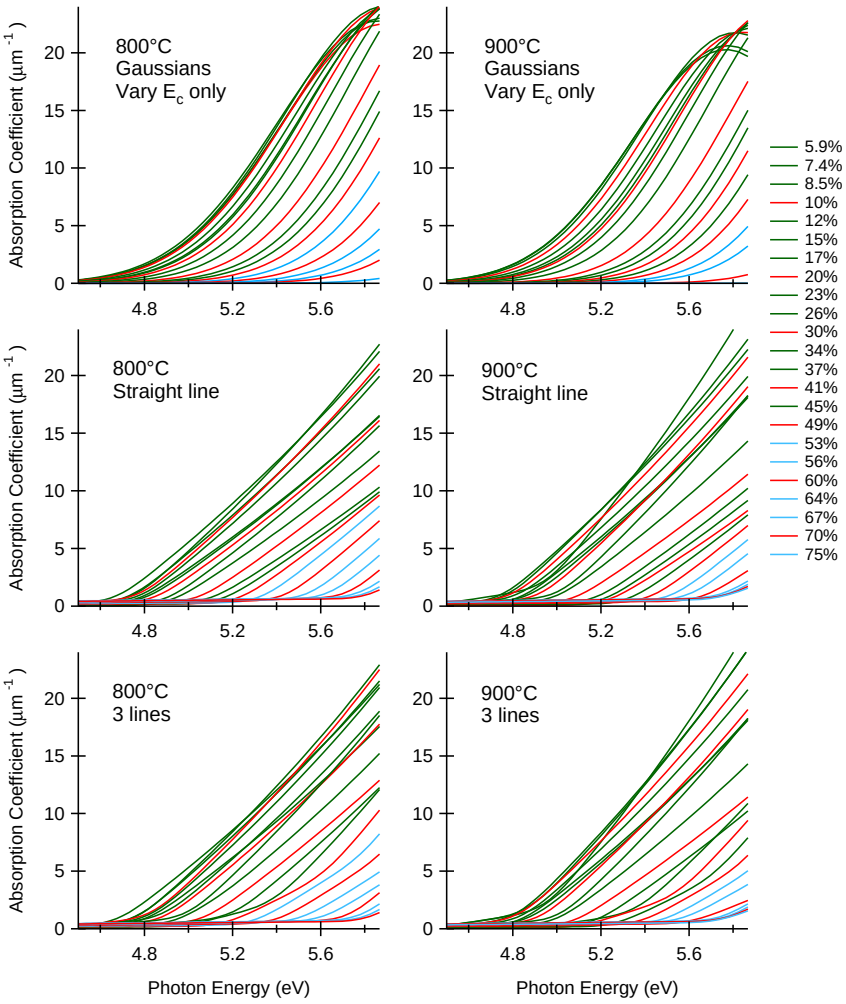

Figure 6.40: Absorption coefficient of sample pa-S1 after annealing to 800 °C and 900 °C. Top row: Gaussian fit, but with all parameters fixed except the center energy E_c. Second row: Straight line fit. Third row: 3 lines fit. Data are highlighted in red at 10 % intervals, and the other color indicates the crystal phase from XRD: Light blue = $\gamma-$phase, Green = $\beta-$phase, and dark blue = amorphous.

the model. After the initial onset, the shape of the absorption coefficient changes when all Gaussian parameters are allowed to vary, becoming less steep from $0 < x < 0.05$, but then very steep from $0.1 < x < 0.2$, and finally less steep again and with a more-or-less constant slope above $x = 0.2$. A similar change from an initial steep onset at $x = 0.05$ to less steep at $x = 0.1$ is seen in the absorption coefficient of sample pa-A2 before crystallization in fig. 6.8, although the change appears to take place at a slightly lower Al concentration. At 300 °C the absorption edge of pa-S1 appears to have shifted to lower energy above $x = 0.3$ relative to the as-deposited data set despite still being in the amorphous state, as evidenced by the non-uniform density of curves.

Above 400 °C, delamination of the film prevented data from being collected at Al concentration less than $x = 0.05$. Nevertheless, the absorption coefficient in the range $0.05 < x < 0.8$ is plotted in fig. 6.39. In addition to the one-oscillator models described above, a fourth model with multiple straight-line oscillators was used to simulate the change from a linear to a curved shape at the boundary from crystalline to amorphous more accurately. Only small differences are seen between the 400 °C and 500 °C data sets, where the initial points are labeled as γ due to their similarity in XRD with the pre-γ phase in sample pa-A1. The absorption shifts less rapidly with concentration at the transition from the pre-γ phase to amorphous, and then the curves are roughly evenly spaced afterwards. At 500 °C the change in the first curve at ($x = 0.05$) is likely due to a slight expansion of the delamination front; however, all other curves appear nearly unchanged. At 600 °C the first β phase peaks appear below $x = 0.1$, and the disordered γ phase peaks extend 10 % farther into the film. Again a slower shift in the absorption edge at the boundary between γ phase and amorphous is observed, but this time at the higher Al concentration. This likely indicates a small negative difference in the band gap between the disordered pre-γ phase and amorphous films at the same Al concentration. At 700 °C the film is in the β phase up to $x = 0.3$, and then a more highly-ordered γ phase from $0.3 < x < 0.6$, and the density of curves appears more uniform until the transition to amorphous, when the onset of absorption actually moves to slightly lower energy with Al concentration before increasing again. The fact that almost no difference exists in the absorption coefficient between films in the β phase and γ phase suggests the two phases have very similar densities of states. Interestingly, the three-line model shows curvature in the absorption coefficient at much lower Al concentration when the films are amorphous than when they are crystalline.

Data sets in the 800 °C and 900 °C range are very similar to 700 °C, except the film is crystalline

throughout and the absorption onset does not exhibit a jog to lower energy at $x = 0.6$. The straight-line and Gaussian fits show similar trends in absorption coefficient for both data sets. The three-line model achieves the best fit with a linear increase below $x = 0.3$, and a more curved shape above $x = 0.3$, and the change occurs at the same Al concentration in both the β and γ phases, providing further evidence of a similar density of states.

Band gaps obtained from the Gaussian and straight-line models are summarized in fig. 6.41, where the gap of Gaussian models was calculated using eq. (6.4). The straight-line and Gaussian models with fixed shape track each other closely, and show excellent agreement with the increase in band gap of post-annealed samples pa-A1 and pa-A2 obtained by UV-Vis spectroscopy (fig. 6.30), and with the powder data obtained by XPS (fig. 5.7). After an initial rapid increase in the band gap of amorphous samples below $x = 0.05$ (possibly related to the huge thickness variation in that region), the trend is more-or-less linear. At 300 °C the band gap of the amorphous film from $x = 0.2$ to $x = 0.8$ moves to a lower trendline with negative bowing, which remains unchanged to 600 °C. Crystallization results in a jump to higher band gap, with the discontinuity dependent on the Al concentration, due to bowing in the amorphous trendline. There is no discontinuity between the β and γ phases, and the increase with Al concentration is quite linear up to 6.0 eV, above which we are unable to measure on our ellipsometer. Band gap trendlines calculated using Gaussian models with variable amplitude and broadening show the same qualitative features as the others, but the changing oscillator shape leads to different values of the band gap when fitting with a tangent line to zero. So there appears to be a trade-off: a freely-varying oscillator produces a more accurate shape of the absorption with lower MSE; however, the fixed-shape Gaussian and straight-line models track the initial onset more sensitively and provide a more consistent estimate of the band gap, defined as the minimum photon energy at which optical absorption begins.

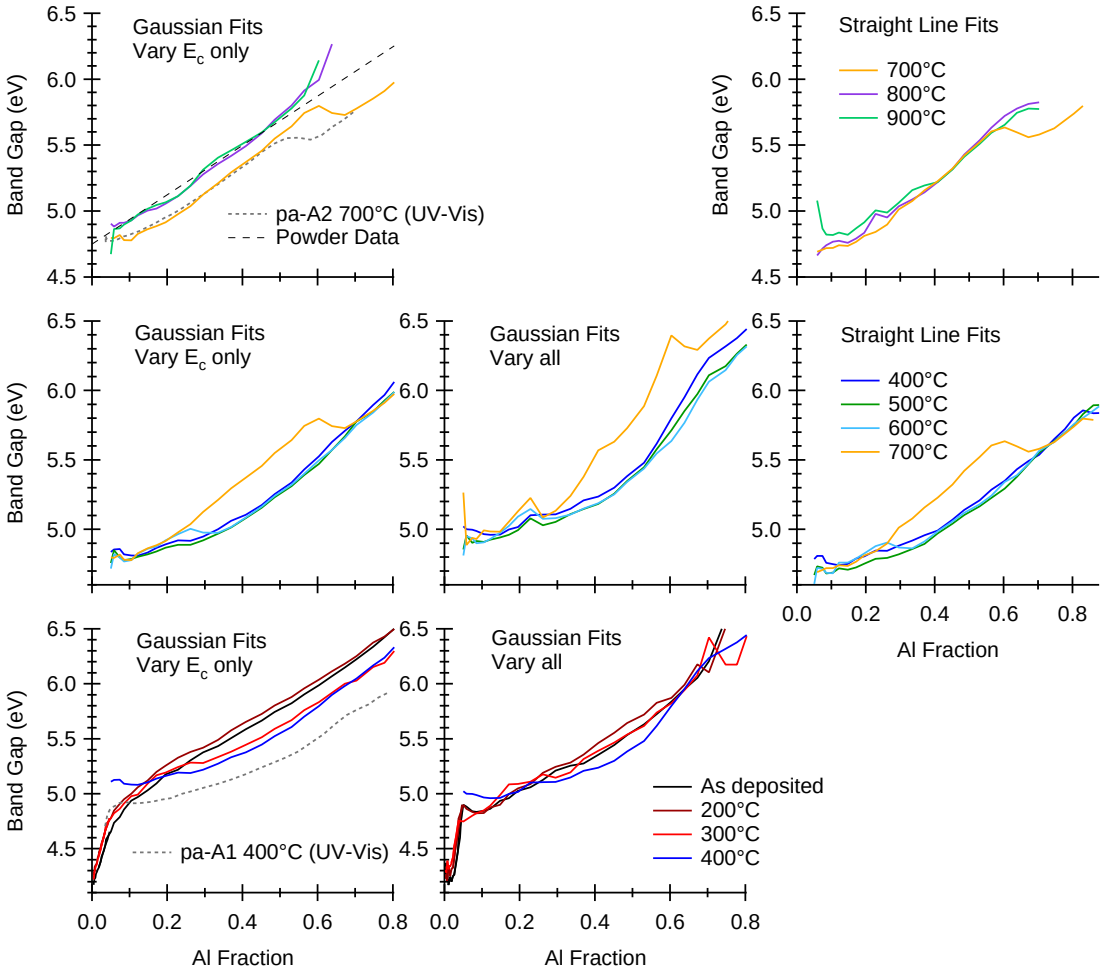

Figure 6.41: Band gaps of sample pa-S1 as determined by three models: Gaussian fit with only E_c allowed to vary, Gaussian fit with all parameters allowed to vary, and a straight line fit to zero. Also appended are the 400 °C data from sample pa-A1 (showing similar disordered γ-phase at low Al concentration), 700 °C data from sample pa-A2, and the linear trendline from single-phase powders in chapter 5.

6.4 Summary of Results from Post-Annealed $(Al_xGa_{1-x})_2O_3$ Films

In this chapter, phase diagrams of $(Al_xGa_{1-x})_2O_3$ thin films vs. annealing temperature in the range 0–1000 °C and alloy composition in the full range $0 < x < 1$ were explored. In two samples, a new phase appears at low $x < 0.1$ after annealing at 400 °C, which was tentatively assigned to orthorhombic $\kappa-Ga_2O_3$, a metastable phase that transitions to β around 870 °C. At intermediate alloy compositions (below $x \approx 0.3$) a diffuse background structure with a maximum at the location of $\gamma - Ga_2O_3$ [311] appears at 400 °C, which was referred to as a disordered "pre-γ" phase. The first appearance of the β phase at $x < 0.05$ (pa-A2) and a more well-defined γ phase at $0.05 < x < 0.2$ occurs at 600 °C. The $(\beta \rightarrow \gamma)$ and $(\gamma \rightarrow$ amorphous) transition temperatures increase steadily with the Al concentration in the alloy. At 700 °C, films below $x \approx 0.25$ are in the β phase, and films in the range $0.25 < x < 0.5$ are in the γ phase; at 800 °C, the β phase extends to $x \approx 0.4$ and the γ phase extends all the way to $x = 1$, and at 900 °C the $(\beta \rightarrow \gamma)$ transition moves to $x \approx 0.5$.

Band gap variation with Al concentration was measured using both UV-Vis spectroscopy and spectroscopic ellipsometry, and correlations between optical properties and crystallinity were established. Downward bowing was observed in the amorphous phase in films without an oxygen deficiency, with some sample-to-sample variation; after crystallization, there was less bowing and better consistency across different samples. The band gap in the β and γ phases seemed to increase more slowly than in my sintered powders, but the discrepancy may just be due to an underestimation caused by fitting to the absorption coefficient α directly rather than to $(\alpha h\nu)^2$. No change in the band gap was observed through the $(\beta \rightarrow \gamma)$ transition, but a discontinuous jump to 0.1–0.2 eV lower band gap was observed when films become amorphous. A sudden jump to higher band gap above $x = 0.5$ in the 800–1000 °C data and longer absorption tails may be evidence of Al diffusion from the sapphire into the film, suggesting that at a certain alloy composition the crystallization temperature is likely higher than the activation energy for diffusion from sapphire into amorphous $(Al_xGa_{1-x})_2O_3$.

Using the data presented in this chapter, it is possible to predict the crystal phase of $(Al_xGa_{1-x})_2O_3$ thin films within the full range $0 < x < 1$ based on the post-annealing temperature up to 1000 °C, and tune the band gap and shape of the absorption onset of $(Al_xGa_{1-x})_2O_3$ within the range 4.7–6.0 eV in the amorphous, γ, and β phases.

Chapter 7

$(Al_xGa_{1-x})_2O_3$ THIN FILMS DEPOSITED AT HIGH TEMPERATURE

Growth of $(Al_xGa_{1-x})_2O_3$ on silicon and sapphire at an elevated temperatures was carried out to explore the suitability of silicon and sapphire as substrates for epitaxial $(Al_xGa_{1-x})_2O_3$ films. Silicon and sapphire wafers are readily available in multiple orientations and inexpensive; epitaxial growth on silicon is particularly desirable for compatibility and ease of integration with modern semiconductor technology. Multiple studies have explored the growth of Ga_2O_3 on sapphire, useful for its excellent transparency into the far ultraviolet, and found an epitaxial relationship between the $(\bar{2}01)$ plane of Ga_2O_3 and the hexagonal (0001) plane of sapphire leading to $[\bar{2}01]$-oriented Ga_2O_3 thin films with six-fold rotational symmetry. Oxygen atoms in the $(\bar{2}01)$ plane of Ga_2O_3 form a distorted hexagon, with two sides 4.96 Å and four sides 5.15 Å, while the (0001) plane of sapphire contains oxygen atoms in a regular hexagonal arrangement with side length 4.76 Å [262]. Therefore Ga_2O_3 has approximately a 6.6 % lattice mismatch to $\alpha - Al_2O_3$ [186].

Single-crystal $\beta - Ga_2O_3$ has been suggested as a lattice-matched substrate for GaN growth, having a smaller mismatch (7.2 %) than sapphire (13.8 %), currently the most common substrate choice [186]. Epitaxial growth of GaN on single-crystal $\beta - Ga_2O_3$ has been demonstrated by MOCVD [29] and improved lattice matching was achieved by nitridizing the $\beta - Ga_2O_3$ substrate prior to GaN deposition [30]. Following the reverse procedure, we attempted epitaxial growth of $(Al_xGa_{1-x})_2O_3$ on wurtzite GaN (0001) and found that a surface reaction takes place between Al and N forming AlN at the interface, which was attributed to the greater heat of formation of AlN than GaN. The hexagonal side length of O atoms on GaN (0001) is approximately 7 % larger than $\beta - Ga_2O_3$ $(\bar{2}01)$, while $\alpha - Al_2O_3$ (0001) is approximately 7 % smaller, so as the Al content is increased the mismatch to $(Al_xGa_{1-x})_2O_3$ would improve for films on sapphire and get worse for films on GaN. Improving the lattice mismatch and preventing a surface reaction by oxidizing the GaN surface prior to deposition, or by first depositing an epitaxial Ga_2O_3 buffer layer was not attempted, but might be interesting to try in a future experiment.

Growth of uniform Ga_2O_3 and Al_2O_3 on HF-etched Si (100) and Si (111), SiOx (Si with native oxide), and *c*-plane sapphire was carried out using the deposition conditions outlined in section 4.2.2. A background O_2 pressure of 20 mT, set-point temperature of 800 °C, laser energy of 200 mJ per pulse ($\sim 3\,J/cm^2$) and low pulse repetition rate of 2 Hz were used for all films, which we found to be optimum conditions for Ga_2O_3 growth after systematically investigating a wide range of deposition parameters (at lower O_2 pressures and/or higher temperatures films were found to be oxygen deficient, and the growth rate slowed dramatically above 800 °C). It is possible that the optimum conditions for Al_2O_3 growth are different. Prior to deposition, samples were sonicated in acetone and isopropanol, and held in vacuum (5×10^{-8} T) at 800 °C for one hour to remove organic contaminants. It was found that the silicon surface forms a native oxide preventing epitaxy to Ga_2O_3 and Al_2O_3 regardless of the etching procedure, but that epitaxial growth of Ga_2O_3 on sapphire was possible. However, Al_2O_3 films on sapphire did not grow homo-epitaxially, instead forming unoriented $\gamma - Al_2O_3$.

Following the natural composition-spread technique described in section 4.2.2, a series of continuous-composition-spread (CCS) $(Al_xGa_{1-x})_2O_3$ alloy films were fabricated on 2-inch SiOx and sapphire substrates, with a gradual composition gradient spanning a wide range in x, to see how the addition of Al affects the epitaxy and to find the solubility limit of Al in the β phase. CCS-related deposition parameters such as the number of pulses per layer and spatial separation between the Ga_2O_3 and Al_2O_3 plumes are summarized in table 7.1. Due to surprising XRD results from samples S1 (on SiOx) and A1 (on sapphire), a 60-layer Ga_2O_3 buffer layer was grown before the composition spread film in samples S2 and A2 to isolate the film from the substrate and determine whether the unexpected findings were intrinsic to $(Al_xGa_{1-x})_2O_3$ or substrate induced. As will be shown, growth on polycrystalline Ga_2O_3 also extended the limit of solubility of Al in the β phase, which may also suggest a higher limit for homoepitaxial growth on single-crystal $\beta - Ga_2O_3$.

Table 7.1: Summary of composition-spread film deposition parameters grown at 800 °C.

Sample	Substrate	Buffer Layers	Layers	Ga:Al Pulses per Layer	Plume Separation	T-S Dist.	Composition Range	Thickness Variation
S0	SiOx	–	1950	8:8	42 mm	55 mm	4 %–80 %	–
S1	SiOx	–	1500	8:8	42 mm	55 mm	5 %–65 %	215–100 nm
A1	Sapphire	–	1500	8:8	42 mm	55 mm	5 %–70 %	130–50 nm
S2	SiOx	60	3600	10:15	38 mm	55 mm	11 %–78 %	480–230 nm
A2	Sapphire	60	4000	10:12	52 mm	55 mm	5 %–81 %	795–270 nm

7.1 X-ray Diffraction of Ga_2O_3 Films

2D X-ray diffraction (XRD) patterns of CCS films S1 and S2 on SiOx substrates on the Ga-rich side (5 % Al and 10 % Al, respectively) are shown in fig. 7.1. Debye rings are observed with no preferred orientation and indexed to $\beta - Ga_2O_3$ using JCPDS PDF card no. 00-043-1012, with a slight offset to higher 2θ due to lattice contraction upon incorporation of Al.

XRD patterns for CCS films A1 and A2 on *c*-plane sapphire on the Ga-rich side (5 % Al) are shown in fig. 7.2. Both samples show $[\bar{2}01]$-oriented $\beta - Ga_2O_3$ relative to the sapphire surface, as has been previously reported [186, 262]. Figure 7.3 shows the angles of all diffraction planes listed on the $\beta - Ga_2O_3$ PDF card (00-043-1012) within the region of the frame ($16° < 2\theta < 52°$) relative to $[\bar{2}01]$ for the identification of off-axis peaks. The only off-axis planes with angles in our experimental windows, which are $-40° < \chi < 40°$ for $16° < 2\theta < 35°$, and $-30° < \chi < 30°$ for $35° < 2\theta < 52°$, are $[\bar{4}01]$ at ($2\theta = 30.5°,\ \chi = -23.4°$), $[\bar{2}02]$ at ($2\theta = 31.7°,\ \chi = 22.5°$), $[\bar{6}02]$ at ($2\theta = 49.6°,\ \chi = -14.5°$), and $[\bar{4}03]$ at ($2\theta = 51.0°,\ \chi = 14.1°$). Therefore we identify $[\bar{4}01]$ and $[\bar{2}02]$ as indicated in fig. 7.2a. $[\bar{6}02]$ and $[\bar{4}03]$ both lie at the high-2θ edge of the detection window and have lower intensities so are not observed. Due to the continuous rotation of ϕ during data collection, $[\bar{4}01]$ and $[\bar{2}02]$ peaks are duplicated above and below the $\chi = 0$ axis. However, pole figures show that the films are six-fold rotationally symmetric (fig. 7.4), so both peaks appear in the frame before ϕ completes the first 60° of rotation, rather than at 180° intervals. The fact that $\beta - Ga_2O_3$ films are six-fold symmetric despite sapphire planes being three-fold symmetric means that the $(\bar{2}01)$ surface nucleates in two opposite directions for each equivalent sapphire direction. This also suggests the possibility of twinning on $(\bar{2}01)$. The relative orientation of $\beta - Ga_2O_3$ and sapphire unit cells is shown in fig. 7.5 for one of the six possible in-plane orientations, and the shared oxygen atoms at the interface are highlighted. From the 30° offset in ϕ between $\beta - Ga_2O_3$ and sapphire peaks in pole figures (fig. 7.4) we find an in-plane epitaxial relationship $[201]_{Ga_2O_3} \parallel [\bar{2}10]_{Sapphire}$ (fig. 7.5).

Examination of the $[400]/[\bar{4}01]$ pole figure from sample A1 (fig. 7.4) taken at $2\theta = 30°$ with a wide enough window to see $[\bar{4}01]$ at $\chi = 23.4°$ and $[400]$ at $\chi = 53.7°$ also shows two extra peaks between $\chi = 10°$ and $\chi = 20°$ (highlighted in blue in the figure). These peaks do not appear for Ga_2O_3 films below ≈ 100 nm and are related to the loss of orientation as film thickness is increased.

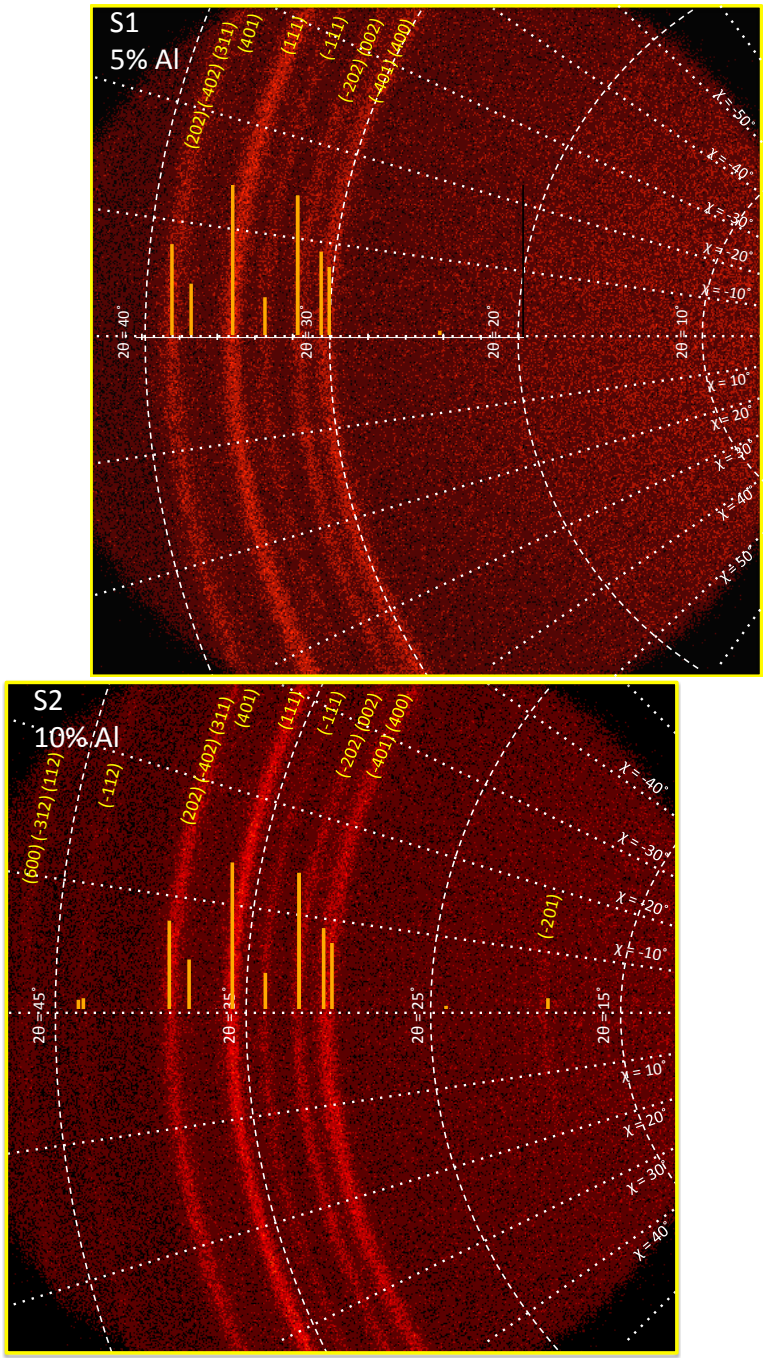

Figure 7.1: 2D diffraction patterns for CCS samples S1 (top) S2 (bottom) on SiOx at the Ga-rich side of the respective films: 5 % Al for S1 and 10 % Al for S2. Overlaid on each figure is the $\beta - Ga_2O_3$ XRD pattern from JCPDS PDF card no. 00-043-1012, slightly offset to higher 2θ (accounting for the lattice contraction relative to pure Ga_2O_3) matching the observed diffraction patterns. Debye rings with uniform brightness indicate no preferred orientation.

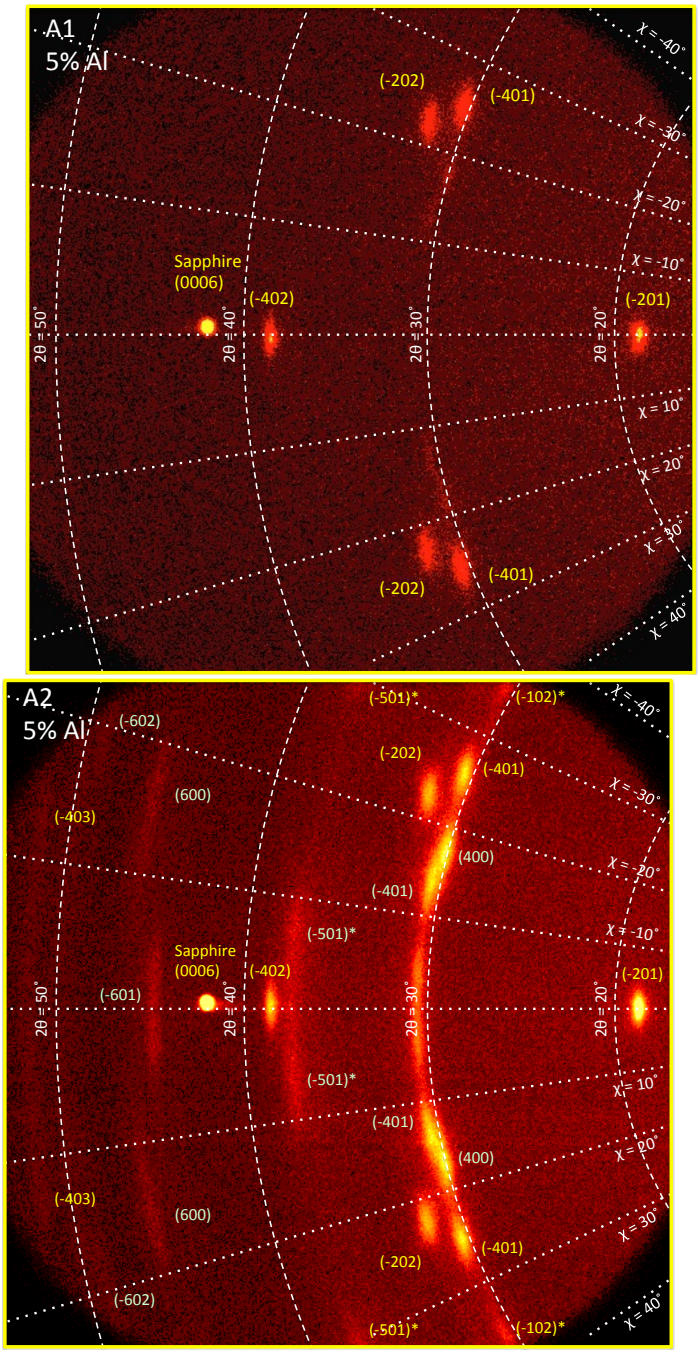

Figure 7.2: 2D diffraction patterns for CCS samples A1 (top) and A2 (bottom) on c-plane sapphire at the Ga-rich side of the film (5 % Al). Peaks in A1 correspond to $[\bar{2}01]$-oriented $\beta - Ga_2O_3$. Sample A2 shows the same $[\bar{2}01]$-oriented $\beta - Ga_2O_3$ pattern, and additional peaks caused by twinning on the (101) plane as film thickness is increased. $[\bar{2}01]$-oriented peaks are labeled in yellow, and twinned peaks are labeled in green. The asterisk indicates a $C2/m$ forbidden peak (table 7.3).

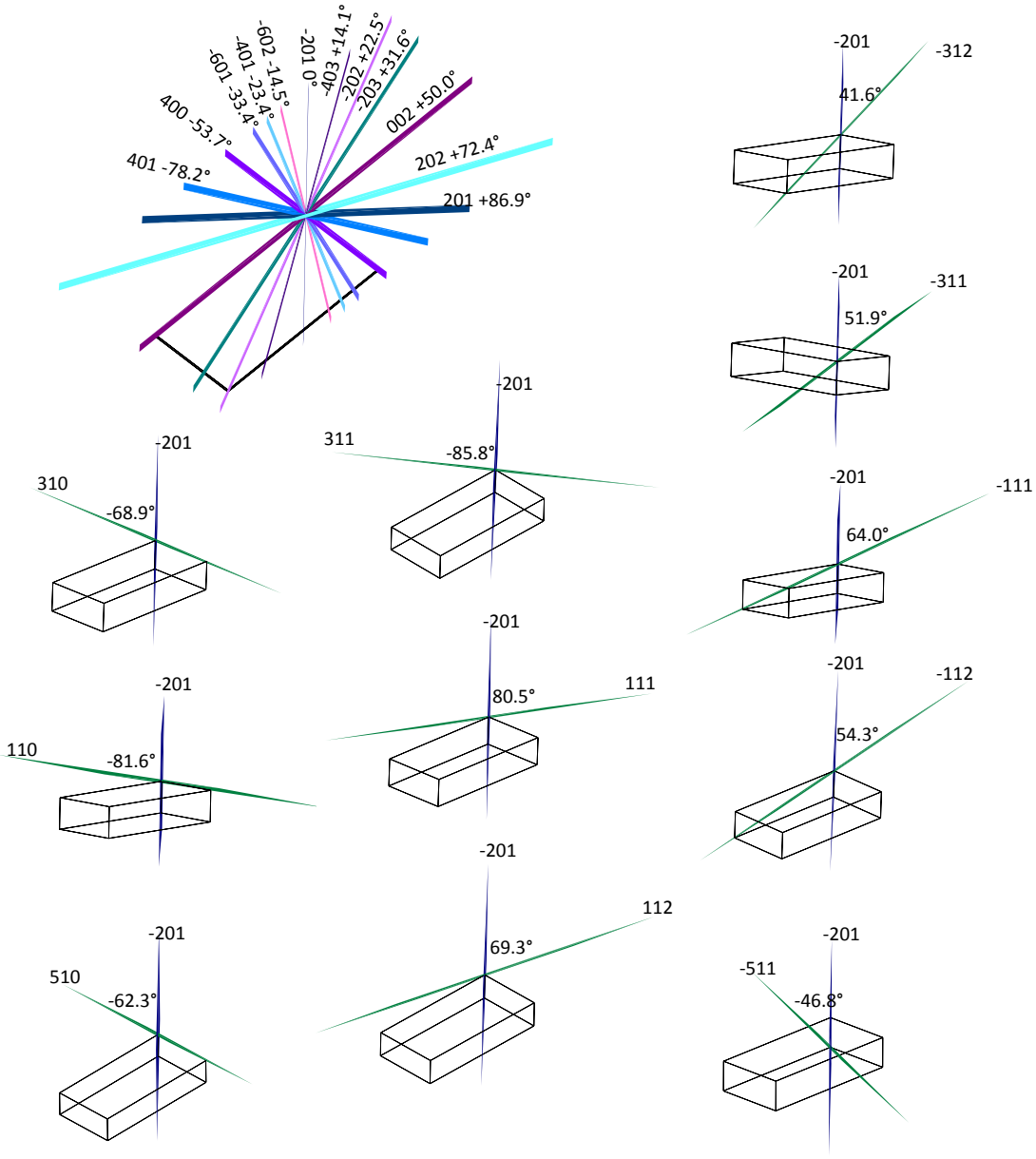

Figure 7.3: χ angles of lattice planes of all reflections listed in JCPDS PDF card no. 00-043-1012 for $\beta - Ga_2O_3$ within the range $16° < 2\theta < 52°$ for a $[\bar{2}01]$-oriented sample positioned vertically in the diffractometer with the surface facing left, and incident X-rays traveling into the page.

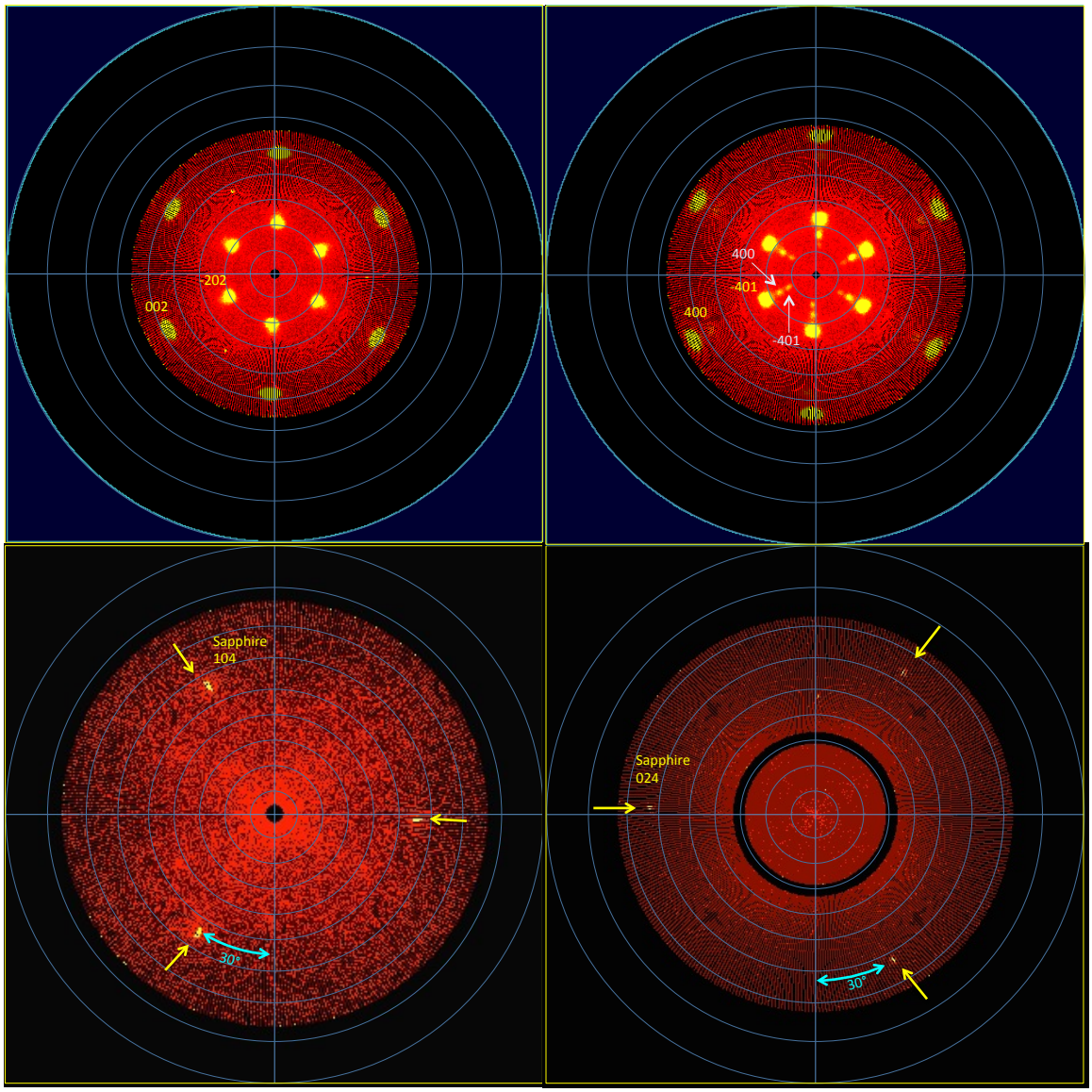

Figure 7.4: Pole figures of CCS sample A1 on the Ga-rich side (5 % Al) showing off-axis angles of $\beta - Ga_2O_3$ lattice planes for a $[\bar{2}01]$-oriented film on *c*-plane sapphire. Sapphire planes are three-fold rotationally symmetric while $\beta - Ga_2O_3$ are six-fold symmetric indicating two film orientations for each sapphire direction. From the 30° offset between sapphire (104) and (024) and $\beta - Ga_2O_3$ lattice planes one can deduce the in-plane epitaxial relationship $[201]_{Ga_2O_3} \parallel [\bar{2}10]_{Sapphire}$. The relative orientation of $\beta - Ga_2O_3$ and sapphire unit cells is depicted in fig. 7.5.

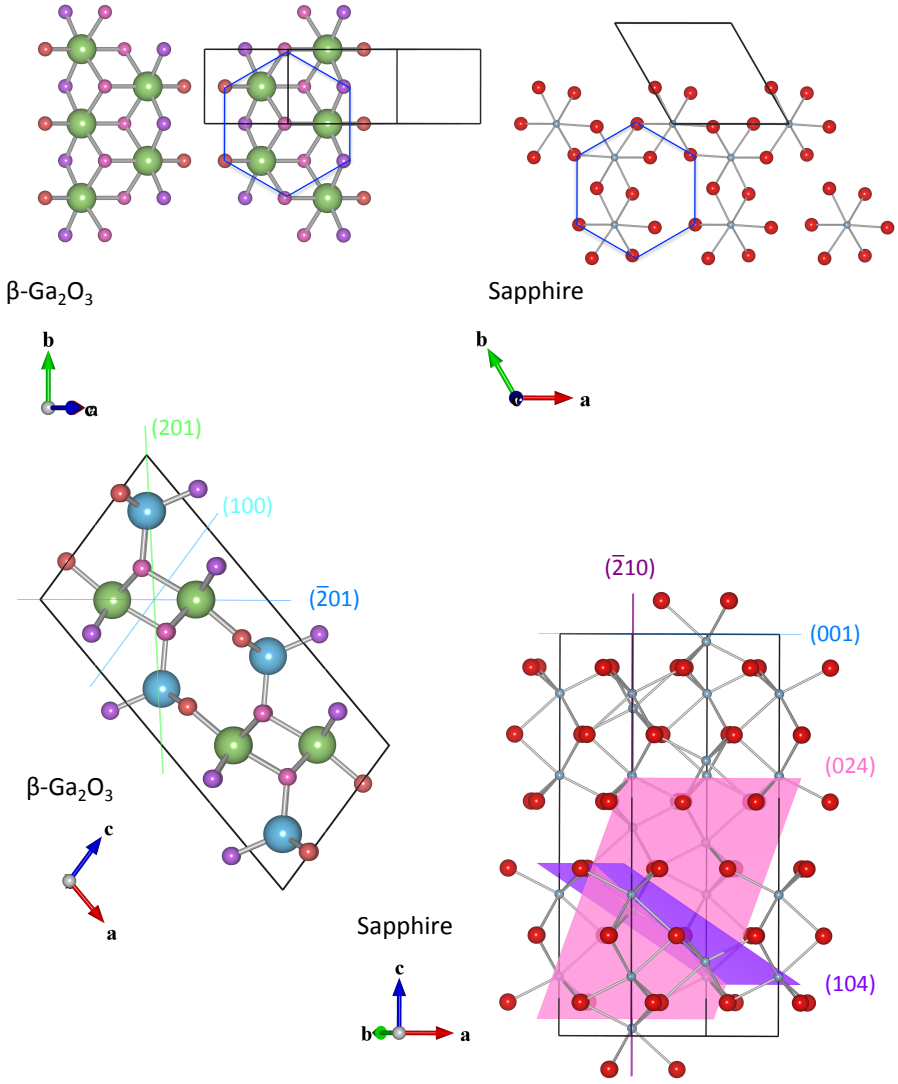

Figure 7.5: Relative orientation of $\beta - Ga_2O_3$ and $\alpha - Al_2O_3$ unit cells for a $[\bar{2}01]$-oriented film on c-plane sapphire, showing a 30° offset between sapphire (104), sapphire (024), and $\beta - Ga_2O_3$ (100) lattice planes as observed in fig. 7.4, and an in-plane epitaxial relationship: $[201]_{Ga_2O_3} \parallel [\bar{2}10]_{Sapphire}$. Hexagons in upper figure highlight matching oxygen atoms at the Ga_2O_3 $(\bar{2}01)$/sapphire (001) interface.

According to the PDF card, the only allowed $\beta - Ga_2O_3$ peaks near that angle in 2θ belong to [400] at $2\theta = 30.1°$, [$\bar{4}$01] at $2\theta = 30.5°$, and [110] at $2\theta = 30.3°$, and [110] has 50x lower intensity than the other two. The two extra peaks are faintly visible in fig. 7.2a, and based on the slight difference in 2θ one may assign the peak closer to $\chi = 10°$ to [$\bar{4}$01] and the peak closer to $\chi = 20°$ to [400]. As mentioned in table 7.1, sample A2 (fig. 7.2b) is about five times thicker on the Ga-rich side than A1 (fig. 7.2a). In A2, the extra [400] and [$\bar{4}$01] peaks are much brighter than in A1, and multiple other peaks are visible as well; however, the original [$\bar{2}$01]-oriented peaks only increase in brightness slightly by comparison. If the extra peaks were due to a simple 40° rotation about the **b** axis then the [$\bar{2}$02] peaks at $2\theta = 31.7°$ would be duplicated as well, and additionally the rotated [002] peak at the same 2θ but initially at $\chi = 50°$ would be visible in the frame, yet neither are observed. Therefore the loss of orientation is most likely a result of twinning. Twinning on ($\bar{2}$01) would not lead to a change in the off-axis angles relative to [$\bar{2}$01], so there must be another twin plane. A prime candidate is (100), which is known to be a twin plane in $\beta - Ga_2O_3$ single crystals [52]; however, twinning on (100) would not explain how (400) peaks become duplicated.

Instead of hoping for a lucky guess to find the correct twin plane, a more systematic way of searching is described. A vector normal to the lattice plane (hkl) is $h\mathbf{h} + k\mathbf{k} + l\mathbf{l}$, where {**h**,**k**,**l**} are the reciprocal lattice vectors obtained from the direct lattice vectors [54]

$$\mathbf{a} = \begin{pmatrix} 12.23 \\ 0 \\ 0 \end{pmatrix} \quad \mathbf{b} = \begin{pmatrix} 0 \\ 3.04 \\ 0 \end{pmatrix} \quad \mathbf{c} = \begin{pmatrix} 5.80\cos(103.7°) \\ 0 \\ 5.80\sin(103.7°) \end{pmatrix}$$

by the transformations

$$\mathbf{h} = 2\pi\frac{\mathbf{b}\times\mathbf{c}}{\mathbf{a}\cdot(\mathbf{b}\times\mathbf{c})} \quad \mathbf{k} = 2\pi\frac{\mathbf{c}\times\mathbf{a}}{\mathbf{a}\cdot(\mathbf{b}\times\mathbf{c})} \quad \mathbf{l} = 2\pi\frac{\mathbf{a}\times\mathbf{b}}{\mathbf{a}\cdot(\mathbf{b}\times\mathbf{c})}$$

The angle ξ between two planes with Miller indices $(h_1k_1l_1)$ and $(h_2k_2l_2)$ can be found by taking the scalar product of the respective vectors $\mathbf{u} = h_1\mathbf{h} + k_1\mathbf{k} + l_1\mathbf{l}$ and $\mathbf{v} = h_2\mathbf{h} + k_2\mathbf{k} + l_2\mathbf{l}$ and solving for ξ

$$u_1v_1 + u_2v_2 + u_3v_3 = |\mathbf{u}|^2|\mathbf{v}|^2\cos\xi_{uv} \tag{7.1}$$

where the subscripts on u and v indicate the vector component. This has been done in fig. 7.3 to calculate the angles of lattice planes in Ga_2O_3 away from ($\bar{2}$01), equivalent to χ for a [$\bar{2}$01]-oriented

film. The transformation matrix to reflect a vector through a plane running through the origin with Miller indices (hkl) and normal vector $\mathbf{n} = \frac{h\mathbf{h}+k\mathbf{k}+l\mathbf{l}}{|h\mathbf{h}+k\mathbf{k}+l\mathbf{l}|}$ is $A = \mathcal{I} - 2\mathbf{n}\mathbf{n}^T$, or

$$A = \begin{pmatrix} 1-2n_1^2 & -2n_1n_2 & -2n_1n_3 \\ -2n_1n_2 & 1-2n_2^2 & -2n_2n_3 \\ -2n_1n_3 & -2n_2n_3 & 1-2n_3^2 \end{pmatrix} \tag{7.2}$$

Since the twinning plane is not known in advance, $\mathbf{n}$ can be defined instead as a function of angle ξ away from the $(\bar{2}01)$ plane using rotation matrices. For rotations on the $\mathbf{b}$ axis the formula is

$$\mathbf{n}(\xi) = \begin{pmatrix} \cos\xi & 0 & -\sin\xi \\ 0 & 1 & 0 \\ \sin\xi & 0 & \cos\xi \end{pmatrix} \frac{-2\mathbf{h}+\mathbf{l}}{|-2\mathbf{h}+\mathbf{l}|} \tag{7.3}$$

Therefore the location χ of a twinned peak with Miller indices (hkl) after twinning on a plane rotated around $\mathbf{b}$ by an angle ξ from $(\bar{2}01)$ can be found by applying eq. (7.2), with $\mathbf{n}(\xi)$ determined by eq. (7.3), to the appropriate vector $\mathbf{v}$ normal to the plane

$$\mathbf{v}_{\text{twin}} = A(\xi)\mathbf{v} = A(\xi)(h\mathbf{h} + k\mathbf{k} + l\mathbf{l})$$

and then computing the angle of $\mathbf{v}_{\text{twin}}$ relative to $(\bar{2}01)$ using eq. (7.1). Applying the above procedure to all peaks with diffraction angle in the range $18^\circ < 2\theta < 52^\circ$, and scanning ξ from -90° to 90° produces a plot of twinned χ locations vs. twinning angle ξ which is shown in fig. 7.6.

Examination of the figure shows that the only twin planes producing [400] and $[\bar{4}01]$ peaks within the range $10^\circ < \chi < 20^\circ$ are at angles $\xi = -18^\circ$ and $\xi = 72^\circ$. Rotating -18° away from $(\bar{2}01)$ does not coincide with any obvious twinning planes (fig. 7.3), but at 72.4° we find (101). Figure 7.7 shows that (101) and $(\bar{2}01)$ both run parallel to different faces of the fcc oxygen sublattice in $\beta - Ga_2O_3$, suggesting that twinning occurs on oxygen atoms in these two planes. The location of other $C2/m$ allowed peaks after twinning on (101) are listed in table 7.2. In addition to $[\bar{4}01]$ and [400] already mentioned, several of the other twinned peaks in fig. 7.2b are identified: $[\bar{6}01]$, [600], $[\bar{6}02]$, and $[\bar{4}03]$. Comparing the relative intensities of these additional peaks to $[\bar{4}01]$ and [400] shows that they are too weak to be observed in sample A1 (fig. 7.2a), which only shows faint signs of twinning due to its smaller thickness. A series of pole figures from sample A2 taken at several (fixed) values of 2θ and covering a wider range in χ (radial axis) show several more peaks appearing at their expected

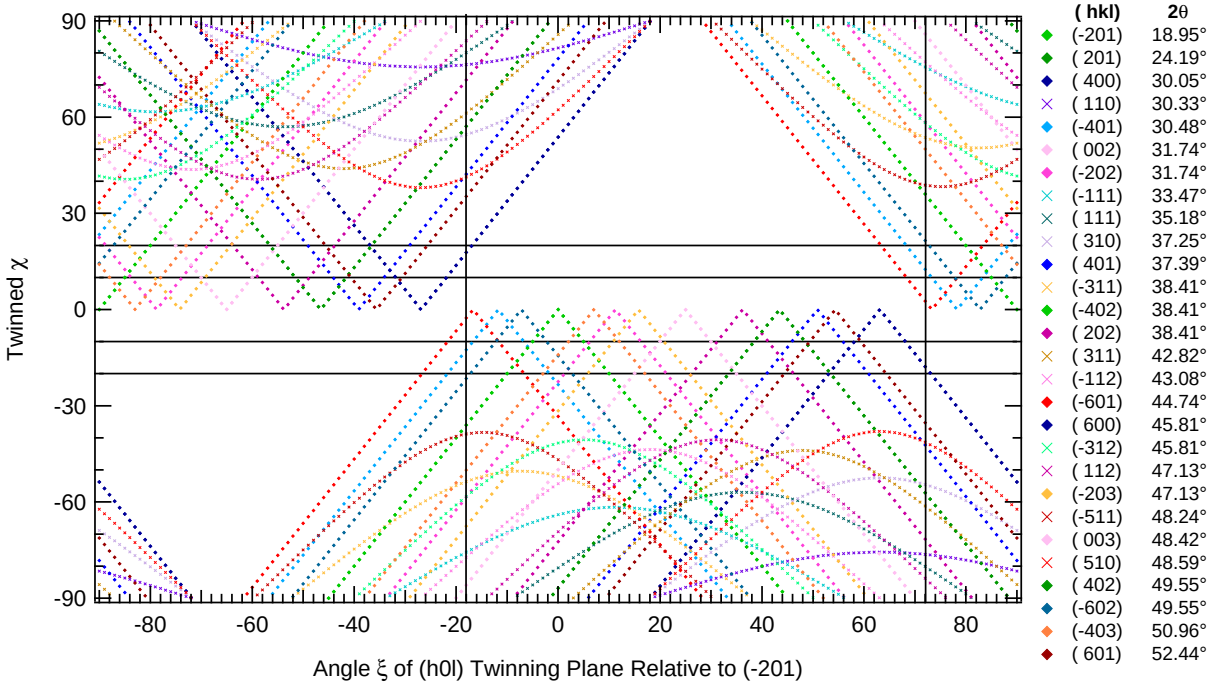

Figure 7.6: χ locations of twinned peaks as a function of the angle of the twinning plane away from $(\bar{2}01)$. The regions between $10° < |\chi| < 20°$ where twinned [400] and $[\bar{4}01]$ peaks appear are highlighted. Twinning at these angles also explains the appearance of $[\bar{6}01]$ at $(2\theta = 44.7°, \chi = -1.6°)$ and $[\bar{6}01]$ at $(2\theta = 44.7°, \chi = -1.6°)$, and the non-appearance of twinned [002] and $[\bar{2}02]$ peaks in the $-40° < \chi < 40°$ window of fig. 7.2b.

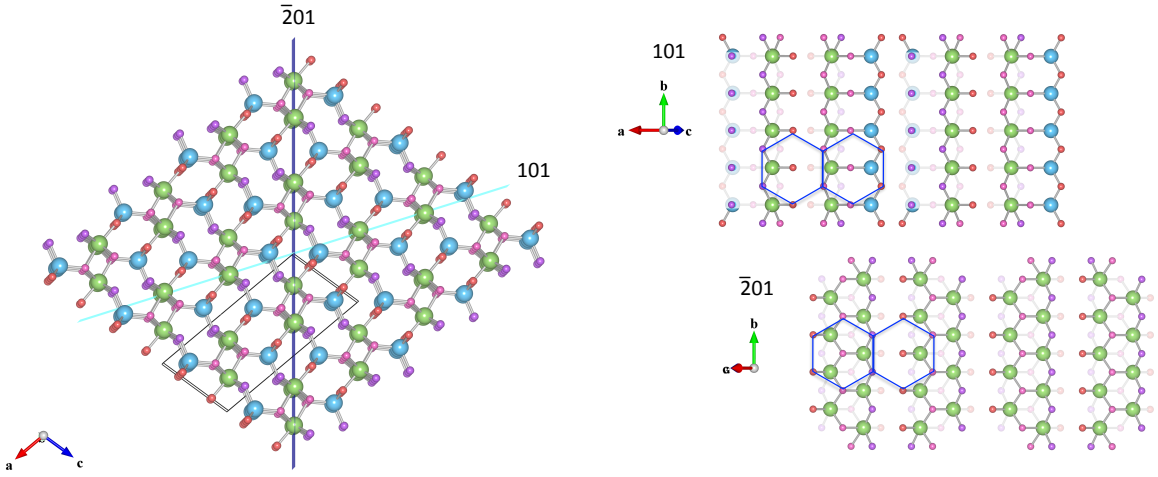

Figure 7.7: $(\bar{2}01)$ and (101) planes in the $\beta - Ga_2O_3$ structure. Left: $\beta - Ga_2O_3$ crystal oriented in the same way as fig. 7.3. These two planes run parallel to different faces of the oxygen fcc sublattice (the third one being (010)). Right: O atomic arrangement in each plane. The blue hexagon in $(\bar{2}01)$ connects the same O atoms as in fig. 7.5, and also connects O atoms in (101), highlighting the similar atomic arrangements in the two planes.

Table 7.2: Off-axis locations of $\beta - Ga_2O_3$ peaks on PDF card no. 00-043-1012 within the range $18° < 2\theta < 52°$ for a $[\bar{2}01]$-oriented thin film before and after twinning on the (101) plane. The χ locations before twinning are calculated using the lattice parameters given in Ahman et al. [106]. The relative intensities (out of 100) are shown in parentheses next to the Miller indices. An asterisk indicates a $C2/m$ forbidden reflection.

Peak (I)	2θ	χ_{orig}	χ_{twin}
$\bar{2}01$ (9)	18.951°	0°	35.15°
201 (4)	24.185°	86.88°	−57.96°
400 (46)	30.054°	−53.78°	−18.62°
110 (1)	30.325°	−81.58°	−76.41°
$\bar{4}01$ (56)	30.484°	23.44°	11.71°
$\bar{1}02$ (*)	30.832°	36.21°	71.36°
002 (93)	31.739°	49.92°	85.08°
$\bar{2}02$ (93)	31.739°	22.49°	57.64°
$\bar{1}11$ (26)	33.472°	63.98°	75.28°
111 (100)	35.179°	80.53°	−80.53°
310 (1)	37.249°	−68.91°	−54.76°
401 (35)	37.393°	−78.26°	−43.10°
$\bar{5}01$ (*)	37.426°	29.30°	5.85°
$\bar{3}11$ (61)	38.405°	51.89°	53.40°
$\bar{4}02$ (61)	38.405°	0°	35.15°
202 (61)	38.405°	72.42°	−72.42°
311 (9)	42.824°	−85.77°	−61.79°
$\bar{1}12$ (8)	43.081°	54.28°	76.63°
$\bar{6}01$ (5)	44.740°	33.35°	1.80°
600 (24)	45.807°	−53.78°	−18.62°
112 (24)	45.807°	69.28°	−84.40°
$\bar{3}12$ (24)	45.807°	41.65°	57.75°
$\bar{2}03$ (1)	47.126°	31.55°	66.71°
$\bar{5}11$ (3)	48.237°	46.83°	38.70°
003 (1)	48.423°	49.92°	85.08°
510 (18)	48.591°	−62.25°	−41.70°
402 (7)	49.552°	86.88°	−57.96°
$\bar{6}02$ (7)	49.552°	14.45°	20.70°
$\bar{4}03$ (3)	50.956°	14.07°	49.23°
601 (2)	52.436°	−71.27°	−36.12°

Table 7.3: XRD selection rules for $C2/m$ space group. [3]

$(h\,k\,l)$:	$h + k = 2n$
$(h\,0\,l)$:	$h = 2n$
$(0\,k\,l)$:	$k = 2n$
$(h\,k\,0)$:	$h + k = 2n$
$(0\,k\,0)$:	$k = 2n$
$(h\,0\,0)$:	$h = 2n$

locations after twinning on (101) (figs. 7.8 and 7.9). In fact, the only allowed peak in table 7.2 that should be observed but isn't (within the visible range of data) is [$\bar{5}11$], most likely due to its low intensity. Some of the remaining peaks can be identified among $C2/m$ forbidden peaks calculated using eqs. (4.7) and (4.8), including ($\bar{5}01$) and ($\bar{1}02$). Interestingly, none of the peaks predicted by twinning again on the duplicated ($\bar{2}01$) plane at $\chi = 35.2°$ are observed, indicating that ($\bar{2}01$) is probably not a twin plane in $\beta - Ga_2O_3$ after all.

Forbidden reflections including ($\bar{1}02$) were observed before in a selected-area electron-diffraction study on float-zone grown $\beta - Ga_2O_3$ single crystals by Villora et al. [124]. In that study a defect domain size of 2.2–2.8 nm was estimated from the width of the ($10\bar{2}$) reflection using Scherrer's formula (eq. 5.1) and found to be on the same order as inhomogeneously-distributed defect clusters observed in a TEM dark-field image, which induce strain in the localized regions surrounding them and disrupt the $C2/m$ symmetry of the $\beta - Ga_2O_3$ lattice. There is not enough information to identify the microscopic origin of symmetry-breaking defects in my CCS thin films, but it may be related to inhomogeneous strain caused by the substitution of Al on Ga sites, broken symmetry along grain boundaries, or surface roughness, which increases with film thickness during columnar growth.

However, the majority of forbidden peaks are not observed, and forbidden reflections do not account for all of the remaining peaks. Therefore another defect has taken place (or perhaps more than one), giving rise to the peak near ($2\theta = 30.5°,\ \chi = 3°$) in fig. 7.2b. Among all the allowed and forbidden reflections, the only choices with diffraction angles in the range $30° < 2\theta < 31°$ are [400], [110], [$\bar{4}01$] or [$\bar{1}02$]. However, twinned [400] is visible in the same frame at $\chi = 18.6°$ and is clearly at a lower 2θ than the unidentified peak (fig. 7.2b). In addition, (400) is 53.7° away from ($\bar{2}01$), and ($\bar{4}01$) is 23.4° away from ($\bar{2}01$), yet no extra [$\bar{4}02$] peaks are observed at those values of χ in the pole figure (fig. 7.9). Similarly, ($\bar{1}02$) is 13.7° away from both (001) and ($\bar{1}01$), yet duplicated [002] and [$\bar{2}02$] peaks are missing in fig. 7.8. Therefore the peak is tentatively assigned to (110), which is at least 76° away (in χ) from any of the ($h0l$) planes considered. Similarly, the unidentified peak in the [400] pole figure of fig. 7.8 near $\chi = 30°$ is tentatively assigned (010) due to the absence of any other possibilities in the range $29° < 2\theta < 30°$. However, (010) is 90° away from all ($h0l$) peaks, and the reason it appears at $\chi = 30°$ is not clear at present.

Comparing the intensities of twinned peaks in fig. 7.2a and fig. 7.2b shows that after twinning

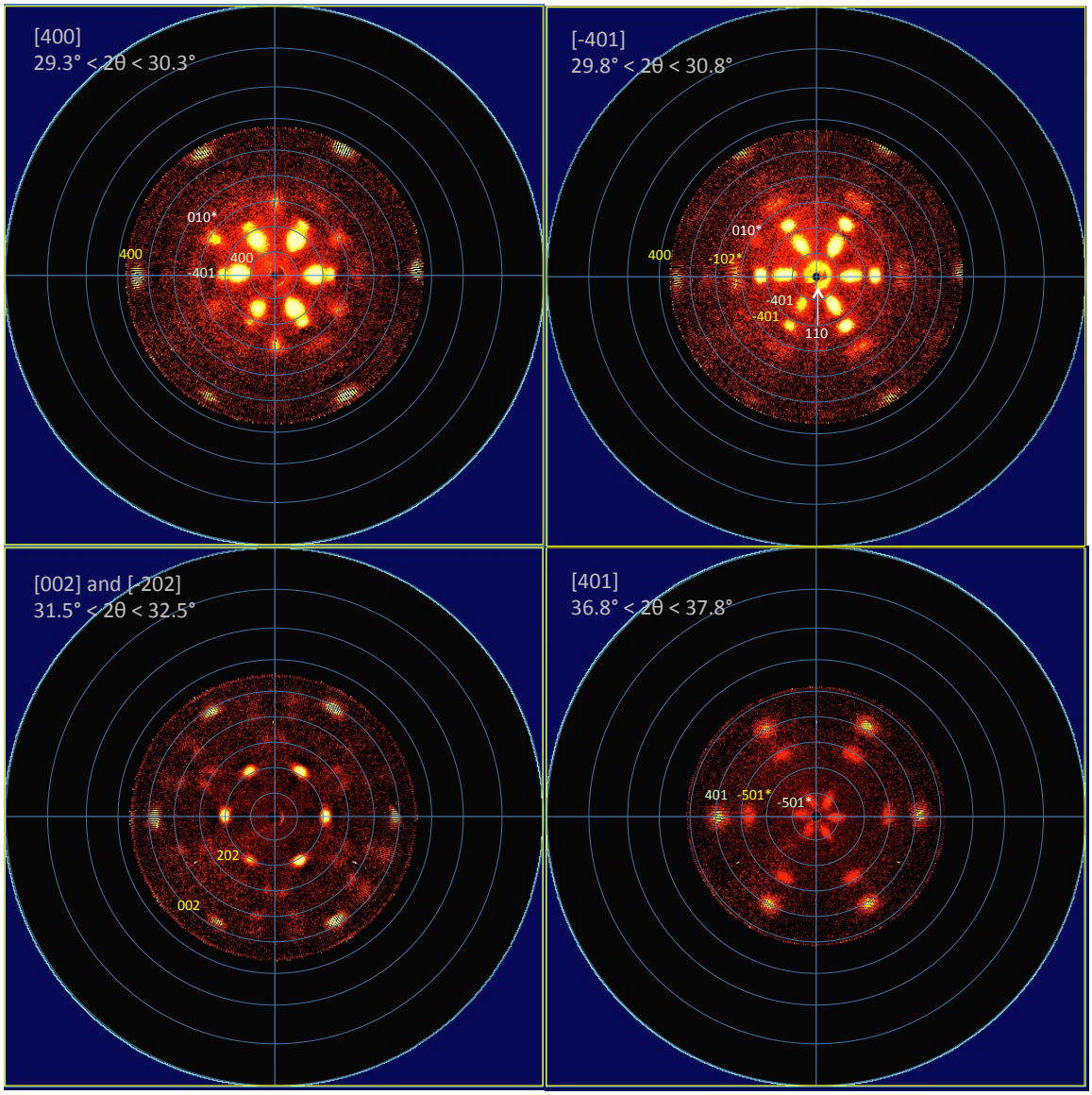

Figure 7.8: Pole figures of CCS sample A2 on the Ga-rich side (5 % Al) showing orientation of $\beta - Ga_2O_3$ lattice planes. [$\bar{2}$01]-oriented peaks are labeled in yellow, (101) twinned peaks are labeled in green, and tentative assignments not arising from twinning are labeled in white. The asterisk indicates a $C2/m$ forbidden peak (table 7.3).

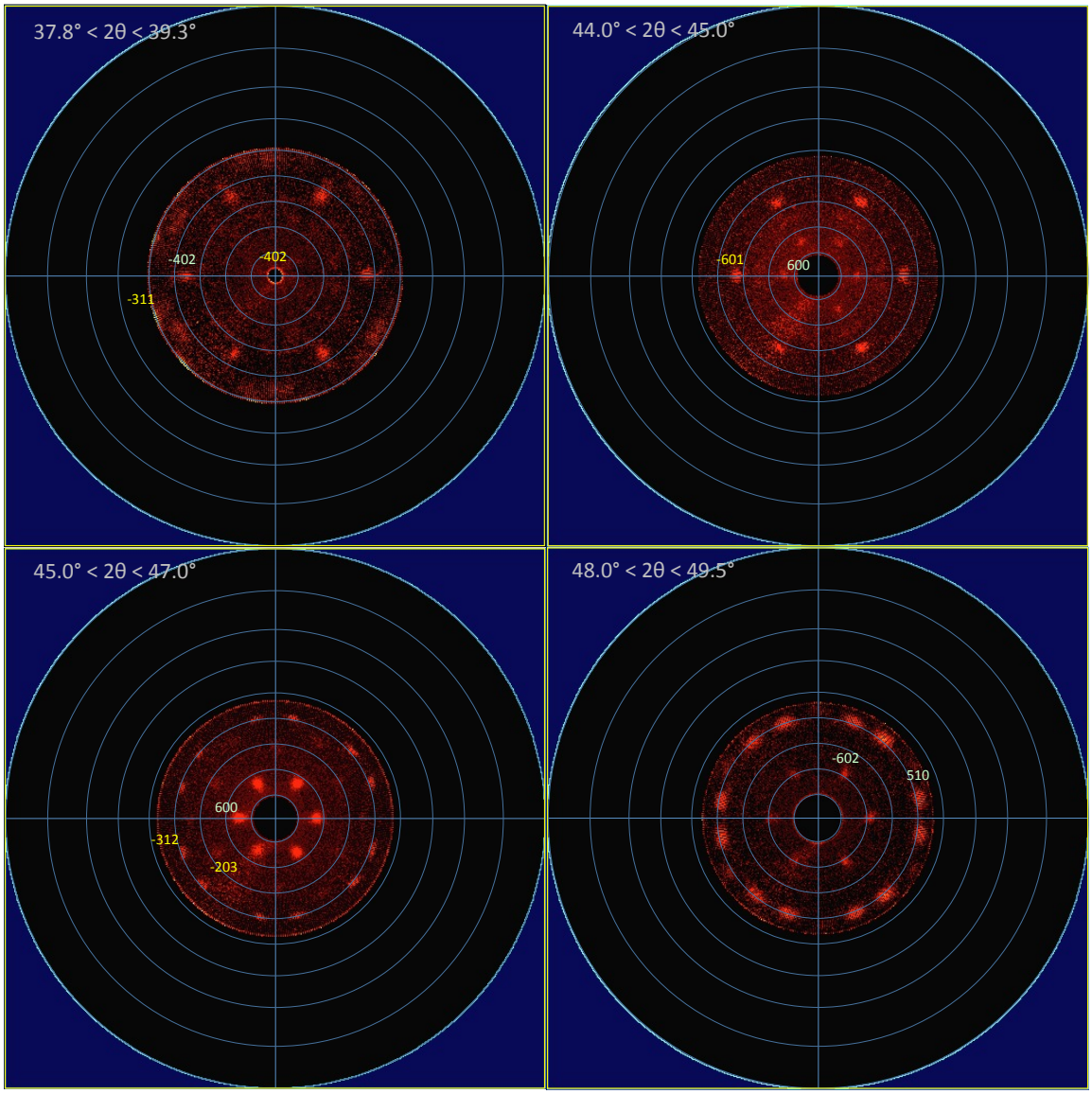

Figure 7.9: Pole figures of CCS sample A2 on the Ga-rich side (5 % Al) showing orientation of $\beta - Ga_2O_3$ lattice planes. [$\bar{2}$01]-oriented peaks are labeled in yellow, and twinned peaks are labeled in green.

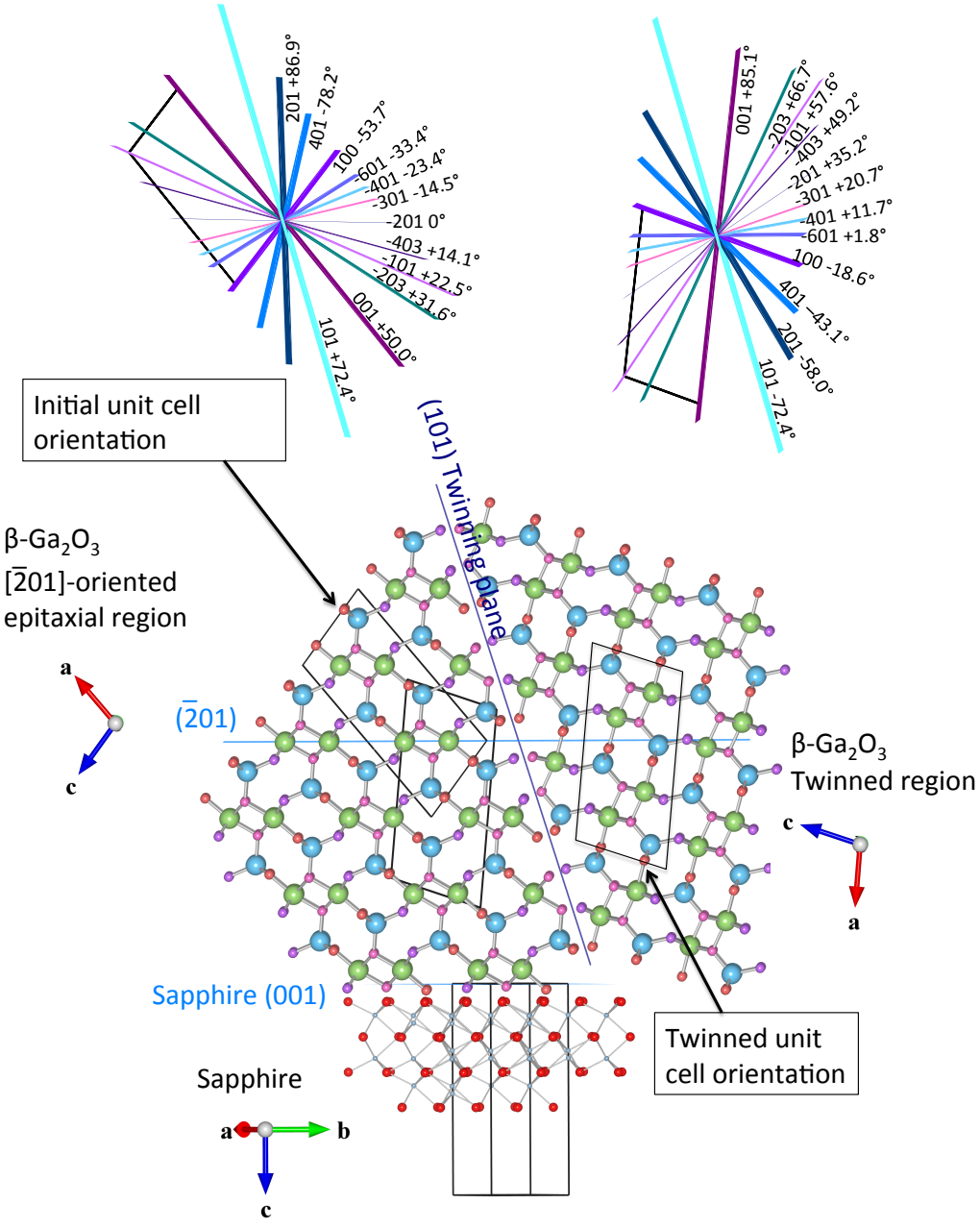

Figure 7.10: Crystal model of a (101)-twinned region on a [$\bar{2}$01]-oriented epitaxial $\beta - Ga_2O_3$ thin film on sapphire (001), and χ angles of ($h0l$) lattice planes before and after twinning. In addition to reflection, translation along (101) has been applied to avoid closely-spaced cation sites at the twin boundary, in such a way that shared O bonds are still either 3- or 4-coordinated.

begins in film thicknesses greater than 100 nm, the twinned [400] and [$\bar{4}$01] peaks increase in brightness faster than [$\bar{2}$01]-oriented peaks, indicating faster growth of twinned regions than epitaxial regions. This could happen if twinning exposes lower-energy surfaces in twinned grains than [$\bar{2}$01]-oriented grains. A crystal model of a (101)-twinned region on a [$\bar{2}$01]-oriented epitaxial $\beta - Ga_2O_3$ thin film (fig. 7.10) shows that the unit cell of the twinned region is more nearly vertically-aligned than in the [$\bar{2}$01]-oriented region, with (100) making an angle of 18.8° away from normal and (001) making an angle of 5.0° away from vertical. A theoretical study by Bermudez [150] found that the two lowest-energy surfaces in $\beta - Ga_2O_3$ are both parallel to (100), and the third-lowest-energy surface is parallel to (001), conclusions which were later verified experimentally using scanning tunneling microscopy by Lovejoy et al. [151]. Therefore it is possible that the twinned region allows for vertical grain growth with more energetically-favorable exposed surfaces than the [$\bar{2}$01]-oriented region, an energy difference which would grow as film thickness and roughness increased. Further TEM study would help elucidate if this is indeed the case, or if the faster growth of twinned regions is simply the result of a lack of substrate-induced strain, which is present in the epitaxial [$\bar{2}$01]-oriented regions due to the 6.6 % mismatch between oxygen atoms in the ($\bar{2}$01) plane of $\beta - Ga_2O_3$ and the (0001) plane of sapphire.

In summary, twinning on (101) has been found to occur in epitaxial $\beta - Ga_2O_3$ films when the film thickness increases past 100 nm. This places an upper limit on the thickness of films on sapphire (0001) if epitaxy is required. To the best of my knowledge, there have been no previous reports of twinning on this plane in $\beta - Ga_2O_3$; a tendency to twin on (100) is well known in $\beta - Ga_2O_3$ single crystals, and [$\bar{2}$01]-oriented $\beta - Ga_2O_3$ films nucleate in opposite directions simultaneously on the sapphire (0001) surface, yet twinning on neither of those planes was observed. As the film thickness increases further to 750 nm additional peaks appear whose origin was not found; however, by using eqs. (7.1) to (7.3), further twinning on any other planes parallel to the **a**, **b**, or **c** axes was ruled out as a possibility.

7.2 XRD of $(Al_xGa_{1-x})_2O_3$: Structural Changes with Al Incorporation

Integrated diffraction patterns of CCS samples S1 and S2 on SiOx, and A1 and A2 on sapphire, are shown in fig. 7.11 as a function of Al concentration. To produce these images, the 2D diffraction pattern at each point was integrated over a wide range of χ to produce line scans of intensity vs. 2θ,

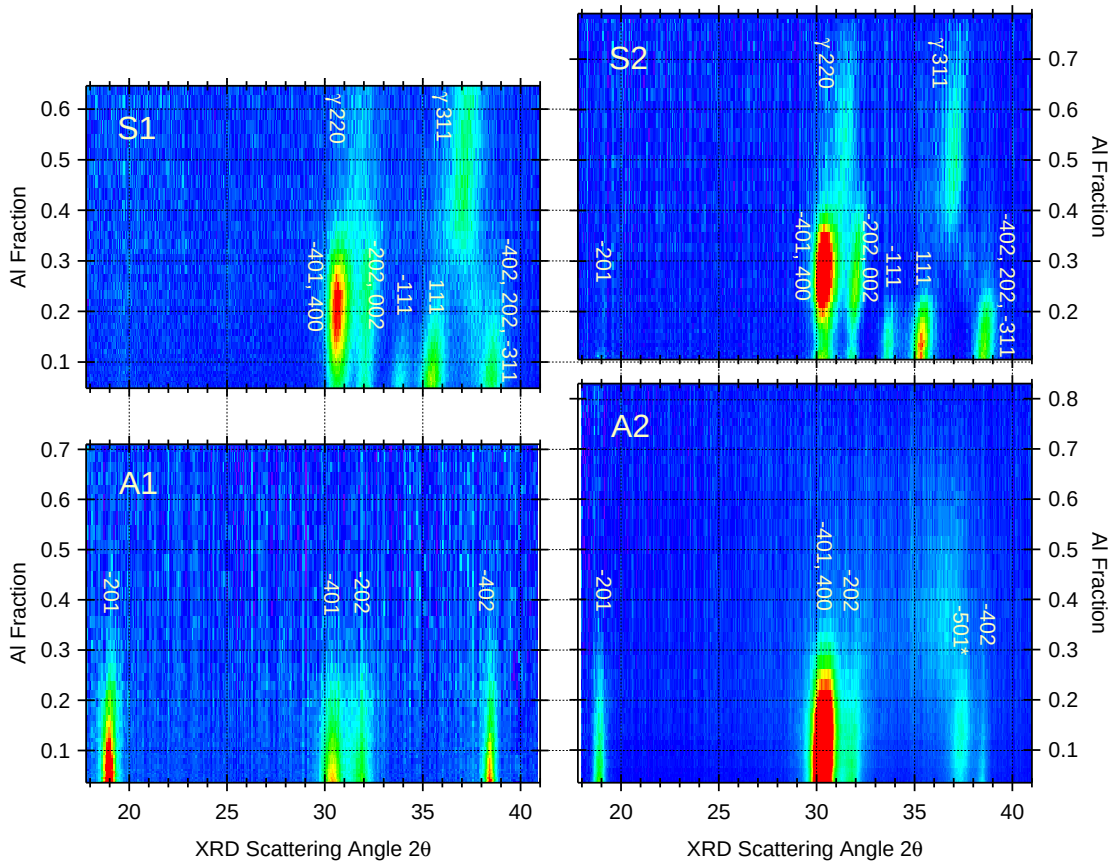

Figure 7.11: Integrated $\theta - 2\theta$ diffraction patterns for CCS samples S1 and S2 on silicon with native oxide, and A1 and A2 on sapphire, as a function of Al fraction x.

the background was subtracted, and the intensity was scaled to normalize for a continually changing film thickness. The y-axis Al concentration comes from XPS fitting as described in section 4.4.3, and the thickness comes from spectroscopic ellipsometry, by fitting the transparent wavelength region to a Cauchy model section 4.6.3. Intensities of diffraction peaks in fig. 7.11 therefore reflect the degree of crystallinity and are comparable between samples.

All samples belong to the $\beta - Ga_2O_3$ phase at low Al concentration, as shown in the previous section. The integrated diffraction patterns of samples on sapphire (A1 and A2) appear different from samples on amorphous silicon oxide due to their $[\bar{2}01]$-orientation, and A2 appears different from A1 due to the inclusion of many more twinned peaks near $2\theta = 30°$. As the alloy parameter x increases

past 0.25 in sample A1, and 0.35 in sample A2, a transition to amorphous is observed, indicated by a lack of diffraction peaks. A2 does show a broad structure at $2\theta \approx 37°$ from $0.25 < x < 0.55$ that doesn't appear in A1. This broad feature was also observed in some of my post-annealed films at annealing temperatures above 400 °C and tentatively assigned to a defective pre-γ phase. In those films, post-annealing to 700 °C caused the feature to become more well-defined so that identification with the γ phase was not as ambiguous (chapter 6). Samples S1 and S2 do not become amorphous as x is increased, but instead transition to the γ phase with well-defined peaks. In post-annealed $(Al_xGa_{1-x})_2O_3$ films with $x > 0.1$, crystal phases are observed to follow the sequence (amorphous $\rightarrow$ pre-$\gamma \rightarrow \gamma \rightarrow \beta$) as the temperature is raised, and the specific temperatures of each transition increase with x.

High-temperature CCS films S1, A1, S2, and A2 were each deposited at a set point temperature of 800 °C, but the thermocouple was located behind the heating element, not at the sample surface; after comparing to post-annealed films, a significant deviation to lower temperature seems likely. When depositing on sapphire, a polycrystalline composite SiC/graphite susceptor was placed between the SiC heating element and the substrate. Sapphire is at least 80 % transparent to infrared radiation up to a wavelength of 5 µm, so the susceptor was intended to absorb radiation and transmit heat to the substrate by conduction. A susceptor was not used when depositing on SiOx because Si was assumed to absorb heat more efficiently due to its lower transparency in the $1 - 5$ µm range—around 55%. In hindsight this was probably a mistake. Although the susceptor absorbs more radiation than sapphire, poor thermal contact could have prevented efficient heat transfer. Furthermore, the spectral emittance of our SiC heating element extends to much longer wavelengths, at least 15 µm, where the transmittance of sapphire is nearly zero. Nevertheless a susceptor was used, and as a result we see a transition to amorphous or pre-γ, rather than to the γ phase, for CCS films on sapphire. Based on the results of our post-annealing experiments, we can estimate that the actual surface temperature was approximately 600 °C for films A1 and A2 on sapphire, and a little over 700 °C for films S1 and S2 on SiOx, based on the fading of $\gamma - Al_2O_3$ peaks above $x = 0.7$.

Detailed XRD results for samples A1 and A2 on sapphire are presented in figs. 7.12 and 7.13, and analogous results for samples S1 and S2 on SiOx are presented in figs. 7.14 and 7.15. Integrated diffraction patterns were fit with symmetric Voigt lineshapes to quantify the changes in intensities and diffraction angles of individual peaks. XRD diffraction angles of each peak are also plotted

against theoretical values of 2θ assuming d-spacings for each peak vary linearly between the endpoint values given in the PDF cards corresponding to the $\beta - Ga_2O_3$ (00-043-1012) and $\gamma - Al_2O_3$ (00-029-0063) phases. Substitutional incorporation of Al in $\beta - Ga_2O_3$ or $\gamma - Ga_2O_3$ is evidenced by constant peak intensities, and agreement between measured and theoretical 2θ shifts.

$\beta - Ga_2O_3$ diffraction peaks for CCS films on sapphire disappear completely above $x \approx 0.25$ (A1) and $x \approx 0.32$ (A2). In sample A1 (no buffer layer) the intensity of peaks decreases linearly as soon as x is increased, and the shift in 2θ is less than expected if Al is substituting for Ga in the $(Al_xGa_{1-x})_2O_3$ structure (fig. 7.12). However, sample A2 (on a thick $\beta - Ga_2O_3$ buffer layer), shows nearly constant peak intensities until $x \approx 0.15$, and the shift in 2θ from $0 < x < 0.15$ is closer to the expected trend (although still low) (fig. 7.13). The superior incorporation of Al in sample A2 compared to A1 may be due to the $\beta - Ga_2O_3$ buffer layer, but not because Al_2O_3 layers prefer to nucleate as $\alpha - Al_2O_3$ on the bare sapphire surface rather than incorporating into the film. In previous experiments, we have found that even at growth temperatures up to 1000 °C, Al_2O_3 films on sapphire take the γ phase, rather than the α phase; therefore it is unlikely that the sapphire surface would induce the α phase at lower temperatures. The actual temperature of sample A2 may have been slightly higher than the temperature of A1 during deposition despite identical set points, resulting in Al incorporation further into the film. A higher deposition temperature may also explain the diffuse background structure at $2\theta \approx 37°$ in A2, which is not observed not A1, although that may also be caused by the greater thickness of A2. Alternatively, the superior incorporation in A2 and appearance of the pre-γ structure may be a result of depositing on epitaxial $\beta - Ga_2O_3$ instead of sapphire (0001) directly.

Both samples S1 and S2 on SiOx show 2θ shifts in better agreement with the expected trendlines than samples A1 and A2 on sapphire, indicating the successful incorporation of Al into $(Al_xGa_{1-x})_2O_3$ due to the presumed higher deposition temperature for each of these samples. Therefore any changes in the band gap will be due to the intrinsic nature of each phase and not a loss of crystallinity.

The most surprising feature of the integrated diffraction patterns for CCS films S1 (fig. 7.14) and S2 (fig. 7.15) is the appearance of an intermediate phase between β and γ, which displaces $\beta - Ga_2O_3$ almost immediately above $x = 0.1$ in sample S1, and above $x = 0.18$ in sample S2. This phase was not seen in a different report on [100]-oriented $(Al_xGa_{1-x})_2O_3$ CCS films on MgO substrates [306]. A series of 2D diffraction patterns for sample S2 (fig. 7.16) shows that the increasing intensity of

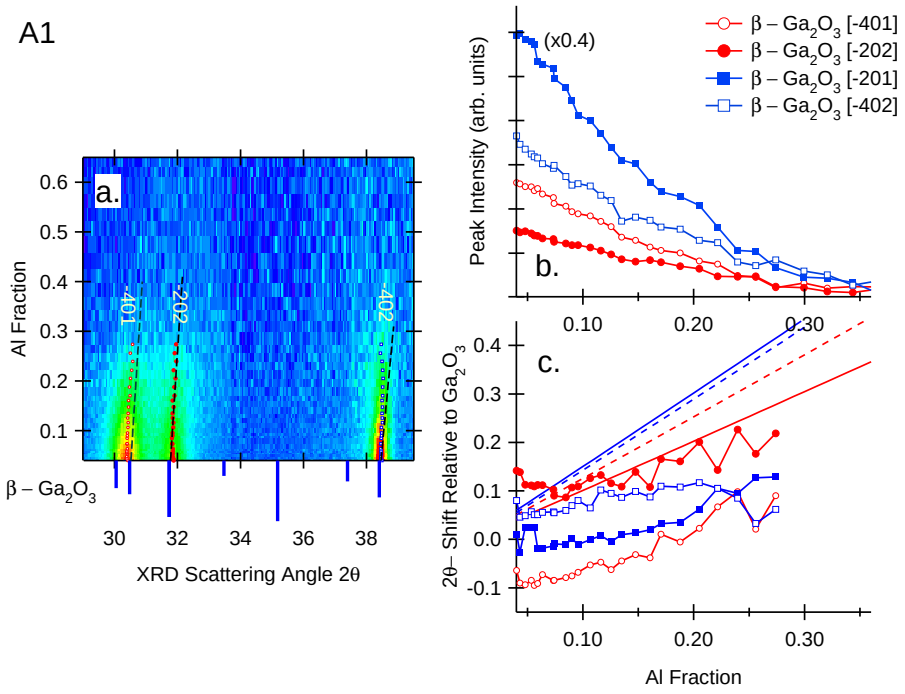

Figure 7.12: a) Integrated XRD pattern for sample A1 (grown directly on sapphire) with markers indicating fitted peak positions. Broken lines are calculated from $\beta - Ga_2O_3$ and $\theta - Al_2O_3$ endpoints given in PDF cards 00-043-1012 and 00-023-1009, assuming no bowing in the d-spacing of each peak as the unit cell contracts. b) Fitted peak intensities as a function of Al concentration. Falling peak intensities mean a growing fraction of the film is not crystalline as x is increased. c) Fitted peak locations relative to their positions in $\beta - Ga_2O_3$ alongside calculated shifts from part a. Deviation from the trendlines is evidence that Al is not incorporating. Diffraction angles of $[\bar{4}01]$ are artificially offset to lower 2θ in the integrated diffraction pattern as a result of twinned [400]. The disappearance of peaks above $x \approx 0.25$ indicates an amorphous $(Al_xGa_{1-x})_2O_3$ film.

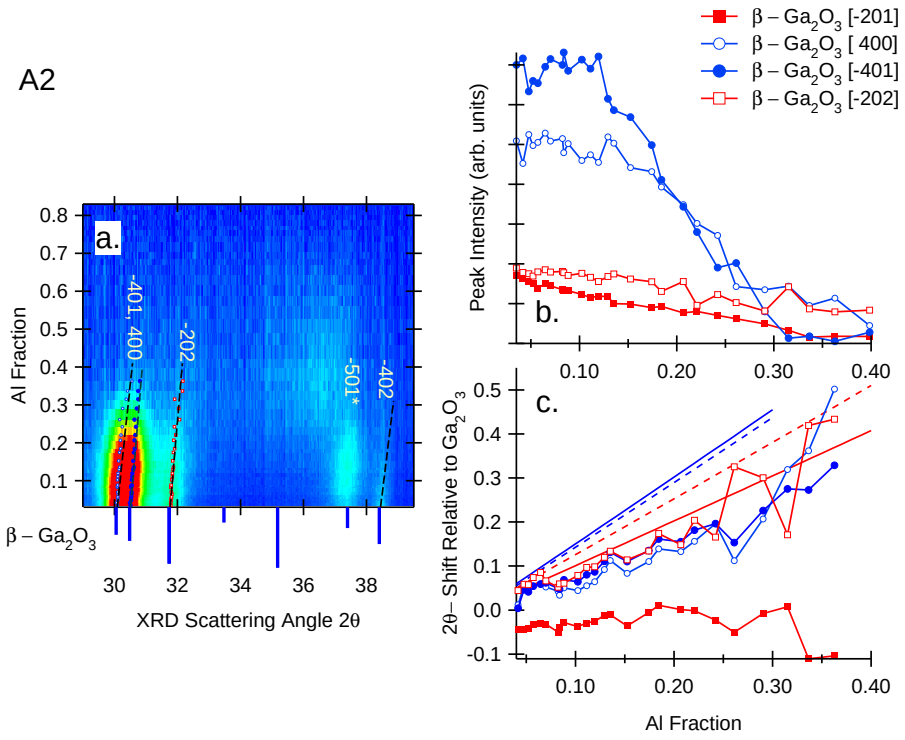

Figure 7.13: a) Integrated XRD pattern for sample A2 (grown on sapphire with a thick $\beta - Ga_2O_3$ buffer layer) with markers indicating fitted peak positions. Broken lines are calculated from $\beta - Ga_2O_3$ and $\theta - Al_2O_3$ endpoints given in PDF cards 00-043-1012 and 00-023-1009, respectively, assuming no bowing in the d-spacing for each peak as the unit cell contracts. b) Fitted peak intensities as a function of Al concentration. Constant peak intensities up to $x \approx 0.15$ indicate substitutional incorporation of Al into $\beta - Ga_2O_3$; falling intensities above $x > 0.15$ mean a growing fraction of the film is not crystalline. Compared to sample A1, the buffer layer appears to extend crystallinity by at least 10 % to higher Al content. c) Fitted peak locations relative to their positions in $\beta - Ga_2O_3$ alongside calculated shifts from part a. Peaks track more closely than in A1, but not as closely as S1 or S2, which may be due to strain induced by the epitaxial relationship with the sapphire substrate at first, or poor incorporation as x is increased.

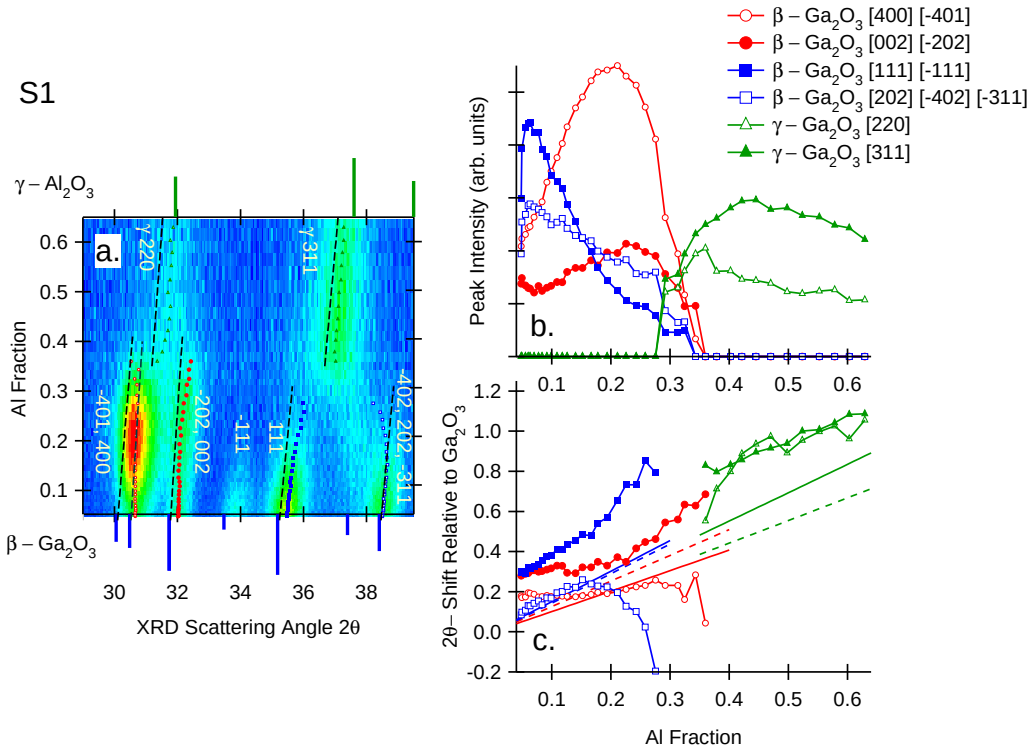

Figure 7.14: a) Integrated XRD pattern for CCS film S1 on SiOx with markers indicating fitted peak positions. Broken lines are calculated from $\beta - Ga_2O_3$ and $\theta - Al_2O_3$ endpoints given in PDF cards 00-043-1012 and 00-023-1009, and $\gamma - Ga_2O_3$ and $\gamma - Al_2O_3$ endpoints given in PDF cards 00-020-0426 and 00-029-0063, assuming no bowing in the d-spacing for each peak as the unit cell contracts. b) Fitted peak intensities as a function of Al concentration. The intermediate phase displaces $\beta - Ga_2O_3$ almost immediately as the Al concentration x is increased. c) Fitted peak locations relative to their positions in $\beta - Ga_2O_3$ and $\gamma - Ga_2O_3$, alongside calculated shifts from part a. Shifts in 2θ parallel to the broken lines indicate incorporation of Al. The 0.2° offset was caused by a slight misalignment when collecting data at a low angle of incidence.

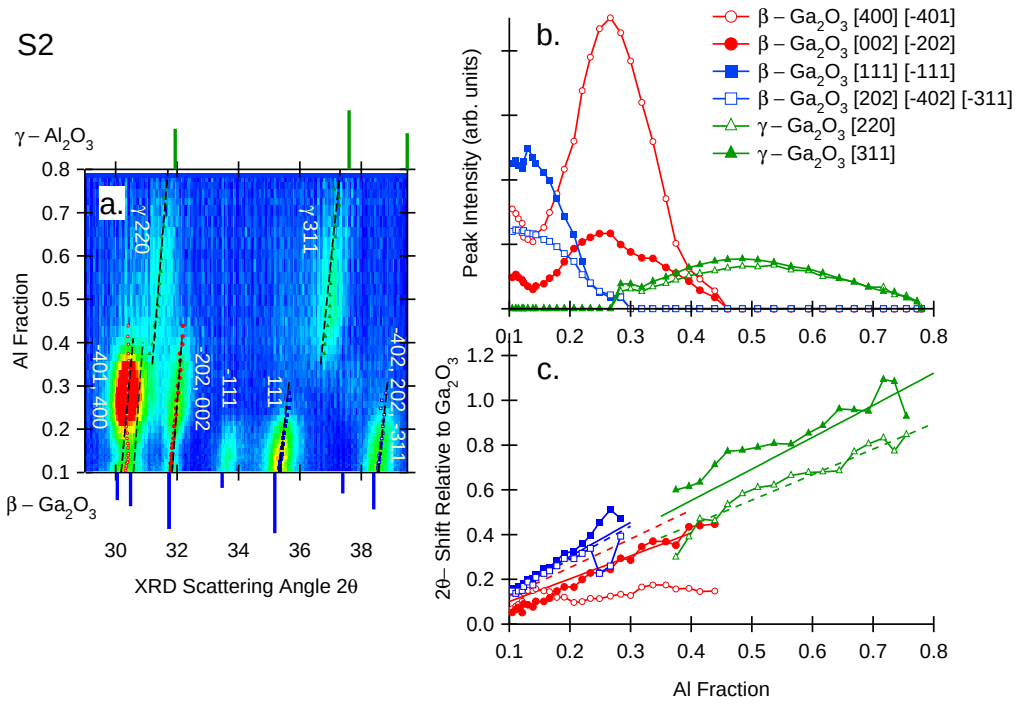

Figure 7.15: a) Integrated XRD pattern for sample S2 on SiOx with a 30 nm unoriented $\beta - Ga_2O_3$ buffer layer. Markers indicate fitted peak positions. Broken lines are calculated from $\beta - Ga_2O_3$ and $\theta - Al_2O_3$ endpoints given in PDF cards 00-043-1012 and 00-023-1009, and $\gamma - Ga_2O_3$ and $\gamma - Al_2O_3$ endpoints given in PDF cards 00-020-0426 and 00-029-0063, assuming no bowing in the d-spacing for each peak as the unit cell contracts. b) Fitted peak intensities as a function of Al concentration. The [400] orientation is stronger here than in sample S1, and so is γ−[220]. c) Fitted peak locations relative to their positions in $\beta - Ga_2O_3$ and $\gamma - Ga_2O_3$, alongside calculated shifts from part a. Shifts in 2θ parallel to the broken lines indicate incorporation of Al, except for the stationary [400] peak.

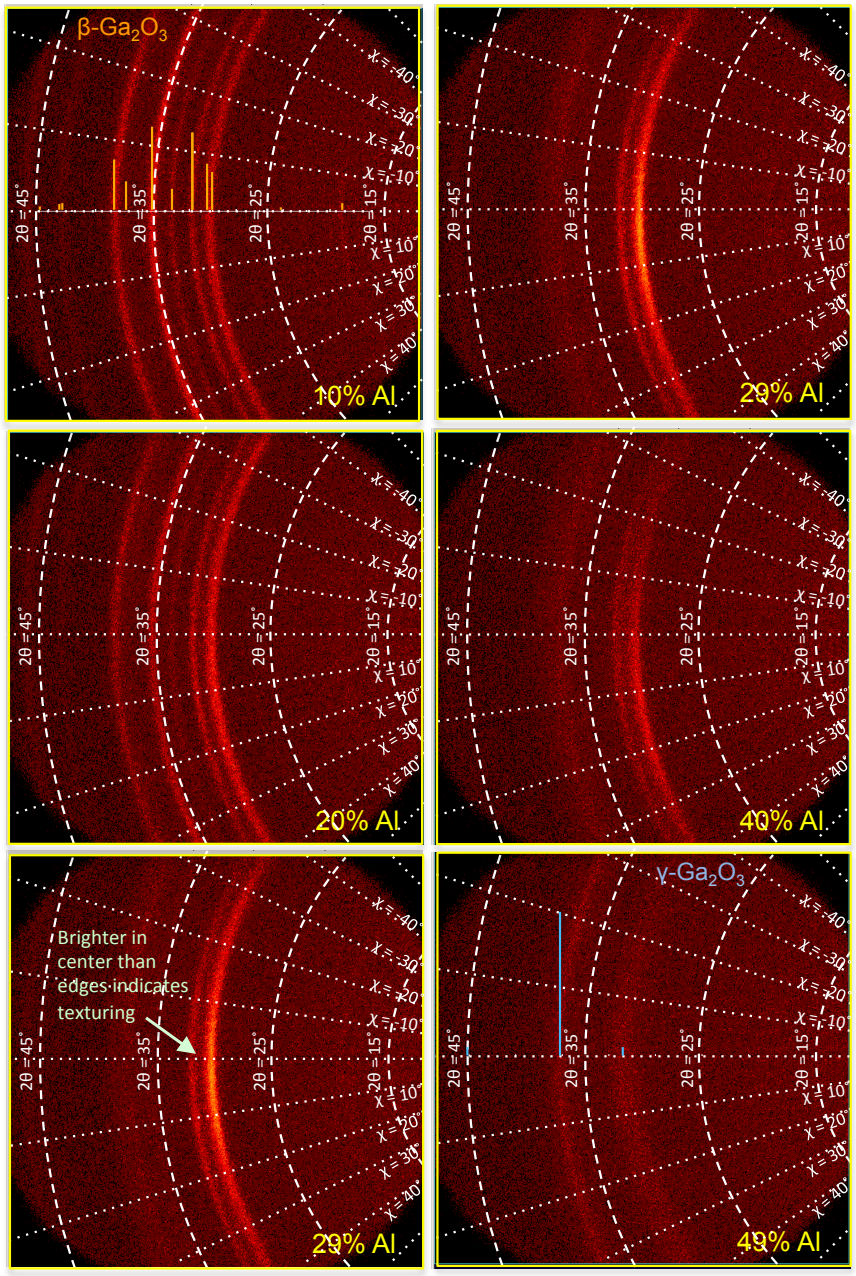

Figure 7.16: 2D diffraction patterns for CCS sample S2, deposited on SiOx with a thick Ga_2O_3 buffer layer, as the Al composition is increased from 10 % to 50 %. Debye rings initially indicate $\beta - Ga_2O_3$ with no preferred orientation on the Ga-rich side, which develop into an intermediate textured phase at 29 % Al (highlighted by the green arrow), and finally unoriented $\gamma - Ga_2O_3$. Diffraction patterns from JCPDS PDF cards 00-043-1012 ($\beta - Ga_2O_3$) and 00-020-0426 ($\gamma - Ga_2O_3$) are overlaid on the first and last frames, respectively, shifted slightly to higher 2θ due to the lattice contraction upon incorporation of Al.

[400]/[$\bar{4}$01] and [$\bar{2}$02]/[002], and simultaneous disappearance of other $\beta - Ga_2O_3$ peaks in figs. 7.14 and 7.15 is at least partially due to texturing, indicated by the stronger diffraction of [400]/[$\bar{4}$01] and [$\bar{2}$02]/[002] near $\chi = 0°$ than at off-axis angles. Randomly-oriented films diffract at every angle with uniform brightness (such as in the first $\beta - Ga_2O_3$ and final $\gamma - Ga_2O_3$ 2D diffraction patterns of fig. 7.16). Sample S2 is nearly twice as thick as sample S1 and was deposited on a $\beta - Ga_2O_3$ buffer layer, whereas sample S1 was deposited directly on the SiOx substrate. If texturing were caused by lattice matching to Si (100), e.g. if oxygen from the amorphous native oxide were scavenged by Al_2O_3 to expose the silicon surface, then the presence of a 30 nm unoriented $\beta - Ga_2O_3$ buffer layer in sample S2 would prevent it. However, comparing the intensities of textured peaks in S2 (fig. 7.15) and S1 (fig. 7.14) shows that texturing in the thicker S2 film is enhanced by nearly a factor of two relative to the initial $\beta - Ga_2O_3$ and final $\gamma - Ga_2O_3$ peaks. Therefore the texture in the intermediate phase must be spontaneous.

An unambiguous identification of the intermediate phase was not achieved by searching our PDF card database, which contains diffraction patterns for most of the various Ga_2O_3 and Al_2O_3 polymorphs in varying qualities, nor was a satisfactory match found using calculated δ and κ−Al_2O_3 XRD patterns based on structures published in refs. [395, 396], or early $(Al_xGa_{1-x})_2O_3$ patterns from Hill et al. [102]. It is reasonable to guess that the intermediate phase is transitory between $\beta - Ga_2O_3$ and $\gamma - Ga_2O_3$ and not something completely different. Optical data supports this conclusion: Schmidt-Grund et al. [306] did not observe a discontinuous jump in band gap through a $\beta \rightarrow \gamma$ transition in an $(Al_xGa_{1-x})_2O_3$ CCS thin film on MgO, and no discontinuous jump is observed in my optical data either, as will be shown. Both the β and γ crystal structures contain a distorted fcc oxygen sublattice, and it is generally accepted that the transition between the two only involves a rearrangement of cations and vacancies around different Wyckoff sites, with minimal disruption to the anions [56, 65]. Playford et al. [63] showed how relative intensities of diffraction peaks belonging to the κ and ϵ structures change dramatically upon a simple rearrangement of cation vacancies in a hcp oxygen sublattice; a similar change in intensities as cations rearrange themselves in the transition from $\beta - Ga_2O_3$ to $\gamma - Ga_2O_3$ may partly explain the intermediate phase we observe. Differences in the relative intensities of peaks also exist between isomorphic phases in several polymorphs of Ga_2O_3 and Al_2O_3, including: $\gamma - Al_2O_3$ and $\gamma - Ga_2O_3$, $\beta - Ga_2O_3$ and $\theta - Al_2O_3$, and $\alpha - Ga_2O_3$ and $\alpha - Al_2O_3$ (fig. 7.17a); in the early diffraction patterns published by

Hill et al. [102] for single-phase $(Al_xGa_{1-x})_2O_3$ powders as the Al fraction is increased (fig. 7.17b); and also in my powder diffraction data (fig. 5.1). The difficulty in making a positive identification may therefore be due to several factors, including fluctuations in relative intensities during cation reordering, variations in relative peak intensities among isostructural Ga_2O_3 and Al_2O_3 polymorphs, the likelihood of mixed phases, and of course spontaneous texturing, which strongly enhances some peaks at the expense of others.

Figure 7.18 shows the integrated diffraction patterns for sample S2 over an extended range of 2θ on the Ga-rich side ($x = 0.1$), in the intermediate region ($x = 0.3$), and after the transition to the γ phase ($x = 0.5$) (corresponding to frames 1, 3, and 5 of fig. 7.16). Overlaid on the intermediate region at $x = 0.3$ are the PDF card diffraction patterns for $\theta - Al_2O_3$ (re-calculated for a lattice expanded isotropically by 3 %), and $\gamma - Ga_2O_3$ (recalculated for a lattice compressed isotropically by 1 %, appropriate for an alloy film with $x = 0.25$ assuming a full-range isotropic lattice parameters variation of 4 %). Agreement between the calculated and measured diffraction patterns is close, except for the unusually high intensities of $\beta - Ga_2O_3$ [400] and [002]. For a textured film, agreement with intensities from a powder reference pattern is not to be expected. Therefore the intermediate region may be a mixed β/γ phase.

Spontaneous orientation usually only occurs on particular low-energy surfaces in the crystal structure of thin films. $\gamma - Al_2O_3$ films grown by several different methods are known to have low energy surfaces (110) and (100) leading to preferential orientation in those directions [56]. The $[220]_\gamma$ peak lies at $2\theta = 30.8°$, nearly coincident with the brightest textured peak $[400]_\beta$, meaning that the observed intensity in the 2D diffraction pattern may actually be the sum of both. Spontaneous $[110]_\gamma$ orientation might also explain why the intensity of $[220]_\gamma$ is comparable to $[311]_\gamma$ in the thicker S2 film, and is about half as intense as $[311]_\gamma$ in thinner S1, despite $[311]_\gamma$ having greater intensity by a factor of five in the powder reference pattern (PDF card 00-020-0426). The lattice mismatch between oxygen ions in a $\gamma - Ga_2O_3$ spinel structure and $[\bar{2}01]$-oriented $\beta - Ga_2O_3$ should be nearly zero except for small distortions, so if $\gamma - Ga_2O_3$ is developing spontaneous texture it may be carried through to $\beta - Ga_2O_3$ peaks of a mixed-phase film as well. As shown in fig. 7.19, the difference in χ between $[400]_\beta$, $[\bar{4}01]_\beta$ and $[220]_\gamma$, or between $[\bar{2}02]_\beta$, $[202]_\beta$, and $[220]_\gamma$, for $[\bar{2}01]$-oriented $\beta - Ga_2O_3$ films nucleating in opposite directions on [111]-oriented $\gamma - Ga_2O_3$, is only about 15°.

An alternative explanation for the spontaneous orientation may be provided by Bermudez [150]

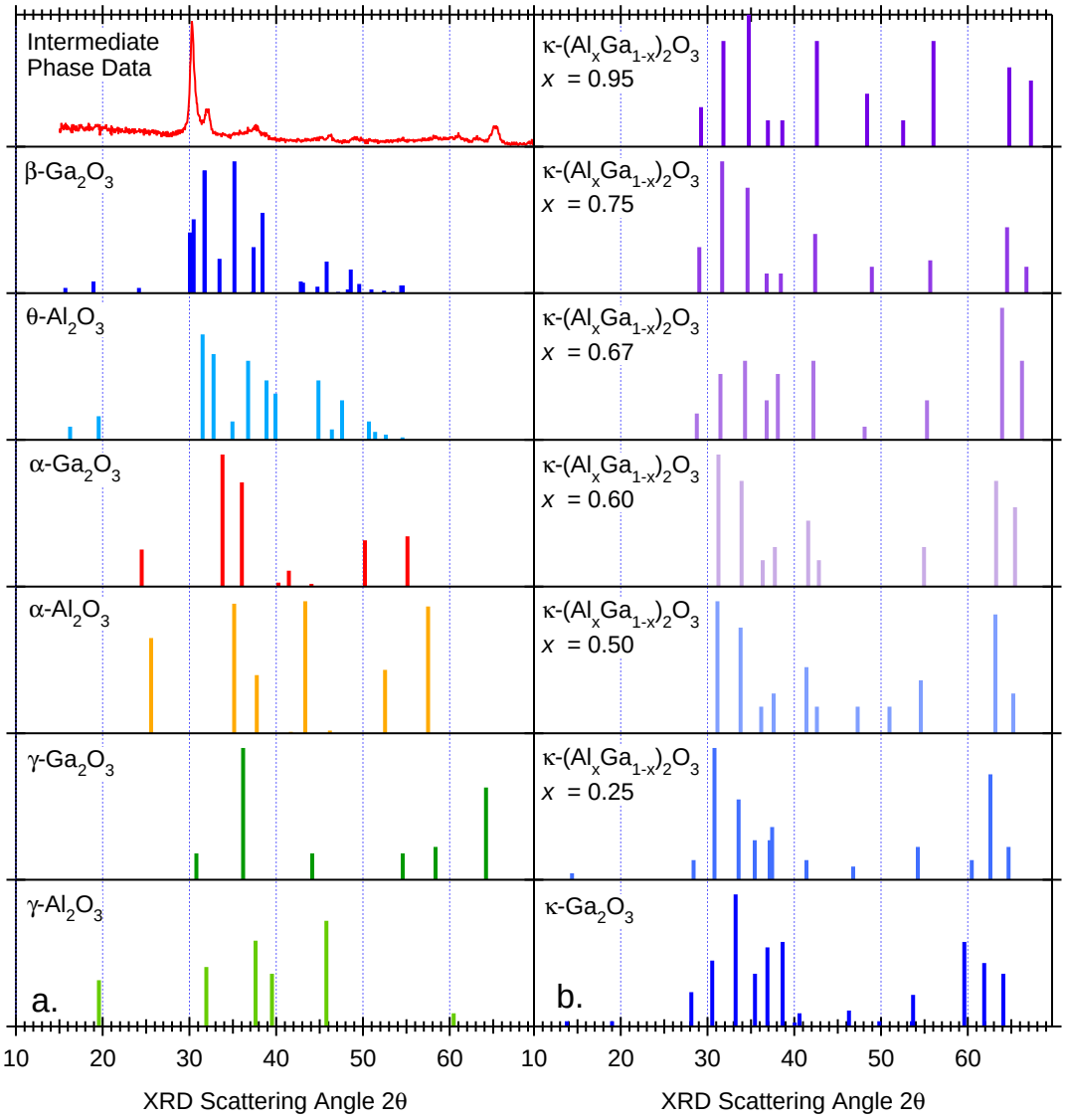

Figure 7.17: a) PDF cards for Ga_2O_3 and Al_2O_3 polymorphs showing differences in relative intensities between isostructural phases (from top to bottom): $\beta - Ga_2O_3$ (00-043-1012), $\theta - Al_2O_3$ (00-023-1009), $\alpha - Ga_2O_3$ (00-043-1013), $\alpha - Al_2O_3$ (00-043-1484), $\gamma - Ga_2O_3$ (00-020-0426), and $\gamma - Al_2O_3$ (00-029-0063). b) Change in peak intensities for a series of $\kappa - (Al_xGa_{1-x})_2O_3$ powders as the alloy parameter x is increased, from ref. [102]. The integrated diffraction pattern for the intermediate phase in S2 at $x = 0.3$ is appended in the top left for comparison.

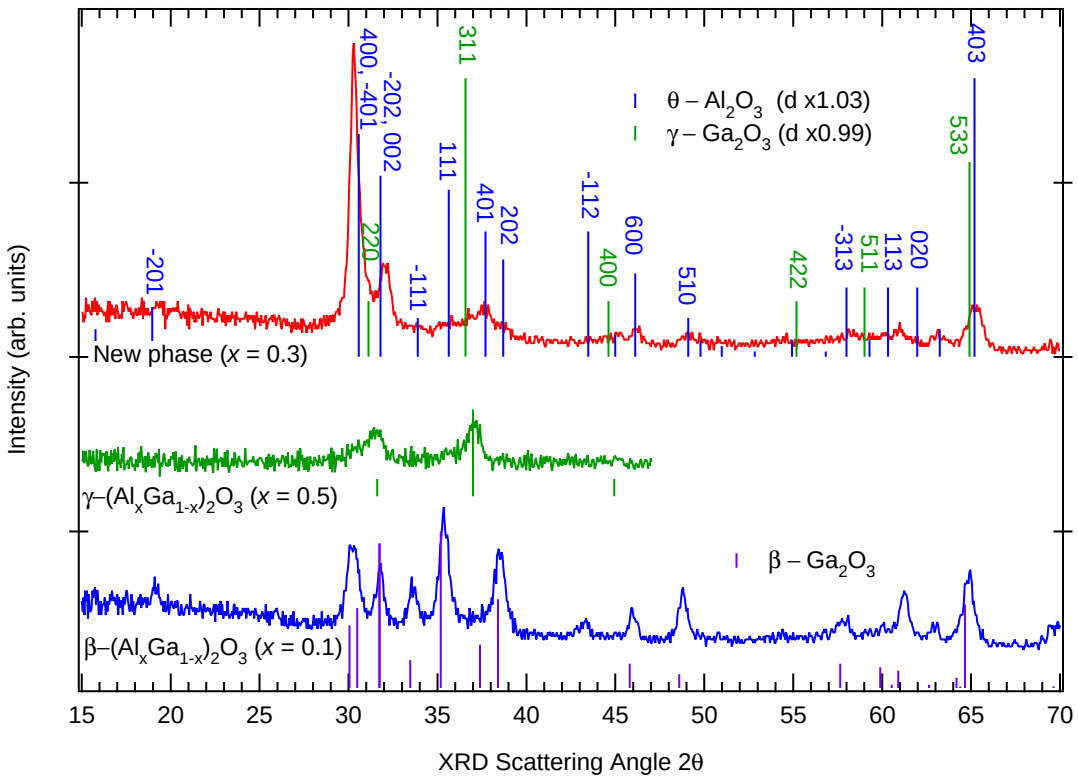

Figure 7.18: Integrated diffraction patterns for sample S2 in the $\beta - Ga_2O_3$ region ($x = 0.1$) in the intermediate region ($x = 0.3$), and in the $\gamma - Ga_2O_3$ region ($x = 0.5$). Overlaid are diffraction patterns for $\theta - Al_2O_3$ (PDF card 00-023-1009) adjusted for an isotropic lattice expansion of 3% and $\gamma - Ga_2O_3$ (00-020-0426) adjusted for an isotropic compression of 1%. Tentative agreement is achieved if texturing on $\gamma - Ga_2O_3$ [220] ($2\theta = 31.1°$) or $\theta - Al_2O_3$ [400] ($2\theta = 30.6°$) is assumed.

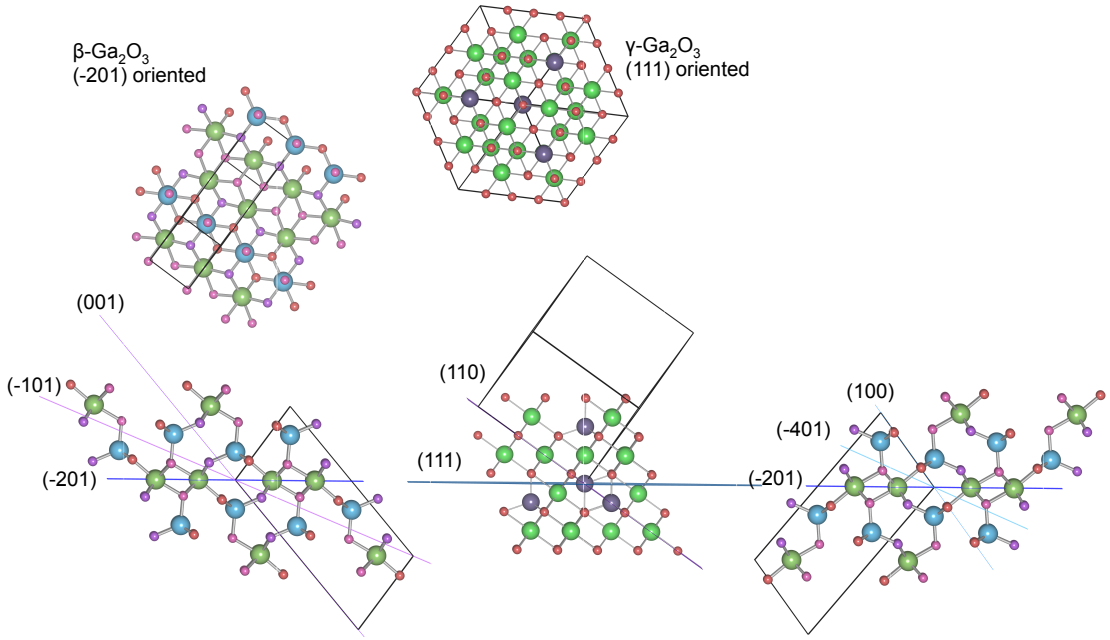

Figure 7.19: (Top) Lattice match between $\beta - Ga_2O_3$ $(\bar{2}01)$ and $\gamma - Ga_2O_3$ (111). Based on the lattice parameters given in refs. [63] and [106] the lattice mismatch is approximately 1%. (Bottom) Similarity in angle between $(\bar{4}01)$ and (100), or $(\bar{1}01)$ and (001) lattice planes in $\beta - Ga_2O_3$, and (110) in $\gamma - Ga_2O_3$ when $[\bar{2}01]_\beta$ is aligned with $[111]_\gamma$.

who calculated that the lowest-energy surfaces in $\beta - Ga_2O_3$ are parallel to (100) and (001), which was also suggested in section 7.1 as a possible explanation for why (101)-twinned regions grow faster than $[\bar{2}01]$-oriented regions in epitaxial $\beta - Ga_2O_3$ films on sapphire with thickness greater than 100 nm. In both samples S1 and S2 on SiOx (fig. 7.14c and 7.15c) the diffraction angle 2θ of the $[400]/[\bar{4}01]$ peak jumps to a lower value at the transition to the intermediate region, suggesting that the oriented peak is [400] only (at $2\theta = 30.1°$) and not $[\bar{4}01]$ (at $2\theta = 30.5°$). Since [002] and $[\bar{2}01]$ are both at the same diffraction angle ($2\theta = 31.7°$), a similar jump in 2θ does not occur for that peak. Spontaneous orientation is not observed in $\beta - Ga_2O_3$ films on amorphous silicon native oxide, but perhaps the addition of Al changes the energetics of the alloy film relative to intrinsic $\beta - Ga_2O_3$. If this model is correct, then the intermediate region is not a mixed phase after all, just spontaneously-oriented $\beta - (Al_xGa_{1-x})_2O_3$. Since there is no observable difference in the band gap of γ-phase and β-phase $(Al_xGa_{1-x})_2O_3$ films, it is not possible for me to definitively rule out either explanation based on optical data collected so far.

Similar to $(Al_xGa_{1-x})_2O_3$ films A1 and A2 on sapphire, growth on a $\beta - Ga_2O_3$ buffer layer extends the stability of the β and intermediate phases to higher Al content x in film S2 (grown on a thick Ga_2O_3 buffer layer) compared to S1 (grown directly on SiOx). Whereas the intermediate phase begins displacing the β phase almost as soon as the Al content is increased in S1, the β phase stays relatively constant until $x \approx 0.15$ in S2, and the intermediate phase persists until $x \approx 0.4$ in S2 compared to $x \approx 0.35$ in S1. These values are consistent with the limits of the β phase in 800 °C post-annealed films (chapter 6), which provides support for the theory that the intermediate phase is spontaneously-oriented $\beta - (Al_xGa_{1-x})_2O_3$ rather than a mixed β/γ phase. If the substrate temperature were raised the transition to γ would move to higher x.

7.3 XPS of $(Al_xGa_{1-x})_2O_3$: Peak Widths and Core Level Shifts

Photoemission peak widths in XPS are influenced by the degree of disorder surrounding individual atoms, which leads to Gaussian broadening in addition to the Lorentzian broadening from the lifetime of individual transitions and the natural width of the X-ray beam. Figure 7.20 shows O $1s$ spectra at several Al concentrations from an early $(Al_xGa_{1-x})_2O_3$ CCS film (S0) deposited on SiOx. Despite similar intensities, peak widths increase substantially with the Al content x. O $1s$ from Al_2O_3 and Ga_2O_3 only differ by 0.2 eV in binding energy, so the changing width is probably not due to two overlapping O $1s$ components, but rather a general broadening caused by poorer crystallinity. At $x = 0.8$, the width is comparable O $1s$ from an intrinsic amorphous Al_2O_3 film, whereas at $x = 0.03$ the width is comparable to single-crystal $\beta - Ga_2O_3$. The O $1s$ width at $x = 0.67$ also agrees with CCS sample A1 on sapphire, as both films are amorphous at that composition. However, sample A1 has noticeably larger width at $x = 0.32$ where it is amorphous, than S0 at $x = 0.32$ where it is crystalline.

An interesting trend was also noticed concerning the relative binding energies (BEs) of Ga, Al and O core levels as the alloy composition was varied through $(Al_xGa_{1-x})_2O_3$ CCS films on SiOx (fig. 7.21a) and sapphire (fig. 7.21b). In these figures, differences between core level binding energies of various Al or Ga photoemission peaks and O $1s$ are plotted for several CCS samples as a function of the Al content x, after subtracting the constant BE difference between corresponding peaks measured in Ga_2O_3 and Al_2O_3 reference samples (section 4.4.3). On the Ga-rich side, the overlap of Ga and Al peaks near zero indicates that Ga, Al, and O core levels all shift together in alloy films on SiOx and sapphire. (Ga and Al are artificially skewed to lower BE in sample A2 at low x, because sample charging did not reach an equilibrium until several mm into the film as data were being collected.)

Above $x \approx 0.35$ in films on SiOx substrates, Al–O BE differences start to diverge upward, indicating that O and Ga core levels are moving together to higher BE more quickly than Al core levels. This starts at roughly the same point as films transition from β to the γ phase, and may be related to the different distribution of octahedral and tetrahedral sites in those two structures (4_{oct}:4_{tet} for $\beta - Ga_2O_3$, and 16_{oct}:8_{tet} for $\gamma - Ga_2O_3$), leading to different degrees of overlap between Al and O atomic orbitals. Divergence starts at around the same Al concentration in films on

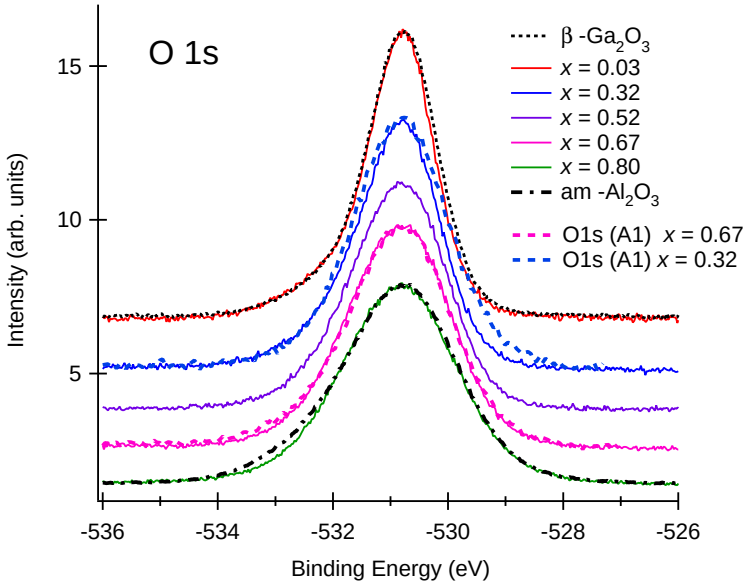

Figure 7.20: O 1s XPS spectra for sample S0 at selected Al concentrations x. Overlaid on the S0 spectra are O 1s from a $\beta - Ga_2O_3$ single crystal (black dots), O 1s from sample A1 at $x = 0.32$ and $x = 0.67$ (colored dots), and O 1s from an amorphous Al_2O_3 thin film (dashed-dotted black line). Sample S0 peak widths match well to the $\beta - Ga_2O_3$ and am-Al_2O_3 spectra at low and high x, respectively. The broad A1 O 1s width at $x = 0.67$ compares well to S0, but the width at $x = 0.32$ is noticeably broader than S0.

sapphire, but in these films Ga moves to higher BE more quickly than O, and Al diverges less. These films are amorphous above $x \approx 0.3$, so one wouldn't necessarily expect the same BE shifts as observed in the γ phase films on SiOx, if the shifting is related to the degree of orbital overlap.

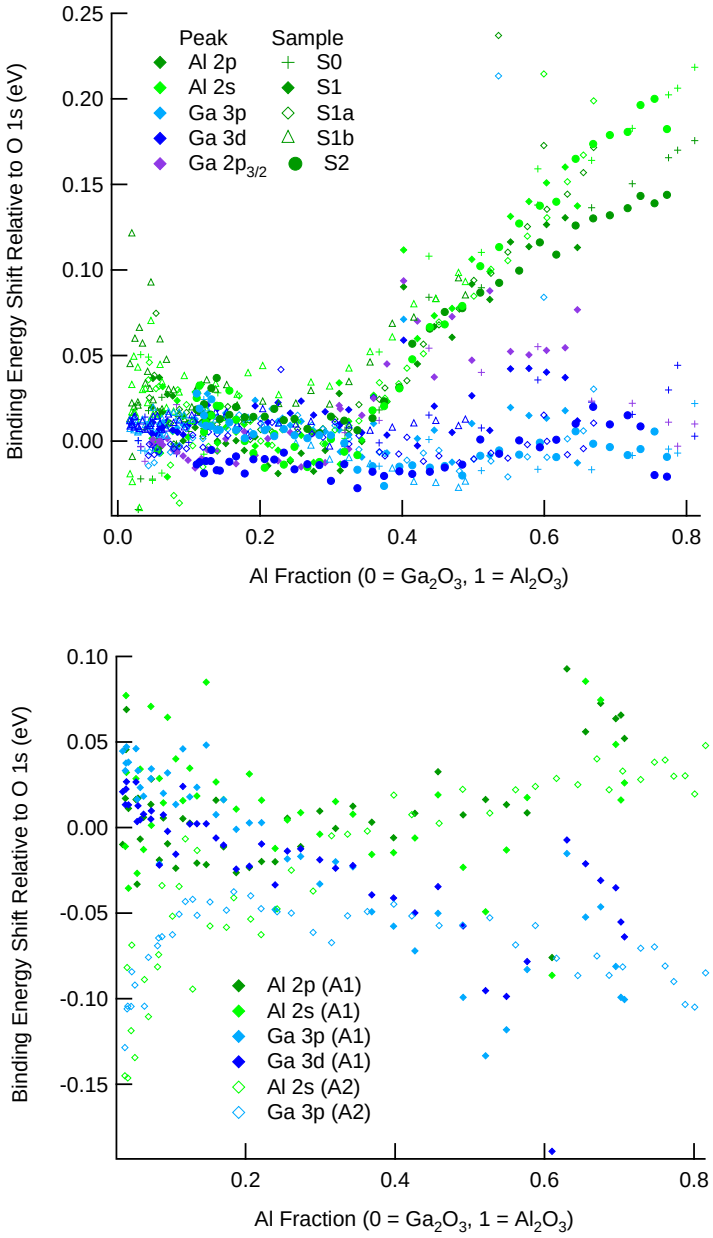

Figure 7.21: Binding energy shifts of Al and Ga core levels relative to O 1s on silicon substrates (top) and on sapphire (bottom).

7.4 Spectroscopic Ellipsometry: Dispersion and Thicknesses

Spectroscopic ellipsometry was performed to measure film thicknesses of CCS $(Al_xGa_{1-x})_2O_3$ films on silicon and sapphire substrates, as well as the variation in bandgap and optical functions with Al concentration.

First, a Cauchy model was used to fit the transparent region from 1–4 eV of intrinsic $\beta - Ga_2O_3$ and $\gamma - Al_2O_3$ films and CCS $(Al_xGa_{1-x})_2O_3$ films S1, A1, S2, and A2 on silicon and sapphire, with and without a $\beta - Ga_2O_3$ buffer layer. In the Cauchy model, the extinction coefficient κ equals zero and the index of refraction is given by the formula (see section 4.6.3)

$$n(\lambda) \approx A + \frac{B}{\lambda^2} + \frac{C}{\lambda^4} + \cdots \tag{7.4}$$

Cauchy parameters after A define curvature in $n(\lambda)$, and therefore are inversely correlated. A represents the index at infinite wavelength and is less strongly affected by differences in higher-order parameters. Fitted Cauchy parameters of intrinsic Ga_2O_3 and Al_2O_3 PLD films are listed in table 7.4. The most accurate fit for Ga_2O_3 made use of all four Cauchy parameters A–D; however when all four parameters are used to fit Al_2O_3, unphysical negative values were obtained for B and D, so instead only the first three (A–C) were used. The band gap of Al_2O_3 is farther out in energy than Ga_2O_3, so it is not surprising that the dispersion between 1–4 eV is less. Since C is similar for both materials, a second Ga_2O_3 fit was performed fixing C at 0.0002. Due to the correlation between B and C this leads to a larger value of B but only a slightly higher MSE.

Table 7.4: Cauchy parameters of $\beta - Ga_2O_3$ and $\gamma - Al_2O_3$ PLD films.

Sample	A	B	C	D
Ga_2O_3	1.885	0.012420	0.00027392	0.000012075
Ga_2O_3 (2)	1.881	0.014080	0.0002 (fixed)	-
Al_2O_3	1.671	0.00066116	0.00019617	-

Cauchy A and B parameters of CCS samples S1, A1, S2, and A2, fitted with fixed $C = 0.0002$, are shown as a function of XPS Al concentration in fig. 7.22. For crystalline films S1 and S2, the A parameter appears to follow a linear trend starting at the intrinsic Ga_2O_3 value, and ending

about 0.02 above the corresponding value for Al_2O_3. A1 and A2 both transition to amorphous at early x along the composition gradient. Where diffraction peaks are visible, A appears to follow a parallel trendline, offset from the other by approximately 0.02; when diffraction peaks disappear, A falls below the line. The difference in trendlines between crystalline films on silicon and sapphire may be a result of anisotropy in the optical constants due to the crystal structure of $\beta - Ga_2O_3$ [11, 12]. Films on SiOx are initially randomly oriented, but develop a [100] and [001] texture in the range $0.1 < x < 0.4$ before transitioning to γ, while films on sapphire are strongly $[\bar{2}01]$-oriented. Random orientation means that both in-plane and out-of-plane indices of refraction are comprised of extraordinary and ordinary values in a $\frac{1}{3} : \frac{2}{3}$ ratio, but if one of the ordinary axes is oriented normal to the surface then the in-plane ratio of extraordinary to ordinary indices becomes $\frac{1}{2} : \frac{1}{2}$. The higher-lying A parameter of sample A2 relative to A1 for $0 < x < 0.5$ is probably due to diffusion from the Ga_2O_3 buffer layer into the $(Al_xGa_{1-x})_2O_3$ film, as will be shown below.

The B parameter follows a similar trend with Al as A for crystalline films on SiOx, except for a deviation in sample S1 at $x = 0.25$. For films on sapphire, B appears to follow a lower trendline in the crystalline phase, and then jump dramatically upon the transition to amorphous. With a sub-100 nm film on sapphire, increased dispersion (represented by B) for the amorphous phase is expected as the onset of absorption moves to lower energy. However, the index of refraction of Si ($n(\lambda)_{\mathrm{Si}}$) is more different from the index of refraction for $(Al_xGa_{1-x})_2O_3$ than the index of refraction of sapphire ($n(\lambda)_{\mathrm{sapphire}}$), which gives rise to stronger interference fringes in the reflected ellipsometric data Ψ and Δ for films on SiOx with similar thickness. Thicknesses for all films are shown in fig. 7.23. For $(Al_xGa_{1-x})_2O_3$ films in the 50–150 nm range there is just a single interference fringe visible between 1–4 eV, and in the case of films on sapphire the amplitude of oscillation is also very small. As a result, the fitted B value depends on the size of the wavelength range $\Delta\lambda$ included in the fit, in contrast to the situation where several cycles are contained within a fitted range, as results in the latter case are generally not senstiive to $\Delta\lambda$. Therefore the deviation in B for samples S1 and A1 from S2 and A2 is probably not important.

The linear variation of Cauchy A and B parameters with Al content for films in the crystalline phase is striking. As shown in chapter 6, a monotonic decrease was not observed in amorphous and post-annealed $(Al_xGa_{1-x})_2O_3$ films, and is not necessarily observed in other alloy systems such as AlGaAs. Taking the linear variation with Al concentration as an assumption allows for

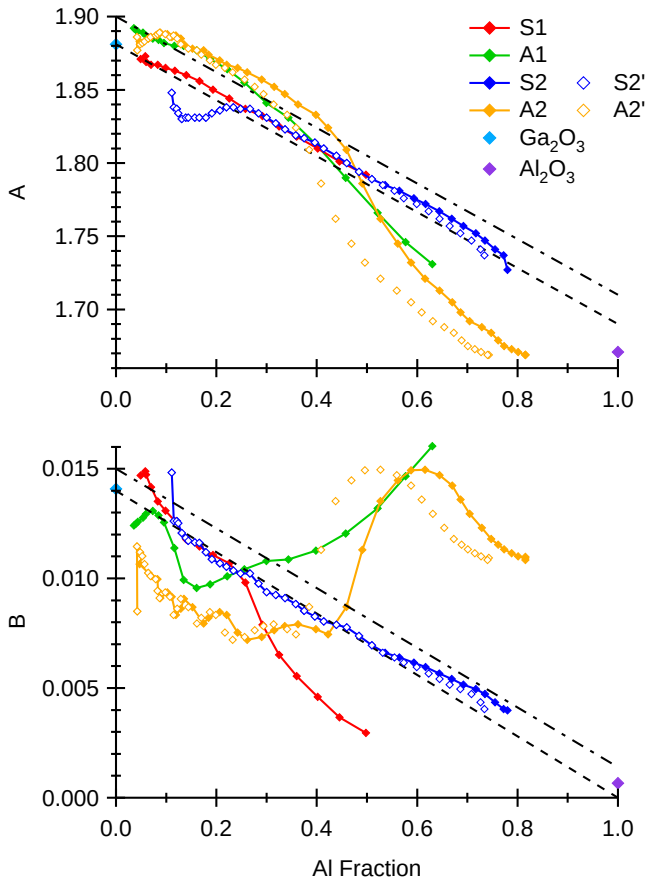

Figure 7.22: Cauchy A and B model parameters for samples S1, A1, S2, and A2 as a function of Al concentration, determined at the surface by XPS (solid markers) and throughout the film depth by ellipsometry (hollow markers). Data from $\beta - Ga_2O_3$ and $\gamma - Al_2O_3$ PLD films on silicon are appended at $x = 0$ and $x = 1$, respectively. In the crystalline region, the Cauchy parameters appear to depend on which substrate is used. Lines connect the Ga_2O_3 and Al_2O_3 endpoint values used for EMA depth profiling in samples S2 and A2; dashed is for sample S2 on silicon, and dashed-dotted is for sample A2.

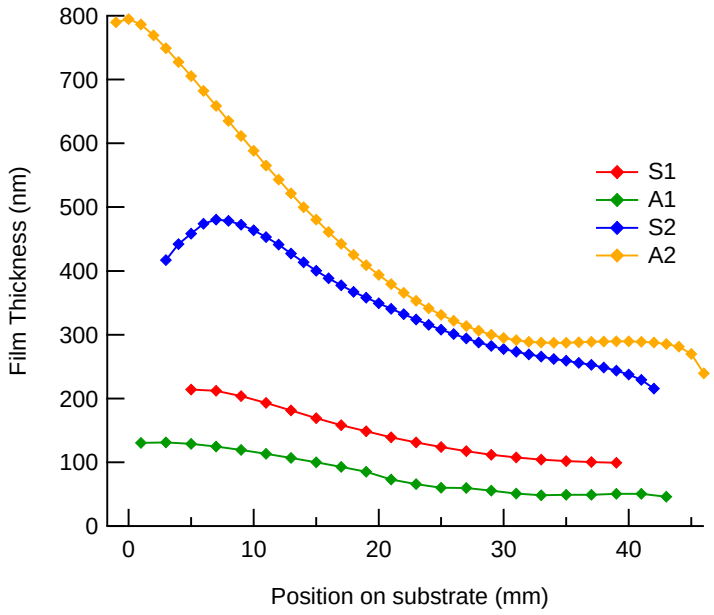

Figure 7.23: Thicknesses of S1, A1, S2, A2 from Cauchy fitting to the transparent 1–4 eV region.

the determination of alloy composition by combining Ga_2O_3 and Al_2O_3 Cauchy parameters in an effective medium approximation (EMA) with a well-defined fraction of Al_2O_3. Unlike XPS, which can only measure the top few nanometers of the film, this provides a depth-sensitive measurement of alloy composition, and even allows for measuring a changing composition as a function of depth below the fllm surface, giving evidence of either a reaction with the substrate or diffusion from a buffer layer into the film. This analysis was carried out for $(Al_xGa_{1-x})_2O_3$ films S2 and A2, which were each deposited on top of a 60-layer Ga_2O_3 buffer layer on SiOx and sapphire substrates, respectively. The uniform Cauchy model was replaced with a 100-layer graded EMA model, with each layer defined by a mixture of Ga_2O_3 and Al_2O_3 in a well-defined Al fraction using the Bruggeman equation (eq. 4.39), where the Al fraction was fixed at zero at the bottom of the film (to match the Ga_2O_3 buffer layer), and fixed to a value matching the XPS composition at the top of the film, but allowed to vary smoothly in between. This model was computationally intensive to simulate and required several days of dedicated CPU time to fit; therefore the fitting program may not have finished converging to a global minimum before being interrupted. However enough iterations were carried out that successive differences in the mean-squared error (MSE) were small and qualitative conclusions can

be drawn. To my knowledge, only one other group has published an ellipsometry depth-profiling procedure similar to the one just described, to measure the damage profile of Ge^+ implanted silicon Tonova and Konova [397].

The results of these computations are shown in fig. 7.24. Based on these figures, diffusion from the buffer layer into the film is minimal in sample S2 until $x > 0.5$, but appears to start much earlier at $x = 0.1$ in sample A2. Above $x > 0.2$, Ga_2O_3 is diffusing all the way through the film. These alloy compositions are precisely where XRD peak intensities begin to decrease in both films (figs. 7.13 and 7.15), suggesting that loss of crystallinity allows diffusion from the buffer layer through the film. In both samples, the diffusion is accompanied by a corresponding decrease in the buffer layer thickness. In A2 the apparent thickness of the buffer layer increases again after 30 mm, reflecting the poorly-defined boundary between buffer layer and film after so much diffusion has taken place. This result suggests that diffusion from the substrate into the film may also occur in amorphous $(Al_xGa_{1-x})_2O_3$ thin films grown at high temperature on single-crystal $\beta - Ga_2O_3$.

Based on these figures, the bulk composition at each position along the substrate was found by averaging the composition of the 100 layers, and compared to the nominal composition at the surface determined by XPS in fig. 7.25. For sample S2, the difference is unnoticeable below 29 mm, or $x = 0.53$. For sample A2 the difference is already significant at 17 mm, or $x = 0.15$, and grows to nearly 10 % above 30 mm; therefore it is most likely incorrect to assume the composition throughout the A2 film is equal to the XPS surface composition when plotting band gap results vs. x from ellipsometry, which is a bulk sensitive measurement. (Diffraction peaks disappear in amorphous films anyway so this is probably not a big issue for XRD). Cauchy parameters are plotted against the updated composition values in fig. 7.22 (S2' and A2').

Absorption coefficients of films on silicon are shown in fig. 7.26, and films on sapphire are shown in fig. 7.27, at several Al concentrations. Perfect fits were rarely achieved, due to a relatively large 1 mm spot size illuminating a range of compositions and thicknesses. Therefore several different models are shown for each sample which produced similar values of the MSE. General descriptions of each of the oscillators can be found in section 4.6.3. B-splines are Kramers-Kronig consistent and use a node spacing of 0.3 eV. "2 P-Semi M0" means two P-Semi M0 oscillators were used instead of one. "Multifit" means data were fit simultaneously using common parameters, with only center energy, amplitude, and broadening allowed to vary from point to point. "P-Semi Tri (wide right)"

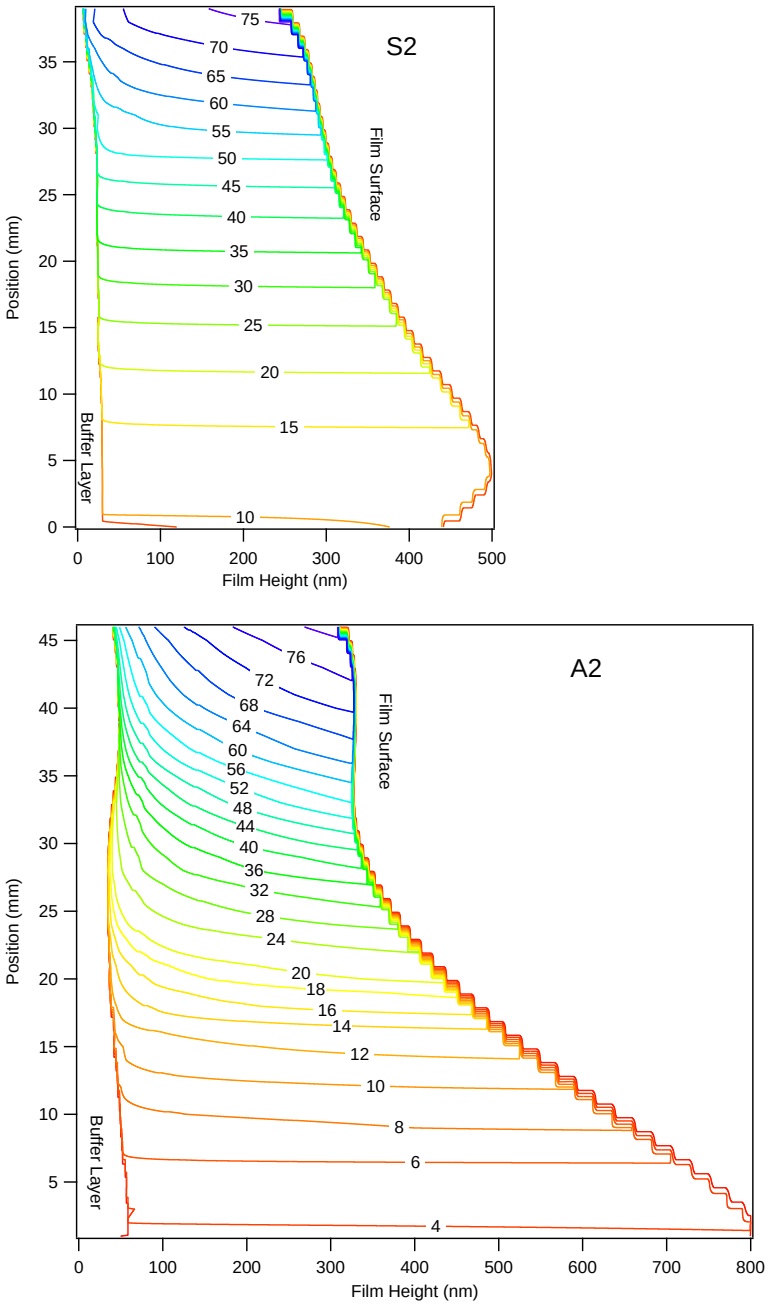

Figure 7.24: Composition vs. depth for CCS films S2 (top) and A2 (bottom) deposited on a 30–60 nm thick Ga_2O_3 buffer layer, estimated by ellipsometry by modeling the film with a graded effective-medium-approximation (EMA) layer that blends Cauchy parameters from Ga_2O_3 and Al_2O_3 PLD films in the Al fraction indicated, which varies in 100 equal steps with depth. The top of the film is held to the XPS composition, and the bottom held to $x = 0$ corresponding to the Ga_2O_3 buffer layer.

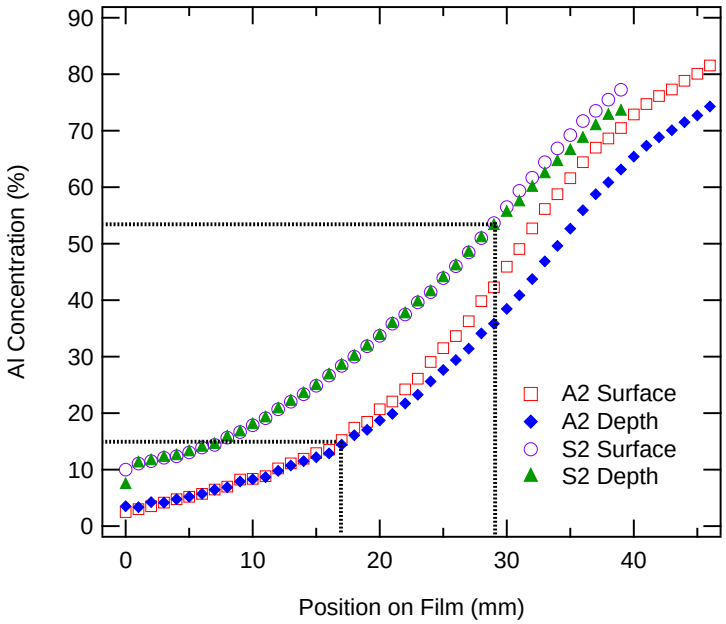

Figure 7.25: XPS surface composition and average composition with depth of CCS films S2 and A2 grown on 30–60 nm Ga_2O_3 buffer layers as determined by ellipsometry. The deviation is caused by diffusion from the buffer layer into the overlying $(Al_xGa_{1-x})_2O_3$ film in the amorphous phase.

oscillators use a linear slope to zero on the left side (amplitude control point = 0.5) and a large tail on the right side (amplitude control point > 1) producing a curve with an amplitude that increases to the right of the center energy. The idea is to simulate the $\sqrt{h\nu}$ dependence of a direct transition with the tail on the right, and a gradual onset due to the composition spread by the tail on the left. In this model, a Lorentzian oscillator was also added in the UV so that its tail could capture possible subgap absorption. In fact, a change in the shape of the absorption from concave down to concave up as the Al concentration increases is most easily seen in this model, although with spurious kinks. The last model used for S1 is a straight line fit (identical to the straight-line model used to fit post-annealed sample pa-S1 in chapter 6), formed by one (or two) P-Semi Tri oscillators anchored in the UV, with the oscillator amplitude and position of the left control point varying and the left amplitude control point fixed at 0.5. Many of the same models were also used to fit samples S2, and in addition a Cody-Lorentz oscillator was tried. Samples on sapphire were fit using P-Semi M0 and straight-line oscillators. B-splines were attempted for sample A1, but the result is

somewhat messy compared to the oscillator models.

Despite the differences between each model used, similar trends can be seen in every sample. For crystalline films on silicon, the absorption edge moves monotonically to higher energy with Al concentration, with a sharper onset at the beginning and a more gradual onset as the Al concentration is increased. This occurs in both samples S1 and S2 and may be due to a faster composition gradient in the middle of the film compared to the edges, rather than an intrinsic change in the shape of the absorption. In addition, there doesn't appear to be an abrupt change as the film transitions from the β to the γ phase. For samples on sapphire, the films start out in the β phase but become amorphous rather than transitioning to γ as the Al concentration is increased. This happens right in the beginning in sample A1, and the absorption coefficient can be seen immediately moving to lower energy and decreasing in amplitude, before moving back to higher energy and with a roughly constant amplitude after the transition is complete. The straight line fit appears to remain fixed and decrease in slope above 34 % because it is fitting to a broad tail rather than the full absorption edge as the absorption edge moves past the upper limit of photon energy. The absorption coefficient in the crystalline region of sample A2 looks like the corresponding region in A1, except it is shifted by approximately 0.2 eV to lower energy. In this sample the crystalline region persists until roughly 20 %, and then a change in shape of the absorption coefficient analogous to sample A1 occurs. However, both the P-Semi M0 and straight line models show an extremely shallow onset of absorption compared to the other three CCS films, which due to the amorphous nature combined with substantial diffusion from the Ga_2O_3 buffer layer into the film. The absorption coefficient in A2 therefore represents an average over a relatively wide range of compositions, as the Al concentration varies by up to 10 % through the depth of the film, and the average composition calculated from graded EMA fitting is shown at the right of the figure. The refraction index variation for crystalline β and γ-phase $(Al_xGa_{1-x})_2O_3$ films as a function of x is shown in fig. 7.28, from CCS films S1 and S2.

Band gaps were calculated for each sample by fitting the absorption coefficient with a line to zero, and the results are shown in fig. 7.29. This method was followed to be consistent with UV-Vis spectroscopy fitting in chapter 6, but may underestimate the gap compared to the value of E_g obtained from direct Tauc plots [$(\alpha h\nu)^2$ vs. $h\nu$]. Jumps are seen as the slope of the absorption onset increases and decreases. However, the overall E_g trend with Al concentration within the crystalline

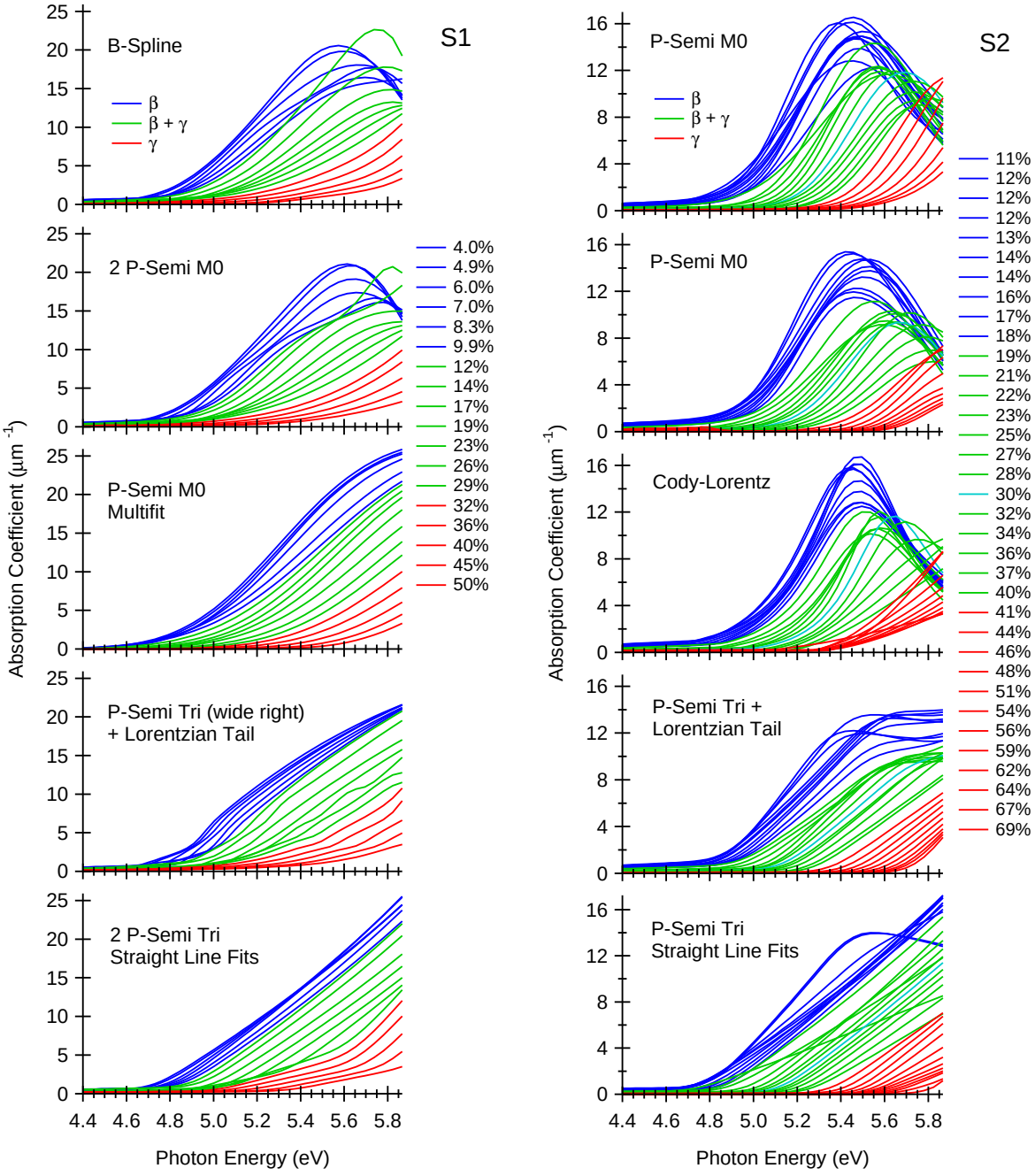

Figure 7.26: Absorption coefficient of CCS films S1 (left) and S2 (right) by ellipsometry using various models. Blue regions are unoriented $\beta - Ga_2O_3$, green regions are in the intermediate phase between β and γ, and red regions are $\gamma - Ga_2O_3$.

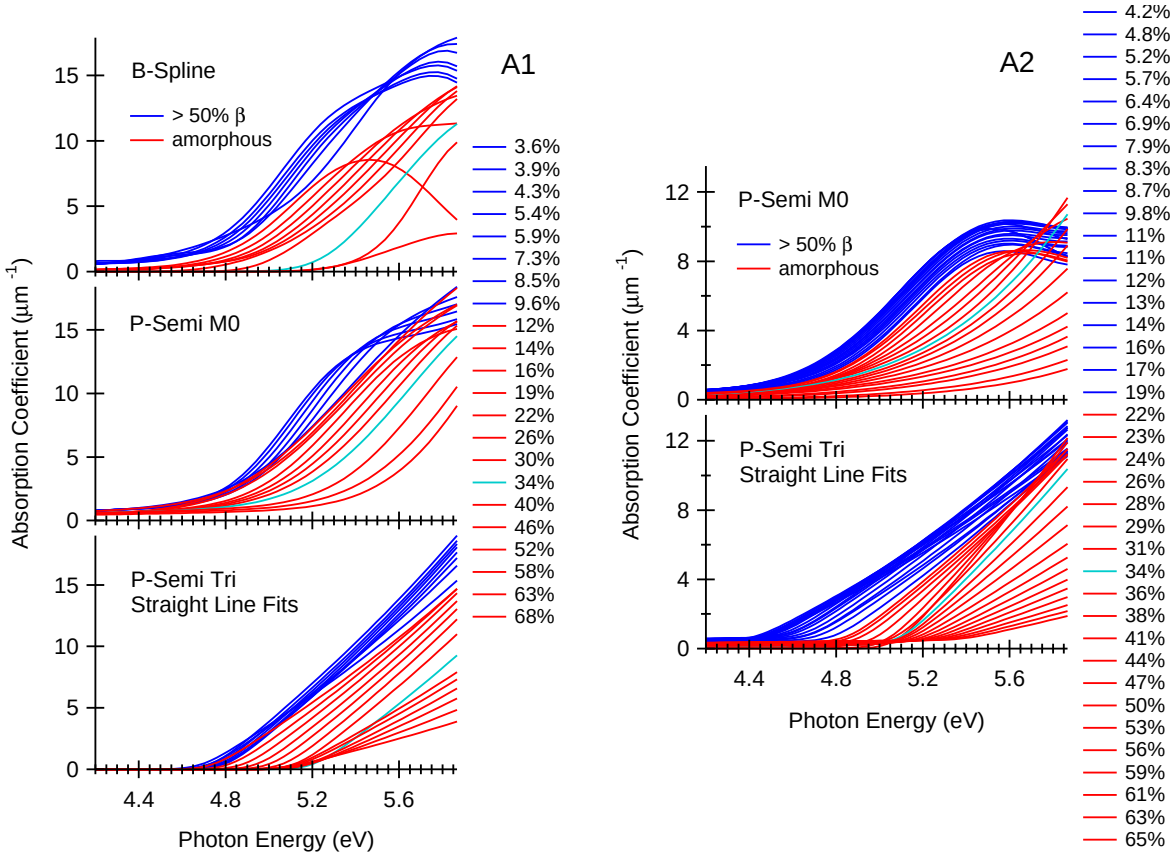

Figure 7.27: Absorption coefficient of CCS films A1 (left) and A2 (right) by ellipsometry using various models. Refions in blue are $[\bar{2}01]$-oriented $\beta - Ga_2O_3$, and regions in red are amorphous.

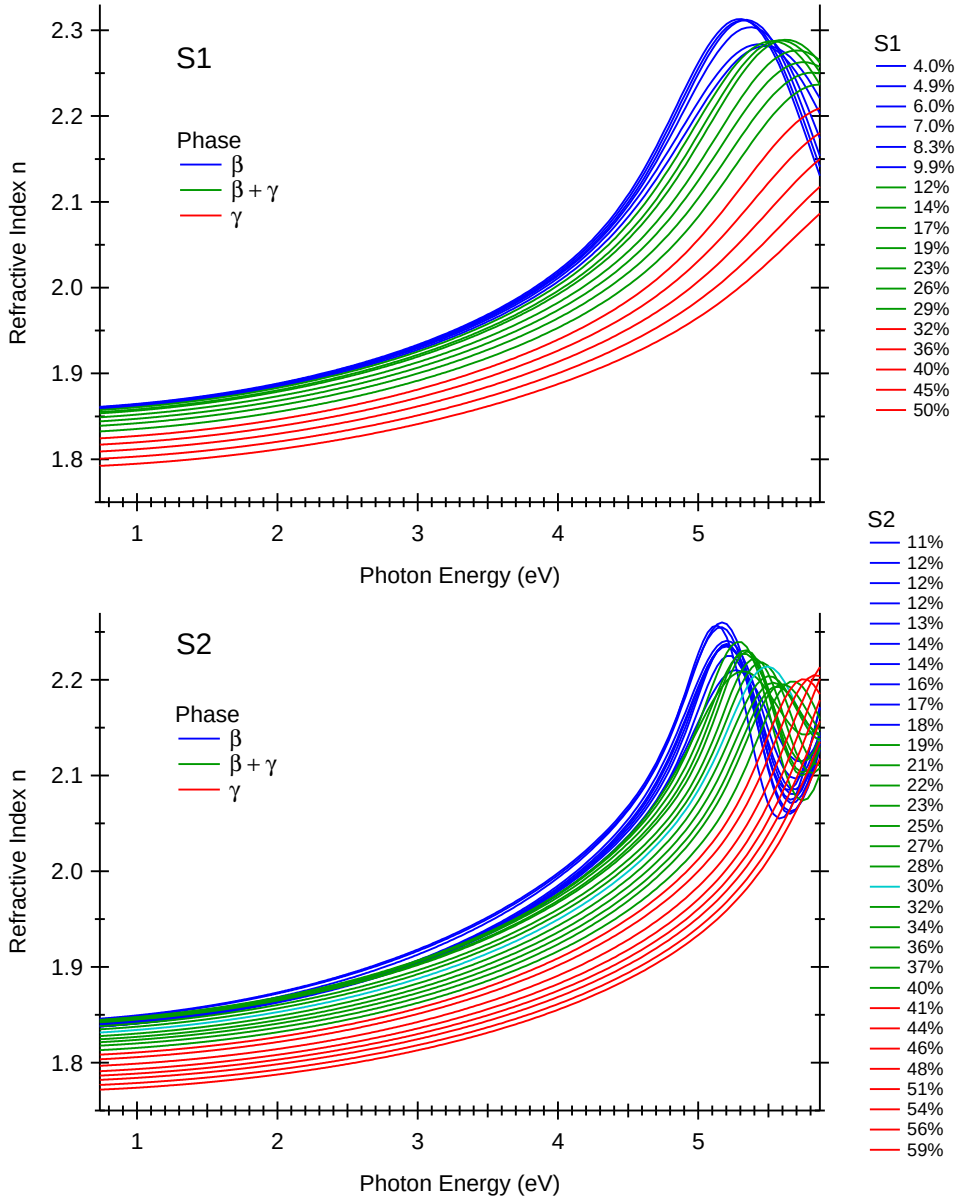

Figure 7.28: Refraction index for crystalline β and γ-phase $(Al_xGa_{1-x})_2O_3$ films in the range $0 < x < 0.6$, from CCS samples S1 and S2 grown on SiOx from spectroscopic ellipsometry.

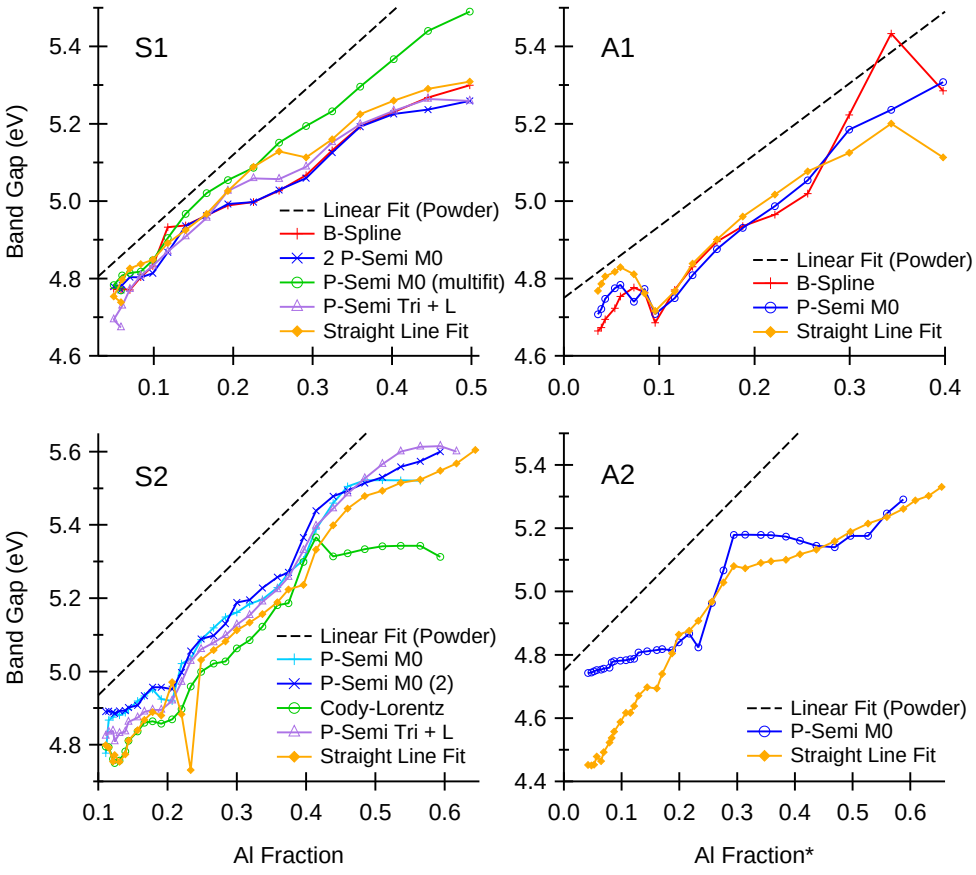

Figure 7.29: Fitted band gaps of CCS films S1 and S2 on SiOx, and A1 and A2 on sapphire, from linear extrapolation to zero of the absorption coefficient. The dotted line is the linear trend in band gap vs x observed in single-phase $\beta - (Al_xGa_{1-x})_2O_3$ powders, for comparison. Sample A2 was plotted against the average bulk composition found by ellipsometry using a graded EMA approximation, as described above; all others are plotted against the surface composition found by XPS.

phase appears to track the powder result, with an constant vertical offset that may just be the result of fitting to the absorption coefficient directly. In sample S1 a deviation to lower E_g occurs above $x = 0.3$, as only the tail of the absorption is visible rather than the full curve; in this case the band gap estimated by the multi-fit model is likely the most accurate. Sample S2 shows a larger vertical offset from the powder line than S1, but the band gap increases with the same slope. In sample A1, the initial trend follows the powder line, but abruptly jumps to a lower value when the film becomes amorphous. However, within the amorphous phase, the trend with Al concentration appears to increase with the same slope as the β phase film from $0.1 < x < 0.4$, but with a 0.1–0.2 eV offset to lower energy. Band gaps were also calculated for sample A2 for, but with an uncertainty in the x-axis of up to 0.1 it's difficult to draw any conclusions other than that the gap generally increases with x.

Close agreement between S2 and post-annealed film pa-A2 is found after heating pa-A2 to 700 °C (fig. 7.30). In addition, the sudden 0.2 eV jump to lower band gap with loss of crystallinity in sample A1 agrees with the offset observed in post-annealed films when they transition to amorphous. Agreement in the band gap variation with Al content between $(Al_xGa_{1-x})_2O_3$ thin films grown at high temperature and post-annealed films grown at room temperature, measured using both ellipsometry and transmission measurements, gives confidence that these results are repeatable within the crystalline β and γ phases for $(Al_xGa_{1-x})_2O_3$ films in general, and may be relied upon to design future devices requiring a carefully-tuned band gap.

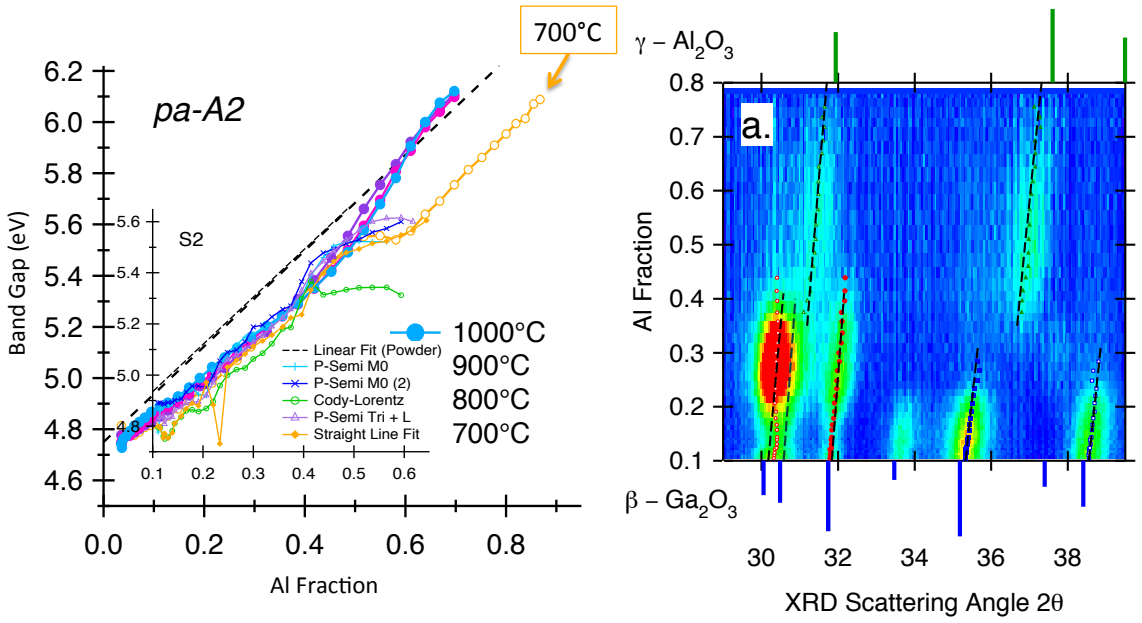

Figure 7.30: Composite figure showing agreement between band gaps (determined by ellipsometry) of high-temperature-grown CCS film S2 on SiOx (with Ga_2O_3 buffer layer), and band gaps measured by UV-Vis spectroscopy of post-annealed CCS film pa-A2 on sapphire after annealing to 700 °C (chapter 6). On the right is the XRD color map showing the changing crystal structure of sample S2 from $\beta - Ga_2O_3$ to $\gamma - Ga_2O_3$ with increasing Al concentration. The abrupt 0.2 eV change to lower band gap at $x \approx 0.6$ corresponds to the loss of crystallinity in both samples.

Chapter 8

SUMMARY

8.1 Key Questions and Results

$(Al_xGa_{1-x})_2O_3$ alloys have attracted renewed interest due to their potential for use in deep-UV optical devices and high-powered transistors, but realization of these technologies depends on the ability to tune the band gap and crystal phase of alloy films for specific applications. Since the stable structures of the parent compounds $\beta - Ga_2O_3$ and $\alpha - Al_2O_3$ are different, there must be a maximum solubility limit of Al in the $\beta - Ga_2O_3$ structure which limits the range of tunability, and within the β phase it is not known whether the increase in band gap proceeds linearly with Al concentration, in accordance with the empirical Vegard's Law, or exhibits significant bowing. Furthermore, depending on the deposition conditions, $(Al_xGa_{1-x})_2O_3$ thin films may grow in a metastable phase rather than the thermodynamically stable β phase, and it was not known how the resulting phase depends on alloy composition and growth temperature, or how the band gap changes between different phases.

These questions on the fundamental structural and optical properties of $(Al_xGa_{1-x})_2O_3$ alloys were thoroughly explored in a series of experiments on single-phase sintered $(Al_xGa_{1-x})_2O_3$ powders produced by solution combustion synthesis, and continuous-composition-spread (CCS) $(Al_xGa_{1-x})_2O_3$ thin films deposited at room temperature on silicon and sapphire by pulsed laser deposition (PLD) and post-annealed to successively higher temperatures in steps of 100 °C to 1000 °C in air, to see how crystallinity develops with alloy composition and measure the corresponding change in band gap. $(Al_xGa_{1-x})_2O_3$ films were also grown on silicon and sapphire at high temperature, with and without an intrinsic Ga_2O_3 buffer layer, to determine limits on substrate epitaxy with those two substrates and to see if films grown at high temperature exhibit similar properties as post-annealed films grown at room temperature.

After sintering at 1600 °C for 12 hours, $(Al_xGa_{1-x})_2O_3$ powders are fully relaxed to the thermodynamically stable phase corresponding to the alloy composition x. X-ray diffraction (XRD) shows

that powders remain in the monoclinic $\beta - Ga_2O_3$ phase until nearly $x = 0.8$, at which point small $\alpha - Al_2O_3$ peaks first start to appear. Lattice parameters are found to contract at slightly different rates from $0 < x < 0.5$ and from $0.5 < x < 0.8$, with a and b decreasing together faster than c at low x, and b diverging from a at higher x, suggesting the possibility of an octahedral site preference for substitutional Al in $\beta - Ga_2O_3$. The band gap was measured using X-ray photoemission spectroscopy (XPS), by locating the onset of inelastic background due to electron-electron scattering behind primary photoemission peaks, and found to increase linearly from the band gap of $\beta - Ga_2O_3$ (4.75 eV) to the band gap of isomorphic $\theta - Al_2O_3$ (6.62 eV) in the range $0 < x < 0.8$. The lack of bowing in the band gap vs. Al concentration trend shows that Al substitutes for Ga without introducing significant strain, charge redistribution or structural relaxation, around the substituted site.

CCS $(Al_xGa_{1-x})_2O_3$ thin films deposited at room temperature and post-annealed up to 1000 °C lose the β phase at much lower Al concentration than sintered powders; the specific transition temperature to β is found to increase steadily with alloy composition from 600 °C to 1000 °C, with a maximum of $x = 0.5$ at 1000 °C. For most of the composition range ($x > 0.1$) $(Al_xGa_{1-x})_2O_3$ films transition first to the metastable γ phase, at temperatures ranging from 500 °C to 800 °C depending on the Al concentration, before transitioning again to the β phase at higher temperature. However, in the Ga-rich region below $x < 0.1$, films transition first from amorphous to a mixed phase, possibly containing $\kappa - Ga_2O_3$, which remains stable to 900 °C before transitioning to β. The transition from β to γ at 800 °C and an Al concentration of $x = 0.25$ is consistent with films deposited at high temperature on silicon substrates.

Band gap and optical constants of post-annealed $(Al_xGa_{1-x})_2O_3$ films were measured using UV-Vis spectroscopy and spectroscopic ellipsometry, and close agreement was obtained in results from both methods. No discontinuity in the band gap was found where films transition from β to γ, suggesting that both structures have similar densities of states near the conduction band minimum. However, a 0.1–0.2 eV jump to lower gap occurs when the films become amorphous. Films in the amorphous phase show downward bowing in the band gap vs. Al concentration trends, and the trends became more linear in the crystalline region. However, the increase in band gap with Al concentration in the crystalline phase is slower than observed for the sintered powders, although the values are close. The difference may be due to improved structural relaxation at the higher sintering

temperature compared to the range of post-annealing temperatures, which were only high enough to crystallize films in the β phase up to $x \approx 0.55$, or it may be an artificial underestimate based on how the fitting was performed. In addition, the development of a broader absorption onset after annealing to 800 °C in the region above $x > 0.5$ may indicate Al diffusion from the sapphire into the film, which means that above a certain composition the crystallization temperature is greater than the activation energy of diffusion into the film, which would limit the composition range achievable in β phase $(Al_xGa_{1-x})_2O_3$ films on sapphire.

In addition to exploring the intrinsic properties of $(Al_xGa_{1-x})_2O_3$, an effort was made to learn about practical issues related to the epitaxial growth of $(Al_xGa_{1-x})_2O_3$ films on commercially important substrates. Therefore Ga_2O_3 and Al_2O_3 CCS films grown at 800 °C on Si (100), Si (111), and SiOx, substrates show unoriented β and γ phases, regardless of whether the native oxide was etched away or not, indicating that the bare Si surface reacts too favorably with oxygen to allow epitaxial growth at that temperature. However, a spontaneous [400]/[002] orientation of the β phase was observed for $x > 0.1$, which occurs regardless of whether a Ga_2O_3 buffer layer was deposited and becomes stronger with increasing film thickness. The orientation is therefore either intrinsic to $(Al_xGa_{1-x})_2O_3$, meaning that the addition of Al changes the film behavior compared to intrinsic unoriented $\beta - Ga_2O_3$, or it is caused by the alignment between $\beta - (Al_xGa_{1-x})_2O_3$ and spontaneously [220]-oriented $\gamma - (Al_xGa_{1-x})_2O_3$. However, the presence of the buffer layer extends the stability region of the β phase from $x = 0.35$ to $x = 0.4$. In addition, ellipsometry showed that the variation of the band gap within the crystalline region of films grown at high temperature is comparable to films that were grown at room temperature and post annealed.

Epitaxial $(Al_xGa_{1-x})_2O_3$ CCS films on sapphire are initially $(\bar{2}01)$-oriented on the Ga-rich side, with an in-plane epitaxial relationship $[201]_{Ga_2O_3} \parallel [\bar{2}10]_{sapphire}$ and six-fold rotational symmetry. Films with thickness greater than 100 nm start to lose their orientation by twinning on the (101) plane, parallel to one of the faces of the distorted oxygen fcc sublattice, and accumulate additional defects above 750 nm. From 100 nm to 750 nm, twinned regions grow much faster than the epitaxial regions, as evidenced by the change in intensity of diffraction peaks. This could be because twinning on (101) orients the unit cell of $\beta - Ga_2O_3$ more nearly vertical to expose the lower energy [100] and [001] surfaces during grain growth. As the Al concentration is increased, CCS films on sapphire quickly lose crystallinity, most likely due to a lower temperature of 500–600 °C, rather than 800 °C,

during growth. As with films on sapphire, a Ga_2O_3 buffer layer was found to extend the stability of the β phase, to about $x \approx 0.15$. However, depth-sensitive ellipsometry revealed Ga_2O_3 diffusion from the buffer layer all the way through the film above $x > 0.15$, where the film became amorphous. This may occur for film growth on single-crystal $\beta - Ga_2O_3$, as well, unless the temperature is high enough to crystallize $(Al_xGa_{1-x})_2O_3$ at the appropriate alloy composition x.

8.2 Future Directions

In this work, fundamental relationships between alloy composition, annealing temperature, crystal structure, and band gap of $(Al_xGa_{1-x})_2O_3$ powders and thin films have been found, which are consistent across different samples and characterization techniques. Sintering of $(Al_xGa_{1-x})_2O_3$ powders in the $0.8 < x < 1$ range could be done at a lower temperature to possibly obtain $\theta - Al_2O_3$ rather than $\alpha - Al_2O_3$, and the variation of the band gap in the full range $0 < x < 1$ could then be determined by XPS. The post-annealed CCS film on silicon (pa-S1) could be repeated with a smaller plume separation to obtain optical constants which do not show unexpected anisotropy at the midpoint of the film. Density functional theory calculations could be performed to test some of my proposed explanations, i.e. why twinned regions grow faster than epitaxial regions for films on sapphire greater than 100 nm, or why unoriented $\beta - Ga_2O_3$ films on SiOx develop a spontaneous orientation upon the addition of Al.

However, practical issues related to the epitaxial growth of $(Al_xGa_{1-x})_2O_3$ films for devices were only explored for a small number of possible cases, with mixed results. Epitaxial $\beta - Ga_2O_3$ films on sapphire are relatively easy to achieve, and the lattice mismatch improves as the Al content is increased, so it would be worthwhile to try depositing a CCS $(Al_xGa_{1-x})_2O_3$ film at at higher temperature to try and achieve crystallinity over a wider range in x. Other substrates could be explored. We found that growth of $(Al_xGa_{1-x})_2O_3$ directly on GaN (001) causes a surface reaction forming AlN at the interface, but such a reaction may be preventable by oxidizing the GaN surface prior to deposition, or using an epitaxial Ga_2O_3 buffer layer. Recently, different authors demonstrated [100]-oriented $(Al_xGa_{1-x})_2O_3$ composition-spread films on MgO (100) substrates, with the β phase extending to $x = 0.5$ followed by an abrupt transition to the γ phase at higher x [306]. Single-crystal $\beta - Ga_2O_3$ wafers have also become commercially available, enabling quasi-homoepitaxial $(Al_xGa_{1-x})_2O_3$ films in multiple orientations. Possible issues with Ga inter-diffusion,

observed in $(Al_xGa_{1-x})_2O_3$ films grown on a crystalline Ga_2O_3 buffer layer on sapphire, as well as enhanced stability of the β phase at higher x when growing on $\beta - Ga_2O_3$ could be explored. In addition, band offsets between ultrathin $(Al_xGa_{1-x})_2O_3$ films and $\beta - Ga_2O_3$ could be measured as a function of the alloy composition, important for the design of high-electron-mobility transistors (HEMTs) and quantum well structures.

In addition to controlling band offsets between $(Al_xGa_{1-x})_2O_3$ and Ga_2O_3, HEMT design requires strong n-type conductivity in the wide-gap layer. Conductivity in $\beta - Ga_2O_3$ has been varied over several orders of magnitude by alloying with extrinsic impurities such as Si or Sn [13, 15], but no reports currently exist on whether those impurities remain shallow donors in $(Al_xGa_{1-x})_2O_3$ over a wide range in x, i.e. if defect states in the gap track the conduction band minimum, or if the impurities move deeper into the band gap as the Al concentration increases. Alternatively, alloying with Mg is known to create deep traps in $\beta - Ga_2O_3$ resulting in highly-insulating single crystals [314], and it would be interesting to see if the same behavior is reproduced in $(Al_xGa_{1-x})_2O_3$. One group reported in 2006 that Sn stabilizes the orthorhombic κ phase [217], but so far no one has followed up on it. Alloying with other transition metals may also stabilize other Ga_2O_3 phases, and our group is well positioned to investigate new alloys efficiently by fabricating composition-spread thin films using PLD. It has also been recently reported that the addition of Al to the metastable $\alpha - Ga_2O_3$ phase pushes the $(\alpha \rightarrow \beta)$ transition to higher temperature [309], allowing for a much wider range of band gap tunability up to 8.7 eV in corundum phase films than β phase films, and quasi-homoepitaxial HEMT and quantum well structures on sapphire instead of single-crystal $\beta - Ga_2O_3$.

BIBLIOGRAPHY

[1] Roy G Gordon. Criteria for Choosing Transparent Conductors. *MRS Bulletin*, 25(8):52–57, 2000.

[2] Toshio Kamiya and Hideo Hosono. Electronic Structures and Device Applications of Transparent Oxide Semiconductors: What Is the Real Merit of Oxide Semiconductors? *International Journal of Applied Ceramic Technology*, 2(4):285–294, jul 2005.

[3] Encarnacion G. Villora, Kiyoshi Shimamura, Yukio Yoshikawa, Kazuo Aoki, and Noboru Ichinose. Large-size $\beta - Ga_2O_3$ single crystals and wafers. *Journal of Crystal Growth*, 270 (3-4):420–426, 2004.

[4] Hideo Hosono. Recent progress in transparent oxide semiconductors: Materials and device application. *Thin Solid Films*, 515(15):6000–6014, 2007.

[5] Aron Walsh, Juarez L F Da Silva, and Su-Huai Wei. Multi-component transparent conducting oxides: progress in materials modelling. *Journal of physics. Condensed matter*, 23(33):334210, aug 2011.

[6] E. Fortunato, P. Barquinha, and R. Martins. Oxide semiconductor thin-film transistors: A review of recent advances. *Advanced Materials*, 24(22):2945–2986, 2012.

[7] Shizuo Fujita. Wide-bandgap semiconductor materials : For their full bloom. *Japanese Journal of Applied Physics*, 54:030101, 2015.

[8] Brian G. Lewis and David C. Paine. Applications and Processing of Transparent Conducting Oxides. *MRS Bulletin*, 25(08):22–27, 2000.

[9] Elvira Fortunato, David Ginley, Hideo Hosono, and David C Paine. Transparent Conducting Oxides for Photovoltaics. *MRS Bulletin*, 32(March):242–247, 2007.

[10] Tadatsugu Minami. Transparent conducting oxide semiconductors for transparent electrodes. *Semiconductor Science and Technology*, 20(4):S35–S44, apr 2005.

[11] H. H. Tippins. Optical absorption and photoconductivity in the band edge of $\beta - Ga_2O_3$. *Physical Review*, 140(1A), 1965.

[12] Naoyuki Ueda, Hideo Hosono, Ryuta Waseda, and Hiroshi Kawazoe. Anisotropy of electrical and optical properties in $\beta - Ga_2O_3$ single crystals. *Applied Physics Letters*, 71(7):933–935, 1997.

[13] Encarnacin G. Vllora, Kiyoshi Shimamura, Yukio Yoshikawa, Takekazu Ujiie, and Kazuo Aoki. Electrical conductivity and carrier concentration control in $\beta - Ga_2O_3$ by si doping. *Applied Physics Letters*, 92(20):202120, 2008.

[14] Naoyuki Ueda, Hideo Hosono, Ryuta Waseda, and Hiroshi Kawazoe. Synthesis and control of conductivity of ultraviolet transmitting $\beta - Ga_2O_3$ single crystals. *Applied Physics Letters*, 70 (26):3561, 1997.

[15] N. Suzuki, S. Ohira, M. Tanaka, T. Sugawara, K. Nakajima, and T. Shishido. Fabrication and characterization of transparent conductive sn-doped $\beta - Ga_2O_3$ single crystal. *Physica Status Solidi (C) Current Topics in Solid State Physics*, 4(7):2310–2313, 2007.

[16] Masahiro Orita, Hiromichi Ohta, Masahiro Hirano, and Hideo Hosono. Deep-ultraviolet transparent conductive $\beta - Ga_2O_3$ thin films. *Applied Physics Letters*, 77(25):4166, 2000.

[17] Masahiro Orita, Hidenori Hiramatsu, Hiromichi Ohta, Masahiro Hirano, and Hideo Hosono. Preparation of highly conductive, deep ultraviolet transparent $\beta - Ga_2O_3$ thin film at low deposition temperatures. *Thin Solid Films*, 411(1):134–139, 2002.

[18] Stefan Müller, Holger von Wenckstern, Daniel Splith, Florian Schmidt, and Marius Grundmann. Control of the conductivity of si-doped $\beta - Ga_2O_3$ thin films via growth temperature and pressure. *Physica Status Solidi (a)*, 211(1):34–39, jan 2014.

[19] Takayoshi Oshima, Keitaro Matsuyama, Kohei Yoshimatsu, and Akira Ohtomo. Conducting

si-doped $\gamma - Ga_2O_3$ epitaxial films grown by pulsed-laser deposition. *Journal of Crystal Growth*, 421:23–26, 2015.

[20] Tadatsugu Minami, Yuki Nishi, and Toshihiro Miyata. High-efficiency Cu_2O-based heterojunction solar cells fabricated using a Ga_2O_3 thin film as n-type layer. *Applied Physics Express*, 6 (044101), 2013.

[21] Takayoshi Oshima, Takeya Okuno, Naoki Arai, Norihito Suzuki, Shigeo Ohira, and Shizuo Fujita. Vertical solar-blind deep-ultraviolet schottky photodetectors based on $\beta - Ga_2O_3$ substrates. *Applied Physics Express*, 1(011202), 2008.

[22] Takayoshi Oshima, Takeya Okuno, Naoki Arai, Norihito Suzuki, Harumichi Hino, and Shizuo Fujita. Flame detection by a $\beta - Ga_2O_3$-based sensor. *Japanese Journal of Applied Physics*, 48(1):011605, 2009.

[23] Zhenguo Ji, Juan Du, Jia Fan, and Wei Wang. Gallium oxide films for filter and solar-blind UV detector. *Optical Materials*, 28(4):415–417, 2006.

[24] Yoshihiro Kokubun, Kasumi Miura, Fumie Endo, and Shinji Nakagomi. Sol-gel prepared $\beta - Ga_2O_3$ thin films for ultraviolet photodetectors. *Applied Physics Letters*, 90(031912):3 pp, 2007.

[25] Pei Guo, Jie Xiong, Xiaohui Zhao, Tuo Sheng, Chao Yue, Bowan Tao, and Xingzhao Liu. Growth characteristics and device properties of mod derived $\beta - Ga_2O_3$ films. *Journal of Materials Science: Materials in Electronics*, 25(8):3629–3632, 2014.

[26] P. Feng, J. Y. Zhang, Q. H. Li, and T. H. Wang. Individual $\beta - Ga_2O_3$ nanowires as solar-blind photodetectors. *Applied Physics Letters*, 88(15):153107, 2006.

[27] W Y Weng, T J Hsueh, and S J Chang. A solar-blind $\beta - Ga_2O_3$ nanowire photodetector. *IEEE Photonics Technology Letters*, 22(10):709–711, 2010.

[28] Y. Tomm, P. Reiche, D. Klimm, and T. Fukuda. Czochralski grown Ga_2O_3 crystals. *Journal of Crystal Growth*, 220(4):510–514, 2000.

[29] Kiyoshi Shimamura, Encarnacion G. Villora, Kay Domen, Keiichi Yui, Kazuo Aoki, and Noboru Ichinose. Epitaxial growth of gan on (1 0 0) $\beta - Ga_2O_3$ substrates by metalorganic vapor phase epitaxy. *Japanese Journal of Applied Physics*, 44(1):L7–L8, jan 2005.

[30] Encarnacion G. Villora, Kiyoshi Shimamura, Kazuo Aoki, and Kenji Kitamura. Molecular beam epitaxy of c-plane wurtzite gan on nitridized a-plane $\beta - Ga_2O_3$. *Thin Solid Films*, 500 (1-2):209–213, 2006.

[31] Shigeo Ohira, Masayuki Yoshioka, Takamasa Sugawara, Kazuo Nakajima, and Toetsu Shishido. Fabrication of hexagonal gan on the surface of $\beta - Ga_2O_3$ single crystal by nitridation with nh3. *Thin Solid Films*, 496(1):53–57, 2006.

[32] M Hong, M Passlack, J P Mannaerts, T D Harris, M L Schnoes, R L Opila, and H W Krautter. A Ga_2O_3 passivation technique compatible with gaas device processing. *Solid State Electronics*, 41(4):643–646, 1997.

[33] M. Rebien, W. Henrion, M. Hong, J. P. Mannaerts, and M. Fleischer. Optical properties of gallium oxide thin films. *Applied Physics Letters*, 81(2002):250–252, 2002.

[34] Toshihiro Miyata, Toshikuni Nakatani, and Tadatsugu Minami. Gallium oxide as host material for multicolor emitting phosphors. *Journal of Luminescence*, 87:1183–1185, 2000.

[35] Masataka Higashiwaki, Kohei Sasaki, Akito Kuramata, Takekazu Masui, and Shigenobu Yamakoshi. Gallium oxide (Ga_2O_3) metal-semiconductor field-effect transistors on single-crystal $\beta - Ga_2O_3$ (010) substrates. *Applied Physics Letters*, 100(013504), 2012.

[36] Kohei Sasaki, Masataka Higashiwaki, Akito Kuramata, and Takekazu Masui. Mbe grown Ga_2O_3 and its power device applications. *Journal of Crystal Growth*, 378:591–595, 2013.

[37] Masataka Higashiwaki, Kohei Sasaki, Takafumi Kamimura, Man Hoi Wong, Daivasigamani Krishnamurthy, Masataka Higashiwaki, Kohei Sasaki, Takafumi Kamimura, and Man Hoi Wong. Depletion-mode Ga_2O_3 metal-oxide-semiconductor field-effect transistors on $\beta - Ga_2O_3$ (010) substrates and temperature dependence of their device characteristics. *Applied Physics Letters*, 103:123511, 2013.

[38] Wan Sik Hwang, Amit Verma, Hartwin Peelaers, Vladimir Protasenko, Sergei Rouvimov, Huili Grace Xing, Wilfried Haensch, Chris Van De Walle, Zbigniew Galazka, Martin Albrecht, Roberto Fornari, Wan Sik Hwang, Amit Verma, Hartwin Peelaers, Vladimir Protasenko, Sergei Rouvimov, Huili Grace Xing, Alan Seabaugh, Wilfried Haensch, Chris Van De Walle, Zbigniew Galazka, Martin Albrecht, and Roberto Fornari. High-voltage field effect transistors with wide-bandgap $\beta - Ga_2O_3$ nanomembranes. *Applied Physics Letters*, 104(20):203111, 2014.

[39] Lakshmi Nagarajan, Roger a De Souza, Dominik Samuelis, Ilia Valov, Alexander Börger, Jürgen Janek, Klaus-Dieter Becker, Peter C Schmidt, and Manfred Martin. A chemically driven insulator-metal transition in non-stoichiometric and amorphous gallium oxide. *Nature materials*, 7(5):391–8, may 2008.

[40] Xu Gao, Yidong Xia, Jianfeng Ji, Hanni Xu, Yi Su, Haitao Li, Chunjun Yang, Hongxuan Guo, Jiang Yin, and Zhiguo Liu. Effect of top electrode materials on bipolar resistive switching behavior of gallium oxide films. *Applied Physics Letters*, 97(19):193501, 2010.

[41] Maximilian Fleischer and Hans Meixner. Gallium oxide thin films: A new material for high-temperature oxygen sensors. *Sensors and Actuators B: Chemical*, 4(3-4):437–441, 1991.

[42] M. Fleischer and H. Meixner. Sensing reducing gases at high temperatures using long-term stable Ga_2O_3 thin films. *Sensors and Actuators B: Chemical*, 6(1-3):257–261, 1992.

[43] Yidong Hou, Ling Wu, Xinchen Wang, Zhengxin Ding, Zhaohui Li, and Xianzhi Fu. Photocatalytic performance of $\alpha-$, $\beta-$, and $\gamma - Ga_2O_3$ for the destruction of volatile aromatic pollutants in air. *Journal of Catalysis*, 250(1):12–18, 2007.

[44] Takayoshi Oshima, Kenichi Kaminaga, Hisanori Mashiko, Akira Mukai, Kohei Sasaki, Takekazu Masui, Akito Kuramata, Shigenobu Yamakoshi, and Akira Ohtomo. $\beta - Ga_2O_3$ single crystal as a photoelectrode for water splitting. *Japanese Journal of Applied Physics*, 52:111102, 2013.

[45] W Y Weng, T J Hsueh, S J Chang, S C Hung, G J Huang, H T Hsueh, Z D Huang, and C J Chiu. Metal-Semiconductor-Metal VUV Photodetector. *IEEE Sensors Journal*, 11(9): 1795–1799, 2011.

[46] Takayoshi Oshima, Takeya Okuno, Naoki Arai, Yasushi Kobayashi, and Shizuo Fujita. $\beta - Al_{2x}Ga_{2-2x}O_3$ Thin Film Growth by Molecular Beam Epitaxy. *Japanese Journal of Applied Physics*, 48(7):070202, jul 2009.

[47] A K Saxena. The conduction band structure and deep levels in $Ga_{1-x}Al_xAs$ alloys from a high-pressure experiment. *Journal of Physics C: Solid State Physics*, 13(23):4323–4334, 1980.

[48] John David Jackson. *Classical Electrodynamics*. Wiley, third edition, 1999.

[49] Peter Y. Yu and Manuel Cardona. *Fundamentals of Semiconductors*. Springer, fourth edition, 2010.

[50] M. S. Dresselhaus. *Solid State Physics*, 2001. accessed on 9/9/2015 from http://web.mit.edu/6.732/www/texts.html.

[51] Hartwin Peelaers and Chris G Van de Walle. Brillouin zone and band structure of $\beta - Ga_2O_3$. *Physica Status solidi (b)*, 252(4):828–832, 2015.

[52] J A Kohn, Gerald Katz, and J D Broder. Characterization of $\beta - Ga_2O_3$ and its alumina isomorph $\theta - Al_2O_3$. *The American Mineralogist*, 42(5-6):398–407, 1956.

[53] Rustum Roy, V G Hill, and E F Osborn. Polymorphism of Ga_2O_3 and the system $Ga_2O_3 - H_2O$. *J. Amer. Chem. Soc.*, 74(7):719–722, 1952.

[54] S. Geller. Crystal structure of $\beta - Ga_2O_3$. *The Journal of Chemical Physics*, 33(3):676–684, 1960.

[55] E. Husson and Y Repelin. Structural studies of transition alumina: Theta alumina. *European Journal of Solid State and Inorganic Chemistry*, 33(11):1223–1231, 1996.

[56] Igor Levin and David Brandon. Metastable alumina polymorphs: Crystal structures and transition sequences. *Journal of the American Ceramic Society*, 81(8):1995–2012, 1998.

[57] J. P. Remeika and M. Marezio. Growth of $(Al_xGa_{1-x})_2O_3$ single crystals at 44 kbars. *Applied Physics Letters*, 8(4):87–88, 1966.

[58] G. Sinha, K. Adhikary, and S. Chaudhuri. Sol-gel derived phase pure $(Al_xGa_{1-x})_2O_3$ nanocrystalline thin film and its optical properties. *Journal of Crystal Growth*, 276(1-2):204–207, 2005.

[59] M. Ristić, S. Popović, and S. Musić. Application of sol-gel method in the synthesis of gallium(iii)-oxide. *Materials Letters*, 59(10):1227–1233, 2005.

[60] Yu V Shvy'ko, M Lucht, E Gerdau, M Lerche, E E Alp, W Sturhahn, J Sutter, and T S Toellner. Measuring wavelengths and lattice parameters with the mossbauer wavelength standard. *Journal of Synchrotron Radiation*, 9:17–23, 2002.

[61] M. Marezio and J. P. Remeika. Bond lengths in the $(Al_xGa_{1-x})_2O_3$ structure and the high-pressure phase of $Ga_{2-x}Fe_xO_3$. *The Journal of Chemical Physics*, 46(5):1862, 1967.

[62] K P Sinha and A P B Sinha. Vacancy distribution and bonding in some oxides of spinel structure. *Journal of Physical Chemistry*, 61(6):758–761, 1957.

[63] Helen Y. Playford, Alex C. Hannon, Emma R. Barney, and Richard I. Walton. Structures of uncharacterised polymorphs of gallium oxide from total neutron diffraction. *Chemistry - A European Journal*, 19(8):2803–2813, 2013.

[64] Guido Busca. The surface of transitional aluminas: A critical review. *Catalysis Today*, 226: 2–13, 2014.

[65] Shu-Hui Cai, Sergey Rashkeev, Sokrates Pantelides, and Karl Sohlberg. Phase transformation mechanism between γ- and θ-alumina. *Physical Review B*, 67(22):1–10, 2003.

[66] E J W Verwey. The crystal structure of $\gamma-Fe_2O_3$ and $\gamma-Al_2O_3$. *Zeitschrift fur Kristallographie*, 91(1):65–69, 1935.

[67] B Ealet, M H Elyakhloufi, E Gillet, and M Ricci. Electronic and crystallographic structure of gamma-alumina thin-films. *Thin Solid Films*, 250(1-2):92–100, 1994.

[68] Y G Wang, P M Bronsveld, J T M DeHosson, B Djuricic, D McGarry, and S Pickering. Ordering of octahedral vacancies in transition aluminas. *Journal of the American Ceramic Society*, 81(6):1655–1660, 1998.

[69] G N Kryukova, D O Klenov, A S Ivanova, and S V Tsybulya. Vacancy ordering in the structure of $\gamma - Al_2O_3$. *Journal of the European Ceramic Society*, 20(8):1187–1189, 2000.

[70] R Dupree, M H Lewis, and M E Smith. A study of the vacancy distribution in nonstoichiometric spinels by magic-angle spinning nmr. *Philosophical Magazine A*, 53(2):L17–L20, 1986.

[71] V. Jayaram and C. G. Levi. The structure of $\delta-$alumina evolved from the melt and the $\gamma - \delta$ transformation. *Acta Metallurgica et Materialia*, 37(2):569–578, 1989.

[72] S J Wilson. Dehydration of boehmite, $\gamma-$alooh, to $\gamma-Al_2O_3$. *Journal of Solid State Chemistry*, 30(2):247–255, 1979.

[73] C.S. John, N.C.M. Alma, and G.R. Hays. Characterization of transitional alumina by solid-state magic angle spinning aluminium nmr. *Applied Catalysis*, 6(3):341–346, 1983.

[74] M.-H. Lee, Chi-Feng Cheng, Volker Heine, and Jacek Klinowski. Distribution of tetrahedral and octahedral a1 sites in gamma alumina. *Chemical Physics Letters*, 265(6):673–676, 1997.

[75] J A Wang, X Bokhimi, A Morales, O Novaro, T Lopez, and R Gomez. Aluminum local environment and defects in the crystalline structure of sol-gel alumina catalyst. *Journal of Physical Chemistry B*, 103(2):299–303, 1999.

[76] L J Alvarez, J F Sanz, M J Capitan, and J A Odriozola. Molecular-dynamics studies of the structure of gamma-alumina. *Chemical Physics Letters*, 192(5-6):463–468, 1992.

[77] S Blonski and S H Garofalini. Molecular dynamics simulations of $\alpha-$alumina and $\gamma-$alumina surfaces. *Surface Science*, 295(1-2):263–274, 1993.

[78] Shang-Di Mo, Yong-Nian Xu, and Wai-Yim Ching. Electronic and structural properties of bulk $\gamma - Al_2O_3$. *Journal of the American Ceramic Society*, 80(5):1193–1197, 1997.

[79] F. Streitz and J. Mintmire. Energetics of aluminum vacancies in gamma alumina. *Physical Review B*, 60(2):773–777, 1999.

[80] Gonzalo Gutiérrez, Adrian Taga, and Börje Johansson. Theoretical structure determination of $\gamma - Al_2O_3$. *Physical Review B*, 65(1):1–4, 2001.

[81] C Wolverton and K C Hass. Phase stability and structure of spinel-based transition aluminas. *Physical Review B*, 63(2):0124102, 2001.

[82] B C Lippens and J H Boer. Study of phase transformations during calcination of aluminum hydroxides by selected area electron diffraction. *Acta Crystallographica*, 17(10):1312–1321, 1964.

[83] V A Ushakov and E M Moroz. Structure of low temperature $\gamma - Al_2O_3$ and $\eta - Al_2O_3$. *Reaction Kinetics and Catalysis Letters*, 24(1–2):113–116, 1984.

[84] R. S. Zhou and R. L. Snyder. Structures and transformation mechanisms of the η, γ and θ transition aluminas. *Acta Crystallographica Section B*, 47(5):617–630, 1991.

[85] Xénophon Krokidis, Pascal Raybaud, Anne Elisabeth Gobichon, Bernadette Rebours, Patrick Euzen, and Hervé Toulhoat. Theoretical study of the dehydration process of boehmite to $\gamma-$alumina. *Journal of Physical Chemistry B*, 105(22):5121–5130, 2001.

[86] M. Digne, P. Sautet, P. Raybaud, P. Euzen, and H. Toulhoat. Use of dft to achieve a rational understanding of acid-basic properties of $\gamma-$alumina surfaces. *Journal of Catalysis*, 226(1): 54–68, 2004.

[87] G. Paglia, C. Buckley, A. Rohl, B. Hunter, R. Hart, J. Hanna, and L. Byrne. Tetragonal structure model for boehmite-derived γ-alumina. *Physical Review B*, 68(14):1–11, 2003.

[88] Gianluca Paglia, Andrew L. Rohl, Craig E. Buckley, and Julian D. Gale. Determination of the structure of gamma-alumina from interatomic potential and first-principles calculations: The requirement of significant numbers of nonspinel positions to achieve an accurate structural model. *Physical Review B - Condensed Matter and Materials Physics*, 71(22):1–16, 2005.

[89] E. Menéndez-Proupin and G. Gutiérrez. Electronic properties of bulk $\gamma - Al_2O_3$. *Physical Review B*, 72(3):1–9, 2005.

[90] Mingyong Sun, Alan E Nelson, and John Adjaye. Examination of spinel and nonspinel structural models for $\gamma - Al_2O_3$ by dft and rietveld refinement simulations. *Journal of Physical Chemistry B*, 110:2310–2317, 2006.

[91] W. Ching, Lizhi Ouyang, Paul Rulis, and Hongzhi Yao. Ab initio study of the physical properties of $\gamma - Al_2O_3$ lattice dynamics, bulk properties, electronic structure, bonding, optical properties, and elnes/xanes spectra. *Physical Review B*, 78(1):1–13, 2008.

[92] Ary R. Ferreira, Mateus J F Martins, Elena Konstantinova, Rodrigo B. Capaz, Wladmir F. Souza, Sandra Shirley X Chiaro, and Alexandre a. Leitão. Direct comparison between two $\gamma-$alumina structural models by dft calculations. *Journal of Solid State Chemistry*, 184(5): 1105–1111, 2011.

[93] Ary R. Ferreira, Emine Küçükbenli, Alexandre a. Leitão, and Stefano De Gironcoli. Ab initio 27al nmr chemical shifts and quadrupolar parameters for Al_2O_3 phases and their precursors. *Physical Review B - Condensed Matter and Materials Physics*, 84(23):1–9, 2011.

[94] Michael F. Peintinger, Michael J. Kratz, and Thomas Bredow. Quantum-chemical study of stable, meta-stable and high-pressure alumina polymorphs and aluminum hydroxides. *Journal of Materials Chemistry A*, 2(32):13143, 2014.

[95] Gianluca Paglia, Craig E. Buckley, and Andrew L. Rohl. Comment on examination of spinel and nonspinel structural models for $\gamma - Al_2O_3$ by dft and rietveld refinement simulations. *Journal of Physical Chemistry B*, 110(5):2310–2317, 2006.

[96] Mathieu Digne, Pascal Raybaud, Philippe Sautet, Bernadette Rebours, and Herve Toulhoat. Comment on examination of spinel and nonspinel structural models for $\gamma - Al_2O_3$ by dft and rietveld refinement simlulations. *Journal of Physical Chemistry B*, 110(ii):20719–20720, 2006.

[97] Lubomír Smrčok, Vratislav Langer, and Jan Krestan. $\gamma-$alumina: A single-crystal x-ray diffraction study. *Acta Crystallographica Section C: Crystal Structure Communications*, 62(9): 83–84, 2006.

[98] Choong-Ki Lee, Eunae Cho, Hyo-Sug Lee, Kwang Seol, and Seungwu Han. Comparative study of electronic structures and dielectric properties of alumina polymorphs by first-principles methods. *Physical Review B*, 76(24):1–7, 2007.

[99] C O Arean, a L Bellan, M P Mentruit, M R Delgado, and G T Palomino. Preparation and

characterization of mesoporous $\gamma - Ga_2O_3$. *Microporous and Mesoporous Materials*, 40(1-3): 35–42, 2000.

[100] S Yoshioka, H Hayashi, A Kuwabara, F Oba, K Matsunaga, and I Tanaka. Structures and energetics of Ga_2O_3 polymorphs. *Journal of Physics: Condensed Matter*, 19(34):346211, 2007.

[101] Helen Y Playford, Alex C Hannon, Matthew G Tucker, Daniel M Dawson, Sharon E Ashbrook, Reza J Kastiban, Jeremy Sloan, and Richard I Walton. Characterization of structural disorder in $\gamma - Ga_2O_3$. *Journal of Physical Chemistry C*, 118:16188–16198, 2014.

[102] V G Hill, Rustum Roy, and E F Osborn. The System Alumina-Gallia-Water. *Journal of the American Ceramic Society*, 35(6):135–142, 1952.

[103] Masao Mizuno, Toyoaki Yamada, and Tetsuo Noguchi. The liquidus curve in the system Al_2O_3-Ga_2O_3 as measured with a solar furnace. *Journal of the Ceramic Association, Japan*, 83(4):175–177, 1975.

[104] Andrea L. Jaromin and Doreen D. Edwards. Subsolidus phase relationships in the Ga_2O_3–$Al_2O_3TiO_2$ system. *Journal of the American Ceramic Society*, 88(9):2573–2577, 2005.

[105] J. P. Remeika. $GaFeO_3$: A Ferromagnetic-Piezoelectric Compound. *Journal of Applied Physics*, 31(5):S263, 1960.

[106] Johan Ahman, Goran Svensson, and Jorgen Albertsson. A Reinvestigation of beta-Gallium Oxide. *Acta Crystallographica*, 52(6):1336–1338, 1996.

[107] G.M. Wolten and A.B. Chase. Determination of the point group of $\beta - Ga_2O_3$ from morphology and physical properties. *Journal of Solid State Chemistry*, 16(3-4):377–383, 1976.

[108] S. Geller. On the structure of $\beta - Ga_2O_3$. *Journal of Solid State Chemistry*, 20:209–210, 1977.

[109] A B Chase. Growth of $\beta - Ga_2O_3$ by the verneuil technique. *Journal of the American Ceramic Society*, 49(9):470, 1964.

[110] Gerald Katz and Rustum Roy. Flux growth and characterization of $\beta - Ga_2O_3$ single crystals. *Journal of the American Ceramic Society*, 49(3):168–169, 1966.

[111] M R Lorenz, J F Woods, and R J Gambino. Some electrical properties of the semiconductor $\beta - Ga_2O_3$. *Journal of Physics and Chemistry of Solids*, 28:403–404, 1967.

[112] B. Hoeneisen, C. A. Mead, and M-A. Nicolet. Permittivity of $\beta - Ga_2O_3$ at low frequencies. *Solid State Electronics*, 14:1057–1059, 1971.

[113] Takahashi Matsumoto, Masaharu Aoki, Akira Kinoshita, and Tomoyoshi Aono. Refractive index of $\beta - Ga_2O_3$. *Jpn. J. Appl. Phys.*, 13(4):737, 1974.

[114] G Blasse and A Bril. Some observations on the luminescence of $\beta - Ga_2O_3$. *J. Phys. Chem. Solids*, 31:707–711, 1970.

[115] T Harwig, G J Wubs, and G J Dirksen. Electrical-properties of $\beta - Ga_2O_3$ single-crystals. *Solid State Communications*, 18(9-10):1223–1225, 1976.

[116] T Harwig and J Schoonman. Electrical properties of $\beta - Ga_2O_3$ single crystals. *Journal of Solid State Chemistry*, 11:205–211, 1978.

[117] T. Harwig, F. Kellendonk, and S. Slappendel. The ultraviolet luminescence of β-galliumsesquioxide. *J. Phys. Chem. Solids*, 39:675–680, 1978.

[118] T. Harwig and F. Kellendonk. Some observations on the photoluminescence of doped β-galliumsesquioxide. *Journal of Solid State Chemistry*, 24(3-4):255–263, 1978.

[119] Vasiltsiv. On the nature of blue and green luminescence bands of $\beta - Ga_2O_3$. *Ukrainskii Fizicheskii Zhurnal*, 33(9):1320–1324, 1988.

[120] Eric Aubay and Didier Gourier. Magnetic bistability and Overhauser shift of conduction electrons in gallium oxide. *Physical Review B*, 47(22), 1993.

[121] Nevill Mott. Metal-insulator transitions. *Proceedings of the Royal Society of London*, 382: 1–24, 1982.

[122] Laurent Binet and Didier Gourier. Origin of the blue luminescence of $\beta - Ga_2O_3$. *Journal of Physics and Chemistry of Solids*, 59(8):1241–1249, 1998.

[123] Laurent Binet and Didier Gourier. Optical evidence of intrinsic quantum wells in the transparent conducting oxide $\beta - Ga_2O_3$. *Applied Physics Letters*, 77(8):1138–1140, 2000.

[124] Encarnacion G. Villora, Yasukazu Murakami, Takasi Sugawara, Toshiyuki Atou, Masae Kikuchi, Daisuke Shindo, and Tsuguo Fukuda. Electron microscopy studies of microstructures in $\beta - Ga_2O_3$ single crystals. *Materials Research Bulletin*, 37(4):769–774, 2002.

[125] J. B. Varley, J. R. Weber, A. Janotti, and C. G. Van de Walle. Oxygen vacancies and donor impurities in $\beta - Ga_2O_3$. *Applied Physics Letters*, 97(14):142106, 2010.

[126] Laurent Binet, Didier Gourier, and C Minot. Relation between electron band structure and magnetic bistability of conduction electrons in beta-ga2o3. *Journal of Solid State Chemistry*, 113(2):420–433, 1994.

[127] E. Aubay and D. Gourier. Bistability of the magnetic resonance of conduction electrons in gallium oxide. *J. Phys. Chem.*, 96(13):5513–5520, 1992.

[128] G. V. Chaplygin and S. a. Semiletov. Preparation, structure and electrical properties of epitaxial films of Ga_2O_3 on sapphire substrates. *Thin Solid Films*, 32:321–324, 1976.

[129] Hyung Gon Kim and Wha Tek Kim. Optical properties of $\beta - Ga_2O_3$ and $(Al_xGa_{1-x})_2O_3$:co thin films grown by spray pyrolysis. *Journal of Applied Physics*, 62(5):2000–2002, 1987.

[130] P Wu, Y-m Gao, R Kershaw, K Dwight, and A Wold. Growth and Characterization of Gallium (III) Oxide Films. *Materials Research Bulletin*, 25:357–363, 1990.

[131] Wolfgang Hanrieder, Maximilian Fleischer, and Hans Meixner. Scanning tunnelling microscopy on oxygen-sensitive Ga_2O_3 thin-film ceramics. *Journal of Physics D: Applied Physics*, 22(3-4): 1938–1941, 1989.

[132] M Fleischer, W Hanrieder, and H Meixner. Stability of Semiconducting Gallium Oxide Thin Films. *Thin Solid Films*, 190:93–102, 1990.

[133] M. Fleischer and H. Meixner. Electron mobility in single- and polycrystalline Ga_2O_3. *Journal of Applied Physics*, 74(1):300–305, 1993.

[134] M. Passlack, N. E. J. Hunt, E. F. Schubert, G. J. Zydzik, M. Hong, J. P. Mannaerts, R. L. Opila, and R. J. Fischer. Dielectric properties of electron-beam deposited Ga_2O_3 films. *Applied Physics Letters*, 64(20):2715, 1994.

[135] M. Passlack, E. F. Schubert, W. S. Hobson, M. Hong, N. Moriya, S. N G Chu, K. Konstadinidis, J. P. Mannaerts, M. L. Schnoes, and G. J. Zydzik. Ga_2O_3 films for electronic and optoelectronic applications. *Journal of Applied Physics*, 77(2):686–693, 1995.

[136] Y Tomm, J.M Ko, A Yoshikawa, and T Fukuda. Floating zone growth of $\beta - Ga_2O_3$: a new window material for optoelectronic device applications. *Solar Energy Materials and Solar Cells*, 66(1-4):369–374, 2001.

[137] Encarnacion Garcia Villora, T Atoua, Takashi Sekiguchi, and Takashi Sugawara. Cathodoluminescence of undoped $\beta - Ga_2O_3$ single crystals. *Solid State Communications*, 120:455–458, 2001.

[138] Z. Galazka, R. Uecker, K. Irmscher, M. Albrecht, D. Klimm, M. Pietsch, M. Brützam, R. Bertram, S. Ganschow, and R. Fornari. Czochralski growth and characterization of $\beta - Ga_2O_3$ single crystals. *Crystal Research and Technology*, 45(12):1229–1236, 2010.

[139] E G Villora, Y Morioka, T Atou, T Sugawara, M Kikuchi, and T Fukuda. Infrared reflectance and electrical conductivity of $\beta - Ga_2O_3$. *Physica Status Solidi (a)*, 193(1):187–195, 2002.

[140] Encarnacion G. Villora, Mitsuo Yamaga, Takafumi Inoue, Satoshi Yabasi, Yuki Masui, Takasi Sugawara, and Tsuguo Fukuda. Optical spectroscopy study on $\beta - Ga_2O_3$. *Japanese Journal of Applied Physics*, 41(Part 2, No. 6A):L622–L625, 2002.

[141] Zoltn Hajnal, Jzsef Mir, Gbor Kiss, Ferenc Rti, Pter Dek, Roy C Herndon, and J Michael Kuperberg. Role of oxygen vacancy defect states in the n-type conduction of $\beta - Ga_2O_3$. *Journal of Applied Physics*, 86(7):3792, 1999.

[142] Mitsuo Yamaga, Encarnacion Villora, Kiyoshi Shimamura, Noboru Ichinose, and Makoto Honda. Donor structure and electric transport mechanism in $\beta - Ga_2O_3$. *Physical Review B*, 68(15):1–9, 2003.

[143] Kenji Yamaguchi. First principles study on electronic structure of $\beta - Ga_2O_3$. *Solid State Communications*, 131(12):739–744, 2004.

[144] Haiying He, Miguel a. Blanco, and Ravindra Pandey. Electronic and thermodynamic properties of $\beta - Ga_2O_3$. *Applied Physics Letters*, 88(26):1–4, 2006.

[145] Haiying He, Roberto Orlando, Miguel Blanco, Ravindra Pandey, Emilie Amzallag, Isabelle Baraille, and Michel Rérat. First-principles study of the structural, electronic, and optical properties of Ga_2O_3 in its monoclinic and hexagonal phases. *Physical Review B*, 74(19):195123, 2006.

[146] Miguel a. Blanco, Munima B. Sahariah, Huitian Jiang, Aurora Costales, and Ravindra Pandey. Energetics and migration of point defects in Ga_2O_3. *Physical Review B - Condensed Matter and Materials Physics*, 72(18):1–16, 2005.

[147] K. Irmscher, Z. Galazka, M. Pietsch, R. Uecker, and R. Fornari. Electrical properties of $\beta - Ga_2O_3$ single crystals grown by the czochralski method. *Journal of Applied Physics*, 110 (6), 2011.

[148] Encarnacion G. Villora, Kiyoshi Shimamura, Kazuo Aoki, and Noboru Ichinose. Reconstruction of the $\beta - Ga_2O_3$ (100) cleavage surface to hexagonal gan after NH_3 nitridation. *Journal of Crystal Growth*, 270(3-4):462–468, 2004.

[149] Shigeo Ohira, Naoki Arai, Takayoshi Oshima, and Shizuo Fujita. Atomically controlled surfaces with step and terrace of $\beta - Ga_2O_3$ single crystal substrates for thin film growth. *Applied Surface Science*, 254(23):7838–7842, 2008.

[150] V. M. Bermudez. The structure of low-index surfaces of $\beta - Ga_2O_3$. *Chemical Physics*, 323 (2-3):193–203, 2006.

[151] T C Lovejoy, E N Yitamben, N Shamir, J Morales, E G Villora, K Shimamura, S Zheng, F S Ohuchi, and M a Olmstead. Surface morphology and electronic structure of bulk single crystal $\beta - Ga_2O_3$ (100). *Applied Physics Letters*, 94(8):081906, 2009.

[152] Jungang Zhang, Bin Li, Changtai Xia, Guangqing Pei, Qun Deng, Zhaohui Yang, Wusheng Xu, Hongsheng Shi, Feng Wu, Yongqing Wu, and Jun Xu. Growth and spectral characterization of $\beta - Ga_2O_3$ single crystals. *Journal of Physics and Chemistry of Solids*, 67(12):2448–2451, 2006.

[153] Jungang Zhang, Changtai Xia, Qun Deng, Wusheng Xu, Hongsheng Shi, Feng Wu, and Jun Xu. Growth and characterization of new transparent conductive oxides single crystals $\beta - Ga_2O_3$: Sn. *Journal of Physics and Chemistry of Solids*, 67:1656–1659, 2006.

[154] Shigeo Ohira, Norihito Suzuki, Naoki Arai, Masahiko Tanaka, Takamasa Sugawara, Kazuo Nakajima, and Toetsu Shishido. Characterization of transparent and conducting sn-doped $\beta - Ga_2O_3$ single crystal after annealing. *Thin Solid Films*, 516(17):5763–5767, 2008.

[155] Kiyoshi Shimamura, Encarnacin G. Vllora, Takekazu Ujiie, and Kazuo Aoki. Excitation and photoluminescence of pure and si-doped $\beta - Ga_2O_3$ single crystals. *Applied Physics Letters*, 92(20):201914, 2008.

[156] F. Litimein, D. Rached, R. Khenata, and H. Baltache. Fplapw study of the structural, electronic, and optical properties of Ga_2O_3: Monoclinic and hexagonal phases. *Journal of Alloys and Compounds*, 488(1):148–156, 2009.

[157] Yijun Zhang, Jinliang Yan, Gang Zhao, and Wanfeng Xie. First-principles study on electronic structure and optical properties of sn-doped $\beta - Ga_2O_3$. *Physica B: Condensed Matter*, 405 (18):3899–3903, sep 2010.

[158] Li Chao, Yan Jin-Liang, Zhang Li-Ying, and Zhao Gang. Electronic structures and optical properties of zn-doped $\beta - Ga_2O_3$ with different doping sites. *Chinese Physics B*, 21(12): 127104, 2012.

[159] Huiyu Yan, Yanrui Guo, Qinggong Song, and Yifei Chen. First-principles study on electronic structure and optical properties of cu-doped $\beta - Ga_2O_3$. *Physica B: Condensed Matter*, 434: 181–184, feb 2014.

[160] M. Mohamed, C. Janowitz, I. Unger, R. Manzke, Z. Galazka, R. Uecker, R. Fornari, J. R.

Weber, J. B. Varley, and C. G. Van de Walle. The electronic structure of $\beta - Ga_2O_3$. *Applied Physics Letters*, 97(21):211903, 2010.

[161] Christoph Janowitz, Valentina Scherer, Mansour Mohamed, Alica Krapf, Helmut Dwelk, Recardo Manzke, Zbigniew Galazka, Reinhard Uecker, Klaus Irmscher, Roberto Fornari, Marcel Michling, Dieter Schmeißer, Justin R Weber, Joel B Varley, and Chris G Van De Walle. Experimental electronic structure of In_2O_3 and Ga_2O_3. *New Journal of Physics*, 13(8):085014, aug 2011.

[162] J B Varley, H Peelaers, A Janotti, and C G Van de Walle. Hydrogenated cation vacancies in semiconducting oxides. *Journal of physics. Condensed matter : an Institute of Physics journal*, 23(33):334212, aug 2011.

[163] Li-Ying Zhang, Jin-Liang Yan, Yi-Jun Zhang, and Ting Li. Effects of n-doping concentration on the electronic structure and optical properties of n-doped $\beta - Ga_2O_3$. *Chinese Physics B*, 21(6):0–6, 2012.

[164] Liying Zhang, Jinliang Yan, Yijun Zhang, Ting Li, and Xingwei Ding. A comparison of electronic structure and optical properties between n-doped $\beta - Ga_2O_3$ and n-zn co-doped $\beta - Ga_2O_3$. *Physica B: Condensed Matter*, 407(8):1227–1231, apr 2012.

[165] T. Zacherle, P. C. Schmidt, and M. Martin. Ab initio calculations on the defect structure of $\beta - Ga_2O_3$. *Physical Review B*, 87(23):235206, 2013.

[166] J L Lyons, D Steiauf, A Janotti, and C G Van De Walle. Carbon as a Shallow Donor in Transparent Conducting Oxides. *Physical Review Applied*, 2(August):064005, 2014.

[167] Weiyan Guo, Yating Guo, Hao Dong, and Xin Zhou. Tailoring the electronic structure of $\beta - Ga_2O_3$ by non-metal doping from hybrid density functional theory calculations. *Phys. Chem. Chem. Phys.*, 17:5817–5825, 2015.

[168] P. D. C. King, I. McKenzie, and T. D. Veal. Observation of shallow-donor muonium in Ga_2O_3: Evidence for hydrogen-induced conductivity. *Applied Physics Letters*, 96(6):062110, 2010.

[169] K. Iwaya, R. Shimizu, H. Aida, T. Hashizume, and T. Hitosugi. Atomically resolved silicon donor states of $\beta - Ga_2O_3$. *Applied Physics Letters*, 98(14):2009–2012, 2011.

[170] Hideo Aida, Kengo Nishiguchi, Hidetoshi Takeda, Natsuko Aota, Kazuhiko Sunakawa, and Yoichi Yaguchi. Growth of $\beta - Ga_2O_3$ single crystals by the edge-defined, film fed growth method. *Japanese Journal of Applied Physics*, 47(11):8506–8509, 2008.

[171] P. Richard, T. Sato, S. Souma, K. Nakayama, H. W. Liu, K. Iwaya, T. Hitosugi, H. Aida, H. Ding, and T. Takahashi. Observation of momentum space semi-localization in si-doped $\beta - Ga_2O_3$. *Applied Physics Letters*, 101(23):2–7, 2012.

[172] T. Onuma, S. Fujioka, T. Yamaguchi, M. Higashiwaki, K. Sasaki, T. Masui, and T. Honda. Correlation between blue luminescence intensity and resistivity in $\beta - Ga_2O_3$ single crystals. *Applied Physics Letters*, 103(4):8–11, 2013.

[173] J. B. Varley, A. Janotti, C. Franchini, and C. G. Van De Walle. Role of self-trapping in luminescence and p-type conductivity of wide-band-gap oxides. *Physical Review B - Condensed Matter and Materials Physics*, 85(8):2–5, 2012.

[174] T. C. Lovejoy, Renyu Chen, X. Zheng, E. G. Villora, K. Shimamura, H. Yoshikawa, Y. Yamashita, S. Ueda, K. Kobayashi, S. T. Dunham, F. S. Ohuchi, and M. a. Olmstead. Band bending and surface defects in $\beta - Ga_2O_3$. *Applied Physics Letters*, 100(18):181602, 2012.

[175] a. Navarro-Quezada, Z. Galazka, S. Alamé, D. Skuridina, P. Vogt, and N. Esser. Surface properties of annealed semiconducting $\beta - Ga_2O_3$ (100) single crystals for epitaxy. *Applied Surface Science*, 349:368–373, 2015.

[176] F. P. Sabino, Luiz Nunes de Oliveira, and Juarez L. F. Da Silva. Role of atomic radius and d-states hybridization in the stability of the crystal structure of M2O3 (M=Al, Ga, In) oxides. *Physical Review B*, 90(15):1–7, 2014.

[177] a. Petitmangin, B. Gallas, C. Hebert, J. Perrière, L. Binet, P. Barboux, and X. Portier. Characterization of oxygen deficient gallium oxide films grown by PLD. *Applied Surface Science*, 278:153–157, 2013.

[178] Hartwin Peelaers, Daniel Steiauf, Joel B. Varley, Anderson Janotti, and Chris G. Van de Walle. $(In_xGa_{1-x})_2O_3$ alloys for transparent electronics. *Physical Review B*, 92(8):085206, 2015. ISSN 1098-0121. doi: 10.1103/PhysRevB.92.085206.

[179] Maria Barbara Maccioni, Francesco Ricci, and Vincenzo Fiorentini. Low In solubility and band offsets in the small-x $\beta - Ga_2O_3/(Ga_{1?x}In_x)_2O_3$ system. *Applied Physics Express*, 8: 021102, 2015.

[180] Joel B Varley and André Schleife. BetheSalpeter calculation of optical-absorption spectra of In_2O_3 and Ga_2O_3. *Semiconductor Science and Technology*, 30(2):024010, 2015.

[181] Rikiya Suzuki, Shinji Nakagomi, Yoshihiro Kokubun, Naoki Arai, and Shigeo Ohira. Enhancement of responsivity in solar-blind $\beta - Ga_2O_3$ photodiodes with a au schottky contact fabricated on single crystal substrates by annealing. *Applied Physics Letters*, 94(22), 2009.

[182] Kohei Sasaki, Masataka Higashiwaki, Akito Kuramata, Takekazu Masui, and Shigenobu Yamakoshi. Ga_2O_3 schottky barrier diodes fabricated by using single-crystal $\beta - Ga_2O_3$ (010) substrates. *IEEE Electron Device Letters*, 34(4):493–495, 2013.

[183] Kohei Sasaki, Akito Kuramata, Takekazu Masui, Encarnacion G. Villora, Kiyoshi Shimamura, and Shigenobu Yamakoshi. Device-quality $\beta - Ga_2O_3$ epitaxial films fabricated by ozone molecular beam epitaxy. *Applied Physics Express*, 5:035502, 2012.

[184] Kohei Sasaki, Masataka Higashiwaki, Akito Kuramata, Takekazu Masui, and Shigenobu Yamakoshi. Si-ion implantation doping in $\beta - Ga_2O_3$ and its application to fabrication of low-resistance ohmic contacts. *Applied Physics Express*, 6(8):6–9, 2013.

[185] M. F. Al-Kuhaili, S. M a Durrani, and E. E. Khawaja. Optical properties of gallium oxide films deposited by electron-beam evaporation. *Applied Physics Letters*, 83(22):4533–4535, 2003.

[186] Shinji Nakagomi and Yoshihiro Kokubun. Crystal orientation of $\beta - Ga_2O_3$ thin films formed on c-plane and a-plane sapphire substrate. *Journal of Crystal Growth*, 349(1):12–18, jun 2012.

[187] Shinji Nakagomi and Yoshihiro Kokubun. Cross-sectional tem imaging of $\beta - Ga_2O_3$ thin films formed on c-plane and a-plane sapphire substrates. *Physica Status Solidi (A) Applications and Materials Science*, 210(9):1738–1744, 2013.

[188] Shinji Nakagomi, Kentaro Kaneko, and Yoshihiro Kokubun. Crystal orientations of $\beta - Ga_2O_3$ thin films formed on m-plane and r-plane sapphire substrates. *Physica Status solidi (b)*, 252 (3):612–620, 2015.

[189] A. A. Dakhel. Structural, optical, and opto-dielectric properties of w-doped Ga_2O_3 thin films. *Journal of Materials Science*, 47(7):3034–3039, 2012.

[190] A. A. Dakhel. Investigation of opto-dielectric properties of ti-doped Ga_2O_3 thin films. *Solid State Sciences*, 20:54–58, 2013.

[191] Yi Cheng, Kun Yang, Yong Peng, Yan Yin, Jixiang Chen, Bo Jing, Hongwei Liang, and Guotong Du. Research on the structural and optical stability of Ga_2O_3 films deposited by electron beam evaporation. *Journal of Materials Science: Materials in Electronics*, 24(12): 5122–5126, 2013.

[192] Yi Cheng, Hongwei Liang, Rensheng Shen, Xiaochuan Xia, Bo Wang, Yuanda Liu, Shiwei Song, Yang Liu, Zhenzhong Zhang, and Guotong Du. Band gap broadening and photoluminescence properties investigation in Ga_2O_3 polycrystal. *Journal of Materials Science: Materials in Electronics*, 24(8):2750–2754, 2013.

[193] Yi Cheng, Hongwei Liang, Yang Liu, Xiaochuan Xia, Rensheng Shen, Shiwei Song, Yunfeng Wu, and Guotong Du. Influence of n2 and o2 annealing treatment on the optical bandgap of polycrystalline Ga_2O_3:cu films. *Materials Science in Semiconductor Processing*, 16(5): 1303–1307, 2013.

[194] Pritty Rao and Sanjiv Kumar. Influence of post-deposition annealing in air and vacuum on the properties of thermally evaporated gallium oxide films. *Superlattices and Microstructures*, 70:117–130, 2014.

[195] M Ogita. Ga_2O_3 thin films for high-temperature gas sensors. *Applied Surface Science*, 142: 188–191, 1999.

[196] Toshihiro Miyata, Toshikuni Nakatani, and Tadatsugu Minami. Manganese-activated gallium oxide electroluminescent phosphor thin films prepared using various deposition methods. *Thin Solid Films*, 373(1-2):145–149, 2000.

[197] Tadatsugu Minami, Toshikuni Nakatani, and Toshihiro Miyata. Multicolor-emitting thin-film electroluminescent devices using Ga_2O_3 phosphors co-doped with mn and cr. *Journal of Vacuum Science & Technology A: Vacuum, Surfaces, and Films*, 18(4):1234, 2000.

[198] Joo Han Kim and Paul H. Holloway. Microstructural characterization of radio frequency magnetron sputter-deposited Ga_2O_3:mn phosphor thin films. *Journal of Vacuum Science & Technology A: Vacuum, Surfaces, and Films*, 20(3):928, 2002.

[199] K. Takakura, T. Kudou, K. Hayama, K. Shigaki, H. Ohyama, K. Kayamoto, and M. Shibuya. Optical property and crystalline quarity of si and ge added $\beta - Ga_2O_3$ thin films. *Journal of Materials Science: Materials in Electronics*, 19(2):167–170, 2007.

[200] K. Takakura, D. Koga, H. Ohyama, J. M. Rafi, Y. Kayamoto, M. Shibuya, H. Yamamoto, and J. Vanhellemont. Evaluation of the crystalline quality of $\beta - Ga_2O_3$ films by optical absorption measurements. *Physica B: Condensed Matter*, 404(23-24):4854–4857, 2009.

[201] Toshio Takeuchi, Hiroki Ishikawa, Norikazu Takeuchi, and Yoshiji Horikoshi. High resolution X-ray photoelectron spectroscopy of beta gallium oxide films deposited by ultra high vacuum radio frequency magnetron sputtering. *Thin Solid Films*, 516(14):4593–4597, 2008.

[202] Yijun Zhang, Jinliang Yan, Qingshan Li, Chong Qu, Liying Zhang, and Wanfeng Xie. Optical and structural properties of cu-doped $\beta - Ga_2O_3$ films. *Materials Science and Engineering: B*, 176(11):846–849, jun 2011.

[203] Yijun Zhang, Jinliang Yan, Qingshan Li, Chong Qu, Liying Zhang, and Ting Li. Structural and optical properties of n-doped $\beta - Ga_2O_3$ films deposited by rf magnetron sputtering. *Physica B: Condensed Matter*, 406(15-16):3079–3082, aug 2011.

[204] S. Sampath Kumar, E.J. Rubio, M. Noor-A-Alam, G. Martinez, S. Manandhar, V. Shutthanandan, S. Thevuthasan, and C.V. Ramana. Structure, Morphology, and Optical Properties

of Amorphous and Nanocrystalline Gallium Oxide Thin Films. *The Journal of Physical Chemistry C*, 117:4194–4200, 2013.

[205] E. J. Rubio and C. V. Ramana. Tungsten-incorporation induced red-shift in the bandgap of gallium oxide thin films. *Applied Physics Letters*, 102(2013):100–104, 2013.

[206] C. V. Ramana, E. J. Rubio, C. D. Barraza, A. Miranda Gallardo, Samantha McPeak, Sushma Kotru, and J. T. Grant. Chemical bonding, optical constants, and electrical resistivity of sputter-deposited gallium oxide thin films. *Journal of Applied Physics*, 115(4):043508, 2014.

[207] Rui Sun, Gui-Gen Wang, Hua-Yu Zhang, Jie-Cai Han, Xin-Zhong Wang, Lin Cui, Xu-Ping Kuang, Can Zhu, and Lei Jin. Microstructure, surface morphology and optical properties of n-incorporated Ga_2O_3 thin films on sapphire substrates. *Journal of Alloys and Compounds*, 580:517–521, 2013.

[208] H.C. Kang. Heteroepitaxial growth of multidomain Ga_2O_3/sapphire(001) thin films deposited using radio frequency magnetron sputtering. *Materials Letters*, 119:123–126, 2014.

[209] Encarnacin G. Vllora, Kiyoshi Shimamura, Kenji Kitamura, and Kazuo Aoki. Rf-plasma-assisted molecular-beam epitaxy of $\beta - Ga_2O_3$. *Applied Physics Letters*, 88(3):031105, 2006.

[210] Takayoshi Oshima, Takeya Okuno, and Shizuo Fujita. Gallium Oxide Thin Film Growth on c-Plane Sapphire Substrates by Molecular Beam Epitaxy for Deep-Ultraviolet Photodetectors. *Japanese Journal of Applied Physics*, 46(11):7217–7220, 2007.

[211] Takayoshi Oshima, Naoki Arai, Norihito Suzuki, Shigeo Ohira, and Shizuo Fujita. Surface morphology of homoepitaxial $\beta - Ga_2O_3$ thin films grown by molecular beam epitaxy. *Thin Solid Films*, 516(17):5768–5771, 2009.

[212] Min-Ying Tsai, Oliver Bierwagen, Mark E. White, and James S. Speck. $\beta - Ga_2O_3$ growth by plasma-assisted molecular beam epitaxy. *Journal of Vacuum Science & Technology A: Vacuum, Surfaces, and Films*, 28(2):354, 2010.

[213] Stephen W. Kaun, Feng Wu, and James S. Speck. $\beta - (Al_xGa_{1-x})_2O_3/Ga_2O_3(010)$ heterostructures grown on $\beta - Ga_2O_3$ (010) substrates by plasma-assisted molecular beam epitaxy.

Journal of Vacuum Science & Technology A: Vacuum, Surfaces, and Films, 33(4):041508, 2015.

[214] Hironori Okumura, Masao Kita, Kohei Sasaki, Akito Kuramata, Masataka Higashiwaki, and James S Speck. Systematic investigation of the growth rate of $\beta - Ga_2O_3$ (010) by plasma-assisted molecular beam epitaxy. *Applied Physics Express*, 7(9):095501, 2014.

[215] M. Orita, H. Ohta, H. Hiramatsu, M. Hirano, S. Den, M. Sasaki, T. Katagiri, H. Mimura, and H. Hosono. Pulsed laser deposition system for producing oxide thin films at high temperature. *Review of Scientific Instruments*, 72(8):3340–3343, 2001.

[216] H Ohta, M Orita, M Hirano, K Ueda, and H Hosono. Epitaxial Growth of Transparent Conductive Oxides. *International Journal of Modern Physics B*, 16(1/2):173–180, 2002.

[217] Kosuke Matsuzaki, Hiroshi Yanagi, Toshio Kamiya, Hidenori Hiramatsu, Kenji Nomura, Masahiro Hirano, and Hideo Hosono. Field-induced current modulation in epitaxial film of deep-ultraviolet transparent oxide semiconductor Ga_2O_3. *Applied Physics Letters*, 88(9):88–91, 2006.

[218] Kosuke Matsuzaki, Hidenori Hiramatsu, Kenji Nomura, Hiroshi Yanagi, Toshio Kamiya, Masahiro Hirano, and Hideo Hosono. Growth, structure and carrier transport properties of Ga_2O_3 epitaxial film examined for transparent field-effect transistor. *Thin Solid Films*, 496 (1):37–41, 2006.

[219] Yongxiang Li, Adrian Trinchi, Wojtek Wlodarski, Kosmas Galatsis, and Kourosh Kalantar-Zadeh. Investigation of the oxygen gas sensing performance of Ga_2O_3 thin films with different dopants. *Sensors and Actuators, B: Chemical*, 93(1-3):431–434, 2003.

[220] H. M. Lam, M. H. Hong, S. Yuan, and T. C. Chong. Growth of $\beta - Ga_2O_3$ nanoparticles by pulsed laser ablation technique. *Applied Physics A: Materials Science and Processing*, 79(8): 2099–2102, 2004.

[221] P. Gollakota, A. Dhawan, P. Wellenius, L. M. Lunardi, J. F. Muth, Y. N. Saripalli, H. Y. Peng, and H. O. Everitt. Optical characterization of eu-doped $\beta - Ga_2O_3$ thin films. *Applied Physics Letters*, 88(22):221906, 2006.

[222] Rong Huang, Hiroyuki Hayashi, Fumiyasu Oba, and Isao Tanaka. Microstructure of mn-doped $\gamma - Ga_2O_3$ epitaxial film on sapphire (0001) with room temperature ferromagnetism. *Journal of Applied Physics*, 101(6):063526, 2007.

[223] Hiroyuki Hayashi, Rong Huang, Fumiyasu Oba, Tsukasa Hirayama, and Isao Tanaka. Epitaxial growth of mn-doped $\gamma - Ga_2O_3$ on spinel substrate. *Journal of Materials Research*, 26(04): 578–583, feb 2011.

[224] Aline Petitmangin, Christian Hbert, Jacques Perrire, Bruno Gallas, Laurent Binet, Philippe Barboux, and Philippe Vermaut. Metallic clusters in nonstoichiometric gallium oxide films. *Journal of Applied Physics*, 109(1):013711, 2011.

[225] Sin-Liang Ou, Dong-Sing Wuu, Yu-Chuan Fu, Shu-Ping Liu, Ray-Hua Horng, Lei Liu, and Zhe-Chuan Feng. Growth and etching characteristics of gallium oxide thin films by pulsed laser deposition. *Materials Chemistry and Physics*, 133(2-3):700–705, apr 2012.

[226] X.H. Wang, F.B. Zhang, K. Saito, T. Tanaka, M. Nishio, and Q.X. Guo. Electrical properties and emission mechanisms of zn-doped $\beta - Ga_2O_3$ films. *Journal of Physics and Chemistry of Solids*, 75(11):1201–1204, 2014.

[227] Minna Nieminen, Lauri Niinist, and Eero Rauhala. Growth of gallium oxide thin films from gallium acetylacetonate by atomic layer epitaxy. *Journal of Materials Chemistry*, 6(1):27, 1996.

[228] F. K. Shan, G. X. Liu, W. J. Lee, G. H. Lee, I. S. Kim, and B. C. Shin. Structural, electrical, and optical properties of transparent gallium oxide thin films grown by plasma-enhanced atomic layer deposition. *Journal of Applied Physics*, 98(2), 2005.

[229] Halit Altuntas, Inci Donmez, Cagla Ozgit-Akgun, and Necmi Biyikli. Electrical characteristics of $\beta - Ga_2O_3$ thin films grown by peald. *Journal of Alloys and Compounds*, 593:190–195, 2014.

[230] G.a. Battiston, R. Gerbasi, M. Porchia, R. Bertoncello, and F. Caccavale. Chemical vapour deposition and characterization of gallium oxide thin films. *Thin Solid Films*, 279(1-2):115–118, 1996.

[231] Liliana Mîinea, Seigi Suh, Simon G. Bott, Jia-Rui Liu, Wei-Kan Chu, and David M. Hoffman. Synthesis of aluminium and gallium fluoroalkoxide compounds and the low pressure metal-organic chemical vapor deposition of gallium oxide films. *Journal of Materials Chemistry*, 9 (4):929–935, 1999.

[232] Dh Kim, Sh Yoo, and Ks An. Chemical vapor deposition of Ga_2O_3 thin films on si substrates. *Bull. Korean Chem. Soc.*, 23(2):225–228, 2002.

[233] Hyoun Woo Kim and Nam Ho Kim. Influence of postdeposition annealing on the properties of Ga_2O_3 films on SiO_2 substrates. *Journal of Alloys and Compounds*, 389(1-2):177–181, 2005.

[234] Russell Binions, Claire J. Carmalt, Ivan P. Parkin, Keith F E Pratt, and Graham a. Shaw. Gallium oxide thin films from the atmospheric pressure chemical vapor deposition reaction of gallium trichloride and methanol. *Chemistry of Materials*, 16(12):2489–2493, 2004.

[235] Volker Gottschalch, Kilian Mergenthaler, Gerald Wagner, Jens Bauer, Hendrik Paetzelt, Chris Sturm, and Ulrike Teschner. Growth of $\beta - Ga_2O_3$ on $Al_2O_3$and gaas using metal-organic vapor-phase epitaxy. *Physica Status Solidi (a)*, 206(2):243–249, 2009.

[236] Lingyi Kong, Jin Ma, Caina Luan, and Zhen Zhu. Journal of solid state chemistry structural and optical properties of Ga_2O_3:in films deposited on mgo (100) substrates by mocvd. *Journal of Solid State Chemistry*, 184(8):1946–1950, 2011.

[237] Wei Mi, Jin Ma, Caina Luan, Yu Lv, Hongdi Xiao, and Zhao Li. Characterization of $\beta - Ga_2O_3$ epitaxial films grown on mgo (111) substrates by metal-organic chemical vapor deposition. *Materials Letters*, 87:109–112, 2012.

[238] Wei Mi, Jin Ma, Zhen Zhu, Caina Luan, Yu Lv, and Hongdi Xiao. Epitaxial growth of Ga_2O_3 thin films on mgo (110) substrate by metalorganic chemical vapor deposition. *Journal of Crystal Growth*, 354(1):93–97, 2012. ISSN 00220248.

[239] Wei Mi, Jin Ma, Caina Luan, and Hongdi Xiao. Structural and optical properties of $\beta - Ga_2O_3$ films deposited on $MgAl_2O_4$ (100) substrates by metalorganic chemical vapor deposition. *Journal of Luminescence*, 146:1–5, 2014.

[240] Wei Mi, Zhao Li, Caina Luan, Hongdi Xiao, Cansong Zhao, and Jin Ma. Transparent conducting tin-doped Ga_2O_3 films deposited on $MgAl_2O_4$ (100) substrates by MOCVD. *Ceramics International*, 41(2):2572–2575, 2015.

[241] Xuejian Du, Wei Mi, Caina Luan, Zhao Li, Changtai Xia, and Jin Ma. Characterization of homoepitaxial $\beta - Ga_2O_3$ films prepared by metal-organic chemical vapor deposition. *Journal of Crystal Growth*, 404:75–79, 2014.

[242] Xuejian Du, Zhao Li, and Caina Luan. Preparation and characterization of sn-doped $\beta - Ga_2O_3$ homoepitaxial films by mocvd. *Journal of Materials Science*, 50:3252–3257, 2015.

[243] Xianjin Feng, Zhao Li, Wei Mi, Yi Luo, and Jin Ma. Mg-doped $\beta - Ga_2O_3$ films with tunable optical band gap prepared on mgo (110) substrates by metal-organic chemical vapor deposition. *Materials Science in Semiconductor Processing*, 34:52–57, 2015.

[244] Yuanpeng Chen, Hongwei Liang, Xiaochuan Xia, Pengcheng Tao, Rensheng Shen, Yang Liu, Yanbin Feng, Yuehong Zheng, Xiaona Li, and Guotong Du. The lattice distortion of $\beta - Ga_2O_3$ film grown on c-plane sapphire. *Journal of Materials Science: Materials in Electronics*, pages 3231–3235, 2015.

[245] D. Gogova, G. Wagner, M. Baldini, M. Schmidbauer, K. Irmscher, R. Schewski, Z. Galazka, M. Albrecht, and R. Fornari. Structural properties of si-doped $\beta - Ga_2O_3$ layers grown by movpe. *Journal of Crystal Growth*, 401:1–5, 2013.

[246] Guenter Wagner, Michele Baldini, Daniela Gogova, Martin Schmidbauer, Robert Schewski, Martin Albrecht, Zbigniew Galazka, Detlef Klimm, and Roberto Fornari. Homoepitaxial growth of $\beta - Ga_2O_3$ layers by metal-organic vapor phase epitaxy. *Phys. Stat. Sol. (a)*, 211 (1):27–33, 2014.

[247] E. Korhonen, F. Tuomisto, D. Gogova, G. Wagner, M. Baldini, Z. Galazka, R. Schewski, and M. Albrecht. Electrical compensation by ga vacancies in Ga_2O_3 thin films. *Applied Physics Letters*, 106(24):242103, 2015.

[248] Daisuke Shinohara and Shizuo Fujita. Heteroepitaxy of corundum-structured $(Al_xGa_{1-x})_2O_3$

thin films on $\alpha - Al_2O_3$ substrates by ultrasonic mist chemical vapor deposition. *Japanese Journal of Applied Physics*, 47(9 part 1):7311–7313, 2008.

[249] Takayoshi Oshima, Taishi Nakazono, Akira Mukai, and Akira Ohtomo. Epitaxial growth of $\gamma - Ga_2O_3$ films by mist chemical vapor deposition. *Journal of Crystal Growth*, 359:60–63, nov 2012.

[250] R. Cusco, N. Domènech-Amador, T. Hatakeyama, T. Yamaguchi, T. Honda, and L. Artús. Lattice dynamics of a mist-chemical vapor deposition-grown corundum-like Ga_2O_3 single crystal. *Journal of Applied Physics*, 117(18):185706, 2015.

[251] Yuichi Oshima, Encarnacion G. Villora, Yoshitaka Matsushita, Satoshi Yamamoto, and Kiyoshi Shimamura. Epitaxial growth of phase-pure $\epsilon - Ga_2O_3$ by halide vapor phase epitaxy. *Journal of Applied Physics*, 118(8):085301, 2015.

[252] Hisashi Murakami, Kazushiro Nomura, Ken Goto, Kohei Sasaki, Katsuaki Kawara, Quang Tu Thieu, Rie Togashi, Yoshinao Kumagai, Masataka Higashiwaki, Akito Kuramata, Shigenobu Yamakoshi, Bo Monemar, and Akinori Koukitu. Homoepitaxial growth of $\beta - Ga_2O_3$ layers by halide vapor phase epitaxy. *Applied Physics Express*, 8, 2015.

[253] A Ortiz, J C Alonso, E Andrade, and C Urbiola. Structural and Optical Characteristics of Gallium Oxide Thin Films Deposited by Ultrasonic Spray Pyrolysis. *Journal of The Electrochemical Society*, 148(2):F26–F29, 2001.

[254] Jianhua Hao and Michael Cocivera. Optical and luminescent properties of undoped and rare-earth-doped Ga_2O_3 thin films deposited by spray pyrolysis. *Journal of Physics D*, 35: 433–438, 2002.

[255] Stuart R. Thomas, George Adamopoulos, Yen-Hung Lin, Hendrik Faber, Labrini Sygellou, Emmanuel Stratakis, Nikos Pliatsikas, Panos A. Patsalas, and Thomas D. Anthopoulos. High electron mobility thin-film transistors based on Ga_2O_3 grown by atmospheric ultrasonic spray pyrolysis at low temperatures. *Applied Physics Letters*, 105(9):092105, 2014.

[256] Tadatsugu Minami, Tetsuya Shirai, Toshikuni Nakatani, and Toshihiro Miyata. Electroluminescent devices with Ga_2O_3 : Mn thin-film emitting layer prepared by sol-gel process. *Japanese Journal of Applied Physics*, 39:L524–L526, 2000.

[257] Godhuli Sinha, Kalyan Adhikary, and Subhadra Chaudhuri. Effect of annealing temperature on structural transformation of gallium based nanocrystalline oxide thin films and their optical properties. *Optical Materials*, 29(6):718–722, 2007.

[258] Yutaka Ohya, Jyunya Okano, Yuki Kasuya, and Takayuki Ban. Fabrication of Ga_2O_3 thin films by aqueous solution deposition. *Journal of the Ceramic Society of Japan*, 117(9):973–977, 2009.

[259] Kohei Sasaki, Masataka Higashiwaki, Akito Kuramata, Takekazu Masui, and Shigenobu Yamakoshi. Growth temperature dependences of structural and electrical properties of Ga_2O_3 epitaxial films grown on $\beta - Ga_2O_3$ (010) substrates by molecular beam epitaxy. *Journal of Crystal Growth*, 392:30–33, 2014.

[260] F.B. Zhang, K. Saito, T. Tanaka, M. Nishio, and Q.X. Guo. Structural and optical properties of Ga_2O_3 films on sapphire substrates by pulsed laser deposition. *Journal of Crystal Growth*, 387:96–100, feb 2014.

[261] Daoyou Guo, Zhenping Wu, Peigang Li, Yuehua An, Han Liu, Xuncai Guo, Hui Yan, Guofeng Wang, Changlong Sun, Linghong Li, and Weihua Tang. Fabrication of $\beta - Ga_2O_3$ thin films and solar-blind photodetectors by laser mbe technology. *Optical Materials Express*, 4(5):1067, 2014.

[262] W. Seiler, M. Selmane, K. Abdelouhadi, and J. Perrière. Epitaxial growth of gallium oxide films on c-cut sapphire substrate. *Thin Solid Films*, 589:556–562, 2015.

[263] Lingyi Kong, Jin Ma, Caina Luan, Wei Mi, and Yu Lv. Structural and optical properties of heteroepitaxial $\beta - Ga_2O_3$ films grown on mgo (100) substrates. *Thin Solid Films*, 520(13): 4270–4274, 2012.

[264] Hyoun Woo Kim and Nam Ho Kim. Annealing effects on the properties of Ga_2O_3 thin films

grown on sapphire by the metal organic chemical vapor deposition. *Applied Surface Science*, 230(1-4):301–306, 2004.

[265] H.W. Kim, N.H. Kim, and C. Lee. Structural and optical properties of annealed Ga_2O_3 films on Si(111) substrates. *British Ceramic Transactions*, 103(4):187–189, 2004.

[266] Anshu Goyal, Brajesh S. Yadav, O.P. Thakur, A.K. Kapoor, and R. Muralidharan. Effect of annealing on $\beta - Ga_2O_3$ film grown by pulsed laser deposition technique. *Journal of Alloys and Compounds*, 583:214–219, jan 2014.

[267] J Robertson, K. Xiong, and S. J. Clark. Band gaps and defect levels in functional oxides. *Thin Solid Films*, 496(1):1–7, 2006.

[268] Kenichiro Takakura, Suguru Funasaki, Isao Tsunoda, Hidenori Ohyama, Daisuke Takeuchi, Toshiyuki Nakashima, Mutsuo Shibuya, Katsuya Murakami, Eddy Simoen, and Cor Claeys. Investigation of the si doping effect in $\beta - Ga_2O_3$ films by co-sputtering of gallium oxide and si. *Physica B: Condensed Matter*, 407(15):2900–2902, 2012.

[269] B Hirschauer, S Sbderholm, and U O Karlsson. Highly oriented α-alumina films grown by pulsed laser deposition. *Thin Solid Films*, 305:243–247, 1997.

[270] Andrew A. Anderson, Robert W. Eason, Miroslav Jelinek, Christos Grivas, David Lane, Keith Rogers, L.M.B. Hickey, and Costas Fotakis. Growth of Ti:sapphire single crystal thin films by pulsed laser deposition. *Thin Solid Films*, 300(1-2):68–71, 1997.

[271] T Kohara, H Tamagaki, Y Ikari, and H Fujii. Deposition of $\alpha - Al_2O_3$ hard coatings by reactive magnetron sputtering. *Surface and Coatings Technology*, 185(2-3):166–171, 2004.

[272] G. Wang, O. Marty, C. Garapon, A. Pillonnet, and W. Zhang. Rare earth doped α-alumina thin films prepared by pulsed laser deposition: structural and optical properties. *Applied Physics A*, 79(4-6):1599–1602, 2004.

[273] J.M. Andersson, E. Wallin, U. Helmersson, U. Kreissig, and E.P. Münger. Phase control of Al_2O_3 thin films grown at low temperatures. *Thin Solid Films*, 513(1-2):57–59, aug 2006.

[274] C. Merckling, M. El-Kazzi, V. Favre-Nicolin, M. Gendry, Y. Robach, G. Grenet, and G. Hollinger. Epitaxial growth and relaxation of $\gamma - Al_2O_3$ on silicon. *Thin Solid Films*, 515 (16):6479–6483, jun 2007.

[275] D. Yu, Y. F. Lu, N. Xu, J. Sun, Z. F. Ying, and J. D. Wu. Preparation of $\alpha - Al_2O_3$ thin films by electron cyclotron resonance plasma-assisted pulsed laser deposition and heat annealing. *Journal of Vacuum Science & Technology A: Vacuum, Surfaces, and Films*, 26(3):380, 2008.

[276] Makoto Hosaka, Yasuyuki Akita, Yuki Sugimoto, Koji Koyama, and Mamoru Yoshimoto. Low-temperature heteroepitaxial growth of $\alpha - Al_2O_3$ thin films on nio layers by pulsed laser deposition. *Japanese Journal of Applied Physics*, 48(8):088003, 2009.

[277] Akihiko Ito, Rong Tu, and Takashi Goto. Amorphous-like nanocrystalline $\gamma - Al_2O_3$ films prepared by mocvd. *Surface and Coatings Technology*, 204(14):2170–2174, 2010.

[278] Satchi Kumari and Alika Khare. Optical and structural characterization of pulsed laser deposited ruby thin films for temperature sensing application. *Applied Surface Science*, 265: 180–186, 2013.

[279] G. Balakrishnan, R. Venkatesh Babu, K.S. Shin, and J.I. Song. Growth of highly oriented $\gamma-$ and $\alpha - Al_2O_3$ thin films by pulsed laser deposition. *Optics & Laser Technology*, 56:317–321, mar 2014.

[280] S W Whangbo, Y K Choi, W S Koh, K B Chung, H K Jang, and C N Whang. Effect of silicon surface states on the properties of epitaxial Al_2O_3 films. *Thin Solid Films*, 398–399: 480–484, 2001.

[281] C. Cibert, H. Hidalgo, C. Champeaux, P. Tristant, C. Tixier, J. Desmaison, and A. Catherinot. Properties of aluminum oxide thin films deposited by pulsed laser deposition and plasma enhanced chemical vapor deposition. *Thin Solid Films*, 516(6):1290–1296, 2008.

[282] Junsoo Shin, Amit Goyal, and Sung-Hun Wee. Growth of epitaxial $\gamma - Al_2O_3$ films on rigid single-crystal ceramic substrates and flexible, single-crystal-like metallic substrates by pulsed laser deposition. *Thin Solid Films*, 517(19):5710–5714, aug 2009.

[283] G. Balakrishnan, P. Kuppusami, S. Tripura Sundari, R. Thirumurugesan, V. Ganesan, E. Mohandas, and D. Sastikumar. Structural and optical properties of gamma-alumina thin films prepared by pulsed laser deposition. *Thin Solid Films*, 518(14):3898–3902, 2010.

[284] Huiyan Wu, Dawei Lu, Kerong Zhu, Guoyong Xu, and Hu Wang. Crystalline and electronic structure of epitaxial $\gamma - Al_2O_3$ films. *Physica B: Condensed Matter*, 413:105–108, mar 2013.

[285] G Balakrishnan, S Tripura Sundari, R Ramaseshan, R Thirumurugesan, E Mohandas, D Sastikumar, P Kuppusami, T G Kim, and J I Song. Effect of substrate temperature on microstructure and optical properties of nanocrystalline alumina thin films. *Ceramics International*, 39(8):9017–9023, 2013.

[286] J. Gottmann and E.W. Kreutz. Pulsed laser deposition of alumina and zirconia thin films on polymers and glass as optical and protective coatings. *Surface and Coatings Technology*, 116-119:1189–1194, 1999.

[287] P. Katiyar, C. Jin, and R.J. Narayan. Electrical properties of amorphous aluminum oxide thin films. *Acta Materialia*, 53(9):2617–2622, 2005.

[288] F. Di Fonzo, D. Tonini, A. Li Bassi, C. S. Casari, M. G. Beghi, C. E. Bottani, D. Gastaldi, P. Vena, and R. Contro. Growth regimes in pulsed laser deposition of aluminum oxide films. *Applied Physics A*, 93(3):765–769, jun 2008.

[289] Shao-Hui Chang, Zhi-Zhan Chen, Wei Huang, Xue-Chao Liu, Bo-Yuan Chen, Zheng-Zheng Li, and Er-Wei Shi. Band alignment ofGa_2O_3/6h-sic heterojunction. *Chinese Physics B*, 20 (11):116101, 2011.

[290] Takafumi Kamimura, Kohei Sasaki, Man Hoi Wong, Daivasigamani Krishnamurthy, Akito Kuramata, Takekazu Masui, Shigenobu Yamakoshi, and Masataka Higashiwaki. Band alignment and electrical properties of $Al_2O_3/\beta - Ga_2O_3$ heterojunctions. *Applied Physics Letters*, 104:192104, 2014.

[291] Ting-Hsiang Hung, Kohei Sasaki, Akito Kuramata, Digbijoy N. Nath, Pil Sung Park, Craig Polchinski, and Siddharth Rajan. Energy band line-up of atomic layer deposited Al_2O_3 on $\beta - Ga_2O_3$. *Applied Physics Letters*, 104(16):162106, 2014.

[292] Ye Jia, Ke Zeng, Joshua S Wallace, Joseph A Gardella, and Uttam Singisetti. Spectroscopic and electrical calculation of band alignment between atomic layer deposited SiO_2 and $\beta - Ga_2O_3$. *Applied Physics Letters*, 106(May):1–5, 2015.

[293] V. I. Vasyltsiv, Ya. I. Rym, and Ya. M. Zakharko. Optical absorption and photoconductivity at the band edge of $\beta - Ga_{2-x}In_xO_3$. *Physica Status Solidi (B)*, 195(2):653–658, 1996.

[294] Yvonne Tomm, Jung Min Ko, Akira Yoshikawa, Takamasa Sugawara, and Tsuguo Fukuda. Crystal Growth and Characterization in the System $(Ga_{1-x}In_x)_2O_3$. *Japanese Journal of Applied Physics*, 39:48–49, 2000.

[295] Takayoshi Oshima and Shizuo Fujita. Properties of Ga_2O_3-based $(In_xGa_{1-x})_2O_3$ alloy thin films grown by molecular beam epitaxy. *Physica Status Solidi (C)*, 5(9):3113–3115, 2008.

[296] Fan Yang, Jin Ma, Caina Luan, and Lingyi Kong. Structural and optical properties of $Ga_{2(1?x)}In_{2x}O_3$ films prepared on $\alpha - Al_2O_3$ (0001) by MOCVD. *Applied Surface Science*, 255:4401–4404, 2009.

[297] Lingyi Kong, Jin Ma, Fan Yang, Caina Luan, and Zhen Zhu. Preparation and characterization of $Ga_{2x}In_{2(1?x)}O_3$ films deposited on ZrO_2 (100) substrates by MOCVD. *Journal of Alloys and Compounds*, 499(1):75–79, 2010.

[298] Yoshihiro Kokubun, Torataro Abe, and Shinji Nakagomi. Sol-gel prepared $(Ga_xIn_{(1?x)})_2O_3$ thin films for solar-blind ultraviolet photodetectors. *Physica Status Solidi (A) Applications and Materials Science*, 207(7):1741–1745, 2010.

[299] M. Baldini, D. Gogova, K. Irmscher, M. Schmidbauer, G. Wagner, and R. Fornari. Heteroepitaxy of $Ga_{2(1-x)}In_{2x}O_3$ layers by MOVPE with two different oxygen sources. *Crystal Research and Technology*, 49(8):552–557, 2014.

[300] M Baldini, M Albrecht, D Gogova, R Schewski, and G Wagner. Effect of indium as a surfactant in $(Ga_{1-x}In_x)_2O_3$ epitaxial growth on $\beta - Ga_2O_3$ by metal organic vapour phase epitaxy. *Semiconductor Science and Technology*, 30(2):024013, 2015.

[301] Christian Kranert, Jörg Lenzner, Marcus Jenderka, Michael Lorenz, Holger von Wenckstern, Rüdiger Schmidt-Grund, and Marius Grundmann. Lattice parameters and Raman-active phonon modes of $(In_xGa_{1?x})_2O_3$ for $x < 0.4$. *Journal of Applied Physics*, 116(1):013505, 2014.

[302] R. Schmidt-Grund, C. Kranert, T. Böntgen, H. von Wenckstern, H. Krauß, and M. Grundmann. Dielectric function in the NIR-VUV spectral range of $(In_xGa_{1-x})_2O_3$ thin films. *Journal of Applied Physics*, 116:053510, 2014.

[303] H Von Wenckstern, D Splith, M Purfürst, Z Zhang, Ch Kranert, S Müller, M Lorenz, and M Grundmann. Structural and optical properties of $(In, Ga)_2O_3$ thin films and characteristics of Schottky contacts thereon. *Semiconductor Science and Technology*, 30(2):024005, 2015.

[304] Fabi Zhang, Katsuhiko Saito, Tooru Tanaka, Mitsuhiro Nishio, Makoto Arita, and Qixin Guo. Wide bandgap engineering of $(AlGa)_2O_3$ films. *Applied Physics Letters*, 105(16):162107, 2014.

[305] Christian Kranert, Marcus Jenderka, Jörg Lenzner, Michael Lorenz, Holger von Wenckstern, Rüdiger Schmidt-Grund, and Marius Grundmann. Lattice parameters and raman-active phonon modes of $\beta - (Al_xGa_{1-x})_2O_3$. *Journal of Applied Physics*, 117(12):125703, 2015.

[306] R. Schmidt-Grund, C. Kranert, H. von Wenckstern, V. Zviagin, M. Lorenz, and M. Grundmann. Dielectric function in the spectral range (0.58.5)ev of an $(Al_xGa_{1-x})_2O_3$ thin film with continuous composition spread. *Journal of Applied Physics*, 117(16):165307, 2015.

[307] Hiroshi Ito, Kentaro Kaneko, and Shizuo Fujita. Growth and Band Gap Control of Corundum-Structured $\alpha - (AlGa)_2O_3$ Thin Films on Sapphire by Spray-Assisted Mist Chemical Vapor Deposition. *Japanese Journal of Applied Physics*, 51(10):100207, 2012.

[308] Shizuo Fujita and Kentaro Kaneko. Epitaxial growth of corundum-structured wide band gap III-oxide semiconductor thin films. *Journal of Crystal Growth*, 401:588–592, 2014.

[309] Sam-dong Lee, Yoshito Ito, Kentaro Kaneko, and Shizuo Fujita. Enhanced thermal stability of alpha gallium oxide films supported by aluminum doping. *Japanese Journal of Applied Physics*, 54(3):030301, 2015.

[310] John Robertson. Band offsets of wide-band-gap oxides and implications for future electronic devices. *Journal of Vacuum Science & Technology B: Microelectronics and Nanometer Structures*, 18(3):1785, 2000.

[311] Kentaro Kaneko, Taichi Nomura, Itsuhiro Kakeya, and Shizuo Fujita. Alloy Thin Films on Sapphire Substrates. *Applied Physics Express*, 2:075501, 2009.

[312] Daoyou Guo, Zhenping Wu, Yuehua An, Xiaojiang Li, Xuncai Guo, Xulong Chu, Changlong Sun, Ming Lei, Linghong Li, Lixin Cao, Peigang Li, and Weihua Tang. Room temperature ferromagnetism in $(Ga_{1-x}Mn_x)_2O_3$ epitaxial thin films. *J. Mater. Chem. C*, 3(8):1830–1834, 2015.

[313] Hiroshi Yanagi, Chiyuki Sato, Yota Kimura, Issei Suzuki, Takahisa Omata, Toshio Kamiya, and Hideo Hosono. Widely bandgap tunable amorphous CdGaO oxide semiconductors exhibiting electron mobilities $10 cm^2 V^{-1} s^{-1}$. *Applied Physics Letters*, 106(8):082106, 2015.

[314] Zbigniew Galazka, Klaus Irmscher, Reinhard Uecker, Rainer Bertram, Mike Pietsch, Albert Kwasniewski, Martin Naumann, Tobias Schulz, Robert Schewski, Detlef Klimm, and Matthias Bickermann. On the bulk $\beta - Ga_2O_3$ single crystals grown by the czochralski method. *Journal of Crystal Growth*, 404:184–191, 2014.

[315] J J Kingsley and K C Patil. A novel combustion process for the synthesis of fine particle α-alumina and related oxide materials. *Materials Letters*, 6(11,12):427–432, 1988.

[316] L.a. Chick, L.R. Pederson, G.D. Maupin, J.L. Bates, L.E. Thomas, and G.J. Exarhos. Glycine-nitrate combustion synthesis of oxide ceramic powders. *Materials Letters*, 10(1-2):6–12, 1990.

[317] Kashinath C. Patil, S. T. Aruna, and Tanu Mimani. Combustion synthesis: An update. *Current Opinion in Solid State and Materials Science*, 6(6):507–512, 2002.

[318] S R Jain, K C Adiga, and V R Pai Verneker. A new approach to thermochemical calculations of condensed fuel-oxidizer mixtures. *Combustion and Flame*, 40(1):71–79, 1981.

[319] D.a. Fumo, M.R. Morelli, and A.M. Segadães. Combustion synthesis of calcium aluminates. *Materials Research Bulletin*, 31(10):1243–1255, 1996.

[320] S. S. Manoharan and K. C. Patil. Combustion synthesis of metal chromite powders. *Journal of the American Ceramic Society*, 75(4):1012–1015, 1992.

[321] V. Srihari, V. Sridharan, H. K. Sahu, G. Raghavan, V. S. Sastry, and C. S. Sundar. Combustion synthesis of Ga_2O_3 nanoparticles. *Journal of Materials Science*, 44(2):671–675, 2008.

[322] V.D. Zhuravlev, V.G. Bamburov, A.R. Beketov, L.a. Perelyaeva, I.V. Baklanova, O.V. Sivtsova, V.G. Vasil'ev, E.V. Vladimirova, V.G. Shevchenko, and I.G. Grigorov. Solution combustion synthesis of $\alpha - Al_2O_3$ using urea. *Ceramics International*, 39(2):1379–1384, 2013.

[323] H M Christen and G Eres. Recent advances in pulsed-laser deposition of complex oxides. *Journal of Physics: Condensed Matter*, 20(26):264005, 2008.

[324] Thomas R Burkholder, Jason T Yustein, and Lester Andrews. Reactions of Pulsed Laser Evaporated Ga and In Atoms with Molecular Oxygen. Matrix Infrared Spectra of New GaO2 and InO2 Species. *Journal of Physical Chemistry*, 96(14):10189–10195, 1992.

[325] Lester Andrews, Thomas R Burkholder, and Jason T Yustein. Reactions of Pulsed-Laser Evaporated Aluminum Atoms with Oxygen. Infrared Spectra of the Reaction Products in Solid Argon. *Journal of Physical Chemistry*, 96(25):10182–10189, 1992.

[326] D. van Heijnsbergen, K. Demyk, M. a. Duncan, G. Meijer, and G. von Helden. Structure determination of gas phase aluminum oxide clusters. *Physical Chemistry Chemical Physics*, 5 (12):2515, 2003.

[327] Howard M. Smith and a. F. Turner. Vacuum Deposited Thin Films Using a Ruby Laser. *Applied Optics*, 4(1):147, 1965.

[328] D. Dijkkamp, T. Venkatesan, X. D. Wu, S. a. Shaheen, N. Jisrawi, Y. H. Min-Lee, W. L. McLean, and M. Croft. Preparation of Y-Ba-Cu oxide superconductor thin films using pulsed laser evaporation from high Tc bulk material. *Applied Physics Letters*, 51(8):619, 1987.

[329] Rajiv K. Singh and J. Narayan. Pulsed-laser evaporation technique for deposition of thin films: Physics and theoretical model. *Physical Review B*, 41(13):8843–8859, 1990.

[330] S. I. Anisimov, D. Bäuerle, and B. S. Luk'Yanchuk. Gas dynamics and lm proles in pulsed-laser deposition of materials. *Physical Review B*, 48(16):12076–12081, 1993.

[331] Mikhail Strikovski and John H. Miller. Pulsed laser deposition of oxides: Why the optimum rate is about 1 A per pulse. *Applied Physics Letters*, 73(12):1733, 1998.

[332] Mikhail Strikovski, John H. Miller, and Jaroslaw Wosik. Deposition rate as the key parameter in pulsed laser deposition of oxide films: a practical model and experiment. *Physica C*, 348: 2349–2350, 2000.

[333] Deepak Marla, Upendra V. Bhandarkar, and Suhas S. Joshi. Critical assessment of the issues in the modeling of ablation and plasma expansion processes in the pulsed laser deposition of metals. *Journal of Applied Physics*, 109(2):021101, 2011.

[334] P Balling and J Schou. Femtosecond-laser ablation dynamics of dielectrics: basics and applications for thin films. *Reports on Progress in Physics*, 76(3):036502, 2013.

[335] a. Sambri, S. Amoruso, X. Wang, F. Miletto Granozio, and R. Bruzzese. Plume propagation dynamics of complex oxides in oxygen. *Journal of Applied Physics*, 104(5):053304, 2008.

[336] S. Trusso, B. Fazio, E. Fazio, F. Neri, and F. Barreca. Influence of the plasma expansion dynamics on the structural properties of pulsed laser ablation deposited tin oxide thin films. *Thin Solid Films*, 518(19):5409–5415, 2010.

[337] P. K. Diwakar, S. S. Harilal, M. C. Phillips, and A. Hassanein. Characterization of ultrafast laser-ablation plasma plumes at various Ar ambient pressures. *Journal of Applied Physics*, 118(4):043305, 2015.

[338] J. Gonzalo, C. N. Afonso, and J. Perrire. Influence of laser energy density on the plasma expansion dynamics and film stoichiometry during laser ablation of BiSrCaCuO. *Journal of Applied Physics*, 79(10):8042, 1996.

[339] B. Toftmann, J. Schou, and J. G. Lunney. Dynamics of the plume produced by nanosecond ultraviolet laser ablation of metals. *Physical Review B*, 67(10):104101, 2003.

[340] S. K. Hau, K. H. Wong, P. W. Chan, and C. L. Choy. Intrinsic resputtering in pulsed-laser deposition of lead-zirconate-titanate thin films. *Applied Physics Letters*, 66(2):245, 1995.

[341] Nini Pryds, Jø rgen Schou, and Sø ren Linderoth. The spatial thickness distribution of metal films produced by large area pulsed laser deposition. *Applied Surface Science*, 253(19): 8231–8234, 2007.

[342] I. Konomi, T. Motohiro, and T. Asaoka. Angular distribution of atoms ejected by laser ablation of different metals. *Journal of Applied Physics*, 106(1):013107, 2009.

[343] T. C. Droubay, L. Qiao, T. C. Kaspar, M. H. Engelhard, V. Shutthanandan, and S. a. Chambers. Nonstoichiometric material transfer in the pulsed laser deposition of LaAlO[sub 3]. *Applied Physics Letters*, 97(12):124105, 2010.

[344] M. Nistor, F. Gherendi, and N.B. Mandache. Angular distribution of species in pulsed energy beam deposition of oxide films. *Applied Surface Science*, 258(23):9274–9277, 2012.

[345] Alejandro Ojeda-G-P, Christof W. Schneider, Max Döbeli, Thomas Lippert, and Alexander Wokaun. Angular distribution of species in pulsed laser deposition of $La_xCa_{1-x}MnO_3$. *Applied Surface Science*, 336:150–156, 2015.

[346] David B. Geohegan and Alexander a. Puretzky. Laser ablation plume thermalization dynamics in background gases: Combined imaging, optical absorption and emission spectroscopy, and ion probe measurements. *Applied Surface Science*, 96-98:131–138, 1996.

[347] Salvatore Amoruso, Bo Toftmann, and Jø rgen Schou. Thermalization of a UV laser ablation plume in a background gas: From a directed to a diffusionlike flow. *Physical Review E*, 69(5): 056403, 2004.

[348] Salvatore Amoruso, Jorgen Schou, and James G. Lunney. Influence of the atomic mass of the background gas on laser ablation plume propagation. *Applied Physics A*, 92(4):907–911, 2008.

[349] J. Gonzalo, C. N. Afonso, and J. Perrire. The role of film re-emission and gas scattering processes on the stoichiometry of laser deposited films. *Applied Physics Letters*, 67(9):1325, 1995.

[350] A. Sambri, S. Amoruso, X. Wang, M. Radovic, F. Miletto Granozio, and R. Bruzzese. Substrate heating influence on plume propagation during pulsed laser deposition of complex oxides. *Applied Physics Letters*, 91(15):151501, 2007.

[351] C. Aruta, S. Amoruso, G. Ausanio, R. Bruzzese, E. Di Gennaro, M. Lanzano, F. Miletto Granozio, Muhammad Riaz, A. Sambri, U. Scotti di Uccio, and X. Wang. Critical influence of target-to-substrate distance on conductive properties of LaGaO3/SrTiO3 interfaces deposited at 10-1 mbar oxygen pressure. *Applied Physics Letters*, 101(3):031602, 2012.

[352] J. Perrière, C. Hebert, N. Jedrecy, W. Seiler, O. Zanellato, X. Portier, R. Perez-Casero, E. Millon, and M. Nistor. On the relevance of large scale pulsed-laser deposition: Evidence of structural heterogeneities in ZnO thin films. *Journal of Applied Physics*, 116(12):123502, 2014.

[353] J. Schou. Physical aspects of the pulsed laser deposition technique: The stoichiometric transfer of material from target to film. *Applied Surface Science*, 255(10):5191–5198, 2009.

[354] Y. Davila, A. Petitmangin, C. Hebert, J. Perrière, and W. Seiler. Oxygen deficiency in oxide films grown by PLD. *Applied Surface Science*, 257(12):5354–5357, apr 2011.

[355] M Nistor, J Perrière, C Hebert, and W Seiler. Nanocomposite indium tin oxide thin films: formation induced by a large oxygen deficiency and properties. *Journal of Physics: Condensed Matter*, 22(4):045006, 2010.

[356] Eric Millon, Magdalena Nistor, Christian Hebert, Yohely Davila, and Jacques Perrière. Phase separation in nanocomposite indium tin oxide thin films grown at room temperature: on the role of oxygen deficiency. *Journal of Materials Chemistry*, 22(24):12179, 2012.

[357] E. Millon. Advanced functional oxide thin films grown by pulsed-laser deposition. *Applied Surface Science*, 278:2–6, 2013.

[358] C. Hebert, A. Petitmangin, J. Perrière, E. Millon, A. Petit, L. Binet, and P. Barboux. Phase separation in oxygen deficient gallium oxide films grown by pulsed-laser deposition. *Materials Chemistry and Physics*, 133(1):135–139, 2012.

[359] M. a. Morales-Paliza, R. F. Haglund, and L. C. Feldman. Mechanisms of oxygen incorporation in indiumtinoxide films deposited by laser ablation at room temperature. *Applied Physics Letters*, 80(20):3757, 2002.

[360] H. M. Christen, S. D. Silliman, and K. S. Harshavardhan. Continuous compositional-spread technique based on pulsed-laser deposition and applied to the growth of epitaxial films. *Review of Scientific Instruments*, 72(6):2673, 2001.

[361] Hans M Christen, Isao Ohkubo, Christopher M Rouleau, Gerald E JellisonJr, Alex a Puretzky, David B Geohegan, and Douglas H Lowndes. A laser-deposition approach to compositional-spread discovery of materials on conventional sample sizes. *Measurement Science and Technology*, 16(1):21–31, 2005.

[362] M. Frumar, B. Frumarova, P. Nemec, T. Wagner, J. Jedelsky, and M. Hrdlicka. Thin chalcogenide films prepared by pulsed laser deposition new amorphous materials applicable in optoelectronics and chemical sensors. *Journal of Non-Crystalline Solids*, 352(6-7):544–561, 2006.

[363] Matthias Batzill and Ulrike Diebold. The surface and materials science of tin oxide. *Progress in Surface Science*, 79(2-4):47–154, 2005.

[364] E Gillet and B Ealet. Characterization of sapphire surfaces by electron energy-loss spectroscopy. *Surface Science*, 273(3):427–436, 1992.

[365] H. M. Rietveld. Line profiles of neutron powder-diffraction peaks for structure refinement. *Acta Crystallographica*, 22(1):151–152, 1967.

[366] M P Seah and W A Dench. Quantitative electron spectroscopy of surfaces: A standard data base for electron inelastic mean free paths in solids. *Surface and Interface Analysis*, 1(1):2–11, 1979.

[367] *Installation and Calibration Manual*. Physical Electronics, Inc., Chanhassan, MN, 2014.

[368] R Hesse, P Streubel, and R Szargan. Product or sum: comparative tests of Voigt, and product or sum of Gaussian and Lorentzian functions in the fitting of synthetic Voigt-based X-ray photoelectron spectra. *Surface And Interface Analysis*, 39(5):381–391, 2007.

[369] Friedrich Reinert and Stefan Hüfner. Photoemission spectroscopy - From early days to recent applications. *New Journal of Physics*, 7(97), 2005.

[370] R. Carli and C.L. Bianchi. XPS analysis of gallium oxides. *Applied Surface Science*, 74(1): 99–102, 1994.

[371] Andreas Klein. Electronic properties of In_2O_3 surfaces. *Applied Physics Letters*, 77(13):2009, 2000.

[372] Paul Erhart, Andreas Klein, Russell G. Egdell, and Karsten Albe. Band structure of indium oxide: Indirect versus direct band gap. *Physical Review B*, 75(15):153205, 2007.

[373] Mousa M Abdul-Gader Jafar. Comprehensive formulations for the total normal-incidence optical reflectance and transmittance of thin films laid on thick substrates. *European International Journal of Science and Technology*, 2(5):214–274, 2013.

[374] D E Aspnes. Optical properties of thin films. *Thin Solid Films*, 89(3):249–262, 1982.

[375] H. Ehrenreich and M. H. Cohen. Self-consistent field approach to the many-electron problem. *Physical Review*, 115(4):786–790, 1959.

[376] M Erman, J B Theeten, P Chambon, S M Kelso, D E Aspnes, M Erman, J B Theeten, and P Chambon. Optical properties and damage analysis of GaAs single crystals partly amorphized by ion implantation. *Journal of Applied Physics*, 56(10):2664, 1984.

[377] Sadao Adachi. Model dielectric constants of GaP, GaAs, GaSb, InP, InAs, and InSb. *Physical Review B*, 35(14):7454–7463, 1987.

[378] Sadao Adachi. Optical properties of $Al_xGa_{1?x}As$ alloys. *Physical Review B*, 38(17):345–352, 1988.

[379] Charles C Kim, J W Garland, H Abad, and P M Raccah. Modeling the optical dielectric function of semiconductors: Extension of the critical-point parabolic-band approximation. *Physical Review B*, 45(20):749–767, 1992.

[380] B Johs, C M Herzinger, J H Dinan, A Cornfeld, and J D Benson. Development of a parametric optical constant model for $Hg_{1-x}Cd_xTe$ for control of composition by spectroscopic ellipsometry during MBE growth. *Thin Solid Films*, 313-314:0–5, 1998.

[381] Y W Jung, T J Kim, J J Yoon, Y D Kim, and D E Aspnes. Model dielectric functions for $Al_xGa_{1?x}As$ alloys of arbitrary compositions. *Journal of Applied Physics*, 013515:1–6, 2008.

[382] T J Kim, T H Ghong, Y D Kim, S J Kim, D E Aspnes, T Mori, T Yao, and B H Koo. Dielectric functions of $In_xGa_{1-x}As$ alloys. *Physical Review B*, 68:1–10, 2003.

[383] J. Tauc, R. Grigorovici, and A. Vancu. Optical Properties and Electronic Structure of Amorphous Germanium. *Physica Status Solidi*, 15(2):627–637, 1966.

[384] A R Forouhi and I Bloomer. Optical dispersion relations for amorphous semiconductors and amorphous dielectrics. *Physical Review B*, 34(10):7018–7026, 1986.

[385] G E Jellison and F A Modine. Parameterization of the optical functions of amorphous materials in the interband region. *Applied Physics Letters*, 69(371):23–26, 1996.

[386] A. S. Ferlauto, G. M. Ferreira, J. M. Pearce, C. R. Wronski, R. W. Collins, Xunming Deng, and Gautam Ganguly. Analytical model for the optical functions of amorphous semiconductors from the near-infrared to ultraviolet: Applications in thin film photovoltaics. *Journal of Applied Physics*, 92(5):2424, 2002.

[387] G Kresse and J Hafner. Ab initio molecular dynamics for liquid metals. *Physical Review B*, 47(1):558–561, 1993.

[388] G. Kresse and J. Furthmüller. Efficient iterative schemes for ab initio total-energy calculations using a plane-wave basis set. *Physical Review B*, 54(16):11169–11186, 1996.

[389] John Perdew, J. Chevary, S. Vosko, Koblar Jackson, Mark Pederson, D. Singh, and Carlos Fiolhais. Atoms, molecules, solids, and surfaces: Applications of the generalized gradient approximation for exchange and correlation. *Physical Review B*, 46(11):6671–6687, 1992.

[390] David Vanderbilt. Soft self-consistent pseudopotentials in a generalized eigenvalue formalism. *Physical Review B*, 41(11):7892–7895, 1990.

[391] G Kresse and J Hafner. Norm-conserving and ultrasoft pseudopotentials for first-row and transition elements. *Journal of Physics: Condensed Matter*, 6(40):8245–8257, 1994.

[392] Shang-Di Mo and W. Ching. Electronic and optical properties of $\theta - Al_2O_3$ and comparison to $\alpha - Al_2O_3$. *Physical Review B*, 57(24):15219–15228, 1998.

[393] James E Bernard and Alex Zunger. Electronic structure of ZnS, ZnSe, ZnTe, and their pseudobinary alloys. *Physical Review B*, 36(6):3199–3228, 1987.

[394] D. Liu, Y. Guo, L. Lin, and J. Robertson. First-principles calculations of the electronic structure and defects of Al_2O_3. *Journal of Applied Physics*, 114(8):083704, 2013.

[395] Libor Kovarik, Mark Bowden, Arda Genc, Janos Szanyi, Charles H F Peden, and Ja Hun Kwak. Structure of delta-Alumina: Toward the Atomic Level Understanding of Transition Alumina Phases. *The Journal of Physical Chemistry C*, 118(31):18051–18058, 2014.

[396] B Ollivier, R Retoux, P Lacorre, D Massiot, and G Ferey. Crystal structure of kappa-alumina: An X-ray powder diffraction, TEM and NMR study. *Journal of Materials Chemistry*, 7 (431484):1049–1056, 1997.

[397] D Tonova and A Konova. Depth profiling of inhomogeneous layers by ellipsometry. *Surface Science*, 349:221–228, 1996.